Optimization of future projects for the measurement of Cosmic Microwave Background polarization

Thuong Hoang Duc

UNIVERSITÉ SORBONNE PARIS CITÉ

UNIVERSITÉ PARIS DIDEROT

École doctorale des Sciences de la Terre et de l'Environnement et Physique de l'Univers (STEP'UP), Paris - ED 560

Laboratoire Astroparticule et Cosmologie (APC)

Optimization of future projects for the measurement of Cosmic Microwave Background polarization

---

HOANG Duc Thuong

Thèse de doctorat d'Université Physique de l'Univers

dirigée par Guillaume Patanchon

présentée et soutenue publiquement le 17 décembre 2018

devant un jury composé de:

Gérard Rousset	Université Paris Diderot, LESIA	*Président du jury*
François Couchot	CNRS, LAL	*Rapporteur*
Giampaolo Pisano	Cardiff University	*Rapporteur*
Sophie Henrot-Versillé	CNRS, LAL	*Examinatrice*
Guillaume Patanchon	Université Paris Diderot, APC	*Directeur de thèse*
Damien Prêle	CNRS, APC	*Co-encadrant*

Abstract

During my Ph.D., my research focused on the development of future projects for the measurement of Cosmic Microwave Background (CMB) polarization aimed to probe primordial B mode. Achieving this goal will not only require sufficient detector array sensitivity but also unprecedented control of all systematic errors inherent to CMB polarization measurements. One of the important effects is the bandpass mismatch error which is the effect of non-uniformity or mismatch of the bandpass filters for different detectors inducing leakage from foreground intensity to polarization after calibrating the data on CMB. I estimated the level of the leakage for a realistic configuration of the forthcoming LiteBIRD JAXA mission with simulation and found that the amplitude of leakage depends on the scanning strategy of the satellite parameterized with precession angle, spin angle, precession and rotation velocities. After the study, I proposed some nearly optimal configurations to archive the target of tensor-to-scalar ratio r. The bias from foreground leakage in the range $2 \leq \ell \leq 10$ (reionization bump) is of the order of about 5×10^{-4} and in the range $10 \leq \ell \leq 200$ (recombination bump) of the order of about 5×10^{-5}.

The second topic of my thesis was an instrumental study: the interaction of particles with a Transition Edge Sensors (TES) array using the focal plane of the ground-based QUBIC (Q & U Bolometric Interferometer for Cosmology) experiment. The goal of this work was to test the behaviour of detectors to cosmic rays (such as time-constants and cross-talk). I placed an Americium 241 radioactive source in front of a 256 TESs array inside a cryostat. When particles hit one of the components of a pixel (eg: Thermometer, absorbing grid, substrate), the deposited energy induced temperature elevation among components and possibly to the neighbor pixels. This could provide an evaluation of the cross-talk between pixels. Moreover, this study allows us to understand the thermal and electronic readout system time constants of a TES.

Keywords: Cosmic Microwave Background polarization, CMB experiments, Data analysis, instrumentation, Observational cosmology

Au cours de ma thèse, mes recherches ont porté sur le développement des projets futurs de mesure de la polarisation du fond diffus cosmologique (CMB) visant à sonder les modes B primordiaux. Pour atteindre cet objectif, il faudra non seulement une sensibilité suffisante des matrices de détecteurs, mais également un contrôle sans précédent de toutes les erreurs systématiques inhérentes aux mesures de polarisation du CMB. Une source importante d'erreur systématique est la non-uniformité ou la non-concordance des filtres passe-bande des différents détecteurs. Cet effet induit des fuites de l'intensité vers la polarisation après l'étalonnage des données. J'ai estimé le niveau de fuite pour une configuration réaliste de la prochaine mission LiteBIRD de la JAXA à l'aide de simulations et montré que l'amplitude de la fuite dépendait de la stratégie de balayage du satellite paramétrée par l'angle de rotation du satellite, l'angle de précession et les vitesses de précession et de rotation. En conclusion de cette étude, j'ai proposé des configurations quasi optimales pour LiteBIRD permettant d'atteindre l'objectif sur le rapport tenseur sur scalaire r. Le biais dû à la fuite des avant-plans dans l'intervalle $2 \leq \ell \leq 10$ (bosse de réionisation) est de l'ordre de 5×10^{-4} et dans l'intervalle $10 \leq \ell \leq 200$ (bosse de recombinaison) de l'ordre de 5×10^{-5}.

Le deuxième sujet de ma thèse était une étude instrumentale : l'interaction des particules avec une matrice de TES. Pour ce faire, j'ai utilisé le plan focal de l'expérience QUBIC (interféromètre bolométrique Q & U pour la cosmologie). Le but de ce travail était de tester le comportement des détecteurs aux rayons cosmiques (tels que les constantes de temps et la diaphonie entre détecteurs). J'ai placé une source radioactive d'américium 241 devant un réseau de 256 TES à l'intérieur d'un cryostat. Lorsque les particules interagissent avec l'un des composants d'un pixel (ex: thermomètre, grille absorbante, substrat), l'énergie déposée provoque une élévation de la température d'un composant et éventuellement celui d'un pixel voisin. Cela pourrait fournir une évaluation de la diaphonie entre pixels. De plus, cette étude nous permet de comprendre les constantes de temps du système de lecture thermique et électronique d'un TES.

Mots clés: Polarisation du fond diffus cosmologique, expériences CMB, analyse de données, instrumentation, cosmologie observationnelle

Acknowledgements

The last three years at the AstroParticle and Cosmology (APC) laboratory have been a time of massive learning and growth for my experiences, both personally and professionally. This thesis would not have been possible without the guidance, support, international collaborations, and motivation from my supervisors, colleagues, friends, family and my willpower.

Firstly, I would like to express from my heart my deepest gratitude to my supervisor Dr. Guillaume Patanchon for the continuous support of my Ph.D study and related research, for his patience, motivation, and immense knowledge. His guidance and discussion helped me in all the time of research and writing of this thesis. As well as, I would like to express my sincere thanks to my co-supervisor Dr. Damien Prêle for his scientific guidance and encouraged supports to widen my research from various perspectives.

I am also indebted to Dr. Giraud-Héraud Yannick for many administrative procedures, many helpful comments on the chapter: interaction of particles with a TES array, he is an unofficial advisor during my thesis.

My sincere thanks also goes to Prof. Jean Christophe Hamilton, Prof. Michel Piat, who provided me an opportunity to join their team, and who gave access to the laboratory and research facilities. Without they precious support it would not be possible to conduct this research. Many difficult problems in instrumentation are solved after discussions with Michel Piat, he is like my technical advisor since I have been studying TES.

Besides my supervisors, I would like to thank the rest of my thesis committee: Prof. Gérard Rousset, Dr. Giampaolo Pisano, and Dr. François Couchot, Dr. Sophie Henrot-Versillé for their insightful comments and encouragement.

I would like to thank my working team on bandpass mismatch systematic effect study Martin Bucher, Tomotake Matsumura, Ranajoy Banerji, Hirokazu Ishino, Masashi Hazumi, Jacques Delabrouille. I gain my knowledge with many scientific discussions in the team. With them I have the first publication of my scientific career, it is always memorable.

I would like to thank to Ken Ganga, Cyrille Rosset, Fabrice Voisin, Laurent Grandsire, Steve Torchinsky, Matthieu Tristram, Joseph Martino and all members of APC laboratory for many scientific discussions.

I thank my fellow labmates (Alessandro, Bastien, Cyrille, Camille, Clara, Dominic, Eleonora, Calum, Jie, Mikhail, Maria, Louise, Pierros, Si, Thomas, Tuan) for the stimulating discussions, for the sleepless nights we were working together before deadlines, and for all the fun we have had in the last three years. I am very thankful to my international friends as well as Vietnamese friends throughout my unforgettable stay in Paris.

Last but not the least, I would like to thank my family: my parents and to my brother for supporting me spiritually throughout doing this thesis and my life in general.

Dedicated to my family

Contents

List of Figures

List of Tables

Abbreviations

APC	Laboratoire **A**stro**P**article et **C**osmologie
ASIC	**A**pplication **S**pecific **I**ntegrated **C**ircuit
CMB	**C**osmic **M**icrowave **B**ackground radiation
COBE	**CO**smic **B**ackground **E**xplorer
CDM	**C**old **D**ark **M**atter
CRs	**C**osmic **R**ays
ETF	**E**lectro**T**hermal **F**eedback
FLL	**F**lux **L**ocked **L**oop
FPGA	**F**ield **P**rogrammable **G**ate **A**rray
HFT	**H**igh **F**requency **T**elescope
HWP	**H**alf **W**ave **P**late
ISM	**I**nter-**S**tellar **M**edium
LFT	**L**ow **F**requency **T**elescope
LNA	**L**ow **N**oise **A**mplification
NEP	**N**oise **E**quivalent **P**ower
NET	**N**oise **E**quivalent **T**emperature
PID	**P**roportional **I**ntegral **D**erivative
PSD	**P**ower **S**pectral **D**ensity
QUBIC	**Q** and **U** **B**olometric **I**nterferometer fo **C**osmology
SQUID	**S**uperconducting **Q**uantum **I**nterference **D**evice
TDM	**T**ime **D**omain **M**ultiplexing
TES	**T**ransition **E**dge **S**ensor
TOD	**T**ime **O**rder **D**ata
WMAP	**W**ilkinson **M**icrowave **A**nisotropy **P**robe

Chapter 1

Introduction

Since the beginning of my Ph.D in November 2015, I have worked on 2 main topics:

- Study of the bandpass mismatch systematic effect for future CMB projects (LiteBIRD, CORE).
- Instrumentation: Behaviour of a TES array (QUBIC) and its electronic readout system, subjected to particles interactions.

1.1 Evaluating the level of the bandpass mismatch systematic effect for the future CMB satellites

The future Cosmic Microwave Background (CMB) satellite concepts LiteBird [78], CORE [32], PIXIE [67] have been proposed to probe B mode polarization to measure the tensor-to-scalar r ratio with a sensitivity $\sigma(r) \leq 10^{-3}$, which is almost two orders of magnitude beyond the Planck sensitivity. Several important systematic effects could contribute to final observation as 1/f noise, asymmetric beams, bandpass mismatches, the interaction of cosmic rays with the focal plane etc.

We learn from Planck mission data analysis that bandpass mismatch error is one of the important systematic effects that can affect the current and next-generation measurements of the polarization of the Cosmic Microwave Background radiation (CMB). The slightly different frequency bandpasses among detectors introduce leakage from intensity into CMB polarization. With the help of full focal plane

simulations, I evaluated the level of the bandpass mismatch systematic effect for future CMB satellites and estimated its possible impact on the final determination of the tensor-to-scalar ratio r. I simulated the time streams with filter variations as observed in Planck HFI. I assumed nominal scan and detector parameters for LiteBIRD. I projected data using the simplest map-making *coaddition* method. Power spectra of residual EE and BB coming from the leakage maps are computed for 80 % sky fraction excluding the galactic plane. The amplitude of leakage depends on the scanning strategy of the satellite parameterized with precession angle α, spin angle β, precession spin $\omega_{\rm prec}$ and rotating spin $\omega_{\rm spin}$. I verified an analytic estimation which has shown the tight correlation between leakage maps and the crossing moment, $\langle \cos 2\psi \rangle$, $\langle \sin 2\psi \rangle$, this is a fast and easy way to predict the magnitude of potential leakage. I found that the spurious signal could potentially bias r for measurements of the reionization bump ($2 \leq \ell \leq 10$) at the level of about 5×10^{-4}, and of the recombination bump ($10 \leq \ell \leq 200$) at the level of about 5×10^{-5} depending on scanning angle parameters. I demonstrated the amplitude scales as the number of detectors. The effect is negligible in case of an ideal HWP. This study has led to a publication [50].

1.2 Interaction of particles with a TES array

In a normal conductor/semiconductor the current is carried by electrons (i.e. fermions: half-integer spin) which obey Fermi-Dirac statistics while in a superconductor the current is carried by cooper-pairs (i.e. bosons: integer spin) which obey Bose-Einstein statistics. The principle of superconductivity is that the phonon lattice slows down the velocity of electrons so that the electrons joined into cooper-pairs. The development of a sensitive superconducting detector allows us to measure a power source with faster responses and a larger heat capacity [61]. A superconducting detector works at a low temperature in that case the noise level is reduced closely to quantum limit. The superconducting transition regime is a tiny change in temperature, of the order of 0.1 mK to 1 mK leading to a large change of resistance. For this reason a superconductor is an ideal candidate for a thermometer in a bolometer. When the thermometer is voltage biased, the Joule power is given by $\mathrm{P_J} = \mathrm{V^2/R_{TES}}$, a rise in temperature leads to an increased resistance of the thermometer, then the Joule power decreased. It means that the Joule power compensates the original rising temperature. This effect is known as

the strong negative electrothermal feedback (ETF) which maintains the transition edge sensor (TES) temperature stable in the superconducting transition regime. This physical characteristic is useful for an array of TESs and is one of the main interest of the use of TES. Furthermore, the effective thermal time constant of a transition edge sensor is divided by the loop gain $\mathcal{L}$ parameter of the ETF. Therefore the TES can be used as very sensitive and linear detectors operated simultaneously in an array.

I have studied the interaction of particles with a 256 TESs array of the ground-based QUBIC (Q&U bolometric interferometer for cosmology) experiment [30]. In order to test the sensitivity of detectors to cosmic rays, an Americium 241 radioactive source was set up in front of the 256 TES array in the mixing chamber inside the cryostat at 300 mK. When particles hit the components of a TES (eg: thermometer, absorbing grid, substrate), the deposited energy induced to temperature elevation of the components and to the neighbor pixels, which provides a evaluation of the cross-talk. Moreover, this study allows us to understand both the intrinsic time constant of a TES and the readout system time constant. First of all, I used a source of α particles from Americium 241 hitting the silicon wafer or the TES. In order to analyze time constants of a glitch, following the thermal response equation of a TES, I found thermal saturating equations of the wafer and the TES. By solving those equations I ended up with the time constants as exponential functions.

On the other hand, the electronic readout system of the TES has the following components the connection of the TESs array, the 128 multiplexing superconducting quantum interference device (SQUIDs), the application specific integrated circuit (ASIC), and the warm digital readout. Applying the block diagram and automatic control algorithm for the readout electronic components, I found that those time constants are inversely proportional to the integral parameter of the proportional integral derivative (PID) controller of the Flux Locked Loop (FLL). The analysis of the glitch timeline indicated that there are two-time constants [131], the thermal time constant of the TES due to the deposited energy by particles and the electronic readout system time constant which depends on the FLL parameter. The thermal cross-talk is constrained to be less than 0.1 percent. The low statistics of events do not allow to put a better constraint. In addition, the electronic readout system can introduce the cross-talk between two successive pixels in the multiplexing timeline.

For pedagogical purposes, I write this thesis with many details, developed calculations in the chapters 2 and 3. The chapter 4 is related to my simulation work on bandpass mismatch systematic effect while the chapter 5 is my contribution in instrumentation and data analysis. The manuscript is organized as follow:

Chapter 2 gives a quick introduction to modern cosmology. In this chapter, I described the hot Big Bang Universe, the standard model of cosmology, the primordial quantum fluctuations in inflation.

Chapter 3 provides the description of Cosmic Microwave Background and its future projects which aim to detect the tensor-to-scalar ratio of the primordial fluctuations by measure B-mode polarization signal. The measurement of cosmic microwave background polarization has to cope with many challenges as foreground and systematic effects.

Chapter 4 details my study of bandpass mismatch error systematic effect for future cosmic microwave background projects in particular the LiteBIRD satellite mission.

Chapter 5 details my study of the interaction of particles with the superconducting transition edge sensors array of the ground-based QUBIC experiment.

Chapter 6 provides the conclusions of my thesis and perspectives after my thesis.

Chapter 2

Introduction to cosmology

Contents

Since the beginning of humankind, we were always curious about the dark and bright sky, the Solar system, the stars, the galaxies, and the Universe. We kept asking ourself what are we? where do we come from? and where are we going? These questions are also represented by Paul Gauguin's masterpiece as shown in figure 2.1. I found that these questions apply to our Universe. The study of the Universe provides scientific answers to our curiosities.

FIGURE 2.1: D'où venons-nous? Que sommes-nous? Où allons-nous? Where Do We Come From? What Are We? Where Are We Going?, 1897, Paul Gauguin, Boston Museum of Fine Arts. The Gauguin's masterpiece should read from right to left, the baby means the beginning of life, where do we come from? in the middle of the painting is human density, ambition, desire, destiny, what are we doing? On the left is a statue, it represents for spiritual belief which is beyond the Earth, at the bottom left, the young woman reflected an old woman who is going to die, where are we going?

In this chapter, I describe the history of the Hot Big Bang theory, then our knowledge about the Universe by studying the standard cosmological model. I also focus on inflation Universe theory which can solve the horizon problem (the homogeneous Universe) and the flatness problem. I also present initial quantum fluctuations during inflation which are the seed of the large-scale structures in the present complex Universe.

2.1 The Hot Big Bang theory

The physical cosmology is the branch of the astronomy that deals with the origin and evolution of the Universe as a whole. In the 16^{th} century, Nicolaus Copernicus,

a Polish scientist suggested that the Sun is center of the Solar system. In the 17$^{\text{th}}$ century, Isaac Newton solved the planetary motion by introducing the gravitation force. The modern cosmology started in the 20$^{\text{th}}$ century, three century after Isaac Newton, in 1917, Albert Einstein published the theory of gravity in the paper cosmological considerations of the General Theory of Relativity [41]. In 1929, Edwin Hubble discovered the redshift of the light of distant galaxies, meaning that they are rushing far away from the Milky Way with a velocity proportional to the distance so that the Universe must be expanding. Therefore the hot Big Bang model which was suggested by Georges Lemaitre in 1927, was accepted. The Big Bang theory described the Universe as a whole and have begun 13.798 $\pm$ 0.037 billion years ago. The Universe contains 4.9 % ordinary matter, 26.8 % dark matter and 68.3 % dark energy [119]. The evolution of the Universe is illustrated in figure 2.2 described by the Big Bang theory.

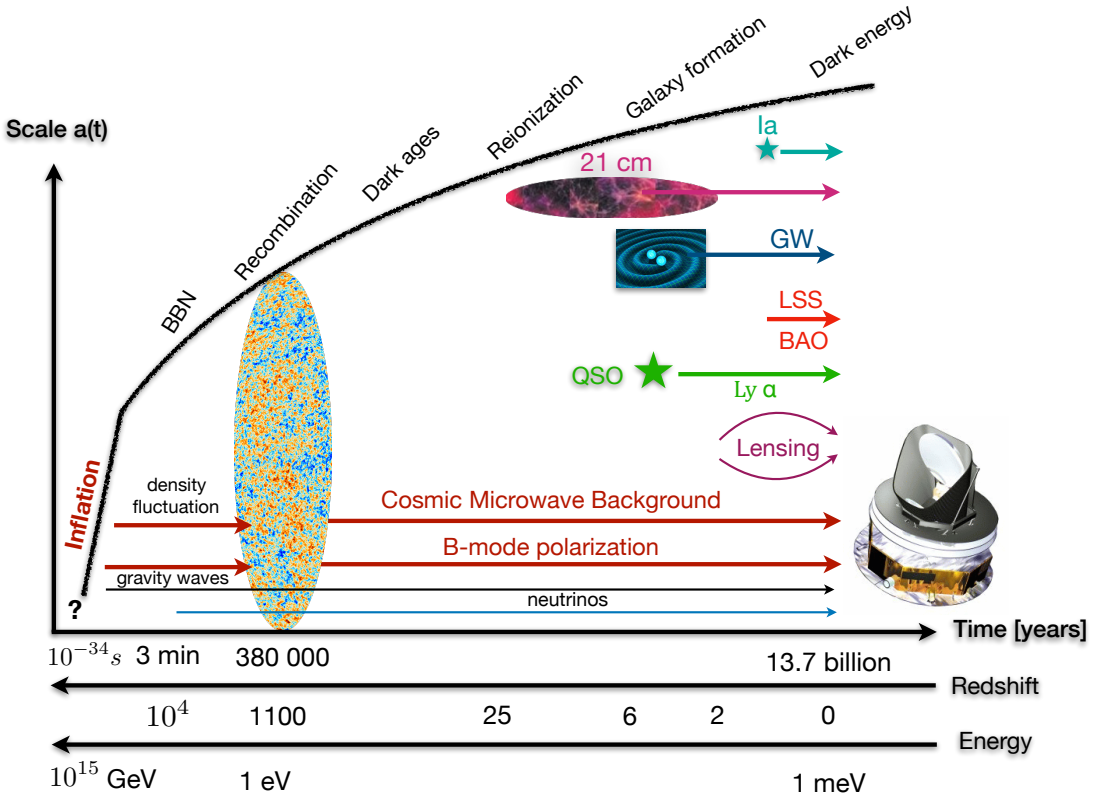

FIGURE 2.2: The history and the evolution of the Universe in time and scale factor. *Acronyms* BBN: Big Bang Nucleosynthesis, Lyα: Lyman alpha, QSO: Quasi-Stellar Objects = Quasars, BAO: Baryon Acoustic Oscillation, LSS: Large-Scale Structure, GW: Gravitational waves, 21cm: Hydrogen transition line and 21 cm cosmology, Ia: Type Ia supernovae

The thermal history of the early Universe is well described by the laws of particle

physics. Figure 2.3 mainly illustrates the evolution of the Universe at the beginning of time to 3 minutes. The events are summarized in the following:

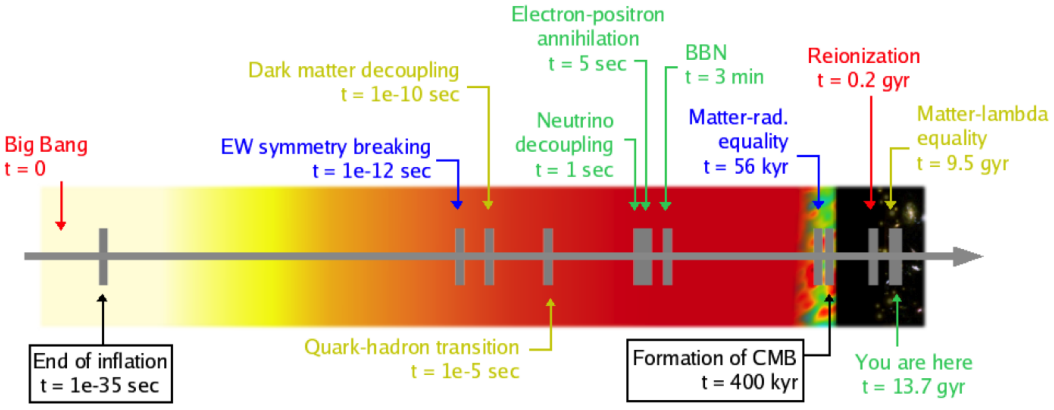

FIGURE 2.3: The early the Universe from the initial singularity to cosmic inflation, quantum gravity epoch, nucleosynthesis, last scattering surface [147].

Inflation epoch. $t \sim 10^{-34}$ s. In 1979 and 1980 Alain Guth proposed a theory of the exponential expansion of space-time in the early Universe to solve possibly the horizon and flatness problems. The theory is developed by contributions of Andrei Linde, Paul Steinhardt and many physicists who believe in the inflation scenario of the Universe.

Baryogenesis. $t < 10^{-10}$ s. If the beginning Universe has equal amount of particle and antiparticle. Then the annihilated process of particles leads to a radiation Universe. However, we observed today that the matter is dominated anti-matter in the present Universe. The hypothesis is that there was a time in the primordial Universe when the symmetry was broken by some dynamic mechanisms which are not known now. This issue is a puzzle in the modern cosmology. The observed ratio of baryons to photons is:

$$\eta \equiv \frac{n_b - n_{\bar{b}}}{n_\gamma} \sim 10^{-9}. \tag{2.1}$$

In 1928, Paul Dirac published the paper "The quantum theory of the electron" [4]. Dirac equation predicted the existence of antimatter. Five years later, in 1932 Carl D. Anderson discovered the positron experimentally since then, every known kind of particle has an anti-particle. Particle and anti-particle have the same mass and opposite charge (e.g., electron and positron), together they annihilate. It is called C-symmetry.

Baryon number is calculated by number of quarks and antiquarks $B = (n_q - n_{\bar{q}})/3$. Baryons made of 3 quarks then baryon number equals +1. Antibaryons made of 3 antiquarks then baryon number equals -1. The thermal equilibrium of the Universe should produce the same amount of matter and antimatter. However we observe in the present Universe the domination of matter, the abundance of anti-matter is very small. This problem is called baryon asymmetry in the Big Bang model. In 1967, Andrei Sakharov indicated three necessary conditions for creating baryon asymmetry in the Universe.

- Violation of Baryon number B
- Violation of C-symmetry and CP-symmetry
- State out of thermal equilibrium

CP-symmetry violation is the violation of charge-parity symmetry or the combination of C-symmetry and P-symmetry. P-symmetry is the change of sign (mirror) in parity transformation. The third condition is that in the state out of thermal equilibrium, the pair-annihilation is decreased then the particles and anti-particles do not reach the equilibrium state.

The Large Hadron Collider (LHCb) accelerator can reach to the energy of the order 10^{13} eV, which corresponds to the quark era of the early Universe. The particle physics, the theory of general relativity and several hypotheses exist to explain the problem, nevertheless the origin of matter-antimatter remains an unsolved problem.

Electroweak phase transition. When the temperature of the Universe was around 100 GeV, at $t \sim 10^{-10}$ s, particles (Z and $W^{\pm}$ Gauge bosons) interacted through the Higgs mechanism. Leptons (electron e, muon μ, tau τ, electron neutrino ν_e, muon neutrino ν_μ, tau neutrino ν_τ) and quarks (up u, charm c, top t, down d, strange s, bottom b) are in thermal equilibrium above 100 GeV. There is a Possible link between the electroweak phase transition and the dark matter of the Universe. If dark matter is made of particles, the dark matter particles interact via gravity and might be weakly interacting massive particles (WIMP). The WIMP model is still an hypothesis and many experiments attempt to detect those. The symmetry between the weak forces and the electromagnetic is broken below 100 GeV.

QCD phase transition. At the temperature of 100 - 300 MeV, t $\sim 10^{-5}$ s, baryons appeared due to the strong interaction between quarks and gluons g (a Gauge bosson). Three quarks systems are baryons as protons, neutrons, and quark-antiquark systems are mesons. There is no observed evidence of this phase transition.

Neutrino decoupling. At t $\approx$ 1 s, Energy $\sim$ 1 MeV. It occurred within one second. The weak interaction between neutrinos and the plasma matter produced a cosmic neutrino background (CNB) which freely propagate into the Universe. This epoch has happened before the recombination.

Electron-positron annihilation. At t $\approx$ 6 s, Energy $\sim$ 500 keV, $e^- + e^+ \rightarrow \gamma + \gamma$. The energy of the electrons and positrons is transferred to the photons energy, and not to neutrinos. It explains why the temperature of CNB is lower than the CMB ($T_\nu < T_\gamma$).

Big Bang Nucleosynthesis (BBN). At t $\approx$ 3 minutes, Energy $\sim$ 0.1 MeV, redshift z $\approx 4 \times 10^8$. The percentage of the light elements - deuterium, helium 3, lithium, helium 4 - in the Universe is an evidence supporting the Hot Big Bang theory. At high temperature, protons and neutrons stay in a thermal equilibrium state. The Universe is expanding and cools down enough, then these particles bind into nuclei. The production of light elements is processed through a series reaction chain.

$$\begin{aligned} p + n &\rightarrow D; \\ D + p &\rightarrow {}^3He; \\ D + D &\rightarrow {}^4He; \\ &\dots \end{aligned}$$

Here D stands for deuterium nuclei. These processes happen when the age of the Universe is $\sim$ 3 minutes. [12] Figure 2.4 shows the observational data is agreement with the predicted abundance of light elements. It means that the result is a good evidence of light elements being formed in the Big Bang Nucleosynthesis theory. The abundance of ^{4}He depends on the abundance of neutrous which started to decay at the time of nucleosynthesis. The heavier elements are made in stars, during stellar evolution or in supernovae. This has originally been described in 1948, R. A. Alpher, H. Bethe and G. Gamow who predicted elements in the Universe by a published paper is The Origin of Chemical Elements ($\alpha\beta\gamma$ paper) [12].

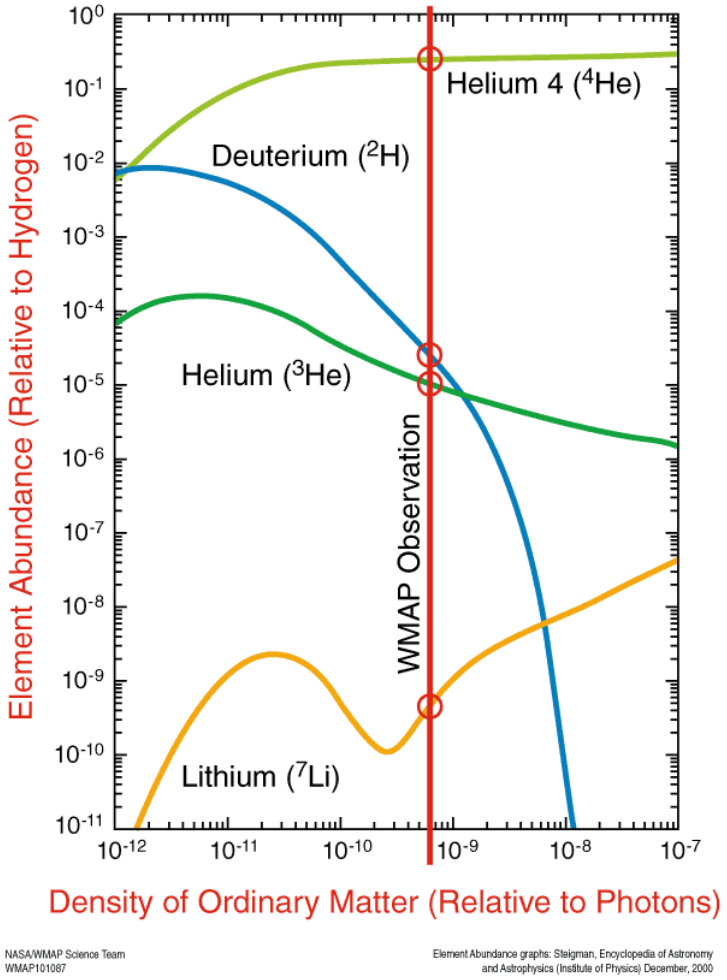

FIGURE 2.4: The primordial predicted abundance of light elements in the Universe on the density of ordinary matter ($\sim 4\%$) and the WMAP satellite. *Credit: WMAP/NASA team*

Recombination. At t $\approx$ 380000 years, Energy $\sim$ 0.1 eV, z $\approx$ 1100. When the temperature cooled down to T $\sim$ 3000 K, the electrons combined with protons and formed neutral Hydrogen through the process: $e^- + p^+ \rightarrow H + \gamma$. This is the first phase change of the Universe with the formation of neutral hydrogen atoms.

Photon decoupling. At t $\approx$ 400000 years, Energy $\sim$ 0.1 eV, z $\approx$ 1100. The photons interact with the electrons through Thomson scattering $e^- + \gamma \rightarrow e^- + \gamma$, those polarized photons (photon decouple) freely traveled entire Universe and we observed today as the Cosmic Microwave Background (CMB) polarization. The fraction of free electrons decrease suddenly because of recombination. I will describe detail the CMB physics in the chapter 3.

The Epoch of Reionization (EoR). At t $\approx 10^8$ years, Energy $\sim$ 1 meV, z $\approx$ 6-25. After the recombination epoch, the Universe is composed of neutral Hydrogen.

The Hydrogen atoms concentrate to form gas clouds due to gravitation. First stars are formed in the interstellar medium (ISM), however, the UV radiation from first stars reionized hydrogen in the ISM. The Universe changed from neutral to ionize state. The 21 cm hydrogen emission line occurred due to the energy level of electron and proton in a hydrogen atom. Observing 21 cm radiation is a useful tool to study the reionization epoch and the properties of the ISM, and the topology (the local and global geometry) of the Universe. The Lyman α forest at redshift z $\approx$ 2.5-6.5, allows to probe the state of the intergalactic medium (IGM) via the absorption of a neutral hydrogen in the spectra of a distant quasi-stellar objects (QSO) [1] when the Universe was filled with gas.

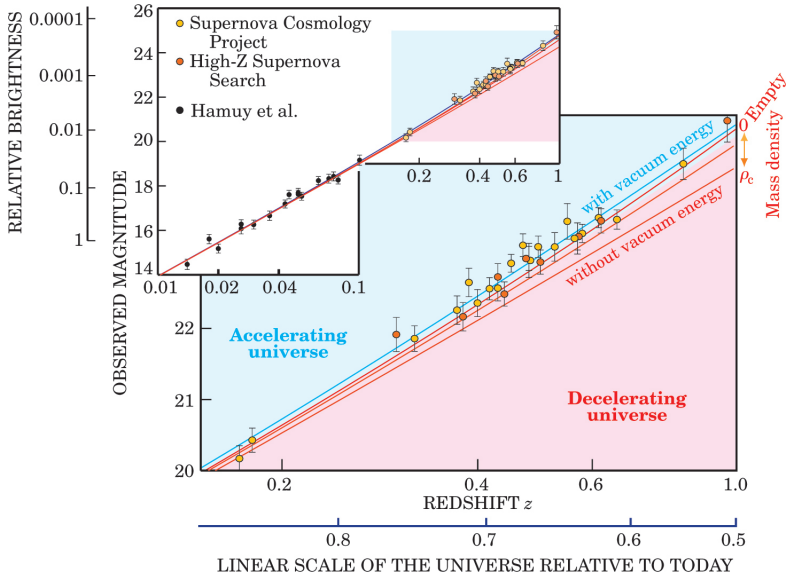

FIGURE 2.5: The plot shows the observed magnitude data of Type Ia supernovae for different experiments versus redshift, it implies that the expanding Universe is acceleration. [95]

Dark energy epoch. At t $\approx 10^9$ years, Energy $\sim$ 1 meV, z $\approx$ 0-2. At this epoch, the Universe is dominated by the dark energy and the expansion is accelerating. We usually assume that the dark energy has negative pressure and distributes homogeneously in space. The accelerating Universe was first evidenced by the observation type Ia supernovae. Supernova is an explosion of a massive star [2] in the universe. Type Ia supernovae result from stars accumulating matter from nearby neighbor stars and collapsing together with a white dwarf. Type Ia supernovae have similar masses, then their luminosity have the same brightness. They are

[1] It is also known as Quasar. A Quasar is an extremely luminous distant object. Quasars energy is believably powered from the accretion disk of massive black holes at the center of an active galactic nucleus (AGN).

[2] Type Ia occurs in binary systems in which two stars orbit each other.

considered as a *standard candle* in the Universe. The dynamics of the Universe can be inferred by measuring luminosity distance of objects then comparing to their corresponded redshift of the standard candle. The result indicated the accelerating Universe as shown in figure 2.5.

Present and observation. Today, we are in the dark energy dominated epoch. Our Universe is $\sim$ 13.7 million years and contains $\sim$ 4.9 % of ordinary matter, $\sim$ 26.8 % of dark matter and $\sim$ 68.3 % of dark energy (Planck result).

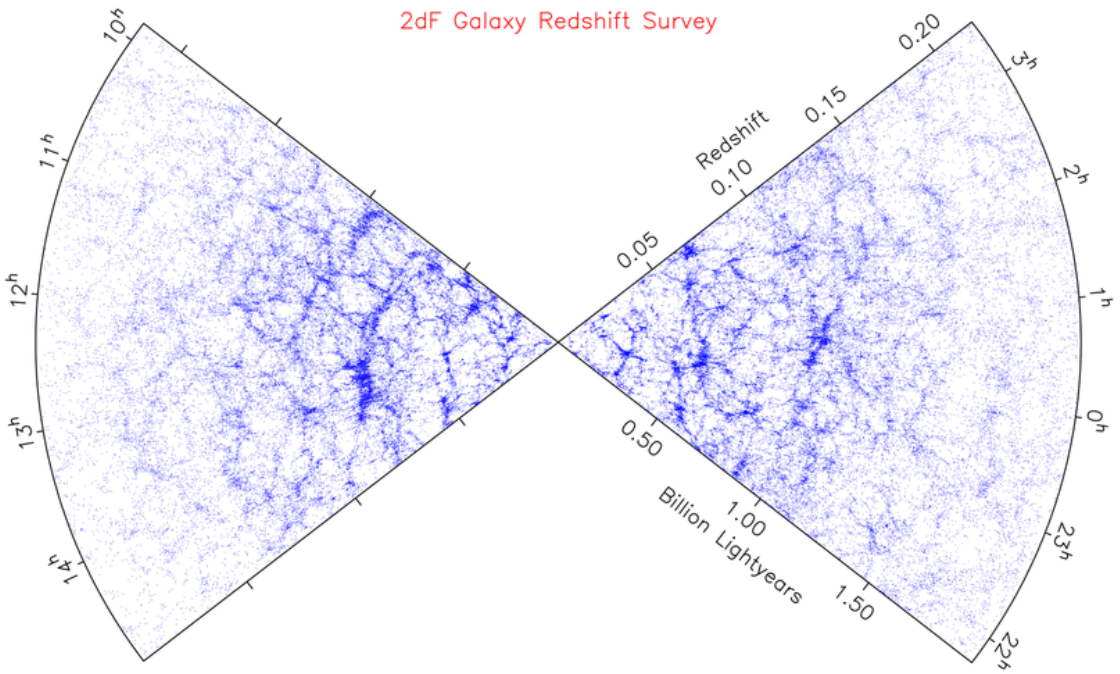

FIGURE 2.6: The 2dF galaxy redshift survey data release. The Earth is placed at the center. The white part is the un-observed sky. Each data point is equivalent to a galaxy. The 2dF galaxy survey observed about hundred thousand galaxies. *Credit: 2dFGRS team*

By surveying the Large-Scale Structure (LSS) of galaxies clusters using redshift which is hundreds of Mpc and more. The 2dF galaxy survey (figure 2.6) and Sloan Digital Sky Survey (SDSS) surveyed typically about hundred thousands or billions of galaxies in the Universe. The smoothness of the Universe is a fundamental assumption in cosmology. The Baryon Acoustic Oscillation (BAO) are acoustic oscillations observed on galaxy-galaxy correlations that can be observed in the large-scale structure of galaxies in the Universe. BAO is a *standard ruler* for the length scale in the Universe. In 2014, the SDSS's Baryon Spectroscopic Survey at redshift $0.2 < z < 0.7$ detected the BAO signal with 7σ [13].

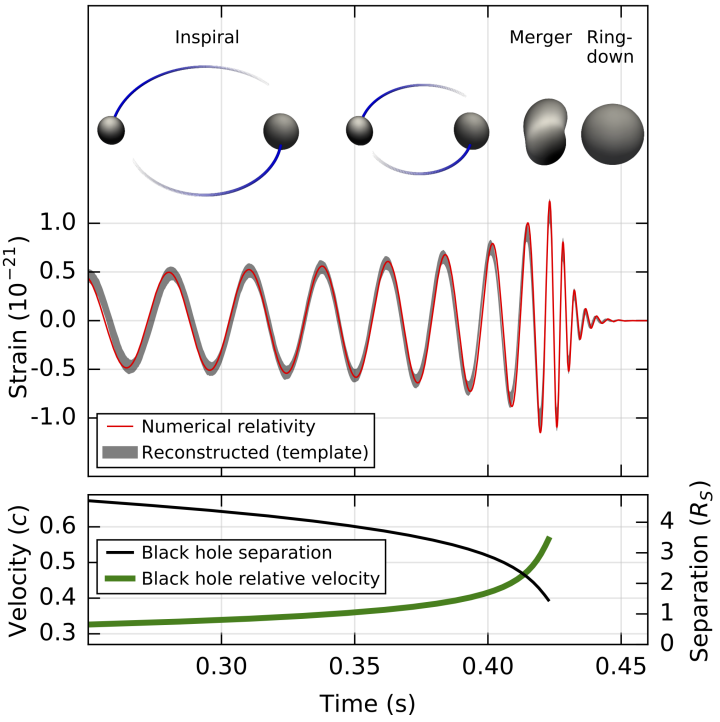

FIGURE 2.7: In 2016, LIGO collaboration discovered the first detection of gravitational waves by observing two black holes merger [11].

In 2016, the LIGO/VIRGO collaboration discovered the existence of gravitational waves which open a new window on the Universe. Gravitational waves are generated by merged massive objects. The existance of gravitational waves was proposed by Henri Poincaré based on the theory of relativity. Gravitational waves travel at the speed of light and transform energy as electromagnetic energy. The first detection results from the merging of a binary black hole with masses 36 M_{sun} and 29 M_{sun} [11] and the second detection concerns the binary neutron star inspiral.

Neutrinos. There have three kinds of neutrino: electron neutrino ν_e, muon neutrino ν_μ, tau neutrino ν_τ. Neutrino oscillations are the phenomenon of changing their types when they travel, for example, an electron neutrino can become a muon neutrino then oscillating back to its original type. Neutrinos are believed to have non-zero rest mass, and they have very weak interaction with matter in the Universe. Along with the cosmic neutrinos background which have not been detected directly but though the effect on CMB at the early Universe, there have some sources of neutrinos directly detected: Our Sun, nearby supernova in 1987, recently the multiteam collaboration-the IceCube Collaboration, Fermi-LAT, MAGIC, AGILE, ASAS-SN, HAWC, H.E.S.S., INTEGRAL, Kanata, Kiso,

Kapteyn, Liverpool Telescope, Subaru, Swift/NuSTAR, VERITAS, VLA/17B-403 teams- has been discovered a high energy neutrino astrophysical source from a blazar flare which is a type of quasar. Blazars also open a new window on multimessenger astronomy for observations of cosmic rays, neutrinos, gravitational waves, and electromagnetic [10].

Since the Hot Big Bang theory has much observational evidence, it is true to state that all of us made up of particles. The behavior of our Universe today depends on the properties of particles at the early Universe.

2.2 The standard cosmological model

The standard cosmological model considers the Universe as a whole and encompasses our knowledge of it.

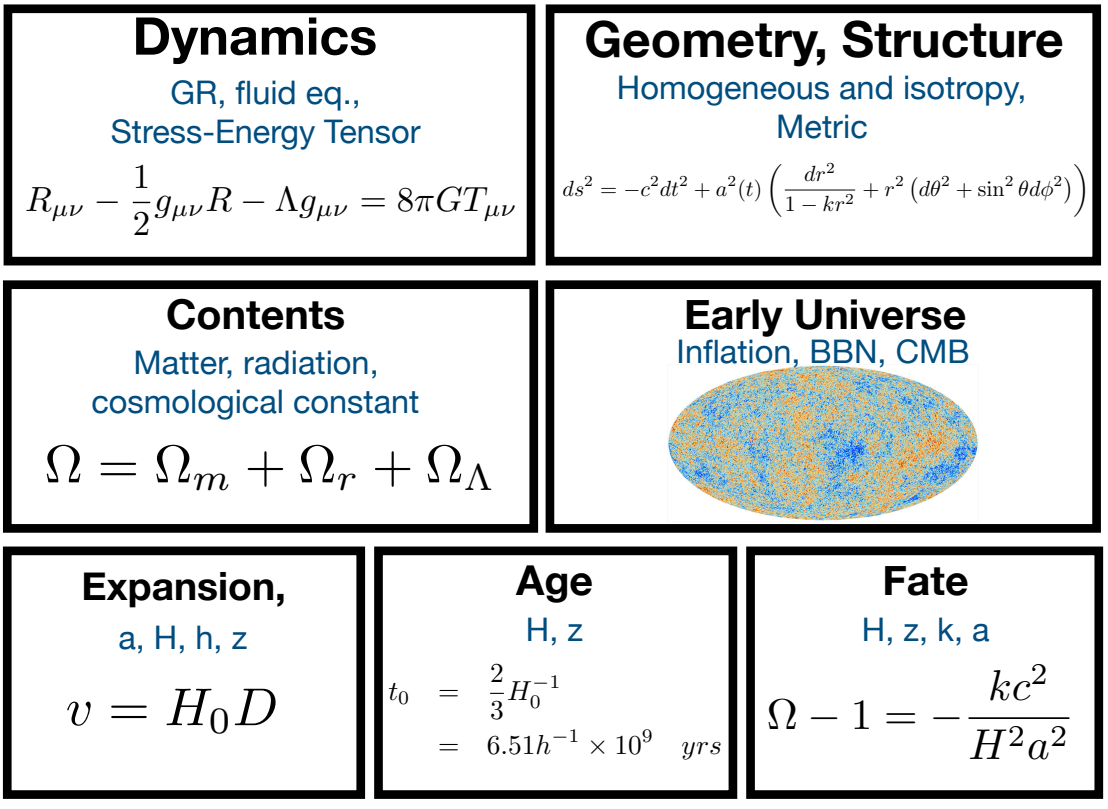

FIGURE 2.8: The standard cosmological model included the accelerating expansion of the Universe, the age, the fate, the contents, the early Universe, the dynamic and geometry. a: scale factor. z: redshift. H, h, H: Hubble parameter, constant. k: curvature Ω density parameters...

Figure 2.8 briefly summaries the standard cosmological model. Einstein introduced the cosmological constant as a term in the general relativity theory to explain a static Universe, however observational data of Hubble showed that the Universe is expanding. The results of supernovae Ia study and also CMB measurements provided evidence of accelerating expansion and then of the presence of a cosmological constant. The cosmic microwave background observation helps us understand many aspects of the Universe including the geometry, the age, and the contents. The early Universe requires more observation to test the inflation theory.

2.3 Expanding Universe

In 1929, at the Carnegie Observatories in Pasadena, California, Edwin Hubble discovered that the galaxies are moving away from us and the velocity of galaxy recession is proportional to their distance from us so the light from distant galaxies was redshifted [58]. This is an evidence of the expansion of the Universe. The so-called Hubble law express a linear relationship the recessional velocity and distance.

$$\mathrm{v} = \mathrm{H_0 D}. \tag{2.2}$$

Here v is the recessional velocity of distance objects km/s, $\mathrm{H_0}$ is the Hubble's constant or the Hubble parameter. D is the distance from the object to the observer. The value of the Hubble constant is measured by many experiments as shown in figure 2.9. The latest Planck 2016 cosmological constraints since [110].

$$\mathrm{H_0} = 67.8 \pm 0.9 \ \mathrm{kms^{-1}Mpc^{-1}}.$$

It is useful to parameterize the Hubble constant as

$$\mathrm{H_0} = \mathrm{h} \cdot 100 \, \mathrm{kms^{-1}Mpc^{-1}}. \tag{2.3}$$

Thus $\mathrm{h} = 0.678 \pm 0.009$, assuming the Planck experimental measurement. Because of the expansion of the Universe, we can measure velocities of moving away objects using the redshift defined as:

$$\mathrm{z} = \frac{\lambda_\mathrm{o} - \lambda_\mathrm{e}}{\lambda_\mathrm{e}}. \tag{2.4}$$

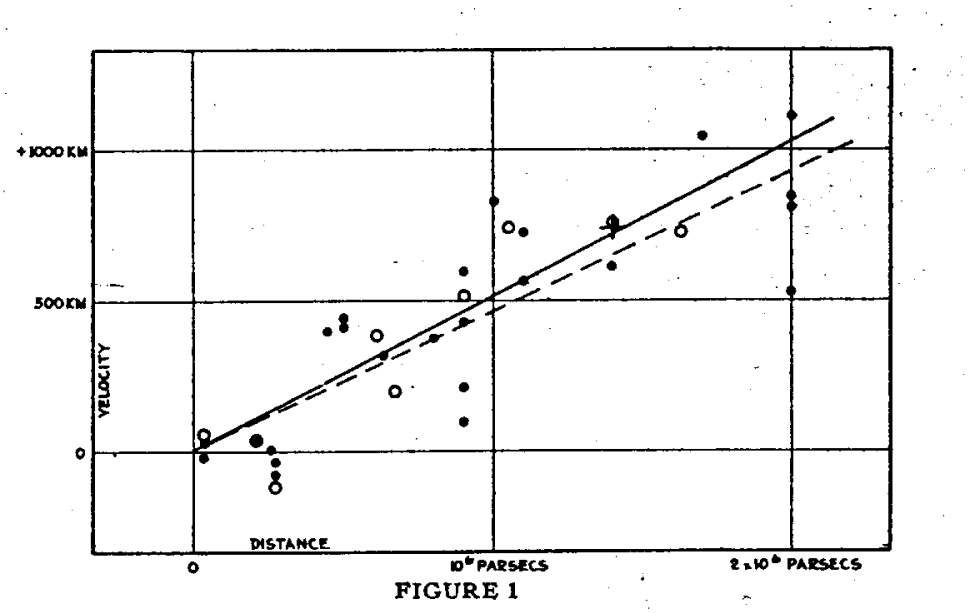

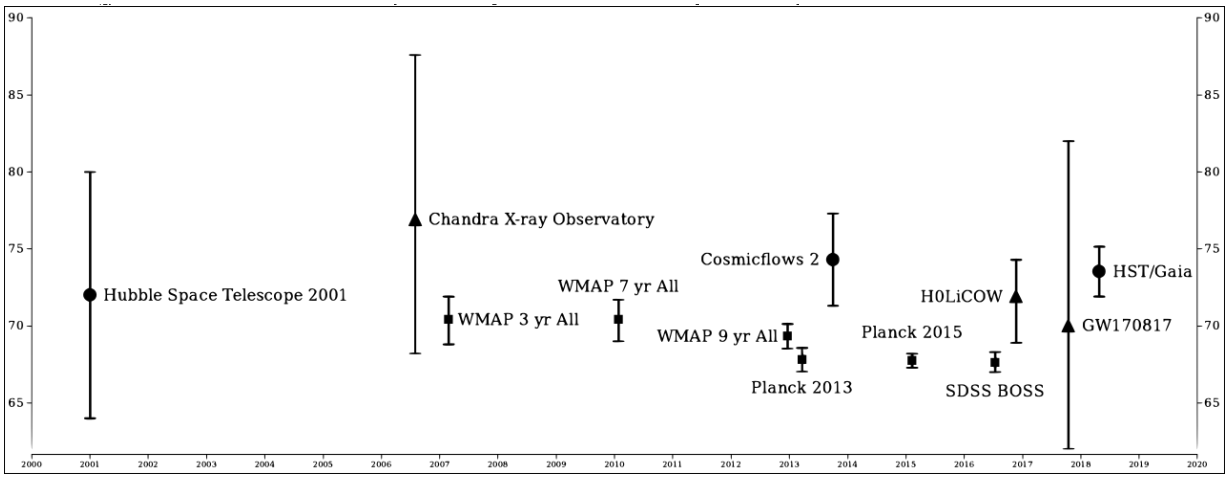

FIGURE 2.9: The Hubble constant from the original paper and the measurements by other experiments from 2001-2018
source: https://en.wikipedia.org/wiki/Hubble%27s_law.

where λ_o, λ_e are the wavelength of the observation and emission, respectively. The scale factor is defined as the distance between two co-moving objects. The redshift can be linked to the scale factor of the expanding Universe.

$$\boxed{1 + z = \frac{\lambda_o}{\lambda_e} = \frac{a(t_0)}{a(t_e)}}. \tag{2.5}$$

2.4 General relativity

The dynamics of the Universe is described by the general relativity. First of all, let us consider the distance between two events in four-dimensional space-time

and is invariant under coordinate transformations. It can be written as

$$ds^2 = \sum_{\mu,\nu} g_{\mu\nu} dx^\mu dx^\nu. \tag{2.6}$$

here $g_{\mu\nu}$ is the metric tensor, μ, ν are index values 0, 1, 2, 3. x^0 is time coordinate and the other are the three spatial coordinates. Notice that, In Einstein notations, the lower indices indicate covariance (the perpendicular projections on the coordinate axes) tensors, the upper indices indicate contravariance (the parallel projections on the coordinate axes) tensors. In special relativity, the space time is the Minkowski metric.

$$g_{\mu\nu} \equiv \eta_{\mu\nu} = \begin{pmatrix} 1 & 0 & 0 & 0 \\ 0 & -1 & 0 & 0 \\ 0 & 0 & -1 & 0 \\ 0 & 0 & 0 & -1 \end{pmatrix}. \tag{2.7}$$

In polar coordinates,

$$g_{\mu\nu} = \begin{pmatrix} 1 & 0 & 0 & 0 \\ 0 & -1 & 0 & 0 \\ 0 & 0 & -r^2 & 0 \\ 0 & 0 & 0 & -r^2 \sin^2\theta \end{pmatrix}. \tag{2.8}$$

2.4.1 Friedmann–Lemaître–Robertson–Walker (FLRW) metric

The structure and evolution of the Universe are described by the Friedmann-Robertson-Walker (FRW) metric. It can be derived the Universe assuming homogeneity (same at every point) and isotropy (same at every direction) properties of the Universe. The FRW metric for the spacetime writes:

$$\boxed{ds^2 = c^2 dt^2 - a^2(t) \left(\frac{dr^2}{1 - kr^2} + r^2 \left(d\theta^2 + \sin^2\theta d\varphi^2 \right) \right)}, \tag{2.9}$$

where a(t) is the scale factor, r is a time dependent comoving coordinate, k is the curvature parameter, k = +1 positive means an open Universe, k = -1 negative means a close Universe, k = 0 means a flat Universe, r, θ, φ are the spherical coordinates.

It is useful to express metric 2.9 in the comoving coordinates (*hypersphere*). This form is convenient for studying the propagation of light in the metric:

$$ds^2 = dt^2 - a(t)^2 \left(d\chi^2 + S_k^2(\chi) \left(d\theta^2 + \sin^2 \theta d\varphi^2 \right) \right), \tag{2.10}$$

where

$$r^2 = S_k(\chi^2) = \begin{cases} \sinh^2 \chi & \text{if} \quad k = -1, \\ \chi^2 & \text{if} \quad k = 0 \\ \sin^2 \chi & \text{if} \quad k = -1, \end{cases}, \tag{2.11}$$

here χ plays a role as a radius or a new angular coordinate. It is sometimes useful to change the coordinate in time by defining the *conformal time*.

$$\eta = \int^t \frac{dt'}{a(t')}. \tag{2.12}$$

Then the FLRW metric becomes:

$$ds^2 = a(\eta)^2 \left[d\eta^2 - d\chi^2 - S_k(\chi^2) \left(d\theta^2 + \sin^2 \theta d\varphi^2 \right) \right]. \tag{2.13}$$

With this coordinate system, it is easy to see how the light propagates on null geodesic $ds^2 = 0$ with respect to the conformal time.

2.4.2 Geodesic

Geodesics are the shortest curve between two points. In such a curved space, trajectories of free particles follow the geodesics with *proper time* τ such that:

$$\frac{d^2 x^\mu}{d\tau^2} + \Gamma^\mu_{\alpha\beta} \frac{dx^\alpha}{d\tau} \frac{dx^\beta}{d\tau} = 0. \tag{2.14}$$

where $x^\mu(\tau)$ is the trajectories of free particles along the geodesics. The Christoffel symbols $\Gamma^\mu_{\alpha\beta}$ are the metric connection.

$$\Gamma^\mu_{\alpha\beta} \equiv \frac{g^{\mu\nu}}{2} \left[g_{\alpha\nu,\beta} + g_{\beta\nu,\alpha} - g_{\alpha\beta,\nu} \right] = \frac{g^{\mu\nu}}{2} \left[\frac{\partial g_{\alpha\nu}}{\partial x^\beta} + \frac{\partial g_{\beta\nu}}{\partial x^\alpha} - \frac{\partial g_{\alpha\beta}}{\partial x^\nu} \right], \tag{2.15}$$

where $(...)_{,\mu} \equiv \dfrac{\partial (...)}{\partial x^\mu} = \partial_\mu$.

2.4.3 Einstein equations and Friedmann equations

The *equivalent principle* of classical mechanics stated the proportionality of the inertial and gravitational mass. It is equivalent to state that in a gravitational field and in the absence of external forces, all masses fall at the same rate of acceleration. The Einstein tensor is described by the Ricci curvature tensor.

$$G_{\mu\nu} \equiv R_{\mu\nu} - \frac{1}{2} g_{\mu\nu} R. \tag{2.16}$$

Where the Ricci curvature tensor [3] and Ricci scalar are given:

$$\begin{aligned} R_{\mu\nu} &= \Gamma^{\alpha}_{\mu\nu,\alpha} - \Gamma^{\alpha}_{\mu\alpha,\nu} + \Gamma^{\alpha}_{\beta\alpha}\Gamma^{\beta}_{\mu\nu} - \Gamma^{\alpha}_{\beta\nu}\Gamma^{\beta}_{\mu\alpha}, \\ R &\equiv g^{\mu\nu} R_{\mu\nu}, \end{aligned} \tag{2.17}$$

The commas means derivatives, for example $\Gamma^{\alpha}_{\mu\nu,\alpha} = \partial\Gamma^{\alpha}_{\mu\nu}/\partial x^{\alpha}$. The Einstein field equations link the curvature space-time (geometry) and the contents in matter and energy through the stress-energy tensor $T_{\mu\nu}$ (illustrated in figure 2.10).

$$\boxed{R_{\mu\nu} - \frac{1}{2} g_{\mu\nu} R - \Lambda g_{\mu\nu} = 8\pi G T_{\mu\nu}}. \tag{2.18}$$

G is the Newton constant. Λ is the cosmological constant that can be added to the equations. The stress-energy tensor describes the density and the flux of energy and momentum in space-time. The stress-energy tensor of the Universe in case of a perfect fluid, in thermodynamic equilibrium is:

$$T^{\mu\nu} = T_{\mu\nu} = \left(\rho c^2 + P\right) \frac{u_\mu u_\nu}{c^2} - P g_{\mu\nu}. \tag{2.19}$$

Where we have introduced the 4-vector velocity u^{μ} of the material object following a time-line curve with respect to the proper time τ of the observer, so that $g_{\mu\nu} u^{\mu} u_{\nu} = -1$. Then

$$u^{\mu} = \frac{dx^{\mu}}{d\tau}. \tag{2.20}$$

Here ρ is the mass density and P is the pressure. Let us assume that the fluid is at rest $u^{\mu} = (1, 0, 0, 0), u_{\nu} = (-1, 0, 0, 0)$ then the stress-energy tensor of a *perfect*

[3] The Ricci curvature tensor is the mathematical object that controls the growth rate of the volume of metric balls in a manifold. In general relativity, the Ricci tensor is the part of the space-time curvature which determines the volume of convergent or divergent matter in time. It relates to the Riemann tensor $R^{\alpha}_{\mu\alpha\nu} \equiv R_{\mu\nu}$.

fluid is:

$$T^{\mu\nu} = \begin{pmatrix} \rho c^2 & 0 & 0 & 0 \\ 0 & P & 0 & 0 \\ 0 & 0 & P & 0 \\ 0 & 0 & 0 & P \end{pmatrix}. \tag{2.21}$$

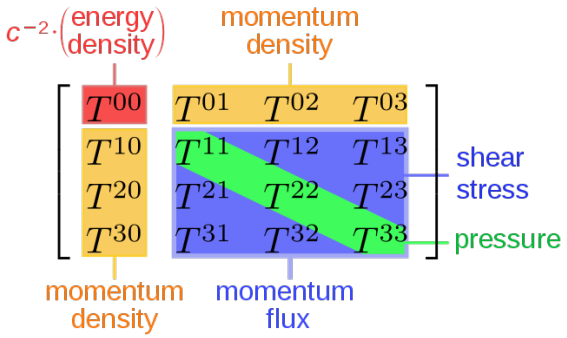

FIGURE 2.10: The intuitive components of the stress-energy tensor $T^{\mu\nu}$ describe the density, pressure, and momentum in spacetime.

Assuming the Universe is homogeneous and isotropic we obtain the FLRW metric 2.4.1 with coordinates $x^\mu = (x^0, x^1, x^2, x^3) = (ct, r, \theta, \phi)$. The metrics FLRW in a spherical coordinate are:

$$g_{\mu\nu} = \begin{pmatrix} 1 & 0 & 0 & 0 \\ 0 & -\dfrac{a^2}{1-kr^2} & 0 & 0 \\ 0 & 0 & -a^2r^2 & 0 \\ 0 & 0 & 0 & -a^2r^2\sin^2\theta \end{pmatrix}. \tag{2.22}$$

$$g^{\mu\nu} = \begin{pmatrix} 1 & 0 & 0 & 0 \\ 0 & -\dfrac{1-kr^2}{a^2} & 0 & 0 \\ 0 & 0 & -\dfrac{1}{a^2r^2} & 0 \\ 0 & 0 & 0 & -\dfrac{1}{a^2r^2\sin^2\theta} \end{pmatrix}. \tag{2.23}$$

After solving the Einstein's equations by calculating Christoffel, Ricci tensor (**Appendix A**). There are two independent Einstein equations, the time-time equation gives the first **Friedmann Equation** relating the expansion of the Universe to the

density, the curvature and the cosmological constant.

$$\boxed{H^2 \equiv \left(\frac{\dot{a}}{a}\right)^2 = \frac{8\pi G}{3c^2}\rho - \frac{kc^2}{a^2} + \frac{\Lambda c^2}{3}}, \tag{2.24}$$

and

$$2\frac{\ddot{a}}{a} + \left(\frac{\dot{a}}{a}\right)^2 = -\frac{8\pi G}{c^2}P - \frac{kc^2}{a^2}. \tag{2.25}$$

By subtracting the equation 2.25 to the first Friedmann equation, we get the second Friedmann equation, so-called **acceleration equation**

$$\boxed{\frac{\ddot{a}}{a} = -\frac{4\pi G}{3c^2}(\rho + 3P) + \frac{\Lambda c^2}{3}}. \tag{2.26}$$

This implies that the acceleration of the expansion of the Universe is slowed down by the first term, gravity and speeded up by the second term, the cosmological constant.

The contents of the Universe

These Friedmann equations describe the dynamics of the expanding Universe. We need an equation describing the density and pressure of matter in the Universe. Under the hypothesis that the expansion of the Universe is an adiabatic process ($TdS \equiv \delta Q = 0$) we have:

$$dE + PdV = TdS. \tag{2.27}$$

This is the first law of thermadynamics in volume V which has scale factor radius a, density ρ. The energy in a co-moving volume is given by:

$$E = \frac{4\pi}{3}a^3\rho c^2. \tag{2.28}$$

If the volume and density change with time then:

$$\begin{aligned} \frac{dE}{dt} &= 4\pi a^2 \rho \frac{da}{dt}c^2 + \frac{4\pi}{3}a^3\frac{d\rho}{dt}c^2; \\ \frac{dV}{dt} &= 4\pi a^2 \frac{da}{dt}. \end{aligned} \tag{2.29}$$

Substitute into the equation 2.27, finally we can derive the **fluid equation**:

$$\boxed{\dot{\rho} + 3\frac{\dot{a}}{a}\left(\rho + \frac{P}{c^2}\right) = 0}. \tag{2.30}$$

The **equation of state** is defined as

$$P = \omega\rho c^2 \Leftrightarrow \omega = \frac{P}{\rho c^2}. \tag{2.31}$$

Then the fluid equation become:

$$\rho \propto a^{-3(1+\omega)} \tag{2.32}$$

Combine those equations above and the Friedmann equation [71], we have the time evolution of the scale factor of the flat Universe.

$$a(t) \propto \begin{cases} t^{2/3(1+\omega)} & \omega \neq -1, \\ e^{Ht} & \omega = -1, \end{cases} \tag{2.33}$$

In case of:
Matter dominated Universe $\omega = 0$: $a(t) \propto t^{2/3}$, $\rho_m \propto a^{-3}$
Radiation dominated $\omega = \frac{1}{3}$: $a(t) \propto t^{1/2}$, $\rho_r \propto a^{-4}$,
Cosmological constant dominated $\omega = -1$: $a(t) \propto e^{Ht}$, $\rho_\Lambda \propto a^0$,

TABLE 2.1: The solutions of fluid equation and Friedmann equation for the Universe in case of matter domination, radiation domination, cosmological domination.

	ω	ρ	a
Matter Domination	0	a^{-3}	$t^{2/3}$
Radiation Domination	$\frac{1}{3}$	a^{-4}	$t^{1/2}$
Cosmological constant Λ	-1	a^0	e^{Ht}

The fate of the Universe

The Friedmann equation connects the density, the space curvature, and the expansion Hubble parameter. The *critical density* is defined as:

$$\rho_c \equiv \frac{3c^2H^2}{8\pi G}. \tag{2.34}$$

Then the *density parameter* as

$$\Omega = \frac{\rho}{\rho_c}. \tag{2.35}$$

Then the Friedmann equation becomes:

$$\boxed{\Omega - 1 = -\frac{kc^2}{H^2a^2} + \frac{\Lambda c^2}{3H^2}}. \tag{2.36}$$

The density parameter for the cosmological constant:

$$\Omega_\Lambda = \frac{\Lambda c^2}{3H^2}. \tag{2.37}$$

The density parameter for the curvature:

$$\Omega_k = -\frac{kc^2}{a^2H^2}. \tag{2.38}$$

The Friedmann equation now can be rewritten as:

$$\Omega + \Omega_\Lambda + \Omega_k = 1, \tag{2.39}$$

if the Universe contains mixing of matter, radiation and cosmological constant today. The density parameters are $\Omega = \Omega_m + \Omega_r + \Omega_\Lambda$.

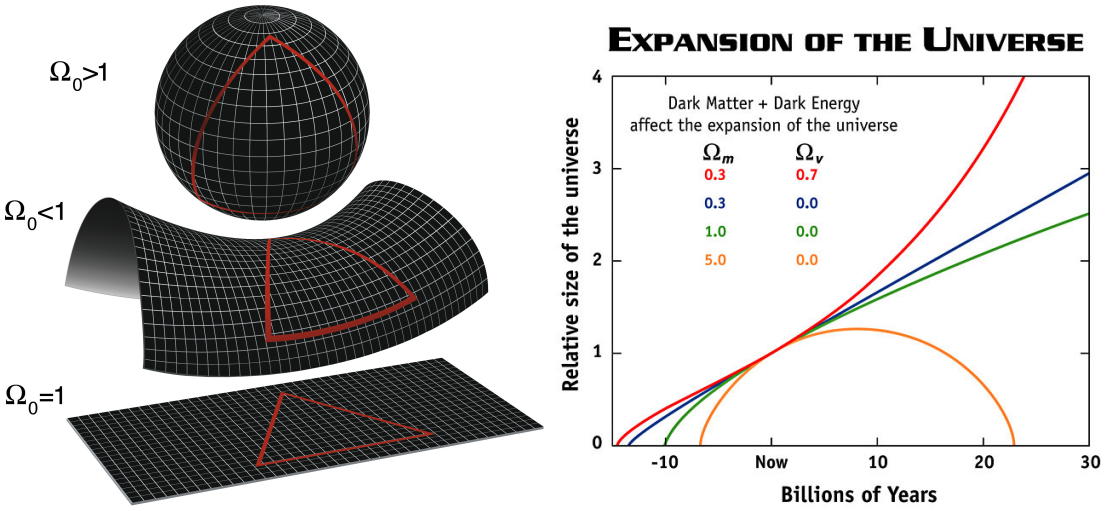

FIGURE 2.11: *Left:* The geometry of the Universe depending on the total density. *Right:* The fate of the Universe with respect to the components of dark matter Ω_m and dark energy Ω_Λ.
Credit: NASA/WMAP team

The value of $\Omega = 1$ implies a flat universe, $\Omega < 1$ an open universe, $\Omega > 1$ a closed universe. The observational data imply that the density of the Universe today is compatible with the critical density Ω_0. Friedmann equations can be solved for different Universe models as: **Empty universe (Milne)** $\Omega = 0$; **Einstein de**

Sitter $\Omega_0 = \Omega_{m;0} = 1$; **Super critical** $\Omega_{m;0} = \Omega_0 > 1$; **Subcritical** k = -1, $\Omega_{m;0} = \Omega_0 < 1$; **Vacuum-dominated universes (de Sitter space)** Only Λ, $\Omega_0 = \Omega_{\Lambda;0} = 1$ this solution is useful to describe the inflationary Universe; **Fluid** k = 0, P = $\rho\omega$; **Flat** k = 0, $\Omega_{m;0} + \Omega_{\Lambda;0} = \Omega_0 = 1$ . . . The evolution of scale factor $a(t)$ and time t depends on Ω_m and Ω_Λ is shown in figure 2.12

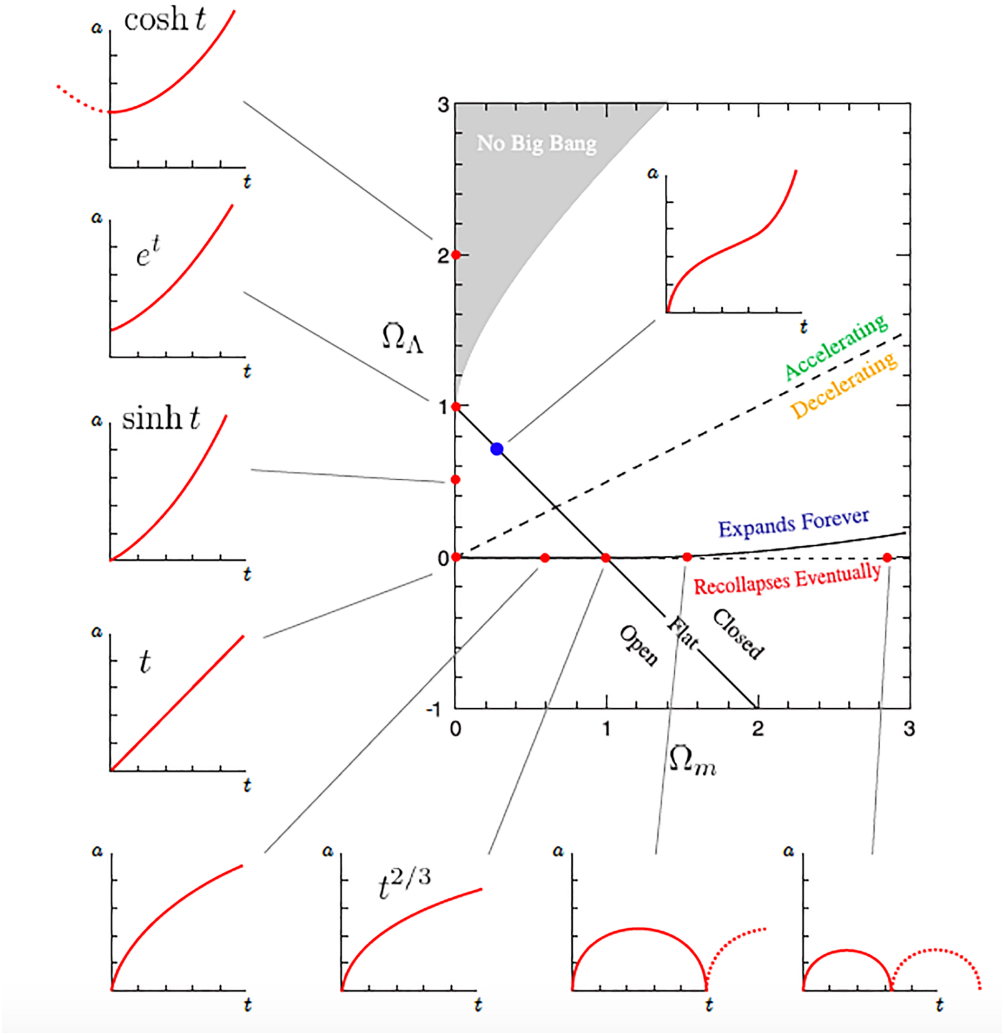

FIGURE 2.12: The evolution of the scale factor $a(t)$ and time t for several Universe models, the blue dot is the de Sitter space, which is an exponential function of the Hubble parameter $a(t) = e^{Ht}$. The de Sitter space is a helpful computation describing the evolution during the inflation.

The Friedmann equation and the acceleration equation tell us that the evolution of the Universe depends on the expansion rate and the gravitational force. The Hubble parameter measures the expansion rate of the Universe, while the gravity force is determined by the density and pressure of the matter in the Universe. The density parameter of radiation today is very small $\Omega_r \approx 10^{-4}$ and is obtained

by accurately measuring the temperature of the cosmic microwave background. The latest measurements from the Planck mission indicate that h ~ 0.678, $\Omega_m \sim 0.3, \Omega_\Lambda \sim 0.7$. Figure 2.11 illustrates the fate of the Universe in time and the scale factor a(t).

The age of the flat Universe with $\Lambda = 0$

At current time t_0, $a(t_0) = 1, H(t_0) = H_0$. The equation 2.36 corresponds to:

$$kc^2 = H_0(1 - \Omega_0) \tag{2.40}$$

Substituting the equation 2.40 into the Friedmann equation 2.24 we get:

$$\boxed{H^2 = \left(\frac{da}{adt}\right)^2 = H_0^2 \left[\Omega_r a^{-4} + \Omega_m a^{-3} + \Omega_\Lambda + (1 - \Omega_0)a^{-2}\right]}. \tag{2.41}$$

Using $dt = \dfrac{da}{aH}$, finally the age of the Universe is given by:

$$\boxed{t_0 = \int_0^{t_0} dt = \frac{1}{H_0} \int_0^{a(t_0)=1} \frac{da}{\sqrt{\Omega_m a^{-1} + \Omega_r a^{-}2 + \Omega_\Lambda a^2 + (1 - \Omega_0)}}}. \tag{2.42}$$

In general, the integral should be computed numerically. In the special case of matter dominated, the open Universe without vacuum energy $\Omega_\Lambda = 0$, $\Omega_r \approx 0$ [71] is:

$$t_0 = \frac{2}{3} H_0^{-1} = 6.51 h^{-1} \times 10^9 \quad \text{years}. \tag{2.43}$$

In order to obtain the relation between the Hubble parameter and redshift, using the definition in the equation 2.5 with $a_0 = 1$ today then $a = 1/(1+z)$, substituting into the equation 2.41, we get the relationship [5]:

$$\boxed{H(z) = H_0 \left[\Omega_{m;0}(1+z)^3 + \Omega_{r;0}(1+z)^4 + \Omega_{k;0}(1+z)^2 + \Omega_{\Lambda;0}\right]^{1/2}}. \tag{2.44}$$

From this equation 2.44 we can derive how the comoving distance relate to redshift, Hubble constant and density parameters.

2.5 Distances

In cosmology, the measurement of distance in the expanding Universe is a very important point. Observational distances depend on the cosmological model of our Universe. There have many ways to determine the distance between two points.

Comoving distance d_χ

The fundamental distance is the distance between two points on a comoving grid. Comoving distance is the distance from a distant emitter at redshift z, or scale factor a and the observer at redshift $z_0 = 0$, or scale factor $a_0 = 1$ following formula:

$$\chi(a) = \int_{t(a)}^{t_0} \frac{c\ dt'}{a(t')}; \tag{2.45}$$

We can apply the changing variable:

$$dt = da\frac{dt}{da} = \frac{da}{aH}.$$

Then we have:

$$\chi(a) = \int_a^1 \frac{c\ da'}{a'^2 H(a')}. \tag{2.46}$$

From the equation 2.5 we have $a = a_0/(1+z)$, it is equivalent to: $da = -\dfrac{a_0\ dz}{(1+z)^2}$, then the cosmoving distance between us and an object at redshift z can be written as

$$\chi(z) = \int_0^z \frac{c\ dz}{H(z)}. \tag{2.47}$$

Here $H(z)$ depends on matter contents of the Universe as shown in the equation 2.44.

The angular diameter distance d_A

In astronomy, if an object has diameter D and subtended angle θ, the angular diameter distance is measured by:

$$d_A = \frac{D}{\theta}. \tag{2.48}$$

We note that the comoving size of the object is D/a. So that the subtended angular size related to comoving distance is $\theta = \dfrac{D/a}{\chi(a)}$, substituting into the equation 2.48,

we show that the angular diameter distance is

$$d_A = a\ \chi(a) = \frac{a_0\chi(a)}{1+z}. \tag{2.49}$$

The luminosity distance d_L

The luminosity distance is defined as the flux of an object known as luminosity L (The energy emitted in a solid angle 4π) and flux density S.

$$(d_L)^2 = \frac{L}{4\pi S}. \tag{2.50}$$

Let us consider an object at scale factor a, $r_0 \equiv \int_{t(a)}^{t_0} c\ dt/a(t)$ is the comoving radius, then the radiation flux accounting for the expansion of the Universe $S = L/(4\pi a^2 r_0^2(1+z)^2)$ [71]. Therefore the equation 2.50 becomes:

$$d_L = a r_0 (1+z). \tag{2.51}$$

For nearby objects $z \ll 1$, the luminosity distance is the physical distance.

2.6 The horizon problem

The horizon problem can be understood as the homogeneity problem, the communication between two opposite regions in the observable Universe. The comoving particle horizon (equivalent to the conformal time) η or the maximum distance a photon can travel between 0 and time t in the Universe is [7]

$$\eta = \int_0^t \frac{dt'}{a(t')} = \int_0^a \frac{da'}{a'}\frac{1}{a'H(a')} = \int_0^a d\ln a' \frac{1}{a'H(a')} \propto \begin{cases} a & \text{radiation dominated.} \\ a^{1/2} & \text{matter dominated.} \end{cases} \tag{2.52}$$

The comoving horizon is the logarithmic integral of the comoving Hubble radius $1/aH$. If we consider two points on the last scattering (LS) surface, as illustrated in figure 2.13, corresponding to looking at the opposite direction in the sky, these regions would have not time to interact on the opposite side of the sky. The observational CMB temperature is nearly isotropic at 2.725 K with tiny fluctuations 10^{-5}. In the matter-dominated epoch, the horizon distance of two regions is

approximately [129].

$$d_{hor}(t_{LS}) = 2\frac{c}{H(t_{LS})} \sim 0.4\, Mpc. \tag{2.53}$$

The angular diameter distance to the last scattering surface is $d_A \approx 14 Mpc$ [129] then the angular between two points is:

$$\theta_{hor} = \frac{d_{hor}(t_{LS})}{d_A} \sim 2^{\circ}. \tag{2.54}$$

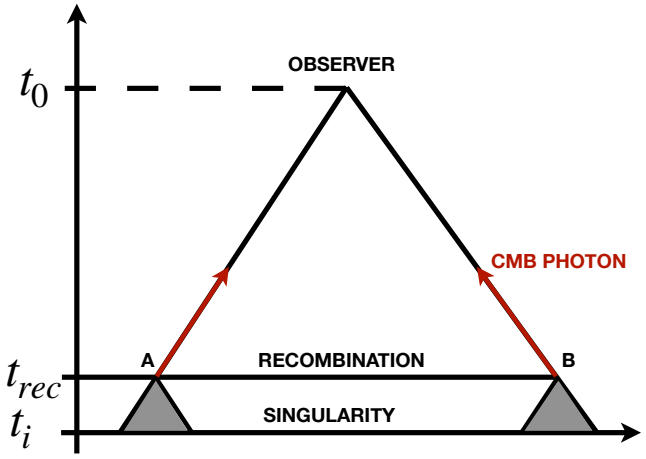

FIGURE 2.13: The horizon problem, two points A and B at the recombination epoch, there is not time for the signal to travel between A and B. How they can have the same temperature with tiny fluctuations?

It means that points separated by more than 2° on the last scattering surface do not have time to interact with each other. However, the angular scale on the CMB map is separated by about 1°. So why does the universe look the same in all directions? The inflationary scenario which is proposed by Alain Guth solves this problem. The idea of inflation scenario is that actually, two regions started really close to each other in the very early Universe, then cosmological inflation has driven the Universe expanded exponentially quickly. The detail ideal and the solution for the horizon problem are described in section 2.8.

2.7 The flatness problem

In the flat Universe (k=0). From the Friedmann equation, the critical density is

$$\rho_c(t) = \frac{3H^2}{8\pi G}(t) = 1.88h^2 \times 10^{-26} \qquad \text{kgm}^{-3}. \tag{2.55}$$

We know that the total density of material in the Universe is closely related to the critical density. The Friedmann equation 2.24 can be rearranged as

$$1 - \Omega_{tot}(t) = \frac{-k}{(aH)^2}. \tag{2.56}$$

where the density parameter is already defined as $\Omega_{tot}(t) \equiv \frac{\rho(t)}{\rho_c(t)}$. The case $\Omega_{tot}(t) = 1$ is an unstable point. Indeed, if the Universe is flat $\Omega_{tot} = 1$, then it remains for all time and independent to the comoving Hubble radius $(aH)^{-1}$ which grows with time. The observation of type Ia supernovae, BAO and the CMB show that $1 - \Omega_{tot}(a) \sim 0.005$ today. Why Ω_{tot} is so close to 1? Why is it not smaller or lager? Again, the rapid exponential expansion in the inflation scenario solves the flatness problem.

2.8 Inflation

In 1981, Alan H. Guth published a paper "A possible solution to the horizon and flatness problems" [47]. The author proposed a scenario of the inflating Universe with a huge expansion factor, and the scale factor is an exponential function of time. This solution implies a negative pressure of the Universe. Particles of whole observational Universe were causally connected together. From the acceleration equation 2.26 we have the requirement of inflation:

$$\frac{d}{dt}\frac{1}{aH} < 0, \Rightarrow \frac{d^2a}{dt^2} > 0, \Rightarrow P < -\frac{\rho c^2}{3}. \tag{2.57}$$

During the inflation, the early Universe behaves as it was dominated by a cosmological constant, then the Friedman equation gives:

$$H^2 = \frac{\Lambda}{3}, \tag{2.58}$$

The Hubble parameter is then constant over the time, then the acceleration equation is

$$\frac{\ddot{a}}{a} = \frac{\Lambda}{3}, \tag{2.59}$$

and the solution for the scale factor is

$$a(t) = \exp\left(\sqrt{\frac{\Lambda}{3}}t\right) = \exp(Ht). \tag{2.60}$$

From this equation 2.60 we can assume the exponential inflation starts at t_i and ends at t_f, the scale factor is

$$\frac{a(t_f)}{a(t_i)} = e^N. \tag{2.61}$$

Where N is the number of e-foldings of inflation:

$$N \equiv H(t_f - t_i) \tag{2.62}$$

For N=60 at least required to explain observational facts, then

$$\frac{a(t_f)}{a(t_i)} \sim e^{60} \simeq 10^{25}. \tag{2.63}$$

This is a huge expansion factor of the early Universe. This also provides explanation of the horizon problem today. Two opposite regions were actually causally connected at the inflation epoch.

Solution of the flat problem

From the equation 2.36 and 2.56, if the Universe is exponentially expanding during the inflation, then [129]

$$1 - \Omega(t) \propto e^{-2Ht}. \tag{2.64}$$

Now we consider the beginning and ending of the inflation, from equation 2.62 we have $t = t_f = t_i + N/H$, substituting into equation 2.64 we obtain:

$$1 - \Omega(t_f) = e^{-2N}(1 - \Omega(t_i)). \tag{2.65}$$

After 60 e-foldings $e^{-2N} \simeq 10^{-52}$, even if at the beginning of the inflation the Universe is not flat, the inflation flatten the Universe by factor of $\sim 10^{52}$. The type Ia supernovae and the CMB observation data indicate that the current limits on the density parameter is $1 - \Omega \leq 0.005$, it implies that the inflation happens with e-fold > 60.

Solution of the horizon problem

At any time t', the horizon distance is with respect to the comoving particle horizon:

$$d_{hor}(t) = a(t)c\int_0^t \frac{dt'}{a(t')}. \tag{2.66}$$

Assuming that the beginning of the inflation is radiation-dominated $a(t_i) \propto t_i^{1/2}$, then the horizon distance at the beginning of the inflation is:

$$d_{hor}(t_i) = a(t_i)c\int_0^{t_i} \frac{dt}{a(t)} = ct_i^{1/2}\int_0^{t_i} \frac{dt}{t^{1/2}} = 2ct_i, \tag{2.67}$$

then the horizon distance at the end of the inflation is calculated as, following equations 2.60 and 2.61:

$$\begin{aligned} d_{hor}(t_f) &= a(t_f)c\int_0^{t_f} \frac{dt}{a(t)} \\ &= a(t_i)e^N c\left[\int_0^{t_i} \frac{dt}{t^{1/2}} + \int_{t_i}^{t_f} \frac{dt}{a(t)}\right]; \\ &= e^N ct_i^{1/2}\left[2t_i^{1/2} + \int_{t_i}^{t_f} \frac{dt}{e^{H(t-t_i)}}\right]; \\ &= e^N c\left(2t_i + \frac{t_i^{1/2}}{H}\left(1 - e^{-N}\right)\right) \end{aligned} \tag{2.68}$$

The horizon is boosted by an exponentional factor. For one possible model, the inflation that it statred around the Grand Unified Theory (GUT) time, $t_i \approx t_{GUT} \approx 10^{-36s}$, with the Hubble parameter $H_i \approx t_{GUT}^{-1}$. The horizon $d_{hor}(t_i) = 2ct_i \approx 6 \times 10^{-28}m$ [129], the Hubble parameter is $H \approx 10^{36}s^{-1}$ for e-folding ≈ 100. Then the horizon after the inflation is immediately $d_{hor}(t_f) \approx e^N c2t_i\left(1 + \frac{t_i^{1/2}}{2}\right) \approx 8 \times 10^{15}m \approx 1.5pc$.

2.9 Physics of inflation

In many inflation models, the simplest way to explain the mechanism of inflation is produced by a scalar field ϕ, *the inflaton*, which is a function of position and time. The dynamic of a scalar field and gravity is the gravitational Einstein-Hilbert action[4] (in a physical system the equation of motion is derived by a dynamic

[4]The action was first proposed by Hilbert, it attributes to the Einstein field equations

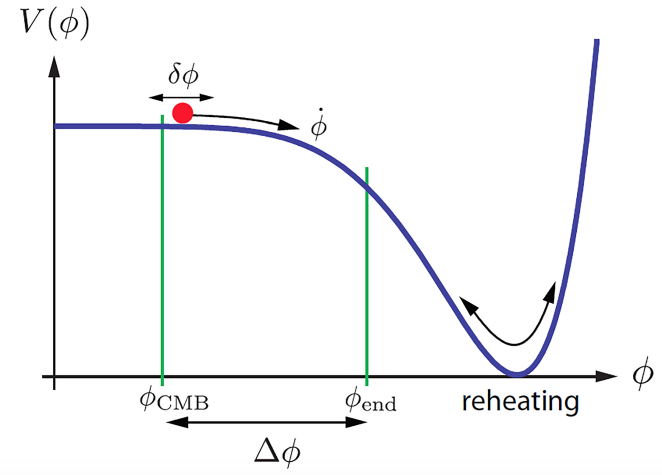

FIGURE 2.14: An example of a scalar field of inflation. The inflation happens when the potential energy accelerates the field. The quantum fluctuations imprint fluctuations on the CMB. The density energy of inflation is transferred into radiation at reheating oscillation around the minimum [18].

attribution) of general relativity and scalar field action [18]. Let us take the Einstein-Hilbert action and a scalar field:

$$S = \int d^4x\sqrt{-g}\left[\frac{M_{Pl}^2}{2}R - \frac{1}{2}g^{\mu\nu}\partial_\mu\phi\partial_\nu\phi - V(\phi)\right] = S_{EH} + S_\phi. \tag{2.69}$$

where $g = det(g_{\mu\nu})$, $R = g^{\mu\nu}R_{\mu\nu}$ is the Ricci scalar, $V(\phi)$ is the potential energy of the scalar field, the reduced Planck mass $M_{Pl} \equiv \frac{1}{\sqrt{8\pi}}m_{Pl} \equiv \frac{\sqrt{\hbar c}}{\sqrt{8\pi G}} = 2.436 \times 10^{18} GeV$ (the Planck mass $m_{Pl} = \sqrt{\frac{\hbar c}{G}}$, $\hbar$ is the reduced Planck constant) and also we can see the starting point in the field theory, the function of space-time, Lagrangian density which is an action of a canonical kinetic term and a scalar field, S_ϕ:

$$\mathcal{L} = -\frac{1}{2}g^{\mu\nu}\partial_\mu\phi\partial_\nu\phi - V(\phi). \tag{2.70}$$

The stress-energy tensor of the evolution of space-time for the scalar field is [18]

$$T_{\mu\nu}^{(\phi)} \equiv -\frac{2}{\sqrt{-g}}\frac{\delta S_\phi}{\delta g^{\mu\nu}} = \partial_\mu\phi\partial_\nu\phi - g_{\mu\nu}\left(\frac{1}{2}\partial^\sigma\phi\partial_\sigma\phi + V(\phi)\right). \tag{2.71}$$

If the inflation field is homogeneous (the gradient of the inflation field equals 0, $\nabla\phi = 0, \nabla^2\phi = 0$) during the inflation then the energy density and the pressure are:

$$\rho_\phi \;=\; T_{00} = \frac{1}{2}\dot{\phi}^2 + V(\phi),$$

$$P_\phi = \frac{1}{3}(T_{11}+T_{22}+T_{33}) = \frac{1}{2}\dot{\phi}^2 - V(\phi). \tag{2.72}$$

We also can get the equation of state

$$\omega_\phi = \frac{P_\phi}{\rho_\phi} = \frac{\dot{\phi}^2 - 2V(\phi)}{\dot{\phi}^2 + 2V(\phi)}. \tag{2.73}$$

The equation of state shows that if the potential energy dominates the kinetic of a scalar field, negative pressure is possible. We can obtain the useful combination:

$$\begin{aligned} \rho_\phi + P_\phi &= \dot{\phi}^2, \\ \rho_\phi + 3P_\phi &= 2(\dot{\phi}^2 - V(\phi)). \end{aligned} \tag{2.74}$$

The equation of motion for the scalar field, assuming the FLRW metric, flat space and homogeneity, is [137]

$$\begin{aligned} &\frac{\delta S}{\delta \phi}\frac{1}{\sqrt{-g}}\partial_\mu(\sqrt{-g}\partial^\mu\phi) + \dot{V}(\phi) = 0. \\ &\Rightarrow \boxed{\ddot{\phi} + 3H\dot{\phi} + \dot{V}(\phi) = 0}. \end{aligned} \tag{2.75}$$

The term $3H\dot{\phi}$ plays a role of friction, it slows down the motion as well as the evolution of the inflaton field in the equation of motion. It is an attractor "slow-roll".

In order to describe the energy of the scalar field during the inflation, inserting in the equation 2.72 into 2.24 we have.

$$\boxed{H^2 = \frac{1}{3M_{Pl}^2}\left(\frac{1}{2}\dot{\phi}^2 + V(\phi)\right)}. \tag{2.76}$$

The equation 2.75 and 2.76 are called the equations of motion and the scalar field equation.

2.9.1 Slow-Roll inflation

The standard approximation to obtain slow-roll parameters is to neglect the small terms in the equation 2.75 and 2.76. They are considered as conditional equations:

$$3H\dot{\phi} \simeq -\dot{V}(\phi), \qquad (\ddot{\phi} \ll 3H\dot{\phi})$$

$$H^2 \simeq \frac{V(\phi)}{3M_{Pl}^2}. \qquad (\dot{\phi}^2 \ll V(\phi)) \tag{2.77}$$

The slow-roll parameters have been introduced by Liddle and Lyth [72].

$$\begin{aligned} \epsilon(\phi) &= \frac{M_{Pl}^2}{2}\left(\frac{\dot{V}}{V}\right)^2 \ll 1. \\ |\eta(\phi)| &= \left|M_{Pl}^2\frac{\ddot{V}}{V}\right| \ll 1. \end{aligned} \tag{2.78}$$

These conditions constrain the shape of the potential energy of the scalar field. The second parameter implies an attractor solution, which starts from arbitrary initial conditions to the basin of attraction by the attractor as illustrated in figure 2.14. These parameters also guarantee a long lived enough inflation for more than 60 e-folds. The first parameter implies a background solution related to the Hubble rate, we can see that by revisiting the condition in the accelerating equation of the inflation.

$$H = \frac{\dot{a}}{a} \Rightarrow \dot{H} = \frac{\ddot{a}}{a} - \frac{\dot{a}^2}{a^2} \Rightarrow \frac{\ddot{a}}{a} = \dot{H} + H^2 > 0 \Rightarrow -\frac{\dot{H}}{H^2} < 1. \tag{2.79}$$

The slow-roll parameter relates to the Hubble parameter, from the conditional equations 2.77 and remembering that $3H\dot{\phi} = -\dot{V}$, we have:

$$\begin{aligned} H^2 = \frac{V}{3M_{Pl}^2} \overset{\text{derivation}}{\Rightarrow} 2H\dot{H} = \frac{\dot{V}\dot{\phi}}{3M_{Pl}^2} \Leftrightarrow H^2\dot{H} = \frac{\dot{V}H\dot{\phi}}{6M_{Pl}^2} = -\frac{\dot{V}^2}{18M_{Pl}^2}, \\ \Rightarrow -\frac{\dot{H}}{H^2} = \frac{1}{2}M_{Pl}^2\left(\frac{\dot{V}}{V}\right)^2 = \epsilon \ll 1. \end{aligned} \tag{2.80}$$

It is useful to notice that:

$$\begin{aligned} H = \frac{\dot{a}}{a} \Rightarrow \dot{a} &= aH, \\ \ddot{a} = \dot{a}H + a\dot{H} &= a(H^2 + \dot{H}), \\ &= aH^2(1-\epsilon) \end{aligned} \tag{2.81}$$

So during slow-roll inflation $\ddot{a} \sim aH^2$ and inflation ends when $\epsilon = 1$. The Hubble parameter slowly changes comparing to the scalar factor a. Number of e-folds from time t_i until to the inflation finish t_f is:

$$N \equiv \ln\frac{a(t_f)}{a(t_i)},$$

$$= \int_{t_i}^{t_f} H(t)dt = \int_{\phi_i}^{\phi_f} \frac{H}{\dot{\phi}} d\phi = \int_{\phi_i}^{\phi_f} \frac{3H^2}{-\dot{V}} d\phi,$$
$$= \frac{1}{M_{Pl}^2} \int_{\phi_f}^{\phi_i} \frac{V}{\dot{V}} d\phi. \tag{2.82}$$

where $dt = \frac{d\phi}{\dot{\phi}}$, $\dot{\phi} = \frac{-\dot{V}}{3H}$. The fluctuations in the CMB provide constrain on value of number e-folds between $N_{CMB} \approx 40 - 60$ for some specific models. The precise value depends on scenarios of the inflation as shown in figure 2.15.

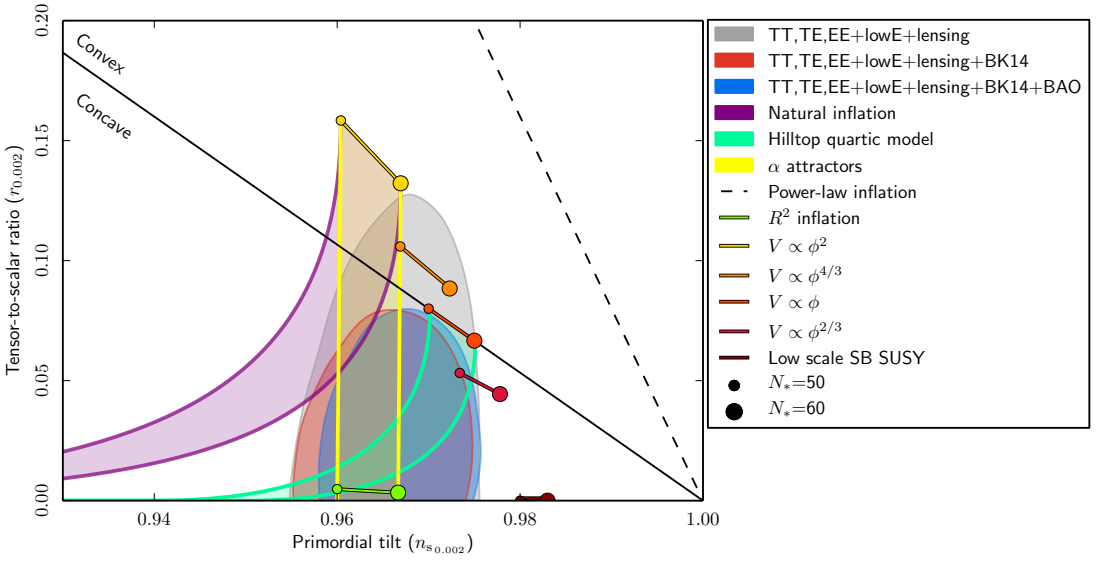

FIGURE 2.15: The theoritical inflation scenarios (Planck 2018 result) are constrained by Planck data and BAO, BICEP [109, 118].

2.10 Primordial quantum fluctuations in inflation and cosmological perturbations

Homogeneity and isotropy of the Universe on large-scale is an usual assumption. On a microscopic scale as the human, the Earth, the Solar system, the stars even galaxy clusters, the Universe is highly inhomogeneous [66]. Recent observations of the Planck satellite measured CMB anisotropics on the full sky with unprecedented accuracy. It observed tiny fluctuations of the temperature $\Delta T/T \sim 10^{-5}$ as shown in figure 2.16. It means that at the epoch of recombination, the Universe was nearly perfectly homogeneous. These fluctuations of the early Universe are the seed of the large-scale structure and originate from cosmological perturbations. The

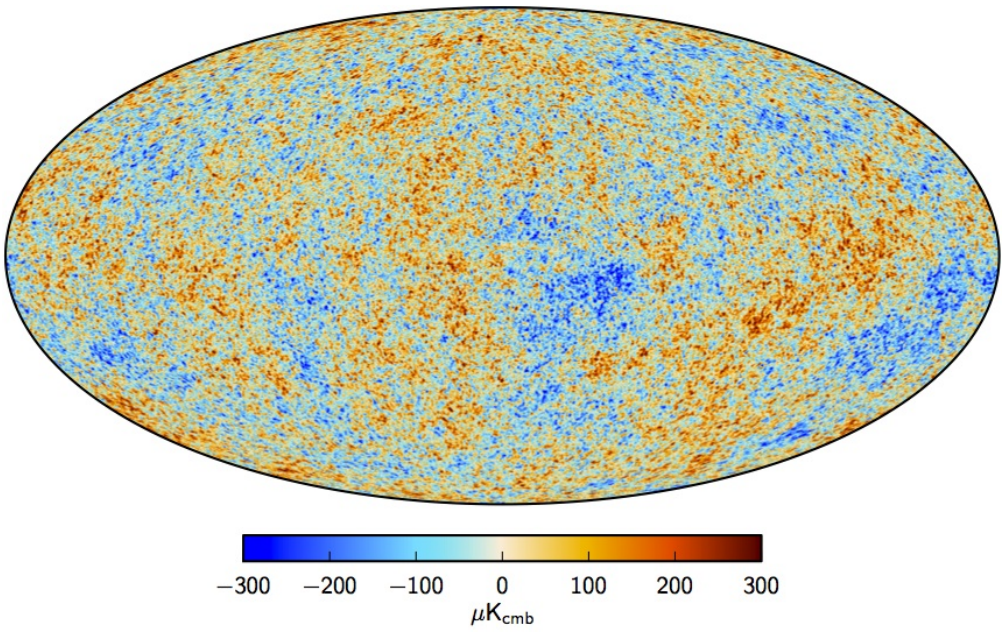

FIGURE 2.16: The CMB anisotropies implies the inhomogeneous Universe. The Plank CMB maps measured a tiny fluctuation in order of 10^{-5}. The structure formation of the Universe today can be analyzed by a linear perturbation of inflation field. *Credit: ESA/Planck team.*

question is what created those tiny primordial fluctuations observed on CMB? The complex structure formation of the Universe is the consequence of the generation and evolution of inhomogeneities. Therefore there are two parts in the theory:

1. The generation of inhomogeneity is speculated by primordial quantum perturbations in the very early Universe. The initial quantum fluctuations of the scalar field ϕ seed the large-scale structure today.

2. The growth of the inhomogeneity is predicted by perturbations of the metric, by gravitational amplification and the effect of the pressure force in the frame of the general relativity depending on the equation of state, density parameters.

2.10.1 Linear perturbation

Because the inhomogeneity of the Universe is small we can describe those with linear perturbations around homogeneity. The linear perturbation is a beautiful and exciting way to treat the initial quantum fluctuations from the inflation field into the macroscopic cosmological perturbations. A quantities $X(t, \mathbf{x})$ of time

and coordinate such as metric $g_{\mu\nu}$ or stress-energy $T_{\mu\nu}$ ($\rightarrow \phi, \rho, P, \ldots$) can be decomposed as a homogeneous background $\bar{X}(t)$ plus a perturbation:

$$\delta X(t, \mathbf{x}) \equiv X(t, \mathbf{x}) - \bar{X}(t). \tag{2.83}$$

Because a transformation of the time coordinate can introduce fictitious perturbations. The split into background and perturbations depends on the chosen coordinates or gauge choice which is precise the transformation between differential geometry [18]. The perturbation for metric, energy density and pressure can be written:

$$\begin{aligned} g_{\mu\nu}(t, \mathbf{x}) &= \bar{g_{\mu\nu}}(t) + \delta g_{\mu\nu}(t, \mathbf{x}). \\ \rho(t, \mathbf{x}) &= \bar{\rho}(t) + \delta\rho(t, \mathbf{x}). \\ P(t, \mathbf{x}) &= \bar{P}(t) + \delta P(t, \mathbf{x}). \end{aligned} \tag{2.84}$$

In order to simplify the differential equations of perturbations, the computation is performed in Fourier space with independent Fourier modes (different wave number) which can be studied independently:

$$X_{\mathbf{k}}(t) = \int d^3\mathbf{x}\, X(t, \mathbf{x}) e^{i\mathbf{k}\cdot\mathbf{x}}. \tag{2.85}$$

Here $X \equiv \delta\phi, \delta g_{\mu\nu}, \delta\rho, \delta P$ and notice that k is wave numbers and $\mathbf{k}$ is wave vectors.

2.10.2 Primordial quantum fluctuations in inflation

Let us discuss briefly the generation of primordial quantum perturbations in inflation. The detail calculation of generation and evolution of the perturbation are available in [16–18, 66, 68, 72, 75, 137]. The generation of primordial perturbations in the framework of inflation are due to quantum fluctuations of the motion of the scalar field, which is the source of tensor, scalar power spectra perturbations $P_t(k), P_s(k)$. The perturbation during inflation is defined as:

$$\phi(t, \mathbf{x}) = \bar{\phi}(t) + \delta\phi(t, \mathbf{x}). \tag{2.86}$$

Inserting the equation 2.86 into the motion equation 2.75 (generally we have to keep the gradient term $\nabla^2\phi$), we get the field equation for a scalar field in FRLW

space with homogeneous background elements and perturbation elements:

$$\left(\bar{\phi}+\delta\phi\right)^{\cdot\cdot}+3H\left(\bar{\phi}+\delta\phi\right)^{\cdot}-a^{-2}\nabla^2\left(\bar{\phi}+\delta\phi\right)+\dot{V}\left(\bar{\phi}+\delta\phi\right)=0. \tag{2.87}$$

Scalar perturbations in inflation (de sitter space-only Λ): Harmonic Oscillations

As mention before, if the inflation field is homogeneous during the inflation, the gradient of the inflation field equals 0, thus $\nabla\phi=0$. By subtracting the equation 2.87 to the background equation 2.75 with notice that $\dot{V}(\bar{\phi}+\delta\phi)=\dot{V}\left(\bar{\phi}\right)+\ddot{V}\left(\bar{\phi}\right)\delta\phi$, we have the perturbation equation during inflation:

$$\delta\ddot{\phi}+3H\delta\dot{\phi}-a^{-2}\nabla^2\delta\phi+\ddot{V}\left(\bar{\phi}\right)\delta\phi=0, \tag{2.88}$$

in Fourier domain:

$$H^{-2}\delta\ddot{\phi}_{\mathbf{k}}+3H^{-1}\delta\dot{\phi}_{\mathbf{k}}+\left[\left(\frac{k}{aH}\right)^2+\frac{m^2}{H^2}\right]\delta\phi_{\mathbf{k}}=0. \tag{2.89}$$

Where $m^2(\phi)\equiv\ddot{V}(\bar{\phi})$. During inflation, H and m^2 change slowly, then we can ignore the m^2/H^2 in the slow-roll approximation ($m^2\ll H^2$). The general solution of the second order different equation of perturbations is:

$$\delta\phi_{\mathbf{k}}(t)=A_{\mathbf{k}}\omega_k(t)+B_{\mathbf{k}}\omega_k^*(t), \tag{2.90}$$

with

$$\omega_k(t)=\left(i+\frac{k}{aH}\right)\exp\left(\frac{ik}{aH}\right). \tag{2.91}$$

The solution implies that before the Hubble horizon exit ($k\gg aH$), as $a(t)$ increase the oscillations are rapid and after the Hubble horizon exit ($k\ll aH$) the oscillations approach to constant values $i\left(A_{\mathbf{k}}+B_{\mathbf{k}}\right)$.

In fact, those calculations above ignored the metric perturbations, however, perturbations depend on the choice of coordinates called gauge choice. We introduce gauge transformation for the curvature perturbation $\mathcal{R}$ which defines the gauge invariant curvature perturbation [18]

$$\mathcal{R}=-H\frac{\delta\phi}{\dot{\bar{\phi}}}. \tag{2.92}$$

Using statistical properties of Gaussian perturbation (which has a stable expectation and a variance) and computational quantum mechanics of the harmonic oscillator [18, 75], the power spectrum describes completely statistical properties of random perturbations of the perturbed universe. During inflation, the amplitude of fluctuation scales with Hubble parameter H. Then we choose the value of $aH = k$ at the horizon exit. Finally, the power spectrum of a scalar perturbation is given by:

$$P_{\mathcal{R}}(k) = \left(\frac{H}{\dot{\phi}}\right)^2 P_{\phi}(k) = \left(\frac{H}{\dot{\phi}}\right)^2 \left(V\frac{k^3}{2\pi^2}\langle|\delta\phi_{\mathbf{k}}|^2\rangle\right) = \left(\frac{H}{\dot{\phi}}\right)^2 \left(\frac{H}{2\pi}\right)^2. \tag{2.93}$$

This scalar primordial spectrum is assumed for the calculation of structure formation and the CMB anisotropy.

Tensor perturbations in inflation (de sitter space-only Λ): Primordial gravitational waves

Similarly, during inflation, we start from the Einstein-Hilbert gravity action plus the matter action. We can rewrite equation 2.69 as:

$$S \equiv \int d^4x \left(\underbrace{\mathcal{L}_g}_{gravity} + \underbrace{\mathcal{L}_m}_{matter}\right) = \underbrace{\frac{M_{Pl}^2}{2}\int d^4x\sqrt{-g}R}_{Einstein-Hilbert\,action} + \underbrace{\int d^4x\sqrt{-g}\left[-\frac{1}{2}g^{\mu\nu}\partial_\mu\phi\partial_\nu\phi - V(\phi)\right]}_{Matter\,action}. \tag{2.94}$$

The metric tensor including a small tensor perturbation $h_{\mu\nu}$ is:

$$g_{\mu\nu} = \bar{g}_{\mu\nu} + h_{\mu\nu}. \tag{2.95}$$

From the FLRW metric we can defined 3×3 tensor h_{ij} as transverse and traceless.

$$ds^2 = a^2(\eta)\left[-d\eta^2 + (\delta_{ij} + h_{ij})\,dx^i dx^j\right]. \tag{2.96}$$

Here η is the conformal time, a is the scale factor. We obtain the second-order action for tensor perturbations due to the fact that the first order is gauge-invariant [18, 151]. From the second-order action, we can calculate the stress-energy tensor and the equation of motion.

$${}^{(2)}S = \frac{M_{Pl}^2}{8}\int d\eta d^3x a^2\left[\left(\dot{h_{ij}}\right)^2 - (\nabla h_{ij})^2\right]. \tag{2.97}$$

The linearized perturbation is applied in Einstein equations [90]:

$$\delta\left[R_{\mu\nu}-\frac{1}{2}Rg_{\mu\nu}\right]=8\pi G\delta T_{\mu\nu}. \tag{2.98}$$

The stress-energy tensor is calculated by integration of the distribution function of momentum space using the action 2.97. The transverse and traceless condition in a spatial metric perturbation is $\partial_i h_{ij} = h_{ii} = 0$. Finally the solution of the equation 2.98 is the equation of motion [8, 90, 151]:

$$\ddot{h}_{ij}+2\mathcal{H}\dot{h}_{ij}-\nabla^2 h_{ij}=16\pi G a^2\Pi_{ij}. \tag{2.99}$$

Where $\mathcal{H}$ is the comoving Hubble parameter, $\mathcal{H} = \frac{1}{a}\frac{da}{d\eta} = aH = k$. Π_{ij} is the transverse ($\partial_i\Pi_{ij} = 0$) and traceless ($\Pi_{ii} = 0$) components of the energy momentum tensor.

$$a^2\Pi_{ij}=T_{ij}-pg_{ij}. \tag{2.100}$$

Likewise we did for a scalar perturbation, we introduce two polarization states h_+, $h_\times$ and we perform the Fourier expansion

$$h_{ij}(\mathbf{x},\eta)=\frac{1}{(2\pi)^3}\int d\mathbf{k}\, e^{i\mathbf{k}\cdot\mathbf{x}}\left[h_+ e^{+}_{ij}+h_\times e^{\times}_{ij}\right]. \tag{2.101}$$

Here $e^{+}_{ij}, e^{\times}_{ij}$ denote for two symmetric polarization tensors, their properties are [90]:

$$\begin{aligned} k^i e^{+}_{ij}=k^i e^{\times}_{ij}=0, \qquad e^{+,i}_{i}=e^{\times,i}_{i}=0,\\ e^{+}_{ij}e^{+,ij}=e^{\times}_{ij}e^{\times,ij}=2, \qquad e^{+}_{ij}e^{\times,ij}=0. \end{aligned} \tag{2.102}$$

In the cartesian coordinate, polarization tensors are [48]:

$$\mathbf{e}^1=\frac{1}{\sqrt{2}}\begin{bmatrix}1&0&0\\0&-1&0\\0&0&0\end{bmatrix} \quad \text{and} \quad \mathbf{e}^2=\frac{1}{\sqrt{2}}\begin{bmatrix}0&1&0\\1&0&0\\0&0&0\end{bmatrix}. \tag{2.103}$$

The left- and right-handed polarizations can be basically defined as:

$$\mathbf{e}^{+,\times}\equiv\mathbf{e}^1\pm i\mathbf{e}^2. \tag{2.104}$$

The simplest way to solve equation 2.99 is that if the inflationary expansion is

driven by a scalar field, since then the energy-momentum tensor is absented. Applying the Fourier transform of $h_{ij}(\mathbf{x}, \eta)$ and substituting again in the motion equation 2.99 (the Laplace operator transforms in Fourier transformation as $\nabla \to -k^2$) we have:

$$\ddot{h}_k + 2\mathcal{H}\dot{h}_k + k^2 h_k = 0. \tag{2.105}$$

Here

$$h_k = \frac{H}{M_{Pl}} i e^{-ikt} k^{-3/2}, \tag{2.106}$$

it is now clear that motion equation of tensor perturbations 2.105 solves the wave equation, hence the solution gives primordial gravitational waves. To solve this equation, it is useful to use the approximation of the de Sitter space. Finally the scale of the power spectrum of tensor perturbation of each polarization mode is given by [18, 26, 72, 90].

$$P_h(k) \equiv \frac{k^3}{\pi^2}\left(|h_+|^2 + |h_\times|^2\right) = \frac{4}{M_{Pl}^2}\left(\frac{H}{2\pi}\right)^2 \tag{2.107}$$

Gravitational waves are tensor perturbations of the metric and these signal imprint in the polarization of the CMB. Many CMB experiments aim to probe these primordial gravitational wave through the B-mode signal.

We already established the scalar perturbation equation 2.93:

$$\boxed{P_s(k) \equiv P_{\mathcal{R}}(k) = \frac{H^2}{(2\pi^2)}\frac{H^2}{\dot{\phi}^2} = \frac{1}{8\pi^2}\frac{H^2}{M_{Pl}^2}\frac{1}{\epsilon}\bigg|_{k=aH}}. \tag{2.108}$$

The power spectrum of tensor perturbations for two polarization modes is calculated by equation 2.107:

$$\boxed{P_t(k) = 2P_h(k) = \frac{2}{\pi^2}\frac{H^2}{M_{Pl}^2}\bigg|_{k=aH}}. \tag{2.109}$$

The tensor-to-scalar ratio is defined as:

$$r = \frac{P_t(k)}{P_s(k)} = 16\epsilon. \tag{2.110}$$

The scale dependence parameters of the spectra are:
- the scalar spectral index:

$$n_s - 1 = \frac{d \ln P_s(k)}{d \ln k}. \tag{2.111}$$

- the tensor spectral index:

$$n_t = \frac{d \ln P_t(k)}{d \ln k}. \tag{2.112}$$

where $\ln k = N + \ln H$ and $\epsilon = -\frac{d \ln H}{dN}$, $\eta = -\frac{d \ln \frac{dH}{d\phi}}{dN}$. In the standard slow-roll approximation:

$$\begin{aligned} n_s - 1 &= 2\eta - 6\epsilon, \\ n_t &= -2\epsilon, \\ r &= 16\epsilon = -8 n_t \end{aligned} \tag{2.113}$$

The Lyth bound provides relationship directly between the tensor-to-scalar and the number of e-folds [74]:

$$r = \frac{8}{M_{Pl}^2} \left(\frac{d\phi}{dN} \right)^2. \tag{2.114}$$

The energy scale of inflation is directly linked to the tensor-to-scalar [18].

$$\boxed{V^{1/4} \sim \left(\frac{r}{0.01} \right)^{1/4} 10^{16} GeV.} \tag{2.115}$$

The measurement of tensor-to-scalar is the main target of the modern cosmology. From its value, we can extract those parameters and understand the inflation model.

2.10.3 Cosmological perturbations and structure formation

So far, we described the quantum fluctuations in inflation epoch in the very early Universe, these fluctuations seed the growth of structures formation and the evolution of large-scale structures. The linear perturbations approach is applied to treat cosmological perturbations. The relativistic perturbation theory is a fully general relativistic treatment of cosmological perturbations in which we can treat perturbations of the metric, the comoving curvature, the scalar, the vector, the tensor

and the matter (the stress-energy tensor). Perturbations evolve in the primordial plasma from the inflation to the CMB emission.

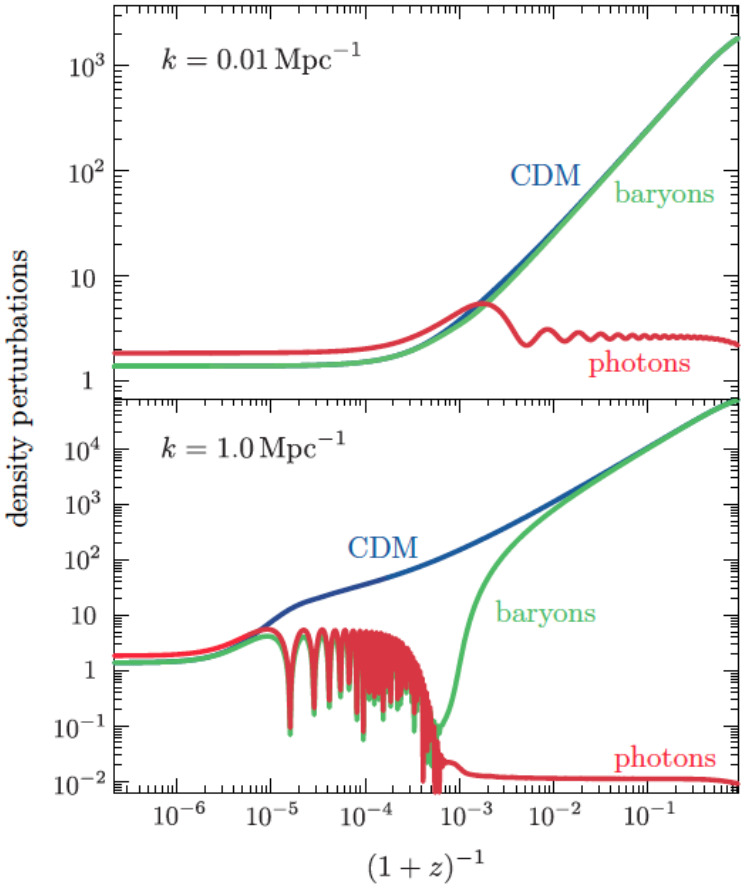

FIGURE 2.17: Evolution of density perturbation of photons, baryons and dark matter [17].

Figure 2.17 presents the evolution of baryons, photons and Cold Dark Matter (CDM) with respect to time in two different wave-numbers k. Before the decoupling epoch $z > z_{dec} \approx 1100$, the radiation era, baryons, and photons are coupled strongly by Compton scattering as a single fluid, on small scales (the large wave-number k) the radiation pressure exceed by photons, pressure opposes the squeezing or compression of the plasma fluid inducing oscillations are called sound waves. Baryon-photon fluid oscillates in the potential wells of dark matter, but fluctuation amplitudes are small of the order of $\mathrm{dT/T} \sim 1$ part in 10^5. Dark matter is not coupled to photons and baryons (except through gravity), so its fluctuations can grow independently. Just after the decoupling, the baryons fall into the potential wells of the grown dark matter density. Radiation is free-streaming after recombination. With the large scale (the smaller wave number) these fluctuation amplitudes of oscillations is invisible due to pressure effects can be neglected.

Dark matter perturbations evolve with different wavelengths. In general, the evolution of the gravitational potential Φ is sourced by the total density fluctuations in the radiation era, radiation-to-matter transition era, and matter era. The gravitational potential is constant on all scales during matter domination [17]. In the radiation era, the perturbed radiation density is the acoustic oscillations which are peaks in the CMB temperature anisotropies spectrum.

Chapter 3

The Cosmic Microwave Background (CMB)

Contents

The evolution of the Universe is illustrated in figure 2.2 under the Big Bang theory. The Cosmic Microwave Background (CMB) is radiation from around 380 000 years after the Universe was born. Before this time, the Universe was so hot, dense and opaque, the early Universe was made of plasma of matter and radiation. Thus photons could not travel freely and no light escaped from those earlier times. The CMB was emitted at the *recombination* era where electrons combined with p and He nuclei atoms and photons were suddenly free to propagate in all directions.

$$e + p \rightleftharpoons H + \gamma.$$

During a small interval time, the Universe suddenly switched from opaque to completely transparent. Therefore CMB photons were freely traveling to the entire the Universe. This process is called as *decoupling*. Then photons reached us from all direction from the last scattering surface[1] [7, 22]. The temperature of the CMB is $T = 2.725 \pm 10^{-5} K$. The temperature anisotropies originate from metric perturbations in the inflation phase of the Universe as seen in the previous chapter. The CMB radiation is polarized because of the last scattering by free electrons (Thomson scattering) during decoupling. The polarization pattern can be decomposed into two components: Curl-free component called 'E-Mode' (electric-field) or 'gradient-mode' and Grad-free component called 'B-Mode' (magnetic-field) or 'curl-mode' [25, 119]. The B-Mode is impacted by gravity waves produced during the inflation epoch at the early Universe. The CMB power spectrum depends on cosmological parameters. The high accuracy measurements the temperature and polarization anisotropies of the CMB allow us to measure the density of energy component such as dark energy, dark matter, baryons. The table 3.1 shows the latest Planck results for fiducial cosmological parameters of the ΛCDM (the Universe has cosmological constant) concordant standard cosmological model which is described in chapter 2.

In 1964, Robert Wilson and Arno Penzias [92] first detected CMB by using a large radio antenna and they got the Nobel Prize in Physics in 1978. The first space

[1]The imaging surface of a sphere which photons travel to us since the decoupling happened around at 3000 K

Parameter	Value	Description
$\Omega_b h^2$	0.02237 ± 0.00015	Physical baryon density parameter
$\Omega_c h^2$	0.1200 ± 0.0012	Physical dark matter density parameter
Ω_Λ	0.6847 ± 0.0073	Dark energy density parameter
τ	0.0544 ± 0.0073	Reionization optical depth
n_s	0.9649 ± 0.0042	Scalar spectral index
$10^9 A_s$	2.092 ± 0.034	Amplitude scalar of power spectrum
H_0	67.36 ± 0.54	Hubble constant
Ω_b	0.0486 ± 0.0010	Baryon density parameter
Ω_m	0.3153 ± 0.0073	Matter density parameter
Ω_c	0.2589 ± 0.0057	Dark matter density parameter
$\rho_c\,(\mathrm{kg/m^3})$	$(8.62 \pm 0.12) \times 10^{-27}$	Critical density
Age/Gyr	13.797 ± 0.023	Age of the Universe
σ_8	0.8111 ± 0.0060	Fluctuation amplitude at $8h^{-1}$ Mpc
N_{eff}	$3.00^{+0.57}_{-0.53}$	Effective number of relativistic degrees of freedom
$\sum m_\nu$	$0.12\,\mathrm{eV/c^2}$	Sum of three neutrino masses (Planck + BAO)
...	...	...

TABLE 3.1: ΛCDM model, the fiducial cosmological parameters table from Planck result 2018 results with 68 % confidence limits (CL) [111, 113, 116, 119].

mission to detect CMB anisotropies is Cosmic Background Explorer (COBE). In 1989 COBE was launched by NASA and placed into Sun-synchronous orbit[2]. COBE measured the CMB temperature and showed that the CMB spectrum is a black-body with a very high accuracy at 2.725 Kelvin. The team got the Nobel Prize in Physics in 2006. Studying these tiny fluctuations in more detail, other balloons and ground-based experiments after COBE such as: BOOMERanG experiment reported that the highest power fluctuation occurs at around 1° in 2000, Degree Angular Scale Interferometers (DASI) experiment detected the polarization of the CMB and the Cosmic Background Image (CBI) experiment measured the E-mode, as well as BICEP, POLABEAR ... The second generation space mission, the Wilkinson Microwave Anisotropy Probe (WMAP) was launched in 2001. The *Planck* mission was launched in 2009 to study the CMB with unprecedented accuracy. After the measurement of the tiny fluctuations of the CMB temperature by WMAP, the *Planck* instrument measured with high accuracy the temperature power spectrum and mapped the CMB as the whole sky. In addition, thanks to a better angular resolution and sensitivity, the *Planck* experiment gave very interesting constraints on primordial B-Modes. A join analysis of BICEP2, the Keck array and Planck data in 2015 set a limit on the tensor-to-scalar ratio of $r < 0.12$

[2]It is geocentric orbit which has the same local mean solar time

[20]. The future CMB experiments aim to detect evidence of inflation Universe using B-modes polarization.

In this chapter, I describe briefly statistic of the CMB, it is decomposition on the spherical harmonic space leading to the monopole, the dipole, multipoles and the angular power spectrum of the CMB temperature. I also describe the angular size to the last scattering surface $\delta\theta_{\rm LS}$, the optical depth to the ionization epoch τ. On the one hand, I present the mechanism of CMB temperature anisotropies which can explain acoustic oscillations peaks in the temperature angular power spectrum. I describe also CMB photons polarization and its angular power spectra. In addition, I describe briefly non-Gaussianity in the CMB, gravitational lensing, CMB spectral distortions. I describe the main foreground components as thermal dust, free-free emission, synchrotron emission, spinning dust, and main systematic effects as beam asymmetry, cosmic rays, 1/f noise, bandpass mismatch. I also present the ground-based QUBIC experiment, the general principle as well as the instrument, and the proposed space mission LiteBIRD.

3.1 The CMB

After $\sim$ 13.7 billions of years, the Universe has expanded and cooled, the wavelength of the photons has stretched (redshift) into roughly 1 millimeter (we can see the CMB on the old analog television snow at the level of $\sim$ 1%) and the CMB temperature has decreased to around $T_0 = 2.725$ Kelvin. These photons fill everywhere in the Universe today and can be detected by far infrared and radio telescopes. The density number is $n_\gamma \approx 400$ photons per cubic centimeter cm^{-3} or 10 trillion photons per second per squared centimeter which is about 2 billion times the baryon density [71]. The CMB is anisotropic at the level of 10^{-3} due to the motion of our Solar system, and the primordial anisotropies are about $10^{-5} \equiv \delta T_{CMB} \approx 30\mu K$.

The CMB is a black body, then following a Planck function of frequency and temperature:

$$\mathrm{B}(\nu, \mathrm{T}) = \frac{2\mathrm{h}\nu^3}{\mathrm{c}^2} \frac{1}{\mathrm{e}^{\mathrm{h}\nu/\mathrm{k_B T}} - 1} \quad [\mathrm{W\,m^{-2}\,sr^{-1}\,Hz^{-1}}]. \tag{3.1}$$

The energy density of radiation is

$$\epsilon_{rad} = \alpha T^4, \tag{3.2}$$

where the radiation constant (or Stefan–Boltzmann constant):

$$\alpha = \frac{\pi^2 k_B^4}{15\hbar^3 c^3} = 7.565 \times 10^{-16}\,\mathrm{Jm^{-3}K^{-4}}. \tag{3.3}$$

We already know that $\rho_{rad} \propto \frac{1}{a^4}$. Then, we have the relationship between temperature and scale factor equation.

$$T \propto \frac{1}{a}. \tag{3.4}$$

From the equation 2.5 we have the equation of the redshift and the temperature

$$T_{\text{emitted}} = T_{\text{observed}}(1+z). \tag{3.5}$$

The CMB temperature maps as observed by COBE and Planck mission are shown in figure 3.1.

The ratio of photon to baryon

The present energy density of photon is given in the equation 3.2 by:

$$\epsilon_{rad}(t_0) = 4.17 \times 10^{-14}\,\mathrm{Jm^{-3}}. \tag{3.6}$$

The energy of photons at temperature T= 2.725 K is

$$E_{rad} \simeq 3k_B T = 7.05 \times 10^{-4}\mathrm{eV}. \tag{3.7}$$

The present number density of photons is calculated as:

$$n_\gamma = \frac{E_{rad}}{\epsilon_{rad}(t_0)} = 3.7 \times 10^8 \quad \mathrm{m^{-3}}. \tag{3.8}$$

We can see that in a cubic metre, there are billion CMB photons. From the table 3.1 we have the baryon density parameter and the critical density parameter. Then we can calculate the baryon energy density

$$\epsilon_b = \rho_b c^2 = \Omega_b \rho_c c^2 \simeq 3.77 \times 10^{-11}\,\mathrm{J\ m^{-3}}. \tag{3.9}$$

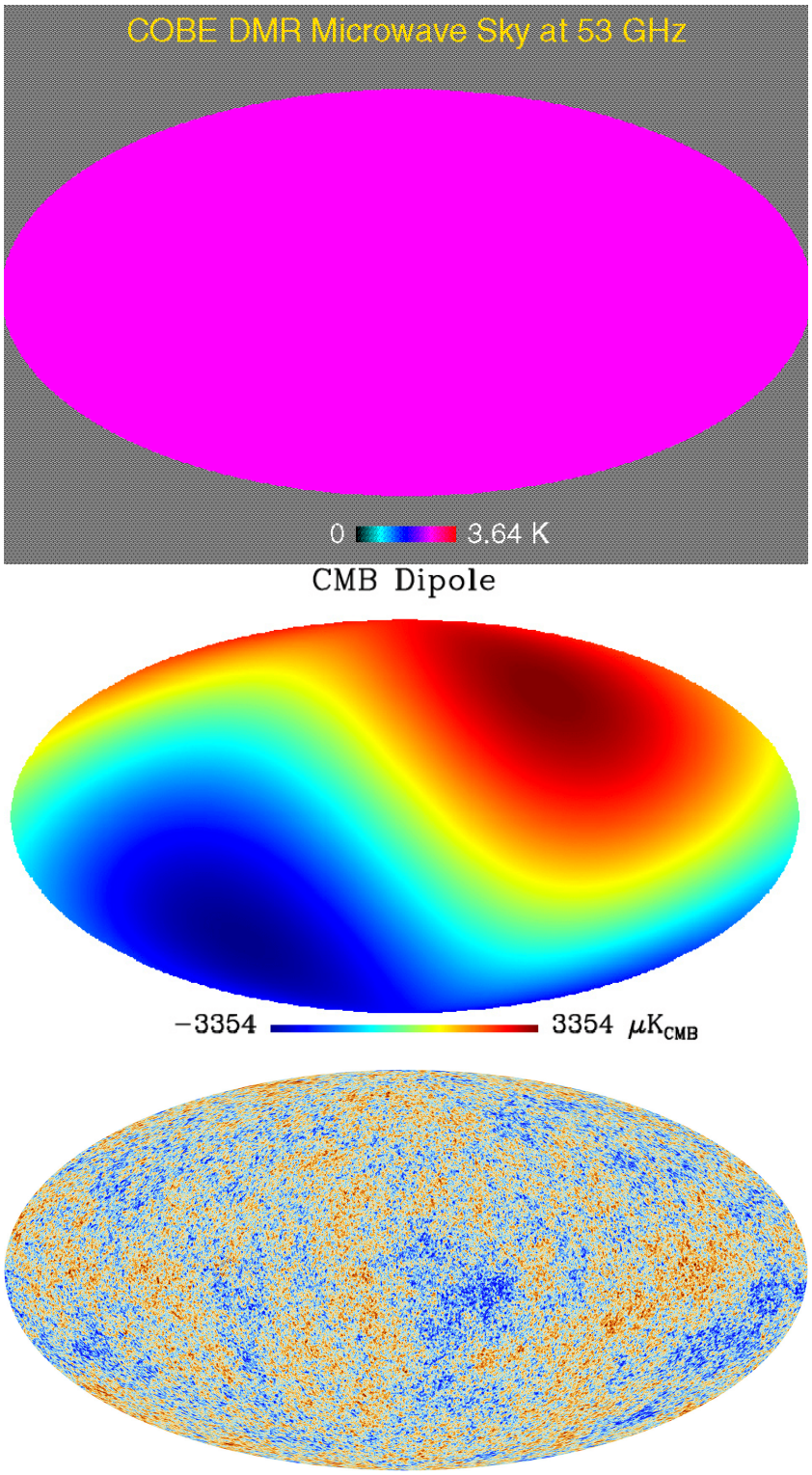

FIGURE 3.1: From top to bottom, the CMB temperature monopole map $T_{CMB} \approx 2.725$K of the COBE Differential Microwave Radiometers (DMR), the CMB dipole map $\delta T_{CMB} = 3.3\,\text{mK}$ and the CMB temperature anisotropies map is measured by the Planck satellite $\delta T_{CMB}/T \approx 10^{-5}$. *Credit: Planck/ESA team*

If we consider that the individual proton and neutron have rest mass about 939 MeV, then we find the number density of baryons is

$$n_b = 0.25\,\mathrm{m}^{-3}. \tag{3.10}$$

The ratio of $\mathrm{n}_\gamma/\mathrm{n}_\mathrm{b} \sim 1.48\times10^9$, it means that the number of photons is around 1.5 billion times the number of baryons today. The Cosmic Microwave Background observed light element abundances and give the constraint on the baryon density in the Universe.

$$\boxed{0.016 \leq \Omega_b h^2 \leq 0.024}. \tag{3.11}$$

Statistical description of the CMB.

We can assume that the CMB temperature in a direction is described by a random Gaussian field. Let us define the dimensionless CMB temperature anisotropies:

$$\Theta(\hat{\mathbf{n}}) \equiv \frac{\delta \mathrm{T}}{\mathrm{T}}(\theta,\varphi) = \frac{\mathrm{T}(\theta,\varphi) - \bar{\mathrm{T}}}{\bar{\mathrm{T}}}. \tag{3.12}$$

Where we denoted in a unit vector $\Theta(\hat{\mathbf{n}}) \equiv \Theta(\theta,\varphi)$. $T(\theta,\varphi)$ is the temperature in the sky direction (θ,φ), $\bar{T}$ is the mean temperature. The CMB temperature anisotropies are decomposed in spherical harmonics basis:

$$\boxed{\frac{\delta T}{T}(\theta,\varphi) = \sum_{\ell=1}^{\infty}\sum_{m=-\ell}^{\ell} a_{\ell m} Y_{\ell m}(\theta,\varphi)}. \tag{3.13}$$

With $Y_{\ell m}$ the spherical harmonic of degree ℓ and order m.

$$Y_{\ell m}(\theta,\varphi) = (-1)^m \sqrt{\frac{2\ell+1}{4}\frac{(\ell-m)!}{(\ell+m)!}} e^{im\varphi} P_\ell^m(\cos\theta). \tag{3.14}$$

This basis is adapted for the decomposition on the surface of a sphere, θ,φ represent colatitude and longitude. P_ℓ^m is the associated Legendre polynomial.

$$\begin{aligned}
P_\ell^m(\cos\theta) &= \frac{(-1)^m}{2^\ell \ell!}\left(1-\cos^2\theta\right)^{m/2}\frac{d^{\ell+m}}{d\cos^{\ell+m}\theta}\left(\cos^2\theta-1\right)^\ell.\\
P_1^1(\cos\theta) &= \sin\theta,\\
P_2^1(\cos\theta) &= 3\cos\theta\sin\theta,\\
P_2^2(\cos\theta) &= 3\sin^2\theta.
\end{aligned} \tag{3.15}$$

The multipoles coefficient is can be expressed as:

$$\boxed{a_{\ell m} = \int Y^*_{\ell m}(\theta, \varphi) \frac{\delta T}{T}(\theta, \varphi) d\Omega}. \tag{3.16}$$

Where $d\Omega$ is the solid angle. This implies the following property of spherical harmonics.

$$\int d\Omega Y_{\ell m}(\hat{\mathbf{n}}) Y^*_{\ell' m'}(\hat{\mathbf{n}}) = \delta_{\ell \ell'} \delta_{m m'}. \tag{3.17}$$

If we sum over the multipole m which is related to orientation, we have multipole number function which is related to the angular size.

$$\sum_m |Y_{\ell m}(\hat{\mathbf{n}})|^2 = \frac{2\ell + 1}{4\pi}. \tag{3.18}$$

CMB monopole

The mean temperature of CMB is T = 2.725 K, and this is the monopole component of the CMB map.

CMB Dipole $\ell = 1$

The dipole pattern (hot and cold are opposite direction on the sky) in the CMB map is dominated by the Doppler shift of the relative motion of the Solar system with respect to the CMB rest frame.

$$\begin{aligned} \mathrm{T} &= \mathrm{T}_{\mathrm{CMB}} \frac{\left(1 - \frac{\mathrm{v}^2}{\mathrm{c}}\right)^{1/2}}{1 - \frac{\mathrm{v}}{\mathrm{c}} \cos\theta}, \\ &= \mathrm{T}_{\mathrm{CMB}} \left(1 + \frac{\mathrm{v}}{\mathrm{c}} \cos\theta + \frac{\mathrm{v}^2}{\mathrm{c}^2} \left(\cos^2\theta - \frac{1}{2}\right)\right). \end{aligned} \tag{3.19}$$

The first order of the dipole is related to the angle between the observer direction and the dipole axis [9, 134, 149].

$$\delta \mathrm{T} = \mathrm{T}_{\mathrm{CMB}} \frac{\mathrm{v}}{\mathrm{c}} \cos\theta = 3.37 \times 10^{-3} \cos\theta \, \mathrm{K}. \tag{3.20}$$

The dipole measurement on the CMB map indicates that the Doppler shift velocity of the Solar system is around 370 km/s with respect to the CMB frame. The motion of the Earth around the Sun is around 30 km/s. This motion is an additional dipole contribution. The effect of the Earth-Sun motion is very well

understood and allow to calibrate and monitor the gain as a function of time for a single detector. The sky map includes only the average dipole. Normally the signal of the dipole is removed for the anisotropies study.

Multipoles moments ℓ

The higher multipole moments are result of density and tensor perturbations of the early Universe. Theoretically, $a_{\ell m}$ are described by a Gaussian random process [134]. The angular wavelength of the fluctuation is $\theta = \frac{180}{\ell}$, the temperature between points on the sky separated by angle θ. For example $\ell = 180$ corresponds to about 1 degree on the sky. The angular resolution of the COBE satellite being 7°, then it can measure up to a resolution of $\ell \simeq 180/7 \simeq 26$. Similarly the WMAP satellite had $0.23° \Rightarrow \ell \simeq 780$, the Planck satellite had the angular resolution of 5 arcminutes, it allows to measure up to $\ell \simeq 2200$.

Angular power spectra

Since the multipoles coefficient $a_{\ell m}$ represent a deviation from the average temperature, the mean value is zero ($\langle \delta T \rangle = 0$).

$$\langle a_{\ell m} \rangle = 0, \tag{3.21}$$

The variance C_ℓ of the coefficients $a_{\ell m}$ is called the *angular power spectrum*,

$$\boxed{C_\ell \equiv \langle |a_{\ell m}|^2 \rangle = \frac{1}{2\ell + 1} \sum_m \langle |a_{\ell m}|^2 \rangle}. \tag{3.22}$$

C_ℓ is independent of m because of the isotropic nature of the random process. The m are represented to the orientation while the ℓ are represented the angular size of the anisotropy of orientation. The two-point covariance of $a_{\ell m}$ is calculated by applying equations 3.17 and 3.22.

$$\begin{aligned} \langle a_{\ell m} a^*_{\ell' m'} \rangle &= \int Y^*_{\ell m}(\hat{\mathbf{n}}) Y_{\ell' m'}(\hat{\mathbf{n}}') \left\langle \frac{\delta T}{T}(\hat{\mathbf{n}}) \frac{\delta T}{T}(\hat{\mathbf{n}}') \right\rangle d\Omega d\Omega' \\ &= \delta_{\ell \ell'} \delta_{m m'} C_\ell. \end{aligned} \tag{3.23}$$

The variance of the temperature anisotropies and the observed angular power spectrum are related to the multipoles ℓ

$$\left\langle \left(\frac{\delta T}{T}(\hat{\mathbf{n}}) \right)^2 \right\rangle = \left\langle \sum_{\ell m} a_{\ell m} Y_{\ell m}(\hat{\mathbf{n}}) \sum_{\ell' m'} a^*_{\ell' m'} Y^*_{\ell' m'}(\hat{\mathbf{n}}) \right\rangle$$

$$
\begin{aligned}
&= \sum_{\ell\ell'}\sum_{mm'} Y_{\ell m}(\hat{\mathbf{n}})Y^*_{\ell' m'}(\hat{\mathbf{n}})\left\langle a_{\ell m}a^*_{\ell' m'}\right\rangle \\
&= \sum_{\ell} C_\ell \sum_{m} |Y_{\ell m}(\hat{\mathbf{n}})|^2 \\
&= \sum_{\ell} \frac{2\ell+1}{4\pi} C_\ell . \qquad (3.24)
\end{aligned}
$$

The angular power spectrum depends on the power spectrum $\mathcal{P}(k)$ of density perturbations as well as CMB temperature anisotropies. If we have a uniform primordial power spectrum in a logarithmic interval, and the inflation predicts that the primordial power spectrum would be nearly a constant, then normally the angular power spectrum is flat in the representation $\frac{\ell(\ell+1)}{2\pi}C_\ell$. The angular power spectrum plays an important role in the statistical analysis of the CMB. The angular power spectrum provides the information on cosmological parameters as well as the early Universe scenario.

The *cosmic variance* is the squared difference between observed spectrum $\hat{C}_\ell$ and the theoretical spectrum C_ℓ, in case of noiseless observation:

$$\left\langle \left(\hat{C}_\ell - C_\ell\right)^2 \right\rangle = \frac{2}{2\ell+1} C_\ell^2 . \qquad (3.25)$$

The cosmic variance is a fundamental limit of experimental measurement of the CMB to compare with theory. And it is important at low ℓ (the large scales). Note that a ground-based experiment can not cover full sky, therefore the cosmic variance is a function of the inverse sky observation f_{obs} [149]:

$$\left\langle \left(\hat{C}_\ell - C_\ell\right)^2 \right\rangle = \frac{2}{(2\ell+1) f_{obs}} C_\ell^2 . \qquad (3.26)$$

The two-point angular correlation function of the temperature on the sky is a function of $\cos\theta = \hat{\mathbf{n}}_\mathbf{1}\cdot\hat{\mathbf{n}}_\mathbf{2}$ [83]:

$$C(\cos\theta) \equiv \langle T(\hat{\mathbf{n}}_\mathbf{1})T(\hat{\mathbf{n}}_\mathbf{2})\rangle = \sum_\ell \frac{2\ell+1}{4\pi} C_\ell P_\ell(\cos\theta) . \qquad (3.27)$$

The measured and theoritical CMB temperature angular power spectrum C_ℓ^{TT} are plotted in figure 3.2. It contains three different regions [134, 149]:

- **The Sachs-Wolfe plateau $\ell \leq 100$:** At the large scales the variation in gravitational potential and temperature fluctuations are statistically nearly

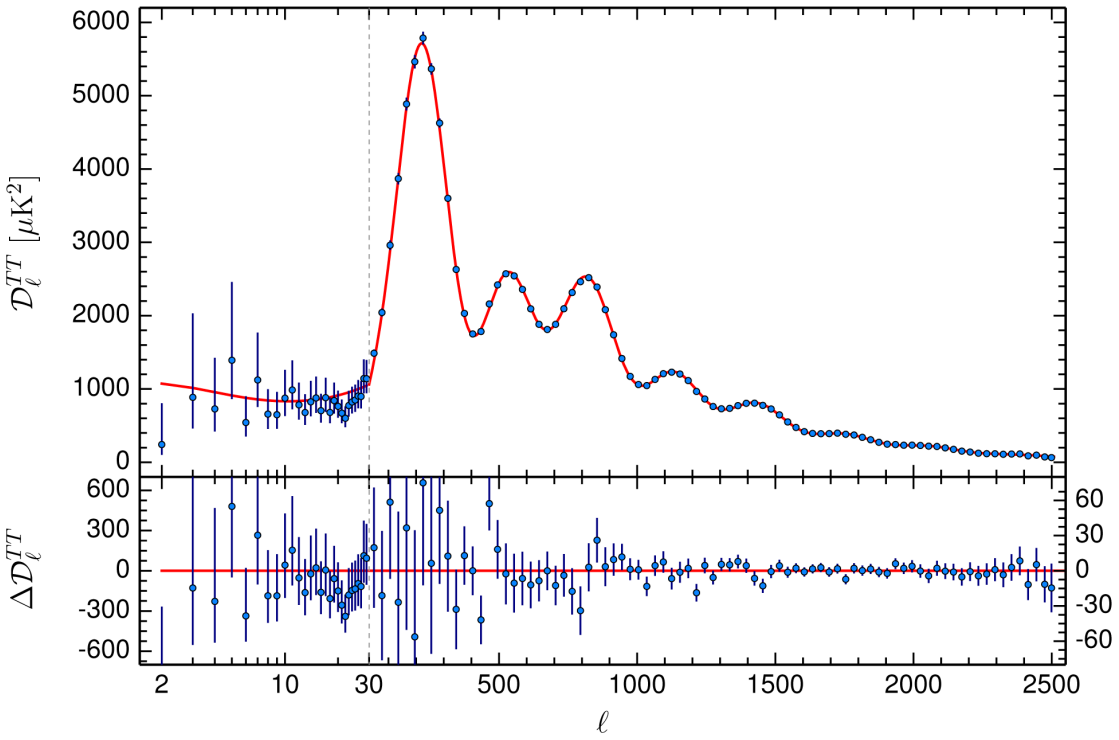

FIGURE 3.2: The temperature angular power spectrum $\frac{\ell(\ell+1)}{2\pi}C_\ell^{TT}$ measured by the Planck mission. The power spectrum has mainly three regions which are Sachs-Wolfe plateau; acoustic oscillation region and the damping. The red curve is the predicted theoretical spectrum while blue dots are the Planck data best-fit with 6 cosmological parameters. *Credit:ESA/Planck team*

flat. It corresponds to mode that did not enter the horizon at the time of CMB emission.

- **Acoustic oscillations peaks** $100 \leq \ell \leq 1000$**:** At the small scale, baryons-photons fluid interacted by photons pressure and baryons inertia, and produced oscillations in the CMB spectrum today.

- **Damping tail** $\ell \geq 1000$**:** At the very small scale, the smoothed damp tail is produced by the diffusion of photons-baryons fluid and imperfect recombination processes.

The first peak has angular scale $\sim 1^\circ \equiv \ell \sim 200$. This scale is related to the geometry of the Universe. The second peak is lower than the first peak, the ratio of the second to the first peak tells us about the baryon density. If we have more baryon matter (increase of the baryon density), the height of peaks is increasing. The damping tail contains information of diffusion of photons at the last scattering surface.

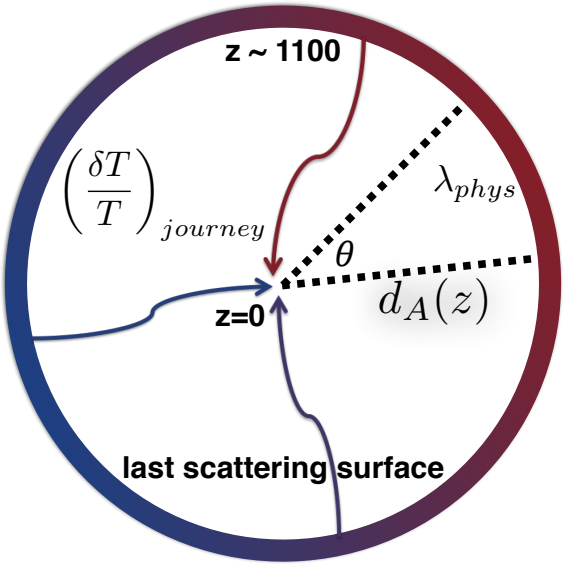

FIGURE 3.3: The surface of last scattering (LS).

Angular size $\delta\theta_{LS}$ to the last scattering surface

The CMB temperature fluctuations at the time of last scattering have the small angular size $\delta\theta$ related to the physical size λ_{phys} on the surface of last scatterings, and to the comoving angular diameter distance $d_A(z)$ to the last scattering surface, such as:

$$\delta\theta_{LS} = \frac{\lambda_{phys}}{d_A(z)}. \tag{3.28}$$

This is illustrated in figure 3.3. The comoving angular diameter distance redshift is related to the horizon distance of two regions on the last scattering surface $d_{hor}(t_{LS})$:

$$d_{hor}(t_{LS}) \equiv d_A(z) = \int_0^{z_{LS}} \frac{cdz}{H(z)}. \tag{3.29}$$

The Hubble parameter is given by the equation 2.44,

$$H(z) = H_0 \left[\Omega_{m;0}(1+z)^3 + \Omega_{r;0}(1+z)^4 + \Omega_{k;0}(1+z)^2 + \Omega_{\Lambda;0}\right]^{1/2}.$$

For a flat Universe, the comoving angular diameter distance and comoving distance are equal. For matter dominated Universe, $H(z) \approx (1+z)^{3/2}$. Then:

$$d_A(z) = \frac{c}{H_0}\int_0^{z_{LS}} (1+z)^{-3/2} dz = \frac{2c}{H_0}\left(1 - (1+z_{LS})^{-1/2}\right). \tag{3.30}$$

Because at the last scattering surface $z_{LS} \sim 1100$, the comoving angular diameter distance redshift is approximated as

$$d_A(z) = \frac{2c}{H_0}. \tag{3.31}$$

The physical distance λ_{phys} at the last scattering surface is the comoving distance or the particle horizon length $d_H(z)$:

$$\lambda_{phys} \equiv d_H(z) = \int_{z_{LS}}^{\infty} \frac{cdz}{H(z)} = \frac{2c}{H_0}(1 + z_{LS})^{-1/2}. \tag{3.32}$$

The angular size is calculated by dividing result of the equation 3.32 to the equation 3.31.

$$\boxed{\delta\theta_{LS} = (1 + z_{LS})^{-1/2} \approx 1.7^\circ}. \tag{3.33}$$

It means that the scale angle larger than 1.7° ($\ell \simeq 105$) were not in contact at the surface of the last scattering. This also refers to the horizon problem of the Universe which we mentioned in the chapter 2 section 2.6, and is solved by inflation.

Optical depth τ

After CMB emission, first stars and galaxies reionize the Universe. The reionization epoch happens at the redshift around $z = 6 - 25$ as illustrated in figure 2.2. The reionization epoch provides information of first stars and galaxies formation. The reionization epoch is constrained by the observed CMB. The optical depth of reionization refers to CMB photons last scattered from free electrons in the intergalactic medium. The Thomson scattering is an interaction of photons with electrons.

$$\gamma + e^- \rightarrow \gamma + e^-. \tag{3.34}$$

The differential cross-section of the interaction in a solid angle $d\Omega$ is [155]:

$$\frac{d\sigma_e}{d\Omega} = \frac{3\sigma_T}{8\pi}|\epsilon \cdot \epsilon'|^2. \tag{3.35}$$

where $\sigma_T = 6.65 \times 10^{-29} m^2$ is the Thomson cross-section. $|\epsilon \cdot \epsilon'|$ is the angle between scattered and incident photons. The mean free path (the distance of traveling photons to electrons) is defined as [129]:

$$\lambda_\gamma = \frac{1}{n_e \sigma_e}, \tag{3.36}$$

where n_e is the number density of electrons, the number density of electrons depends on the redshift $n_e(z)$. Since the speed of photons is c, the scattering rate of photons is given by

$$\Gamma(z) = \frac{c}{\lambda_\gamma} = n_e(z)\sigma_e c, \tag{3.37}$$

When we collect CMB photons at time t_0, these photons have been scattred by free electrons in the intergalactic medium. Thus the optical depth [129] is:

$$\tau(t) = \int_t^{t_0} \Gamma(t')dt', \tag{3.38}$$

at the surface of last scattering, $\tau = 1$. We can change the variable into the scale factor and remembering that $H = \dot{a}/a$:

$$\tau(a) = \int_a^1 \Gamma(a)\frac{da}{\dot{a}} = \int_a^1 \frac{\Gamma(a)}{H(a)}\frac{da}{a}. \tag{3.39}$$

We can express the optical depth as a function of redshift using $1 + z = 1/a$:

$$\boxed{\tau(z) = \int_0^z \frac{\Gamma(z)}{H(z)}\frac{dz}{1+z} = \int_0^z \frac{dz}{H(z)(1+z)} n_e(z)\sigma_e c}. \tag{3.40}$$

The Hubble parameter is given as a function of redshift in the equation 2.44. According to the Beer-Lambert law of attenuation of light traveling in the material and physics of CMB photons, the amplitude of temperature angular power spectrum at the reionization bump is approximately

$$\boxed{C_\ell \approx A_s e^{-2\tau}}, \tag{3.41}$$

where A_s is the scalar amplitude. The measurement of τ value plays an important role to determine the primordial B-mode power spectrum as well as the tensor-to-scalar value and to study the epoch of reionization. On the other hand, the Sunyaev-Zeldovich effect which is distortions of CMB photons through the InterGalactic Medium (IGM) by interaction with high energy electrons (inverse Compton scattering), effects the temperature fluctuations on all scales [91]:

$$\frac{\delta T}{T} \rightarrow \frac{\delta T}{T} e^{-\tau}. \tag{3.42}$$

3.2 Physics of CMB temperature anisotropies

Many physical sources contribute to CMB anisotropies. We classify them into primary and secondary anisotropies. The primary anisotropies arise at the recombination epoch while the secondary anisotropies are caused by the anisotropies of photons distribution between the last scatering surface and the observers. As we already described, the early Universe was filled by baryons-photons fluid in a gravitational potential interaction, baryons matter attract each other and fall in the dark matter potential well. When the baryons density increases, the pressure will be increase then the repulsion force due to radiation pressure appears. There are some of the primary anisotropies sources which described the mechanism of temperature anisotropies on large, intermediate and small angular scale [7, 91]:

- **The Sachs-Wolfe (SW) effect [130]:** Gravitational perturbations lead the intrinsic temperature variations at the last scattering surface due to photons climbing out or fall into gravitational potential wells $\delta\Phi$. There is also effect of higher temperature in higher density. This process links temperature anisotropies and gravitational potential fluctuations in the early Universe. The Sach-Wolfe effect is the combination of two effects arising from gravitational potential perturbations. Firstly, gravitational redshift effect due to photons climb out or fall into of the gravitational potential wells. The gravitational redshift is determined by:

$$\frac{\delta\nu}{\nu} \approx \frac{\delta\Phi}{c^2}, \tag{3.43}$$

  where ν is the frequency of the photons. Secondly, the time dilation at the last scattering surface, it occurs at the higher temperature at an overdensity region. The gravitational redshift effect is caused of the time dilation of scatering photons $\delta t/t = \delta\Phi/c^2$. Remember that the CMB temperature $T \propto 1/a(t)$, and in the matter-domonated era $n_\gamma \propto \rho_m \propto a^{-3} \propto T^3$, it follows that $\delta\rho/\rho = 3\delta T/T$. Moreover we can imply also $a \approx t^{2/3}, \rho \propto t^{-2}$. Finally we get [52, 148]:

$$\frac{1}{3}\frac{\delta\rho}{\rho} = \frac{-2}{3}\frac{\delta t}{t} = \frac{2}{3}\frac{\delta\nu}{\nu} \approx \frac{-2}{3}\frac{\delta\Phi}{c^2}. \tag{3.44}$$

The combining two processes are Sach-Wolfe effect, these fluctuations dominate at the large scale [126, 130]:

$$\boxed{\frac{\delta T}{T} \approx \frac{1}{3}\frac{\delta \Phi}{c^2}}. \tag{3.45}$$

- **Density (Adiabatic) perturbations:** The tight coupling of baryonic matter and radiations can compress the radiation resulting on the increasing of the temperature. The fraction of temperature perturbations in the radiation is as same as the fraction of density perturbations.

$$\boxed{\left(\frac{\delta T}{T}\right)_{obs} = \frac{\delta \rho}{\rho}}. \tag{3.46}$$

- **Doppler effect:** The Doppler velocity perturbations, there has a variation in wavelength of the photons when they are emitted by measuring structures with respect to us. If $\mathbf{v}$ is the photon fluid velocity in the last scattering surface and $\hat{\mathbf{r}}$ is the direction along the line of sight:

$$\boxed{\frac{\delta T}{T} = \frac{\delta \mathbf{v} \cdot \hat{\mathbf{r}}}{c}}. \tag{3.47}$$

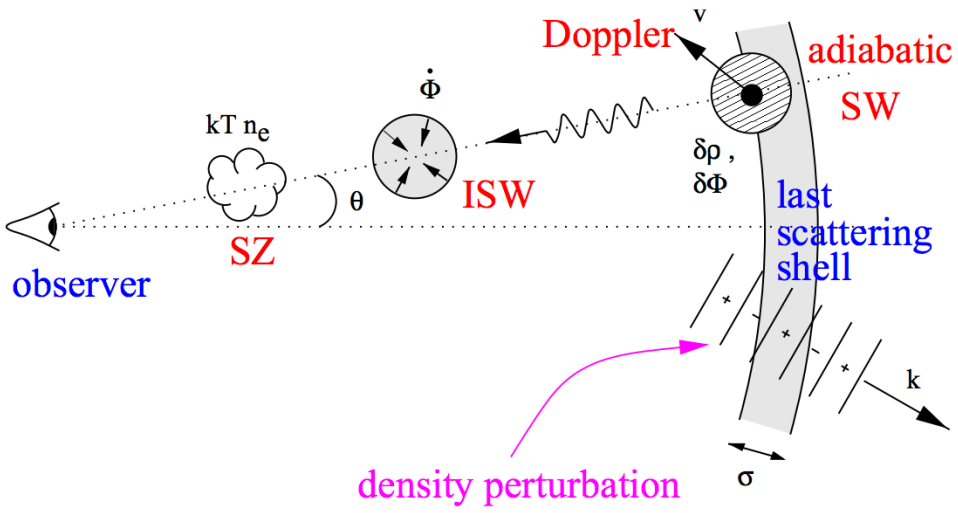

FIGURE 3.4: The physical mechanism of CMB temperature anisotropies. SZ stands for the Sunyaev-Zeldovich effect, ISW stands for the Integrated Sachs-Wolfe Effect. The desity perturbation at last scattering surface can be analysed in Fourier space with modes of wavevector $\mathbf{k}$ [91].

A full treatment solution of the mechanism of temperature anisoptropies was described in Wane Hu thesis in 1995 [51, 54, 56]. The mechanism of the original

anisotropies from baryons and gravity is that gravity introduced potential wells and affected to the amplitude of temperature oscillations. Baryons-photons perturbations oscillated the process created acoustic peaks in the temperature fluctuations by compression and expansion of photons-baryons plasma fluid. During their travel, photons interacted with the large-scale structures of the Universe from the last scattering surface. Consequently, secondary anisotropies are present in the CMB maps, and then these oscillation peaks depend on the dark matter, the dark energy, the baryons density and so on. Figure 3.5 shows the shift of the temperature angular power spectrum with respect to cosmological parameters.

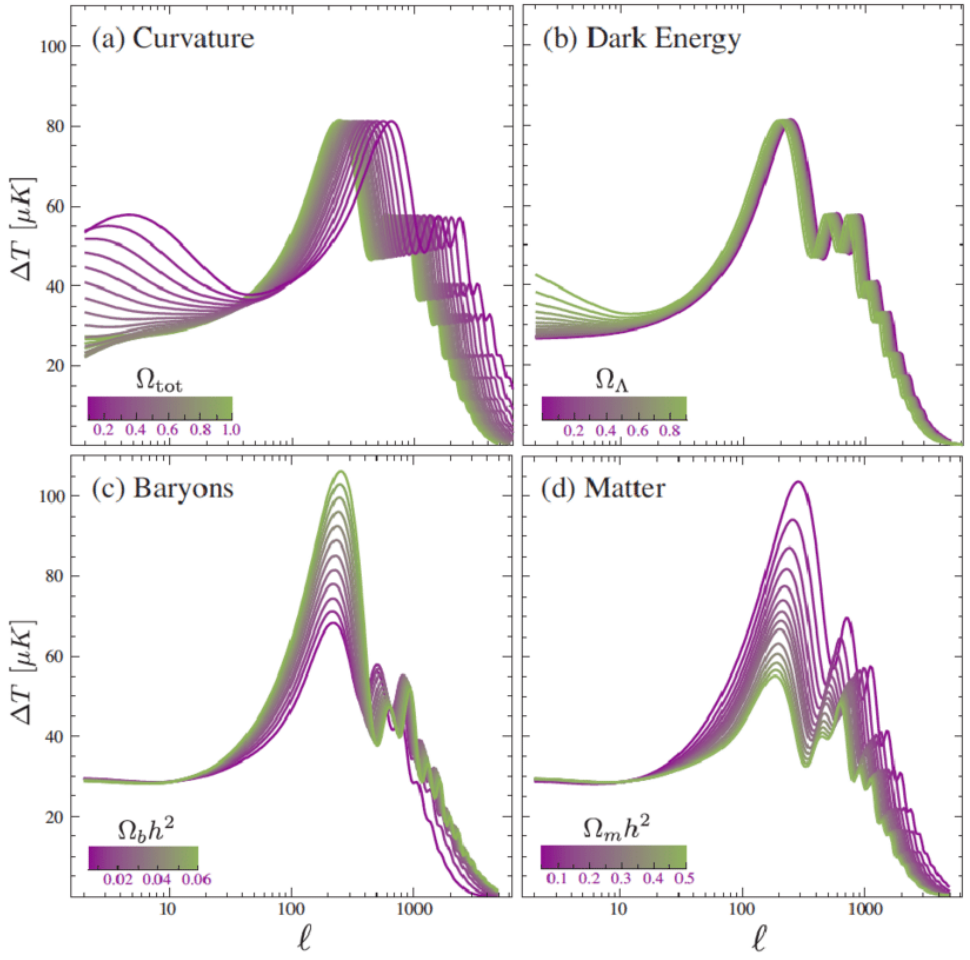

FIGURE 3.5: The variation of Baryon acoustic peaks of the temperature angular power spectrum and 4 cosmological parameters which are varied around the fiducial point: The curvature $\Omega_{tot} = 1$, the cosmological constant or dark energy $\Omega_\Lambda = 0.65$, the physical baryon density $\Omega_m h^2 = 0.02$, the physical matter density $\Omega_m h^2 = 0.147$ [52].

3.3 CMB polarization

Temperature anisotropies at the last scattering surface are evidence of primordial fluctuations at the early Universe. Local temperature anisotropies at the last scattering surface lead to the polarization of photons via Thomson scattering as shown in figure 3.6.

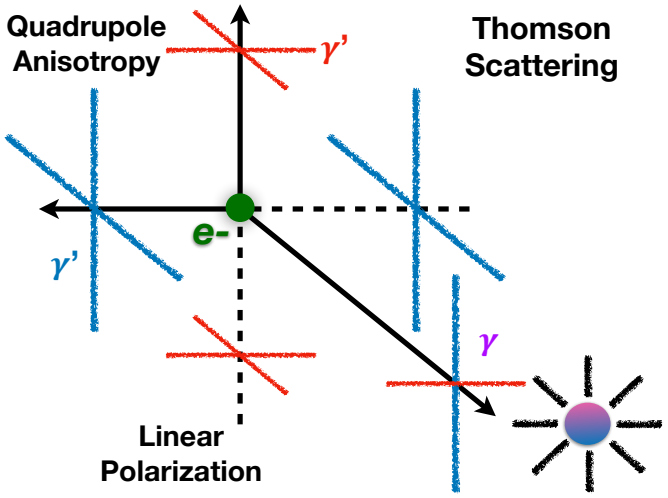

FIGURE 3.6: The temperature perturbation via quadrupole anisotropies with Thomson scattering of hot, cold radiations and electrons generated linear horizontal/vertical polarization.

Thomson scattering is the interaction of an electromagnetic wave with a free electron. The scattered wave is polarized perpendicular to the incidence direction. Because of incident photons from a perpendicular direction have different intensities, then the result is linearly polarized. Local quadrupole anisotropies in the distribution on photons produces a net polarization (because the poles of an anisotropy are $360°/4 = 90°$) ($\ell = 2$, $m = 0, \pm 1, \pm 2$). The CMB photons only scatter when there are still free electrons in the last scattering surface. Thus the polarization could be produced during a short time at the end of recombination epoch. Consequently, we only have a small fraction of polarization of CMB photons. It depends on the thickness of the last scattering duration. The polarized signal is at about 10^{-6} or several μK which is $\sim 10\%$ of the temperature anisotropies of 10^{-5} level. This order of magnitude is the reason for experimental challenges [57]. These quadrupole anisotropies are created by scalar and tensor perturbations.

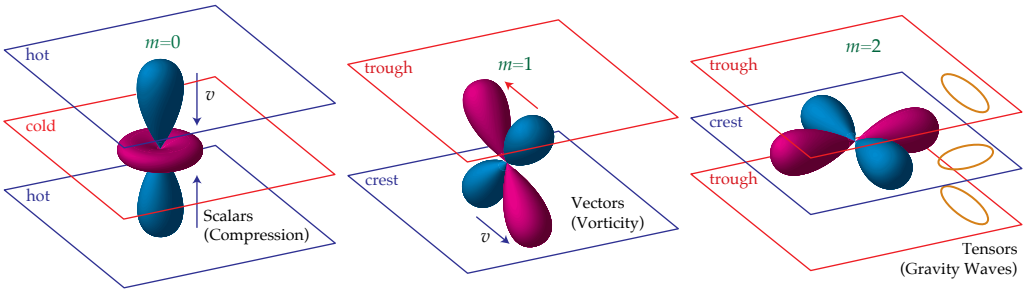

FIGURE 3.7: There have three different sources of quadrupoles anisotropies. Scalar perturbations originated from density perturbations, vector perturbations originated from the primordial fluid. In the physic of inflation, these vector perturbations are decay with the expansion of the Universe then we are negligible them. Tensor perturbations are evidenced by primordial gravitational waves from inflation which affected to density fluctuations resulting from the transformation of gravitational well [57, 149]. *credit: Wayne Hu*

If a monochromatic light wave propagates in the $z-$direction, the electric field at a given point:

$$E_x = E_{0x}\cos\left(\omega_0 t - \vartheta_x(t)\right) \quad ; \quad E_y = E_{0y}\cos\left(\omega_0 t - \vartheta_y(t)\right), \tag{3.48}$$

In order to simplify understanding of the polarization properties, the polarization of the CMB can be described by the Stokes parameters. The Stoke parameters are defined as:

$$\begin{aligned} I &\equiv \langle E_{0x}^2\rangle + \langle E_{0y}^2\rangle; \\ Q &\equiv \langle E_{0x}^2\rangle - \langle E_{0y}^2\rangle; \\ U &\equiv \langle 2E_{0x}E_{0y}\cos(\vartheta)\rangle; \\ V &\equiv \langle 2E_{0x}E_{0y}\sin(\vartheta)\rangle. \end{aligned} \tag{3.49}$$

Where $\vartheta = \vartheta_y - \vartheta_x$, E_{ox} and E_{oy} are components orthogonal to the propagation. The Stoke parameter I represents for intensity of the radiation which can be the CMB temperature. The linear polarization is Q and U parameters, Q parameter states in x-y directions while U parameter is rotated by 45°. The V parameter is the circular-polarization, in the Thomson scattering process, V is vanished. Nature light or unpolarized radiation has $Q = U = V = 0$. If the CMB radiation is rotated during its propagation because of Faraday rotation with a rotated angle

α, we can write:

$$\begin{pmatrix} Q' \\ U' \end{pmatrix} = \begin{pmatrix} \cos 2\alpha & \sin 2\alpha \\ -\sin 2\alpha & \cos 2\alpha \end{pmatrix} \begin{pmatrix} Q \\ U \end{pmatrix}. \tag{3.50}$$

The linear polarization parameters Q, U can be described as a symmetric trace-free 2×2 tensor, and depend on the coordinate system. Nevertheless it is possible to decompose the polarization Q, U in 2 fields which are independent of the coordinate system. We can decompose the polarization Q, U in the second-order spin spherical harmonics space are [144]:

$$(Q \pm iU)(\hat{\mathbf{n}}) = \sum_{\ell m} a_{\pm 2\ell m}\, Y_{\pm 2\ell m}(\hat{\mathbf{n}}). \tag{3.51}$$

We can then define the two orthogonal combination of E-mode and B-mode by analogy to the to electric (also known as Gradient-G) and magnetic (also known as Curl-C) fields. Their spherical harmonics coefficents are introduced as [24, 135, 153, 154]:

$$\begin{aligned} a^E_{\ell m} &= -\frac{a_{2\ell m} + a_{-2\ell m}}{2} \\ a^B_{\ell m} &= i\frac{a_{2\ell m} - a_{-2\ell m}}{2}. \end{aligned} \tag{3.52}$$

Then the two scalar (spin 0) E and B are defined as

$$\begin{aligned} E(\hat{\mathbf{n}}) &= \sum_{\ell m} a^E_{\ell m} Y_{\ell m}(\hat{\mathbf{n}}) \\ B(\hat{\mathbf{n}}) &= \sum_{\ell m} a^B_{\ell m} Y_{\ell m}(\hat{\mathbf{n}}). \end{aligned} \tag{3.53}$$

The E and B modes completely describe the linear polarization, E-mode polarization is represented as *curl-free* modes which are radial around cold spots and tangential around hot spots. B-mode polarization is a *divergence-free* which has *curl-free* also. B-mode polarization has vorticity around spots. Figure 3.8 shows the pure maps of E- and B- mode patterns. They are invariant under coordinate rotations but in a parity transformation, the E-mode is unchanged while the B-mode changes sign. Scalar perturbations only produce E-mode, vector perturbations produce B-mode but they are sub-dominated because of the expansion of the Universe, therefore, believed to be negligible, tensor perturbations produce both E-modes and B-modes thus detection of B-mode polarization is the evidence

of primordial gravitational waves of the inflation epoch [18, 24, 136, 153].

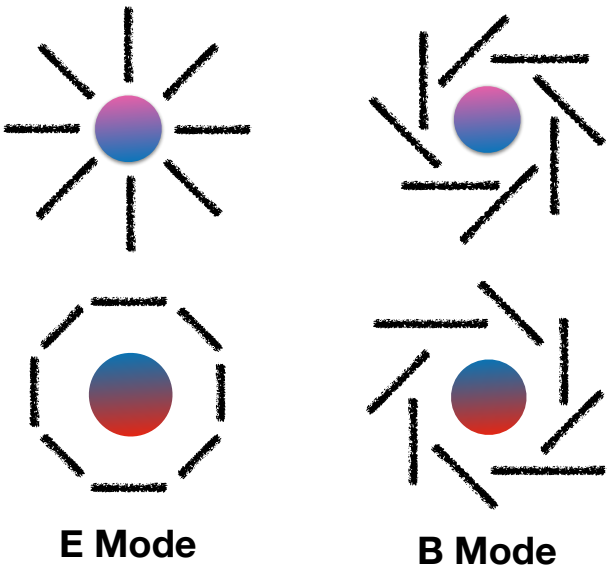

FIGURE 3.8: The representation of pure E- and B-modes.

As for equation 3.22, the angular power spectra of pure polarization, and temperature cross polarization are defined as:

$$\begin{aligned} C_\ell^{EE} &= \left\langle |a_{\ell m}^E|^2 \right\rangle \\ C_\ell^{BB} &= \left\langle |a_{\ell m}^B|^2 \right\rangle \\ C_\ell^{TE} &= \left\langle a_{\ell m}^T a_{\ell m}^{*E} \right\rangle \\ C_\ell^{TB} &= \left\langle a_{\ell m}^T a_{\ell m}^{*B} \right\rangle \\ C_\ell^{EB} &= \left\langle a_{\ell m}^E a_{\ell m}^{*B} \right\rangle . \end{aligned} \tag{3.54}$$

The second-order spin spherical harmonics have C_ℓ^{TB}, C_ℓ^{EB} equal 0. Figure 3.9 plotted the theoretical angular power spectra of temperature, polarization and cross term. The temperature angular power spectrum is well understood nowadays. The E-mode polarization is measured by many experiments while the amplitude of B-mode is not yet known.

As discussions in the chapter 2 section 2.10.2 the scalar perturbations produce E-modes polarization due to density perturbations while gravitational waves space-time produces B-mode. The definition of h_+ and $h_\times$ depend on coordinates system, but definitions of E-mode and B-mode polarisation do not depend on coordinates system. Therefore, h_+ does not always give E, $h_\times$ does not always give B. The important point is that h_+ and $h_\times$ always coexist. When a linear combination

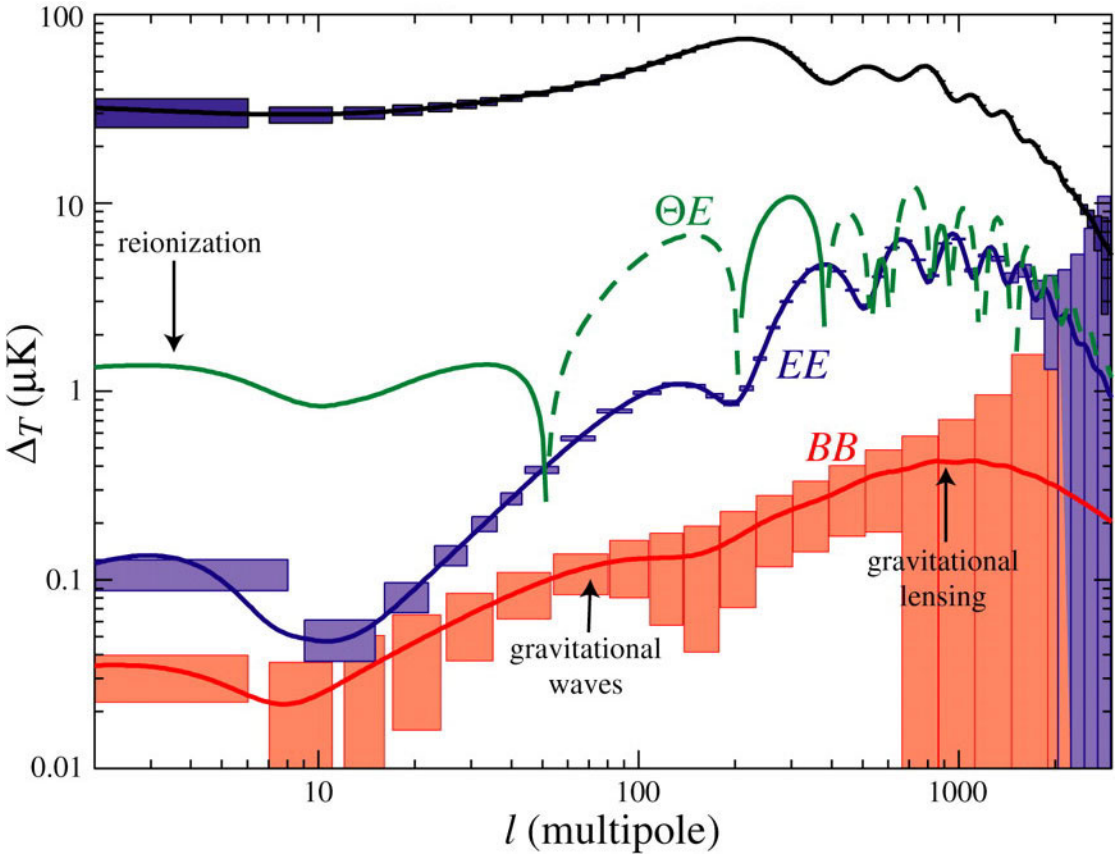

FIGURE 3.9: The temperature, polarization and temperature cross polarization angular power spectra. The 1σ statistical errors of the Planck satellite are shown by color boxed [52].

of h_+ and $h_\times$ produces E, another combination produces B. At the small angular scale, gravitational lensing produces B-mode from E-mode. The amplitude of B-mode at large angular scales is related to the tensor-to-scalar ratio r which gives the information of inflation scenarios, the energy of inflation in the early Universe as shown in equation 2.115 [57].

We can compute the power spectra in the Fourier space with the helppf spherical Bessel transfer functions $\Delta_{T\ell}(k), \Delta_{E\ell}(k), \Delta_{B\ell}(k)$. The details of the function can be found in the [Seljak & Zaldarriaga, Kamionkowski] papers [64, 136, 153]. The angular power spectrum of polarization E-mode and the cross term TE is dominated by scalar perturbation in inflation, it means:

$$\begin{aligned} C_\ell^{TE} &\approx (4\pi)^2 \int k^2 dk \underbrace{P_{\mathcal{R}}(k)}_{inflation} \Delta_{T\ell}(k)\Delta_{E\ell}(k), \\ C_\ell^{EE} &\approx (4\pi)^2 \int k^2 dk \underbrace{P_{\mathcal{R}}(k)}_{inflation} \Delta^2_{E\ell}(k). \end{aligned} \tag{3.55}$$

For B-mode which are only created by tensors perturbation in inflation:

$$C_\ell^{BB} = (4\pi)^2 \int k^2 dk \underbrace{P_h(k)}_{inflation} \Delta^2_{B\ell}(k). \tag{3.56}$$

The measurement of C_ℓ^{BB} is the unique way to access tensor perturbation information.

3.4 Primordial non-Gaussianity in the CMB

The inflation scenarios predict that the amplitude and the phase of energy density fluctuations in the early Universe are random variables following a very nearly Gaussian statistics, small deviations from Gaussianity might be expected for same inflationary models. These deviations are called non-Gaussianity (NG). Therefore, the statistical study of non-Gaussianity will tell us about the different theoretical models of inflationary paradigm. So far we have studied the second order statistics of the angular power spectrum of CMB fluctuations which depend on the primordial power spectrum $P_\mathcal{R}(k)$ in the Fourier space.

The primordial power spectrum contains all the information for a Gaussianity field. We need to go to higher order statistics to study the non-Gaussianity, the next order being the three-point function giving the primary measurement of non-Gaussianity. The computation of non-Gaussianity requires careful expansion of the third order of the action. Therefore I just show the main physical definition. The bispectrum of 3-point function in Fourier space is:

$$\langle \mathcal{R}_{\mathbf{k}_1} \mathcal{R}_{\mathbf{k}_2} \mathcal{R}_{\mathbf{k}_3} \rangle = (2\pi)^3 \delta(\mathbf{k}_1 + \mathbf{k}_2 + \mathbf{k}_3) B_\mathcal{R}(\mathbf{k}_1, \mathbf{k}_2, \mathbf{k}_3). \tag{3.57}$$

$B_\mathcal{R}(\mathbf{k}_1, \mathbf{k}_2, \mathbf{k}_3)$ is the primordial bispectrum, it has degree -6 [18], the primordial bispectrum leaves a signature in the CMB angular bispectrum on the sphere is

$$B^{\ell_1\ell_2\ell_3}_{m_1m_2m_3} = \langle a_{\ell_1 m_1} a_{\ell_2 m_2} a_{\ell_3 m_3} \rangle . \tag{3.58}$$

The *local non-Gaussianity* $\mathcal{R}_\mathbf{x}$ is defined through the curvature perturbation around the Gaussian $\mathcal{R}_g$ using a Taylor expansion. The local primordial non-Gaussianity is parametrized by the non-linear constant parameter f_{NL} which quantifies the

amplitude of non-Gaussianity for different shapes [18]:

$$\boxed{\mathcal{R}_{\mathbf{x}} = \mathcal{R}_g + \frac{3}{5} f_{NL} \left[\mathcal{R}_g(\mathbf{x})^2 - \left\langle \mathcal{R}_g(\mathbf{x})^2 \right\rangle \right]}. \tag{3.59}$$

The bispectrum of the local non-Gaussianity is

$$B_{\mathcal{R}}(k_1, k_2, k_3) = \frac{6}{5} f_{NL} \left[P_{\mathcal{R}}(k_1) P_{\mathcal{R}}(k_2) + P_{\mathcal{R}}(k_2) P_{\mathcal{R}}(k_3) + P_{\mathcal{R}}(k_3) P_{\mathcal{R}}(k_1) \right]. \tag{3.60}$$

The experimental measurements set constraints on the f_{NL} parameter. In addition, the gravitational lensing of CMB also produced a level of non-Gaussianity, hence the study of non-Gaussianity is important to test the fundamental inflation physics.

3.5 Gravitational lensing

The CMB photons propagation is affected by the gravitational field of the large-scale structure, galaxies, and stars. Gravitational lensing was studied by Einstein in 1912 and also predicted by the general relativity theory. By generating spacetime curvature bright object can induce blending the propagation of light. Microlensing is the lensing effect of stars in a galaxy, this effect is a useful tool to probe small scale substructures as well as dark matter in a galaxy, dark matter halos, while cosmic shear is produced by gravitational lensing at large-scale structure of the Universe.

The CMB photons travel through the large-scale structure to us from the last scattering surface. Like cosmic shear of galaxy clusters, the temperature and polarization anisotropies of CMB is a type of the gravitational lensing effect and it distorts the hot and cold spots. In contrast to the cosmic shear, CMB lensing is the lensing of Gaussian random fields. The weak lensing effect converts E mode to B mode at small angular scales $\ell \geq 300$ and gravitational weak lensing has contamination of B mode from primordial gravitational waves. We can calculate the lensing effect in the CMB power spectrum, as well as the mixing of E-mode and B-mode polarization. Many studies of gravitational lensing in the CMB can be found in the [7, 53, 55, 133, 138].

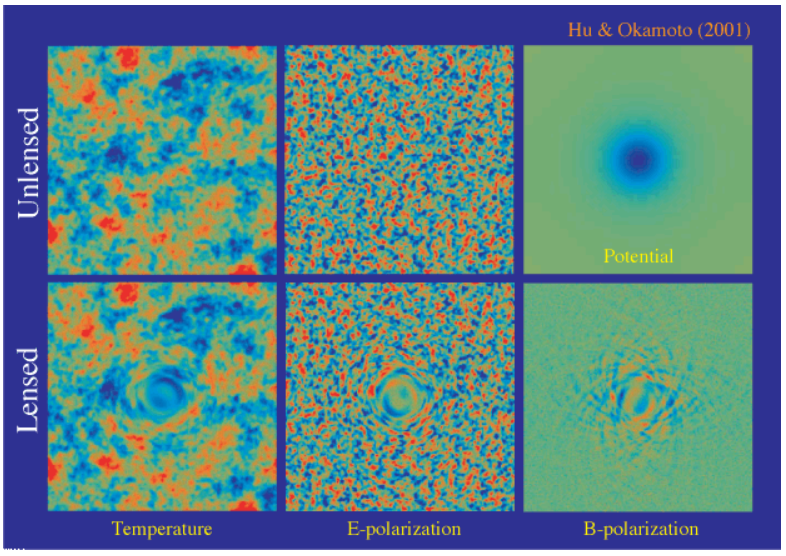

FIGURE 3.10: An example of CMB lensing effect on $10° \times 10°$. *Credit: Wayne Hu & Takemi Okamoto.*

3.6 CMB spectral distortions

CMB spectral distortions are departure the CMB spectrum from a pure black body spectrum due to its interaction with the matter in the Universe. Many processes are sources of spectral distortions such as reionization and structure formation, decaying or annihilating particles, dissipation of primordial density fluctuations, cosmic string, primordial black hole, small-scale magnetic fields, adiabatic cooling of matter, cosmological recombination ... [27]. The spectral distortions reach the level of $\sim 10^{-7}$–10^{-6} relative to the CMB. There are two types of the CMB spectral distortions which are the chemical potential $\mu \leq 9 \times 10^{-5}$ and Compton $y \leq 1.5 \times 10^{-5}$ distortions as shown in figure 3.11. μ distortions is created by photon injection due to particle decays via Compton scattering at the early Universe [28, 143]. y distortions is also named the thermal Sunyaev-Zel'dovich effect. The CMB photons travel through galaxy clusters thus CMB photons can be scattered by hot electrons in the gas via Compton scattering, this phenomenon is so-called the thermal Sunyaev-Zel'dovich (SZ) effect [139, 140]. Consequently, the temperature of CMB photons is changed in the blackbody spectrum. The Compton y parameter is calculated as [29]:

$$y = \int \frac{kT_e}{m_e c^2} n_e \sigma_T dl, \tag{3.61}$$

here σ_T is Thomson cross section, n_e and T_e are the electron number density and temperature respectively, dl is the path length through clusters. Basically, we have $kT_e/m_e c^2 \sim 0.01$ and the Thomson optical depths $\tau_T = \int n_e \sigma_T dl \sim 0.01$. Thus the

value of y distortion is typically of the order of 10^{-4}. The change in temperature of CMB photons due to thermal SZ effect is [29]:

$$\frac{\Delta I(\nu, \hat{\mathbf{n}})}{I_{CMB}(\nu, \hat{\mathbf{n}})} = y \frac{x e^x}{e^x - 1} \left[x \frac{e^x + 1}{e^x - 1} - 4 \right], \tag{3.62}$$

where $x = \dfrac{h\nu}{kT_{CMB}}$.

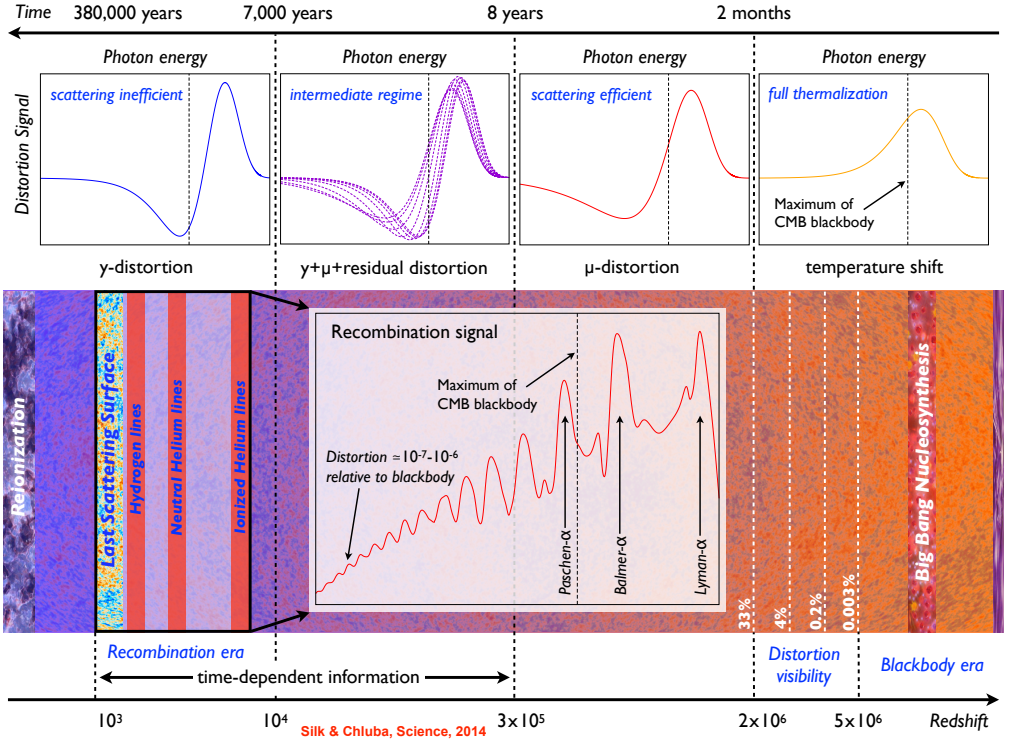

FIGURE 3.11: Different signals of CMB spectral distortions in the early Universe. μ and y distortions are redshift independent. After the BigBang Nucleosynthesis, the energy is release at redshift at $\sim 5 \times 10^6$. μ distortions arises at $3 \times 10^5 \leq z \leq 2 \times 10^6$. The transition μ, y distortions is at $10^4 \leq z \leq 3 \times 10^5$. y distortion arises at recombination epoch due to atomic transitions of hydrogen and helium. *Credit: Silk & Chluba*

From the study of spectral distortions, we can learn the reionization and structure formation history, the cosmological recombination spectrum, the dissipation of small scale acoustic modes, constraints on the tensor-to-scalar ratio B-modes and various scenarios [27].

3.7 Foreground components

In order to estimate the CMB signal, we have to perform foreground component separation. There are many sources of foregrounds which consists of emissions between us and the CMB. The most important are Glactic dust emission and Galactic synchrotron. Figure 3.12 shows the instrumental noise, the galactic foreground, the galaxie cluster SZ emission. The transmission bands of future CMB missions are expected to avoid the rotational lines of carbon monoxide which is emitted in the epoch of star formation in the Universe. CO lines: CO J $= 1 \rightarrow 0$ (115.3 GHz), CO J $= 2 \rightarrow 1$ (230.5 GHz), CO J $= 3 \rightarrow 2$ (345.8 GHz), CO J $= 4 \rightarrow 3$ (461.0 GHz), CO J $= 5 \rightarrow 4$ (576.3 GHz), CO J $= 6 \rightarrow 5$ (691.5 GHz), CO J $= 7 \rightarrow 6$ (806.7 GHz), J is the angular-momentum quantum number [128].

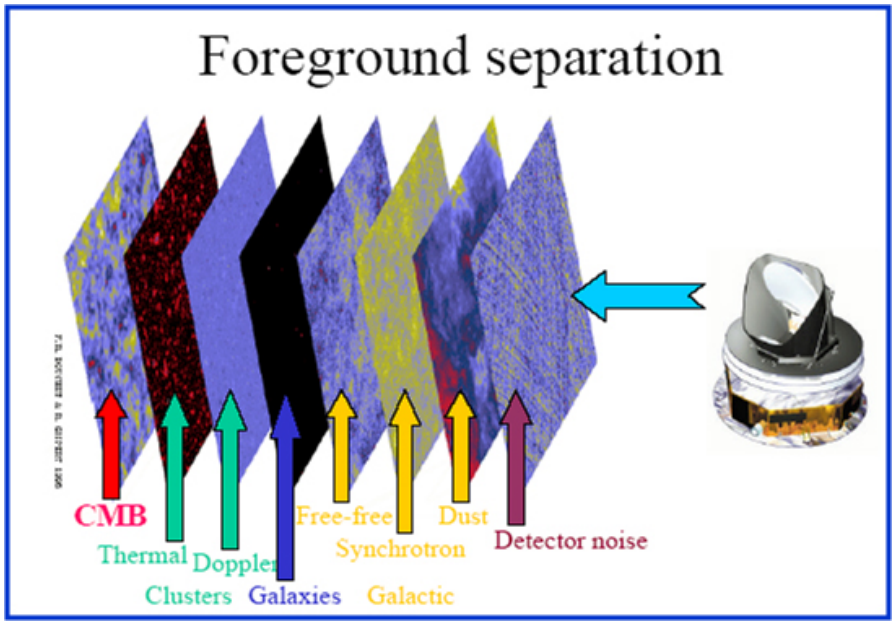

FIGURE 3.12: The foreground components, the detector noise, galactic emission: Dust, Free-free, synchrotron, cluster: Doppler effect, thermal SZ effect.

Figure 3.13 indicates the dominated source of galactic components at frequencies relevant to CMB observation. Foreground emissions are polarized, the B-mode signal has ≤ 1 % of the level of the foreground emission. The sum of the foreground signal is always larger than the CMB B-mode signal at all frequencies. So that the foreground subtraction and separation play an important role in data analysis at different frequencies for CMB measurements [60, 106]. In this small section I focus on the contamination of our galactic foreground emissions which are free-free, spinning dust, synchrotron and thermal dust.

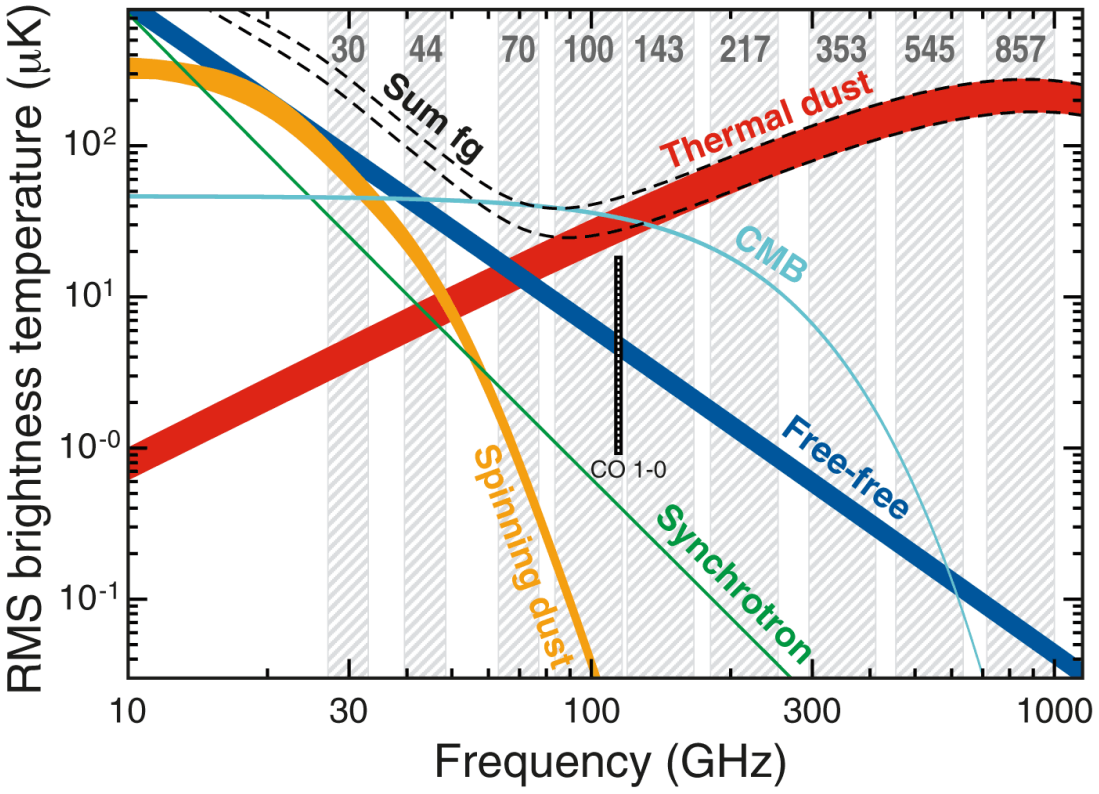

FIGURE 3.13: The microwave sky components, the frequency bands are the Planck focal plane [105].

There have several component separation methods classified as internal template fitting, parametric methods, and non-parametric methods (internal linear combination, independent component analysis). **Commander** is a Bayesian procedure for the CMB and foreground components and Monte Carlo method used Gibbs sampling for CMB power spectrum [42]. **NILC (Needlet Internal Linear Combination)** for which, the CMB component is computed minimizing variance by linear combination while the foreground is removed out using multi-frequency infarction [37]. **SEVEM (Spectral Estimation Via Expectation Maximisation)** is an internal template subtraction method. The method estimates foreground components using high and low frequency channels, then subtracting them out at CMB frequencies [44], **SMICA (Spectral Matching Independent Component Analysis)** is a method of the independent component analysis applied in the angular spectrum domain [36, 60, 112]. These methods normally assume that observed maps are a linear mixture of unknown components [127]. The methods assume the sky temperature at a pixel position $\hat{\mathbf{n}}$ and the frequency ν is a

superposition of components $X_i(\hat{\mathbf{n}})$ and noise $n(\hat{\mathbf{n}}, \nu)$:

$$T\left(\hat{\mathbf{n}}, \nu\right) = \sum_i \alpha_i(\nu) X_i(\hat{\mathbf{n}}) + n(\hat{\mathbf{n}}, \nu), \tag{3.63}$$

here $\alpha_i(\nu)$ are the component amplitude coefficients which depend on frequency of foreground emission.

3.7.1 Thermal dust

One of the major foreground component effecting to the study of CMB is the galactic thermal dust emission which arises from the interstellar dust grain in the microwave sky at $\geq 70\,GHz$ frequencies [101] and it is heated by stars light. The spectrum of thermal dust is a modified black-body

$$\mathrm{I}_{\mathrm{dust}}\left(\hat{\mathrm{n}}\right) = \tau_{\nu_0}\left(\hat{\mathrm{n}}\right) \times \left(\frac{\nu}{\nu_0}\right)^{\beta_\mathrm{d}} \times \mathrm{B}(\nu, \mathrm{T_d}). \tag{3.64}$$

Here $\tau_{\nu_0}\left(\hat{n}\right)$ is the dust optical depth at frequency ν_0, orientation $\hat{n}$, β_d is the spectral index. $B(\nu, T)$ is the Planck function at frequency ν and the dust temperature T_d [96]. The spectral index of dust is an important parameter of separation the dust and the CMB polarization [115]. Figure 3.14 represents the Planck 2018 re-

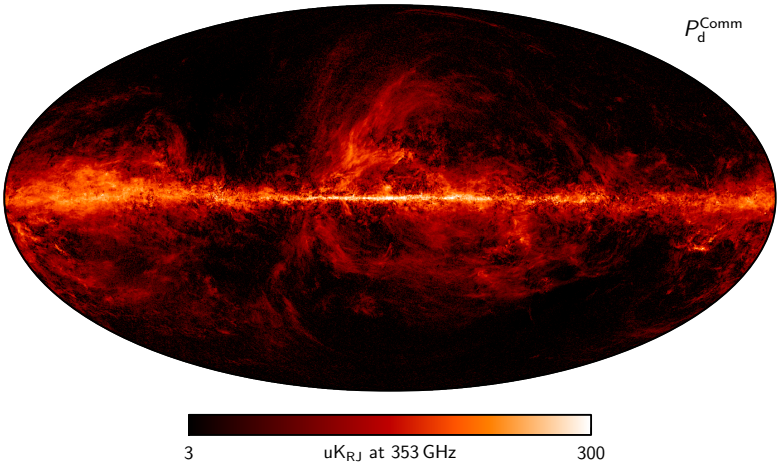

FIGURE 3.14: The Planck 2018 result of thermal dust polarization at 353 GHz using Commander method with 5′ FWHM resolution [117].

sult of the galactic thermal dust at 353 GHz. In the Galactic plane regions the dust temperature gradient can be observed from 14 K to 19 K. Because of differences in size and component then the emitted photons from thermal dust can be

polarized. Observations have showed that the level of thermal dust polarization is about 10 % [34, 114].

3.7.2 Synchrotron

Synchrotron radiation or magnetobremsstrahlung is emitted due to free electrons cosmic rays spiraling in the magnetic field of the Milky Way. The contamination of synchrotron is 10 % polarization of CMB signal at low frequencies ($\leq 80\,GHz$), it gets higher at lower frequency for the P06 mask $|b| < 5^{\circ}$ [60]. The intensity and the energy depend on the electron density and the strength of the magnetic field, the energy distribution of electrons follows a power law $N_e(E) \propto E^{-p}$ with index p and the spectrum of synchrotron emission is:

$$\mathrm{T}_{\mathrm{sync}}\,(\nu) \propto \mathbf{B}^{(\mathrm{p}+1)/2}\nu^{\beta_{\mathrm{s}}}. \tag{3.65}$$

Here $\mathbf{B}$ is the magnetic field of our Galaxy ($\mathbf{B} \approx 5 \times 10^{-6}\,G$). The spectral index $\beta_s = -(p+3)/2$ has the value ≈ -2.5. In order to model synchrochon emission for component separation, the variation and uncertainty in the spectral index is an important issue in foreground studies. In addition, the galactic cosmic rays and the magnetic field are necesary to model accurately and remove foreground polarization [34, 38, 146]. Figure 3.15 represents Planck 2018 result of synchrotron polarization map at 30 GHz. The larger polarization region at high latitudes are the local structures of the Milky Way. These directions are not good to observe CMB polarization.

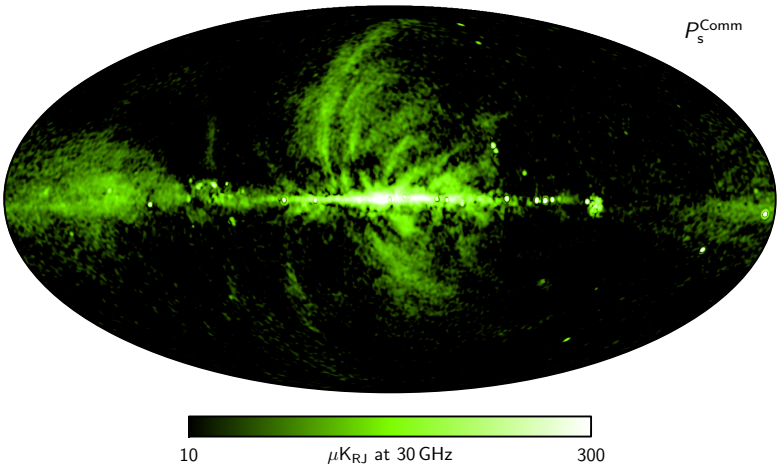

FIGURE 3.15: The Planck 2018 result of syncrochon polarization at 30 GHz using Commander method with 40′ FWHM resolution [117].

3.7.3 Free-free

Free-free or thermal Bremsstrahlung is an emission mainly at low frequencies of the electron-ion (warn ionized medium) scattering through the interaction of free electrons with positive charge nuclei in interstellar plasma [34]. It is unpolarized emission because of the isotropic and random direction of scattering electrons [60]. The spectral index of free-free emission depends only on the electron temperature T_e. Planck measured the $T_e \approx 8000K$ the the brightness temperature of the free-free emission follows a power law with the spectral index ~ -2.14 [146].

$$T_B \approx \nu^{-2.14}. \tag{3.66}$$

3.7.4 Spinning dust

Anomalous microwave emission (AME) or spinning dust is a observed Galactic foreground which is compatible with the model of Draine and Lazarian [39] of very fast spinning of nano dust grains. Another candidate for AME is thermal fluctuations of the magnetic pole of small silicate grains [146]. The spectral index of AME is close to the thermal dust spectral index $\beta_{AME} \approx -2.5$. The AME is expected to have a very small amount of polarization and it falls rapidly at high-frequency [60].

3.8 Systematic effects

In this section, I will present the most important systematic effects which impact to the measurement of CMB polarization from learned lessons of Planck mission for future CMB projects. Figure 3.16 shows the contribution of systematic effect to final angular power spectra of Planck high-frequency instrument at 100 GHz and 143 GHz [103]. We have instrumental noise, pointing uncertainty, near and far sidelobes, ADC nonlinearity, temperature fluctuation. The main systematic effects are shown in the table 3.2. Generally, some of the systematic effects produce leakage from intensity to polarization signal. These effects lead to observe the spurious primordial B mode angular power spectrum. I will introduce some of the main systematics as an example that are relevant for future mission.

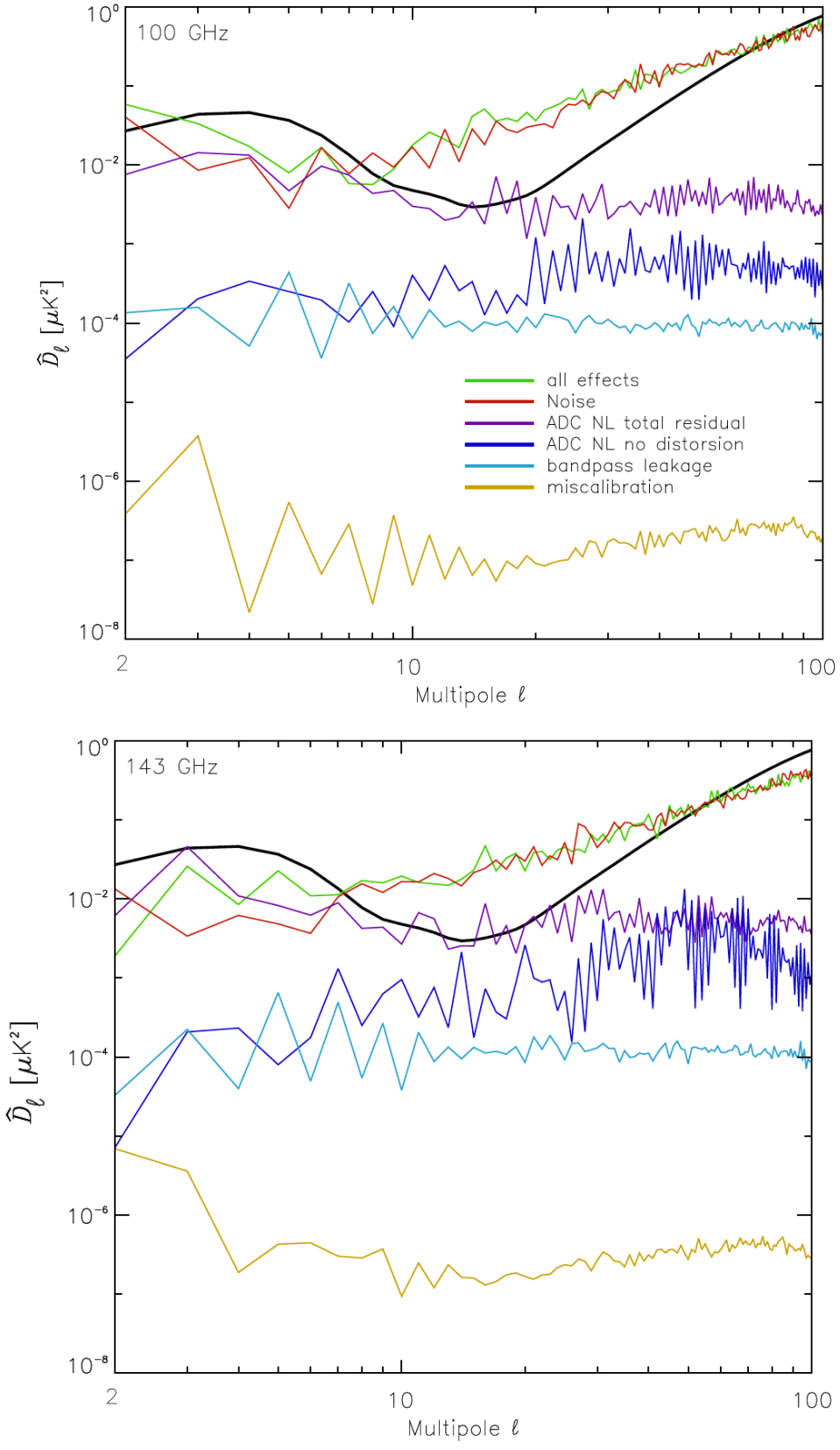

FIGURE 3.16: Power spectra of Planck HFI systematic effects, the black curves are EE angular power spectrum. [108].

Effect	Source	Leakage & issue
Cosmic rays	at Lagrange point 2	Loss data
Gain mismatch	Detector pair	T $\rightarrow$ E,B
Beam asymetry	Optical beams	T $\rightarrow$ E, B; E $\rightarrow$ B
1/f noise	RF amplifiers	T $\rightarrow$ E, B
Pointing uncertainty	Attitude control, Pointing reconstruction,	T $\rightarrow$ E, B
Bandpass mismatch	RF spectral filters	T $\rightarrow$ E, B
HWP ...	Imperfection HWP, 4f noise	T $\rightarrow$ E, B

TABLE 3.2: The main systematic effects table.

3.8.1 Cosmic rays

Planck had a significant contribution from cismic rays. The cosmic rays are high energy particles: 89 % proton 10 % α particles 1 % nuclei heavier elements and electrons. The main source of CRs at L2 is from the Milky Way galaxy and is affected by Solar flares. The flux of cosmic rays at L2 is about 5 $cm^{-2}s^{-1}$. Figure 3.17 shows contributions of glitches to the data. Cosmic rays penetrated the focal plane and produced glitches in Planck data. The Planck data experiences that CRs hit the silicon die, the absorber and the thermometer of bolometers. Their thermal energy produces short glitches (the time constant is of the order of a few miliseconds), long glitches (time constants are of the order of 60 ms and 2 s) and longer glitches (0.5-5s) and the rate is 2 glitches per second [100, 145]. After Planck, the technology of CMB projects evolved the use of Transition Edge Sensor (TES) or Kinetic inductance detector(KID). In order to study behavior respond times of detectors towards CRs, in the laboratory we can use a radioactive source. The detail of TES time constants study is described in chapter 5.

3.8.2 Beams

The beam is an instrumental angular response to the signal. We can clasify in [107, 120]:

- The optical beam is the response of an optical system which can be horns, antenna coupled to the telescope mirror. The optical beam represents the pure transfer function of the optical system.

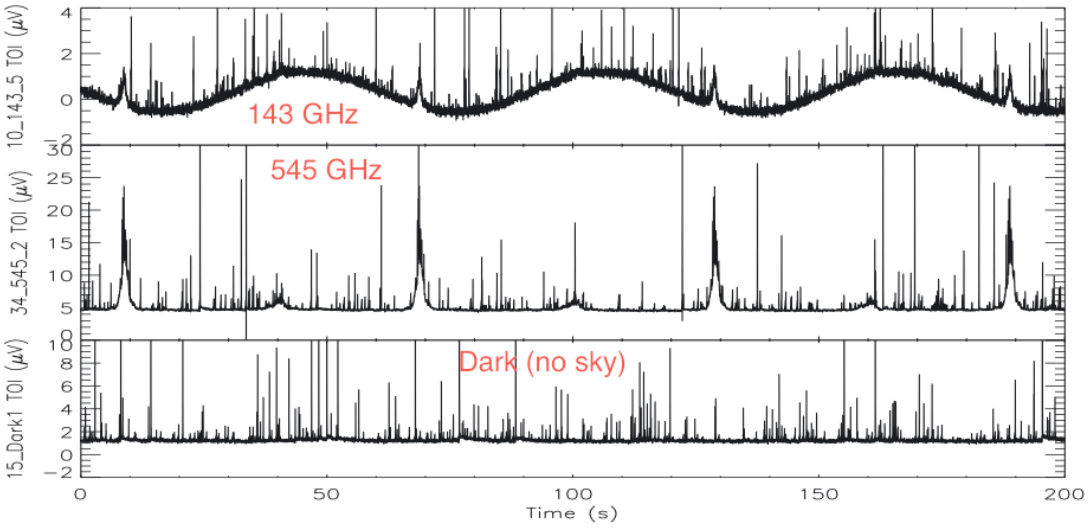

FIGURE 3.17: The Planck data of some detectors in around 200 seconds, the data is dominated by CMB dipole, galactic and cosmic rays.

- The scanning beam is defined by the beam in-flight. The scanning beam has three different components as the main beam which has angular up to 30', the near sidelobes have angular between 30' and 5°, the far sidelobes have angular beyond 5°.
- The effective beam is defined in the map domain for a given pixel by averaging scanning beams associated with a scanning strategy.

The convolution of the observed CMB signal and instrumental beam along the scanning strategy would produce leakage from intensity to polarization E mode, B modes. This convolution also induced mixing of E and B modes due to asymmetric beam so-called elliptical, gain mismatch and pointing mismatch. Beam ellipticity or beam mismatch is the result of astigmatic aberrations and detector time constants. The gain mismatch is caused by bandpass mismatch of detectors leading to different beam response functions. Pointing mismatch is the mismatch of center beams. Basically, we can write the signal $\mathbf{S}_i$ at the measurement i [49]

$$\mathbf{S}_i = \int d\mathbf{\Omega}\ \mathbf{b}_i\left(\mathbf{\Omega}\right)\ \Theta(\mathbf{\Omega}) + \mathrm{n}_i. \tag{3.67}$$

where $\Theta(\mathbf{\Omega})$ is the CMB signal at a solid angle location $\mathbf{\Omega}$. n_i is the instrumental noise, $\mathbf{b}_i\left(\mathbf{\Omega}\right)$ is the beam response. There have two approachs to study asymmetry of beam reponse systematic effect and correct from the data, the first implementation is directly in real space convolution (Fourier space). The second

implementation is in the spherical harmonics space convolution (angular power spectrum).

3.8.3 Bandpass mismatch

This effect is induced by differences in detector filters. These differences at the edges and shape of bandpass filters are measured and described in Planck publications [99, 103]. This effect is observed at percent level of variation. Figure 3.18 illustrates transmitted filters of many detectors of Planck satellite. The bandpass mismatch error produces leakage from temperature to polarization. The Bandpass mismatch error is an important systematic effect and impacts the estimation of primordial B-mode for future CMB experiments. The bandpass mismatch systematic effect is one of my PhD topics, this study is described in detail in Chapter 4.

3.9 State of the art

As we know the CMB power spectrum is close to a perfect blackbody. Since the discovery of CMB in 1964 by Penzias and Wilson using horn antenna, there have been 4 satellites RELIKT-1[3], COBE(Time observation: 1989-1993), WMAP(Time observation: 2001-2010), Planck(Time observation: 2009-2013) and many ground-based as well as balloon borne experiments. The European Space Agency's Planck mission made public final results in 2018. Figure 3.19 presents results of Planck 2018 and current different experiments. The temperature TT and E-mode polarization are well fit with concordance 6 parameters ΛCDM model while the next generation of experiments expects to measure B-mode polarization and will improve lensing measurements.

After two decades of Planck, the temperature anisotropies are measured with high accuracy. Now, scientists are moving to smaller projects including ground-based, balloon-borne experiments alongside with the space telescopes. The main focus is to measure the CMB polarization signal meeting the inflation. There always

[3]RELIKT-1 is a Soviet CMB anisotropies experiment. It launched 1 July 1983, its result reported a blackbody spectrum and anisotropies of CMB in January 1992. Nevertheless, the Nobel Prize in physics for 2006 was awarded to COBE team who announced the result on April 23, 1992.

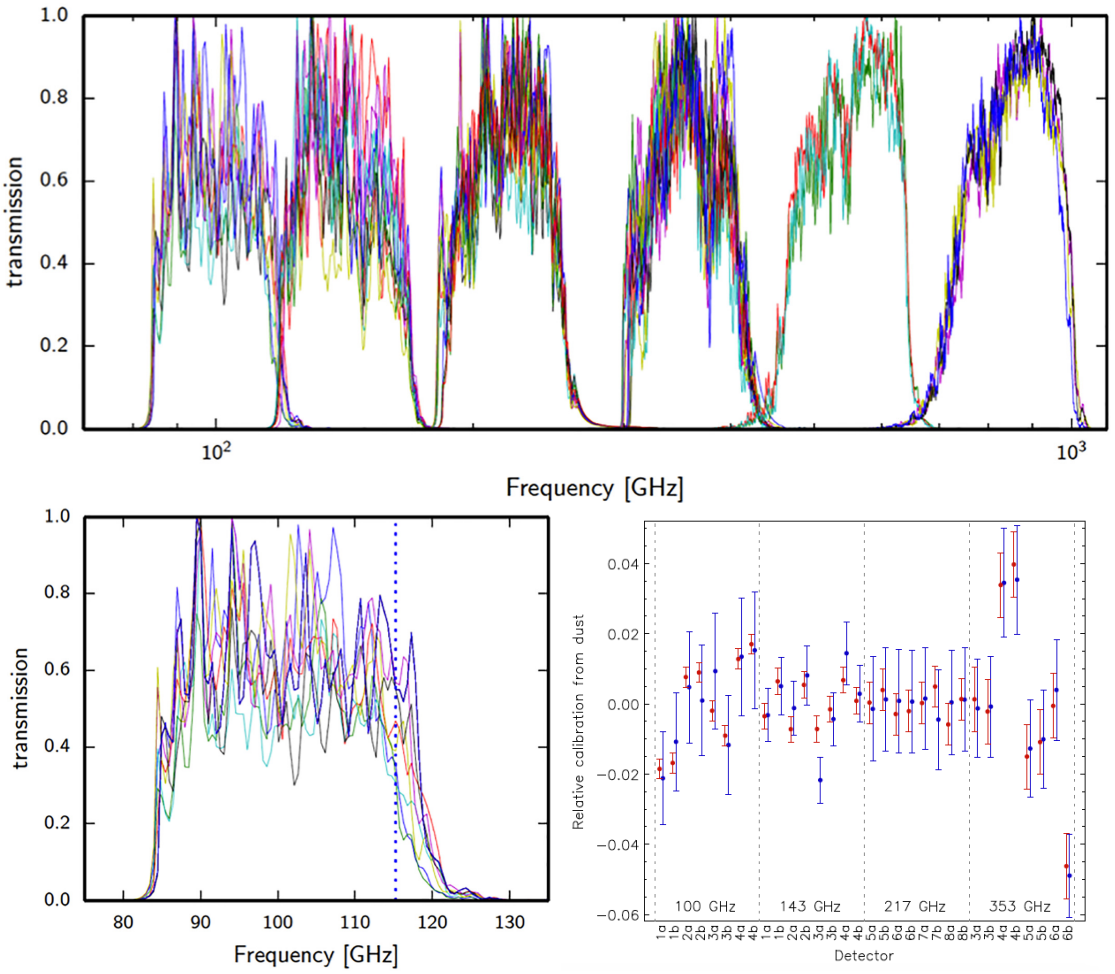

FIGURE 3.18: The spectral filters of Planck satellite. There are variations on the edges and top of filters. (*Bottom right*) The calibration from dust for each detector, blue points are ground test, red points are flight data [99, 103].

have advantages and disadvantages of satellites, ground-based, balloon-borne experiments. A satellite can cover full sky observation while the balloon-borne and ground-based can only cover a fraction of the sky. Due to constraints of weight and cost, the focal plane or the telescope size of satellites and balloons are usually limited in resolution compared to ground-based experiments that use a large telescope. The obvious difference between satellites and ground-based experiments is the atmosphere of the Earth. The ground-based experiments usually have to operate at a dry location and high attitude such as the South Pole, Atacama desert of Chile and Tibet. The balloon-borne experiments fly at around tens kilometers at attitudes with less effect of atmosphere but still receive some emission. Last but not least the time observation for balloons are usually short few days while for satellite and ground are several years [149]. All the observation has to face with astrophysical foreground emissions and systematic effects of the experiment.

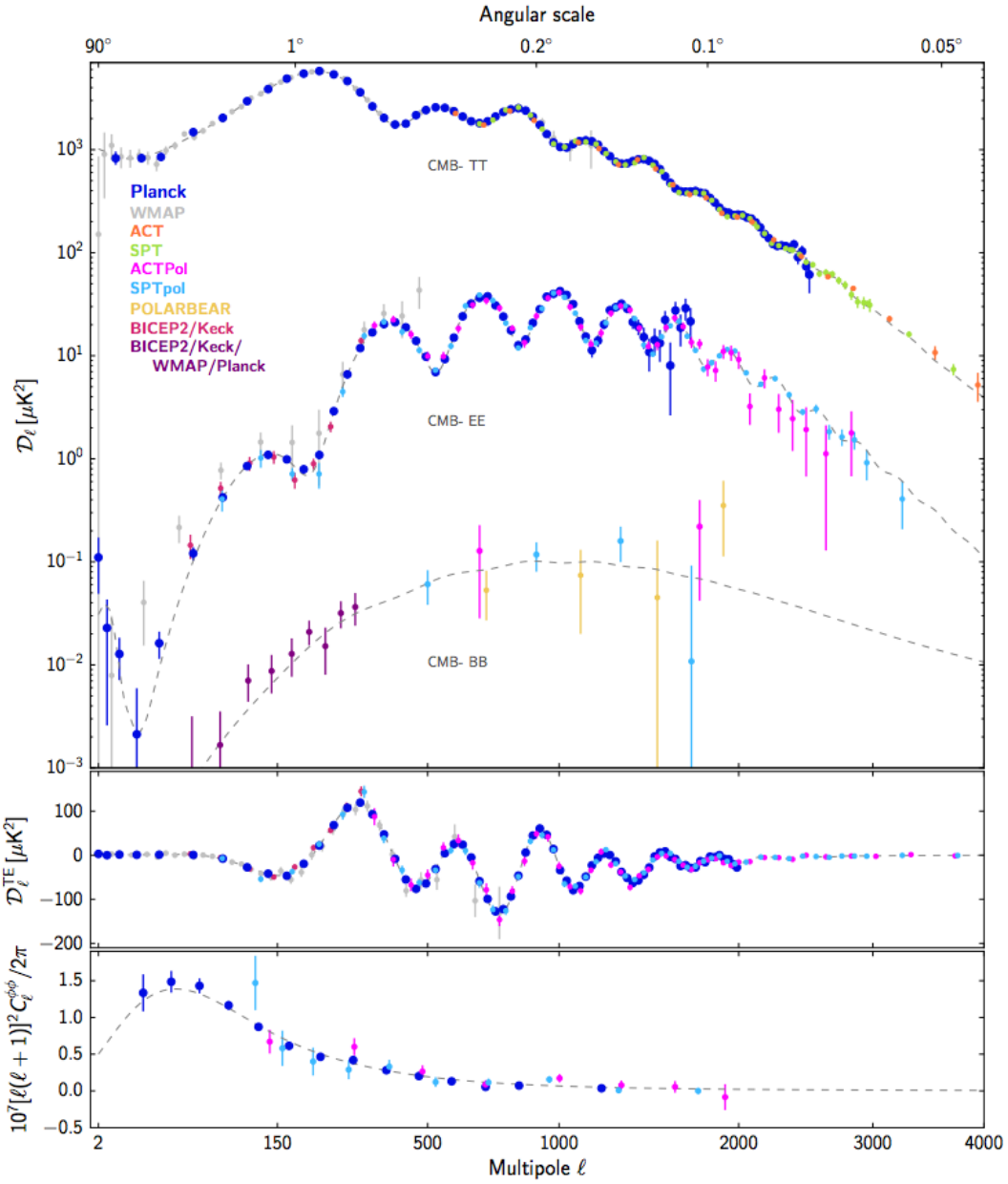

FIGURE 3.19: The state of the art after Planck 2018 result. The top panel shows the angular power spectrum of temperature TT, and polarization EE, BB. The middle panel shows the cross-correlation spectrum TE. The bottom panel shows the lensing defection angular power spectrum. Different colours mean different projects.

Currently, most of CMB projects are on-going or planned by the USA community such as BICEP3/KECK, CLASS, SPT3G, AdvACT, Simon Observatory ... QUBIC, QUIJOTE are ground-based and LSPE is the balloon-borne CMB B-mode experiment of the European community. QUBIC experiment is undergoing the construction phase and is preparing to move to Argentina for observing the sky at the beginning of 2019. In space, LiteBIRD (Light satellite for the studies of B-mode polarization and Inflation from cosmic background Radiation Detection) is a proposed satellite to Japan Aerospace Exploration Agency (JAXA). LiteBIRD currently is in phase A1, concept design study.

3.10 QUBIC and LiteBIRD

3.10.1 Ground base experiment: QUBIC

QUBIC (the Q&U Bolometric Interferometer for Cosmology) is a ground based experiment designed to measure the B-mode polarization signal at intermediate angular scales ($30 \leq \ell \leq 200$). The science objective is measurement tensor-to-scalar r with constraint $\sigma(r) = 0.01$ with foreground (0.006 no foreground) with 95 % confident level as shown in figure 3.20 [31]. QUBIC will observe the sky with three frequencies 90 GHz, 150 GHz and 220 GHz at Alto Chrorrillos in Argentina. QUBIC uses a novel kind of instrument, a bolometric interferometer concept. This technology allows to take advance of interferometry (control systematic effects) and bolometer detectors imagers (image the sky on a focal plane and directly measure temperature in a given direction [31]) which have high signal sensitivity. The table 3.3 describes basic general information as well as requirements of the QUBIC experiment from the cryostat, the instruments, the focal plane to scanning strategy.

3.10.1.1 General principle

The QUBIC bolometric interferometer principle is that a dual reflector telescope is selected by horns (diffractive apertures make spatial filtering i.e. the entrance pupil is a square array of gaussian-illuminated apertures) and then recombined beam. QUBIC uses the Fizeau interferometer approach which is a linear combination of summing outputs beam. The correlation between two receivers (detectors)

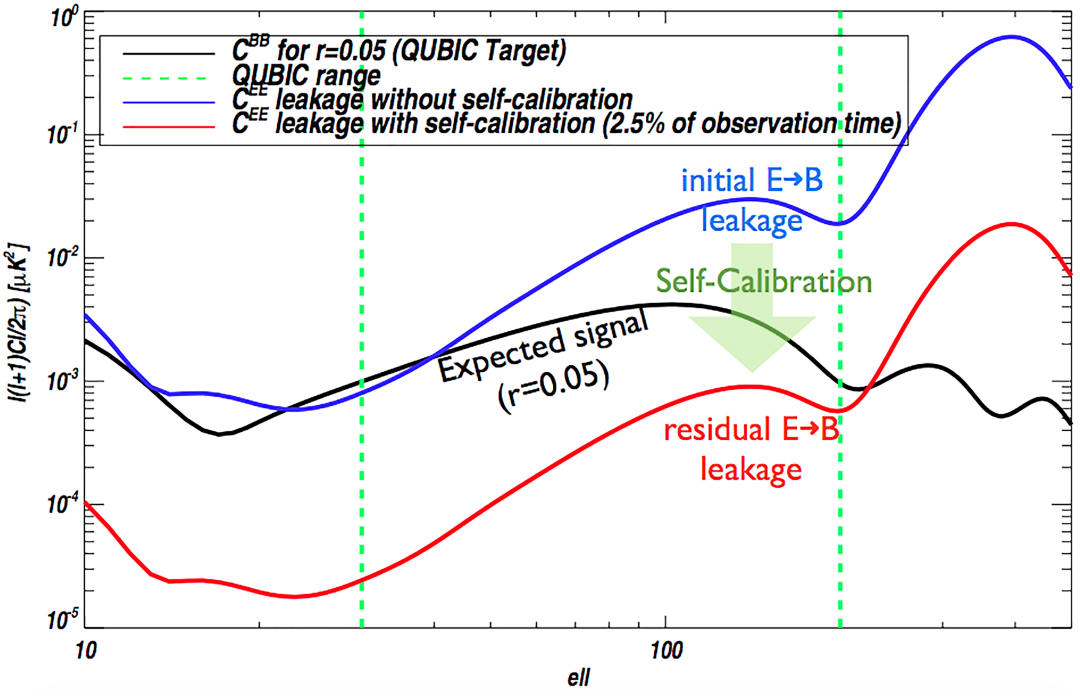

FIGURE 3.20: QUBIC self-calibration sensitivity.

contains interferometer terms which allow us to access directly the Fourier modes (so-called visibilities) of Stokes parameters I, Q and U [31, 84]. We can model the QUBIC instrument using the formalism of Jones matrices which is 2×2 dimension. A Jones matrix represents for an instrument, for several instruments the Jones matrix is simply multiplications matrices. Basically, we can assume that the incident radiation has orthogonal electric field amplitude E_x, E_y passing through receivers: (i) A rotating half wave plate before (ii) the polarizing grid and (iii) horns as described in figure 3.21.

$$\begin{pmatrix} E_x^{\rm rec} \\ E_y^{\rm rec} \end{pmatrix} = \mathbf{J}_{\rm QUBIC} \begin{pmatrix} E_x \\ E_y \end{pmatrix}, \tag{3.68}$$

here the Jones matrix for QUBIC instrument

$$\begin{aligned} \mathbf{J}_{QUBIC} &= \mathbf{J}_{{\rm horn};i}\mathbf{J}_p\mathbf{J}^{\mathbf{T}}{}_{\rm rot}\mathbf{J}_{\rm hwp}\mathbf{J}_{\rm rot}; \\ &= \mathbf{J}_{{\rm horn};i}\mathbf{J}_p \begin{pmatrix} \cos(\psi_{\rm hwp}t) & -\sin(\psi_{\rm hwp}t) \\ \sin(\psi_{\rm hwp}t) & \cos(\psi_{\rm hwp}t) \end{pmatrix} \begin{pmatrix} 1 & 0 \\ 0 & -1 \end{pmatrix} \begin{pmatrix} \cos(\psi_{\rm hwp}t) & \sin(\psi_{\rm hwp}t) \\ -\sin(\psi_{\rm hwp}t) & \cos(\psi_{\rm hwp}t) \end{pmatrix}, \end{aligned}$$

Name tag	Information
Instrument Diameter	< 1.6 m
Instrument Height	< 1.8m
Instrument Weight	< 800 kg
Window diameter	39.9 cm
Filters diameters	39.2 cm
Polarizer diameter	32.6 cm
Half-Wave plate diameter	32.7 cm
Back-to-back Horn array	400 (diameter 33.078 cm)
Optical combiner focal length	30 cm
M1 shape and diameter	480mm $\times$ 600 mm
M2 shape and diameter	600 mm $\times$ 500 mm
Frequency channels	150 GHz and 220GHz
Bandwidth	25 %
Primary beam FWHM at 150 GHz, 220 GHz	12.9° , 15°
Blue center peak FWHM 150GHz, 220GHz	23.5 arcmin, 16 arcmin
Number of bolometers / focal plane	1024
Detector stage temperature goal	320 mK
Bolometers NEP	$5 \times 10^{-17} W.Hz^{-1/2}$
Scientific Data sampling rate	100 Hz
Bolometers time constant	< 10 ms
TES size	2.6 mm
Rotation in azimuth	-220° / + 220°
Rotation in elevation	+30° / +70°
Rotation around the optical axis	-30° / +30°
Pointing accuracy	< 20 arcsec
Angular speed	Adjustable between 0 and 5°/s with steps < 0.2°/s

TABLE 3.3: QUBIC experiment general information [31].

$$= \mathbf{J}_{\text{horn};i}\mathbf{J}_p \begin{pmatrix} \cos(2\psi_{\text{hwp}}t) & \sin(2\psi_{\text{hwp}}t) \\ \sin(2\psi_{\text{hwp}}t) & -\cos(2\psi_{\text{hwp}}t) \end{pmatrix}. \tag{3.69}$$

Here $\mathbf{J}_{\text{horn};i}$ is the Jones matrix for the horn i. $\mathbf{J}_p$ is the Jones matris for the polarizing grid. ψ_{hwp} is the angular velocity of the half-wave plate. $\mathbf{J}_{\text{rot}}$ and $\mathbf{J}_{hwp}$ are the rotational matrix and the ideal Jones matrix of the half wave plate, respectively. After the QUBIC's receiver system, an ideal detector j measures the signal at time t, for the frequency ν is [84]

$$S(j,\nu,t) = S_I(j,\nu) + S_Q(j,\nu)\cos(4\psi_{\text{hwp}}t) + S_U(j,\nu)\sin(4\psi_{\text{hwp}}t). \tag{3.70}$$

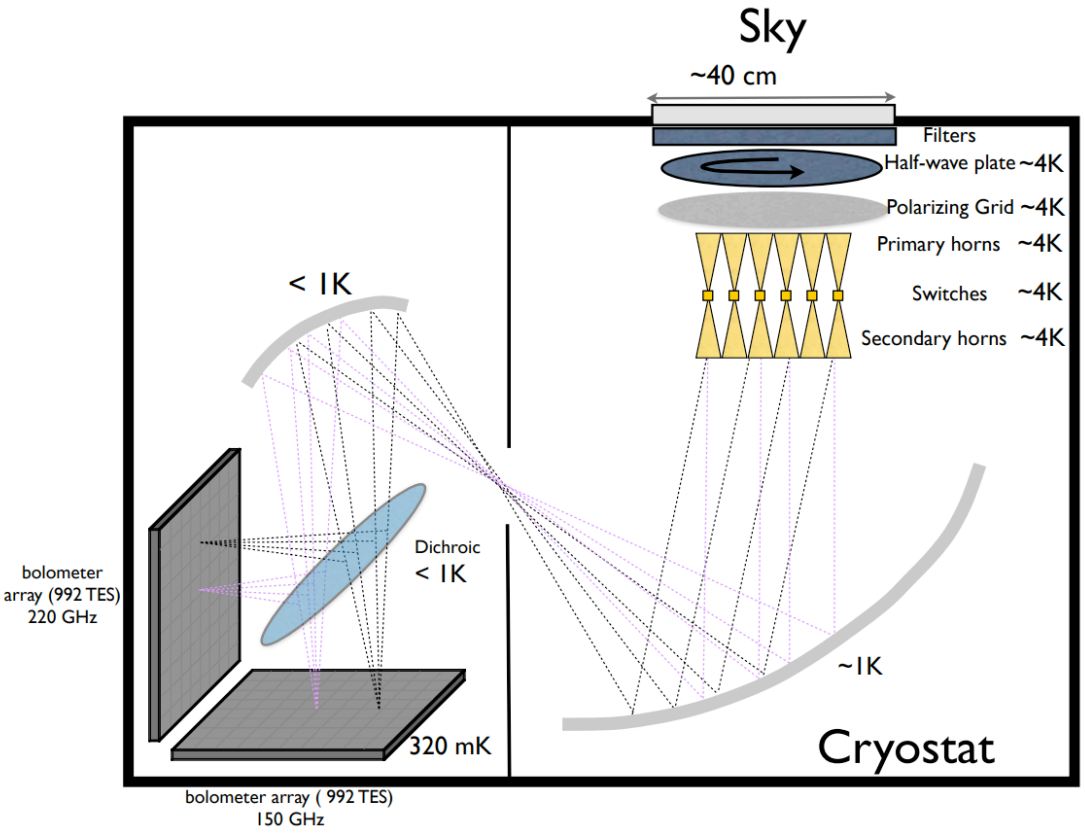

FIGURE 3.21: The basic elements of the QUBIC's cryostat are cooled down to 320 mK at the focal plane, the optical system is worked at the level of 1 K. The quasi-optical system including a half-wave plate, polarizing grid and horns system is maintained at 4 K.

These terms $S_{I,Q,U}$ are intensity and polarization signal convolved with the synthetic beam. Due to the fact that the half-wave plate and horns have imperfection. Therefore, in order to study systemmatic errors, we introduce the complex gain parameters g_x, g_y, h_x, h_y in diagonal terms and the complex coupling parameters e_x, e_y, ξ_x, ξ_y in non-diagonal terms [21] [88], finally we have the Jones matrix for the half-wave plate is

$$\mathbf{J}_{\text{hwp}} = \begin{pmatrix} 1 - h_x & \xi_x \\ \xi_y & -(1 + h_y) \end{pmatrix}. \tag{3.71}$$

The Jones matrix for the horn i

$$\mathbf{J}_{\text{horn};i} = \begin{pmatrix} 1 - g_{x;i} & e_{x;i} \\ e_{y;i} & 1 - g_{y;i} \end{pmatrix}. \tag{3.72}$$

The nature of the bolometric interferometer of QUBIC is so-called *self-calibration*.

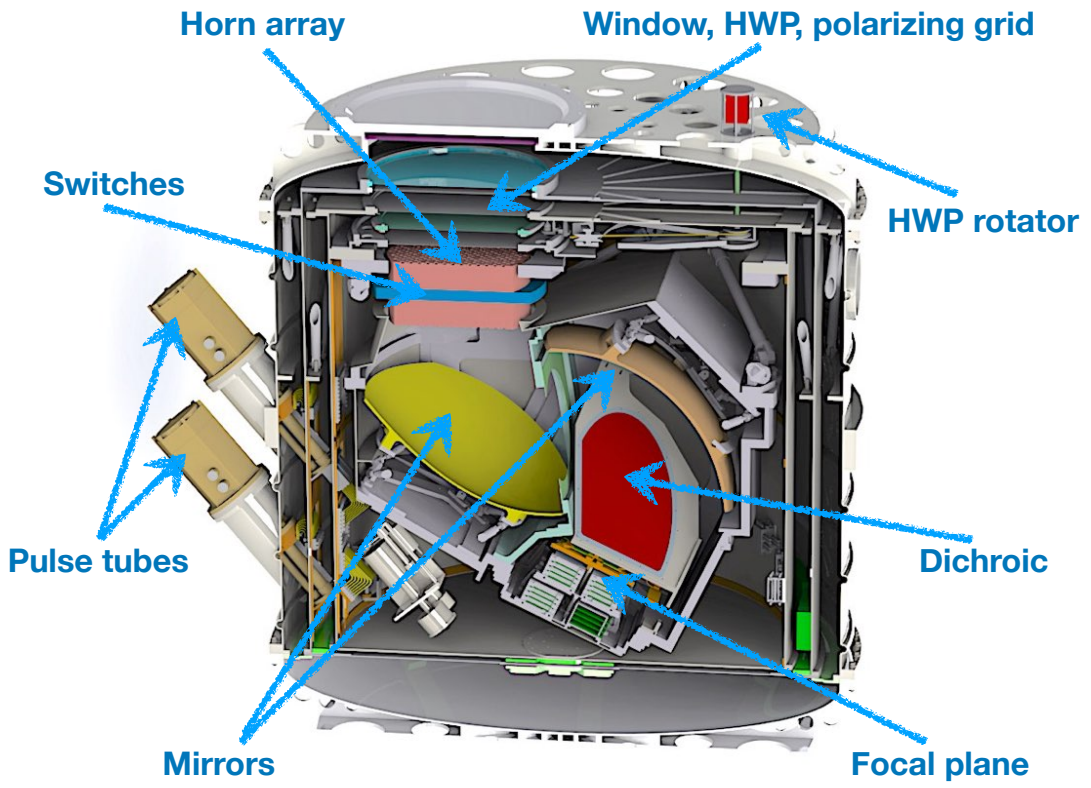

FIGURE 3.22: QUBIC instrument

The basic idea is that the image of an open horn pair (named a baseline) is repeatably observed with many different pairs (redundant baselines). So that the systematic errors are able to control. The mechanism of horns is that they have shutter switches which are placed between primary and secondary horns. The switches can on/off a single horn pair. This procedure allows measuring the image of a polarized source with all baselines or a fraction of baselines and control instrumental systematic effects.

3.10.1.2 Instrument

The QUBIC instrument is located inside a cryostat which is cooled down to 4K using pulse-tubes. Figure 3.21 and 3.22 shows QUBIC's instrument in its cryostat. The quasi optical components (mesh filters, HWP, polarizer, dichroic) are manufactured by the Astronomy Instrumentation Group (AIG) in Cardiff with high TRL technology readliness level [31]. An open **window** (high density polyethylene) $\sim 45\,\text{cm}$ scan the incident sky light with set of filters. **The rotating half**

wave plate and Polarizing grid: The QUBIC's HWP made of metamaterials with the embedded mesh filters technology. The bandwidth requirement of 2 channel frequencies is 73 %. The rotational QUBIC's HWP (3K) modulates the polarization using a rotational mechanism and a stepping rotator (300K) mounted outside the cryostat. The rotational HWP has 8 positions corresponding to 11.25° for a step. Polarization states are selected by a polarizing grid [31]. **Horns, switches:** The feed horn array contains 400 back-to-back horns with movable switches in the middle. The shutters of switches can open or close independently the optical path. This mechanism is used in the self-calibration phase. **Mirrors:** There have 2 Aluminium mirrors for the optical combiner. Each of them has 9 attached supported points which allow to alignment the mirror system. Focal lengths of the primary and the secondary mirror are 231 mm, 196 mm respectively. They are set at a distance of 578 mm. Thus the focal length of the system is $\approx$ 300 mm. **Dichroic/polarizer/filters** is an ecliptic optical element which is designed to transmit the 220 GHz band and reflect the 150 GHz band with an efficiency of $>$ 90%. **The focal plane** of QUBIC will be used around 2048 Transition Edge Sensors (TES) detectors with total noise equivalent power NEP $\sim 5 \times 10^{-17} WHz^{-1/2}$. Each frequency band has 4 arrays of 256 TES pixels. The requirement of time constants is in the range of 10-100 ms.

3.10.2 Space satellite mission: LiteBIRD

The concept design of the LiteBIRD spacecraft is shown in figure 3.23. The payload module consists of the low-frequency telescope and the high-frequency telescope with half-wave plate, the focal plane, cryogenic system. The Service module of the BUS module supports, power supply, communication system. The mass and consumption power of LiteBIRD is estimated at 2.6 tons and 3.0 kW, respectively [73]

The science goal of LiteBIRD is to detect B-mode polarization and to measure tensor-to-scalar r of the order of 10^{-3}. The concept design of LiteBIRD is an optimized mission of light and small satellite for the B-mode detection at large scale to intermediate scale ($2 \leq \ell \leq 200$). The key concept of LiteBIRD is the half-wave plate (HWP) modulation. The satellite will be located at the Sun-Earth Lagrange point 2 with 3 years observation. The study of an optimized scanning strategy of LiteBIRD is described in the chapter 4, the scanning parameters are

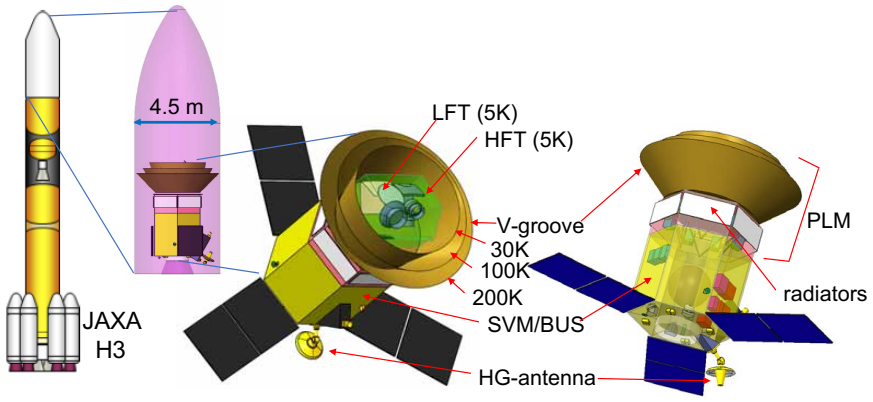

FIGURE 3.23: The concept design of the LiteBIRD spacecraft which composed of the payload module (PLM) and the service module (SVM).

precession angle α, spin angle β, precession period τ_{prec} and spin period τ_{spin} as shown in figure 4.1. The instrument is designed to sense $\sim 4.1\ \mu K$. The Low-Frequency Telescope (LFT) 40 GHz - 235 GHz has a 400 mm aperture, Crossed-Dragone telescope. The transition edge sensor (TES) detectors array of LFT has been developed for the POLARBEAR experiment by the University of California (UC) Berkeley and UC San Diego. The High-Frequency Telescope (HFT) from 280 GHz to 400 GHz has a 200 mm aperture refractor with two silicon lenses. The TES array of HFT with corrugated feedhorn has been developed for ABS, ACTpol, SPTpol by UC Boulder, NIST, and Stanford. The layout of the focal plane unit and the main cold system are shown in figure 3.24.

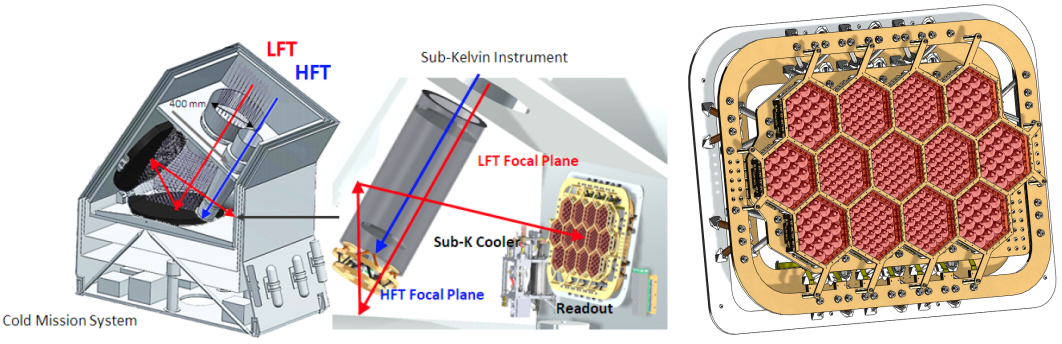

FIGURE 3.24: The concept design of the cold system needs to be cooled to $\sim$ 5K. The focal plane unit of the low, mid-frequency, the dimension of the unit is 420 mm $\times$ 600 mm.

Half wave plate

LiteBIRD will use continuous rotating half-wave plates (HWP) for both telescopes. The HWP can modulate the polarized angle of an incident radiation, mitigate systematic effects as $1/f$ noise by shifting the signal above free frequency, bandpass

mismatch as well as beam mismatch [142]. The polarization signals can be measured by a single detector, thus it removes out systematic error of combining multi-detector. Basically, HWP (or birefringence) is an optical element called as a retarder. The output from the HWP will have different phases and different polarizations. The incident angle will be rotated twice after an HWP. The characteristic equation is the retarder of a single wave plate [80]

$$\Delta\delta = 2\pi\frac{\nu}{c}|n_0 - n_e|d = (2m+1)\,\frac{\lambda_0}{2}. \tag{3.73}$$

here ν is the frequency and λ_0 is its equivalent wavelength, d is the thickness of the material, n_0, n_e are the ordinary and extraordinary refractive indices of a wave plate. m=0,1,2,3... is the number of wave plates in a stack HWP. We can study transformation of radiation through a HWP using Mueller 4×4 matrix formalism which is an overlapping generalization of 2×2 Jones matrices:

$$\mathbf{M} = \mathbf{A}\,(\mathbf{J}\otimes\mathbf{J}^*)\,\mathbf{A}^{-1}, \tag{3.74}$$

where $\otimes$ is the tensor product, * is the complex conjugate and

$$\mathbf{A} = \begin{pmatrix} 1 & 0 & 0 & 1 \\ 1 & 0 & 0 & -1 \\ 0 & 1 & 1 & 0 \\ 0 & -i & i & 0 \end{pmatrix}. \tag{3.75}$$

Fully polarized light can be treated by Jones formalism or Mueller formalism while unpolarized or partially polarized light must be treated by Muller formalism. In the literature both formalism are used for HWP. We described Jones formalism in the section 3.10.1, this is a motivation to use the two formalism in this thesis. The output signal along the z axis with rotation angle ρ of the HWP around its axis after m wave plates is [80]

$$S_{\text{out}} = \prod_{i=1}^{\text{m}} \mathbf{R}\,(-\rho)\;\; \mathbf{M}\;\mathbf{R}\,(\rho) \begin{pmatrix} I \\ Q\cos 2\psi \\ U\sin 2\psi \\ V \end{pmatrix}. \tag{3.76}$$

ψ is the polarized angle of incident radiations. An ideal HWP has the Muller matrix:

$$\mathbf{M} = \begin{pmatrix} 1 & 0 & 0 & 0 \\ 0 & 1 & 0 & 0 \\ 0 & 0 & -1 & 0 \\ 0 & 0 & 0 & -1 \end{pmatrix}, \tag{3.77}$$

with a reference frame along the ordinary and extroordinary axis. The rotation matrix is introduced as

$$\mathbf{R}(\rho) = \begin{pmatrix} 1 & 0 & 0 & 0 \\ 0 & \cos 2\rho & \sin 2\rho & 0 \\ 0 & -\sin 2\rho & \cos 2\rho & 0 \\ 0 & 0 & 0 & 1 \end{pmatrix}. \tag{3.78}$$

Due to the fact the the HWP is imperfection, in order to study the systematic of a HWP, the Muller matrix can be expressed as

$$\mathbf{M} = \begin{pmatrix} M_{II} & M_{IQ} & M_{IU} & M_{IV} \\ M_{QI} & M_{QQ} & M_{QU} & M_{QV} \\ M_{UI} & M_{UQ} & M_{UU} & M_{UV} \\ M_{VI} & M_{VQ} & M_{VU} & M_{VV} \end{pmatrix}, \tag{3.79}$$

and those coefficients in the matrix can be obtained by simulation tools or experimentation in laboratory. The equation 3.76 is useful for simulations and study LiteBIRD measurements as map making, and systematic effects.

The focal plane of LiteBIRD

LiteBIRD will observe the sky with 15 frequency bands from 40 to 400 GHz of about 2622 TES detectors [78, 79]. The frequency bands have been defined to avoid CO lines. The observing frequency bands, bandwidth, noise equivalent power (NEP) are showed in the table 3.4 and figure 3.25. The focal plane unit is cooled down to $\sim$ 100 mK. The fabrication of the LiteBIRD focal plane unit will be implemented at the NIST Microfabrication facility in Boulder and the Marvell Nanofabrication laboratory in Berkeley. The low/mid frequency array technology is multi-chroic lenslet coupled sinuous antenna detectors. This technology has been implemented for POLARBEAR, Simons Array, SPT-3G and Simon Observatory experiments. The low frequency has a baseline of 18 mm diameter per pixel.

Type	ν [GHz]	BW [%]	Beam [arcmin]	N_{Pix}	Loading [pW]	$\mathrm{NET}_{\mathrm{CMB,Arr}}$ [$\mu\mathrm{K}\cdot\sqrt{s}$]	Sensitivity [$\mu\mathrm{K}-\mathrm{arcmin}$]
LF-1	40	30	69.2	114	0.15	25.0	36.8
LF-2	50	30	56.9	114	0.18	16.0	23.6
LF-3	60	23	49.0	114	0.16	13.2	19.5
LF-4	68	23	40.8	114	0.17	10.8	15.9
LF-5	78	23	36.1	114	0.19	9.0	13.3
LF-6	89	23	32.3	114	0.20	7.8	11.5
MF-1	100	23	37.0	296	0.18	6.1	9.0
MF-2	119	30	31.6	222	0.25	5.1	7.5
MF-3	140	30	31.6	296	0.25	3.9	5.8
MF-4	166	30	24.2	222	0.24	4.3	6.3
MF-5	195	30	21.7	296	0.22	3.9	5.7
MF-6	235	30	19.6	222	0.18	5.1	7.5
HF-1	280	30	13.2	128	0.13	8.8	13.0
HF-2	337	30	11.2	128	0.10	13.0	19.1
HF-3	402	23	9.7	128	0.05	25.0	36.9

TABLE 3.4: Summary of detector configuration and sensitivity, LF, MF and HF stand for low, mid and high frequency respectively. BW is fraction of bandwidth. NET stands for noise equivalent temperature as well as noise equivalent power.

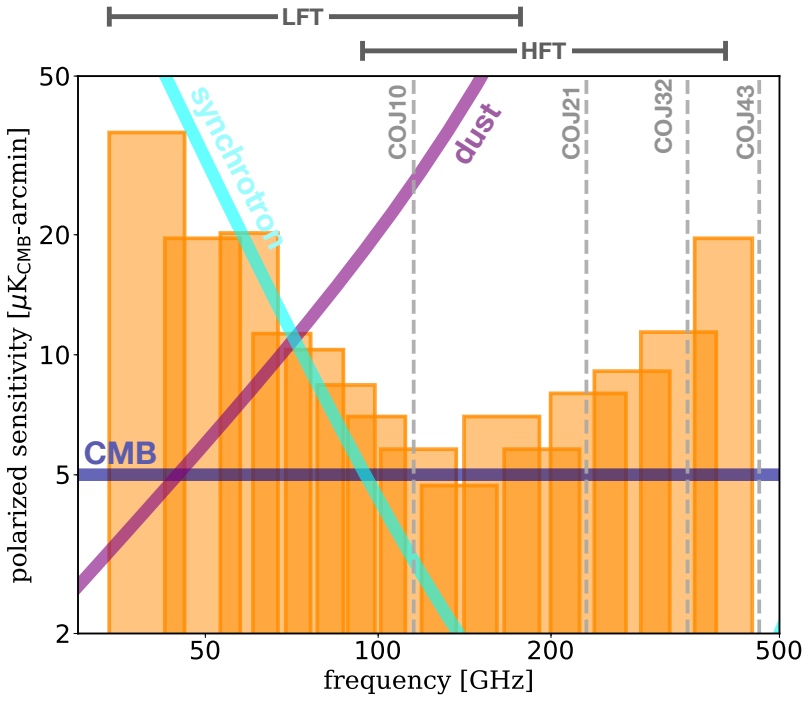

FIGURE 3.25: LiteBIRD frequencies.

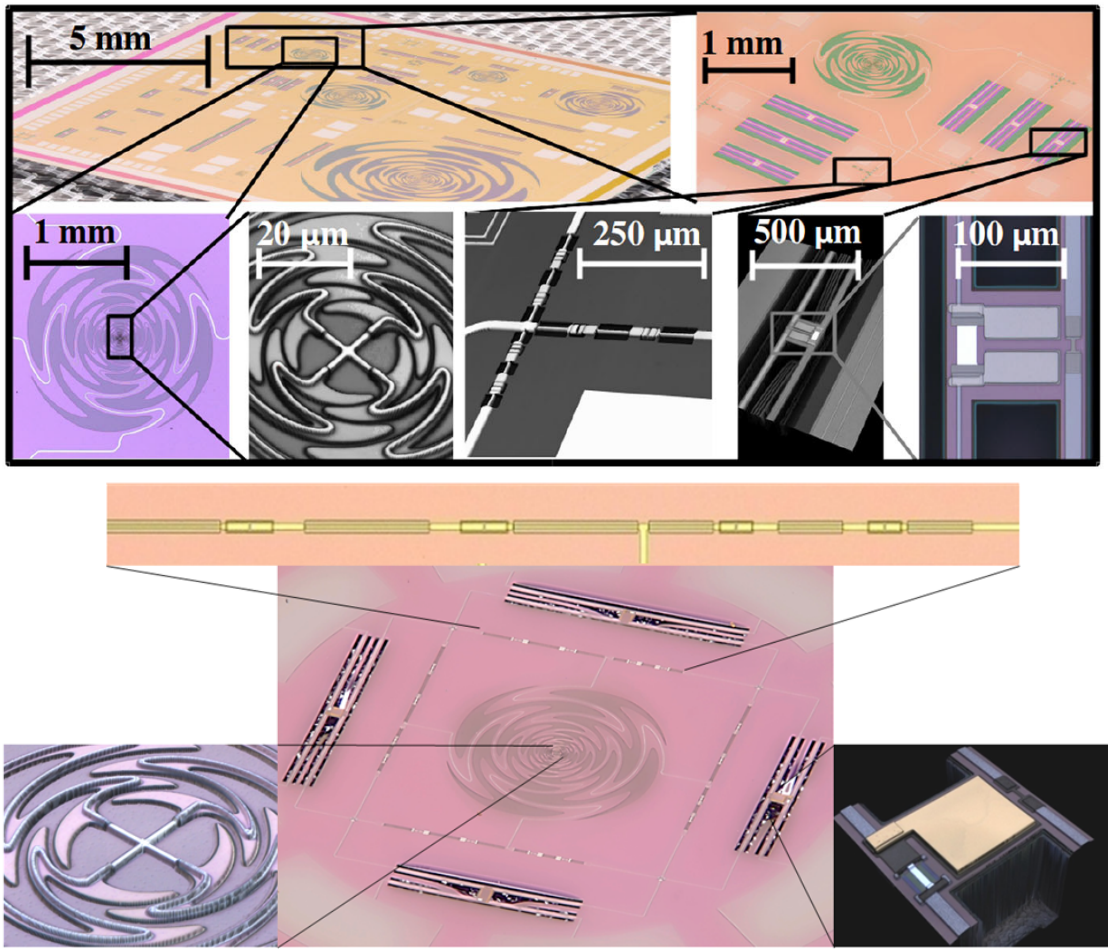

FIGURE 3.26: The low/mid frequency technology: *Top:* The low, mid frequency pixel is fabricated by the Marvell Nanofabrication laboratory in Berkeley [152]. *Bottom:* The main components of a pixel are the sinuous antenna at the center, four diplexer bandpass filters, four TES surround these filters. A pixel has 3 millimeters in diameter.

The mid frequency has a baseline of 12 mm diameter. The bandwidth, number of pixels, beam size are given in the table 3.4. Each pixel is a dual polarized sinuous antenna (log-periodic) coupled with radio frequency transmission lines, Chebyshev bandpass filters [4] for several frequency bands and TES bolometers which measure power in each frequency band. The sinuous antenna-coupled is a four-armed antenna with the self-similar structure (16-cell) as shown in figure 3.26. The sinuous antenna is (i) sensitive to the CMB linear polarization by a pair of opposite arms if we have power and 180° phase difference, (ii) planar antenna for large arrays, (iii) the sinous antena has the inner and outer radius of antenna defining the frequency bands (broadband), (iiii) high gain amplitude

[4]Comparing Butterworth and Chbyshev filters, we know that a Chebyshev filter has a sharp rise and steeper drop thus the cut off frequency is better determination.

which is compatible with telescope, and a stable impedance. The sinuous coupled antenna is placed under lenslet in order to boost the gain of an antenna [40, 141].

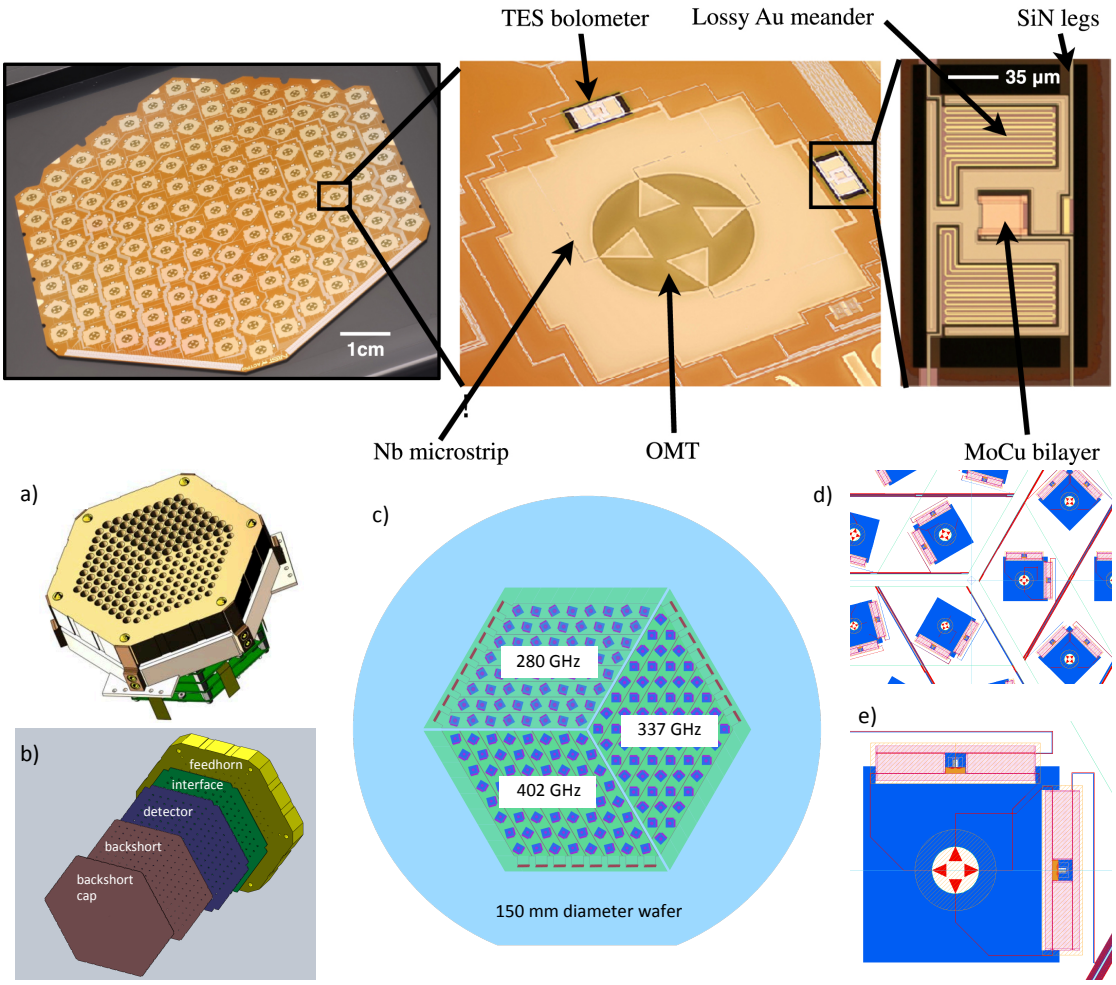

FIGURE 3.27: The high frequency technology: a) The high frequency pixel is fabricated by NIST. The technology shows the feedhorn coupled array and the readout board. b) A detector stack assembly. c) The hexagonal detector array has three frequency bands in a 150 mm diameter wafer. Each band has 64 pixels with only one low pass filter. d) Zoom in at the center of the array. e) Zoom in a single pixel design which indicates two orthogonal polarized bolometers.

The high-frequency array technology is the single color of an orthomode transducer (OMT) coupled corrugated horn detectors. This technology has been implemented for ACT-pol, SPT-pol and SPIDER experiments as shown in these figures 3.27. Each frequency band has 64 dual polarized pixels. The orthomode transducer detector technology has high Technology readiness level (TRL) level at high frequency, symmetry of beam, clean polarized property [142]. The corrugated feedhorns, a gold-plated silicon-platelet, transmit radiation through a coplanar waveguide (CPW) directly to microstrip (MS), then isolated TES bolometers area [87]. The OMT circle design has the orthogonal polarization independently for each

frequency, the incident radiation will be transmitted to MS by CPW transmission lines independently from OMT then the signals pass through the bandpass filter which is set of resonant MS in a pixel. Now the incident signals are measured for each polarization by TES [43, 59, 81, 82].

Chapter 4

Band-pass mismatch

Contents

The future Cosmic Microwave Background (CMB) satellite concepts LiteBird [79], CORE [32], PIXIE [67] have been proposed to probe B modes polarization to measure the tensor-to-scalar r ratio with a sensitivity $\sigma(r) \leq 10^{-3}$, which is almost two orders of magnitude beyond the Planck sensitivity. LiteBIRD is a proposed CMB polarization satellite project to JAXA aims to probe the inflationary B-mode signal [45, 62, 78, 79]. It will observe the full sky with more than 2000 detectors, frequency coverage spans 40–402 GHz from the second Lagrange point for 3 years. LiteBIRD is an optimized satellite for the observation of the large-scale of the CMB B-mode polarization and it is a reasonably light and small satellite to maximize the chance for launch. LiteBIRD has a half-wave-plate modulation, which rotates the polarization of linearly polarized light. Typical CMB experiments observe in a number of different frequency channels with many detectors for each channel. The effect of non-uniformity, or unbalance, of the bandpass filters for different detectors induces leakage from intensity to polarization after calibrating the data

on the CMB. In this chapter, I will present the results of the study of the bandpass mismatch systematic effect.

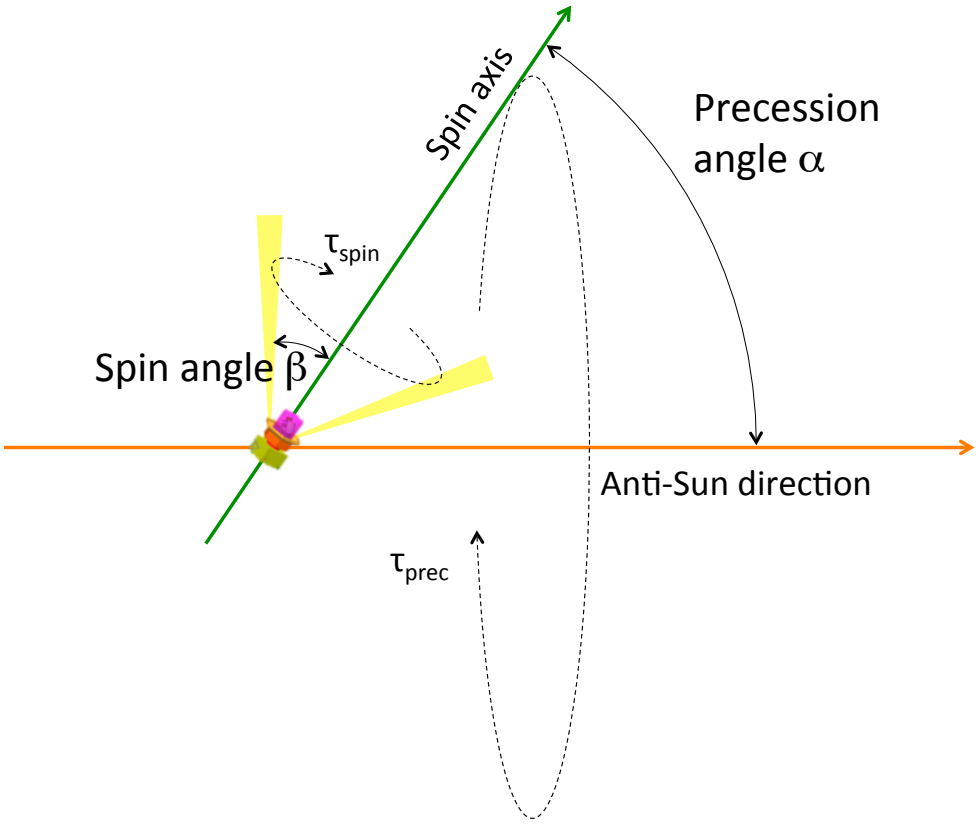

FIGURE 4.1: Representation of typical satellite scanning strategy, the spin angle: β, precession angle: α, rotating spin: $\tau_{\rm spin}$ or $\omega_{\rm spin}$, precession spin: $\tau_{\rm prec}$ or $\omega_{\rm prec}$.

My study first focuses on the evaluation of the level of the bandpass mismatch effect impact on the final determination of the tensor-to-scalar ratio r in the case without a Half Wave Plate (HWP) at 140 GHz. I have studied also bandpass mismatch effect for CORE scanning strategy parameters. I have done a code for bandpass mismatch simulation based on a *co-addition* map making method. The code has been integrating into the Japanese LiteBIRD simulation tool package, which operated in the high energy accelerator research organization known as KEK computers. The final tool intergrating previous work can simulate the boresight pointing, the data and the map making for the full focal plane of LiteBIRD. As a conclusion of this study, the level of leakage depend strongly on the scanning strategy of a satellite (α: Precession angle and β: Spin angle) which are illustrated in figure 4.1. Furthermore, we have studied the importance of choosing scanning strategy parameters ratios $\frac{\omega_{\rm prec}}{\omega_{\rm spin}}$ to avoid Moiré patterns which produce features on the power spectrum. The results of the study allow us to choose the scanning strategy of future CMB satellites. In addition, I have verified the analytic estimation

of the bandpass mismatch effect with simulation. The method indicated the tight correlation between leakage maps and crossing moment maps $\langle \cos 2\psi \rangle$, $\langle \sin 2\psi \rangle$, the analytic estimation method is a useful approach to cross-check, fast and easy ways to predict the magnitude of potential leakage. Moreover, I also studied a correction method for the bandpass mismatch error systematic effect.

The amplitude of the angular power spectrum is decreased when the precession angle α is larger, as explained by a more uniform angle coverage for larger α. The magnitude of the tensor-to-scalar in the reionization bump ($2 \leq \ell \leq 10$) is of the order of 10^{-3}, in the recombination bump ($10 \leq \ell \leq 200$) is of the order of 10^{-5} depending on scanning angle parameters. So that the bandpass mismatch error is not a negligible effect at the reionization bump that can impact to current and next generation of CMB polarization missions.

In addition, I also verified that the bandpass mismatch effect is greatly mitigated with an ideal rotating HWP without any achromaticity or other non-idealities. But the imperfect HWP has systematic effects.

The simulation pipeline is illustrated in the flowchart figure 4.2. These processes start from the filter coefficient to the sky simulation, the map making equation and the computation of angular power spectra. For more details, this systematic effect has been discussed in the paper "Bandpass mismatch error for satellite CMB experiments I: Estimating the spurious signal", Journal of Cosmology and Astroparticle Physics December 2017 [50].

4.1 Sky emission model and mismatch errors

In order to model the emission of the sky, we only use CMB intensity and thermal dust intensity as a start. The input maps at 140 GHz are shown in figure 4.3 for CMB intensity and thermal dust intensity in μK.

For the integration on the frequency band, we need to model the spectra of components. As we known, the spectrum of CMB is a black body at T=2.7255 K. We remind the Planck function with respect to temperature and frequency:

$$\mathrm{B}(\nu;\mathrm{T}) = \frac{2\mathrm{h}\nu^3}{\mathrm{c}^2}\frac{1}{\exp(\frac{\mathrm{h}\nu}{\mathrm{kT}})-1} \qquad [\mathrm{Wsr}^{-1}\mathrm{m}^{-2}\mathrm{Hz}^{-1}]. \tag{4.1}$$

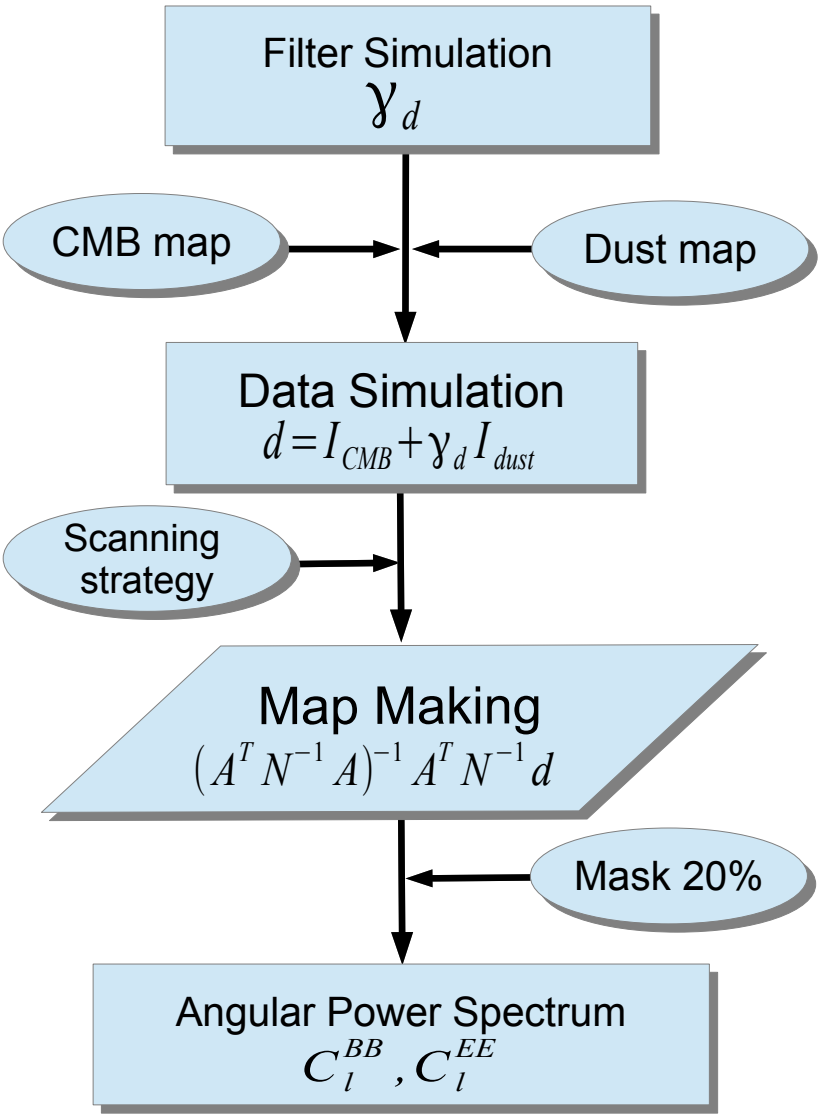

FIGURE 4.2: The simulation process

T is the brightness temperature of the source. We often express the sky emission in CMB temperature units. The relationship between intensity I and δT is obtained by linearizing the Planck formula around $T = T_0$:

$$\frac{\delta \mathrm{I}(\nu)}{\delta \mathrm{T}} = \left(\frac{\partial \mathrm{B}(\nu;\mathrm{T})}{\partial \mathrm{T}}\right)_{\Big|\mathrm{T}_0} = \frac{2\mathrm{h}^2\nu^4}{\mathrm{kc}^2\mathrm{T}_0^2} \frac{\exp(\frac{\mathrm{h}\nu}{\mathrm{kT}_0})}{\left(\exp(\frac{\mathrm{h}\nu}{\mathrm{kT}_0}) - 1\right)^2}. \tag{4.2}$$

The spectrum of thermal dust is a modified blackbody. In the sub-mm domain, the dust is optically thin $\mathrm{I}_{\mathrm{dust}}(\hat{\mathrm{p}}, \nu) = \tau_{(\hat{\mathrm{p}},\nu_0)} \left(\frac{\nu}{\nu_0}\right)^{\beta_{\mathrm{d}}(\hat{\mathrm{p}})} \mathrm{B}\left(\nu; \mathrm{T_d}\right)$ where $\tau_{(\hat{p},\nu_0)}$ is the optical dept at frequency center ν_0, $\beta_d(\hat{p})$ is the spectral emissivity index in a position, its value is in range $1.5 - 2$. Assuming that the spectral index is a

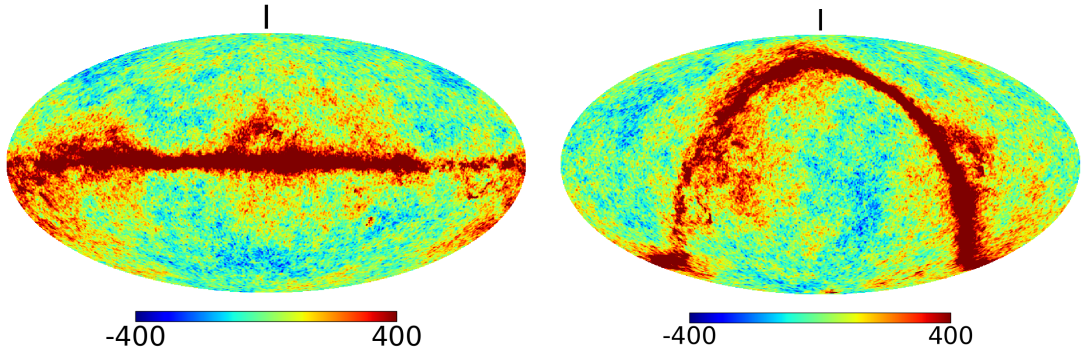

FIGURE 4.3: Input intensity I maps containing CMB and thermal dust at 140 GHz in galactic (*left*) and ecliptic (*right*) coordinates. The unit is in μK

constant, we can relate the intensity at two different frequencies with the following formula for any location on the sky:

$$\mathrm{I}_{\mathrm{dust}}(\hat{\mathrm{p}},\nu) = \left(\frac{\nu}{\nu_0}\right)^{\beta_\mathrm{d}} \frac{\mathrm{B}(\nu;\mathrm{T_d})}{\mathrm{B}(\nu_0;\mathrm{T_d})}\mathrm{I}_{\mathrm{dust}}(\hat{\mathrm{p}},\nu_0). \tag{4.3}$$

We assume the same emission law for intensity and polarization, and a constant spectral index over the sky but this is not critical for this study.

Generally, the total intensity $I_{\mathrm{tot}}(\hat{p},\nu)$ of the microwave sky can be expressed as the sum of components, the model of the unpolarized sky is:

$$I_{\mathrm{tot}}(\hat{p},\nu) = I_0(\nu) + \left.\frac{\partial B(\nu;T)}{\partial T}\right|_{T_0} \Delta T_{\mathrm{CMB}}(\hat{p}) + \sum_{(c)} I_{(c)}(\hat{p},\nu) \tag{4.4}$$

where $B(\nu;T)$ is the spectrum of a blackbody at temperature T, T_0 is the average CMB temperature of about 2.7255 K, $\Delta T_{\mathrm{CMB}}(\hat{p})$ is the CMB temperature fluctuation around this mean value, $I_{(c)}(\hat{p},\nu)$ the emission spectrum of component (c) as a function of electromagnetic frequency ν, $I_0(\nu)$ is the monopole including all components. The carbon monoxide (CO) emission at transition line frequencies $\nu = 115\,GHz$ for $J = 1 \rightarrow 0 \ldots$ was a main source of leakage in Planck experiment [97], the future satellite will avoid these lines. We have similar relationships for the Q and U Stokes parameters.

Let us define $g_i(\nu)$ is the bandpass filter transmission for detector i. The intensity $I(\hat{p},\nu)$ and polarization $Q(\hat{p},\nu)$ and $U(\hat{p},\nu)$ are the result of the integration of the

emission of components on the detector band-pass.

$$\mathrm{I}(\hat{\mathrm{p}},\nu) = \frac{\int \mathrm{g_i}(\nu)\mathrm{I_{cmb}}(\nu)\mathrm{d}\nu + \int \mathrm{g_i}(\nu)\mathrm{I_{dust}}(\nu)\mathrm{d}\nu + ...}{\int \mathrm{g_i}(\nu)\mathrm{d}\nu}, \tag{4.5}$$

where $I_{\mathrm{cmb}}(\nu)$ and $I_{\mathrm{dust}}(\nu)$ are the intensity of cmb and dust at the frequency ν. The denominator term $\int g_i(\nu)d\nu$ is for the normalization. We then inject equations 4.3 and 4.2 into the equation 4.4. We obtain the fluctuation of the signal measured by the detector i:

$$\begin{aligned}\int \mathrm{d}\nu\ \mathrm{g_i}(\nu)\ \Big(\mathrm{I}(\hat{\mathrm{p}},\nu) - \mathrm{I_0}(\nu)\Big) = \int \mathrm{d}\nu\ \mathrm{g_i}(\nu)\frac{\partial \mathrm{B}(\nu;\mathrm{T})}{\partial \mathrm{T}}\Big|_{\mathrm{T_0}} \Delta\mathrm{T_{CMB}}(\hat{\mathrm{p}}) \\ + \int \mathrm{d}\nu\ \mathrm{g_i}(\nu)\ \mathrm{I_{dust}}(\hat{\mathrm{p}},\nu_0)\ \left(\frac{\nu}{\nu_0}\right)^{\beta_\mathrm{d}(\hat{\mathrm{p}})} \frac{\mathrm{B}(\nu;\mathrm{T_d})}{\mathrm{B}(\nu_0;\mathrm{T_d})} + \ldots,\end{aligned} \tag{4.6}$$

where ν_0 is the central frequency of a band. $\mathrm{I_0}(\nu) = \mathrm{B}(\nu;\mathrm{T_0})$ is the CMB monopole. $\mathrm{I_{dust}}(\hat{\mathrm{p}},\nu_0)$ is the intensity of the dust component at the reference frequency ν_0, and where these dots stand for other components (such as synchrotron and free-free) not explicitly written here. For our study we assume that the galactic thermal dust emission is a greybody of temperature $T_d \approx 19.7\,\mathrm{K}$ [98] with an emissivity spectral index $\beta(\hat{p})$, which depends on sky positions and whose average value is ≈ 1.62 as measured by Planck [98, 102]. The synchrotron and the free-free emissions can be described by power law spectra with the negative spectral indices ≈ -3.1 and ≈ -2.3, respectively [104].

The CMB temperature is a constant and independent in frequency observations. Therefore, we divide two sides of equation 4.6 for $\int \mathrm{g_i}(\nu)\left(\frac{\partial \mathrm{B}(\nu;\mathrm{T})}{\partial \mathrm{T}}\right)_{|\mathrm{T_0}} \mathrm{d}\nu$ and express to the first order we obtain for the total sky intensity $\mathrm{I_{sky}}(\nu_0)$ after converting the CMB temperature ΔT_{CMB} (by multiplying with $\left(\frac{\partial \mathrm{B}(\nu_0;\mathrm{T})}{\partial \mathrm{T}}\right)\Big|_{\mathrm{T_0}}$) to intensity $I_{\mathrm{CMB}}(\nu_0)$:

$$I_{\mathrm{sky}}(\nu_0) = I_{\mathrm{CMB}}(\nu_0) + \gamma_d\, I_{\mathrm{dust}}(\nu_0) + \gamma_s\, I_{\mathrm{sync}}(\nu_0) + \ldots, \tag{4.7}$$

where

$$\boxed{\gamma_d = \left(\frac{\int d\nu\ g_i(\nu)\left(\frac{\nu}{\nu_0}\right)^{\beta_d}\frac{B(\nu;T_d)}{B(\nu_0;T_d)}}{\int d\nu g_i(\nu)\left(\frac{\partial B(\nu;T)}{\partial T}\right)\Big|_{T_0}}\right)\left(\frac{\partial B(\nu_0;T)}{\partial T}\right)\Big|_{T_0}}. \tag{4.8}$$

The factor γ_s is similarly defined integrating over the synchrotron spectrum, etc. The equation (4.7) also holds for the polarization when I is replaced with Q and

U. The unit normalization for the CMB component is justified because the data are calibrated using the CMB dipole (or higher order temperature anisotropies).

Differences in the bandpass function $g_i(\nu)$ from detector to detector result in corresponding variations in γ from detector to detector for each non-CMB component. Such variations have been observed in Planck data (see Figs. 5 and 28 of [99] for the measured Planck filters and the mismatch parameters, respectively). The variations of the bandpass functions of the filters from a detector to a detector for a future satellite experiment will depend on the kind of detector technology used (see also [63] regarding the WMAP experiment). As already stressed, for the above sky emission model where each component has a fixed (factorizable) frequency dependence, the bandpass mismatch maps depend only on the γ parameters and not on the other details of the filters. Consequently, the intensity to polarization leakage due to bandpass mismatch can be obtained using only the γ and no additional properties of the bandpass functions. The γ_d parameter in front of $\mathrm{I}_{\mathrm{dust}}$ are close to unity when the bandwidth is narrow bands and differences in $\mathrm{g_i}(\nu)$ will induce some variations around 1.

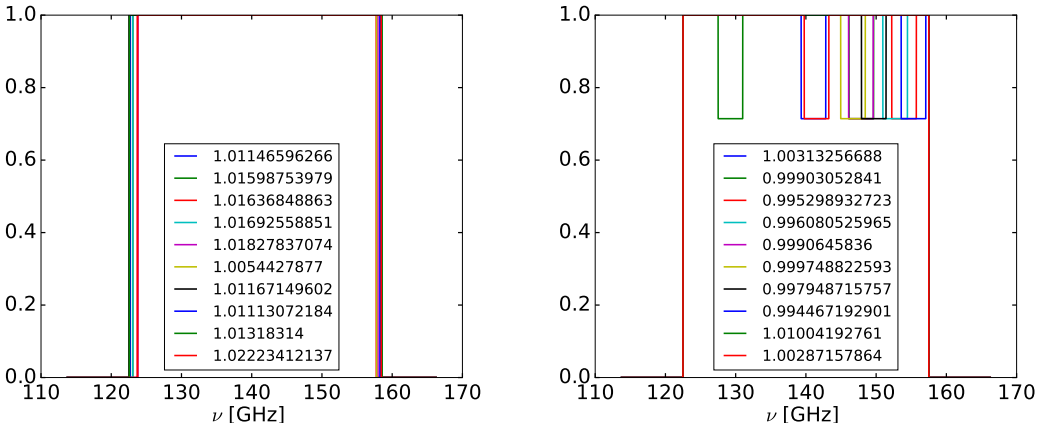

FIGURE 4.4: The simulation of bandpass miss-match function at $\nu_0 = 140\,GHz$ for 10 detectors, the left is the boxcar function which is vary on the edge of a filter and the right is the tophat fuction which is vary at the top with the surface 1 GHz.

At this stage, we use a boxcar function for the bandpass $\mathrm{g}(\nu) = \Pi(\frac{\nu-\nu_0}{\Delta\nu})$ (figure 4.4), for which $g(\nu) = 1$ in the interval $[\nu_{\min}, \nu_{\max}]$ and $g(\nu) = 0$ elsewhere. The center frequency is $\nu_0 = 140\,\mathrm{GHz}$ and the equation (4.8) uses to simulation bandpass mismath γ_d parameter with CMB temperature $T_0 = 2.725\,K$, thermal dust $T_d = 19.7\,K$, $\beta_d = 1.62$, but in principle we could use any function. We assume that the variations in $\nu_{\min}$ and $\nu_{\max}$ for each detector are generated independently

according to a uniform distribution with a width of 1%[1]. We also assume a bandwidth $(\nu_{\max} - \nu_{\min})/\nu_0$ of 0.25 on average, with $\nu_0 = 140.7\,\mathrm{GHz}$. We also simulated the tophat function as figure 4.4 on the right with average 1 GHz surface of the tophat.

In some micro-fabricated technologies for Transition Edge Sensor (TES) or Kinetic Inductance Detector (KID), each detector is designed of a feed antenna in a single band or broadband, a superconducting radio frequency (RF) filter circuit, and a transmission termination line of the characteristic impedance. A frequency band is defined by the combination of the antenna impedance and the integrated RF filter circuit. The fabrication of a bandpass filter on a silicon wafer with a Niobium ground plan, a dielectric insulator, and a Niobium strip layer actually could contribute variously to non-ideality in reality. These fabrication parameters are:

- **Layer to layer misalignment:** Due to the machines during fabrication, misalignment could contribute to the mismatch between two orthogonal detectors. In practical experience, the fabricated machines can align each layer up to 0.5 μm. However, we believe this effect does not shift much the shape of the filter.
- **Line width:** The center frequency of a bandpass filter could shift as a function of line width this error could introduce 1 GHz per 0.2 micron of changing width due to non-uniform etch a part of a lumped filter.
- **Dielectric constant:** The center frequency of a bandpass filter depends on the dielectric constant because of changing capacitance of capacitors. If we change 0.1 in the dielectric constant, the center frequency of a bandpass filter will shift 1 GHz. We expect that the value of the dielectric constant is fixed on the whole silicon wafer.
- **Dielectric thickness:** The impedance of a microstrip line and the capacitance of parallel capacitors depend on the dielectric thickness of a material.

[1]We thank Aritoki Suzuki for sharing with us that the measurement errors with Fourier Transform Spectrometer (FTS) in the bandpass of the third-order Chebyshev filter placed between the broadband sinuous antennas and the bolometers of the focal plane panels of the Simons Array [152] give approximately this spread. Obviously, since these are values dominated by measurement error, the actual bandpass mismatch for these filters could be much smaller. These measurements merely serve to establish an upper bound on the mismatch. These values are also of the same order of magnitude as the values representing the bandpass mismatch of the metal mesh filters used as part of the Planck satellite HFI instrument. [See [103] for a discussion of the Planck bandpass mismatch.]

For example, if we have 100 A (Angstrom unit $\sim 10^{-10}$) change in the thickness, the center band of a lumped filter will vary 1GHz.

- **Kenetic Inductance:** The quality of Niobium could also change due to incident radiations. The changing quality effect to the kinetic inductance of a microstrip filter [65]. If we have a change of 0.03 pH/square in the kinetic inductance, we will make 1 GHz shift in the frequency band.

The resulting RMS of γ_d simulation is 0.6% for these simple filter models. This is similar to the variations observed for Planck at 143 GHz. The fact that actual bandpass functions are more complex functions of ν does not affect the applicability of the present work as long as the corresponding γ coefficients remain of the same order of magnitude. Results for other values may be obtained by trivial rescaling. We verified the expected linear scaling by increasing the width of the uniform distribution from 1% to 2% and observed that the leakage increases by a factor of 2, as expected.

4.2 Calculating the bandpass mismatch

In this section, we assume a simplified model of the single source of the systematic effect. We study the bandpass mismatch error in isolation and in the simplest possible context. We assumed that the beams are azimuthally symmetric and identical. We also assumed that the monopole and the dipole, as well as gain variations, are already well calibration.

The scanning strategy of a satellite is characterized by the following parameters: α (precession angular radius), β (spin angular radius), $\tau_{\rm prec}$ (precession period), and $\tau_{\rm spin}$ (spin period). The motion of a satellite and definitions of the scanning parameters are indicated in Figure 4.1. Many of the proposed future CMB polarization space missions have adopted such a scan strategy [35, 79].

The large focal plane of the LiteBIRD mid-frequency spreads over 10 degrees wide. Figure 4.5 indicates the position of pair detectors in the focal plane for 5 wafers. Each wafer contains 37 orthogonal detectors. As described in [79], 222 detectors are designed at 140 GHz.

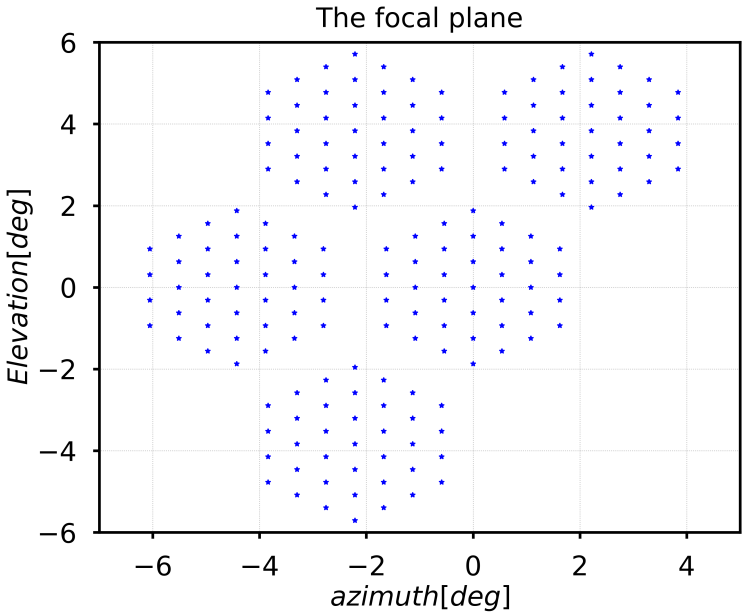

FIGURE 4.5: The position of 370 detectors at 140 GHz in the 5 wafers of the focal plane, each position is a pair of orthogonal detectors.

I used HEALPix [2] [46] (with $n_{\rm side} = 256$) to simulate the celestial sphere pixelized maps. In order to obtain several hits in a pixel, a fast sampling rate is chosen, the sampling rate parameter does not affect to the results of the study of the effect comparing with the scanning strategy parameters. We also assumed white instrument noise, and we solve the map making equation as a solution of maximum Likelihood:

$$\widehat{\mathbf{m}} = (\mathbf{A}^T\mathbf{N}^{-1}\mathbf{A})^{-1}(\mathbf{A}^T\mathbf{N}^{-1}\mathbf{d}). \tag{4.9}$$

Here $\widehat{\mathbf{m}}$ includes the estimated maps of Stokes parameters $\widehat{I}$, $\widehat{Q}$ and $\widehat{U}$. $\mathbf{A}$ is the pointing matrix. $\mathbf{N}$ is the noise covariance matrix in the time domain, ψ is the polarization angle of a detector with respect to a reference axis. The data measurements vector $\mathbf{d}$ are given by

$$S_j = I(p) + Q(p)\cos 2\psi_j + U(p)\sin 2\psi_j + n_j \tag{4.10}$$

where n_j represents a stationary white noise source for observations indexed by j. Here the index j ($j = 1, \ldots, N_p$) labels the observations falling into the pixel labeled by p. Under the hypothesis of white instrument noise, the map making

[2] http://healpix.sourceforge.net

equation 4.9 can be expressed into a block diagonal form for different pixels.

$$\begin{pmatrix} \widehat{I}(p) \\ \widehat{Q}(p) \\ \widehat{U}(p) \end{pmatrix} = \frac{1}{N_p} \times \begin{pmatrix} 1 & \langle \cos 2\psi_j \rangle & \langle \sin 2\psi_j \rangle \\ \langle \cos 2\psi_j \rangle & \frac{1+\langle \cos 4\psi_j \rangle}{2} & \frac{\langle \sin 4\psi_j \rangle}{2} \\ \langle \sin 2\psi_j \rangle & \frac{\langle \sin 4\psi_j \rangle}{2} & \frac{1-\langle \cos 4\psi_j \rangle}{2} \end{pmatrix}^{-1} \times \begin{pmatrix} \sum_j S_j \\ \sum_j S_j \cos 2\psi_j \\ \sum_j S_j \sin 2\psi_j \end{pmatrix} \tag{4.11}$$

where the hats indicate the maximum likelihood estimator maps, and $\langle \cdot \rangle$ denotes the average over all data samples j. We have also assumed that the noise variance is identical all detectors [33] and there is no correlation in time, nor variance of the r.m.s noise with time between detectors.

Following the equation 4.10, bandpass mismatch error maps are given by

$$\begin{pmatrix} \delta\widehat{I}_{\rm BPM} \\ \delta\widehat{Q}_{\rm BPM} \\ \delta\widehat{U}_{\rm BPM} \end{pmatrix} = \begin{pmatrix} 1 & \langle \cos 2\psi_j \rangle & \langle \sin 2\psi_j \rangle \\ \langle \cos 2\psi_j \rangle & \frac{1+\langle \cos 4\psi_j \rangle}{2} & \frac{\langle \sin 4\psi_j \rangle}{2} \\ \langle \sin 2\psi_j \rangle & \frac{\langle \sin 4\psi_j \rangle}{2} & \frac{1-\langle \cos 4\psi_j \rangle}{2} \end{pmatrix}^{-1} \times \begin{pmatrix} \delta \langle S_j \rangle \\ \delta \langle S_j \cos 2\psi_j \rangle \\ \delta \langle S_j \sin 2\psi_j \rangle \end{pmatrix}. \tag{4.12}$$

Here $\delta \langle S_j \rangle$, $\delta \langle S_j \cos 2\psi_j \rangle$, and $\delta \langle S_j \sin 2\psi_j \rangle$ are sky component maps. We assumed perfect calibration of normalization of the CMB component for each detector.

For future studies of the CMB polarization, the error of greatest concern arises from the leakage of the I component of the foregrounds into the Q and U components of the maximum likelihood band sky maps. From equation (4.12) we observe that the three terms $\delta \langle S_j \rangle$, $\delta \langle S_j \cos 2\psi_j \rangle$, and $\delta \langle S_j \sin 2\psi_j \rangle$ can potentially induce a bias on the polarization Stokes parameters. The first term $\delta \langle S_j \rangle$ has no impact

if the maps of $\langle \cos 2\psi \rangle$ and $\langle \sin 2\psi \rangle$ vanish. This is the case in particular if the detectors are arranged in sets of perfectly orthogonal pairs observing the sky. If in addition for each such pair there is a matching pair observing at an angle of 45° relative to the first one, we get an optimized configuration [33] for which the 3×3 matrix in equation (4.11) takes the form

$$\begin{pmatrix} 1 & 0 & 0 \\ 0 & \frac{1}{2} & 0 \\ 0 & 0 & \frac{1}{2} \end{pmatrix}^{-1} . \tag{4.13}$$

This simple form is 'optimized configuration' of detectors orientation which was used for the Planck mission and this type of detector arrangement is now standard for all proposed CMB polarization experiments. We then get

$$\begin{aligned} \delta \widehat{\mathrm{Q}}_{\mathrm{BPM}}(\mathrm{p}) &= 2\delta \langle S_j \cos 2\psi_j \rangle , \\ \delta \widehat{\mathrm{U}}_{\mathrm{BPM}}(\mathrm{p}) &= 2\delta \langle S_j \sin 2\psi_j \rangle , \end{aligned} \tag{4.14}$$

According to the sky model presented in Sect. 4.1 we known that

$$\begin{aligned} \delta \langle \mathrm{S_j} \cos 2\psi_\mathrm{j} \rangle &= \sum_{(\mathrm{c})} \mathrm{I}_{(\mathrm{c})}(\mathrm{p}) \sum_{\mathrm{i}} \gamma_{(\mathrm{c}),\mathrm{i}} \mathrm{f_i}(\mathrm{p}) \langle \cos 2\psi_{\mathrm{i,j}} \rangle , \\ \delta \langle \mathrm{S_j} \sin 2\psi_\mathrm{j} \rangle &= \sum_{(\mathrm{c})} \mathrm{I}_{(\mathrm{c})}(\mathrm{p}) \sum_{\mathrm{i}} \gamma_{(\mathrm{c}),\mathrm{i}} \mathrm{f_i}(\mathrm{p}) \langle \sin 2\psi_{\mathrm{i,j}} \rangle . \end{aligned} \tag{4.15}$$

Here (c) labels the non-CMB components of the sky model and i labels the detectors. The coefficients $\gamma_{(c),i}$ parameters vary from detector to detector and it depends on the $g_i(\nu)$ function. $f_i(p)$ represents the fraction of the total hits in the pixel p from the detector i, and $\langle \cos 2\psi_{i,j} \rangle$ and $\langle \sin 2\psi_{i,j} \rangle$ are the components of the second-order crossing moments in pixel p for the detector i.

4.2.1 Results

In this section, I present the numerical results for the bandpass mismatch error maps and their angular power spectra using simulations. The exact correspondence of the pointing with the center of the pixel is an approximation which is performed in order to isolate the effect of band-pass mismatch an to avoid introducing other effects. The timestreams for each detector is constructed by reading

a CMB map and a galactic thermal dust map $N_{\rm side} = 256$. The value of $N_{\rm side}$ is compatible with the proposed instrumental beam size. The input maps have been previously convolved with a Gaussian kernel to account for the instrument beam $\theta_{\rm FWHM} = 32'$. We use an instrumental model with actual locations of detectors in the focal plane as described in [79] or [35]. We have noticed that the details of the arrangement of the detectors on the focal plane have little or no impact on the leakage angular power spectra. We simulate time streams by scanning input template maps without polarization, nor noise as well as same pixelization between input and output maps using several detectors. We use detectors with nominal locations in the focal plane and polarizer orientations for LiteBIRD. Because the map making method is linear and the noise does not affect the bias induced by the mismatch. For the same reason, we do not introduce sky emission polarization in simulations. The bandpass mismatch properties of each detector are generated randomly and in a statistically independent manner. We use the pointing information in an ecliptic coordinate as well as a galactic coordinate. The hit map for 222 detectors and a year observation is shown in figure 4.6 in the galactic and ecliptic coordinates. Scanning strategy creates symmetric pattern in ecliptic coordinates with respect to angles θ, ϕ after one year observation. The simulation assumed 222 detectors, which is the number of detectors composing the LiteBIRD arrays described in [79], spread over a large focal plane approximatively 10 degrees wide observing with no HWP. The observation time is a sidereal year length 365 days to ensure that the full and uniform sky is surveyed. We assume the fiducial scanning parameters $\alpha = 65°$, $\beta = 30°$, $\tau_{\rm spin} = 10\,{\rm min}$, and $\tau_{\rm prec} = 96.1803\,{\rm min}$ for the center of the focal plane (see Section 4.2.3 for a discussion of the choice of $\tau_{\rm spin}$ and $\tau_{\rm prec}$ to minimize the inhomogeneity of the scanning pattern which is responsible for Moiré effects in the crossing moment maps).

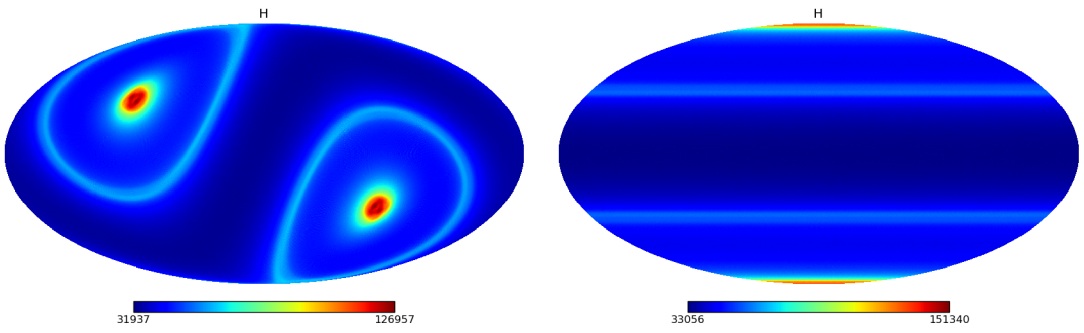

FIGURE 4.6: Hitcount map of 222 detectors and 365 days for a fiducial scanning strategy in the galactic and ecliptic coordinates.

Figure 4.7 shows the Q and U leakage maps δQ_{BPM} and δU_{BPM} for one particular realization in galactic and ecliptic coordinate. The output polarization maps result from optimal map making using our simulated noiseless and polarizationless timestreams for the 140 GHz channel. The bands at equal latitude visible in the leakage maps correspond to regions where the second order crossing moments depart significantly from zero (Fig. 4.6), the strong correlation between the relative leakage amplitude and these moments will be demonstrated in the section 4.2.2.

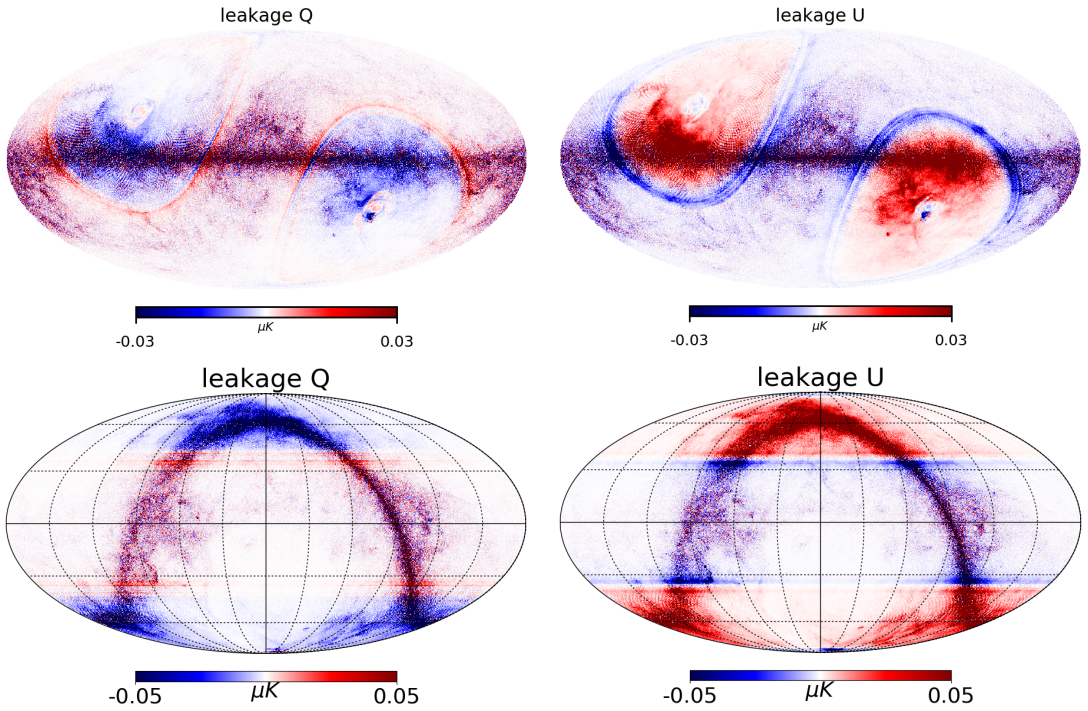

FIGURE 4.7: Q and U leakage maps, in galactic and ecliptic coordinates, with fiducial scanning parameters and $N_{\mathrm{det}} = 222$, a sidereal year survey.

Figure 4.8 shows the mask of 20 % sky fraction which is the galactic plane. This sky fraction number is verified by the temperature angular power spectrum comparison. Since we have intensity I component of the only CMB and the CMB plus the thermal dust output map after applying the map making equation 4.9, we mask the galactic plane and compute the angular power spectrum using "healpy.anafast" method. The result is plotted in the same figure with the angular power spectrum of the input CMB map. The sky fraction 20 % is a suitable masked sky fraction to have the same amplitude of angular power spectra between the input and output. The smaller sky fraction is tested by applying larger than 20 % masked galactic plane, the result is that the power spectrum is decreased as expected.

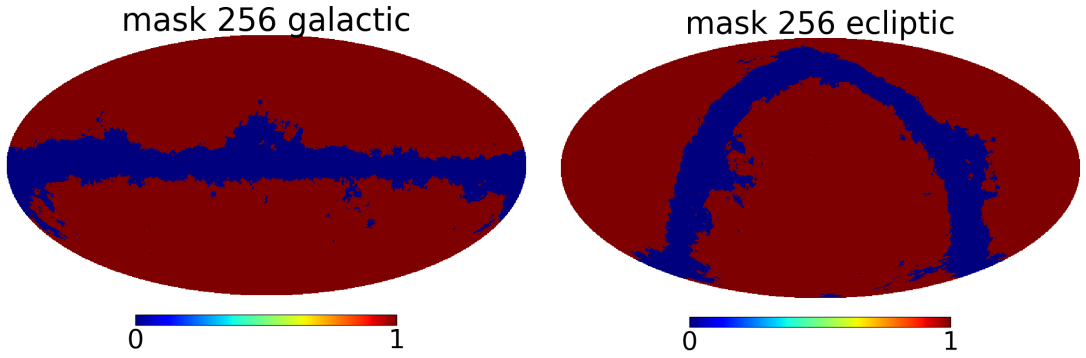

FIGURE 4.8: Mask 20 % sky in galactic and ecliptic coordinate.

Figures 4.9, 4.10 and 4.11 show the bandpass mismatch leakage contributions to the EE and BB power spectra in different observing configurations. The power spectra are computed after masking the 20% of the sky where the thermal dust emission is the strongest. These plots also show the primordial power spectrum of BB mode model for two different values of tensor-to-scalar $r = 10^{-2}, 10^{-3}$. The dashed curves indicate how the signal is attenuated by convolution with a Gaussian beam $\theta_{FWHM} = 32'$. The power spectra are averaged of 10 realizations simulation.

Figure 4.9 indicates that the bandpass mismatch error amplitude of the power spectrum scales as $1/N_{\rm det}$ the number of detectors. This scaling becomes more accurate when $N_{\rm det}$ becomes large, as shown by comparing the EE and BB leakage power spectra for $\tau_{\rm spin} = 10\,{\rm min}$, $\tau_{\rm prec}$= 96.1803 min and $N_{\rm det}$ of either 74 or 222. The pairs of spectra have the same shape but the ratio of power spectrum amplitudes is consistent with the predicted ratio $222/74 = 3$.

Figure 4.10 shows the BB power spectra for $\alpha = 65°$, $\beta = 30°$ for several spin and precession period ratio. We see that the characteristics of the leakage angular power spectrum particularly in the peaks locations at $\ell \geq 100$) depend on the exact ratio of $\tau_{\rm spin}$ and $\tau_{\rm prec}$. A proper value of the ratio $\tau_{\rm prec}/\tau_{\rm spin}$ moves the peaks in the bandpass leakage spectrum to higher ℓ, away from the location of the maximum of the primordial B-mode recombination bump. The more detail study will be described in the section 4.2.3.

Figure 4.11 compares the BB leakage power spectra for different configuration of scanning strategy of precession angles α and β, and also different spin period, precession period. With the constraint $\alpha+\beta = 95°$, scan strategies with larger precession angle produce less leakage because they allow for more homogeneous scan

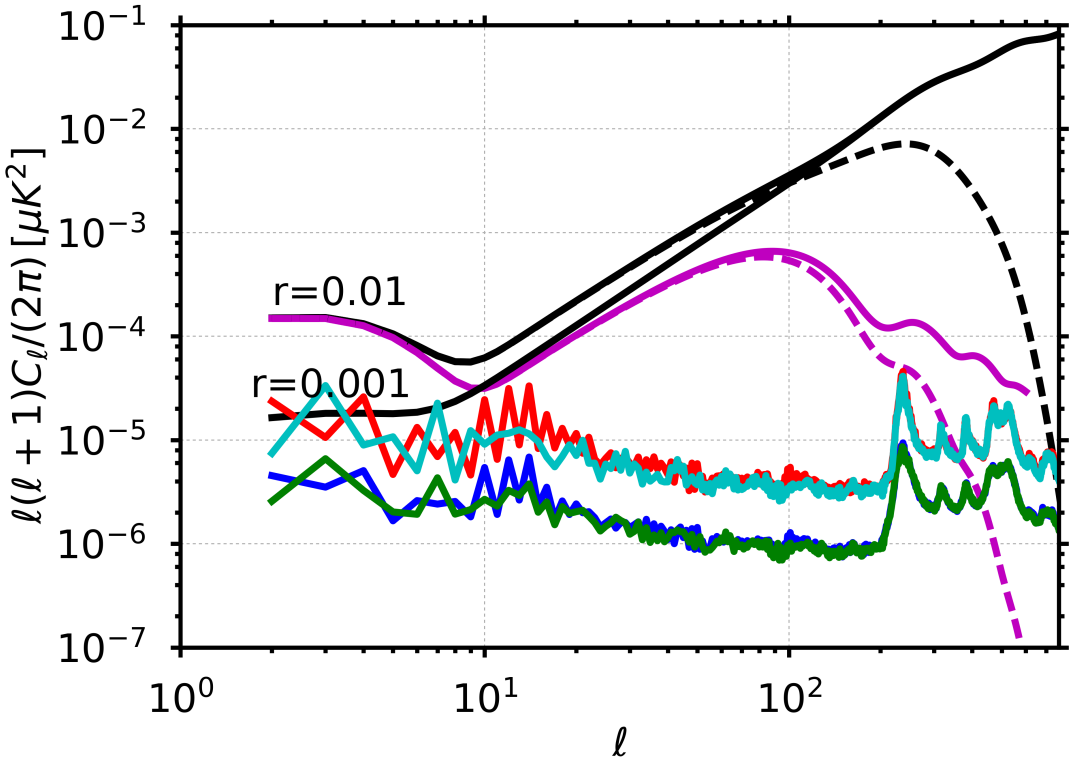

FIGURE 4.9: EE and BB leakage power spectra for $\alpha = 65°$, $\beta = 30°$, $\tau_{\rm spin} = 10\,{\rm min}$, $\tau_{\rm prec} = 96.1803\,{\rm min}$, and combining data for either 74 or 222 detectors. The red curve corresponds to BB with 74 detectors, the cyan to EE with 74 detectors, the blue to BB with 222 detectors and the green to EE with 222 detectors. The purple curve represents a model of primordial B mode power spectrum with fiducial cosmological parameters after Planck for $r = 0.01$, the black curves are including lensing for $r = 0.01$ and $r = 0.001$. The dashed curves show the effect of convolving with a 32 arcmin beam. This plot demonstrates the $1/N_{\rm det}$ dependance of the level of the power spectra.

angle coverage per pixel, and hence lower $|\langle\cos 2\psi_j\rangle|$ and $|\langle\sin 2\psi_j\rangle|$ per individual detector.

We observe that the power spectra above (without an HWP) are approximately proportional to $\ell^{-\eta}$ where $\eta \approx 2.5$. We also observe some dependence of the amplitude of the leakage spectra with respect to the scanning strategy parameters α and β. Scanning strategies with more uniform angular coverage (provided by larger precession angles for the studied cases) have a lower leakage amplitude.

Overall, the amplitude of the leakage due to bandpass mismatch error is nearly a Gaussian with a zero mean and the variations of γ_d impact all multipoles of the leakage map power spectrum in a correlated way. For this reason, an accurate estimate of the average leakage power spectrum requires averaging many independent

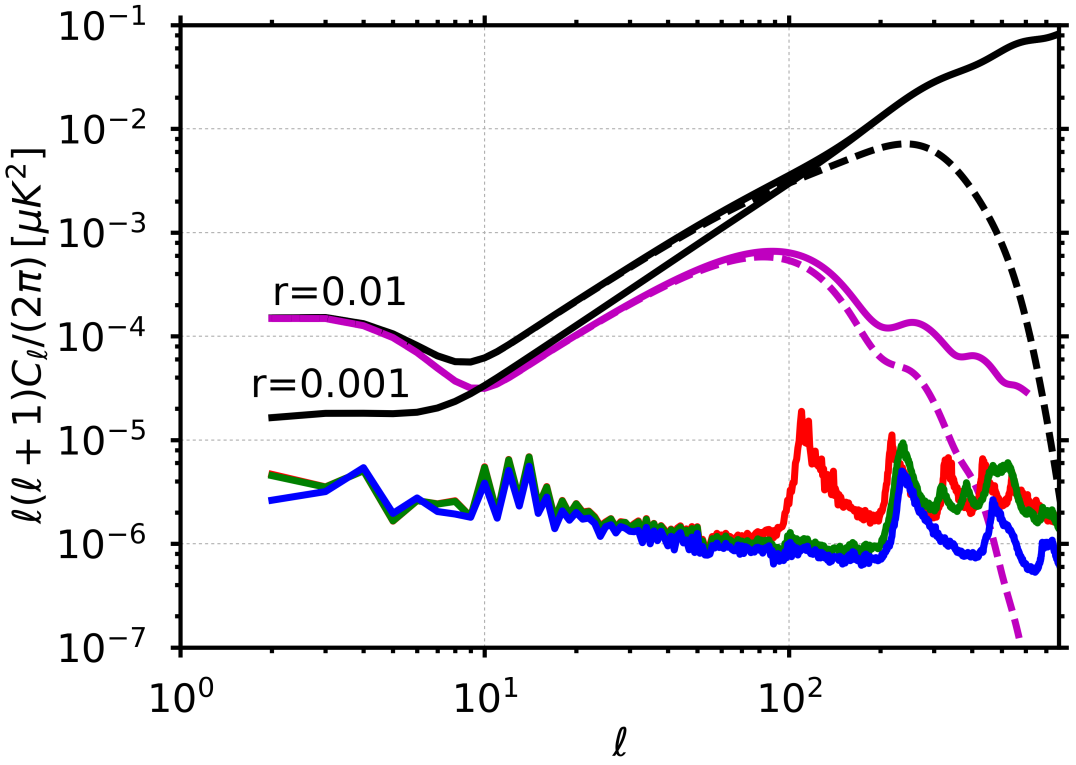

FIGURE 4.10: BB leakage power spectra for $\alpha = 65°$, $\beta = 30°$, $\tau_{\rm spin}$=10 min, $\tau_{\rm prec}$=93 min (red); $\tau_{\rm spin}$=10 min, $\tau_{\rm prec}$=96.1803 min (green); and $\tau_{\rm spin}$=10/3 min, $\tau_{\rm prec}$=96.1803 min (blue). Simulations include 222 detectors and 365 days observation. See the Fig. 4.9 caption for a description of the model curves.

realizations even if many detectors are used for the simulations. At least on large angular scales, the fluctuations in the power spectrum due to different realizations is roughly an overall amplitude varying as the square of a Gaussian. Figure 4.12 shows 10 single realizations of the bandpass mismatch error, it indicates the fluctuation of the angular power spectrum for variations of γ_d.

As a conclusion, the study of bandpass mismatch error help to choose an optimal scanning strategy of future CMB polarization satellite. The amplitude of the bandpass leakage depends on the scanning strategy configuration of open precession angle α and spin angle β, these peaks on the angular spectrum depends on the ratio between precession period and spin period, the study is described in the section 4.2.3. The sample rate does not impact to the leakage of the bandpass mismatch error, I already tested the case of the faster sampling rate, the result indicated that the amplitude of angular power spectrum is not affected. I have performed many simulations with $N_{side} = 256 \times 2 = 512$ to verify the dependence

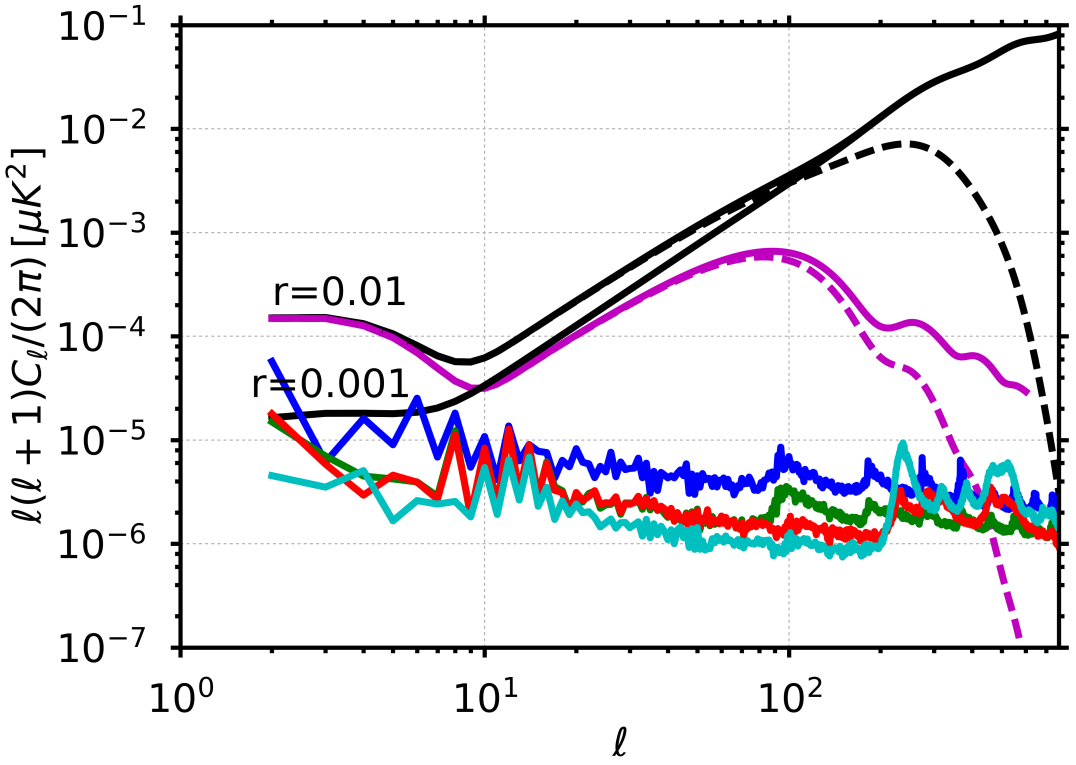

FIGURE 4.11: BB leakage power spectra for different scanning parameters. In cyan: $\alpha = 65°$, $\beta = 30°$, $\tau_{\rm spin}$=10 min, $\tau_{\rm prec}$=96.1803 min, red: $\alpha = 50°, \beta = 45°$, $\tau_{\rm spin}$=10 min, $\tau_{\rm prec}$=96.1803 min, green: $\alpha = 50°$, $\beta = 45°$, $\tau_{\rm spin}$=2 min, $\tau_{\rm prec}$=4 day, blue: $\alpha = 30°, \beta = 65°$, $\tau_{\rm spin}$=2 min, $\tau_{\rm prec}$=4 day. Spectra are computed for 222 detectors. Curves for the B mode model are described in Fig. 4.9 caption. For the scanning strategies with a long precession period, we computed spectra for 100 detectors rescaling to 222 equivalent detectors using the $1/N_{\rm det}$ dependance.

with resolution of those results. The results are similar. The best sampling rate choice could be determined by studying other systematic effects such as 1/f noise performance, cosmic rays interaction with detectors.

Table 4.1 shows the contribution of bandpass miss match error leakage to tensor-to-scalar r based on its angular power spectrum averaged over many realizations. The calculation is using chi-square estimation:

$$\hat{\delta}r = \frac{\sum_{\ell=\ell_{\rm min}}^{\ell_{\rm max}} (2\ell+1) C_\ell \hat{C}_\ell}{\sum_{\ell=\ell_{\rm min}}^{\ell_{\rm max}} (2\ell+1) C_\ell^2}. \tag{4.16}$$

Here C_ℓ is the power spectrum for the primordial B mode signal normalized to $r = 1$. $\hat{C}_\ell$ is the angular power spectra signal due to the bandpass mismatch leakage. The Table shows δr calculated for two ranges of ℓ: one with $\ell \in [2, 10]$ to

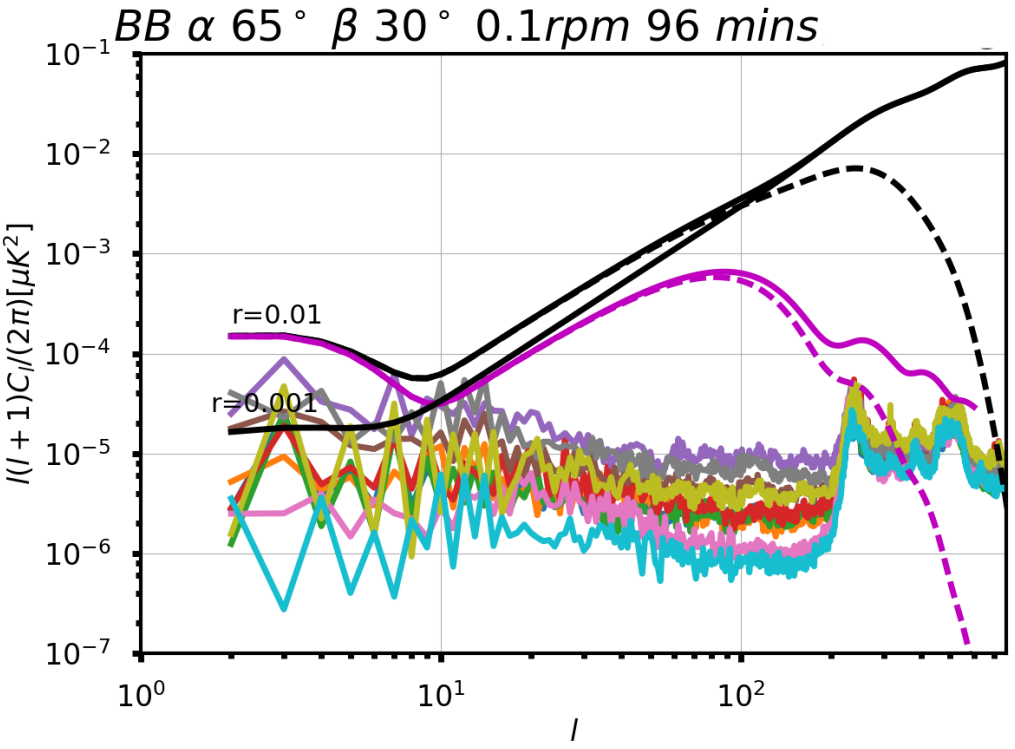

FIGURE 4.12: The angular power spectrum of 10 realizations with different set of γ_d parameter.

	$2 \leq \ell \leq 10$	$10 \leq \ell \leq 200$
$\alpha = 30°$; $\beta = 65°$; $\tau_{\rm prec} = 4\,$days; $\omega_{\rm spin} = 0.5\,$rpm	1.83×10^{-3}	9.32×10^{-5}
$\alpha = 50°$; $\beta = 45°$; $\tau_{\rm prec} = 4\,$days; $\omega_{\rm spin} = 0.5\,$rpm	6.49×10^{-4}	4.66×10^{-5}
$\alpha = 50°$; $\beta = 45°$; $\tau_{\rm prec} = 96\,$min; $\omega_{\rm spin} = 0.1\,$rpm	6.32×10^{-4}	3.08×10^{-5}
$\alpha = 65°$; $\beta = 30°$; $\tau_{\rm prec} = 93\,$min; $\omega_{\rm spin} = 0.1\,$rpm	3.29×10^{-4}	7.61×10^{-5}
$\alpha = 65°$; $\beta = 30°$; $\tau_{\rm prec} = 96\,$min; $\omega_{\rm spin} = 0.1\,$rpm	3.27×10^{-4}	2.11×10^{-5}
$\alpha = 65°$; $\beta = 30°$; $\tau_{\rm prec} = 96\,$min; $\omega_{\rm spin} = 0.3\,$rpm	3.03×10^{-4}	1.77×10^{-5}

TABLE 4.1: Contribution of bandpass mismatch error to the tensor-to-scalar ratio r computed according to the equation (4.16) for 222 detectors and 365 days observation. The level of the bandpass leakage relative to primordial B-mode signals is acceptable at the angular scale of the recombination bump, but problematic in the reionization bump at $\ell \leq 10$. Scanning strategies with larger α and smaller β perform better, as they provide more uniform angular coverage in each pixel.

isolate the signal from the re-ionization bump, and another with $\ell \in [10, 100]$ to isolate the signal arising from the recombination bump. The results in the table assume $N_{\rm det} = 222$ detectors but can be rescaled based on the $1/N_{\rm det}$ dependence to other numbers of detectors. These results are only an order of magnitude estimate because they are based on a single 140 GHz channel, and it has been assumed

that very low and very high-frequency channels have been used to remove the non-primordial components completely. We stress that the bandpass mismatch power spectrum is not a simple bias that can be predicted and subtracted away because its overall amplitude suffers large fluctuations, which is of the same order of magnitude as the average bias itself.

The adopted model for the band-passes uncertainty assumes a 1 % deviation from nominal value of $\nu_{\rm min}$ and $\nu_{\rm max}$. I checked how the result scales with the value of this uncertainty, moving this for example to 2%. I have verified that the resulting γ_d are increased by a factor of 2, as was predicted. The result in figure 4.13 shows that the angular power spectrum is scaled by a factor of 4. The simulation used the fiducial scanning strategy and 10 realizations.

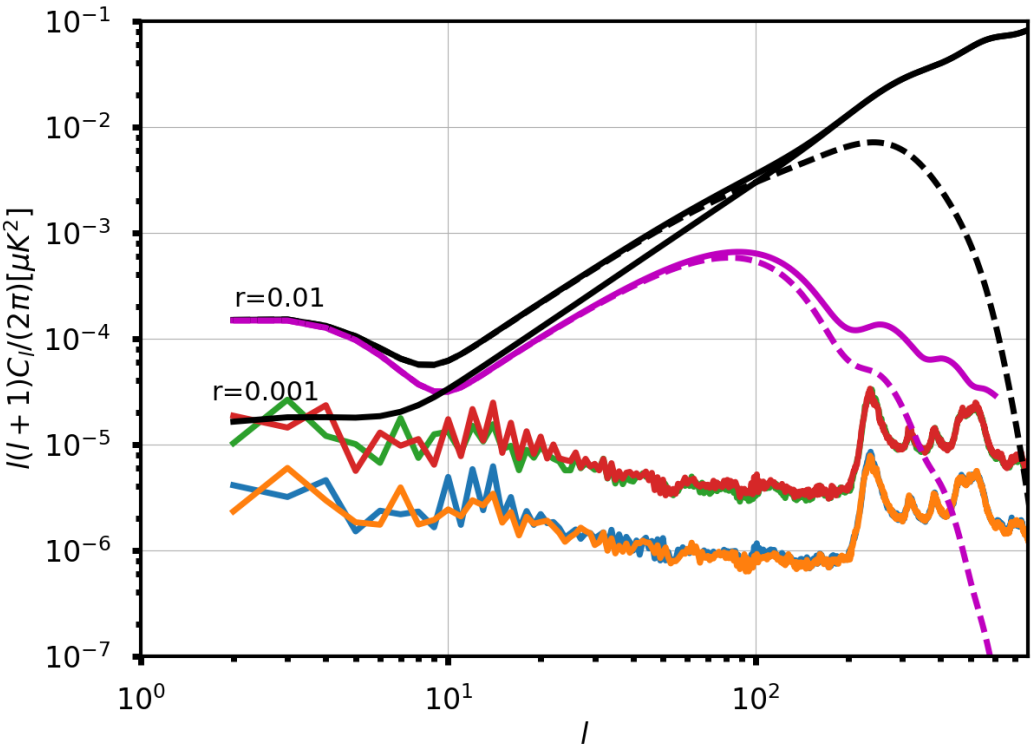

FIGURE 4.13: The angular power spectrum of 2 % variation of the filters, the power spectrum is scaled by 4.

One more point, the errors on the band definition are a uniformly distributed. What if there is a global offset or some systematic variation across the focal plane? This is important but difficult to address in absence of instrumental models of the origin of bandpass mismatches. In the most pessimistic case, there is a constant difference between detector γ_a and detector γ_b coherent across the

focal plane as shown in figure 4.14, where the "a" bolometers are the ones for which the orientation of the polarizer is closer to the horizontal axis in the detector frame. In that case, we observe that the leakage is boosted by a large factor compared to the uncorrelated case resulted in figure 4.15. This is because the leakages for each pair do not tend to cancel each other in the global leakage map including all detectors. However as we mentioned before we use detectors with nominal locations in the focal plane and polarizer orientations, each detector has a different value of γ_d, these pairs are orientated following $(0°, 90°), (-45°, 45°), (-120°, -30°), (-165°, -75°), (-180°, -90°), (-225°, -135°)$ on the focal plane. Figure 4.16 presents the leakage bandpass mismatch error maps for each pair orientation for a year observation and fiducial configuration scan. We can observe obviously that there have negative and positive patterns on the leakage maps of several pair orientations. Therefore there have cancellation across the focal plane when we use multi-detectors, this also implies the scale of $1/N_{\rm det}$ in the amplitude of power spectrum.

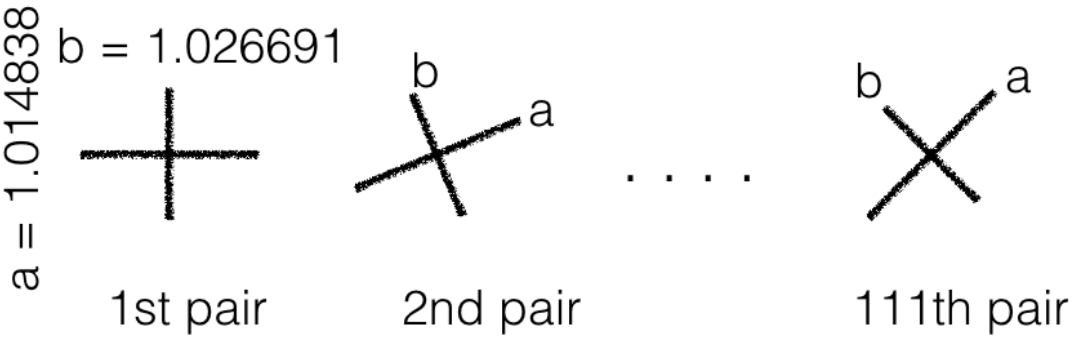

FIGURE 4.14: The global offset across the focal plane

Figure 4.17 shows that the amplitude of the angular power spectrum of each pair with nominal locations on the focal plane is the same as expected.

I have also computed the bandpass errors in case of Planck scanning strategy $\alpha = 7.5°$, $\beta = 85°$, $\tau_{\rm spin} = 1\,{\rm min}$, $\tau_{\rm prec} = 6\,{\rm month}$. Figure 4.18 shows the polarized leakage maps for 222 detectors and a sidereal year observation. In order to compare the level of the bandpass mismatch systematic error of the Planck satellite scanning strategy and the fiducial scanning strategy, the angular power spectra are plotted in figure 4.19. We observe that the leakage is higher by more than an order of magnitude in the power spectrum. It is obviously understandable because of the small opening angle α used to measure temperature anisotropies of Planck mission.

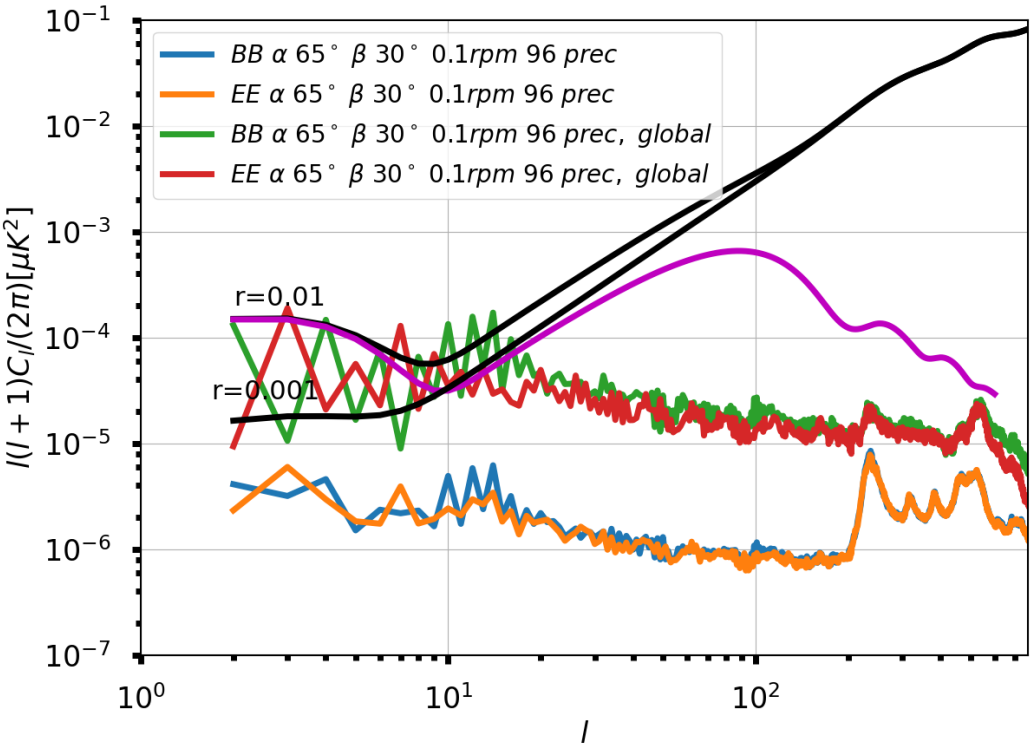

FIGURE 4.15: Angular power spectrum of the global offset across the focal plane compares with the nominal focal plane.

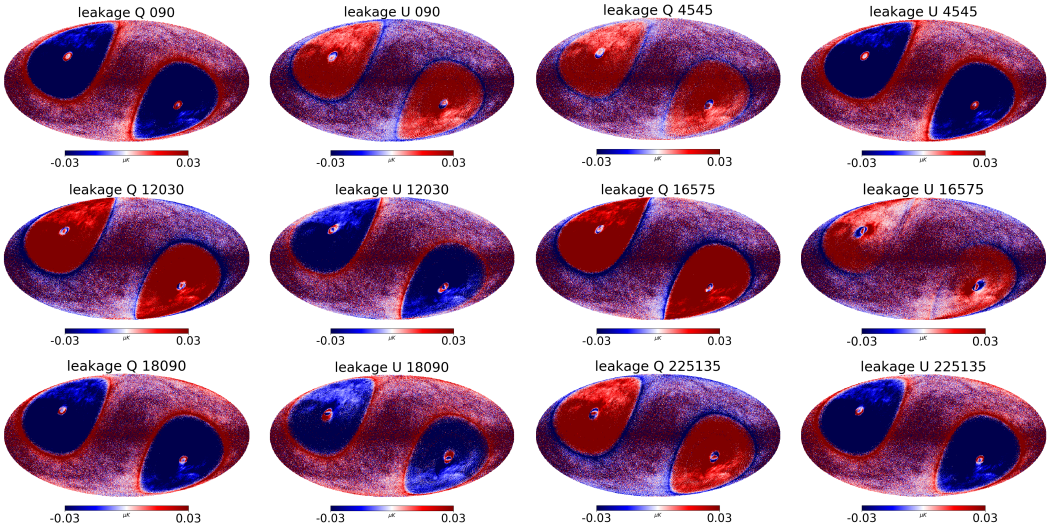

FIGURE 4.16: The leakage map of pair detectors with nominal locations. The title indicates the oriental angle of a pair detector.

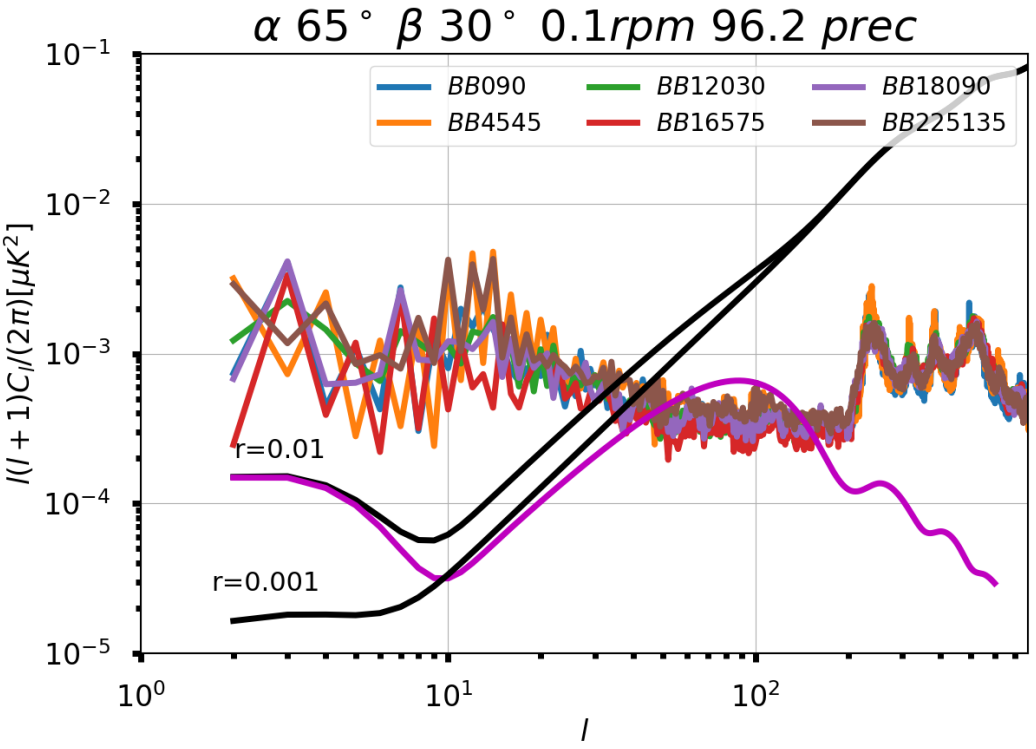

FIGURE 4.17: The BB angular power spectrum for each pair detector with nominal locations, the orientation of pair detector is labeled.

Thanks to the fast scanning with the Planck mission, we do not observe peaks on the high multipoles on the angular power spectrum.

So far, I presented the results of the case of no half-wave plate. Future studies will consider an imperfection of a rotating half-wave plate case. In case of a perfect HWP, we perform a simple set of simulations in which the input sky (smoothed by a 32′ beam) is a HEALPix map pixelized at $n_{\rm side} = 256$. The pixel size is well matched to the rotation speed of the HWP, which makes about one turn while it crosses a pixel. However, numerical effects will generate unevenness in the angular coverage of each pixel, and thus, when multi-detector maps are made using the equation 4.9, small bandpass leakage mismatch effects will subsist. Simulating the observation of this model sky with the use of a HWP spinning at 88 rpm and other parameters set to $\alpha = 65°$, $\beta = 30°$, $\tau_{\rm spin}$=10 min, $\tau_{\rm prec} = 96.1803$ min, we obtain the small residual leakage shown in figure 4.20, which confirms the effectiveness of the HWP in reducing bandpass leakage by homogenizing the angular coverage in each pixel. The shape of the spectrum of the residual is similar to that of white noise. Its origin is in the small unevenness of the angle distributions across the

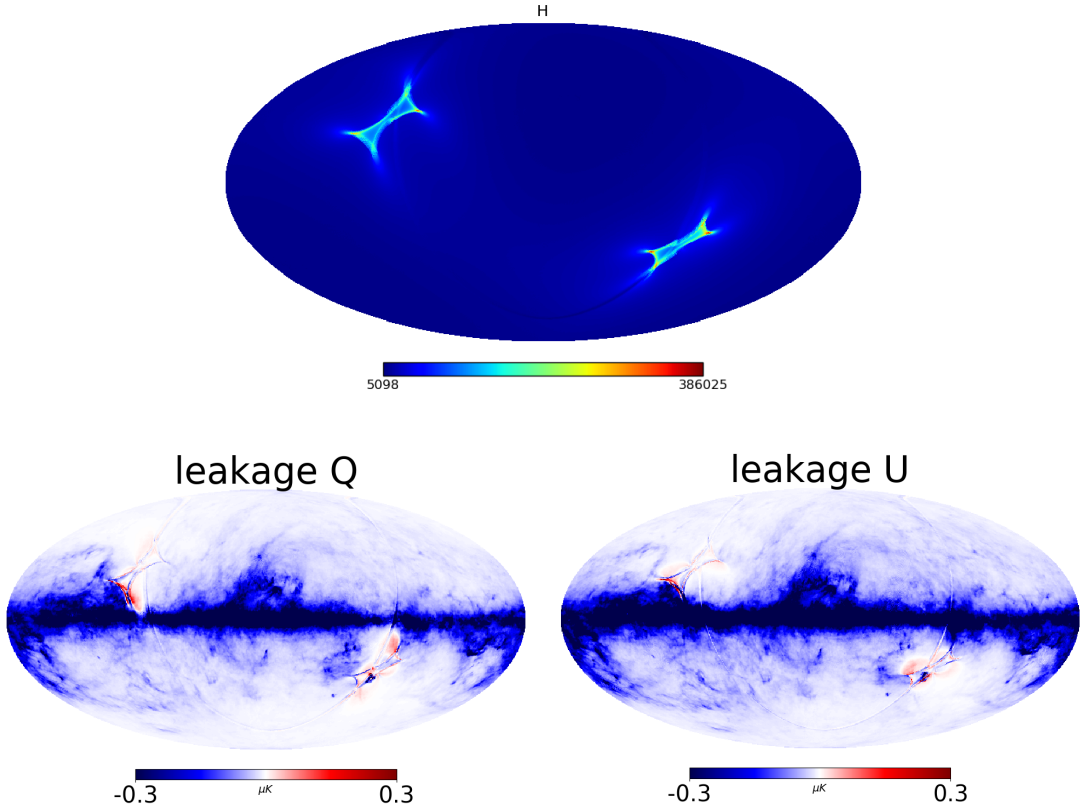

FIGURE 4.18: The hitcount map and leakage maps of the Planck scanning strategy case, $\alpha = 7.5°$, $\beta = 85°$, $\tau_{\rm spin} = 1\,{\rm min}$, $\tau_{\rm prec} = 6\,{\rm month}$, and combining data for 222 detectors and 365 days observation a single realization. The power spectrum of the fiducial scanning strategy is also plotted with purpose of comparison.

pixels and is an artefact of sky pixelization.

I verified that in case of a perfect HWP, the multi-detector solution for the polarization is close to the solution consisting in combining single detector polarization maps, as the residual leakage and its impact of r that can be read off the plot, is negligible.

4.2.2 Analytic estimates

In order to understand the features in the leakage maps related to the scanning strategy configuration. The correlation of leakage amplitude and crossing moment $\langle \cos 2\psi \rangle$ and $\langle \sin 2\psi \rangle$ provides an easy and fast way to predict the magnitude of leakage. We now consider the signal of the leakage from a pair i detector $S_{i;a}(t)$

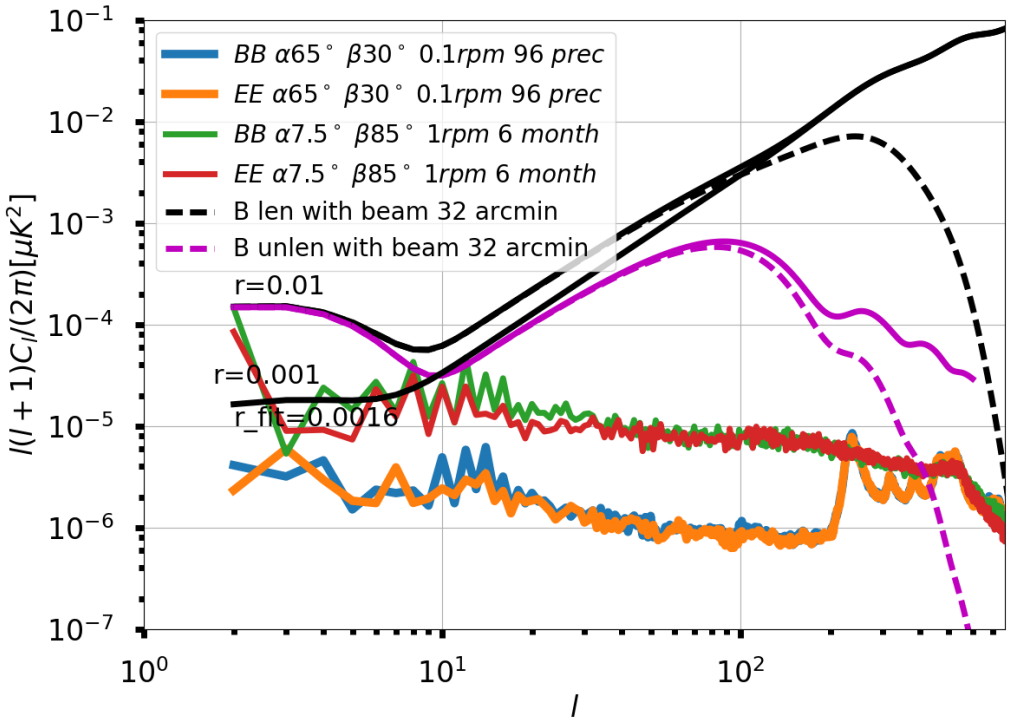

FIGURE 4.19: Power spectrum of the Planck scanning strategy case which is described in figure 4.18, I also plotted the plot of the fiducial scanning strategy is $\alpha = 65°$, $\beta = 30°$, $\tau_{\rm spin} = 10\,{\rm min}$, $\tau_{\rm prec}= 96\,{\rm min}$, and combining data for 222 detectors and 365 days observation

and $S_{i;b}(t)$ at time t in pixel p with no noise assumption.

$$\begin{aligned} {\rm S_{i;a}(t)} &= I_{i;p} + Q_p \cos 2\psi(t) + U_p \sin 2\psi(t) + M_{i;p}, \\ {\rm S_{i;b}(t)} &= I_{i;p} - Q_p \cos 2\psi(t) - U_p \sin 2\psi(t) - M_{i;p}. \end{aligned} \tag{4.17}$$

Here ψ is the polarizer angle of detector a and $I_{i;p}$, Q_p, U_p are the Stokes parameters. The bandpass mismatch component $M_{i;p}$ is given by

$${\rm M_{i;p}} = \frac{1}{2} \sum_{\rm (c)} \left(\gamma^{\rm a}_{\rm (c)} - \gamma^{\rm b}_{\rm (c)}\right)\ {\rm I_{p,(c)}}. \tag{4.18}$$

Here (c) denotes for foreground components. As mentioned before, the $\left(\gamma^{\rm a}_{\rm (c)} - \gamma^{\rm b}_{\rm (c)}\right)$ is vary from detector pair to detector pair. Each pair detector is orthogonality then $\langle \cos 2\psi \rangle$ and $\langle \sin 2\psi \rangle$ vanish.

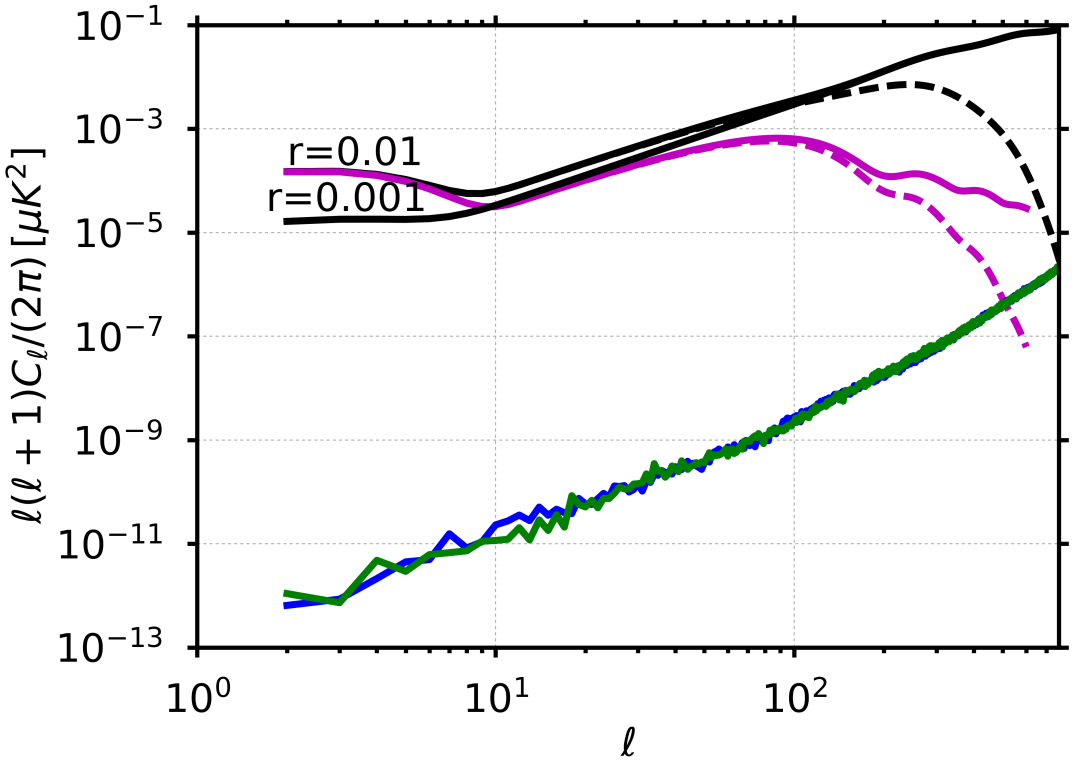

FIGURE 4.20: ***EE* and *BB* leakage power spectra with rotating HWP** for $\alpha = 65°$, $\beta = 30°$ and spin period of 10 min with a HWP rotating at 88 rpm for 50 detectors.

From the equation 4.12, the map making equation of bandpass mismatch error for a pair is given by

$$\begin{pmatrix} \widehat{I}_p \\ \widehat{Q}_p \\ \widehat{U}_p \end{pmatrix} = \begin{pmatrix} 1 & 0 & 0 \\ 0 & \frac{1}{2}\left(1 + \langle\cos 4\psi\rangle\right) & \frac{1}{2}\langle\sin 4\psi\rangle \\ 0 & \frac{1}{2}\langle\sin 4\psi\rangle & \frac{1}{2}\left(1 - \langle\cos 4\psi\rangle\right) \end{pmatrix}^{-1} \begin{pmatrix} \langle S\rangle \\ \langle\frac{1}{2}(S_a - S_b)\cos 2\psi\rangle \\ \langle\frac{1}{2}(S_a - S_b)\sin 2\psi\rangle \end{pmatrix}. \tag{4.19}$$

We neglected the index of detector label i with purpose of simplification. The estimated Stokes parameter maps $\widehat{Q_p}$ and $\widehat{U_p}$ can be decomposed as $\widehat{Q_p} = Q_p + \delta Q_p$ and $\widehat{U_p} = U_p + \delta U_p$, where δQ and δU represent the leakages to polarization resulting from bandpass mismatch. The leakage maps of intensity to polarization

is described by

$$\begin{aligned}\begin{pmatrix}\delta Q_p\\ \delta U_p\end{pmatrix} &= \begin{pmatrix}\frac{1}{2}(1+\langle\cos 4\psi\rangle) & \frac{1}{2}\langle\sin 4\psi\rangle\\ \frac{1}{2}\langle\sin 4\psi\rangle & \frac{1}{2}(1-\langle\cos 4\psi\rangle)\end{pmatrix}^{-1}\begin{pmatrix}\langle M_p\cos 2\psi\rangle\\ \langle M_p\sin 2\psi\rangle\end{pmatrix}\\ &= \frac{2}{(1-\langle\cos 4\psi\rangle^2-\langle\sin 4\psi\rangle^2)}\begin{pmatrix}1+\langle\cos 4\psi\rangle & -\langle\sin 4\psi\rangle\\ -\langle\sin 4\psi\rangle & 1-\langle\cos 4\psi\rangle\end{pmatrix}\\ &\quad\times\begin{pmatrix}\langle M_p\cos 2\psi\rangle\\ \langle M_p\sin 2\psi\rangle\end{pmatrix}. \end{aligned} \tag{4.20}$$

We can assuming the average distribution angles of $\langle\cos 4\psi\rangle^2+\langle\sin 4\psi\rangle^2 \ll 1$. This assumption is not so bad an approximation except very near the poles, then we obtain a relationship between leakage maps and distribution angles

$$\begin{pmatrix}\delta Q_p\\ \delta U_p\end{pmatrix} \approx 2\begin{pmatrix}\langle M_p\cos 2\psi\rangle\\ \langle M_p\sin 2\psi\rangle\end{pmatrix}. \tag{4.21}$$

Substituting M_p expression in the equation 4.18 and dividing the leakage map to the galactic components, we obtain the correlation function of the amplitude of the leakage and the distribution angle

$$\begin{pmatrix}\frac{\delta Q_p}{I_{\mathrm{Gal};p}}\\ \frac{\delta U_p}{I_{\mathrm{Gal};p}}\end{pmatrix} = \left(\gamma^{\mathrm{a}}_{\mathrm{Gal}}-\gamma^{\mathrm{b}}_{\mathrm{Gal}}\right)\begin{pmatrix}\langle\cos 2\psi\rangle\\ \langle\sin 2\psi\rangle\end{pmatrix}. \tag{4.22}$$

We can define that these distribution angles $\langle\cos 2\psi\rangle, \langle\sin 2\psi\rangle$ are crossing moments of a single detector. With the help of simulation for a pair detector I have verified the relationship of leakage maps and crossing moments. Figure 4.21 shows these maps in the equation 4.22 the relative leakage map $\delta\mathrm{Q_p}/\mathrm{I_{Gal;p}}$ and the crossing moment map $\sum\cos 2\psi/n_p$. The $\delta\mathrm{U_p}/\mathrm{I_{Gal;p}}$ and $\sum\sin 2\psi/n_p$ components have similar properties.

The tight link of the leakage map and the crossing moment map due to bandpass mismatch error is shown in figure 4.22 using scattering histogram two dimensions plot for a subset of pixels of these maps. We observed that the high correlation of two maps has a linear slope following $\Delta\gamma=\gamma_a-\gamma_b$ as the equation 4.22. It means that the approximations made to derive equation 4.22 are verified. The exception of the linear slope dues to pixels near to poles where the angle coverage of crossing moment is less uniform for the fiducial scanning strategy.

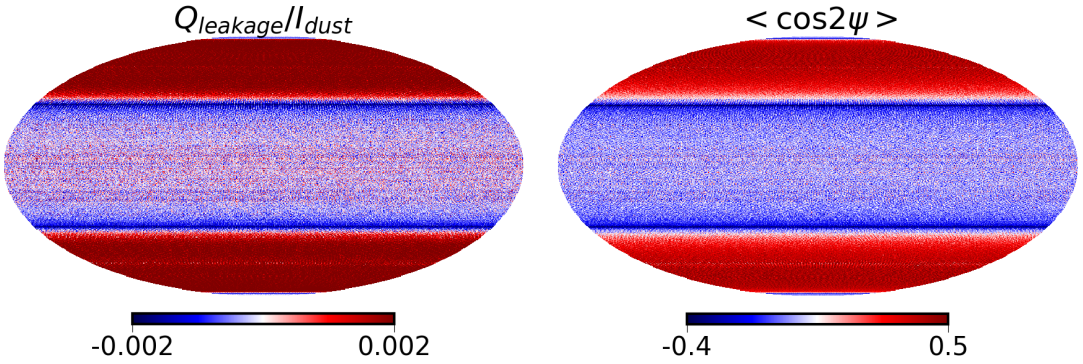

FIGURE 4.21: Left: Leakage for the Q component relative to the dust temperature ($\delta Q/I_{Gal}$) after polarization reconstruction using one bolometer pair only and a one year observation time. Right: Averaged $\cos 2\psi$ in each pixel for one bolometer after one year of observation time. This quantity is strongly correlated to the relative leakage Q component with respect to the dust intensity.

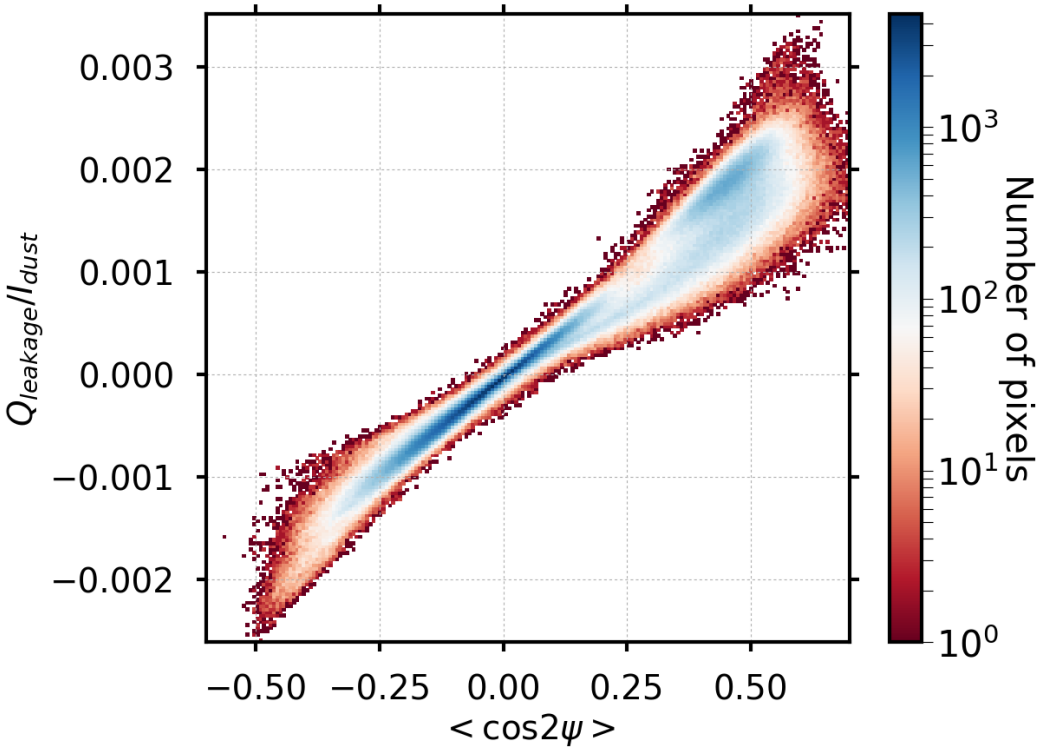

FIGURE 4.22: Values of the relative leakage $\delta Q_p/I_{Gal;p}$ for a pair of detectors with orthogonal polarizations of a function of the scanning strategy parameter $(1/n_p)\sum \cos 2\psi$ (see text) after map making with two detectors only. We observe a tight correlation between the relative leakage and the second order crossing moments.

We can develop the equation 4.22 to find the solution combining many detectors. We also start from the equation 4.20, the leakage component of multi-detector is

given by

$$\begin{pmatrix}\delta Q_p\\ \delta U_p\end{pmatrix} = \begin{pmatrix}\frac{1}{2}\sum_{\mathrm{i}}\sum_{\mathrm{j}}(1+\cos 4\psi_{\mathrm{i}}^{\mathrm{j}}) & \frac{1}{2}\sum_{i}\sum_{j}\sin 4\psi_i^j\\ \frac{1}{2}\sum_{\mathrm{i}}\sum_{\mathrm{j}}\sin 4\psi_{\mathrm{i}}^{\mathrm{j}} & \frac{1}{2}\sum_{i}\sum_{j}(1-\cos 4\psi_i^j)\end{pmatrix}^{-1}\begin{pmatrix}\sum_{\mathrm{i}}\sum_{\mathrm{j}}\cos 2\psi_{\mathrm{i}}^{\mathrm{j}}\,\mathrm{M_{i,p}}\\ \sum_{\mathrm{i}}\sum_{\mathrm{j}}\sin 2\psi_{\mathrm{i}}^{\mathrm{j}}\,\mathrm{M_{i,p}}\end{pmatrix} \tag{4.23}$$

Here we labeled the detector pairs i and all falling samples j in pixel p. Since the number of detector pair is increased, the covariance matrix in the equation 4.23 becomes closely diagonal. So that we obtain a simple approximation:

$$\frac{\delta\mathrm{Q_p}}{\mathrm{I_{Gal;p}}} \approx \frac{2}{\mathrm{N_{hit}}}\sum_{\mathrm{i}}\Delta\gamma_{\mathrm{i}}\sum_{\mathrm{j}}\cos 2\psi_{\mathrm{i}}^{\mathrm{j}}, \tag{4.24}$$

Here $\mathrm{N_{hit}}$ is the total number of hit counts of all detectors and $\Delta\gamma_i = \gamma_i^a - \gamma_i^b$. Because γ parameter is random and independently, we can express variance of the equation 4.24 into separated terms

$$\mathrm{Var}\left(\frac{\delta\mathrm{Q_p}}{\mathrm{I_{Gal;p}}}\right) \approx \sum_{\mathrm{i}}\mathrm{Var}(\Delta\gamma_{\mathrm{i}})\left(\sum_{\mathrm{j}}\cos 2\psi_{\mathrm{i}}^{\mathrm{j}}\right)^2\left(\frac{2}{\mathrm{N_{hit}}}\right)^2, \tag{4.25}$$

we have $\mathrm{Var}(\Delta\gamma) = 2\mathrm{Var}(\gamma)$ then we obtain the variance of the leakage maps and crossing moment cosine in case of multi-detectors is

$$\mathrm{Var}\left(\frac{\delta Q_p}{I_{\mathrm{Gal};p}}\right) \approx 4\frac{\mathrm{Var}(\gamma)}{N_{\mathrm{det}}}\left\langle\left(\frac{\sum\cos 2\psi_i^j}{\bar{n}_p}\right)^2\right\rangle_{\mathrm{det}}, \tag{4.26}$$

Here $\langle\,\cdot\,\rangle_{\mathrm{det}}$ means average over all detectors, and $\bar{n}_p = \frac{N_{\mathrm{hit}}}{N_{\mathrm{det}}}$ is definition of the average number of hits per detector. The equation 4.26 is the expression for Q component, the U component has similar variance of leakage map with the crossing moment sine map. The comparison of variance leakage map the quantity $\mathrm{Var}\,(\delta Q_p/I_{\mathrm{Gal};p})$ and crossing moment the quantity $\left\langle\left(\,(1/\bar{n}_p)\sum\cos 2\psi_i\right)^2\right\rangle_{\mathrm{det}}$ shows in the figure 4.23. The result is simulated by 10 times Monter Carlo realizations.

Similarly in case of a pair detector, figure 4.24 shows the correlation of the equation 4.26 in the scatter plot. We observed that the significant correlation between two quantities is especially on large scales. The dispersion is partly due to the limited number of realizations to estimate the variance. Nevertheless, the result shows that

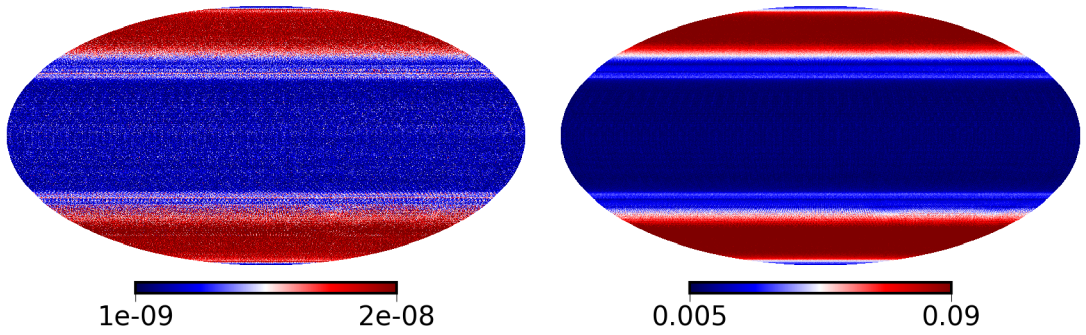

FIGURE 4.23: Left: Estimated leakage variance of the Q component relative to the dust temperature ($\mathrm{Var}\,(\delta Q_p/I_{\mathrm{Gal};p})$) after polarization reconstruction using all bolometer pairs and one year of observations. We used 10 independent realizations of the bandpass to estimate the variance. Right: Averaged $\left\langle \left((1/\bar{n}_p) \sum \cos 2\psi_i^j \right)^2 \right\rangle_{\rm det}$ in each pixel for all bolometers after one year of observation time. As for the detector pair case, we observe a tight correlation between the two maps on large angular scales

we can evaluate the level of bandpass mismatch error by study only the second order crossing moments maps cosine and sine without the need of running large simulations of map making. This method also explains the result in figure 4.11, it means that the scanning strategies (α and β parameters) with more uniform angle distribution (larger precession angle α) have lower the impact of bandpass mismatch error (see also [150] for the link with other systematic effects).

4.2.3 Precession period and spin period ratio $\tau_{\rm prec}/\tau_{\rm spin}$

The observing strategy of a CMB polarization mission must be designed to cover the complete sky with adequate polarization angle coverage at each point. Homogeneous observing time among all pixels and all polarization angles provides the lowest noise power spectrum, uncorrelated between maps of I, Q, and U. The homogeneity of the sky and angle coverage can be optimized with a proper choice of the values of the various angles, and with an optimization of the spinning and precession period. In this section, we discuss how to optimize precession and spin period scanning parameters.

Moiré effects in the leakage maps, generating peaks in the bandpass leakage angular power spectrum, arise from concentrations of scans in particular regions of sky and with sharp discontinuities in the angle coverage maps. The most notable effect arises for $\tau_{\rm spin} = 10\,\mathrm{min}$ and $\tau_{prec} = 93\,min$, $\alpha = 65°$ and $\beta = 30°$ as shown in

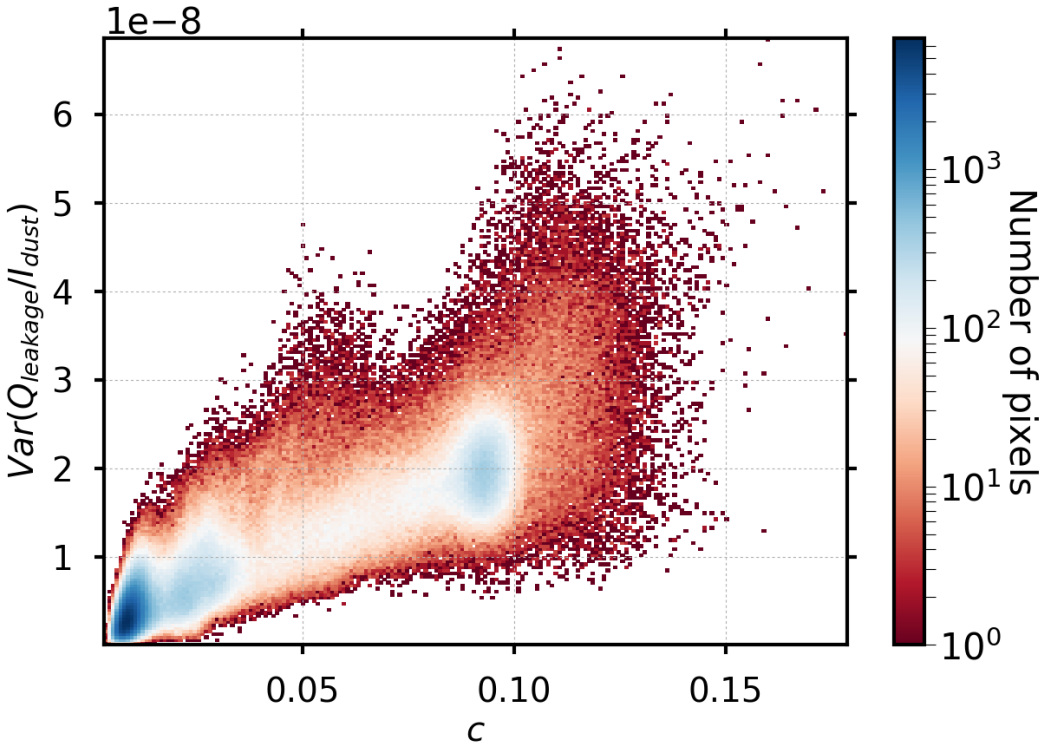

FIGURE 4.24: Estimated variance distribution of the relative leakage parameter: $\mathrm{Var}\,(\delta Q_p/I_{\mathrm{Gal};p})$ as a function of $c = \left\langle \left((1/\bar{n}_p) \sum \cos 2\psi_{t;i} \right)^2 \right\rangle_{\rm det}$ (see text) after map making including all detectors. We have averaged over ten realizations to estimate the variance.

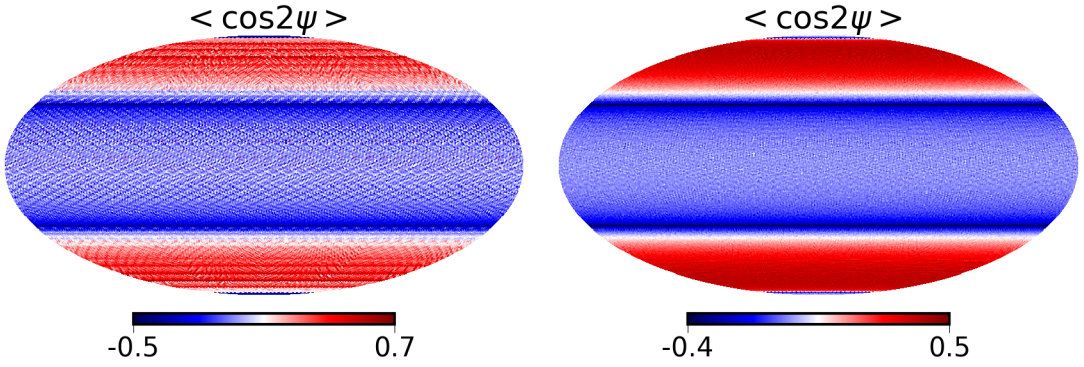

FIGURE 4.25: Effect of a poorly chosen scanning frequency ratios. *left* The map has $\tau_{\rm prec}/\tau_{\rm pin} = 9.3$, *right* the map has the more irrational ratio $\tau_{\rm prec}/\tau_{\rm pin} = 9.61803,$. A series of Moiré patterns on intermediate angular scales is clearly visible in the map on the left, which lead to spikes in the crossing moment map power spectra, and also in the final bandpass mismatch power spectra. The artefacts can be avoided by choosing ratios of frequencies judiciously in order to avoid good rational approximations.

figure 4.10. We can adjust $\tau_{\rm prec}/\tau_{\rm spin}$ concerning to crossing moment while the sky

is scanned. The figure 4.25 shows crossing moment maps for two different ratios of precession period and spin period ratio.

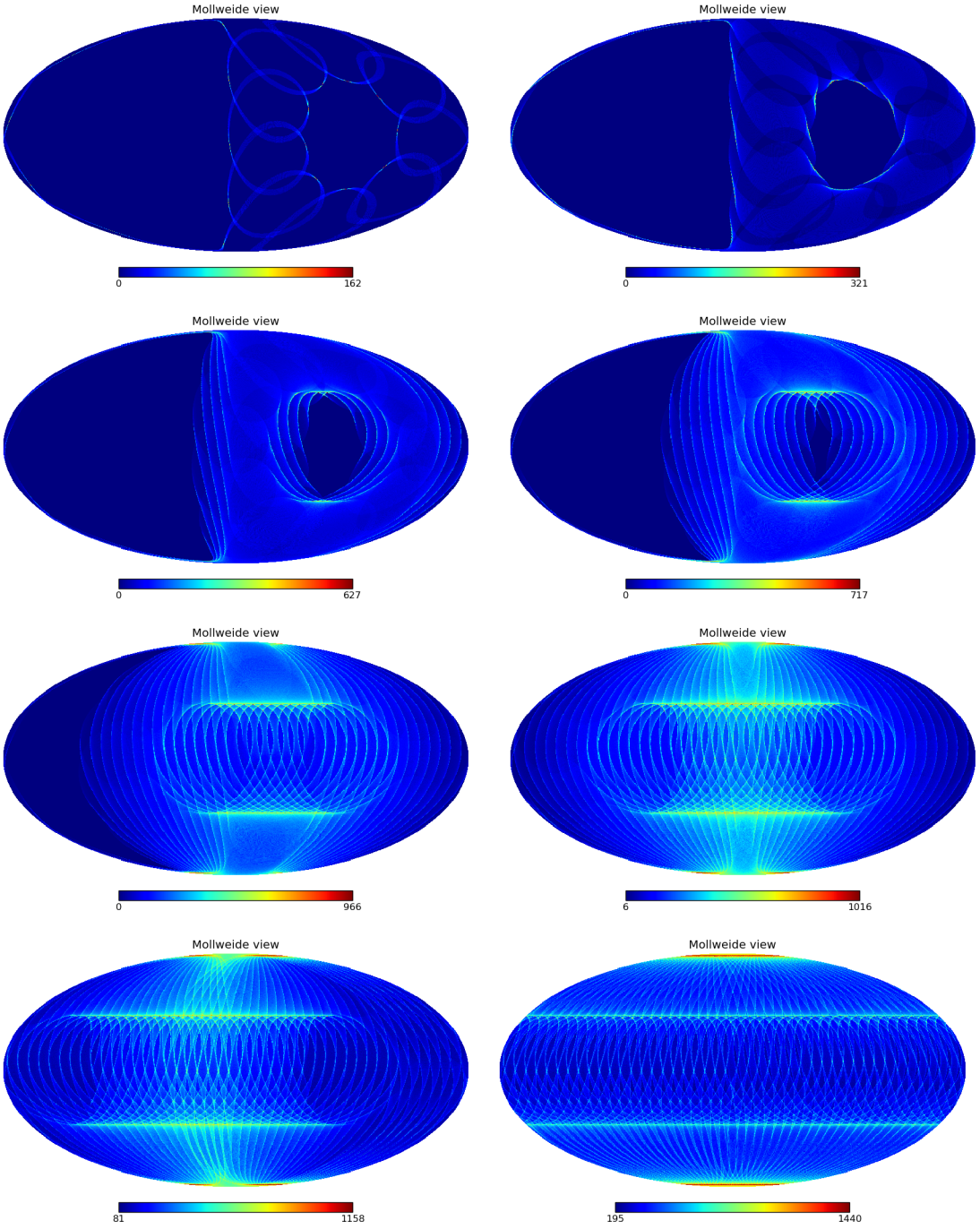

FIGURE 4.26: The hit count map of a pair detector in a assumed pessimistic configuration: $\tau_{\text{spin}} = 10\,\text{min}$, $\tau_{\text{prec}} = 89.95\,\text{min}$. The time integration of each scan running for 1 day, 6 days, 1 month, 2 months, 4 months, 6 months, 8 months and 1 year, from left to right and top to bottom, respectively.

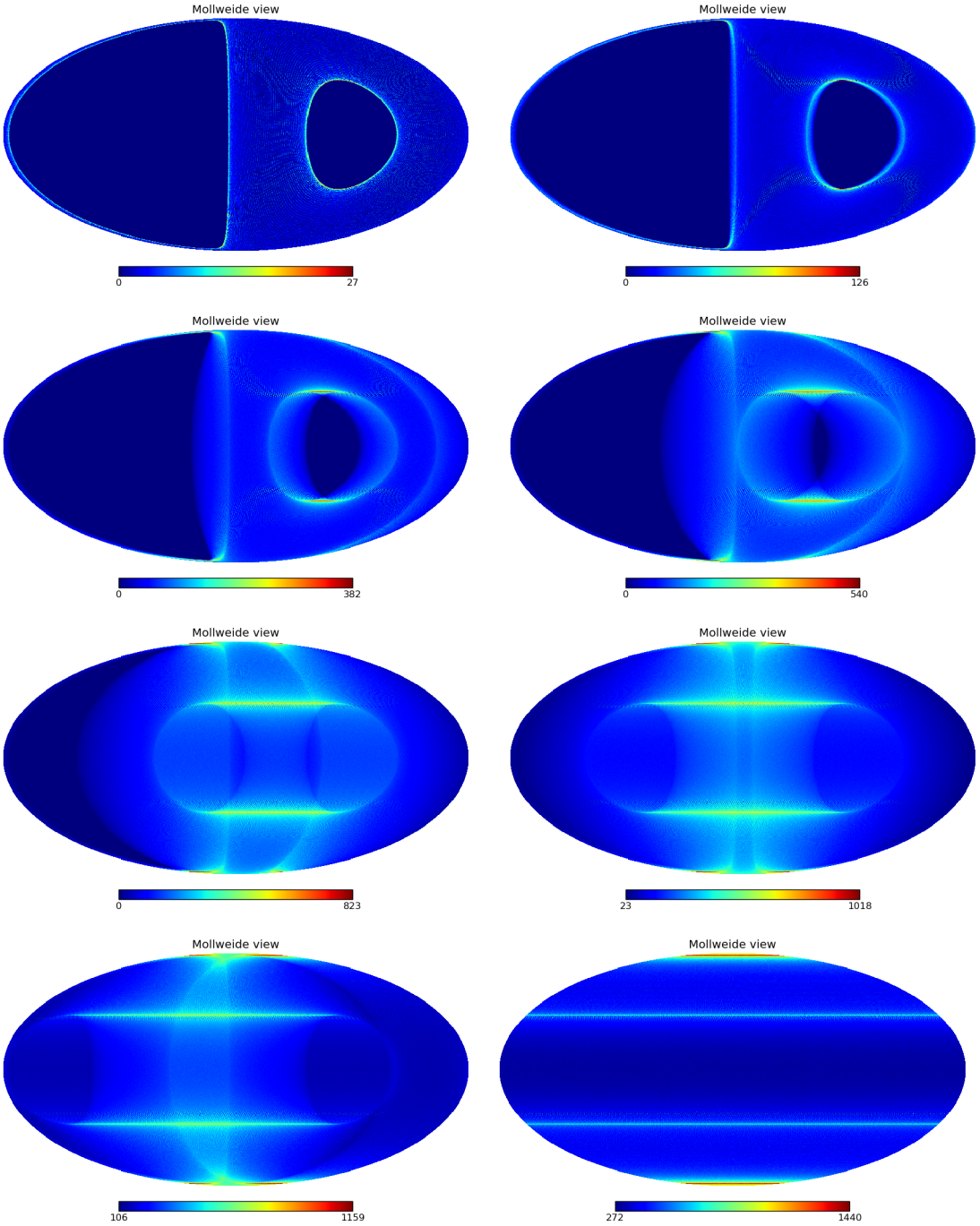

FIGURE 4.27: The hit count map of a pair detector for the fiducial scanning strategy $\alpha = 65°$, $\beta = 30°$, $\tau_{\rm spin}$=10 min, $\tau_{\rm prec} = 96.1803$ min. The time integration of each scan running for 1 day, 6 days, 1 month, 2 months, 4 months, 6 months, 8 months and 1 year, from left to right and top to bottom, respectively.

As an example, in a assumed pessimistic case, we choose a bad ratio of parameter of precession and spin period, as $\tau_{\rm spin} = 10\,{\rm min}$, $\tau_{\rm prec}= 89.95\,{\rm min}$. Figure 4.26 and figure 4.27 illustrate the evolution of scanning hit count maps of a pair detector for the pessimistic case $\tau_{\rm spin} = 10\,{\rm min}$, $\tau_{\rm prec}= 89.95\,{\rm min}$ and the figucial configuration $\alpha = 65°$, $\beta = 30°$, $\tau_{\rm spin}=10\,{\rm min}$, $\tau_{\rm prec} = 96.1803\,{\rm min}$. The fiducial configuration has been chosen a good ratio of the precession period and the spin period, $\tau_{\rm prec}/\tau_{\rm spin}$ which follows an irrational number as Golden ratio, so that the hit count maps present homogeneous angle coverage. In contrast, the hit count maps of the assumed pessimistic configuration have many inhomogeneous features.

In order to observe these feature in the pessimistic case in the leakage maps as well as in the final angular power spectrum compare with the fiducial scanning strategy, the simulation implements for the configuration $\alpha = 65°$, $\beta = 30°$, $\tau_{\rm spin} = 10\,{\rm min}$, $\tau_{\rm prec}= 89.95\,{\rm min}$, 222 detectors and a year observation, these leakage maps are also obvious features in the hit count maps. Figure 4.28 shows the hitcount map and leakage maps of the assumed pessimistic case in the galactic coordinate. Figure 4.29 indicates that the amplitude of the power spectrum is as same as the

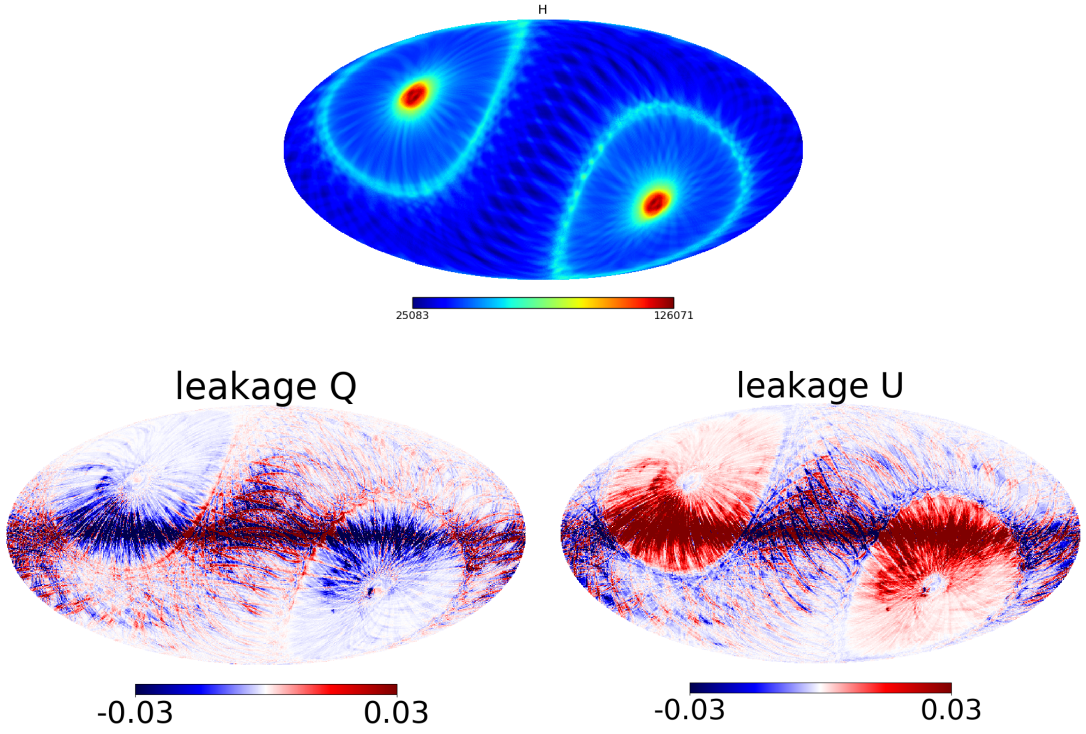

FIGURE 4.28: The hit count and leakage maps of a bad chosen parameter of the precession time, the scanning parameters are $\alpha = 65°$, $\beta = 30°$, $\tau_{\rm spin} = 10\,{\rm min}$, $\tau_{\rm prec}= 89.95\,{\rm min}$ in the galactic coordinate, and combining data for 222 detectors and 365 days observation for one realization

fiducial scanning strategy at the reionization bump. However the feature in the

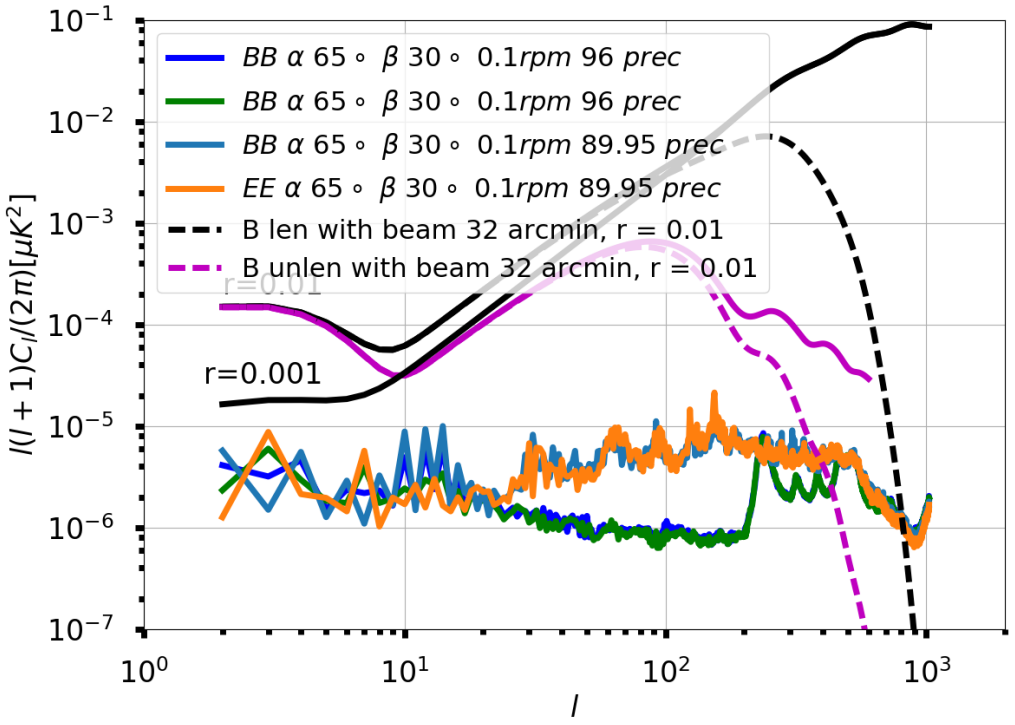

FIGURE 4.29: Power spectrum of the badly chosen parameter of precession period, the scanning strategy parameters are described in figure 4.28. The power spectrum of the fiducial scanning strategy is also plotted together with the purpose of comparison.

hitcount maps (it implies crossing moment maps) produces booting in the power spectrum at the recombination bump.

In order to investigate the position of peaks on the power spectra on the multipoles ℓ axis. The scanning angles are fixed $\alpha = 65°$ and $\beta = 30°$, with the same 222 detectors and 365 days observation. Firstly the spin period is fixed, the precession period is variation from ~ 96.1803 min to ~ 101.1803 min. The simulations have take into account the float number of the scanning parameter. Figure 4.30 shows the result of power spectra for different precession periods, the amplitude of each configuration is rescaled by order of magnitudes with the purpose of comparison. We observed that these positions of peaks tend to shift to smaller multipoles ℓ, the number of peaks also have variation in the power spectrum depending on the ratio of precession and spin period. These hitcount maps leakage maps are not shown here but these power spectra mean these maps have different features.

Secondly, the spin period is varied including a tiny change with many numbers after

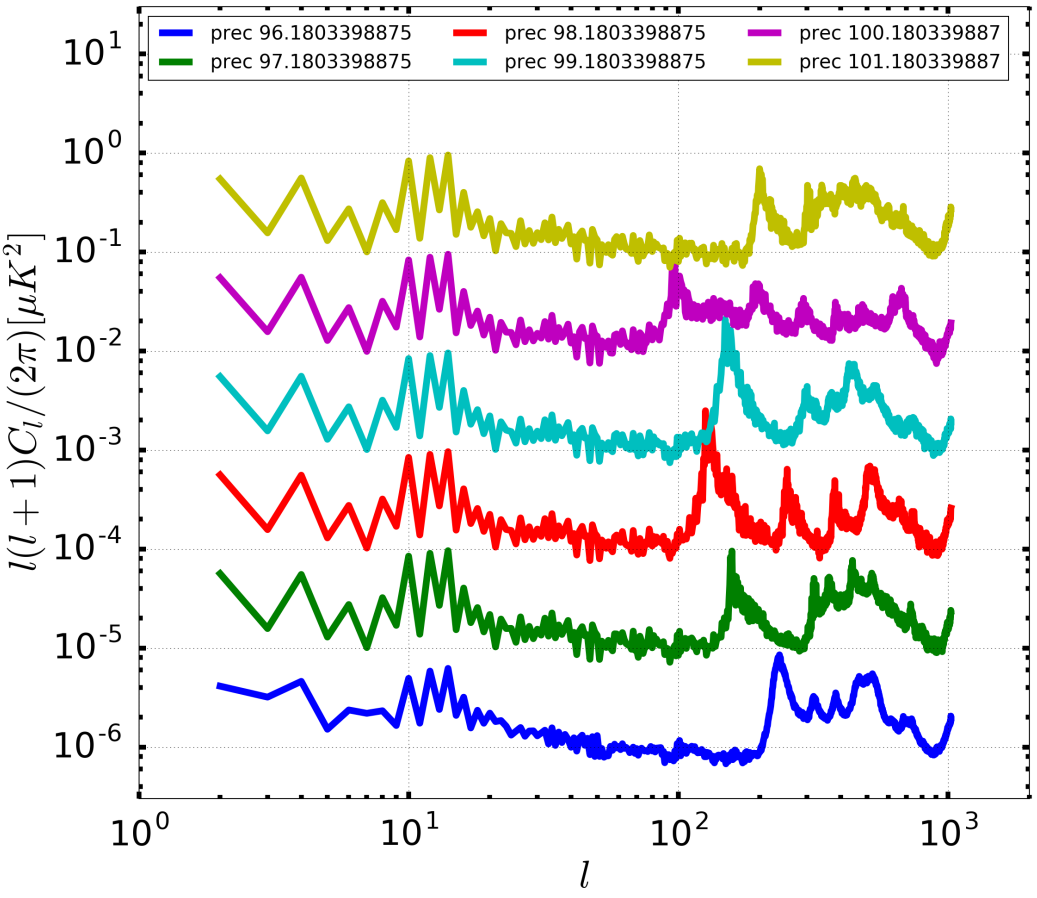

FIGURE 4.30: Variation of precession time parameter and the amplitudes are rescaled to easily observe. The other canning strategy parameters are fixed as $\alpha = 65°$, $\beta = 30°$, $\tau_{\rm spin} = 10\,{\rm min}$, 222 detectors and a year of observation. The value of precession period is labeled on the plot.

the dot of a float number fixing other parameters. With the same configurations, we observed that the position and amplitude of these peaks are not affected since the spin period is smaller than 0.3 rpm. In the case of spin period is 0.5 rpm these peaks are moved away as shown in figure 4.31. Thirdly the ratio of precession period and spin period $\tau_{\rm prec}/\tau_{\rm spin}$ is varied for example precession is 32.06 minutes and the spin period is 0.3 rpm. Figure 4.31 shows that these peaks are located at the same position on the multipoles axis. Since the ratio is varied if we change the spin or precession period, the location of these peaks is changed. We also applied a tiny change in the float number of the spin period, the result shows that there is a change in the amplitude of peaks.

As a conclusion, to obtain good crossing moment maps (it means lower the power

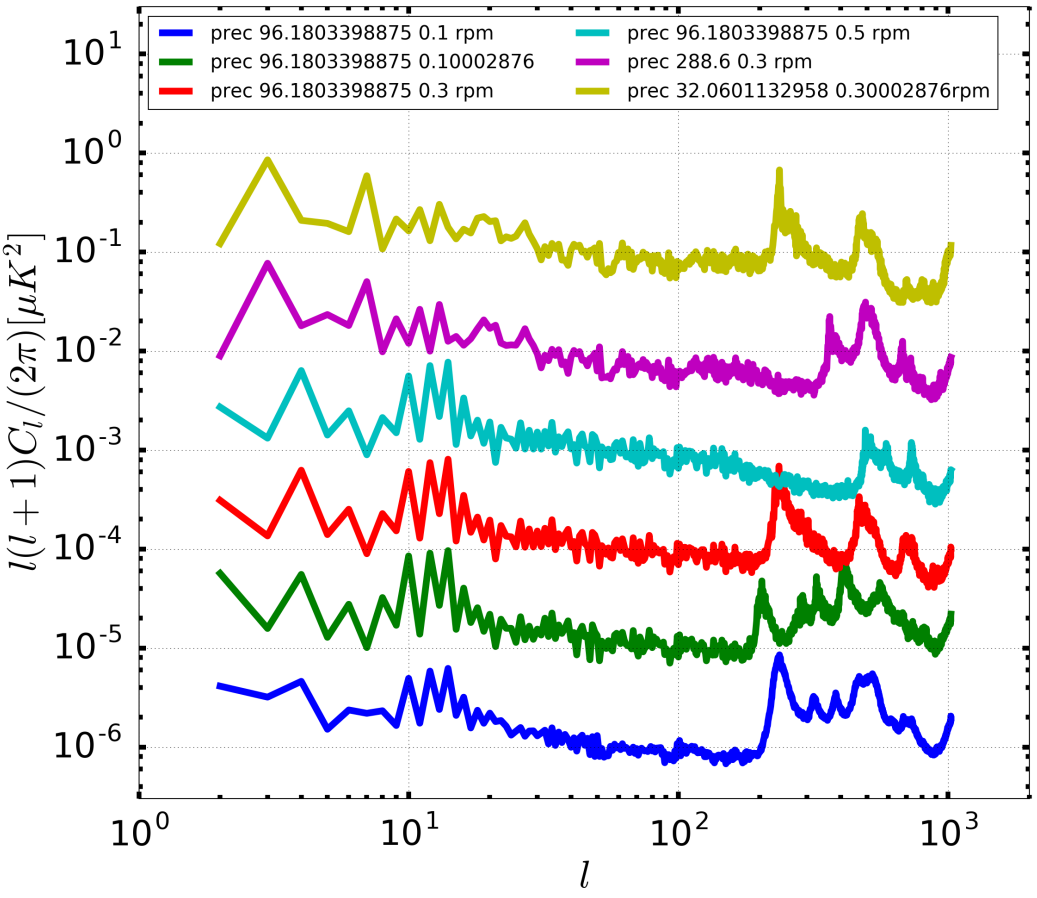

FIGURE 4.31: Variation ratio of precession time and spin parameters. The amplitudes are rescaled to easily observe. The canning strategy parameters are fixed $\alpha = 65°$, $\beta = 30°$. (*from bottom to the top*) The blue green red and cyan curves have different spin period from $\tau = 0.1$ *rpm* up to $\tau = 0.5$ *rpm*. The violet and yellow curves are the power spectra in case of changing ratio of precession and spin period together.

spectrum also), we have to carefully consider the ratio of scan frequencies of precession and spin period. Those peaks at multipole numbers on the bandpass mismatch power spectrum are caused by Moiré effects. The detailed study of this ratio jumps to the number theory of regular and irregular motion[3]. The first study was carryed out for $\tau_{spin} = 10\,\text{min}$ and $\tau_{prec} = 93\,\text{min}$ and we obtain the hitcount and crossing moment maps with clearly visible Moiré effects as shown in the figure 4.25 on the left. After that the map with ratio $\tau_{\rm prec}/\tau_{\rm spin} = 9.61803$, has the more

[3]See detail discussion in Michael Berry, (1978, September), *Regular and irregular motion*, in S. Jorna (Ed.), AIP Conference proceedings (Vol. 46, No. 1, 16-120), the discussion of perturbed integrable systems in classical mechanics and the stability of the solar system.

irrational number. The detailed description of the importance of avoiding resonances and theory of choosing ratios number theory is described in the published paper of this bandpass mismatch error for future CMB satellite experiment [50].

4.3 A correction method

There have several correction methods which are studied in the companion paper [14]. In this section, I present the study of correction method for a detector pair which is difined in equation 4.17. The procedure has been used for the WMAP data analysis [63] which cancels leakage form intensity to polarization due to bandpass mismatch. We assume perfectly uniform angle coverage in each pixels for more than three revisit. We also assume white noise with identical variance for a pair. The method consists in estimating an extra component as the leakage on a pair by pair basic. This is equivalent to estimating I, Q, U components for each detector and then combine the Q and U parameters obtained for each detector.

$$\begin{aligned} \mathrm{Cov}_{3;p} &= (\mathbf{A}^T\mathbf{N}^{-1}\mathbf{A})^{-1} \\ &= \frac{\sigma_n}{N_p} \times \begin{pmatrix} 1 & \langle\cos 2\psi\rangle & \langle\sin 2\psi\rangle \\ \langle\cos 2\psi\rangle & \dfrac{1+\langle\cos 4\psi\rangle}{2} & \dfrac{\langle\sin 4\psi\rangle}{2} \\ \langle\sin 2\psi\rangle & \dfrac{\langle\sin 4\psi\rangle}{2} & \dfrac{1-\langle\cos 4\psi\rangle}{2} \end{pmatrix}^{-1} . \end{aligned} \quad (4.27)$$

In the second case the polarization covariance matrix is the submatrix covariance which is formed by the lower tight corner of 4.27. Here σ_n is the root mean square of noise in each pixel.

$$\mathrm{Cov}_{2;p} = \sigma_n \times \begin{pmatrix} \dfrac{1+\langle\cos 4\psi\rangle}{2} & \dfrac{\langle\sin 4\psi\rangle}{2} \\ \dfrac{\langle\sin 4\psi\rangle}{2} & \dfrac{1-\langle\cos 4\psi\rangle}{2} \end{pmatrix}^{-1} . \quad (4.28)$$

We study the loss of accuracy in two cases by computing numerically the two covariance matrices with and without leakage components. In case of scanning strategy $\alpha = 65°$, $\beta = 30°$, $\tau_{\mathrm{spin}} = 0.1\,\mathrm{rpm}$ the noise of the covariance matrices associated with the level of leakage is about 4 %. In case of $\alpha = 50°$, $\beta = 45°$, the loss accuracy of the Q component is of the order of 10 % for a given arbitrary

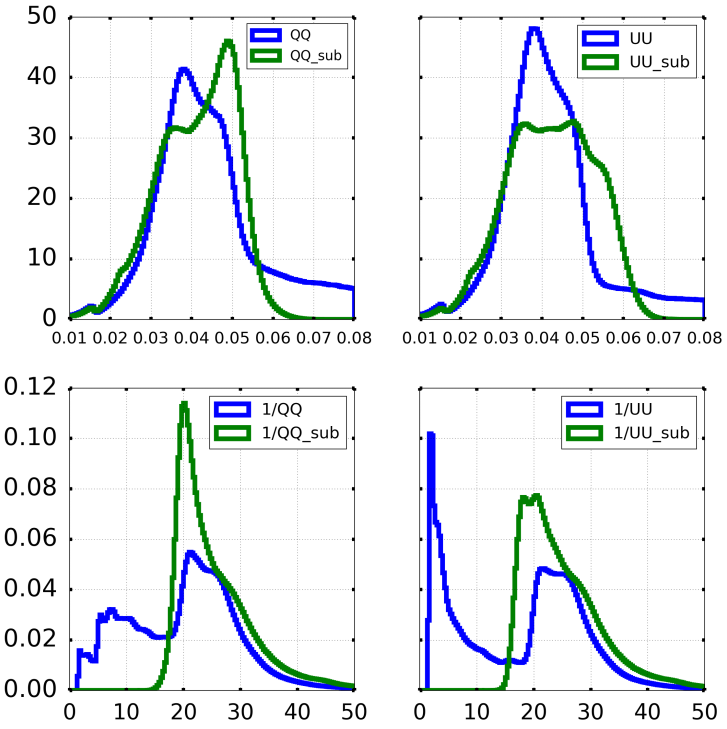

FIGURE 4.32: Histogram of the covariance matrix and sub-covariance matrix for the configuration $\alpha = 30°$, $\beta = 65°$, $\tau_{\text{spin}} = 2\,\text{min}$, $\tau_{prec} = 4$ day.

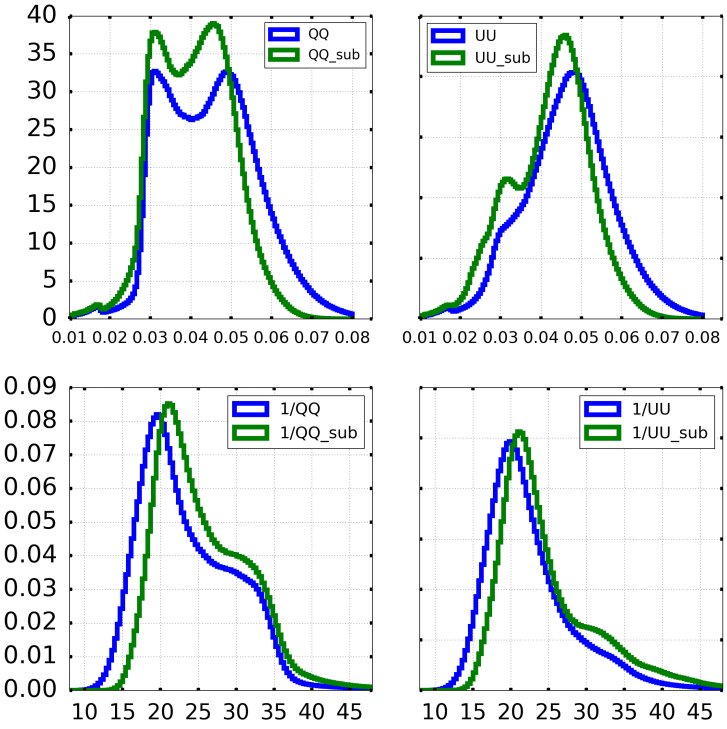

FIGURE 4.33: Histogram of the covariance matrix and the sub-covariance matrix for the configuration $\alpha = 50°$, $\beta = 45°$, $\tau_{\text{spin}} = 2\,\text{min}$, $\tau_{\text{prec}} = 4$ day.

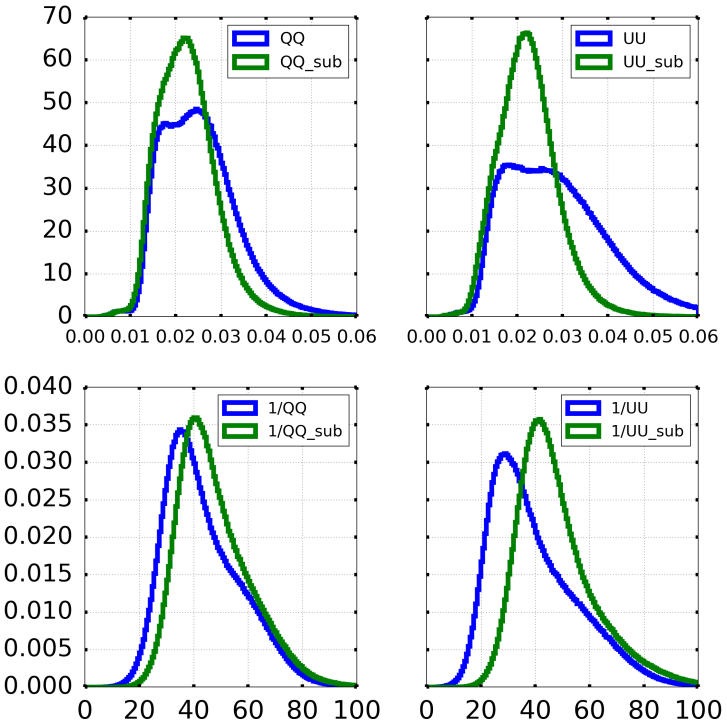

FIGURE 4.34: Histogram of the covariance matrix and the sub-covariance matrix for the configuration $\alpha = 50°$, $\beta = 45°$, $\tau_{\text{spin}} = 10\,\text{mins}$, $\tau_{\text{prec}} = 96.1803\,\text{mins}$.

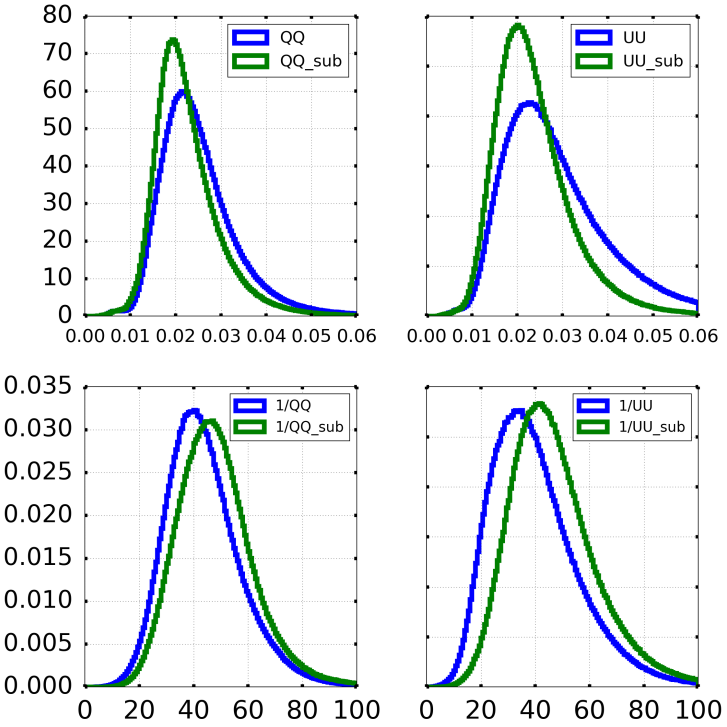

FIGURE 4.35: Histogram of the covariance matrix and the sub-covariance matrix for the configuration $\alpha = 65°$, $\beta = 30°$, $\tau_{\text{spin}} = 10\,\text{min}$, $\tau_{\text{prec}} = 96.1803$ minutes.

detector pair. These histograms in figure 4.32, 4.33, 4.34, 4.35 carry out for different configurations of scanning strategy parameters. QQ and UU polarization maps in case of temperature leakage components are estimated as equation 4.27. $\mathrm{QQ_{sub}}$ and $\mathrm{UU_{sub}}$ are in case of null leakage as equation 4.28. The histogram of inverse of the covariance matrices respectively $\frac{1}{QQ}$, $\frac{1}{\mathrm{QQ_{sub}}}$, $\frac{1}{UU}$, $\frac{1}{\mathrm{UU_{sub}}}$. The root mean square of noise $\sigma_n = 1$.

As a conclusion, if we assume, there is no leakage, we will estimate the sub-covariance matrix Q, U. In contrast in case of leakage we will estimate the level leakage of a pair similar to a single detector with covariance matrix I, Q, U. This is estimation of the total budget of noise (3 components I, Q, U) of leakage components of a single detector maps as equation 4.27 comparing with null the leakage assumption of the detector pair which has the orthogonal polarization as equation 4.28. The comparison of the full focal plane is left for a future study. The second method which is base on a template fitting method is studied in the companion paper [14].

4.4 Conclusions

This chapter described estimation of the level of bandpass mismatch error to the final determination of power spectrum as well as tensor-to-scalar value r for several scanning strategies. This study helps to choose an optimal scanning strategy for future CMB polarization satellite. In case of without an HWP, bandpass mismatch error is a non-negligible systematic effect. The amplitude of bandpass mismatch error depends on the scanning strategy of the satellite: precession angle α, spin angle β, precession spin τ_{prec} and rotating spin τ_{spin}. The amplitude scales as the number of detectors. I found that the spurious angular power spectrum could potentially bias r for measurements of the reionization bump ($2 \leq \ell \leq 10$) at the order of about 5×10^{-4}, and of the recombination bump ($10 \leq \ell \leq 200$) at the order of about 5×10^{-5} depending on scanning angle parameters and for variations of band-pass observed by Planck. The amplitude of the power spectrum is scaled $\frac{1}{\mathrm{N_{det}}}$ the number of detectors. I observed a tight correlation between leakage maps and the crossing moment, $\langle \cos 2\psi \rangle$, $\langle \sin 2\psi \rangle$, this is a fast and easy way to predict the magnitude of potential leakage. The companion paper [14] presents correction methods for bandpass miss match error [in preparation].

Chapter 5

Interaction of particles with a TES array

Contents

We know from the Planck mission that the cosmic ray particles interaction with the focal plane produces thermal glitches on the data due to deposit energies. Examples of Planck data are shown in figure 3.17, the cosmic rays systematic is described in the chapter 3 the section 3.9. For future CMB missions, we need to study this systematic effect and find a way to reduce its impact.

QUBIC is a ground-based experiment, aiming at measuring B-mode polarization of the CMB. The QUBIC instrument design is based on a novel concept of bolometric interferometry with high sensitivity and extremely good control of the systematic effects by the self-calibration technique. The QUBIC focal plane contains a total of 2048 pixels Transition-Edge-Sensors (TES) in the focal plane. A TES, also called a superconducting phase-transition thermometer, consists of a superconducting film operated in the narrow temperature region between the normal and superconducting state. The concept of QUBIC is described in the section 3.10.1. In the "mm lab" of APC laboratory we set up an Americium 241 source in front of a QUBIC's 256-TES detector array inside the cryostat, which can cool down to the level of hundreds of mK. When a particle hits components of a TES pixel(e.g.: Thermometer, absorbing grid membrane, substrate), the deposited energy could be transformed to temperature elevation between components and to the neighbor pixels (called cross-talk). This study does not only help to understand the TES thermal behaviors but also prepares for future CMB missions. In addition, the study of cross-talk for TESs pixel array also carry out. The idea is that when we have a glitch event in the signal, we also detect the behavior on pixels around.

In this chapter, I am going to describe (1) the theory of superconductivity associated with the transition regime, (2) principles of a superconducting transition edge sensor, I figure out the electrical time constant, the thermal time constant basing on a TES responding equations, noise performance in a TES. (3) I also describe the TES array and the electronic readout system of the QUBIC experiment, the time constant of the electronic readout chain. (4) In the end, I present my work on data analysis of glitches and the cross-talk.

5.1 Theory of a superconducting Transition-Edge Sensor

In a normal conductor/semiconductor the current is carried by electrons (i.e. Fermions) which obey Fermi-Dirac statistics while in a superconductor the current is carried by Cooper-pairs (i.e. Bosons) which obey Bose-Einstein statistics. The principle is that the phonon lattice net slows down the velocity of electrons so that the electrons joined into Cooper-pairs. The development of a sensitive superconducting detector allows us to measure a power source with faster responses and a larger heat capacity [61]. A superconducting detector works at low temperature in that case the noise level is reduced closely to quantum limit.

5.1.1 Theory of superconductivity

In 1911, Heike Kamerlingh Onnes (figure 5.1), a Dutch professor of experimental physics, cooled mercury at the temperature of liquid helium to 4.2 K [89]. This experiment does not only determine the boiling point temperature of Helium but also measures the electrical resistance of the mercury. He discovered that the resistance of the metal dramatically drops to zero. The phenomenon called superconductivity at low temperature and opened a new area in physics. In 1913, lead was discovered as a superconductor at critical temperature $T_c = 7.2$ K, then 17 years after niobium was found as a superconductor at $T_c = 9.2$ K. Over the time many metals and alloys were superconductors in between 1K and 18K.

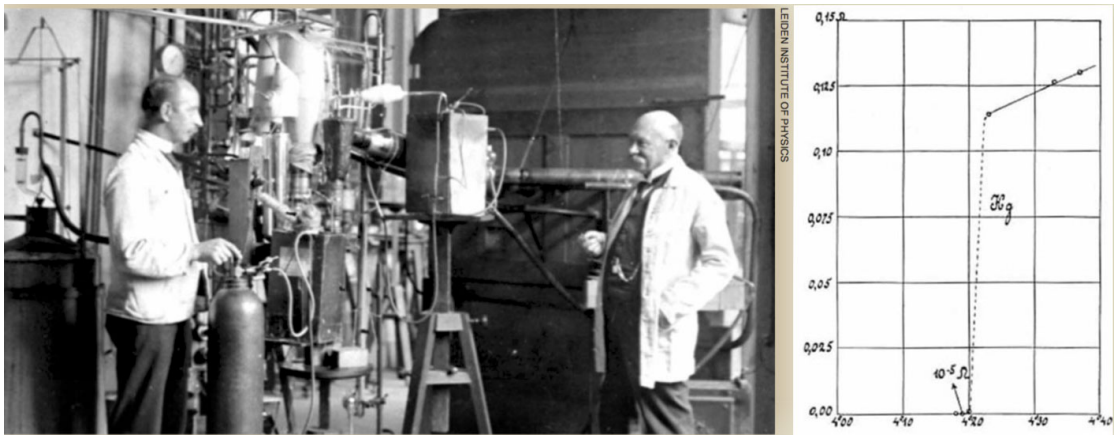

FIGURE 5.1: The liquid helium experiment of Heike Kamerlingh Onnes (on the right) and his chief technician Gerrit Flim. The historic superconducting plot of resistance versus temperature of the mercury at low temperature.

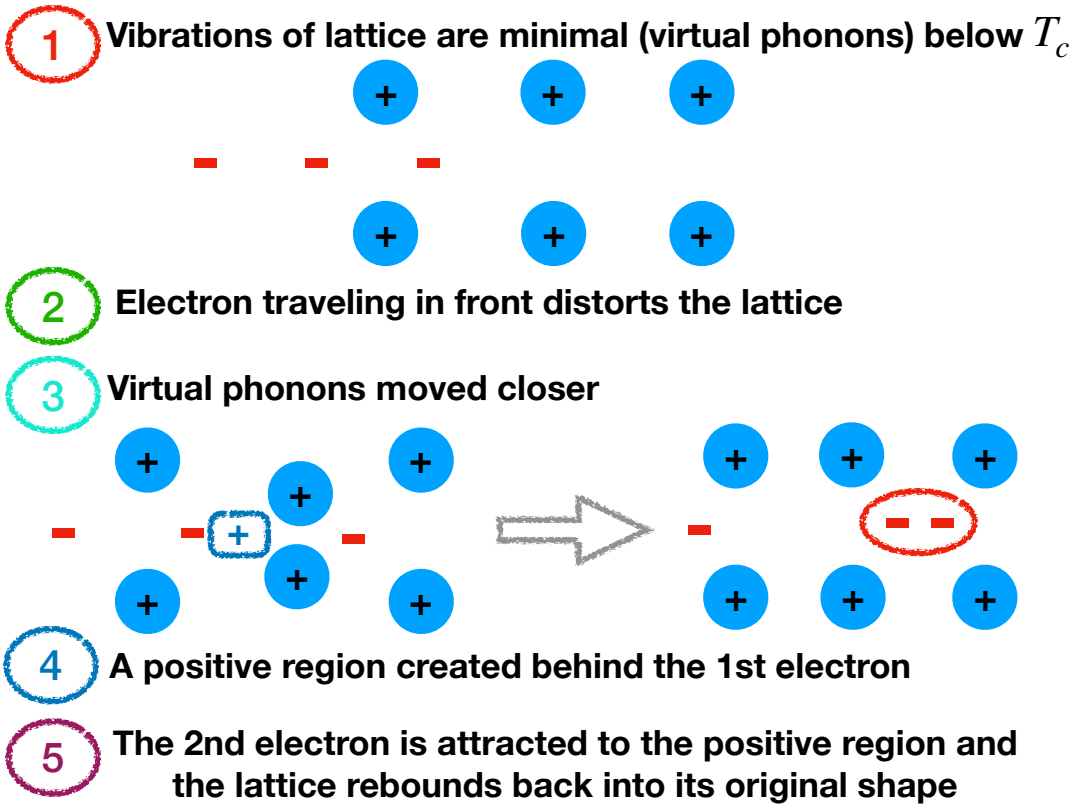

FIGURE 5.2: The BCS theory of superconductivity

In order to understand the quantum process of a superconductor, we need to investigate into the atomic study. In semiconductors or insulators, the energy gap of the order of $\frac{3}{2}k_B T_0$ occurs between electrons and the periodic lattice. However, the energy gap of superconductors mainly occurs due to phonon interaction of electron and electron ($\approx$ 100 nm), which is called *Cooper-pairs* [15]. The idea was presented by John Bardeen, Leon Cooper, and Robert Schrieffer in 1957 and they received the Nobel Prize in 1972 for the BCS theory of superconductivity. Cooper-pairs are considered as Bosons ($q\overline{q}$) and condense into the ground state. The BCS microscopic theory of superconductivity was successfully described type I superconductor using quantum mechanics by the key idea Cooper-pairs. (1) When we cool down the sample into the critical temperature, the vibration of lattices are minimal (virtual phonon). (2) The electron traveling in front distort the lattice. Therefore (3) the virtual phonon moved closer in lattice because of attracted negative first electron and thus (4) a positive region is created behind the first electron. (5) The second electron has enough time to be attracted by the virtual phonon before the lattice vibrated recoil to its shape, the pair of opposing spin electron is formed [6, 15]. The process is described in figure 5.2. In the end,

there is no resistance for Cooper-pairs, it means that electron does not slow down with the lattice, then we have a perfect conductor or superconductor.

In simple words, the requiring energy to break the Cooper-pairs to normal electrons (quasi-particles) is the energy gap of the superconducting state. At low temperature, the zero resistivity of superconductor due to the thermal energy is less than the energy gap of the Cooper-pairs. The energy gap is decreased gradually to break the Cooper-pair when the temperature increased to the transition of the critical temperature. The energy gap plays an important role in the theoretical explanation of superconductivity and superconducting detectors. The BCS microscopic theory of superconductivity predicted that the energy gap is proportional to the critical temperature T_c:

$$\mathrm{E_g} \approx \frac{7}{2}\mathrm{k_B T_c} \quad \approx 10^{-3}\mathrm{eV}. \tag{5.1}$$

5.1.2 The superconducting transition region

In solid state physics, a phase is defined by its structure, therefore, a phase transition is a change of structure in geometry terms. Ehrenfest classified that there are only two ways of phase transition first-order and second-order in thermodynamics [86]. The first-order phase is usually known as the transitions between different crystal modifications involving latent heat absorption or relaxation, sudden volume change, discontinuous entropy, likely the water transforms into ice at the zero degrees (from liquid to solid). Landau theory developed the second-order phase which specifically emphasized on the crystal symmetry changes continuously. The shape of the transition region depends on the material. The critical temperature of a thin film can be adjusted by its thickness because of exchanging Cooper-pairs and quasiparticles or by using an alloy as the NbSi. The superconducting transition region is extreme temperature sensitivity, a tiny changing temperature, order 0.1 mK to 1 mK leads to a large changing resistance. Therefore the superconducting transition edge sensor can be used as very sensitive detectors by breaking Cooper-pairs which is order of meV compatible with mm detection which has energy around $\mathrm{E_{1mm}} = \mathrm{hc}/\lambda_{1\mathrm{mm}} \sim 1.2$ meV.

5.1.3 Principle of a Transition-Edge Sensor (TES)

In 1941, D.H. Andrews, American chemical professor, designed an experiment of an infrared source and a fine tantalum wire, which is operated in its superconducting phase transition at 3.2 K. He measured temperature versus resistance of the tantalum wire. The D.H. Andrews experiment was made the first Transition-Edge Sensor (TES), also called a superconducting phase transition thermometer. The main difficulty is to read out the low resistance of TES (few Ω). The superconducting quantum interference device (SQUID) with associated input loop is finally used to current read out a voltage biased TES [70].

5.1.3.1 Electrical and thermal response

Figure 5.3 illustrated a bolometer [1] and the electrothermal feedback playing an important role for TES. Bolometer converts energy to temperature and the natural time constant is the ratio of the heat capacity and the thermal conductance. A TES is a bolometer exhibiting a strong electrothermal feedback. The electrothermal feedback of the TES plays a key concept of the TES technology. The block diagram figure 5.4 illustrated the feedback. The incident power is compensated by the Joule dissipation.

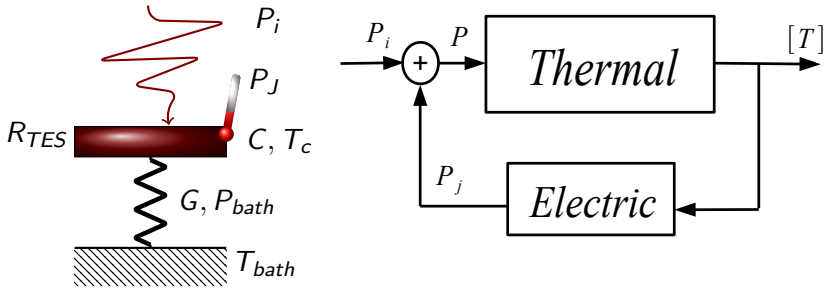

FIGURE 5.3: *Left:* The simple thermal bolometer model, P_i [W] , P_J [W] and P_{bath} [W] are the incident signal power, the Joule power dissipated by the thermometer and the power to the bath temperature, respectively. C $[J/K]$ is the heat capacity, G $[W/K]$ is the thermal conductance, T_c $[K]$ is the critical temperature of the TES, T_{bath} [K] is the reference bath temperature. *Right:* The electrothermal feedback model.

[1] A bolometer measures the power of incident radiation via the heating of a material.

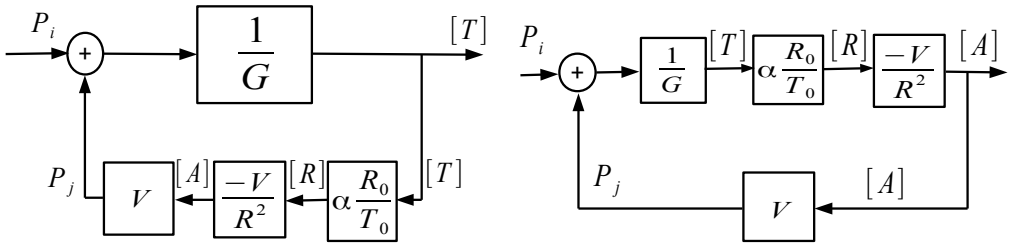

FIGURE 5.4: The left look likes a standard bolometer model: $T(P_i)$. The right is a rearrange one highlighting the $I(P_i)$ TES transfer function when it is voltage biased. R_0, T_0 are the steady state value of the TES resistance and TES temperature respectively. α is the logarithmic sensitivity to temperature parameter. R is the TES resistance under the voltage-biased operation.

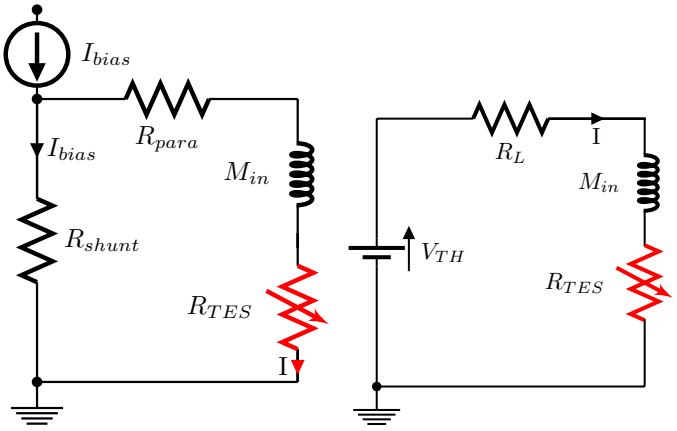

FIGURE 5.5: (*left*) The practical TES bias circuit and (*right*) its Thevenin equivalent circuit $V_{TH} = I_{bias}R_{shunt}$, the current is applied in the shunt resistor then the load resistor in the Thevenin circuit $R_L = R_{para}+R_{shunt}$, the inductance coil L with M_{in} and the TES. The value of R_{shunt} and R_{para} is of the order of 10 mΩ.

The block diagram in figure 5.4 is useful to understand the TES response and the mechanism of the negative electrothermal feedback effect which drives the thermometer back to the set point in its transition region. In the voltage-biased mode $P_J = \frac{V^2}{R_{TES}}$, a rise in temperature of the thermometer leads to a rise in resistance, then the Joule power is decreased, it means that there is less power in the thermometer, thus it cools down because the Joule power compensated for the original rising temperature. This process keeps a TES self-regulation in a set point of the critical temperature.

The thermal and electrical response of the TES are described by circuits in figure 5.5 and the figure 5.3 and follow two differential equations, which are *the electrical*

equation for the current I though the TES, with the electrical resistance R_{TES}.

$$\begin{aligned} V_{TH} &= V_{TES} + V_L + V_{R_L}, \\ L\frac{dI}{dt} &= V_{TH} - IR_L - IR_{TES}. \end{aligned} \tag{5.2}$$

and conventional energy, *the thermal equation for the temperature T:*

$$\frac{dE}{dt} = C\frac{dT}{dt} = P_i + P_J - P_{bath}. \tag{5.3}$$

where I and T are the electrical current and the temperature of the TES, L is the input inductance of the SQUID, V_{TH} and R_L is the Thevenin equivalent voltage and the resistance.

The electrical time constant of TES: τ_{el}

Following the current conservation and the energy conservation, we can solve the Thevenin circuit by understanding basic electric equations $V_R = IR_L, V_L = L\frac{dI}{dt}$ in the biasing circuit figure 5.5. Then we develop the equation 5.2 by rearranging, integration to find the solution.

$$\begin{aligned} \frac{dI}{V_{TH} - (R_L + R_{TES})\,I} &= \frac{dt}{L}, \\ \int \frac{dI}{V_{TH} - (R_L + R_{TES})\,I} &= \int \frac{dt}{L}, \\ -\frac{\ln\left(V_{TH} - (R_L + R_{TES})\,I\right)}{R_L + R_{TES}} &= \frac{1}{L}t + cst. \end{aligned}$$

Since $I = 0$ and $t = 0$, we have $cst = -\frac{\ln V_{TH}}{R_L + R_{TES}}$, substituting back to the equation, we get:

$$\ln\left(V_{TH} - (R_L + R_{TES})\,I\right) - \ln V_{TH} = -\frac{(R_L + R_{TES})}{L}t.$$

Take exponentially to both sides then we have:

$$I = \frac{V_{TH}}{R_L + R_{TES}}\left(1 - e^{-\frac{R_L + R_{TES}}{L}t}\right). \tag{5.4}$$

The equation 5.4 indicates the transition period of current adjust from its initial value of zero to the final value $\frac{\mathrm{V_{TH}}}{\mathrm{R_L + R_{TES}}}$, which is the steady state. The intrinsic time constant of the TES bias circuit is known as the electrical time constant:

$$\boxed{\tau_{\mathrm{el}} = \frac{L}{R_{\mathrm{L}} + R_{\mathrm{TES}}}}. \tag{5.5}$$

The electrical time constant is the time for the current get to the final steady state. Indeed the inductor L creates a magnetic field in the circuit and store energy, below T_c the resistance of the TES is zero therefore the time constant increases up to $\frac{\mathrm{L}}{\mathrm{R_L}}$.

In order to solve fully the electrical equation 5.2 and the thermal equation 5.3, we will calculate independently each term of these equations such as the TES resistance $\mathrm{R_{TES}}$, the thermal bath power $\mathrm{P_{path}}$, the Joule power $\mathrm{P_J}$. We will end up with TES's time constants, the discussion of the electrothermal feedback effect, energy resolution and TES responsivity.

The resistance of the TES: $\mathrm{R_{TES}}$

We can write the resistance of TESs as a function of temperature and current. This is called as non-linearity behavior of the thermometer resistance, $\mathrm{R_{TES}\,(T, I)} = \mathrm{R_0} + \delta\mathrm{R\,(T, I)}$. $\mathrm{R_0}$, $\mathrm{T_0}$, $\mathrm{I_0}$ are steady state values, then we can expand a small signal to the first order:

$$\mathrm{R_{TES}\,(T, I)} \approx \mathrm{R_0} + \left.\frac{\partial \mathrm{R}}{\partial \mathrm{T}}\right|_{\mathrm{I_0}} \delta\mathrm{T} + \left.\frac{\partial \mathrm{R}}{\partial \mathrm{I}}\right|_{\mathrm{T_0}} \delta\mathrm{I}. \tag{5.6}$$

Conveniently, we define two unitless sensitive parameters:

$$\begin{cases} \alpha \equiv \left.\dfrac{\partial \log \mathrm{R}}{\partial \log \mathrm{T}}\right|_{\mathrm{I_0}} = \dfrac{\mathrm{T_0}}{\mathrm{R_0}} \left.\dfrac{\partial \mathrm{R}}{\partial \mathrm{T}}\right|_{\mathrm{I_0}}, \text{ the logarithmic sensitivity to temperature.} \\ \beta \equiv \left.\dfrac{\partial \log \mathrm{R}}{\partial \log \mathrm{I}}\right|_{\mathrm{T_0}} = \dfrac{\mathrm{T_0}}{\mathrm{R_0}} \left.\dfrac{\partial \mathrm{R}}{\partial \mathrm{I}}\right|_{\mathrm{T_0}}, \text{ the logarithmic sensitivity to current.} \end{cases} \tag{5.7}$$

For a semiconductor the value of α is around -1 to -10, in contrast, it is 100 - 1000 for a superconductor, the electrothermal feedback is strong when α is high. We can see the value of α for several TESs in the array P57 of the QUBIC experiment

in figure 5.6. The resistance of the TES now is:

$$\mathrm{R_{TES}}\left(\mathrm{T},\mathrm{I}\right) \approx \mathrm{R_0} + \alpha\frac{\mathrm{R_0}}{\mathrm{T_0}}\delta\mathrm{T} + \beta\frac{\mathrm{R_0}}{\mathrm{I_0}}\delta\mathrm{I}. \tag{5.8}$$

From the equation 5.8 we can derive the dynamic resistance of the TES is

$$\begin{aligned}\mathrm{R_{dyn}} &= \left.\frac{\partial\mathrm{V}}{\partial\mathrm{I}}\right|_{\mathrm{T_0}} = \frac{\partial\left[\mathrm{R}\left(\mathrm{T_0},\mathrm{I}\right)\mathrm{I}\right]}{\partial\mathrm{I}} = \frac{\partial\left[\left(\mathrm{R_0}+\beta\frac{\mathrm{R_0}}{\mathrm{I_0}}\right)\left(\mathrm{I_0}+\delta\mathrm{I}\right)\right]}{\partial\mathrm{I}},\\ &= \frac{\partial\left(\mathrm{R_0I_0}+\beta\mathrm{R_0}\delta\mathrm{I}+\mathrm{R_0}\delta\mathrm{I}+\beta\frac{\mathrm{R_0}}{\mathrm{I_0}}\delta\mathrm{I}^2\right)}{\partial\mathrm{I}}.\end{aligned}$$

The $\mathrm{R_0I_0}$ is a constant, we can neglect the second order of the current term $\beta\frac{\mathrm{R_0}}{\mathrm{I_0}}\delta\mathrm{I}^2$, then the dynamic resistance of the TES is approximately expressed as:

$$\mathrm{R_{dyn}} \approx \beta\mathrm{R_0} + \mathrm{R_0} = \mathrm{R_0}\left(1+\beta\right). \tag{5.9}$$

The thermal bath power: $\mathrm{P_{bath}}$

The thermal response of the TES around steady-state ($\mathrm{R_0}$, $\mathrm{T_0}$, $\mathrm{I_0}$) values can be derived from the thermal equation 5.3. Firstly we have the thermal conduction is defined:

$$\mathrm{G}\left(\mathrm{T}\right) = \frac{\partial\mathrm{P_{bath}}}{\partial\mathrm{T}} = \mathrm{n}\,\kappa\,\mathrm{T}^{\mathrm{n}-1}. \tag{5.10}$$

The heat bath is assumed as an exponential function:

$$\mathrm{P_{bath}} = \int_{\mathrm{T_{bath}}}^{\mathrm{T_0}} \mathrm{G}\left(\mathrm{T}\right) = \kappa\left(\mathrm{T_0^n} - \mathrm{T_{bath}^n}\right). \tag{5.11}$$

In the equilibrium state T_0, the rising temperature of the absorber $\mathrm{T_0}+\delta\mathrm{T}$ flows to the thermal conduction of the thermal link to the bath temperature.

$$\begin{aligned}\left.\mathrm{P_{bath}}\right|_{\mathrm{T_0}} &\approx \int_{\mathrm{T_{bath}}}^{\mathrm{T_0}+\delta\mathrm{T}} \approx \mathrm{G}\left(\mathrm{T}\right)\mathrm{dT},\\ &\approx \mathrm{P_{bath_0}} + \left.\frac{\partial\mathrm{P_{bath}}}{\partial\mathrm{T}}\right|_{\mathrm{T_0}},\\ &\approx \mathrm{P_{bath_0}} + \mathrm{G}\delta\mathrm{T},\\ &\approx \kappa\left(\mathrm{T_0^n} - \mathrm{T_{bath}^n}\right) + \mathrm{n}\kappa\mathrm{T_0^{n-1}}\delta\mathrm{T}.\end{aligned} \tag{5.12}$$

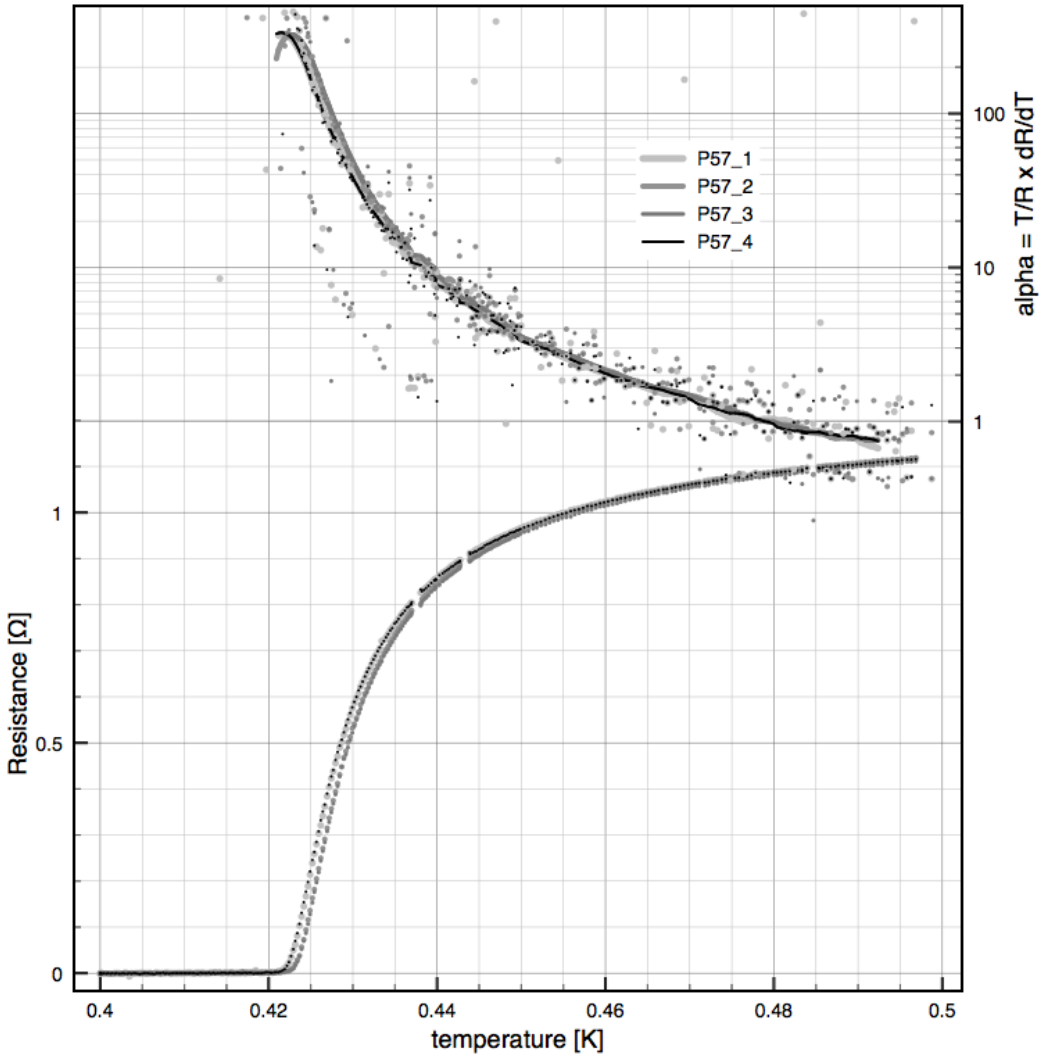

FIGURE 5.6: The plot of temperature versus resistance and the α parameter for pixel 1, 2, 3, 4 of the 256 TES array named P57. *[Damien Prêle-APC/Stefanos Marnieros-CSNSM, personal communication, 2018]*

where $\delta T = T - T_0$, κ, and n depends on the natural thermal link and the heat bath temperature. In practice, for the TES the value of n $\sim$ 3 or 4. κ depends on the type of using materials of pixel's legs, in this case of the TES, we are using SiN. The equilibrium state of the bath temperature is $P_{bath_0} = P_{J_0} + P_{i_0}$. P_{i_0} is the equilibrium state of the incident signal and the equilibrium state of the Joule power is $P_{J_0} = I_0^2 R_0$.

The Joule power: P_J

In the current biased operating mode, the Joule power is calculated as $P_J = R_{TES}(T, I) \times I_{bias}^2$ while in the voltage biased operating mode, the first order of the

Joule power can be calculated around (R_0, T_0, I_0).

$$\begin{aligned} P_J &= \frac{V_{TES}^2}{R_{TES}(T,I)} = I^2 R_{TES}(T,I) = (I_0+\delta I)^2 R_{TES}(T,I), \\ &\approx P_{J_0} + 2I_0 R_0 \delta I + \alpha \frac{P_{J_0}}{T_0}\delta T + \beta \frac{P_{J_0}}{I_0}\delta I. \end{aligned} \tag{5.13}$$

We will discuss after that the TES is stable in the voltage biased operating mode via the presence of the strong negative electrothermal feedback effect. We define the low-frequency loop gain constant in the voltage-biased operation and natural time constant of thermal response [61].

$$\begin{aligned} \mathscr{L} \equiv \frac{P_{J_0}\alpha}{GT_0} = \frac{I_0^2 R_0 \alpha}{GT_0}, \\ \tau \equiv \frac{C}{G}. \end{aligned} \tag{5.14}$$

The thermal time constant: τ_{th}

We substitute the TES resistance equation 5.8, the bath power equation 5.12, the Joule power equation 5.13 and the low frequency loop gain equation 5.14 into the thermal and the electrical different equations 5.3, 5.2. In addition, we substitute also the variables $T - T_0 = \delta T$, $I - I_0 = \delta I$ and we just only consider the first order of those equations, finally we got new equations [61]

$$\begin{cases} \dfrac{d\delta I}{dt} = -\dfrac{R_L + R_0(1+\beta)}{L}\delta I - \dfrac{\mathscr{L} G}{I_0 L}\delta T + \dfrac{\delta V_{TH}}{L}. \\ \dfrac{d\delta T}{dt} = \dfrac{I_0 R_0 (2+\beta)}{C}\delta I - \dfrac{1-\mathscr{L}}{\tau}\delta T + \dfrac{\delta P_i}{C}. \end{cases} \tag{5.15}$$

Where $\delta V_{TH} \equiv V_{bias} - V_0$ is the changing voltage bias around the equilibrium state, $\delta P_i \equiv P_i - P_{i_0}$ is the changing signal around the equilibrium state. We can recognize that the electrical time constant of TES is described in the equation 5.4

$$\tau_{el} = \frac{L}{R_L + R_0(1+\beta)} = \frac{L}{R_L + R_{dyn}}. \tag{5.16}$$

and the thermal time constant is defined by the nature time constant of the TES and the low-frequency loop gain constant:

$$\boxed{\tau_{\mathrm{th}} \equiv \tau_{\mathrm{eff}} \equiv \tau_1 = \frac{\mathrm{C}}{\mathrm{G}(1+\mathscr{L})} = \frac{\tau}{1+\mathscr{L}}}. \tag{5.17}$$

Notice here that $\mathscr{L}$ is the negative loop gain feedback in a voltage biased operating mode, it is equivalent to $\mathscr{L}_V$ and $\mathscr{L}_{\mathrm{V}} = -\mathscr{L}_{\mathrm{I}}$ due to the α the logarithmic sensitivity temperature parameter. The equation 5.17 proved the advantage of a TES, the $|\mathscr{L}| > 1$ then the natural time constant of a bolometer τ is decreased by the effective loop gain of the electrothermal feedback effect and thus the speed of a TES is increased.

So far we have demonstrated the electrical and thermal responding time constants of a TES thought TES differential equations. The 2 time constants and the feedback imply that the response of the TES can be stable or unstable.

TES responsivity: $s(\omega)$

We can rearrange equations 5.15 in the matrix form.

$$\frac{\mathrm{d}}{\mathrm{dt}}\begin{pmatrix}\delta \mathrm{I}\,(\mathrm{t}) \\ \\ \delta \mathrm{T}\,(\mathrm{t})\end{pmatrix} = -\begin{pmatrix}\dfrac{1}{\tau_{\mathrm{el}}} & \dfrac{\mathscr{L}G}{I_0 L} \\ \\ \dfrac{\mathrm{I_0 R_0}\,(2+\beta)}{\mathrm{C}} & \dfrac{1-\mathscr{L}}{\tau}\end{pmatrix}\begin{pmatrix}\delta \mathrm{I}\,(\mathrm{t}) \\ \\ \delta \mathrm{T}\,(\mathrm{t})\end{pmatrix} + \begin{pmatrix}\dfrac{\delta \mathrm{V_{TH}}}{\mathrm{L}} \\ \\ \dfrac{\delta \mathrm{P_i}}{\mathrm{C}}\end{pmatrix}. \tag{5.18}$$

The solution of electrical and thermal response equations 5.18 are exponential function by taking the non-homogeneous term $\delta \mathrm{V_{TH}}, \delta \mathrm{P_i}$ to zero [61]. After calculating eignvalues and rewriting in term of the inductance, we found that the power to the current responsivity is expressed by [61]:

$$\mathrm{s}(\omega) = -\frac{1}{\mathrm{I_0 R_0}}\left[\frac{\mathrm{L}}{\tau_{\mathrm{el}}\mathrm{R_0}\mathscr{L}} + \left(1 - \frac{\mathrm{R_L}}{\mathrm{R_0}}\right) + \mathrm{j}\omega\frac{\mathrm{L}\tau}{\mathrm{R_0}\mathscr{L}}\left(\frac{1-\mathscr{L}}{\tau} + \frac{1}{\tau_{\mathrm{el}}}\right) - \frac{\omega^2\tau\mathrm{L}}{\mathscr{L}\mathrm{R_0}}\right]^{-1}. \tag{5.19}$$

The equation 5.19 is the TES responsivity related to the loop gain $\mathscr{L}$. The TES model in figure 5.3 also implies that a fluctuation of the incident power to the TES is transformed to the resistance of the thermometer by a fluctuation in the Joule power.

$$\mathscr{L} = \frac{\partial \mathrm{T}}{\partial \mathrm{P}}\frac{\partial \mathrm{P_J}}{\partial \mathrm{T}} = \frac{\partial \mathrm{T}}{\partial \mathrm{P}}\frac{\partial \mathrm{P_J}}{\partial \mathrm{R}}\frac{\partial \mathrm{R}}{\partial \mathrm{T}}. \tag{5.20}$$

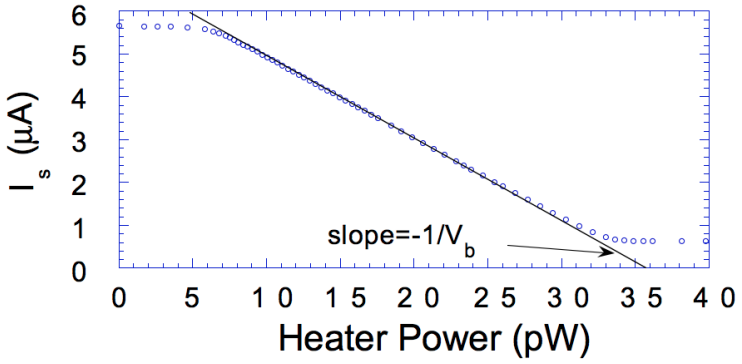

FIGURE 5.7: The linear response of the current versus the heat power [69].

$\frac{\partial T}{\partial P}$ is the expected transfer function of a bolometer from power to temperature. The signal depends on the fluctuation of the TES resistance $\frac{\partial R}{\partial T}$, the sensitive temperature parameter α and the operating mode of voltage-bias or current-bias. $\frac{\partial P_J}{\partial R}$ is the transfer function of the electrical feedback system, it depends on the operating mode of voltage-bias or current-bias.

In the voltage-biased mode of the supercondicting TES, the strong negative electrothermal feedback reduces the nature time constant of a TES up to two orders of magnitude which is necessary to produce a high resolution signal, and the current responsivity to the absorbed power is proportional to the inverse of the voltage bias. From the equation 5.19, the current responsivity of the superconducting TES is given [69, 70, 125]:

$$s_I(\omega) = -\frac{1}{V_{bias}} \frac{|\mathscr{L}|}{1+|\mathscr{L}|} \frac{1}{1+j\omega\tau_{eff}} [A/W]. \tag{5.21}$$

Figure 5.7 presents the historic experiment which demonstrates the voltage-biased superconducting TES has a linear response of the current to the heat power following the $\frac{1}{V_{bias}}$ [69].

The electrothermal feedback (ETF) effect

The electrothermal feedback (ETF) effect is the interaction between the electric current and the thermal temperature through the change in the resistance of the TES. It has shown in the cross terms of the electrical and thermal equations 5.18. The value of the α parameter of the transition edge sensor is positive as shown in figure 5.6, the increasing temperature will increase the electrical resistance of the TES and the electric current in the TES dissipates the thermal power to the

resistance of the TES by Joule power. In case of current-bias ($R_L \gg R_{TES}$), the Joule power is calculated by the formula $P_J = I^2 R_{TES} \Longrightarrow$ the ETF is positive, it means unstable. In the case of voltage-bias ($R_{TES} \gg R_L$), the Joule power is calculated by the formula $P_J = \frac{V^2}{R_{TES}} \Longrightarrow$ the ETF is negative, it means stable. There has no stable margin in case of $R_L = R_{TES}$. Advantages of the current-bias are that the voltage can be easily amplified. Nevertheless, the TES become unstable. Furthermore, we implement the Superconducting QUantum Interference Devices (SQUID) which makes possible to do voltage-bias [70]. In the voltage-biased mode, the Joule power is given by $P_J = \frac{V^2}{R_{TES}}$ then an increasing incoming signal (it means also increase of T and R_{TES}) will decrease the Joule power, then the total power on the TES will be staying to a constant. This is called the negative ETF effect:

- A strong negative ETF speeds up the detector, the thermal time constant of the effective thermal time constant of a TES is divided by the loop gain $\mathscr{L}$, the result is demonstrated by theory and experiment.
- In the voltage-biased mode, the TES is self-calibrating staying within its transition temperature, this physical characteristic is useful for an array of TESs and is one of the main interest of the use of TES instead of other kinds of bolometer.
- The current response is $-\frac{1}{V_{bias}}$.

5.1.3.2 Noise performance

Noise is unwanted and random signals, the main types of noise are thermodynamic noise, low frequency (1/f) noise and shot noise. The thermal noise is observed by J. B. Johnson in the Bell Telephone Laboratory in 1927 and studied by H. Nyquist in 1928 [2]. The electrons in a conductor are random vibrations in the lattice and depend on the temperature thus there have many tiny currents inside a conductor because an electron has charged 1.6×10^{-19} *Coulomb*. The thermal noise power is basically calculated by the temperature and a bandwidth of a measurement Δf.

$$P = k_B T \Delta f. \tag{5.22}$$

where T is the temperature of the conductor in Kelvin, k_B is the Boltzmann's constant. In the room temperature, for 1 Hz bandwidth, the noise power is in order of $4 \times 10^{-21}\,W$. It is equivalent to - 204 dBW [2].

The sensitivity of an operating TES is determined by different noise sources:

- The thermal fluctuation noise (TFN) or phonon noise dues to the link between the intrinsic detector and the bath.
- The Johnson or Nyquist noise which is associated with the resistors of the TES circuit.
- The noise from the different stage of the electronic readout system as SQUID noise, ASIC noise ...

Noise Equivalent Power (NEP)[2] is understood as the harmonic input noise $W/\sqrt{Hz}$. The low value of NEP means the highly sensitive detector. In general, we can express the NEP through the power spectral density (PSD), which characterizes a stationary random process by taking the square of the signal, in the frequency domain the PSD of the signal $x\,(t)$ is calculated:

$$\mathrm{PSD_{x(\omega)}} = \frac{1}{2\mathrm{T}} \int_{-\mathrm{T}}^{\mathrm{T}} \left| \mathrm{x\,(t)\,e^{-j2\pi\omega t}} \right|^2 \mathrm{dt}. \tag{5.23}$$

Because a stationary stochastic process is typically not an absolute integration then the signal has to be truncated before the Fourier transform. The relationship of the NEP and the PSD is given by:

$$\mathrm{NEP} = \sqrt{\mathrm{PSD}}\ \left[\mathrm{W}/\sqrt{\mathrm{Hz}}\right]. \tag{5.24}$$

In case of noise sources are not correlated, the total NEP_{tot} can be understood as variations and we can sum separately:

$$\begin{aligned} \mathrm{NEP_{tot^2}} &= \mathrm{NEP^2_{h\nu}} + \mathrm{NEP^2_{int}} + \mathrm{NEP^2_{elec}}. \\ \mathrm{NEP^2_{int}} &= \mathrm{NEP^2_{phonon}} + \mathrm{NEP^2_{J_{R_L}}} + \mathrm{NEP^2_{J_{TES}}}. \end{aligned} \tag{5.25}$$

[2]Noise Equivalent Power (NEP) is defined as the ratio of an input signal and the electrical output signal given by $W/\sqrt{Hz}$ or in simple words, the NEP is the necessary power to equalizing noise level during a second.

where $\mathrm{NEP}_{\mathrm{h}\nu}$ and NEP_{elec} are the photons noise and the electronic system noise, respectively. $\mathrm{NEP}_{\mathrm{int}}$ is the intrinsic noise of TES components.

Photons noise

when an experiment observes the CMB photons by its focal plane, obtaining photons in a TES follow a Poisson distribution. The measurement of photons gives intrinsic photons noise. An average number of photons $\langle n \rangle$ (bosons) obey Bose-Einstein statistic.

$$\langle \mathrm{n} \rangle = \left(\frac{\mathrm{h}\nu}{\mathrm{e}^{\frac{\mathrm{h}\nu}{\mathrm{k_B T}}} - 1} \right)^{-1}. \tag{5.26}$$

with ν is the frequency of electromagnetic waves and T is the source temperature. The variance of number of photons is given

$$\langle \Delta \mathrm{n}^2 \rangle = \langle \mathrm{n} \rangle + \langle \mathrm{n} \rangle^2. \tag{5.27}$$

The power of the photons is multiplication of a single photon energy and the average number of photons considering the efficient responding frequency $\eta(\nu)$:

$$\mathrm{P}_\gamma = \int_\nu \mathrm{h}\nu \langle \mathrm{n} \rangle \ \eta(\nu)\, \mathrm{d}\nu = \int_\nu \mathrm{h}\nu \left(\frac{\mathrm{h}\nu}{\mathrm{e}^{\frac{\mathrm{h}\nu}{\mathrm{k_B T}}} - 1} \right)^{-1} \eta(\nu)\, \mathrm{d}\nu. \tag{5.28}$$

Apply the equation 5.27 we have the variance of power formula

$$\left(\Delta \mathrm{P}^2\right) = \int_\nu (\mathrm{h}\nu)^2 \eta(\nu) \langle \mathrm{n} \rangle \left(1 + \eta(\nu) \langle \mathrm{n} \rangle\right) \mathrm{d}\nu. \tag{5.29}$$

The variance power is calculated in a second which is corresponded 0.5 Hz bandwidth in the Fourier domain so that the integration is from 0 to 1/2. Then the power spectral density is square of the NEP over 2 [76].

$$\frac{\mathrm{NEP}_\gamma^2}{2} = \left(\Delta \mathrm{P}^2\right) = \int_\nu (\mathrm{h}\nu)^2 \eta(\nu) \langle \mathrm{n} \rangle \left(1 + \eta(\nu) \langle \mathrm{n} \rangle\right) \mathrm{d}\nu. \tag{5.30}$$

In case of a square function or a box car filter the $\eta(\nu) = 1.$ and the bandwidth is less than the frequency center $\Delta\nu \ll \nu_0$.

$$\mathrm{NEP}_\gamma \approx \sqrt{2\mathrm{h}\nu_0 \mathrm{P}_\gamma + 2\frac{\mathrm{P}_\gamma^2}{\Delta\nu}}. \tag{5.31}$$

with $P_\gamma = h\nu_0\langle n_0\rangle\Delta\nu$. When $h\nu \ll k_BT$ photons noise is called Bose bunching noise, and $h\nu \gg k_BT$ is called Poisson noise.

Thermal fluctuation noise or phonon noise

The exchange energy of a detector (thermometer) with the thermal bath link at low-temperature dues to processes of phonons or quasi-particles under the quantum mechanic physics which are vibrations of atoms in the lattice because fluctuations in the temperature lead to fluctuations in the resistance as well as the electrical current. In the TES the approximation of the NEP for the phonon noise at the temperature T with the thermal conduction G is given by the formula [77]

$$\mathrm{NEP_{TFN}} = \sqrt{4\mathrm{k_B T^2 G}} \qquad \left[\mathrm{W^2/Hz}\right]. \tag{5.32}$$

Johnson noise of the thermometer resistance (R_{TES}) and the load resistance (R_L)

The ETF reduces the TES Johnson noise by the Loop gain of the TES. Then the power spectral density of the current noise due to the Johnson noise of the resistor of the TES thermometer is given [61]:

$$\mathrm{PSD_{I_{TES}}} \approx 4\mathrm{k_B T_0/R_0}/\mathscr{L}^2, \tag{5.33}$$

for the shunt resistor, the noise is not affected by the feedback of Loop gain of the TES and stay:

$$\mathrm{PSD_{I_{shunt}}} \approx 4\mathrm{k_B T_L/R_{shunt}} \tag{5.34}$$

Electronic gain

The SQUID is the first stage of readout the TES signal, then the noise of the SQUID amplifier noise is encountered with the gain of the amplifier.

$$\mathrm{G_{elec}} = \frac{\mathrm{M_{in}}}{\mathrm{M_{fb}}}\mathrm{R_{fb}}. \tag{5.35}$$

Where $\mathrm{M_{in}}, \mathrm{M_{fb}}$ are transformer coils of a SQUID and the flux-locked loop. $\mathrm{R_{fb}}$ is the feedback resistor of the flux-locked loop.

5.2 TES arrays of the QUBIC experiment

The QUBIC's TES array is an array of 256 TES pixels. Each pixel has 30 nm thickness of superconductor NbSi thin film with 15.45 % of niobium[3], absorbing grids are made of TiV. The sheet resistance of the TiV thin film is matched (increases) to the vacuum impedance Z_0 by shaping the absorber as a grid. The sheet resistance of the absorber is then given by equation 5.36

$$R_S = \frac{\rho}{t} \times \frac{L}{l}. \tag{5.36}$$

Where ρ is the resistivity Ωm of the TiV, t is the thickness and L, l the geometry parameters of the grid as shown in figure 5.8. The critical temperature of the TES

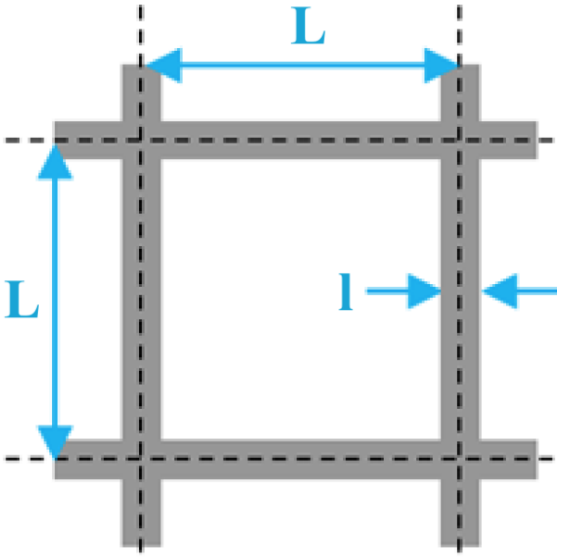

FIGURE 5.8: Geometry parameters of the absorbing grid

depends on the percentage components of the niobium and silicon as shown in figure 5.9. The ratio of niobium and the thickness of the film decides to the goal critical temperature thus the requiring critical temperature of the QUBIC's TES array is $T_c \approx 400\,mK$ [85].

To build a TES array, the first point is that we have to define the dimension of a pixel as well as the architecture of the array that has to fit with the focal plane of the QUBIC experiment at 150 GHz ($\lambda = 2\,mm$) and 220 GHz ($\lambda = 1.4\,mm$). Due to the incident photons, we want to measure, the absorbing grid surface of the QUBIC's TES is required $\geq 2\,mm$. The resolution of the instrument relates to the

[3]Niobium (Nb) has atomic number 41.

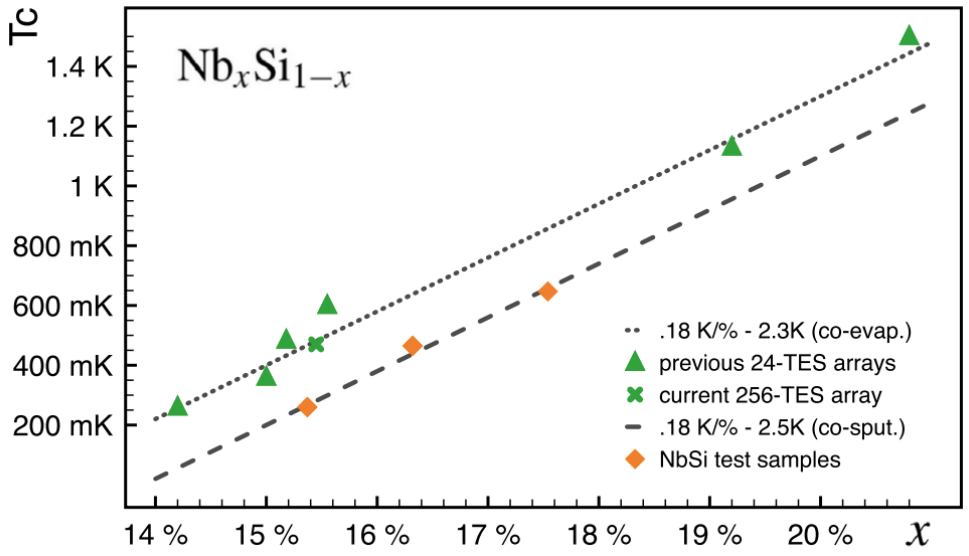

FIGURE 5.9: The critical temperature of a TES depending on the percentage of niobium. Two techniques have been presented in the plot, co-evaporation (*dot line*) and co-sputtering (*bar line*) [94].

limited diffraction for a collected photons mirror (diameter D) which is express:

$$\theta = 1.22\frac{\lambda}{\mathrm{D}}. \tag{5.37}$$

The QUBIC telescope has a primary mirror diameter of about $D = 317$ mm then we have the table of angular resolution.

TABLE 5.1: The table of angular resolution

150 GHz	D = 317 mm	$\theta = 26.5$ arcminus
220 GHz	D = 317 mm	$\theta = 18.5$ arcminus

The TES array is fabricated in the clean room using microfabrication technologies which are performed in the Center for Nanoscience and Nanotechnology (C2N)[4] laboratory and the Centre de Sciences Nucléaires et de Sciences de la Matière (CSNSM). The cross section of the successive processes to build one pixel is shown in figure 5.11. Microfabrication is a sequential multi-processes technology , its complexity is described by mask count layers. The mask of the 256 TESs is shown in figure 5.10. We use 500 μm thick of a silicon on insulator (SOI) substrate with 3 inches ($\sim$ 7.6 cm) perimeter, the substrate is two layers of silicon and a thin layer of

[4]C2N was established in 2016 by the joint of CNRS and University Paris Sub laboratories on the same campus: Laboratory for Photonics and Nanostructures (LPN) and Institut d'Electronique Fondamentale (LEF).

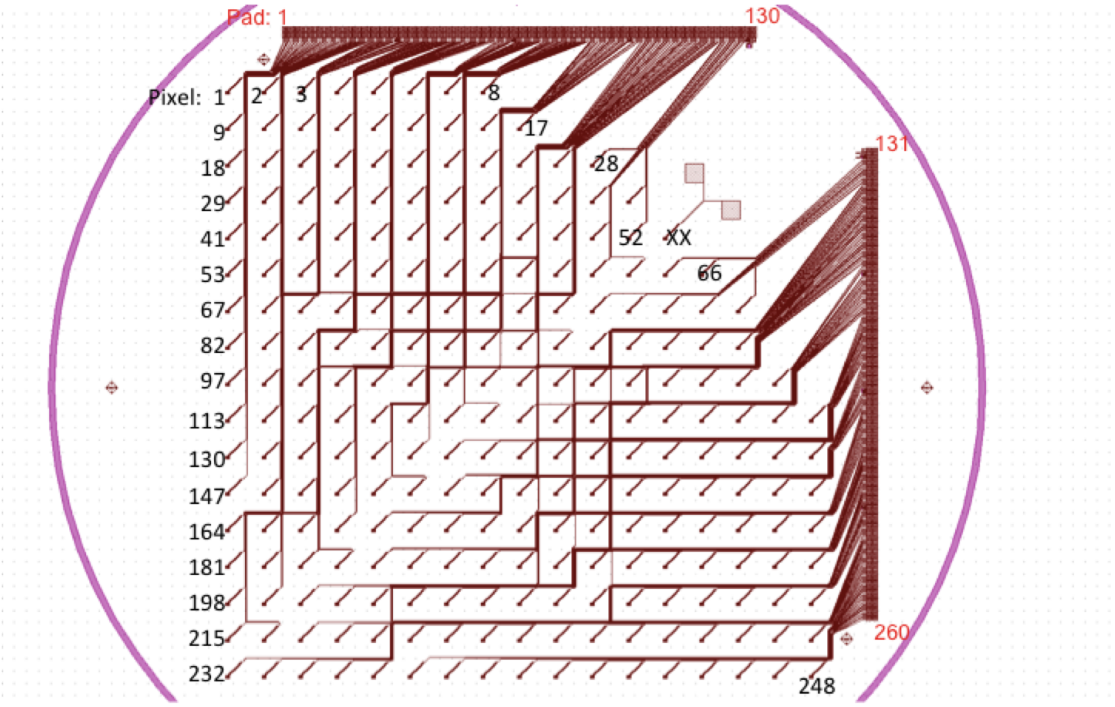

FIGURE 5.10: The mask of 256 TES pixels array, the magenta curve is 3 inch (7.6 cm) wafer perimeter. Each TES has Al wires connection to the bonding wire.

silicon dioxide SiO_2 5 μm. The SiO_2 layer not only helps to stop the deep etching un-uniform between different areas on the array but also helps to produce a homogeneous pixel array. The membrane layer is 1 μm thick silicon nitride Si_3N_4 and then a superconducting NbSi-thermometer and aluminum-wires are evaporated in order on the top of the membrane layer. The next step, the metallic absorbing grid (TiV or Pd) is added on the top and releasing the membrane. Finally, the legs are excavated [93]. Figure 5.11 illustrates the microfabrication performance of a pixel. There are 12 steps in the process, *the detail of the microfabricating performance is given in the Camille Perbost thesis (in French) and her team in CSNSM, C2N and APC laboratories [94].*

The Si_3N_4 membrane has high strength and has been widely used in micromachining, then legs and absorber structures can be fabricated. The thermal properties of this membrane at a low temperature allowing the mean free path of phonons is long then the heat from the absorber can transform immediately to the superconducting thermometer. The thermal conduction of the Si_3N_4 is also limited by

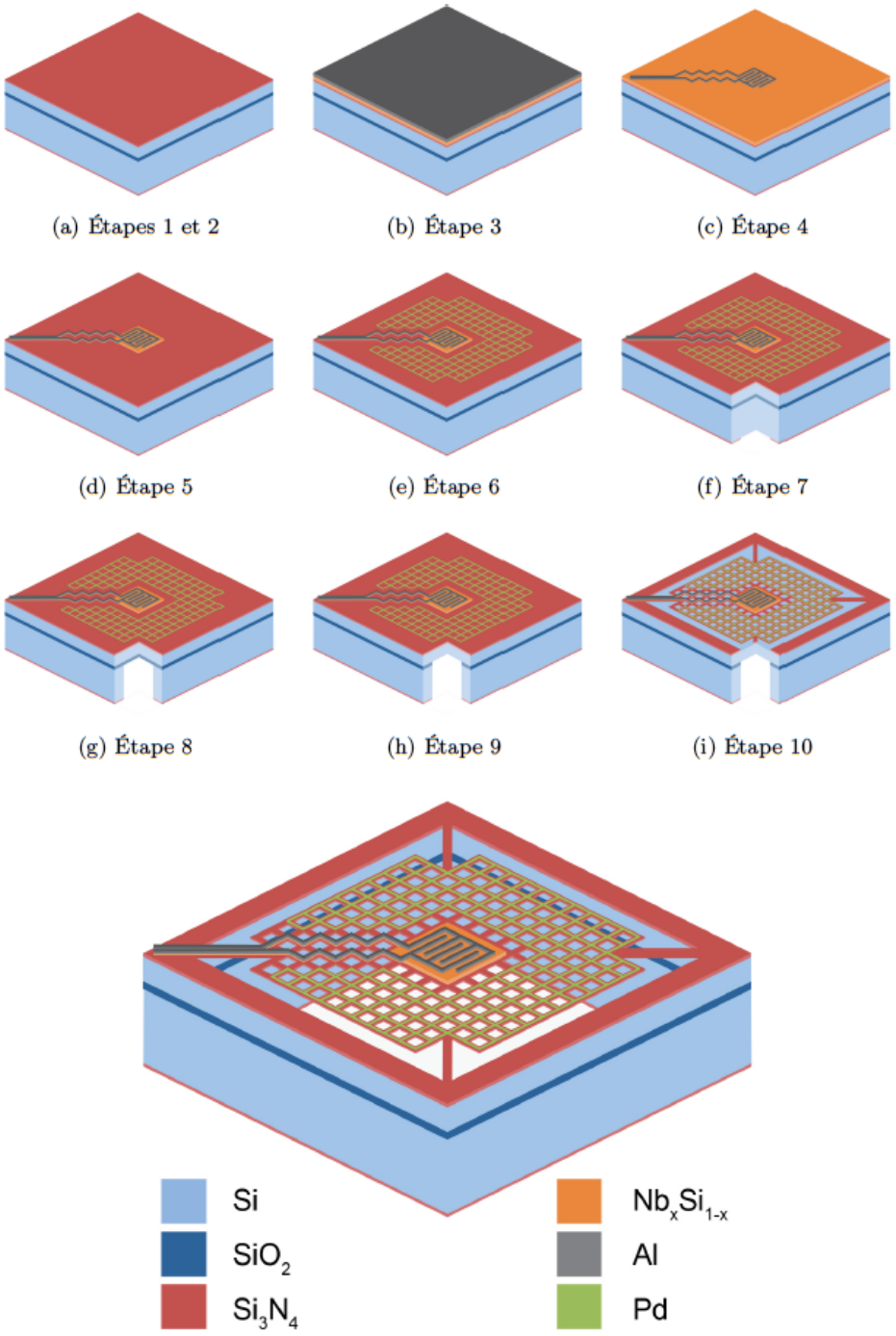

FIGURE 5.11: TES fabrication is used the microelectromechanical systems (MEMS). The processes are preparing substrate, evaporated membrane, added thermometer and wire, added absorbing grid. *credit: Camille Perbost/Christelle Carré* [94].

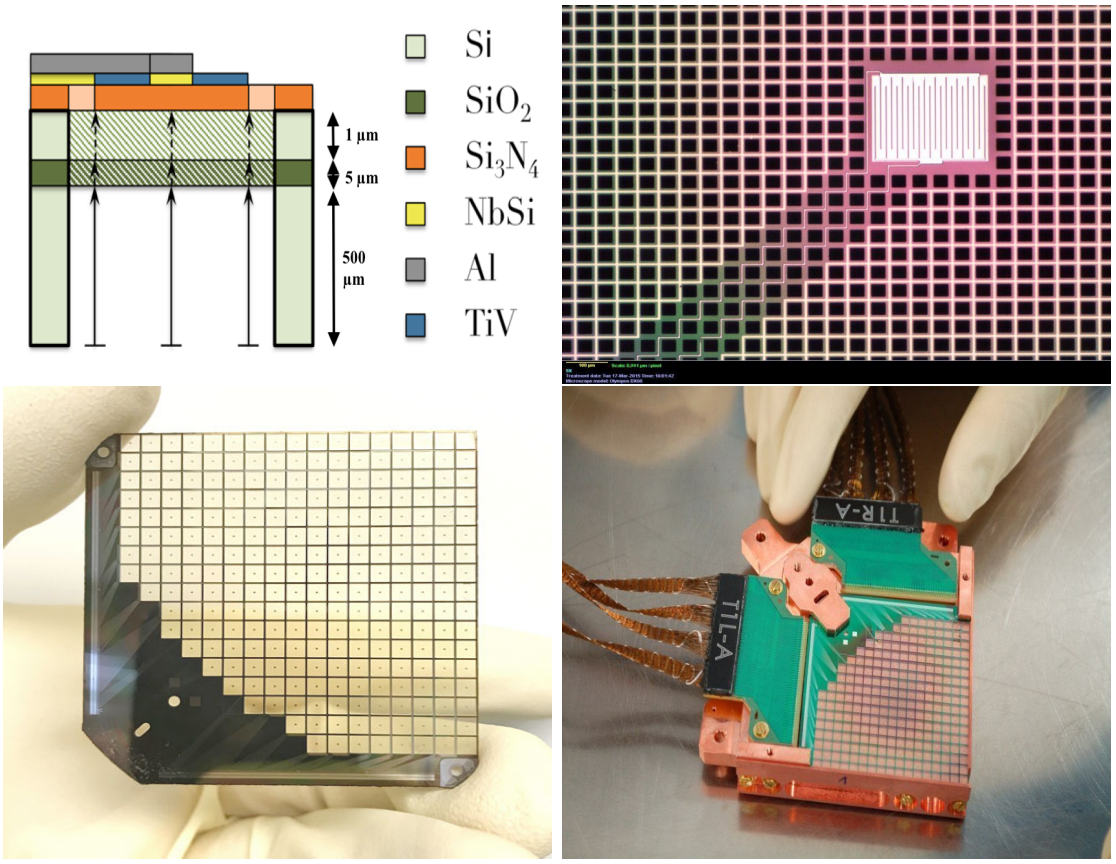

FIGURE 5.12: From the top to the bottom, the left to the right: A single pixel components, the substrate is layers of Si, SiO_2, the pixel is layers of Si_3N_4, Al, TiV and NbSi. The dimension of a pixel is $\approx$ 3 mm. The microphotography of a superconducting NbSi thermometer which is located at the center of the pixel. The 256 TESs array (named P90) and the copper backshort.

the scattering of phonons in the surface, therefore the low thermal conductivity is maintained. The silicon-on-insulator wafer has two layers of Si which are separated by an amorphous SiO_2, this technology allows reach to low thermal conductivity G structures.

Figure 5.12 shows the dimension of a pixel as well as a zooming of the superconducting NbSi thermometer at the center of a pixel. This figure also presents a fabricated array P90 and its bonding wires with the copper backshort which allows mounting on the focal plane of a cryostat. These superconducting wires will be connected to the SQUIDs.

After the successful fabrication of a TES array which occurs 10 % of the case, we need to do some tests. (1) The first test is the connection of Al wires and TES using measurements of TES resistances at room temperature. We applied a DC bias measuring current from -0.1V to 0.1V (step 0.02V) to the aluminum

wires which always connect with the superconducting NbSi thermometers. The resistance of aluminum wires and the thermometer metal is deduced $I = \frac{V}{R}$. Figure 5.13 presents the cartography and histogram of the TESs resistance of the array at room temperature measurement. We can approximately an Al wire ($\sim$ 10 cm length, $\sim$ 200 nm thickness, $\sim$ 6 μm width). Therefore the value of the TESs resistance at the room temperature test is of the order of $2\,k\Omega$. Due to the fact that we carry out measurements of the superconducting NbSi thermometer plus the Al wires thus the values of TES resistance of the array P90 in figure 5.13 are of the order of $\sim$ 4000 Ω compatibly cause aluminum resistance wires. The values of TES resistance have varied from different arrays. The goal of this measurements is the test of connections between TESs and Al wires and through it evaluating the yield of a TES array. The cartography demonstrated a yield of the TES array about 85 % at room temperature test. Due to the SQUID and wire bonding issue, 10 % more of TESs will be lost, finally, the yield of the TES array inside the cryostat is $\approx$ 75 % after the electronic readout system. This measurement helps primarily to know the yield as well as resistors distribution of the array, therefore we can decide the array is useful or useless. Table 5.2 presents array names and its yield of good pixels. Some arrays perform a good yield number in the connection test in the room temperature, however, there have some reasons such as the values of TES resistance are too high or un-uniform, many broken pixels or problems of the silicon wafer ... We base on that measurements and reasons to evaluate and decide a TES array. (2) The next step, the good TES arrays will be bonded and fixed in a copper backshort as shown in figure 5.12, which can be plugged with the focal plane and keep the array safe in movements. Then the TES array is installed into the focal plane inside the cryostat, which is cooled down to 300 mK. The TES resistance, the I-V curves, radioactive source test will be tested and readout by the electronic system.

5.3 The cryostat and the electronic readout system

The test cryostat in the APC laboratory is a component of a Triton 200/400 system. The Triton system has 6 connected independent components: the cryostat cooled system, the control box, the power supply, the pump system, the compressor, and the liquid nitrogen. The detail of the Triton system is described in the

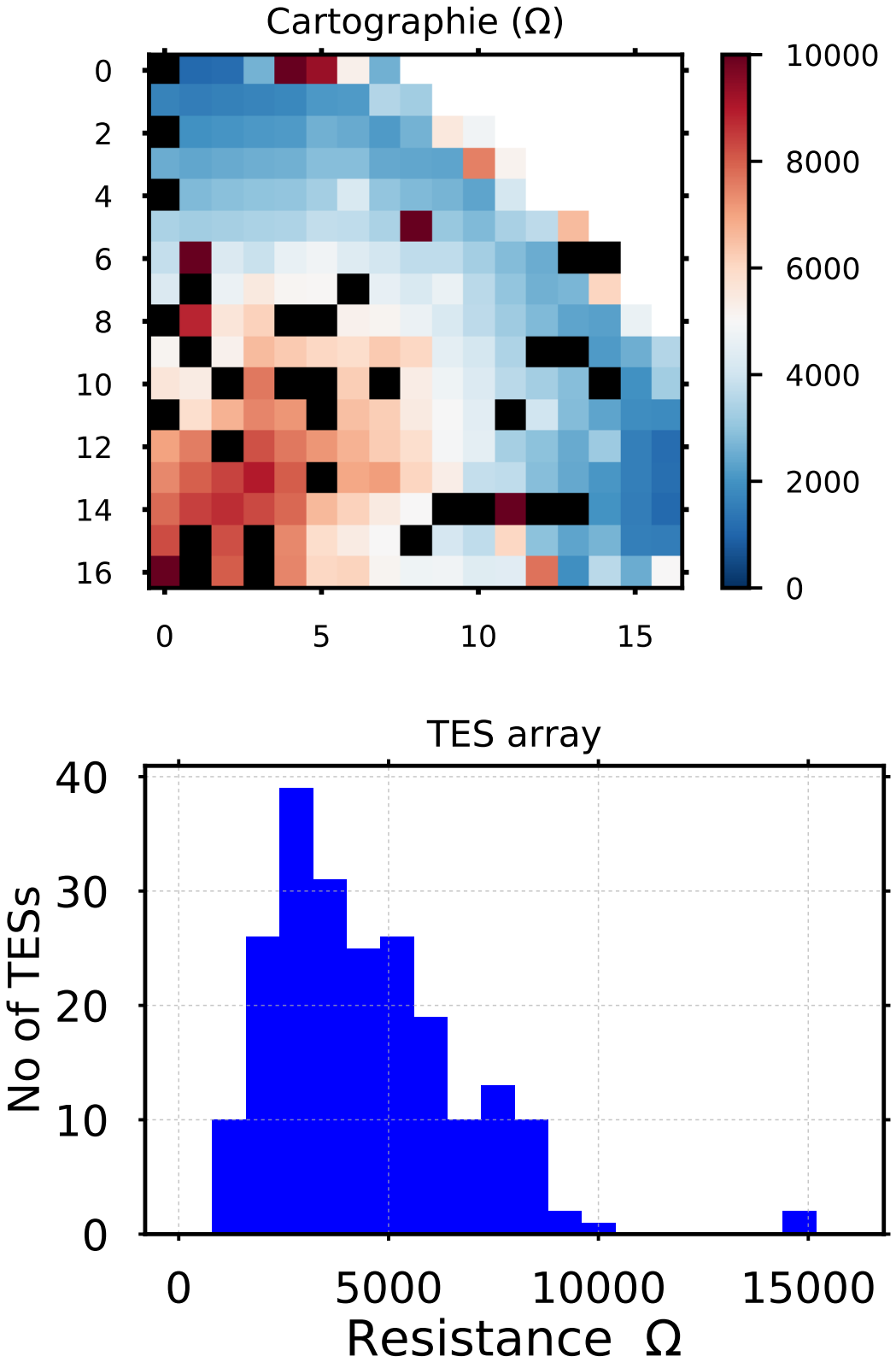

FIGURE 5.13: The measured resistor result of connection between NbSi and Al wires for the array P90 at room temperature. The cartography of TESs resistance indicates that there are 15 % of dead pixels which are in the black color. The histogram of TES resistance for good pixels, these values of resistance are of the order of 4000 Ω.

Number	Array name	Yield (good pixels)	Evaluation & Current status
1	P63	84 %	Good & Usable
2	P65	84 %	Ok & Usable
3	P68	77 %	Ok & Usable
4	P71	75 %	Not good & Useless
5	P73	89 %	Good & Usable
6	P82	77 %	Not good & Useless
7	P86	92 %	Ok & Usable
8	P88	84 %	Ok & Usable
9	P90	88 %	Good & Usable

TABLE 5.2: The table of TES arrays.

technical manual [3]. Figure 5.14 describes different temperature stages of the cryostat, a TES array is located and operated in superconducting temperature at the mixing chamber (MC plate).

In the vacuum tube, the cryostat system cools the temperature of the mixing chamber down to the temperature (mK) base on the helium dilution refrigerator. Basically, the principle is that a mixture of $^3He + ^4He$ is in equilibrium with ^3He in the mixing chamber. When ^4He is added to the mixture, ^3He is evaporated, this diluting process is an endothermic process, thus the temperature of the system is cooled down by the absorbed heat process. The system has the pump loop to pump the ^3He back the mixture, then the temperature of the mixing chamber continues to cool down to the setpoint of the controlled system.

The TESs array is mounted in the focal plane and the wire is connected to 256 SQUIDs multiplexer, the ASIC, the warm digital readout FPGA board which has included PID controller and the scheme of a TES array is showed on the screen computer by the QUBIC studio software. Figure 5.15 shows the order of the electronic readout system devices while Figure 5.16 illustrates its equivalent scheme. The focal plane of the QUBIC experiment is kilo-pixel TESs composed of 4 quadrants of 256 TESs, each read out by 256 SQUIDs and 2 ASICs. The readout of kilo-pixel TESs requires a high and complex technology readout system as the cryogenics system, the ultra-low noise cryogenic amplification, the flux locked loop, ADC, FPGA.

Descriptions of readout components:

- **A 128-to-1 Time-Domain SQUID Multiplexer:** Superconducting QUantum Interference Device (2 mm x 3 mm) is used to readout voltage-bias

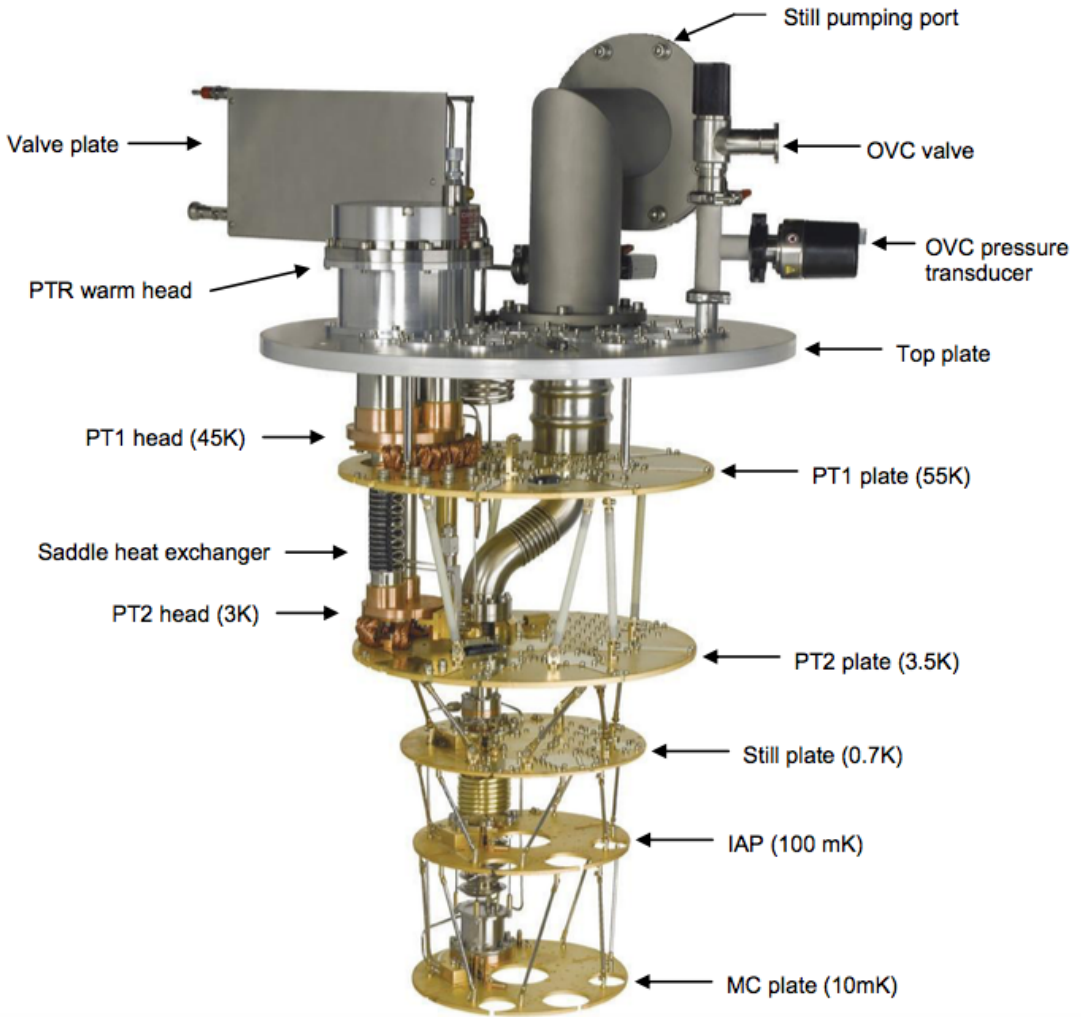

FIGURE 5.14: The vacuum chamber of Triton 200/400, dilution refrigerator is the stage of under 3.5 K. OVC, PTR stand for Outer Vacuum Chamber and Pulse Tube Refrigerator, respectively. PT1, PT2 are Pulse Tube first, second stage. IAP is Intermediate Anchoring Plate (100 mK plate). MC plate stands for the mixing chamber plate [3].

TESs, SQUIDs are operated around 0.1-4 K. Due to the fact that the yield of SQUIDs is not 100 %, then independently a TES is read out by a SQUID. A 128-to-1 Time-Domain SQUID Multiplexer has been investigated and manufactured for the QUBIC experiment to readout kilo-TESs [123]. Therefore each quadrant focal plane has a 256 TESs array which is composed of 2 Time-domains SQUID multiplexers. 128 SQUIDs are arranged in 4 columns and 32 rows as shown in figure 5.17.

The second multiplexing stage acts as 128-to-4 multiplexer, the ASIC and the low noise amplifier (LNA) at 40 K stage read out the SQUIDs as a 4-to-1 mux. A SQUID adds about 10 pW per TES and this power is dissipated

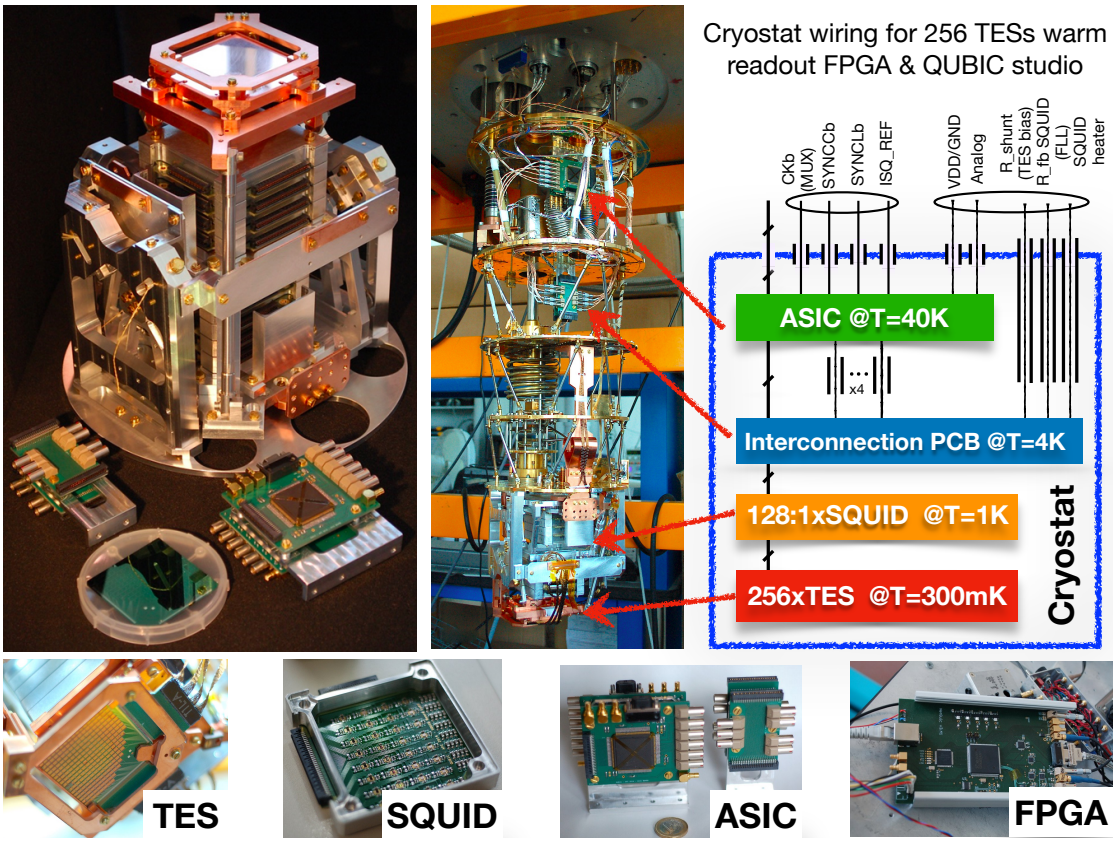

FIGURE 5.15: Readout electronic components of the cryostat in the APC laboratory in order of connection the TES array is mounted with the $\frac{1}{4}$ QUBIC focal plane, the SQUID, the ASIC, the warm readout FPGA board.

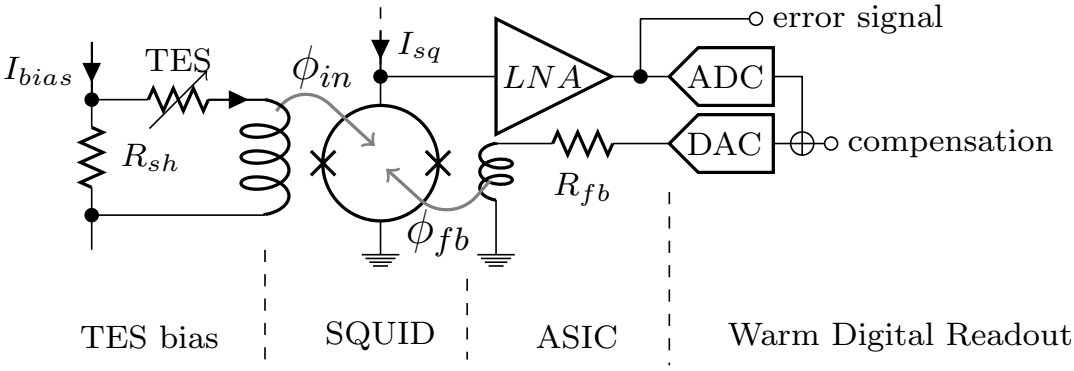

FIGURE 5.16: The scheme of the TES readout system from sub Kelvin to warm digital readout.

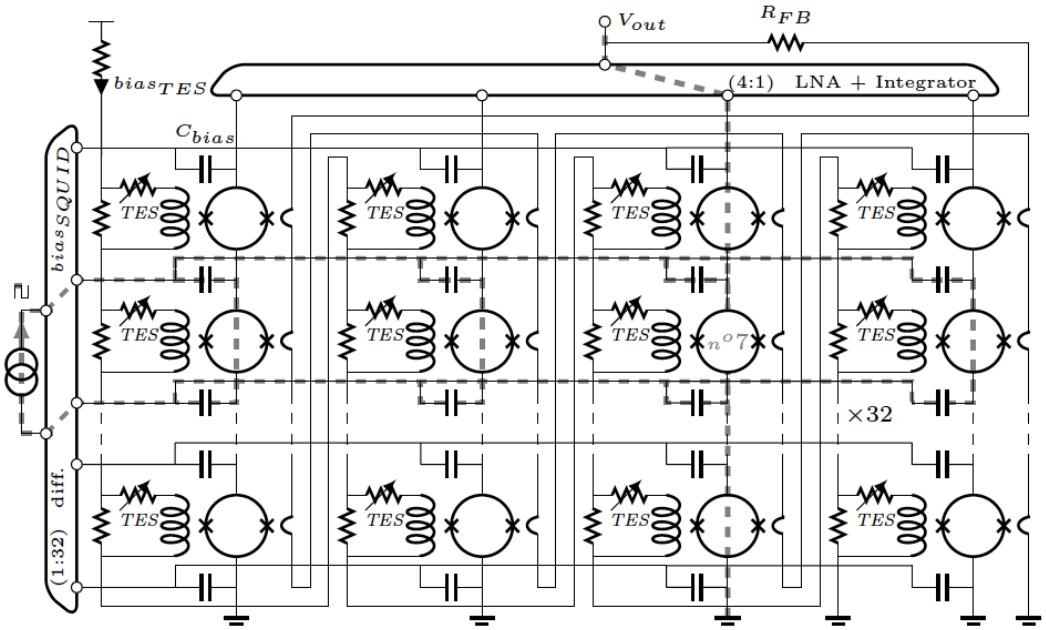

FIGURE 5.17: The topology of the 128:1 Time-Domain SQUID multiplexer. Each column has 32 rows of SQUIDs. 4 columns are read out by ASIC and a low noise amplifier (LNA). Capacitors C_{bias} allows to isolate the voltage of each SQUID [123].

to the cryostat shield. The sample rate of the readout 128 TESs in the time domain is shown in figure 5.18. The first cycle sample is "Mux" of the 1^{st} pixel to the 128^{th} pixel then return to the 1^{st} pixel. A frequency sample f_s is chosen by "QUBIC studio" then we can calculate the "Line", it is corresponding to the sample rate of each pixel or inverting of frequency acquisition f_{acq}. There has mismatch step between each pixel due to the constraint of the dynamic readout range, in practice with "QUBIC studio", we will not take data of some beginning points of "Mux".

$$\text{sample rate} = \frac{1}{\mathrm{f_{acq}}} = \frac{1}{\mathrm{f_s}}\mathrm{N_{dets}}\mathrm{N_{pts}} \qquad [\mathrm{s}]. \tag{5.38}$$

where $\mathrm{f_{acq}}$ is the frequency acquisition, $\mathrm{N_{dets}}$ is number of pixels, $\mathrm{N_{pts}}$ is number of measurements done for each pixels. For example, we read 128 TESs with frequency 2 MHz for 1000 samples per pixel, then we got the sample rate of each pixel is $0.064\,s$.

- **The ASIC:** Application Specific Integrated Circuit is designed to read out SQUID/TES at cryogenic temperature, in addition, Low Noise Amplification (LNA). The electronic circuit of the resistor and heterojunction bipolar

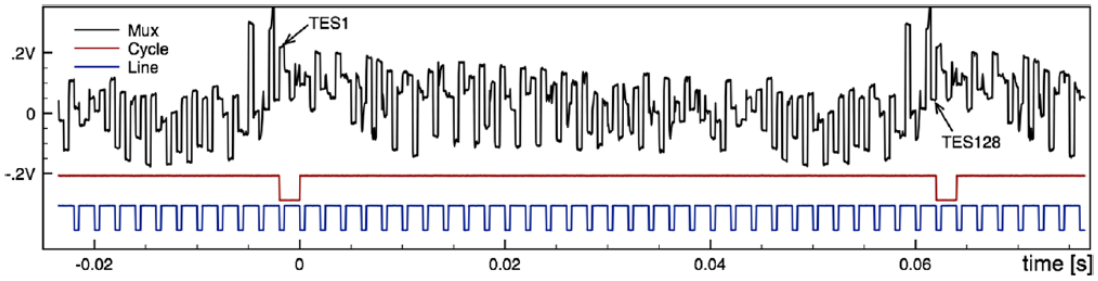

FIGURE 5.18: The sampling rate of 128 TESs, the Mux read out 128 TESs, Cycle and Line signal provided by ASIC [123].

transistors, on a few mm^2 chip is needed to fit with the intrinsic voltage SQUID noise ($nV/\sqrt{Hz}$). The functions of LNA are used to provide a large gain bandwidth ($\gg$ 1 GHz), small 1/f noise, basically, the noise is affected by a factor of square root of the number of detectors $\sqrt{N_{dets}}$ because of the mux. The ASIC of the QUBIC experiment uses commercial of BiCMOS SiGe 0.35 μm technology, and operates around 2 - 300 K. The ASIC amplifies and reads the signal from the 4 SQUID columns of 32 SQUIDs through 4 multiplexed inputs of the LNA. Sequentially, the analog signal is a timeline of 128 TESs through SQUIDs and LNAs [124].

- **The FPGA** is the abbreviation for Field Programmable Gate Array, which is programmed by Very high speed integrated circuit Hardware Description Language (VHDL) language. FPGA is a warn electronic readout at the room temperature. We are using FPGA XEM3005 Xilinx Spartan-3E, 32 MB, 16-bit wide SDRAM, USB connection, fast configuration, easy communication, and access. The purposes of the FPGA board are compensated offset to characterize the SQUID signal, controlled and feedback the flux locked loop of the system by loading PID controller parameters from the user (developed by the Research Institute in Astrophysics and Planetology (IRAP)).

- **The PID controller:** PID stands for Proportional Integral Derivative. PID controller is widely used in an automation system. In this system it controls a loop feedback. The PID controller is programmed and embedded inside the FPGA board. P is using to control compensated error between the setpoint value and the real value. I learn from past values of the system and control to eliminate the residual error. D estimates the future trend of the setpoint.

- **The QUBIC studio** is a software tool. It is installed on a window computer. The QUBIC studio can perform TES readout signal by an intuitive

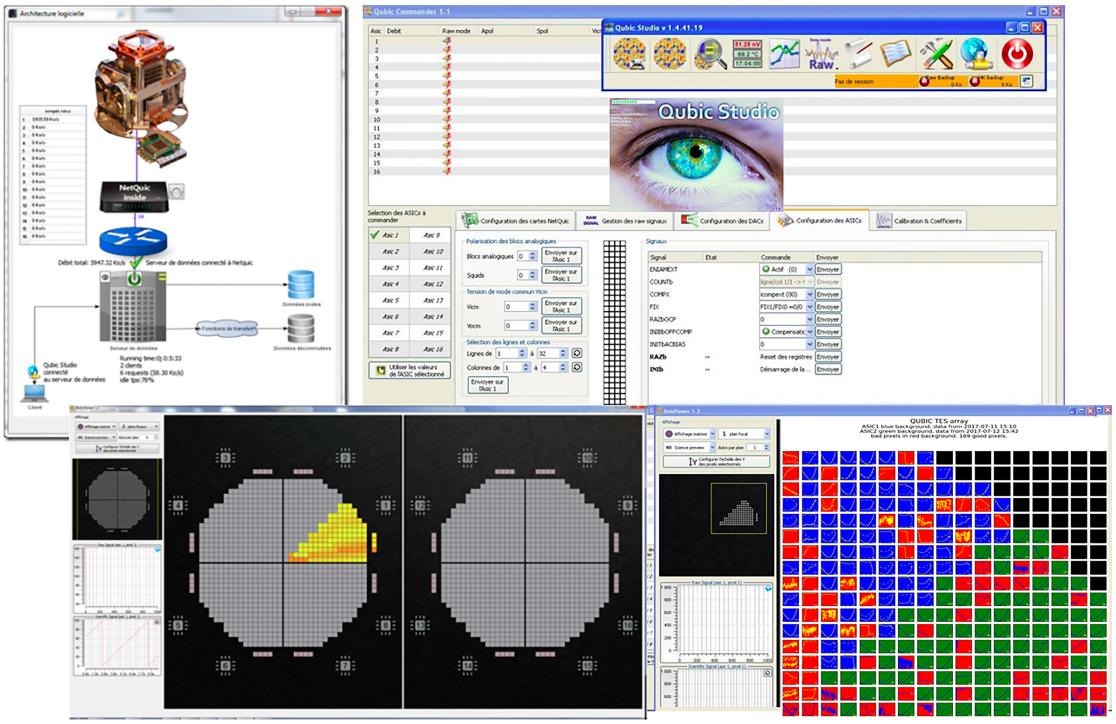

FIGURE 5.19: The QUBIC studio interfaces on a window operation computer.

cartography on a computer screen, saved data, compensated offset, voltage-biased TESs. The QUBIC studio helps to calibrate the TES array, measure I-V curves. The interface of the QUBIC studio is shown in figure 5.19. The software is integrated a pystydio and a qubic pack. They are python interfaces control locally or remotely read and write, data analysis, data plotting. The pystudio and the qubic pack are available on the GitHub: https://github.com/satorchi/pystudio

The TES and the readout system can be transformed to block diagrams as shown in figure 5.20. This algorithm can be used to express the electrical time constant of the TES and the electric readout system. We notice the negative sign of the flux locked loop (FLL) feedback, due to periodic transfer function (sin-like) of the SQUID, the FLL is stable whatever the sign. Indeed, If the feedback is positive the system is unstable and thus the operating point of the SQUID jump to the other slope of the SQUID characteristic (the transfer function H_{SQ} become $-H_{SQ}$). So that the periodic SQUID transfer function leads to always operate in a negative feedback which is in steady state. In addition, it is possible to invert the connection to the loops of the transformer coils: $M_{in} \rightarrow -M_{in}$ and/or $M_{fb} \rightarrow -M_{fb}$. So that, in the end, we do not really know exactly the sign, but we are sure that the system can find a stable state.

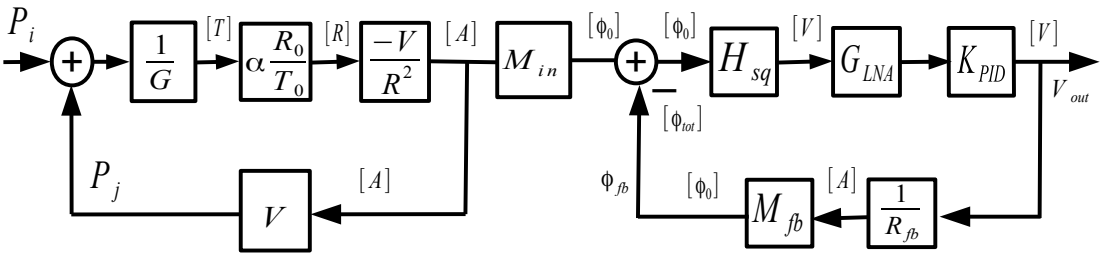

FIGURE 5.20: The block diagram of a TES and the electric readout system which included the SQUID, the low noise amplifier, the PID controller and the flux locked loop feedback.

Figure 5.21 shows the output signal of I-V measurements for a 256 TESs array. There are 2 ASICs in the interface (green-ASIC2 and blue-ASIC1 color online), we can observe number good or bad pixels.

A DC-SQUID consists of two Josephson junctions[5] connecting parallel on a superconducting loop. It is extraordinarily sensitive to convert magnetic flux to voltage(V-Φ) and current voltage. A fundamental property of a closed superconducting loop is that they can maintain the magnetic flux in a universal constant called the flux quantum. A flux quantum can be understood as the ratio of Planck constant h and the absolute value of the Cooper-pair charge 2e, $\Phi_0 = \frac{\mathrm{h}}{2\mathrm{e}} \approx 2 \times 10^{-15}$ Wb [1, 122].

The current passes by a SQUID, normally it is divided equally by two $2 \times \mathrm{I}_1 = 2 \times \mathrm{I}_2 = \mathrm{I}_{\mathrm{sq}} = \mathrm{I}_0 \sin\Delta\phi$, where $\Delta\phi$ is the different phase. The output voltage of a SQUID is a periodic function of magnetic flux, this is explained in the superconducting electromagnetic theory of the relationship between phase change and wavefunction in canonical momentum. Hence we could measure the magnetic signal by an integer number of flux quanta sensitively. If we applied a magnetic field to a SQUID, the superconducting loop opposes the magnetic field by generating a screening current I_s, which is equal but opposite the applied magnetic field and the

[5]Josephson junction: weak link thin insulator or normal regions of superconductors, the current can flow with zero resistance called Josephson current, the maximum current before having resistance is called the critical current (I_c).

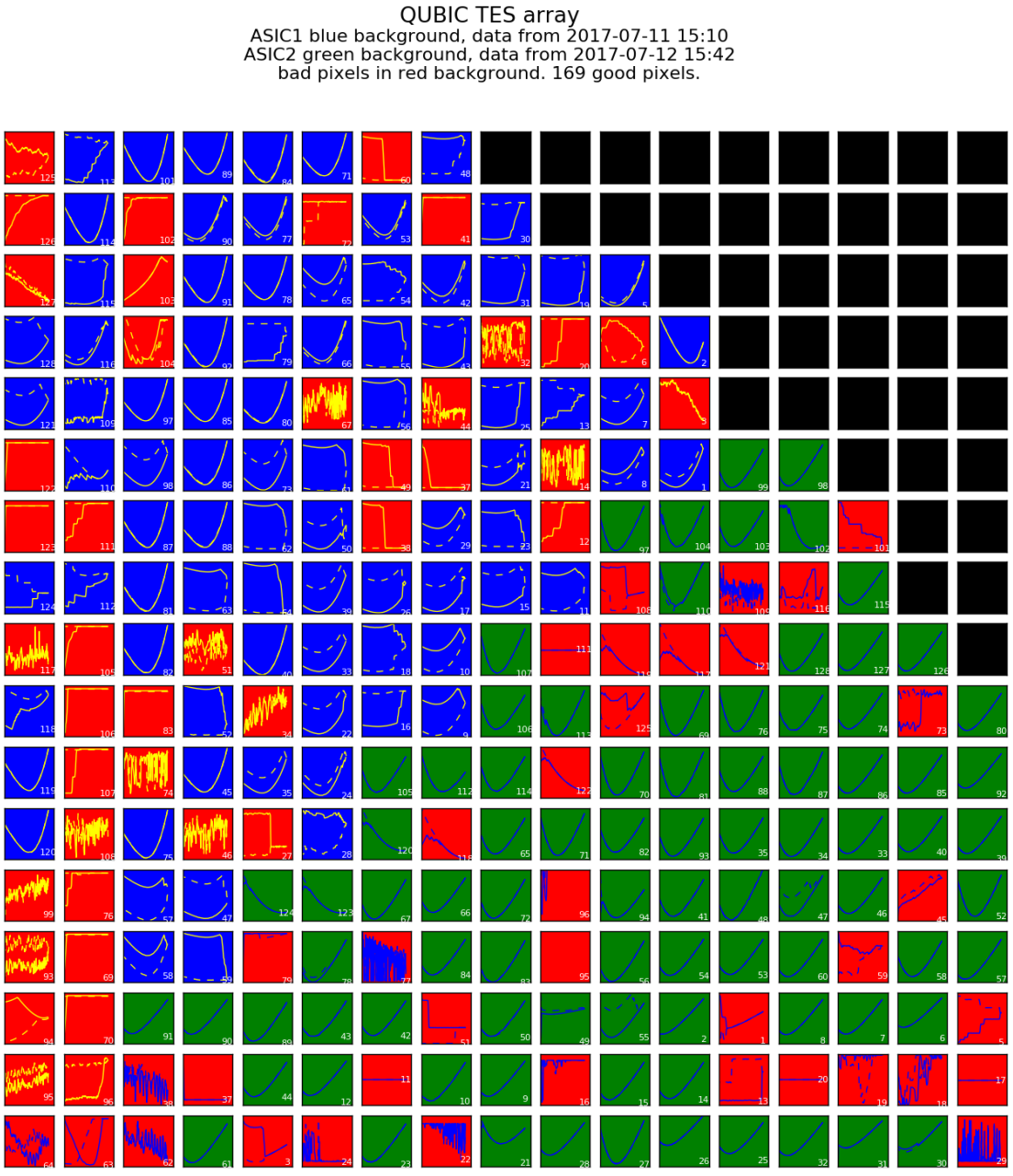

FIGURE 5.21: The read out result of the QUBIC studio tool and read out system for a 256 TESs array, half-bottom pixels (green) are read by ASIC2 and the half-top pixels(blue) are read by ASIC1. The curves in the pixels are the IV measurements for each TES.

screening current cancels the flux in the Josephson junctions ring. This current is periodic in the applied flux, the critical currents of Josephson junctions depend on the screening current [1].

$$\begin{aligned} I_1 &= \frac{\mathrm{I_{sq}}}{2} - \mathrm{I_s}, \\ I_2 &= \frac{\mathrm{I_{sq}}}{2} + \mathrm{I_s}. \end{aligned} \tag{5.39}$$

When we applied a magnetic flux in the order of one flux quantum to one and a half flux quantum, this is equivalent to increase continuously the magnetic flux from zero to a determined value. The SQUID I-V curve oscillates between two regimes with a period of one flux quantum. This physical concept helps to make a magnetometer detector. The input flux and the output voltage across the SQUID look sine-like oscillation as shown in figure 5.22.

In fact we use SQUIDs with a feedback coil in a Flux-Locked Loop (FLL) [122], it means the current from SQUID will be fed again the second coil of the SQUID. Consequently the negative feedback can compensate external flux to help operating system in the constant flux between Φ_{in}, Φ_{fb}.

The FLL technology can measure tiny voltage-bias using a SQUID. The principle is that when we apply an unknown voltage to one of SQUID coils, the screening current appears, the FLL coil will create a canceling magnetic flux of the unknown voltage. The current of the FLL is measure then the voltage is determined by a resistor $\mathrm{R_{fb}}$. The block diagram in figure 5.20 and 5.23 illustrate the FLL operation. The relationship among the voltage, the feedback resistor, the transformer coil, and original from a TES is:

$$\begin{aligned} \mathrm{V_{out}} &= \mathrm{G} \times \mathrm{K_{PID}} \times \mathrm{V_{SQUID}}, \\ \Phi_{\mathrm{in}} &= \mathrm{M_{in}I_{in}}, \\ \Phi_{\mathrm{fb}} &= \mathrm{M_{fb}I_{fb}} = \frac{\mathrm{M_{fb}}}{\mathrm{R_{fb}}} \times \mathrm{V_{out}}. \end{aligned} \tag{5.40}$$

If the FLL loop gain is $\ll 1$ then:

$$\begin{aligned} \Phi_{\mathrm{in}} - \Phi_{\mathrm{fb}} &= 0, \\ \mathrm{M_{in}I_{in}} &= \frac{\mathrm{M_{fb}}}{\mathrm{R_{fb}}} \times \mathrm{V_{out}}. \end{aligned} \tag{5.41}$$

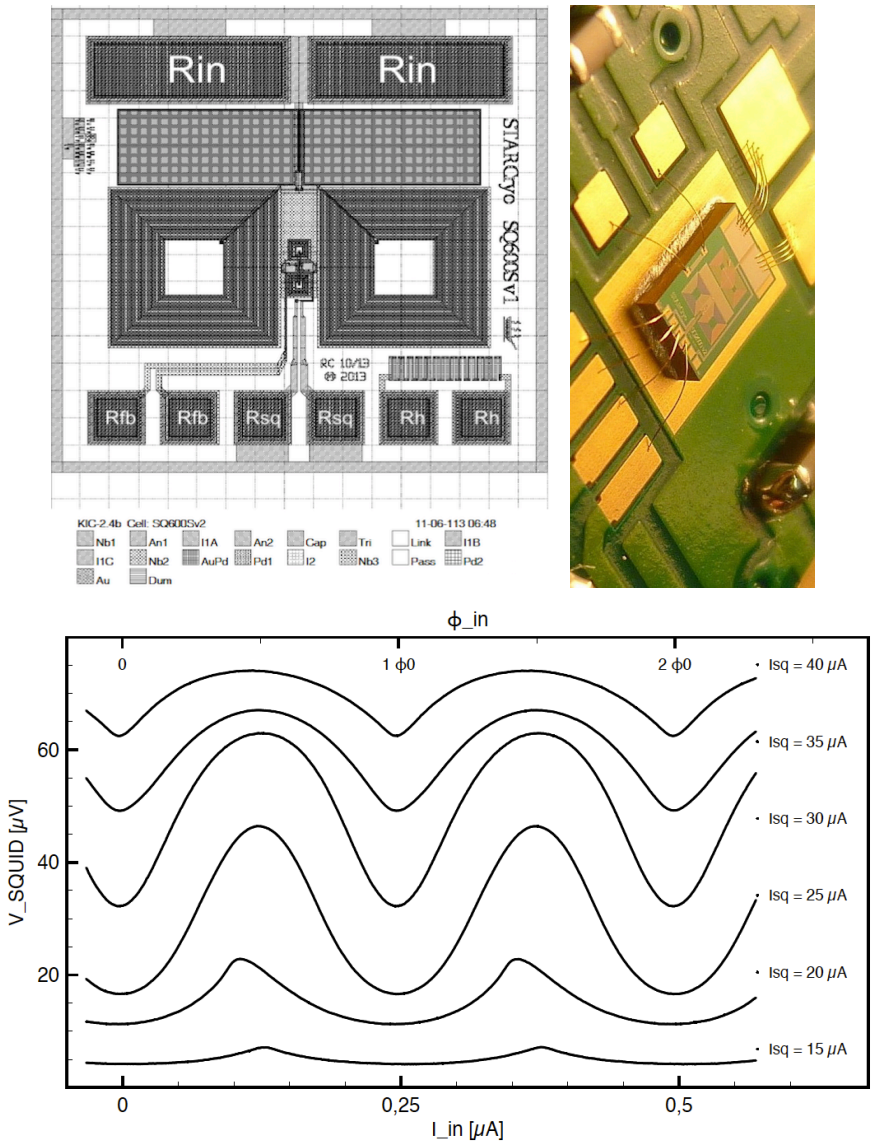

FIGURE 5.22: (*top*) A microphotograph of the SQUID pins scheme, glued and bonded on a printed circuit board (PCB) for a flux locked loop operating in superconducting temperature.(*bottom*) The sine-like SQUID characteristic output voltage as function of magnetic flux Φ_{in}. The different lines are obtained by different currents bias I_{sq} [31].

In the language of an automatic controlled system, the block diagram of the TESs close-loop feedback readout system is model as figures 5.23 and 5.20:

- $H_{sq} = \dfrac{dV_{sq}}{d\Phi_{tot}}$ is the dynamic transfer function of the SQUID.
- G is the gain of the cryogenic SiGe followed by a preamplifier Stanford Research SR560 at room temperature providing a total gain G = 200000 ($G_{SiGe=200}, G_{SR560} = 1000$).

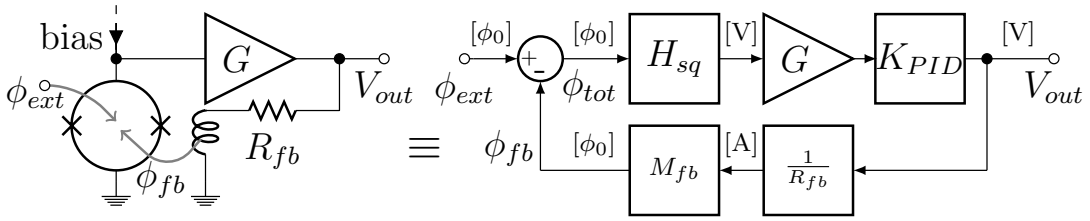

FIGURE 5.23: SQUID readout system and its corresponding block diagram in a Flux Locked Loop. This block diagram is associated with the block diagram in figure 5.20

- K_{PID} is the transfer function of the PID controller, which is embedded in the FPGA board. In practice, we used to configure PI or I controllers.
- R_{fb} is the feedback resistor of the FLL, $R_{fb} = 10\,k\Omega$ or $110\,k\Omega$.
- M_{fb} is the transformer coil of the FLL.

The electrical time constant of the readout chain

We can study the stability of the system in the Laplace domain[6], the transfer function of the PID controller is expressed $L(s) = K_{PID} = K_P + \frac{K_I}{s} + sK_D = \frac{K_I + sK_P + s^2K_D}{s}$ where s is the complex frequency. The transfer function of the close loop, negative feedback system is calculated in Laplace domain:

$$\begin{aligned} FB &= \frac{H_{sq}GK_{PID}}{1 + H_{sq}GK_{PID}\frac{M_{fb}}{R_{fp}}}, \\ &= \frac{H_{sq}G\frac{K_I + sK_P + s^2K_D}{s}}{1 + H_{sq}G\frac{M_{fb}}{R_{fp}}\frac{K_I + sK_P + s^2K_D}{s}}, \\ &= \frac{H_{sq}G\left(1 + \frac{K_P}{K_I}s + \frac{K_D}{K_I}s^2\right)}{\frac{s}{K_I} + H_{sq}G\frac{M_{fb}}{R_{fb}}\left(1 + \frac{K_P}{K_I}s + \frac{K_D}{K_I}s^2\right)}, \\ &= \frac{R_{fb}}{M_{fb}}\frac{1 + \frac{K_P}{K_I}s + \frac{K_D}{K_I}s^2}{1 + \frac{K_P}{K_I}s + \frac{R_{fb}}{H_{sq}GM_{fb}K_I}s + \frac{K_D}{K_I}s^2}. \end{aligned} \tag{5.42}$$

[6]it transfers a variable from real domain to the complex domain. Normally it is transformation of time to frequency.

Due to the fact that we do not often design a full three PID components system. We use to set the derivative $\mathrm{K_D} = 0$. Then we can define responded time constants of the system in the equation 5.42

$$\begin{cases} \tau_0 = \dfrac{\mathrm{R_{fb}}}{\mathrm{H_{sq}GM_{fb}K_I}} + \tau_{01}, \\ \\ \tau_{01} = \dfrac{\mathrm{K_P}}{\mathrm{K_I}}. \end{cases} \tag{5.43}$$

Especially, the QUBIC studio has separated scripts, which are compensated signal to the zero baseline. Consequently we also set the proportional $K_P = 0$. Finally the electronic readout time constant of the system is depended only on the integral K_I term of the PID controller since we know $R_{fb}, H_{sq}, G, M_{fb}$ [122]:

$$\boxed{\tau_0 = \frac{\mathrm{R_{fb}}}{\mathrm{H_{sq}GM_{fb}K_I}}}. \tag{5.44}$$

5.3.1 IV, PV, RV curves

The TES Current-Voltage characteristic (I-V curves) represents the TES operating current, voltage, resistance..., as a function of bias voltage in the electrothermal feedback (ETF) regime. The I-V curves measurements also establish a relationship between the voltage and the current of a TES, particularly in the TES transition regime. The measurements of TES I-V curves have a vital role for several reasons [156]:

- The I-V curves help us to determine saturation energy of the pixels, the maximum dissipated energy of the TES without driving the TES to the normal regime.
- The I-V curves provide information such as the TES operating current and resistance as a function of bias voltage, when I-V curves are taken at multiple bath temperatures, the thermal conductance of the TES to the thermal bath helps determine the TES behaviors such as the TES noise and responsivity and the optimal TES operating condition.

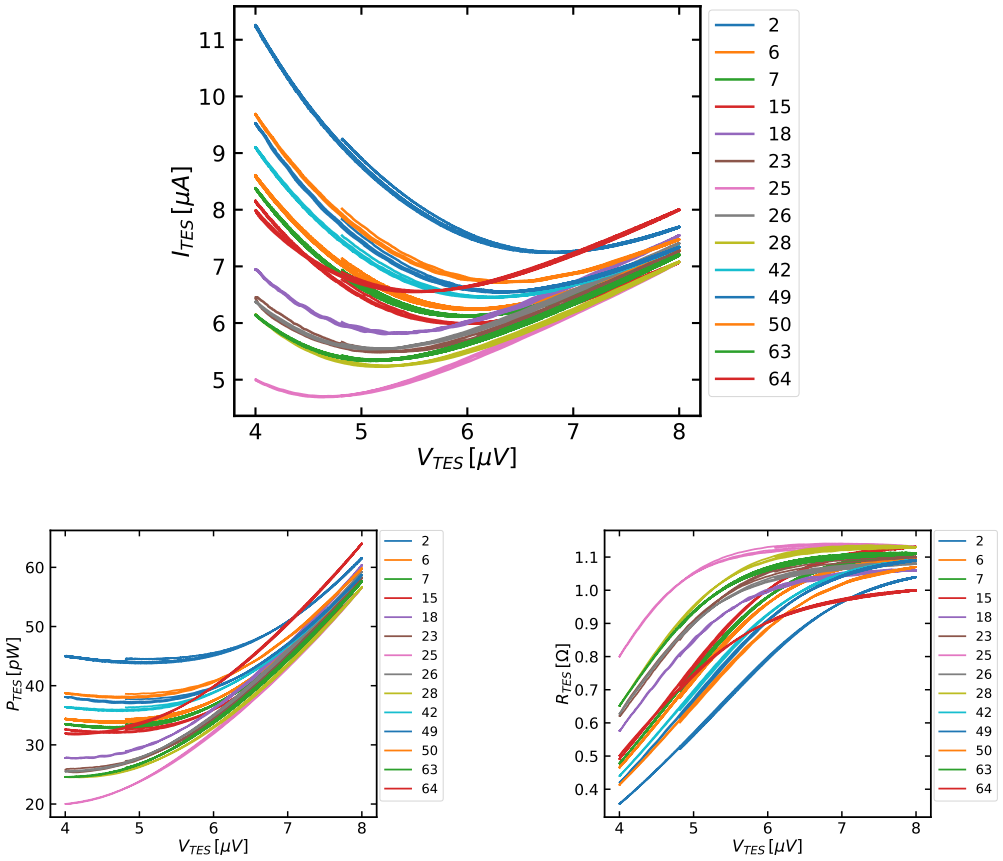

FIGURE 5.24: I-V, V-R and P-V curves of the several pixels on a 256-TES at T_{bath} = 300 mK. We apply changing voltage-biased source and measure the output current.

- The I-V curves also help to calibrate the TES complex impedance and the TES noise spectrum, which are necessary for establishing an electrothermal model of the TES.

Figure 5.24 represents I-V, R-V and P-V curves of several pixels on a 256 TES array. A typical TES I-V curve is divided into three states: the normal state, the transition state, and the superconducting state. First I-V curves describe that from the right part of the curves, the TESs are in their normal state following the metallic behavior of Ohm's law. Then, the TESs tend to transit to their superconducting state, and the electrothermal feedback starts to take place when the I–V curves reach their minimum. Once the electrothermal feedback is operational, the TESs are self-regulated and work at quasi-constant power, which corresponds to the P–V plateau. As the TESs travel further on their transition, their resistance continues to drop, which leads to I–V portions of a parabola on the left part of

the curves. The flat region of the P-V curve shows that the total dissipated power is a constant regardless of changes in the voltage bias which is an evidence of an electrothermal feedback regime [93]. The R-V curves represent for currents in the TESs, TESs operate in the normal regime obey Ohm's law, they transit to the superconducting regime, a small change of the resistance equivalents to a large change of the current then these curves are not linear.

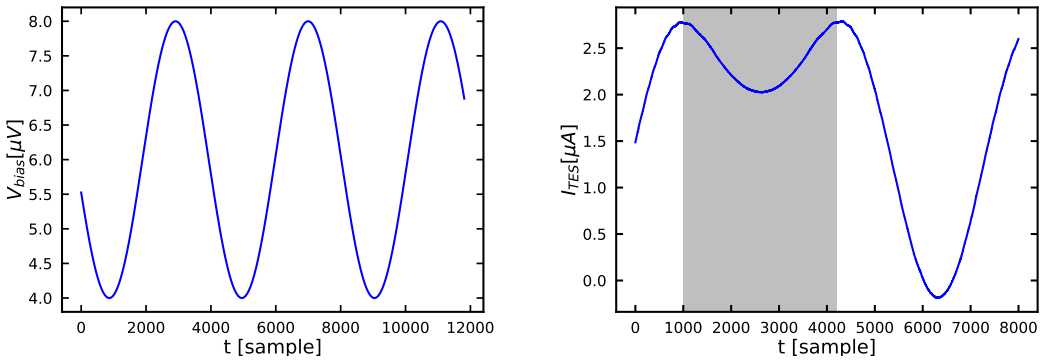

FIGURE 5.25: *left:* The input sine V_{bias} signal, which is sent to the TES. *right:* The output signal of the readout system when the TES array is cooled down to the superconducting temperature. The grey area indicates the TES signal in the transition regime while outside the grey area, the TES signal is in the normal regime.

In addition, in order to estimate the resistance of the TES below T_c, practically we vary the TES bias voltage following very low-frequency sine waves (0.1 Hz) we change decreasingly the temperature of the cryostat to the superconducting regime. We can observe the behavior of the signal between the normal state and the superconducting state by result of the changing output signal in *QUBIC studio* tool as shown in figure 5.25. The resistance values of the TES is calculated using the formula 5.8:

$$R_{TES} = \frac{V_{bias} R_{para}}{R_{bias} + R_{para}} \frac{1}{N_{pts} \Delta S_{sig} G \frac{M_{fb}}{M_{in} R_{fb}}}. \tag{5.45}$$

The left term of the equation $\frac{V_{bias} R_{para}}{R_{bias} + R_{para}}$ is the TES voltage as described in the principal circuit of a TES while the right term is $\frac{1}{I_{TES}}$ from the electronic readout system with ΔS_{sig} is the dynamic (amplitude with no offset) of the output which is measured in the sample unit. When a TES is in the normal state, the value of R_{TES} is close to $\approx 1\ \Omega$, figure 5.6 shows the curves of temperatures in K and resistances Ω and also the values of the sensitivity temperature parameter α for

some TESs. When the TES enters the superconducting regime, the value of α is high and it decreases steadily in the normal regime. Figure 5.25 illustrates the changing of the signal of a TES between the normal state and the superconducting state. The voltage of the TES evolves faster in the superconducting state than in the normal state while the V_{bias} follows a sine wave. This point has been figured out by analysis the SQUID signal as well as experiments. In the QUBIC studio software, we can see the changed signal in the screen when the detectors enter the superconducting temperature.

5.4 Radioactive source Americium 241

The ^{241}Am[7] half-life ($t_{1/2} = 432.2\,years$) source has diameter 3 mm. It has an activity of 8 Bq and the α particles are emitted with an energy of 5.44 MeV ($\lambda \approx 0.23$ pm), the γ rays are emitted with an energy of 60 keV. The source is placed at 5mm distance from a TES array which could be in front of a determined pixel. In order to minimize the thermal background, we designed a copper holder which can be mounted to the bonded TES array. The copper holder is covered by copper tape which is placed in front of the TES array. On the copper cover, we attach the radioactive source. The configuration of the experiment is shown in figure 5.26.

In order to estimate simply the deposited energy of particles through pixel structures, we can present an approximate formula:

$$\Delta \mathrm{E} = \mathrm{e}\frac{\mathrm{dE}}{\mathrm{dx}}\rho \ [\mathrm{MeV}], \tag{5.46}$$

where e and ρ are the thickness $[cm]$ and the density $[g/cm^3]$ of materials, respectively. Firstly we calculated the stopping power $\frac{dE}{dx}$ of materials which made the TES pixel. We used SRIM[8] with the range of incident energy from keV to GeV.

[7] ^{241}Am radioactive source can be found in residential smoke detectors. ^{241}Am emits α particles and γ rays. α particles or $^4_2He^+$ consists of two protons and two neutrons. γ rays are electromagnetic waves of very short wavelength. According to Public Health Statement of National Technical Information Service (NTIS), Virginia USA, we may be exposed to ^{241} Am a little by breathing air, drinking water or eating food. Alpha particles do not penetrate the skin and gamma rays emitted from americium sources are low energy. Then exposure to americium is not usually considered to be a danger to human health. The ^{241}Am source emitted α particles at $\sim$ 5.44 MeV, then the penetration is around 4 cm in air.

[8] The **S**topping and **R**ange of **I**ons in **M**atter: calculates many features of the transport of ions in matter http://www.srim.org/

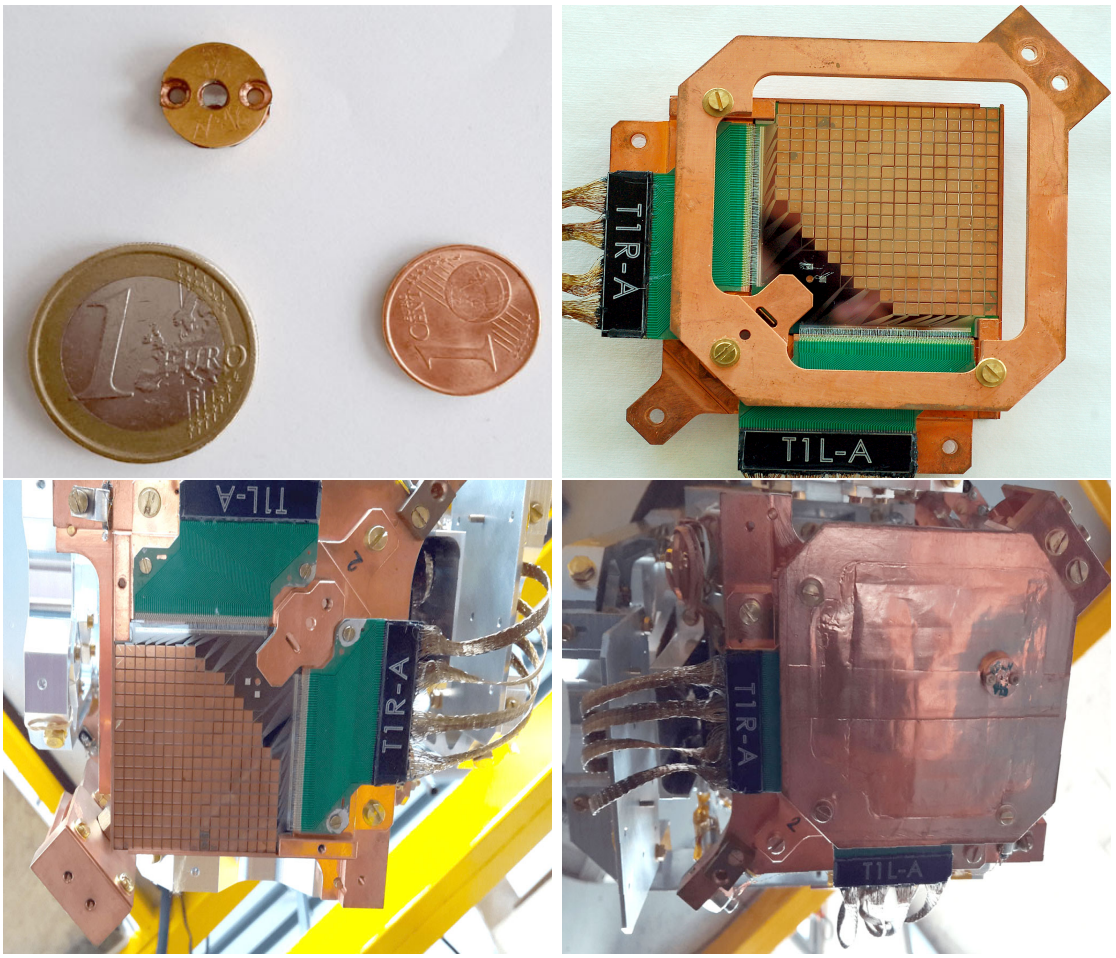

FIGURE 5.26: Configuration of Americium source and the TES array for the experiment. *Top left*: The americium source. *Bottom right*: The source is set up in font of the TES array in the cryostat.

With compound materials we assumed 50 % of each ingredient except the NbSi that is taken 15.45 % of Nb. The result of stopping power is shown in figure 5.27.

Apply the equation 5.46 we obtain the deposited energy in the table 5.3. Due to the thickness of the substrate, the energy of alpha particles is absorbed in the substrate layer.

5.5 TES model approach

We can model a basic TES pixel as a film of a heat capacity linked to a silicon wafer substrate and a cooling bath by thermal conductances. The temperature elevation of a detector is evaluated by the Joule heating and the losing heat to the

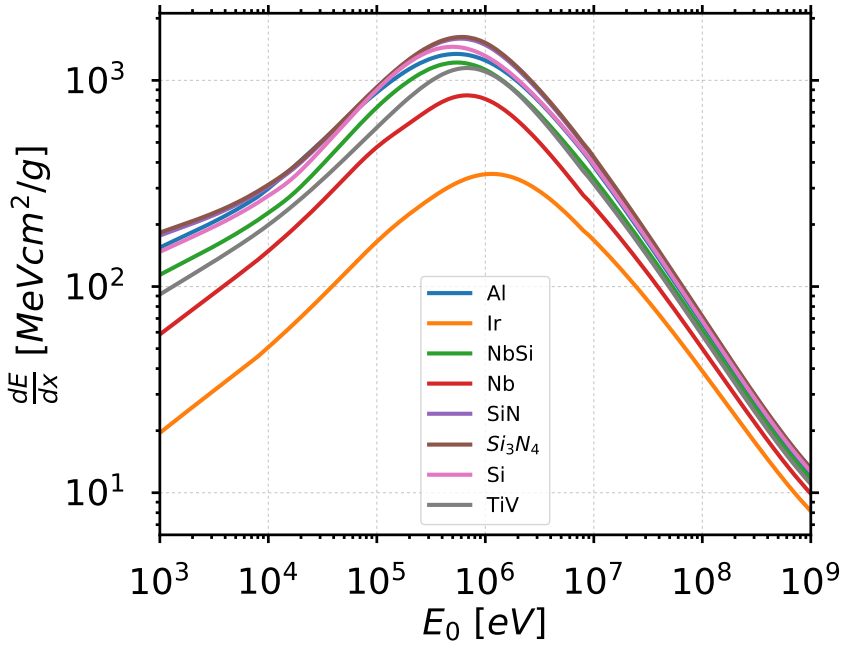

FIGURE 5.27: The stopping power of alpha particles in different materials, data is exported by SRIM software.

Element	Material	Thickness [μm]	Density [g/cm^3]	Deposit energy [keV]
Thermometer	NbSi	0.1	6.8	33.495
Grid	TiV	0.1	5.0717	23.7374
Wires	Al	0.2	2.7	30.7372
Membrane	Si_3N_4	0.5	3.44	109.538
Substrate	Si	500	2.329	5400 (absorbed)

TABLE 5.3: The table of the deposited energy of alpha particles in different materials and its thickness. Due to the thickness of Silicon substrate, the emitted energy of α particles is absorbed.

substrate. The Joule heating provides ETF to hold a constant temperature of the TES. An equilibrium state is set when the Joule heating matches the heat going to the thermal bath. Figure 5.28 shows the heat capacities of TESs C_2 and the silicon wafer substrate $C_1(J/K)$. G_1 is the thermal link of the silicon wafer substrate to the bath temperature T_b of the cryostat whereas C_b is considered infinite. T_b must be below T_c. In order to solve the thermal model in a simple way, we assume $G_2(W/K)$ the effective thermal link of TESs with the silicon wafer, in this case, the thermal conductance G_2 is increased by the electrothermal feedback effect then they are equivalent to the effective thermal conductance $G_{eff} \approx G(1+\mathscr{L})$ in a TES. So that we have effective time constants $\tau_1 = \frac{C_1}{G_1}$ and $\tau_2 = \frac{C_2}{G_2}$. Notice that the definition is not the same as the natural time constant of a TES which is

$$\tau = \frac{C}{G}.$$

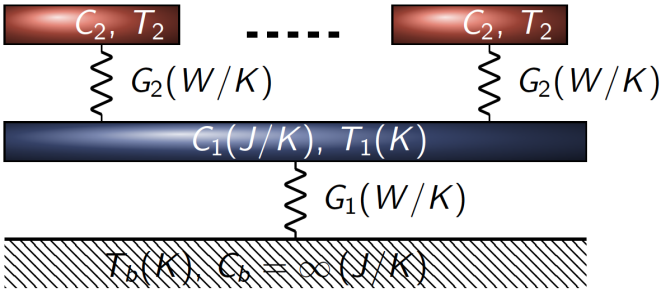

FIGURE 5.28: The simple model of TESs array, TESs link to the silicon wafer substrate by a thermal link, and it is similar for the silicon wafer and the thermal bath.

We assume particles from the radioactive source with energy E_{in} and hitting the pixel which could be absorbed by the grids, the substrate, the thermometer .... The deposited energy will induce temperature variations to the thermometer NbSi ($\Delta T = \frac{E}{C}$) and effect on the TES signal. We define $\Delta T_1(t)$ and $\Delta T_2(t)$ are the rising temperature on the silicon wafer substrate and TES, respectively. Following the simple model in figure 5.28 and *the thermal equation for the temperature* 5.3, we have the thermal saturation of the silicon wafer and TESs over time are:

$$\begin{cases} \frac{dE_1}{dt} = C_1 \frac{d\Delta T_1}{dt} = G_2 \left(\Delta T_2(t) - \Delta T_1(t)\right) - G_1 \Delta T_1(t). \\ \\ \frac{dE_2}{dt} = C_2 \frac{d\Delta T_2}{dt} = G_2 \left(\Delta T_1(t) - \Delta T_2(t)\right). \end{cases} \tag{5.47}$$

we perform in the companion matrix form of the thermal equations.

$$\frac{d}{dt}\begin{pmatrix} \Delta T_1(t) \\ \\ \Delta T_2(t) \end{pmatrix} = \begin{pmatrix} -\frac{G_1 + G_2}{C_1} & \frac{G_2}{C_1} \\ \\ \frac{G_2}{C_2} & -\frac{G_2}{C_2} \end{pmatrix} \begin{pmatrix} \Delta T_1(t) \\ \\ \Delta T_2(t) \end{pmatrix}. \tag{5.48}$$

This matrix equation is similar form with the linear algebra equation $y' = \mathbf{A}y$, then the general solution of the equation is:

$$\begin{pmatrix} \Delta T_1(t) \\ \\ \Delta T_2(t) \end{pmatrix} = c_1 \left(\mathbf{k_1}\right) e^{\lambda_1 t} + c_2 \left(\mathbf{k_2}\right) e^{\lambda_2 t}$$

$$= c_1 \begin{pmatrix} \dfrac{G_2}{C_1} \\ \\ \lambda_1 + \dfrac{G_1+G_2}{C_1} \end{pmatrix} e^{\lambda_1 t} + c_2 \begin{pmatrix} \dfrac{G_2}{C_1} \\ \\ \lambda_2 + \dfrac{G_1+G_2}{C_1} \end{pmatrix} e^{\lambda_2 t}.$$

$$\text{or} \quad = c_1 \begin{pmatrix} \lambda_1 + \dfrac{G_2}{C_2} \\ \\ \dfrac{G_2}{C_2} \end{pmatrix} e^{\lambda_1 t} + c_2 \begin{pmatrix} \lambda_1 + \dfrac{G_2}{C_2} \\ \\ \dfrac{G_2}{C_2} \end{pmatrix} e^{\lambda_2 t}. \tag{5.49}$$

where $c_{1,2}$ are constants, $\mathbf{k_{1,2}}$ are eigenvectors $((\mathbf{A} - \lambda \mathbf{I})\,\mathbf{k} = 0)$, we can choose 2 vectors which satisfy the solution. $\lambda_{1,2}$ are eigenvalues $(det\,(\mathbf{A} - \lambda \mathbf{I}) = 0)$ which basically inverse of time constants.

$$\lambda_{1,2} = -\frac{\left(\dfrac{G_1+G_2}{C_1} + \dfrac{G_2}{C_2}\right) \pm \sqrt{\text{Delta}}}{2};$$

$$\text{Delta} = \left(\frac{G_1+G_2}{C_1} + \frac{G_2}{C_2}\right)^2 - \frac{4G_1G_2}{C_1C_2}. \tag{5.50}$$

We define $\Lambda_{1,2} = \lambda_{1,2} + \dfrac{G_1+G_2}{C_1}$ then we can rearrange the solution equations 5.49, notice that $\Lambda_1 - \Lambda_2 = \lambda_1 - \lambda_2$.

$$\begin{pmatrix} \Delta T_1(t) \\ \\ \Delta T_2(t) \end{pmatrix} = \begin{pmatrix} c_1 \dfrac{G_2}{C_1} e^{\lambda_1 t} + c_2 \dfrac{G_2}{C_1} e^{\lambda_2 t} \\ \\ c_1 \Lambda_1 e^{\lambda_1 t} + c_2 \Lambda_2 e^{\lambda_2 t} \end{pmatrix}. \tag{5.51}$$

In order to find those constants $c_{1,2}$, we have to consider the initial condition, simply and firstly, we can assume α particles hit the substrate silicon wafer at time $t = 0$, $\Delta T_1\,(t) = \dfrac{E_{in}}{C_1}$, $\Delta T_2\,(t) = 0$. The equation 5.51 is now

$$\begin{pmatrix} \dfrac{E_{in}}{C_1} \\ \\ 0 \end{pmatrix} = \begin{pmatrix} c_1 \dfrac{G_2}{C_1} + c_2 \dfrac{G_2}{C_1} \\ \\ c_1 \Lambda_1 + c_2 \Lambda_2 \end{pmatrix}. \tag{5.52}$$

We get

$$\begin{cases} c_1 = -\dfrac{E_{in}}{G_2}\dfrac{\Lambda_2}{\Lambda_1 - \Lambda_2}, \\ c_2 = \dfrac{E_{in}}{G_2}\dfrac{\Lambda_1}{\Lambda_1 - \Lambda_2}. \end{cases} \tag{5.53}$$

Substituting to the equation 5.51 we have

$$\begin{pmatrix} \Delta T_1(t) \\ \\ \Delta T_2(t) \end{pmatrix} = \begin{pmatrix} \dfrac{E_{in}}{C_1}\dfrac{1}{\lambda_2 - \lambda_1}\left(\Lambda_2 e^{\lambda_1 t} - \Lambda_1 e^{\lambda_2 t}\right) \\ \\ \dfrac{E_{in}}{G_2}\dfrac{\Lambda_1\Lambda_2}{\lambda_2 - \lambda_1}\left(e^{\lambda_1 t} - e^{\lambda_2 t}\right) \end{pmatrix}. \tag{5.54}$$

Secondly we also can assume α particles hit the TES at the time $t = 0$, $\Delta T_2(t) = \dfrac{E_{in}}{C_2}$, $\Delta T_1 = 0$. Then we obtain

$$c_1 = -c_2 = \frac{E_{in}}{C_2}\frac{1}{\Lambda_1 - \Lambda_2}. \tag{5.55}$$

substituting to the equation 5.51 we have

$$\begin{pmatrix} \Delta T_1(t) \\ \\ \Delta T_2(t) \end{pmatrix} = \begin{pmatrix} \dfrac{E_{in}}{C_2}\dfrac{G_2}{C_1}\dfrac{1}{\lambda_1 - \lambda_2}\left(e^{\lambda_1 t} - e^{\lambda_2 t}\right) \\ \\ \dfrac{E_{in}}{C_2}\dfrac{1}{\lambda_1 - \lambda_2}\left(\Lambda_1 e^{\lambda_1 t} - \Lambda_2 e^{\lambda_2 t}\right) \end{pmatrix}. \tag{5.56}$$

The equations 5.54 and 5.56 represent for the time constants of the interaction of particles with a pixel including the silicon wafer substrate and the TES thermometer. Notice that we are interested in the TES rising temperature $\Delta T_2(t)$ while ΔT_1 is important for the thermal cross-talk. In order to estimate the time constants of the QUBIC's TES array using those equations above, the table 5.4 presents the heat capacity and the thermal conductance of a TES pixel which considers as the summation of the thermometer, the absorbing grid, and the membrane. We also investigate the ratio $\dfrac{C}{G}$.

Element	Material	C $[pJ/K]$	G $[pW/K]$	$\frac{C}{G}$ [ms]
A pixel	NbSi + TiV + Si_3N_4	3.79	140 ± 70	27 (18-54)

TABLE 5.4: The table of materials, a pixel has three main components: The thermometer (NbSi), the metallic absorber grid and the membrane Si_3N_4 [94].

5.6 Glitches data analysis

In this section, I describe the data analysis of glitches induced by interaction of α particles. In order to fitted glitches, I introduce an exponential function template of an amplitude a and two time constants: the electric readout system time constant τ_0 and the thermal time constant τ_1. Due to the fact that, the intrinsic electrical time constant of TES $\tau_{\text{el}} = \frac{\text{L}}{\text{R}_\text{L} + \text{R}_\text{TES}} \propto \frac{600\,\text{nH}}{20\,\text{m}\Omega + 1\,\Omega} \approx 0.6\,\mu\text{s}$ is too small then it is neglected. I propose an interpretation of time constants. In addition, I present the dependence of (i) the electric readout system time constant τ_0 and the Flux Locked Loop, (ii) the voltage bias V_bias and time constants. Finally the thermal cross-talk among TES pixels and the electronic readout chain cross-talk are studied.

First, we consider that when a particle hits the pixel, it can be either (1) the silicon wafer substrate, (2) the absorbed grid or (3) the NbSi thermometer. In 3 cases, the deposition of energy causes on increase of temperature of the medium which at the end induces a signal in the thermometer (TES). Figure 5.29 describes that (a) the TES is in the transition region, the current follows in the R_TES + the inductor L (the TES readout circuit is already described in figure 5.5), (b) when particles hit the pixel, its energy is converted into heat transferred to the TES, (c) the small change in the temperature leading to the changing resistance of the thermometer, due to the value of R_shunt is as small as the value of R_para then the current follows to the R_shunt during very short time. This changing signal contributed to the signal of the SQUID as well as the readout system. When the electrothermal feedback and thermal bath set again the equilibrium state, (d) the TES returns to the superconducting transition state.

First, we performed some measurements with the array P63, the frequency acquisition was set at 156.25 Hz, equivalent to a sample rate of 6.4 ms per bin sample on the time order data (TOD). The data was mainly taken during around 4 minutes at different bath temperatures, thus we can study the I-V curves measurements. We also vary the PID controller parameters of the electric readout system. After

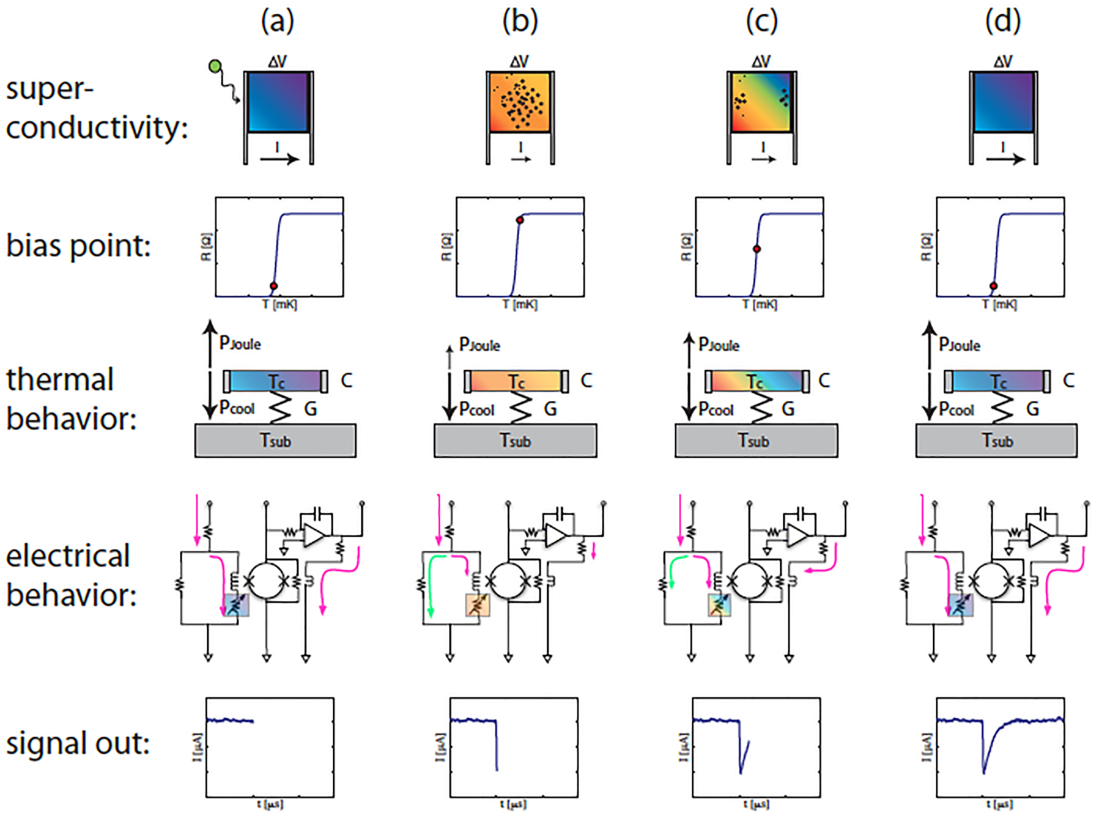

FIGURE 5.29: A single particle (Ex: an alpha particle, a single photon, cosmic rays . . .) hits the pixel and behaviors of the electric system to the output signal. *Credit: Jennifer Anne Burney* [23].

the P63, we performed other measurements with the array P73, the frequency acquisition was set at 1562.5 Hz (0.64 ms). The data was collected during 10 minutes, several sets of data are collected for an hour. Due to the fact that the frequency acquisition is high then we have a huge amount of data to store. We have chosen to work on 10 minutes of data to ensure a stability of the behavior and which are compatible with data analysis on a personal computer. Table 5.5 gives data information of 27 times collected data. We are going to present the obtained results with the array P73 as the results. The array P63 has obtained similar conclusions.

The cryostat system is cooled down to 350 mK, the value of R_{fb} is 110 $k\Omega$, applying a voltage-biased. The TESs array is in the superconducting transition regime. When the readout system is well calibrated, glitches started to be observed. In order to understand the behavior of TESs, we will measure its time constants depending on the electronic readout system parameters, especially the integral term of the PID controller, the K_I parameter is varied with a fixed voltage-bias.

Array	Frequency acquisition	Number of runs	Remark
P63	156.25 Hz ($\sim$ 6.4 ms)	27	TOD $\sim$ 4', 30' Different bath temperatures Different PID controller parameters
P73	1562.5 Hz ($\sim$ 0.64 ms)	27	TOD $\sim$ 10', 1h Different PID controller parameters Different voltage-biased parameters

TABLE 5.5: The table of measurements data.

In contrast, the voltage-bias (V_{bias}) is varied with a fixed K_I parameter. After the voltage bias, there is a bias resistance $R_{bias} = 10\,k\Omega$, then the bias current is applied to a TES as shown in the practical TES bias circuit figure 5.5. Finally the voltage applied to the TES is $V_{TES} = \frac{R_L}{R_{bias}} V_{bias}$ which is of the order of μV. Due to the position of the radioactive source compared with the TES array, several pixels are investigated to analyze the data. The study of time constants not only helps to interpret the interaction of particles with pixel components but also determines the best PID controller parameter for the TESs electronic readout system of the QUBIC experiment.

Figure 5.30, we show $\approx$ 10 minutes timeline of the data with glitches and noise for 2 typical pixels close to the radioactive source. The pixel 88 is in front of the radioactive source. The baseline is set to zero by applying the median of the original data. The y-axis shows the current in nano Ampere while on the x-axis is the bin sample. The sample rate is calculated using formula 5.38. This is a conventional parameter, according to the setting readout system 128 pixels, 2 MHz readout for 10 samples, it derives that a bin is equivalent to 0.64 ms. Figure 5.31 presents the data processing of glitches. From the original time order data, we applied methods for glitches detection, and glitches processing. After that, a template model is used to fit the glitches signal. The time constants of glitches provide interpretations of particles on pixel components. The study of the crosstalk among pixels is also addressed.

5.6.1 Glitches detection

In order to detect glitches (the fast signal compare to CMB), the noise is assumed to have a Gaussian distribution. We have been carried out three methods. In the first method, when we detect events greater than the threshold of the mean

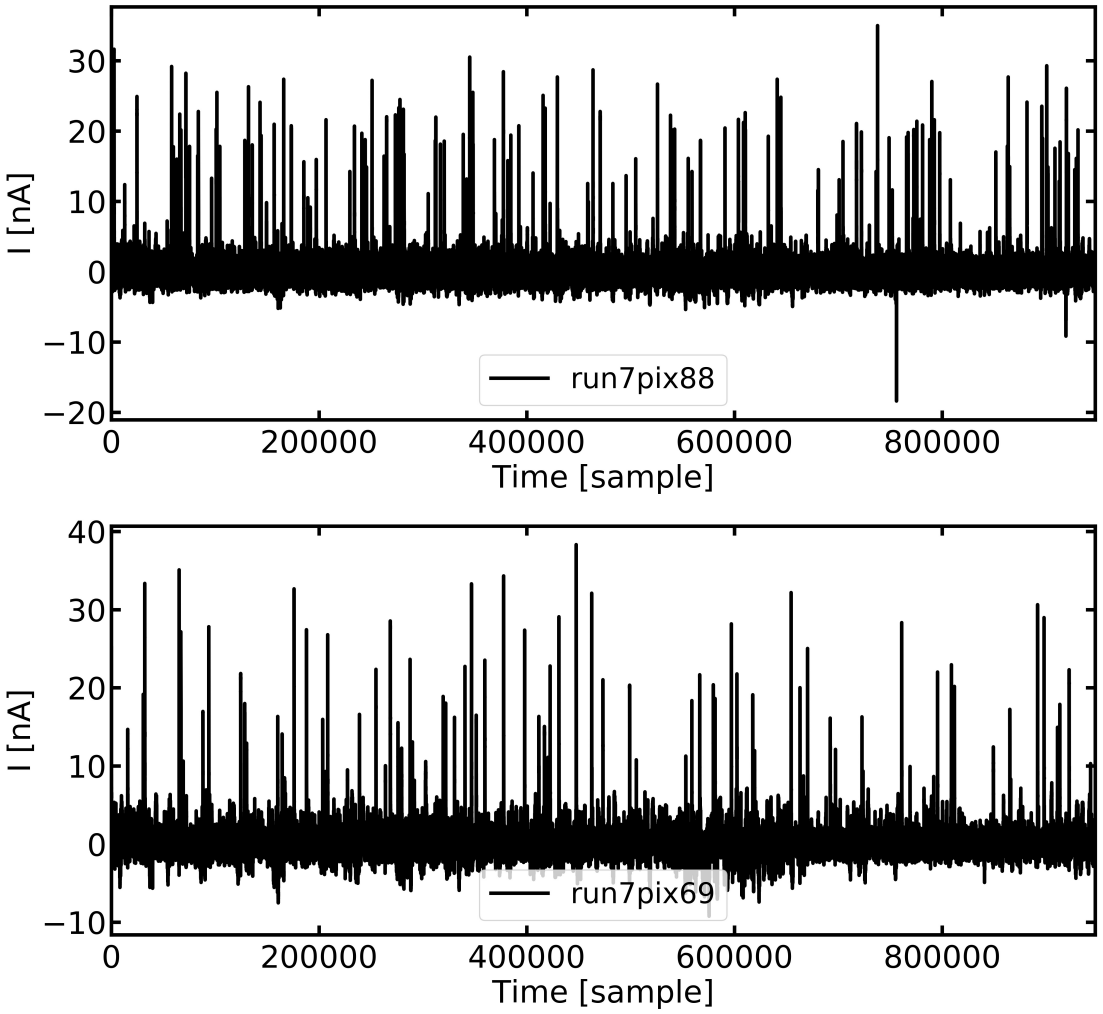

FIGURE 5.30: The glitches data of 2 TES pixels the 88 (in front of the radioactive source) and the 69 in the sample unit (time 0.64 ms) and the current amplitude I in nano-Ampere.

and 3 times the standard deviation $\mu_s + 3\sigma_s$ of the data, we consider that events are glitches. However, this first method has the disadvantage of small glitches detection even though we have a fine-tuned threshold. The second method is an improvement of the first method, we use the same threshold of $\mu_s + 3\sigma_s$ of the data. After that we separate the noise signal and the glitches signal, we only calculate the mean μ_n and the standard deviation σ_n of the noise signal, iteratively we applied the threshold of $\mu_n + 3\sigma_n$ for the whole data again to detect the glitches. Nevertheless, the fluctuations of the data signal in the small scales lead to wrong detected glitches. Finally, the third method is chosen to present the results, the data processing follows as:

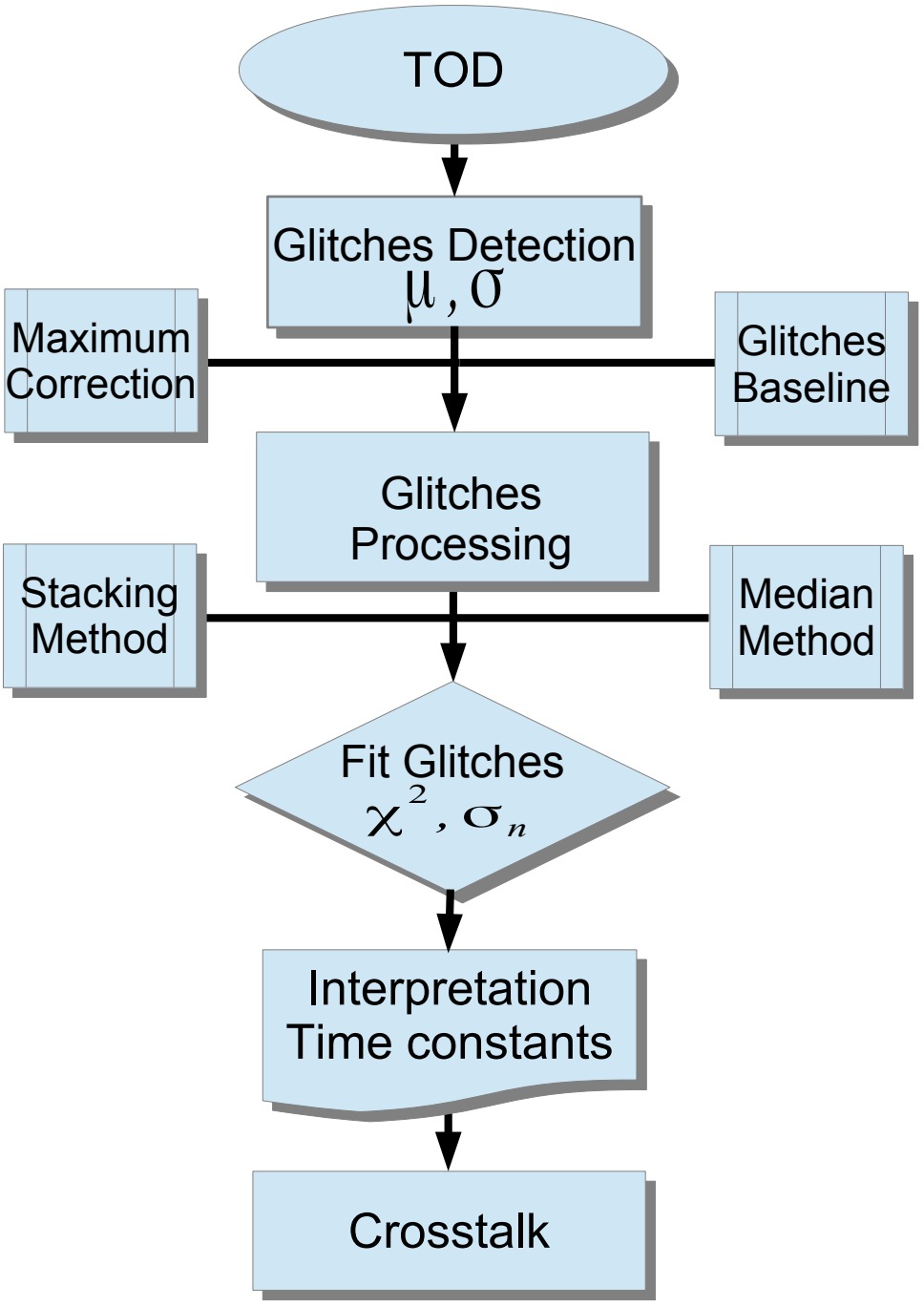

FIGURE 5.31: The flow chart of glitches data analysis. TOD stands for the time order data. μ, σ are the mean and the standard deviation of the data. χ^2 method is used to estimate the best fit associated with the standard deviation of the noise σ_{n}.

- The baseline of the whole data is processed using a median window of 2000 bin samples. This method is so-called the median filter.
- The mean and the standard deviation of the signal are calculated $\mu_{\rm s}$, $\sigma_{\rm s}$.
- The stated threshold to detect glitches is the mean and 2 times the standard deviation $\mu_{\rm s} + 2\sigma_{\rm s}$. This threshold means that we will detect 5% which are not glitches. The next step solves this issue.
- When a glitch event is detected at a level greater than $\mu_{\rm s} + 2\sigma_{\rm s}$, we compare the value of event with the local noise of a 100 bins sample window, iteratively the threshold of the mean noise $\mu_{\rm n}$ pluses $3\sigma_{\rm n}$ of the local noise is applied to determine glitches. This threshold implies that 99.7 % of noise is rejected, it means that 3 events will be detected as glitches due to the noise or signal fluctuations in a total of 1000 detected events.
- A sliding window of 750 bin samples is taken to study the glitch, starting 200 bin samples before the position of maximum glitch. This window is equivalent to 0.48 second. This choosing window takes into account the number of glitches over the timeline. In general, we have about 200 detected glitches for 10 minutes, it corresponds to 1 glitch per 3 seconds.
- The amplitude of a glitch is chosen as the maximum peak value of the sliding window data. The peaks of detected glitches are stored as well as their bin positions. Then the rising time of a glitch is defined by 200 bin samples and the decay time of a glitch is defined by 550 bin samples. The local noise is also taken for a window of 100 bins sample starting from the beginning of the window.

Figure 5.32 shows the distribution of the data with the threshold $2\sigma_s$ and $3\sigma_s$ for two typical pixels. The position of the maximum of the distribution is close to zero because of the baseline signal resulting from the median filter method. The tails is due to the glitches signal.

Because the signal has small scales fluctuations in the timeline, the noise can vary over the threshold. A similar detection method is applied for the inverted data to evaluate the level of noise. After detecting peaks, the mean of the local noise is calculated. The absolute amplitude of a glitch is computed by subtracting the peak and the mean of the local noise. Figure 5.33 shows the histograms of the

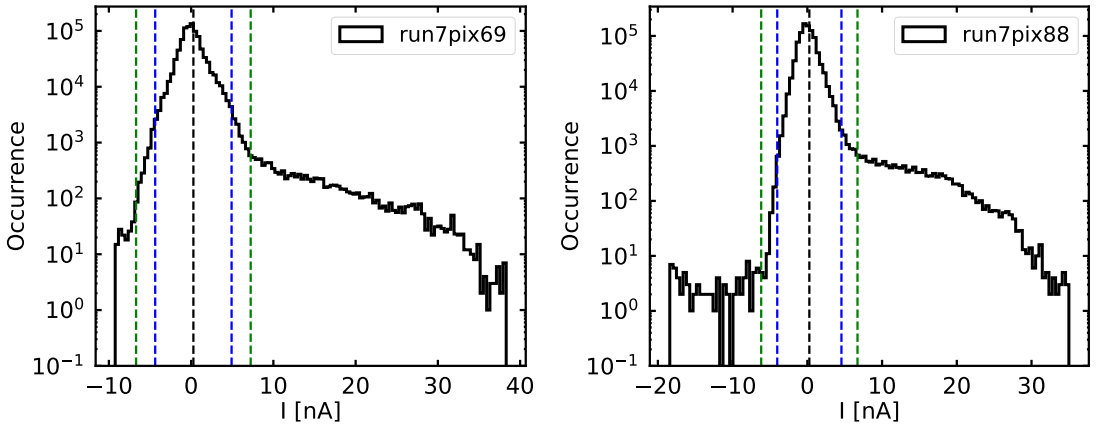

FIGURE 5.32: The histogram of data for run7 detector 69 and detector 88. The black vertical line is the mean μ_s value of the signal, the vertical blue lines indicate the $2\sigma_s$ of the signal, the vertical green lines indicate the $3\sigma_s$ of the signal. The tail of the signal is the glitches data. The negative populations are the noise signal.

absolute amplitude of detected glitches and the level of the noise contribution. These peaks values indicate that the amplitudes of glitches peaks are in a range of $\sim 10-37$ nA. There are two populations in the distribution. The high amplitude region could be the contribution of α particles ($E_\alpha \sim 5.4\,\text{MeV}$) interaction with pixels while there is lower amplitudes beside the noise level that is a possible contribution of gamma rays ($E_\gamma \sim 60\,\text{keV}$).

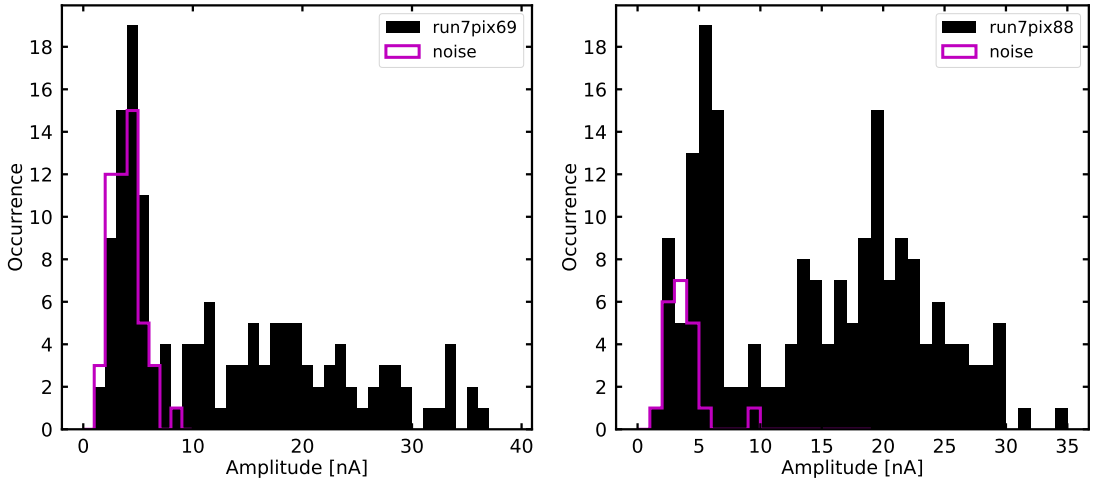

FIGURE 5.33: The histogram of glitches peaks of the signal (the black color) and the inverted data which is represented by noise level (the pink color).

Glitches baseline

In order to obtain a better evaluation of the glitches baseline, the data processing of detected glitches follows steps:

1. To the signal of each detected glitch, we subtracted each bin value to the mean value of the detected local noise → Absolute glitches signal.

2. After that, we subtracted again each bin value to the median of a window of 100 bins sample starting from the beginning of the window → Glitches baseline.

3. According to the peaks of the inverted data as shown in figure 5.33, a filtered noise which is the median or the mean plus 4 or 5 σ of the negative peaks distribution, is applied to reject the noise contribution in the signal. Only glitches with the amplitude of peaks greater than this filter threshold are consider as glitches.

4. Because small-scale fluctuations of the signal could happen around the maximum of the glitches. We use a median window of 9 bins sample to determine again the glitches maximum positions then we reprocess the glitches timeline with corrected maximum positions.

Figure 5.34 is an example of a typical glitch (left) and all glitches (right) after selection. The first impression is that glitches look to have similar shapes and just varying amplitudes, probably the glitches occur due to the interaction of the α particles, and the evidence of glitches due to γ particles are too difficult to recognize because of the incident energy is very small and the noise is complex. The baseline is not exactly stayed at the zero due to small shapes fluctuations of the noise signal (not flat), these fluctuations will be rejected when we average glitches to study time constants.

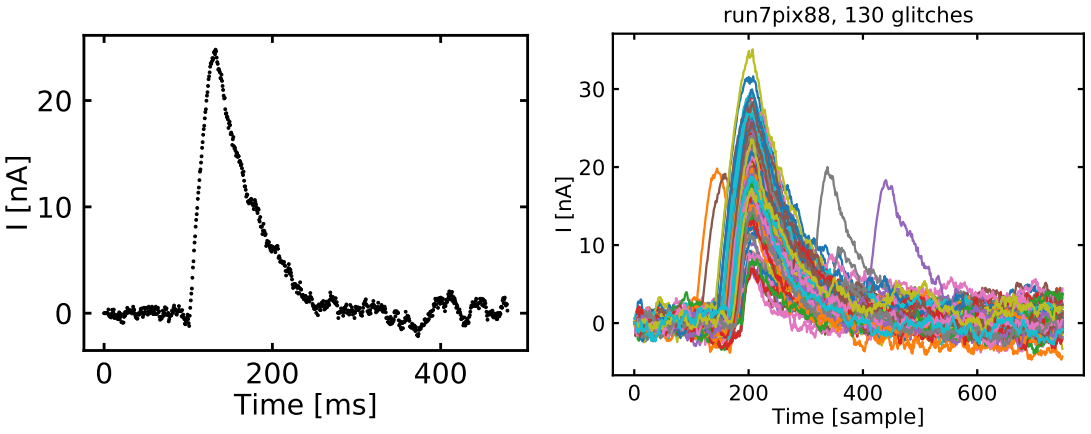

FIGURE 5.34: An example glitch and all the 130 glitches after data processing for the pixel 88 which is in front of the radioactive source.

5.6.2 Fit glitches

I will describe results obtained on the "run7" taken with voltage-bias of the TES $V_{TES} = 5.0\ \mu V$, and the PID controller K_I parameter equals 1000. In order to investigate time constants of a glitch, we based on the simple model and the solution which has been represented in the equations 5.54 and 5.56. A general template model (equation 5.57) is used to fit the data. On the right-hand side of the equation, the first term is the rising time constant of the glitch, the electrical readout system time constant τ_0, and the second term is the decay time constant of a glitch, the TES responding time constant τ_i of an event (the thermal time constant).

$$S(t) = a\left(1 - \exp^{-(t-t_0)/\tau_0}\right)\sum_{i=1}^{n}\exp^{-(t-t_0)/\tau_i} + c. \tag{5.57}$$

Here a is the amplitude parameter of the glitch, t is the bin sample data corresponding with $S(t)$ value. For the initial starting fit values, t_0 is set at 100 bin sample (64 ms), the offset c is set to zero, the bound of amplitude a is a positive value.

Figure 5.35 presents some fitted glitches, all fitted glitches are presented in the **Appendix C**. The χ^2 estimator is calculate for each glitch. We consider the noise for the χ^2 estimation as the standard deviation of a window of 100 bins samples starting from the beginning of the glitch window. The reduced χ^2 will be used to determine the quality of the fit. We express the first exponential function of equation 5.57 in Taylor series, $a\left(1 - \exp^{-(t-t_0)/\tau_0}\right) \approx \frac{a}{\tau_0}(t - t_0)$, and we can see that we have the degeneration of the amplitude a and the electronic time constant of the readout chain τ_0. The degeneration can be observed in parameters of the fitted glitches.

Figure 5.36 shows the plot of estimated time constants versus glitches maximum. Because of the degeneration of the a and the τ_0, the maximum value of glitches are a good alternative way to study behaviors of glitches. The histogram of the maximum has a mean of the order of 20 nA. The histogram of the decay time constant τ_1 has a mean of the order of 40 ms. The histogram distribution of the rising time constant τ_0 shows two populations which help us to understand the interaction of particles with TES pixel components.

To improve the global understanding of the glitches, we applied two methods to determine average glitches:

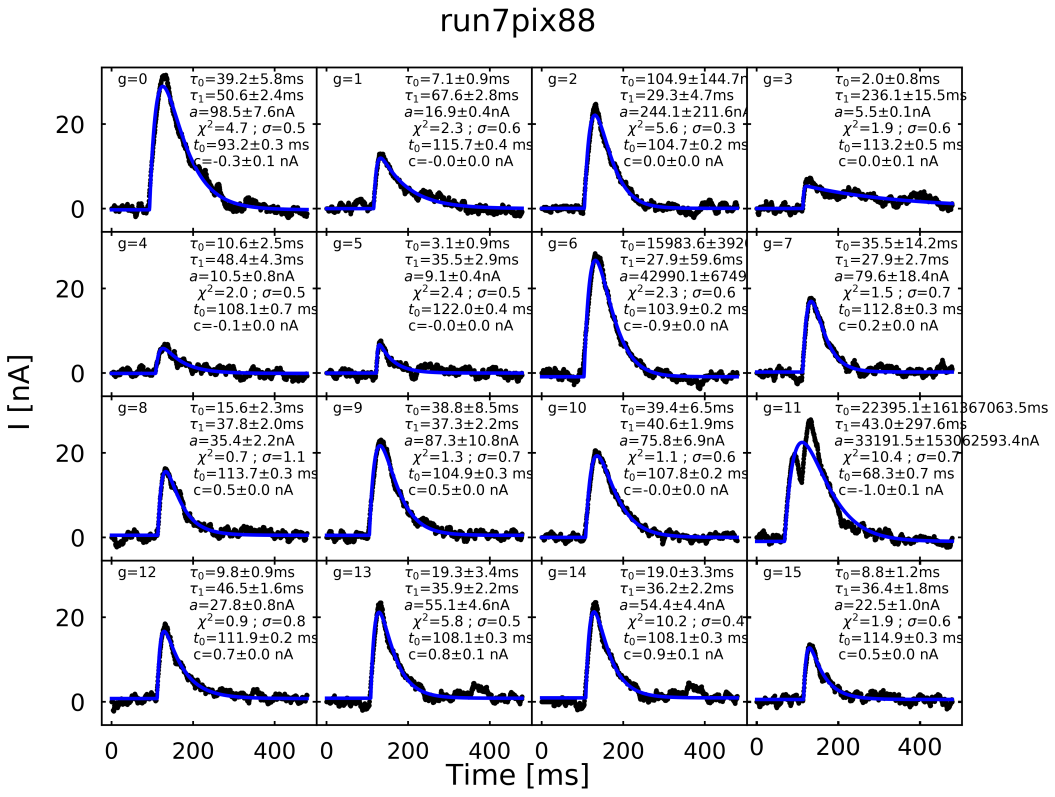

FIGURE 5.35: Example of fitted glitches for pixel 88. The glitch identification is label g. Parameters of the fitted template model are labeled. The reduced χ^2 is used to evaluate the fit.

- **Stacking glitches method:** For this mean method, all the glitches data are summed to become a final mean glitch when divided by the number of glitches.

- **Median glitches method:** Each glitch is divided by the maximum value to obtain the normalized glitch. After that, the median of all glitches for each individual bin data point is applied to obtain the final normalized glitch.

Figure 5.37 presents the result of the stacking glitches method and the median method for all glitches in the run7 pixel 88 while figure 5.38 and 5.39 present for the different populations of the electrical time constant of the readout chain τ_0. The stacking glitches method provides the estimation of the amplitude of the glitch while the median glitches method estimates more accurately the time constants values. In fact, the process of stacking small and big glitches together affects the rising edge of the glitch. Consequently, the baseline of the median glitches method is better than the baseline of the stacking glitches method. This can be proofed

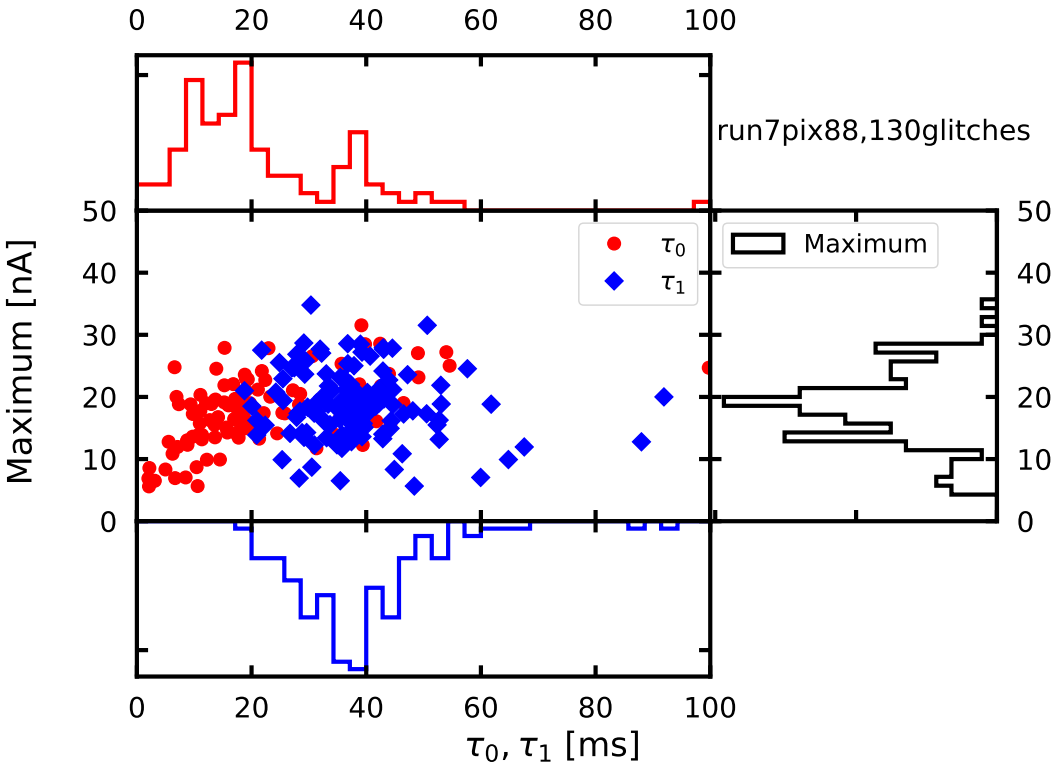

FIGURE 5.36: Time constant and peak values of glitches. Two populations of the rising electrical time constant τ_0 are observed on the histogram.

by the estimation of the χ^2 value. Therefore, we will present time constants using the median glitches method and the amplitude using the stacking glitches method.

Figure 5.40 presents the results of the fit on the median glitches method for several pixels. The table 5.6 shows the results for different pixels, the fitted time constants values τ_0, τ_1 are estimated using the median glitches method, and the amplitude using estimated by the stacking glitches method. We will not talk about the mismatch fitted model values because sometimes the fitted model does not fit the data mathematically. (i) On the case of the peaks of the glitches could be resulted of scattering operating points in the superconducting transition regime for different pixels. When an event of high energy (big glitch) happens, the operating point should transit to the normal regime ($\tau_1 \sim \frac{C}{G}$), when the thermal bath and the strong ETF operates the operating point is pulled back to the superconducting transition regime ($\tau_1 \sim \frac{\mathrm{C}}{\mathrm{G}\mathscr{L}}$). Finally the thermal time constants decays with the contribution of two regimes. This case represents a better fit on the peaks glitches. Furthermore the logarithmic sensitivity to temperature parameter α is small in the normal state, the loop gain parameter $\mathscr{L}$ is proportional to α. The

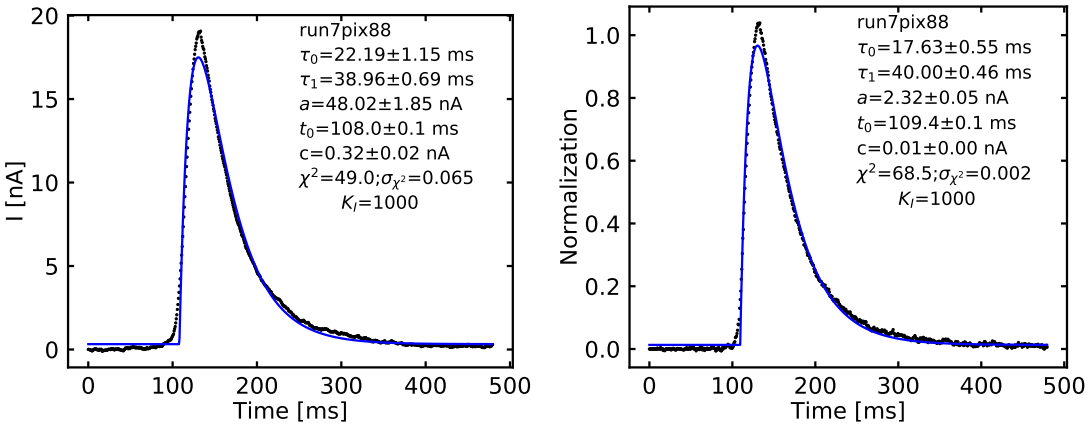

FIGURE 5.37: *Left:* The stacking glitches method and *Right:* The median glitches method apply for all 130 glitches. These fitted parameters of the template model are labeled on the plot, together with the estimation of χ^2 associated with the standard deviation of the noise σ_{χ^2}. The value of the PID controller parameter K_I equals 1000 for the run7.

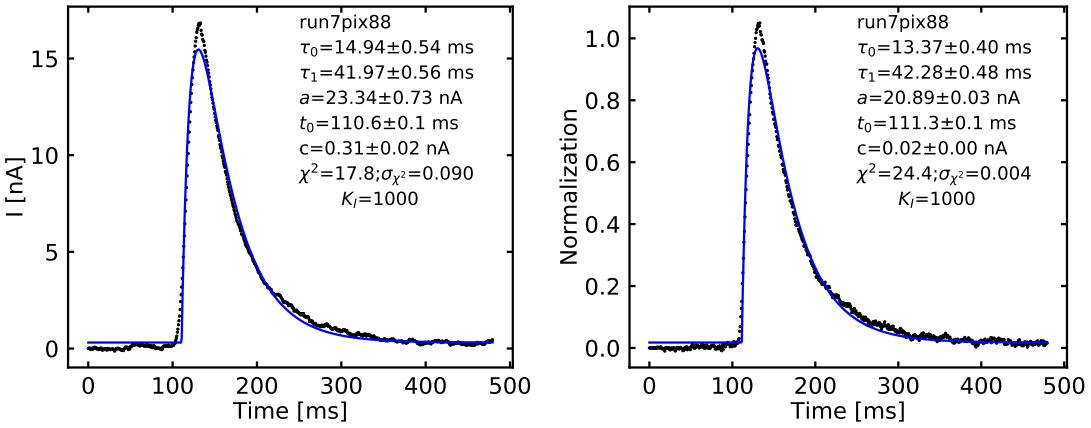

FIGURE 5.38: The first population of the electrical time constant τ_0: The stacking glitches method (*left*) and the median glitches method (*right*) applied for the 75 glitches.

time constant is the inverted proportion to $\mathscr{L}$. Therefore, this case has a bigger value of the time constant, it also means that the fit is well fit. (ii) On the other case, the low operating point, the adding transition is still in the superconducting transition regime ($\tau_1 \sim \frac{C}{G\mathscr{L}}$), this case represents not well fit around peaks of the glitches. In addition, the different values of time constants in different pixels can be explained by the readout of SQUIDs, due to the fact that each TES is read out by an independent SQUID. The characterized SQUIDs are not uniform including noise performance also. Then the final outputs signal are not uniform among pixels. This feature also can be observed by taking I-V calibrated measurements as shown in figure 5.24. The relative positions of pixels compared to the radioactive

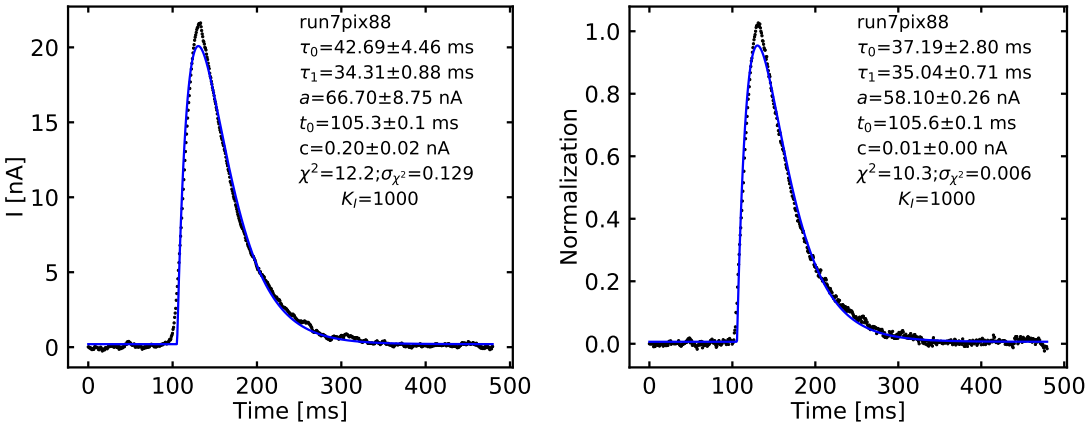

FIGURE 5.39: The second population of the electrical time constant τ_0: The stacking glitches method *Left* and the median glitches method *Right* applied for the 33 glitches.

source are different, hence the number of detected glitches has to be different.

Run	V_{bias} (μV)	K_I	Pixel	Glitches	τ_0 (ms)	τ_1 (ms)	a (nA)
7	5	1000	69	80	11.41±0.15	64.31±0.33	33.28±0.38
7	5	1000	70	54	7.89±0.16	35.91±0.27	54.25±2.08
7	5	1000	75	77	23.07±0.95	53.64±0.84	37.01±1.28
7	5	1000	81	94	23.76±0.35	72.97±0.43	32.15±0.70
7	5	1000	87	70	10.17±0.13	47.11±0.22	36.52±0.53
7	5	1000	88	130	17.63±0.55	40.0±0.46	48.02±1.85
7	5	1000	93	75	15.99±0.36	43.33±0.36	51.14±2.14
7	5	1000	106	23	35.57±1.34	71.84±1.05	86.54±15.32
7	5	1000	107	73	60.72±9.75	39.01±1.35	103.74±60.06

TABLE 5.6: The table indicates the number of glitches for several good pixels with around 10 minutes recorded data which is labeled "run7" and the time constants from the median glitches method for different pixels. The amplitude is computed with the stacking glitches method.

Following the template model equation 5.57, a fitted model with a third or a fourth time constant does not work. We also fitted the only decay glitches with several time constants model. In addition, we make a template model with the rising time constant inside the decay time constant term, however, it was not conclusive. Therefore, we choose to have only one time constant for τ_0, the rising time constant of the electronic readout system and one τ_1 for the decay time constant (the thermal time constant). The value of the electric readout time constant is typically 7-30 ms and the TES time constant is typically 20-60 ms. In addition, we simply estimated the energy of the alpha particles in the range

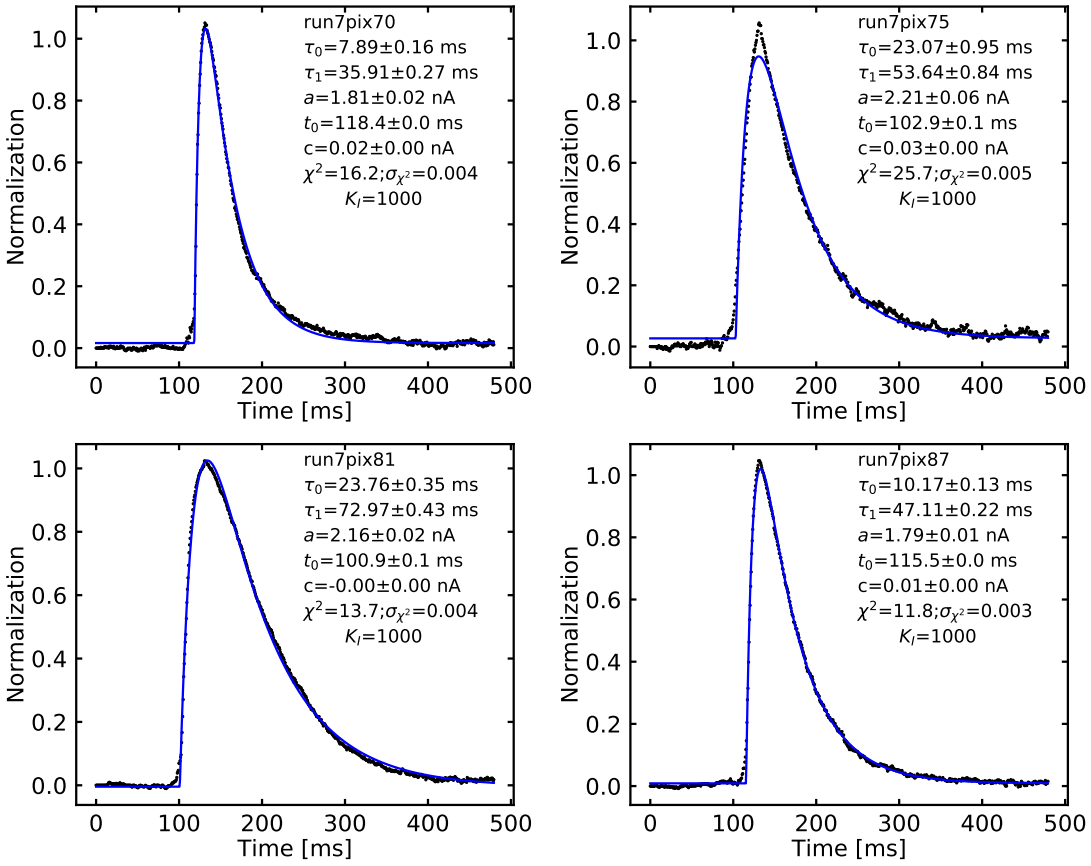

FIGURE 5.40: The fitted parameters of the template model for different pixels in the same taken data run7. The K_I parameter of the PID controller for run7 is 1000 and the median glitches method is applied.

2-5 MeV, in agreement with theoretical predictions. Our results demonstrate the capability of our readout electronics in performing tests of sensitivity towards CRs [131].

5.6.3 Interpretation

We can calculate the surface of a pixel components as shown figures 5.11 and 5.12. A pixel (TES thermometer + absorber + membrane) has:

1. A surface of the absorber grid $\sim 2800\ \mu m^2$ and $\sim 1\,\mu m$ thickness.
2. Each square grid has dimension of $50 \times 50\ \mu m$ hole and $5\ \mu m$ width frame.
3. The TES (NbSi) has a surface of $\sim 293\ \mu m^2$.
4. Between two pixels, the Si substrate has a surface of $2800 \times 200\ \mu m$ and its thickness is $500\ \mu m$.

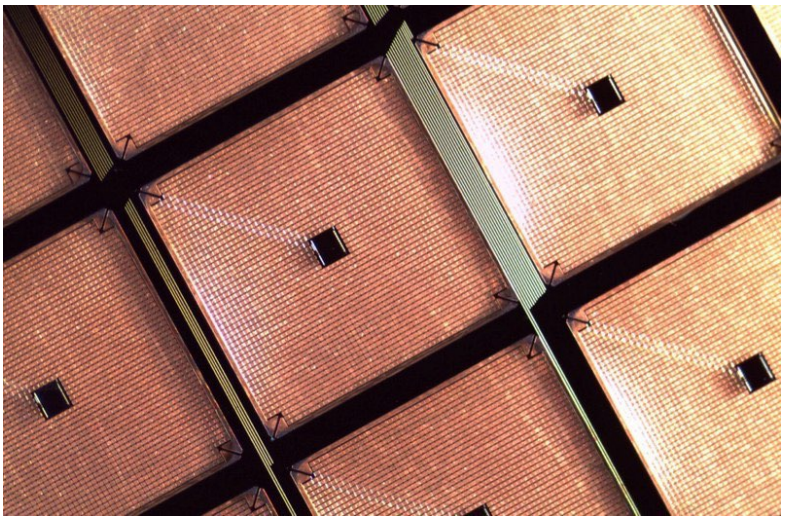

FIGURE 5.41: The micro-photography of several pixels, the thermometer is at the center of a pixel, the absorber is the metal grid, and the Silicon substrates are among pixels.

5. The Al wires have a geometry of $\sim$ 10 cm length, $\sim$ 200 nm thickness, $\sim$ 6 μm width.

Figure 5.41 shows a micro-photography of a TES array and its components. The surface of a pixel compared to the Si substrate is very high, however, the thickness of the pixel is very small compared to the Si substrate. In table 5.3 we estimate the deposited energy by an α particle of 5.44 MeV versus the thickness of pixel components. In general, if the particles hit one of the pixel components, the deposited energy on the pixel is of the order of keV while the deposited energy on the substrate is of the order of MeV.

As already said, the rising time constant τ_0 estimation in figure 5.36 indicates two populations of the rising time τ_0 which is the electrical readout time constant for the short one and could be a thermal time constant for the long one. According to the cross-section, the thickness and the deposited energy, the design, the fabrication and the assembly of a TES array, we can provide a hypothesis to interpret this result:

- In an equilibrium state, the Joule dissipation due to the voltage bias V_{TES} on a TES evacuates to the thermal bath (reference/fixed temperature).
- The fist population: Particles hit directly to the sensor (thermometer TES or the absorber), thermal effect propagates very quickly to the thermometer

and the rising time constant τ_0 is the electronic readout time constant. The thermal equilibrium process is rapidly established due to the deposited energy on the absorber which has a thickness of 1 μm (τ_1). A discussion of the thermal behaviour of the absorber and the TES thermometer can be found on [19]. These events correspond to the first population.

- The second population: Particles could hit the Si substrate, the deposited energy is huge due to the thickness of 500 μm. To reach the sensor, the heat has to affect the temperature of the TES through the thermal link between this sensor and the Si substrate. The rising time constant should be close to the thermal time constant. Because the thermal coupling is not perfect between the Si wafer and the back copper (which is a better fixed thermal bath), there have several reasons affecting the thermal decoupling of this two layers. First, the assembly of the array is that the edge of the array is well pressed over the back copper in order to hold the array with the back short. The discussion of the applied force and thermal contact conductance between material layers can be found in the paper [132]. However the center of the array is not uniformly pressed over this copper thermal bath, then the heat flows could transfer slower than the edge. Consequently, these heat flows arise the increment of the background reference temperature in which is finally detected by the sensor through a rising time τ_0 dominated by the thermal time constant (more or less equal to τ_1).

- A proposed solution to fix this substrate thermal decoupling is that we can add a gold layer on the back side of the Si substrate in order to fix and uniform the Si bulk temperature which thus could played better the role of thermal bath.

- Space application: In the aspect of Cosmic Rays and a satellite's focal plane using TES arrays, the Silicon substrate surface plays an important role to reduce the impact of CRs.

Following our hypothesis, we explain the two populations seen in the τ_0 distribution. The long τ_0[9] glitches are observed on the presentation of neighbor pixels at the same time order data. Figure 5.42 presents an example of a glitch which has the long time constant τ_0. We observe that there have fluctuations of the signal of neighbor pixels. The observation reinforces the interpretation of the hypothesis.

[9]The long τ_0 means $\tau_0 \geq 32\,\text{ms}$

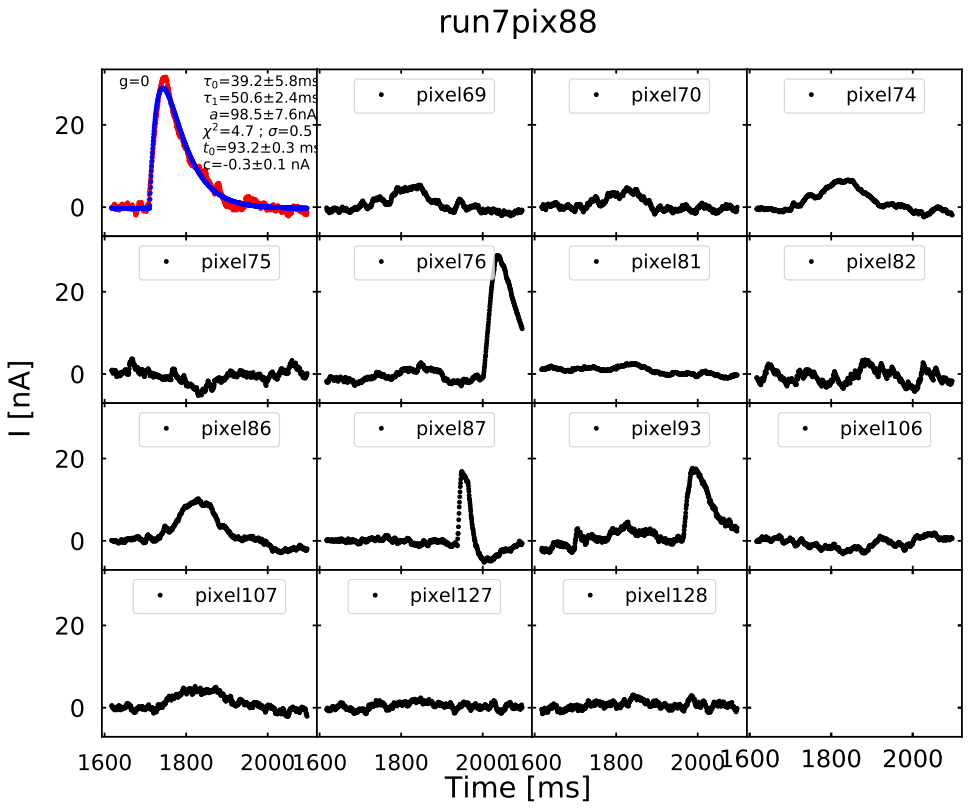

FIGURE 5.42: The top left glitch is the glitch of the run7 pixel 88. This is the evidence of crosstalk

It means that particles hit the substrate, the heat is dissipated to among pixels. The discussion of the crosstalk estimator is described in the section 5.7 below.

5.6.4 Time constants and the K_I parameter of the PID controller

As described in the section 5.3, the K_I parameter of the PID controller affect the rising time of the glitches as well as the amplitude of glitches. This demonstration is described in the transfer function equation of the readout system 5.44. K_I parameter relates to the loop gain of the Flux Lock Loop (FLL) which changes the bandwidth of the readout chain. *When we increase K_I parameter, the time constant corresponding to the readout bandwidth must decrease*. The equation 5.44 is equivalent to $y = 1/x$ form.

Table 5.7 and figure 5.43 show very well how the time constants depend on the electronic readout system K_I parameter of the PID controller. Note that the value

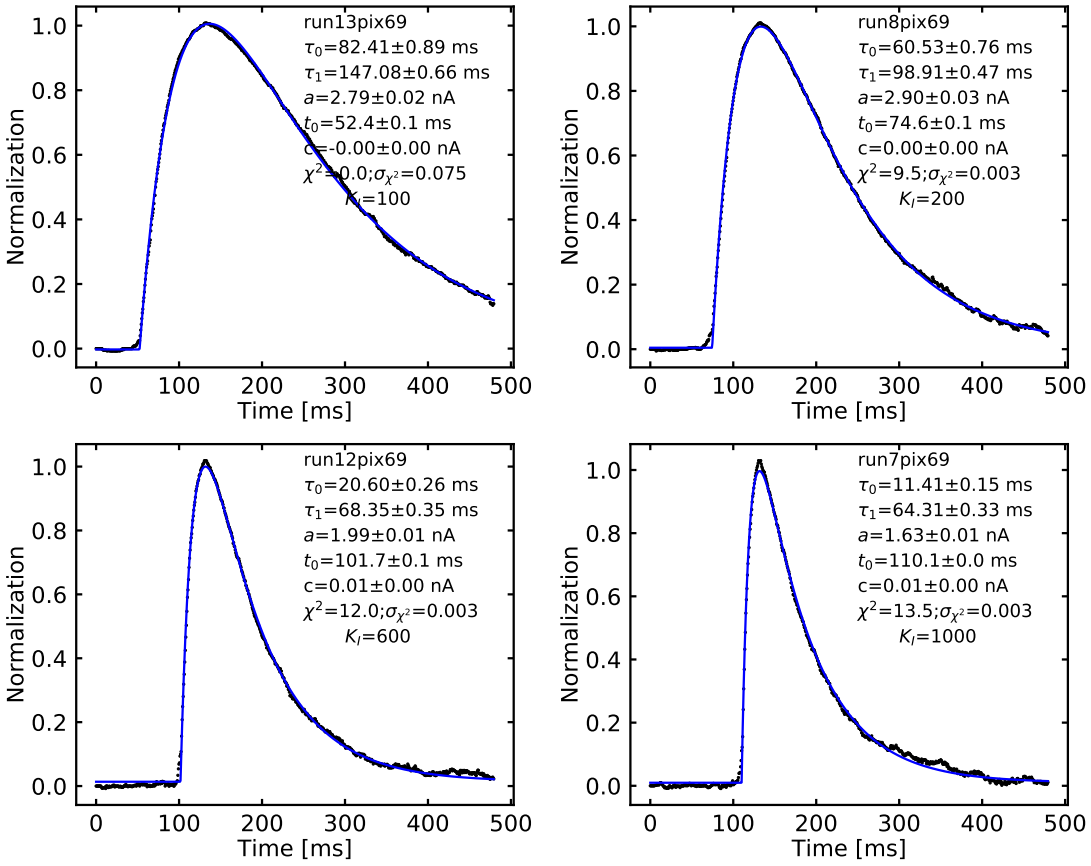

FIGURE 5.43: The fitted model of time constants for the pixel 69 with different K_I parameters of the PID controller with fixed voltage-bias $V_{TES} = 5\mu V$. The K_I parameter value is between 100, 200, 600 and 1000 as shown detail in the table 5.7. The slope of rising time increase with K_I according to the expected evolution of the readout bandwidth with K_I.

of K_I parameter is an input on the QUBIC studio software to be changed by hand. If we increase the value of the parameter K_I, the time constant will decrease. The analysis is shown for the pixel 69, but other analyzed pixels give similar results. A simple evaluation of the deposited energy is given by the product of the amplitude and the time constant. The values are compared with the table 5.3 and we can see that the values are compatible. However, this estimation is not accurately correct because we have to take into account the proportion of V_{TES} to amplitude because of electrothermal feedback effects to the TESs voltage.

Figure 5.44 shows the behavior of time constants respect to the changing K_I parameter. It is possible to fit the plot of time constants versus K_I parameter with a $y = 1/x$ function model. Because of the complexity of the electronic readout system of TES technology, in particularly the QUBIC's TES array, the calibration parameters for a working stable system play an important role. As an

Run	V_{bias} (μV)	K_I	Pixel	Glitches	τ_0 (ms)	τ_1 (ms)	a (nA)
13	5.0	100	69	76	84.62±0.97	148.57±0.69	22.75±0.37
8	5.0	200	69	63	60.53±0.76	98.91±0.47	36.80±0.89
9	5.0	300	69	73	39.22±0.60	88.87±0.56	29.03±0.31
10	5.0	400	69	62	30.61±0.36	76.94±0.36	39.19±0.52
11	5.0	500	69	73	23.73±0.22	70.13±0.27	43.75±0.64
12	5.0	600	69	71	20.60±0.26	68.35±0.35	46.78±1.02
7	5.0	1000	69	80	11.41±0.15	64.31±0.33	33.28±0.38
14	5.0	1500	69	70	10.81±0.30	40.25±0.42	38.50±0.79

TABLE 5.7: This table is given the measured time constants versus K_I parameters of the PID controller. Time constants are estimated using the median glitches method while the amplitude is estimated using the stacking mean method.

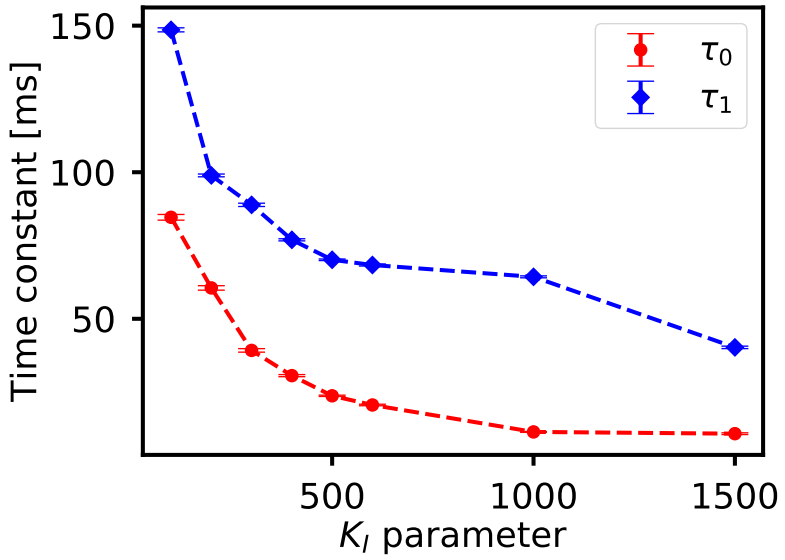

FIGURE 5.44: Time constants respect to the K_I parameter of the PID controller. The voltage bias is fixed at 5.0 μV. The error bar is 1σ.

output of the study, in order to calibrate the QUBIC's TES array, the value of $K_I \geq 1000$ is a good parameter value for the electronic readout system. This value of the K_I parameter is also satisfied requirements of time constants of the QUBIC experiment. For a higher value of K_I, the FLL become unstable and extra noises start to appear.

5.6.5 Time constants, amplitude and the voltage bias V_{TES}

As discussed before, from the equation 5.21, we know that the current responsivity of the superconducting TES is proportional to the inverse of the voltage bias $s_I \sim -\frac{1}{V_{TES}}$. It means also that *if we increase the voltage bias, the electrical time constants (τ_0) will decrease.* In practice, a study has been executed by varying the voltage bias parameter V_{TES} with a fixed K_I parameter. In order to have many data points, overall, the pixel 69 has been chosen as it was a good pixel for many runs and it is very close to the pixel 88 (in front of the radioactive source).

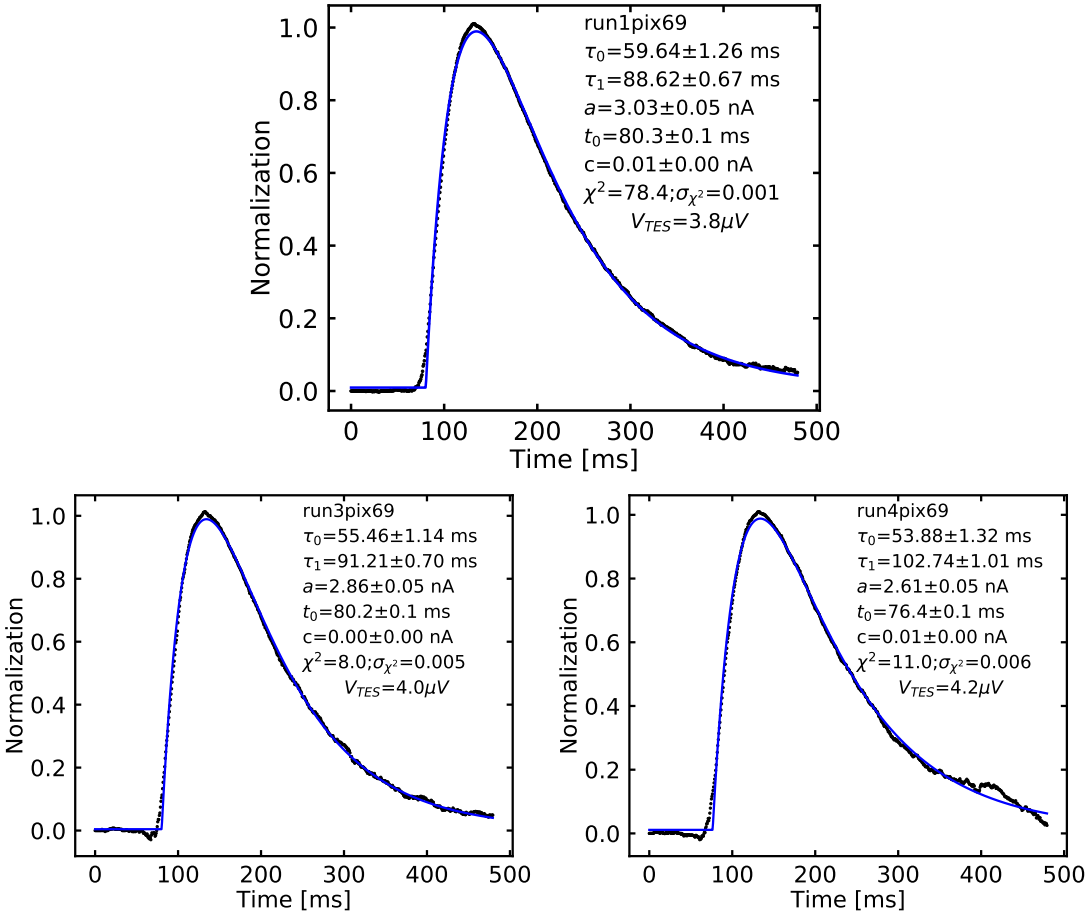

FIGURE 5.45: The fitted model of time constants for the different voltage-bias V_{TES}. The fixed $K_I = 200$ parameter of the PID controller equals 200.

Figure 5.45 shows the data and fitted curves for several runs of the pixel 69. In the table 5.8 we give results of the behavior of the time constants in respect of the changing voltage biased at a fixed $K_I = 200$ parameter of the PID controller. The voltage-bias ranged between 3.8 μV and 5.8 μV. The range of the voltage-bias is chosen based on the behavior of TES from a normal state to the transition regime

state and the superconducting state as shown on the study of I-V curves figure 5.24, when we increase the voltage-bias, the TES array went close to the normal state. Hence the TES time constants also could represent different meaning.

Run	V_{TES} (μV)	K_I	Pixel	Glitches	τ_0 (ms)	τ_1 (ms)	a (nA)
1	3.8	200	69	81	59.64±1.26	88.62±0.67	81.28±4.57
3	4.0	200	69	73	55.46±1.14	91.21±0.70	36.49±1.00
4	4.2	200	69	50	53.88±1.32	102.74±1.01	32.35±0.67
5	4.5	200	69	78	75.90±2.24	89.25±0.86	71.89±3.61
6	4.8	200	69	68	54.69±1.19	96.32±0.81	41.80±1.17
8	5.0	200	69	63	60.53±0.76	98.91±0.47	36.80±0.89
15	5.3	200	69	62	48.27±0.85	93.49±0.65	25.32±0.70
16	5.5	200	69	37	41.25±0.73	122.08±0.97	11.38±0.18
17	5.8	200	69	60	54.38±0.90	104.25±0.69	14.04±0.32

TABLE 5.8: The table shows the relationship of time constants, the amplitude and the applied voltage-bias V_{TES}. Time constants are estimated by the median glitches method while the amplitude is estimated by the stacking mean method.

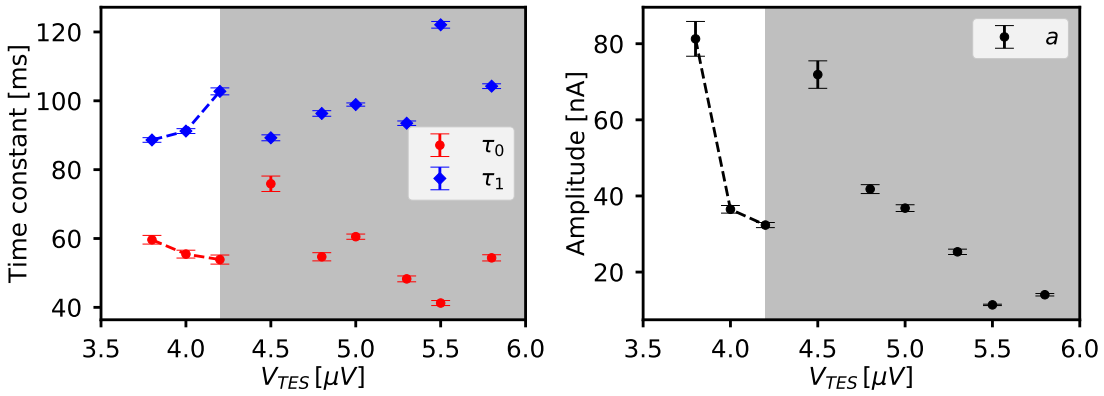

FIGURE 5.46: *Left:* Time constants versus voltage biases V_{TES}. *Right:* The amplitude versus voltage biases V_{TES}. The grey color area means that TESes enter to the normal state. The K_I is fixed at 200. The error bar is 1σ.

Figure 5.46 presents the behavior of time constants, and amplitudes with respect to the changing voltage-bias. In general, *when we increase the* V_{TES}*, the thermal time constant* (τ_1) *increases because TES enters to the normal state, the logarithmic sensitivity to temperature parameter* α *is small, the amplitude behavior has a negative slope.* Unfortunately, the data point at $V_{TES} = 4.5\,\mu V$ is affected by the changing state of the TES from the superconducting state to transition regime. as we can deduce from the TES behavior at $V_{TES} = 4.5\,\mu V$ in I-V curves figure 5.24. On the other hand, the PID controller parameter K_I equals 200 is not an

optimal parameter for the electronic readout system as shown in figure 5.44. The behavior of the electronic readout system changes very quickly at that regime, this could affect the results and the slope of the relationship. In conclusion, this study would need more investigated data points as well as more fine-tuned PID controller parameter due to the fact that voltage-bias changes the state of the TES from a strong electrothermal feedback to a superconducting transition regime to a normal regime.

5.7 Cross-talk

When a TES array is hit by α particles, cross-talk can happen at the stage of thermal dissipation or electronic readout chain.

5.7.1 Thermal cross-talk

What we call thermal cross-talk is the fact that a deposition of energy in a given pixel could also induce temperature elevation of neighbors pixels. For thermal cross-talk analysis we fix a reference pixel, located in front of the radioactive source, assuming that this pixel is the one mostly hit by α particles and then we observe the signal of the neighboring pixels. Firstly we analyzed I-V curves of full 256 TES pixels to identify the best radioactive source position which has many good pixels around as shown in figure 5.47. The position of the radioactive source was chosen in front of the pixel 88. What we wanted to evaluate is if after a particle interaction in the central pixel, the temperature increase will propagate gradually from the red circle to the green circle and then to the blue circle, expecting that the level of the thermal cross-talk will probably be related to the distance of pixels compared with the pixel 88.

First of all, figure 5.48 presents the TOD of several pixels at the same time during 3.84 s. We can observe independent glitches occuring in different pixels. The expression of the thermal cross-talk estimator is given in equation 5.58. Let us consider a reference pixel where a glitch event happens: the glitch event g has the bin position i of the maximum and the data of the maximum value of the reference pixel is $d^0_{e;i}$ (in our study the reference pixel is the pixel 88). At that maximum position i of a glitch, the data of all around pixels j is sum, however, the

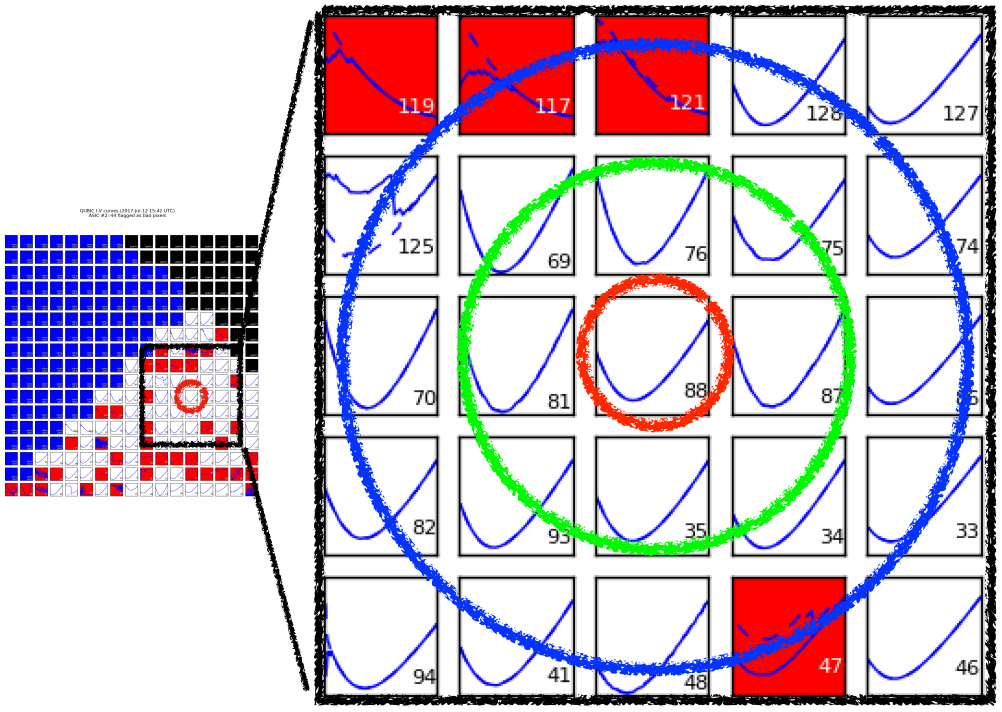

FIGURE 5.47: The scheme of a 256 TES array, the IV curves represent good or bad pixels in an ASIC. The position of the Americium source is located in front of the pixel 88 (the red circle) and the relative pixels around. The thermal cross-talk estimator C_1 of *round 1 (the green circle - pixels: 69, 76, 75, 87, 34, 35, 93, 81)* and C_2 of *round 2 (the blue circle - pixels: 128, 127, 74, 86, 33, 46, 47, 48, 41, 94, 82, 70)* are considered due to the distance of pixels respect to the radioactive source position. The thermal cross-talk estimator C *of the black square - whole pixel of the green circle and the blue circle* - is considered for all pixels except the pixel 88.

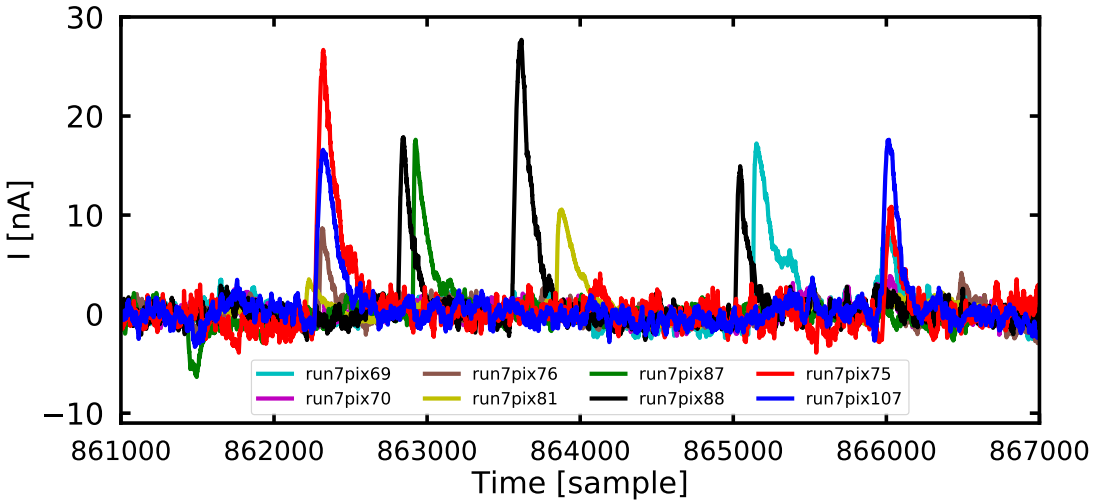

FIGURE 5.48: 3.84 s TOD for several pixels which are the closest ones to the radioactive source.

limited position has to consider the baseline then the baseline position b is given for two positions which explain the factor of 0.5 in equation 5.58, statistically we can divide by a smaller factor to obtain a high efficiency based on the variation concept. All the glitches occurring in pixel 88 during the 10 minutes TOD are used and normalized by the number of glitches and the number of pixels. Finally, the thermal cross-talk estimator depends on the number of glitches, number of pixels, and the baseline. To estimate the thermal cross-talk, we try to evaluate if there is a correlated signal in pixels close to the central pixel where glitches are detected:

$$\mathrm{C(b, pixel \quad area)} = \frac{1}{\mathrm{N_g}} \frac{1}{\mathrm{N_j}} \sum_{\mathrm{g=1}}^{\mathrm{N_g}} \sum_{\mathrm{j=1}}^{\mathrm{N_j}} \frac{\mathrm{d^j_{i(g)} - 0.5 d^j_{i(g)-b} - 0.5 d^j_{i(g)+b}}}{\mathrm{d^0_{i(g)}}}. \tag{5.58}$$

In this formula:
- g is the glitch number on the reference pixel (pixel 88).
- $i(g)$ is the sample number where occurs the maximum of the glitch in pixel 88.
- $\mathrm{d^0_{i(g)}}$ is the TOD value for the maximum of glitches in the reference pixel (pixel 88).
- d_i^j is the TOD value of sample i of pixel $\mathrm{j^{th}}$ (the reference pixel having $j = 0$).
- b is a constant chosen to estimate the baseline of a given pixel TOD around the central sample defined as the glitch maximum position. The estimated baseline will be given by $\left(\mathrm{d^j_{i(g)-b} + d^j_{i(g)+b}}\right)/2$.
- N_g is the number of glitches events in the reference pixel 88.
- N_j is the number of pixels included in the set of pixels selected to evaluate the cross-talk:

- $N_j = 8$ for the green circle corresponding to the pixels near the pixel 88.
- $N_j = 12$ for the blue circle corresponding to the pixels external to pixel 88.
- $N_j = 20$ if we consider all the pixels included inside the back square of figure 5.47.

Firstly, we applied different baseline positions b for the estimation of the baseline as a first step, we decided to study the level of cross-talk estimator for different round of pixels as shown in figure 5.47. The table 5.9 shows the values of cross-talk estimator in percent for different baseline positions b for the round 1, round 2 and round of all pixels in the black square as illustrated in figure 5.47 respect to the

Baseline position b	pixel	$C_1(b)\%$	$C_2(b)\%$	$C(b)\%$
5	88	0.0354	0.0157	-0.0026
20	88	-0.1957	0.1996	0.0565
50	88	-0.2838	0.2842	0.0518
100	88	-0.4423	0.2965	0.0045
200	88	-0.0758	-0.0067	0.017
300	88	0.1725	0.1240	0.1792
400	88	0.1782	0.1338	0.2131
500	88	0.0687	0.2923	0.3047
700	88	0.2157	-0.3502	-0.1325
1000	88	0.3343	-0.3702	-0.0757
1500	88	0.2065	-0.6317	-0.2844

TABLE 5.9: The table of cross-talk estimators calculated using the equation 5.58 by choosing randomly baseline positions b. All glitches g (130 glitches) of the reference pixel 88 was taken into account. $C_1(b)$ is the cross-talk estimator is calculated for 8 pixels in round 1 (the green circle as shown in figure 5.47). Similarly, $C_2(b)$ the cross-talk estimator is calculated for 12 pixels in round 2 (the blue circle as shown in figure 5.47). Finally, $C(b)$ the cross-talk estimator is calculated for whole 20 pixels.

radioactive source position pixel 88. With very far baseline position b (big values of b), it means that the outside of the glitch window is the dominated noise signal. The contribution of complex noise affects to give a constraint on the cross-talk estimator.

Secondly, in order to observe the cross-talk estimator as a function of the number of glitches event g. We can consider this is the distribution of the cross-talk estimator respected to glitches. Figure 5.49 shows the distribution of cross-talk estimator $\mathrm{C(b} = 200, \mathrm{pixel\ \ area)}$ and $\mathrm{C(b} = 300, \mathrm{pixel\ \ area)}$ for the different defined round of pixels for examples of the baseline position $b = 200$ and $b = 300$. The distributions can be fitted by the Gaussian-like and zero-like center, those fitted values of mean μ and standard deviation σ are labeled in the figure. The negative part means that the distribution of cross-talk estimators has contributed by noise.

Cross-talk of the long τ_0 (the second population of the time constant τ_0) As discussed in the subsection 5.6.3, we also decided to study the level of cross-talk when a second population glitch (figure 5.36) occurs. For this reason, we select glitches with $\tau_0 > 32\,\mathrm{ms}$ and a validated fit ($\chi^2 < 5.0$). In order to obtain better

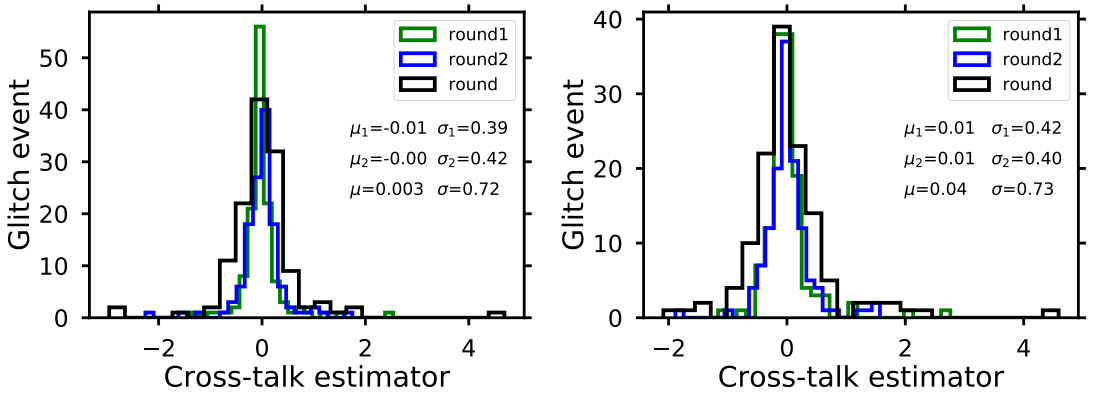

FIGURE 5.49: The histograms of cross-talk estimator respects to the number of glitch event. The green, blue and the black curves represent for round 1 (the green circle - pixels: 69, 76, 75, 87, 34, 35, 93, 81), round 2 (the blue circle - pixels: 128, 127, 74, 86, 33, 46, 47, 48, 41, 94, 82, 70), round square (whole pixel of the green circle and the blue circle), respectively. The corresponding values of μ and σ of the fitted Gaussian are labeled in the plot. The x-axis shows amplitudes of the cross-talk estimators while the y-axis indicates occurrence of glitch maximum. The baseline positions are 200 (*left*) and 300 (*right*) compared with the maximum position.

statistical estimations of the cross-talk estimator (equation 5.58), a window of the baseline position b from the glitch maximum position is considered.

While a full glitch signal was defined as 750 bin samples. Each cross-talk estimator $C(b)$ is calculated for each baseline position b in a chosen window, then the final cross-talk estimator C is evaluated by calculation the mean and the standard deviation of all $C(b)$ in that chosen window. With different windows of the baseline position b, the table 5.10 shows the value of the mean and the standard deviation of the cross-talk estimator in percentage for all pixels in the black square as illustrated in figure 5.47. The result shows that the cross-talk estimator depends on the considered window of the baseline position b and the value of cross-talk estimator is of the order of 0.1 %. When the window of the baseline position b is very large, it means that the outside a full glitch signal is noise signal, then these results give the information of noise among pixels.

On the other hand, the contribution of noise plays an important role in the estimation of the thermal cross-talk estimator. The exactly same analysis method for the data but the position of all pixels is shifted to the noise position n instead of

Window of baseline b	Pixel	$\mu\%$ (C)	$\sigma\%$ (C)
20	88	0.083	0.060
50	88	0.1613	0.0830
70	88	0.1934	0.0896
100	88	0.1774	0.0802
200	88	0.0107	0.1990
300	88	-0.1010	0.2344
500	88	-0.1452	0.2017
750	88	-0.0389	0.259

TABLE 5.10: The table of thermal cross-talk values calculated using the equation 5.58 by choosing randomly windows of the baseline position b.

the position of glitch maximum i. The equation 5.58 become:

$$\mathrm{C_n(b, pixel \quad area)} = \frac{1}{\mathrm{N_g}}\frac{1}{\mathrm{N_j}}\sum_{\mathrm{g=1}}^{\mathrm{N_g}}\sum_{\mathrm{j=1}}^{\mathrm{N_j}}\frac{\mathrm{d^j_{i(g)+n} - 0.5d^j_{i(g)+n-b} - 0.5d^j_{i(g)+n+b}}}{\mathrm{d^0_{i(g)}}}. \quad (5.59)$$

Here n is the noise position which is considered to outside the glitch window. The reference pixel is pixel 88. Because of fluctuation of noise then a window of the baseline position b is also taking for the estimation of the cross-talk estimator of noise. The cross-talk estimator is calculated for each baseline position b in a window then the final cross-talk estimator of noise is the mean and standard deviation of those values. Comparing results in the table 5.11 and the table 5.10

Position n	Window baseline b	Pixel	$\mu_n\%$ (C_n)	$\sigma_n\%$ (C_n)
1500	20	88	-0.0736	0.0559
1500	50	88	-0.150	0.0760
1500	70	88	-0.1746	0.0726
1500	100	88	-0.1489	0.0769
1500	200	88	-0.0087	0.27845
1500	300	88	0.3460	0.3130
1500	500	88	0.5077	0.3756
1500	750	88	0.5934	0.3324

TABLE 5.11: The table of contribution of noise level to thermal cross-talk estimator following the equation 5.59.

we observe that the behavior of noise performance in the signal is complex, it affects to the thermal cross-talk among pixels. As a conclusion, the thermal cross-talk is constrained to less than 0.1 percent. The low statistic of events does not allow to put a better constraint.

5.7.2 Cross-talk of the electronic readout chain

As described in section 5.3 (electronic readout system), we have been developed a 128-to-1 time domain multiplexer (TDM) for the readout of the TES array. At the first multiplexing stage, each TES is readout by a SQUID. The 128 SQUIDs are arranged in 32 rows and 4 columns as shown in figure 5.17. The C_{bias} capacitor aimed to isolate each SQUID column to avoid cross-talk has a value of 100 nF [123]. At the second multiplexing stage, the ASIC provides sequentially readout 4 columns multiplexing ("Mux") as shown in figure 5.50. The steps between two successive pixels can introduce electronic cross-talk related to the frequency acquisition f_{acq}. Therefore, to do our measurements and to be able to analyze precisely the glitches we use a fast sampling rate of 0.64 ms (1562.5 Hz). The fact is that QUBIC experiment has been first developed to use a lower frequency acquisition ($\sim$ 156 Hz) for observing CMB photons, and to match a typical scanning strategy.

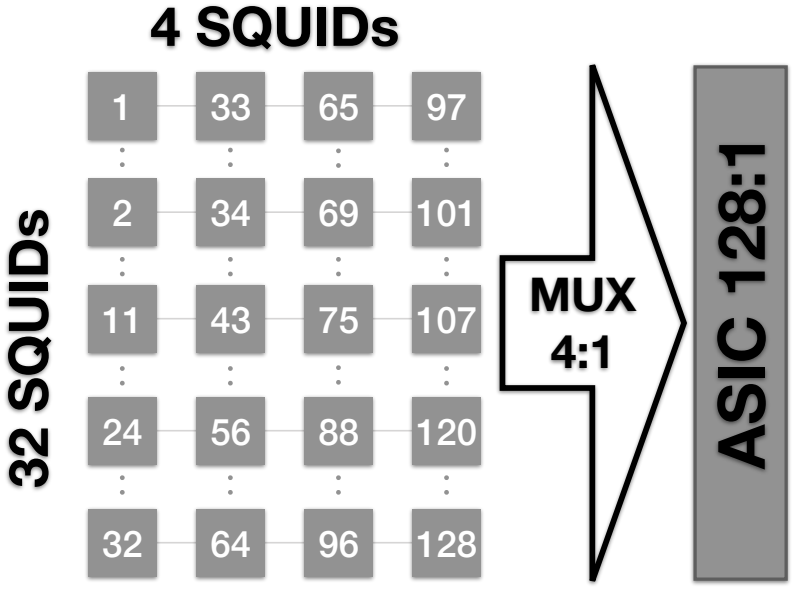

FIGURE 5.50: The 32x4 SQUIDs and the ASIC multiplexing readout. Steps between two successive pixels can introduce cross-talk.

Figure 5.51 shows the data of pixel 75 and pixel 107, these two successive pixels are sequential steps in multiplexing time, note that the pixel 75 is close to the radioactive source while the pixel 107 is far. The pixel 107 presents evidence of electronic readout cross-talk at each glitch events. The perturbed signal between negative and positive can be understood as resulting of C_{bias} by the changing sign

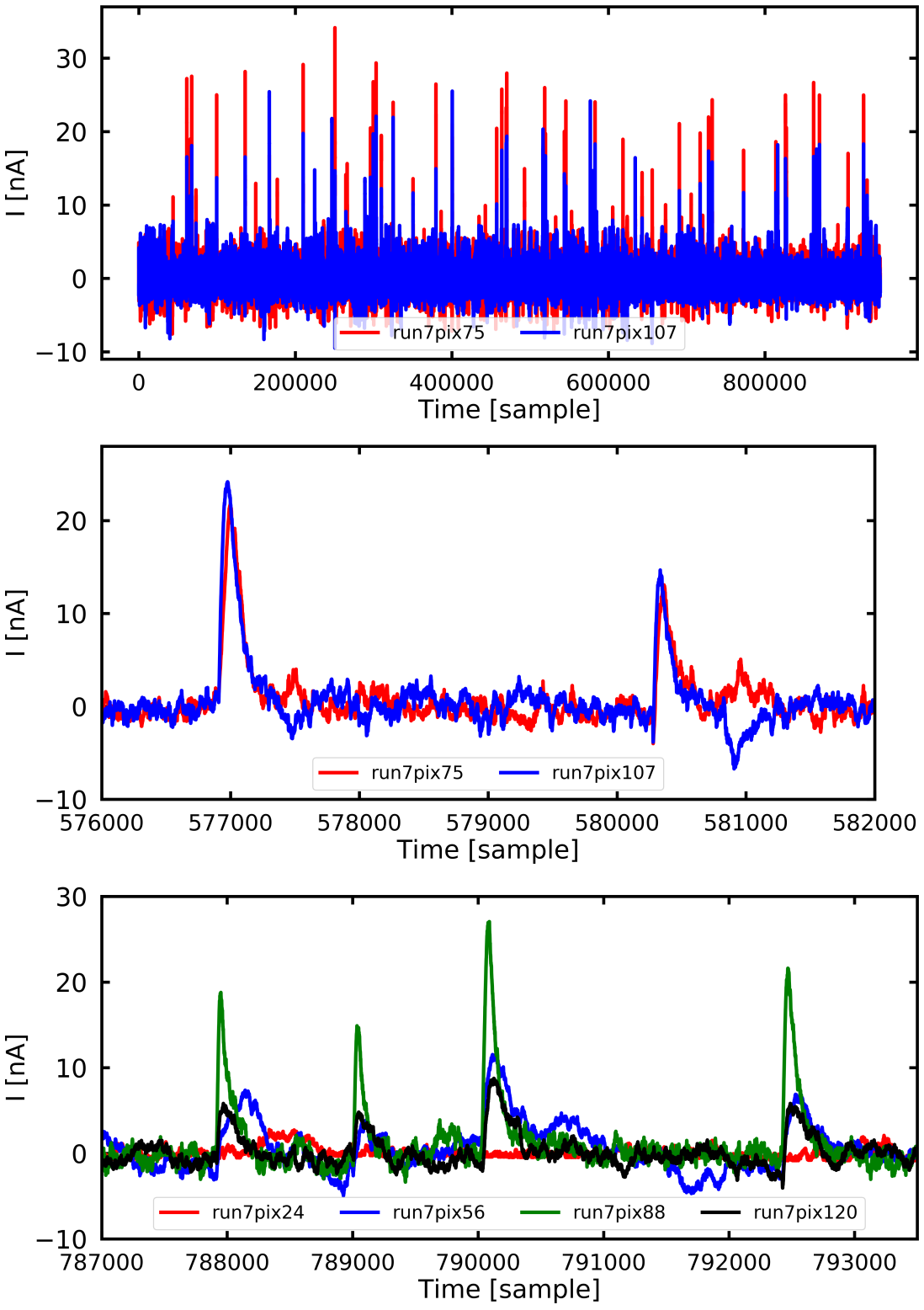

FIGURE 5.51: cross-talk of the electronic readout chain between successive pixels. The negative and positive fluctuated signal regime is probably due to the successive positive and negative readout of the 4 SQUIDs columns used to charge and discharge capacitors C_{bias}.

of the amplifiers. On the other hand, the plot also shows the group pixels 24, 56, 88 (in front of radioactive source), 120, they are sequential in the readout timeline and the cross-talk is present at each glitch events. Let us consider three pixels in the sequential multiplexing timeline. The glitch event occurs at pixel 88, the electronic readout cross-talk on pixel 120 is understandable in the readout timeline because pixel 120 is read after. Nevertheless, the signal appears on pixel 56 which is a past signal in the multiplexing timeline. Thus the interpretation of the cross-talk of the electronic readout chain dose not work this case. We also consider the case of particles which could hit directly the electronic readout chain, however the distance of the SQUID stage and the radioactive source is very far and separated by the back copper of the TES array. This study needs more investigation to have final conclusions.

Finally, there is many manners to study cross-talk than the thermal one or the one intrduced by multiplexing. The frequency acquisition of multiplexing can introduce one important cross-talk between two successive pixels (in the multiplexed timeline). Indeed, it could also inductive between 2 SQUIDs nearby, or due to unmatched capacitors C_{bias} used to separate the SQUID biasing. The radioactive source method allow the study of cross-talk, however this study requires a deeper work. This thesis introduces the problem.

5.8 Conclusion and discussion

In order to understand time constants of a TES detector, I studied the fundamental theory of superconductivity, the principle of the electrical and thermal response of a TES and its readout system. I developed a thermal model of TES to understand the interaction of particles with a TES array. Thanks to presence of the cryostat equiped with the electronic feedback system including FLL, SQUID, ASIC, FPGA, PID, QUBIC studio ... in the "mm lab" of APC laboratory, the data have been collected and analyzed. The first step was to analyze TES I-V curves which represent the operating regime (the normal state, the superconducting transition, and the superconducting state) of a TES as a function of the voltage-bias in the electrothermal feedback regime. We understand that we have 3 time constants in the system: (1) the intrinsic electric time constant of TES τ_{el} which is to small to be observable, (2) the electronic time constant of the readout chain, (3) one thermal time constant describing the thermal behaviour of the TES. Time

constants of the TES depend on the biasing power applied to the TES and on the PID controller of the electronic feedback system. Those parameters are V_{bias} and K_I(PID), respectively. In particular, if we apply the same power for TES (V_{bias}), we increase the K_I(PID) parameter, time constants will decrease. In conclusion, we can choose an optimal parameter of K_I for a QUBIC's TES array based on time constants behavior.

In a second part of this work, I studied cross-talk between TESs. Due to the fact that the collected data of signal and noise have different behavior when we change the frequency acquisition. This might have an effect on the time constant and cross-talk of the electronic readout chain. Indeed, two successive pixels introduced the electronic cross-talk in the multiplexing timeline. Furthermore, the study of cross-talk needs more careful investigation especially the cross-talk of the electronic readout system between two successive pixels which is necessary to improve for the QUBIC experiment. In addition, a discussion of time domain multiplexing and frequency domain multiplexing (FDM) can be found in the paper [121]. Future studies will rely on a study of the sampling rate and cosmic rays.

On the other hand, the TES array used for this data analysis is one of the QUBIC TES arrays. Due to the fact that the QUBIC technical demonstrator is developing steadily after each fabricated TES array, many tests are carrying on and improving effectively the future TES arrays, they should have a better yield. Therefore, the same study for the future TES arrays will have to be performed to get a better result. For example, the material, Niobium compound, size grid are studied and evaluated carefully after each fabricated TES array.

In the aspect of technological discussion on the cross-talk, a QUBIC's TES array has different design as compared to a TES array of other experiments. For example, POLARBEAR uses a sinuous antenna-coupled TES through bandpass filters, the BICEP uses a planar antenna-coupled TES though bandpass filters. QUBIC has a dichroic mirror in which separates incident radiations into different frequency bands directly to a TES array in the focal plane. As Expected, this procedure somehow mitigates the cross-talk between frequency band level while for the antenna coupled TES and bandpass filter, the interference might happen between different bands.

Chapter 6

Conclusion and perspectives

In this manuscript, I report the work I have been done during my Ph.D. I have focused on systematic effect for future CMB satellite mission in a first part and then I work on TES bolometer testing for the QUBIC experiment.

The first part is dedicated to bandpass mismatch systematic effect as one of the important systematic effects that can affect the current and next-generation measurement of the polarization of the Cosmic Microwave Background radiation. The slightly different frequency bandpasses among detectors introduce leakage from intensity into CMB polarization. I have evaluated the level of the bandpass mismatch systematic effect for several observational strategies. The amplitude of the leakage depends on the scanning strategy and impacts the estimation of the tensor-to-scalar ratio r. The result of the study allows us to optimize the scanning strategy of future CMB projects. Particularly in case without a half-wave plate, with the help of a full focal plane simulations at 140 GHz, random variation of detector filters is of the order of 0.6 % I found that the spurious angular power spectrum could potentially bias on r at the reionization bump ($\ell \leq 10$) at the level of 5×10^{-4} and the amplitude scale as $\frac{1}{\mathrm{N_{det}}}$. I have shown and verified the tight correlation between leakage maps and the average angle $\langle \cos 2\psi \rangle$; $\langle \sin 2\psi \rangle$. In case of an ideal continuously rotating HWP, the spectrum of the bandpass mismatch error leakage is similar to white noise. In order to obtain accuracy evaluations on the bandpass mismatch error, we have to concern to precise assumptions on (1) the scanning pattern strategy, (2) the variations in the bandpass filters, and (3) foreground removal process, (4) frequency band (5) 1/f noise in the modeling.

In the second part of the manuscript, in order to study the interaction of cosmic rays with the focal plane unit of future CMB projects, I studied the behavior of TES arrays of the ground-based QUBIC experiment in the laboratory. We have mounted on the front of a TES array an ^{241}Am source extracted from common smoke detectors. This source is particularly suitable for our tests as its main decay products are alpha particles with 5.5 MeV energy. Our analysis of the TES response to the glitch interaction, the study indicates that (1) we have clearly measured two time constants, the rising time constant τ_0, which is mostly due to the system limited bandwidth of the electronic readout chain and the thermal time constant (τ_1), which represents decay time of a glitch. Typical values for τ_0 and τ_1 are (7-30) ms and (20-60) ms, respectively. Moreover, we estimated the energy of the alpha particles in the range (2-5) MeV, in agreement with theoretical predictions. Our results demonstrate the capability of our readout electronics in performing tests of sensitivity towards CRs. (2) The rising time constant (τ_0) of the pixel 88 (in front of the radioactive source) has two populations, the first population can be interpreted as particles hit directly to the thermometer or the absorber of the sensor, the thermal equilibrium is rapidly established due to the deposited energy on the 1 $\mu\, m$ thickness of the absorber. The second population can be interpreted as particles hit the Si substrate which has the thickness of 500 $\mu\, m$, so that the deposited energy is huge. The heat flows increase the background reference temperature which affects the sensor through the thermal link between the sensor and the Si substrate. The sensor finally detected through a rising time τ_0 dominated by the thermal time constant (more or less equal to τ_1). The result of other pixels have difficulties to observe clearly the second population of the rising time τ_0 of the electronic readout chain. Several factors could affect the result such as the position of the pixel compared to the radioactive source, the thermal cross-talk among pixels, the behavior of the electronic readout system. (3) The thermal cross-talk has been estimated using an estimator. On the other hand, I found that the frequency acquisition of the multiplexing readout chain can introduce the cross-talk between two successive pixels in the multiplexing timeline. This could be a problem for the electronic readout system, however we studied interactions of α particles (fast signal compare to CMB) with the TES array using a very high frequency acquisition (1562.5 Hz). In fact QUBIC experiment has been first developed for a lower frequency acquisition ($\sim$ 156 Hz). Furthermore the study of the cross-talk of the electronic readout system needs a deeper work, this is a prospective of the thesis.

In this manuscript, I described the chapter 2 introduction to modern cosmology, standard cosmological model and the chapter 3 description of CMB in spherical harmonic, temperature anisotropies, CMB polarization, foreground components, and systematic effects. I am happy to state that there have plenty of avenues for improving and extending the work after my Ph.D.

Systematic effects

I have studied bandpass mismatch systematic effect, with similar procedures I could also study others systematic effects as the gain mismatch, cosmic rays effect, 1/f noise performance as well as beam asymmetry ... The study of imperfection in frequency bands of a half-wave plate is also an interesting topic close to bandpass mismatch.

Foreground components separation

A perspective of the bandpass mismatch study is that we need to study accuracy requirements of bandpass filters variation for future CMB experiment. Furthermore, the bandpass mismatch among detectors will have an impact to the component separation of the foreground. In fact that the bandpass mismatch study is achieved at 140 GHz dominated by thermal dust and synchrotron. If the foregrounds turn out to be complicated, we might have large bandpass errors thus a foreground cleaning and calibration method are necessary. In addition, the study of bandpass mismatch effect for multi-channel frequency bands also can be a future interesting topic.

Sensor Technology

In this manuscript especially chapter 5, I described the principle of TES as well as the behavior of a TES array to particle interactions. One thing missing is the TES design architecture and fabrication which should be pursued to cope the problem which has been identified and it is a straightforward direction in my research career. The fact is that the fabrication processes of an array are difficult, specially suspended membranes. It is also mandatory to have a good control over film and layers. The readout system of TES is very complex, SQUIDs are tricky and extremely expensive, difficult to multiplex and readout. Therefore I have put my eyes on the perspective of Kinetic Inductance Detector (KID) which has a simple readout system that uses a resonance circuit to see resonance frequency change when photons strike.

Appendix A

Solutions of Einstein equations

A.1 FLRW solution and Friedmann equations

The FLRW metric is:

$$ds^2 = c^2dt^2 - a^2(t)\left(\frac{dr^2}{1-kr^2} + r^2\left(d\theta^2 + \sin^2\theta d\varphi^2\right)\right).$$

The diagonal metric coefficients are

$$g_{00} = 1; \qquad g^{00} = \frac{1}{g_{00}} = 1;$$

$$g_{11} = -\frac{a^2(t)}{1-kr^2}; \qquad g^{11} = \frac{1}{g_{11}} = -\frac{1-kr^2}{a^2(t)};$$

$$g_{22} = -a^2(t)r^2; \qquad g^{22} = \frac{1}{g_{22}} = -\frac{1}{a^2(t)r^2};$$

$$g_{33} = -a^2(t)r^2\sin^2\theta; \qquad g^{33} = \frac{1}{g_{33}} = -\frac{1}{a^2(t)r^2\sin^2\theta};$$

$g^{\nu\beta}g_{\alpha\beta} = \delta^\nu_\alpha; \quad g^{\mu\nu} = g^{\mu\alpha}g^{\nu\beta}g_{\alpha\beta}; \quad A_\mu = g_{\mu\nu}A^\nu; \quad A^\mu = g^{\mu\nu}A_\nu.$

A.1.1 Christoffel symbols for the FLRW metric

$$\Gamma^{\mu}_{\alpha\beta} \equiv \frac{g^{\mu\nu}}{2}\left[g_{\alpha\nu,\beta} + g_{\beta\nu,\alpha} - g_{\alpha\beta,\nu}\right] = \frac{g^{\mu\nu}}{2}\left[\frac{\partial g_{\alpha\nu}}{\partial x^{\beta}} + \frac{\partial g_{\beta\nu}}{\partial x^{\alpha}} - \frac{\partial g_{\alpha\beta}}{\partial x^{\nu}}\right].$$

$$\Gamma_{\nu\mu\rho} = \frac{1}{2}\left[g_{\mu\nu,\rho} + g_{\nu\rho,\mu} - g_{\rho\mu,\nu}\right].$$

$\Gamma^0_{00} = 0$
$\Gamma^0_{0i} = \Gamma^0_{i0} = 0$
$\Gamma^{\mu}_{\alpha\nu} = \Gamma^{\mu}_{\nu\alpha}$
The non-zero Christoffel symbols are:

$$\Gamma^0_{11} = \frac{1}{c}\frac{a\dot{a}}{1-kr^2}; \quad \Gamma^0_{22} = \frac{1}{c}a\dot{a}r^2; \quad \Gamma^0_{33} = \frac{1}{c}a\dot{a}r^2\sin^2\theta;$$

$$\Gamma^1_{01} = \Gamma^1_{10} = \frac{1}{c}\frac{\dot{a}}{a}; \quad \Gamma^1_{11} = \frac{kr}{1-kr^2}; \quad \Gamma^1_{22} = -r\left(1-kr^2\right); \quad \Gamma^1_{33} = -r\left(1-kr^2\right)\sin^2\theta;$$

$$\Gamma^2_{02} = \Gamma^2_{20} = \Gamma^3_{03} = \Gamma^3_{30} = \frac{1}{c}\frac{\dot{a}}{a}; \quad \Gamma^2_{12} = \Gamma^2_{21} = \Gamma^3_{13} = \Gamma^3_{31} = \frac{1}{r};$$

$$\Gamma^2_{33} = -\sin\theta\cos\theta; \quad \Gamma^3_{23} = \Gamma^3_{32} = \frac{\cos\theta}{\sin\theta};$$

A.1.2 Ricci tensor and Einstein's tensor

The Ricci tensor is:

$$R_{\mu\nu} = \Gamma^{\alpha}_{\mu\nu,\alpha} - \Gamma^{\alpha}_{\mu\alpha,\nu} + \Gamma^{\alpha}_{\beta\alpha}\Gamma^{\beta}_{\mu\nu} - \Gamma^{\alpha}_{\beta\nu}\Gamma^{\beta}_{\mu\alpha},$$

$$R_{00} = -\frac{3}{c^2}\frac{\ddot{a}}{a} \overset{c=1}{=} \frac{3\ddot{a}}{a};$$

$$R_{11} = \frac{1}{1-kr^2}\left(\frac{\ddot{a}a}{c^2} + \frac{2\dot{a}^2}{c^2} + 2k\right) \overset{c=1}{=} \frac{a\ddot{a} + 2\dot{a}^2 + 2k}{1-kr^2};$$

$$R_{22} = r^2 \left(\frac{\ddot{a}a}{c^2} + \frac{2\dot{a}^2}{c^2} + 2k \right) \overset{c=1}{=} r^2 \left(a\ddot{a} + 2\dot{a}^2 + 2k \right);$$

$$R_{33} = r^2 \sin^2\theta \left(\frac{\ddot{a}a}{c^2} + \frac{2\dot{a}^2}{c^2} + 2k \right) \overset{c=1}{=} r^2 \sin^2\theta \left(a\ddot{a} + 2\dot{a}^2 + 2k \right);$$

Ricci Scalar is:

$$R \equiv g^{\mu\nu} R_{\mu\nu} = R^{\alpha}_{\alpha} = -6 \left[\frac{\ddot{a}}{a} \frac{1}{c^2} + \frac{\dot{a}^2}{a^2} \frac{1}{c^2} + \frac{k}{a^2} \right] \overset{c=1}{=} -6 \frac{a\ddot{a} + \dot{a}^2 + k}{a^2};$$

Einstein's tensor is:

$$G_{00} = 3 \frac{\dot{a}^2}{a^2} \frac{1}{c^2} + 3 \frac{k}{a^2};$$

$$G_{ii} = g_{ii} \left[2 \frac{\ddot{a}}{a} \frac{1}{c^2} + \frac{\dot{a}^2}{a^2} \frac{1}{c^2} + \frac{k}{a^2} \right];$$

A.2 Stress-energy tensor $T_{\mu\nu}$

$$T^{\mu\nu} = T_{\mu\nu} = \left(\rho c^2 + P \right) \frac{u_\mu u_\nu}{c^2} - P g_{\mu\nu},$$

The stress-energy tensor components are:

$$\begin{aligned}
T_{ii} &= P g_{\mu\nu}; \\
T_{00} &= (\rho + P) \frac{u_0 u_0}{c^2} - P g_{00} = \rho; \\
T_{11} &= P \frac{a^2}{1 - kr^2}; \\
T_{22} &= P r^2 a^2; \\
T_{33} &= P a^2 r^2 \sin^2\theta;
\end{aligned}$$

Using those calculations above, we could find the Friedmann equations.

A.3 Schwarzschild Solution and Black Holes

The Schwarzschild metric so-called Schwarzschild solution of Einstein equations is

$$ds^2 = -\left(1 - \frac{2GM}{c^2 r}\right) cdt^2 + \left(1 - \frac{2GM}{c^2 r}\right)^{-1} dr^2 + r^2 \left(d\theta^2 + \sin^2 \theta d\varphi^2\right).$$

Where G is the universal gravitational constant, M is a Newtonian mass. The equation is the static spherically symmetric vacuum solution of Einstein equations. The equation describes space-time around a point mass. There are two interesting points at $r = 0$ which represents a real singularity and at the Schwarzschild radius $r_S = \frac{2GM}{c^2}$, the radius at which mass M collapses into a black hole.

Appendix B

χ^2 and fit C_ℓ

If we have an equation $d = ax + n$, then $n = d - ax$, where d is the data measurement, x is a model of data, a is an estimate solution and n is the noise contribution. The probability distribution function of noise is assumed as a Gaussian distribution: $P(n) = \frac{1}{N(\sigma)} e^{-n^t N^{-1} n}$
$\chi^2 = -\log(P(n))$, maximum $P(n)$ corresponds to minimum χ^2

$$\chi^2 = n^t N^{-1} n = \sum (d_i - ax_i) \frac{1}{\sigma_i^2} \sum (d_i - ax_i) = \frac{\sum (d_i - ax_i)^2}{\sigma_i^2}.$$

Minimum χ^2, it means that

$$\frac{\partial \chi^2}{\partial x_{|a}} = \frac{-2}{\sigma_i^2} \sum x_i (d_i - ax_i) = 0.$$

$$\frac{\sum x_i d_i}{\sigma_i^2} = \frac{\sum a {x_i}^2}{\sigma_i^2},$$

$$a = \frac{\frac{\sum x_i d_i}{\sigma_i^2}}{\frac{\sum {x_i}^2}{\sigma_i^2}},$$

We can imply the form of the solution:

$$a = \sum \left(x_i \frac{1}{\sigma_i^2} x_i \right)^{-1} \sum x_i \frac{1}{\sigma_i^2} d_i,$$

We can apply the χ^2 method to fit the cosmic variance C_ℓ to estimate the tensor to scalar value r

$$\chi^2 = \sum_\ell \frac{\left(\tilde{C}_\ell - 100 r C_{\ell 0.01}\right)^2}{\frac{2C_\ell^2}{2\ell+1} + \frac{N_\ell^2}{2\ell+1}},$$

then we apply the equation above by consider noise amplitude N_ℓ is $>>$ than C_ℓ, and $\tilde{C}_\ell, C_\ell$ are the data measurement and the model respectively.

$$100r = \sum_\ell \left(C_\ell^2 \frac{2\ell+1}{N_\ell^2}\right)^{-1} \sum_\ell \left(C_\ell \tilde{C}_\ell \frac{2\ell+1}{N_\ell^2}\right),$$

$$100r = \sum_\ell \left(C_\ell^2 (2\ell+1)\right)^{-1} \sum_\ell \left(C_\ell \tilde{C}_\ell (2\ell+1)\right).$$

Appendix C

Fitted glitches

In this appendix, I present the fitted glitches for the data run7 and the pixel 88 which is in front of the radioactive source. The glitch identification is label g. Parameters of the fitted template model are labeled.

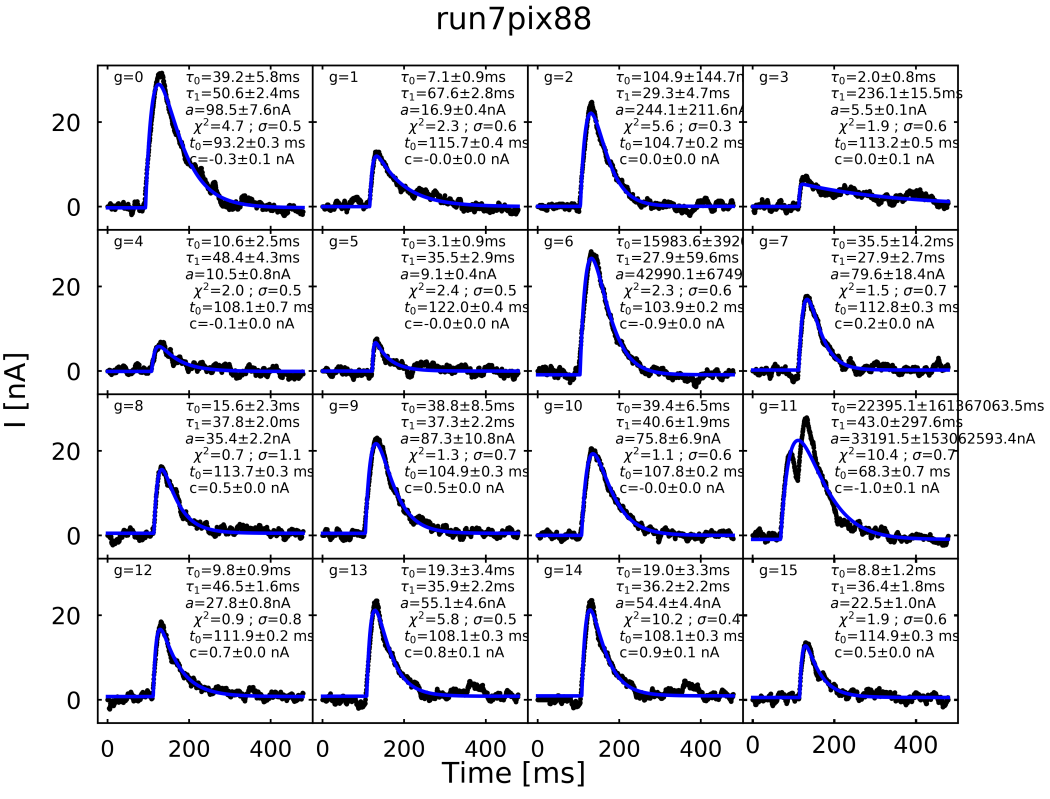

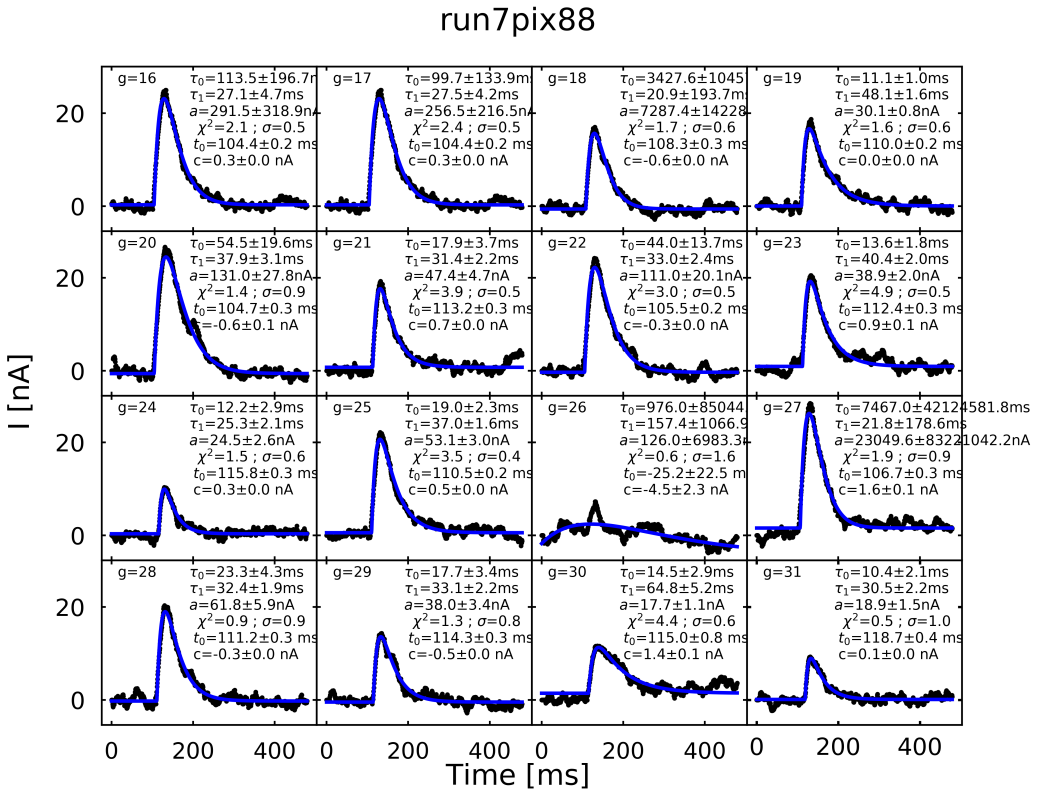
run7pix88
g=16 τ0=113.5±196.7r τ1=27.1±4.7ms a=291.5±318.9nA χ²=2.1 ; σ=0.5 t0=104.4±0.2 ms c=0.3±0.0 nA
g=17 τ0=99.7±133.9m τ1=27.5±4.2ms a=256.5±216.5nA χ²=2.4 ; σ=0.5 t0=104.4±0.2 ms c=0.3±0.0 nA
g=18 τ0=3427.6±1045 τ1=20.9±193.7m a=7287.4±14228 χ²=1.7 ; σ=0.6 t0=108.3±0.3 ms c=-0.6±0.0 nA
g=19 τ0=11.1±1.0ms τ1=48.1±1.6ms a=30.1±0.8nA χ²=1.6 ; σ=0.6 t0=110.0±0.2 ms c=0.0±0.0 nA
g=20 τ0=54.5±19.6ms τ1=37.9±3.1ms a=131.0±27.8nA χ²=1.4 ; σ=0.9 t0=104.7±0.3 ms c=-0.6±0.1 nA
g=21 τ0=17.9±3.7ms τ1=31.4±2.2ms a=47.4±4.7nA χ²=3.9 ; σ=0.5 t0=113.2±0.3 ms c=0.7±0.0 nA
g=22 τ0=44.0±13.7ms τ1=33.0±2.4ms a=111.0±20.1nA χ²=3.0 ; σ=0.5 t0=105.5±0.2 ms c=-0.3±0.0 nA
g=23 τ0=13.6±1.8ms τ1=40.4±2.0ms a=38.9±2.0nA χ²=4.9 ; σ=0.5 t0=112.4±0.3 ms c=0.9±0.1 nA
g=24 τ0=12.2±2.9ms τ1=25.3±2.1ms a=24.5±2.6nA χ²=1.5 ; σ=0.6 t0=115.8±0.3 ms c=0.3±0.0 nA
g=25 τ0=19.0±2.3ms τ1=37.0±1.6ms a=53.1±3.0nA χ²=3.5 ; σ=0.4 t0=110.5±0.2 ms c=0.5±0.0 nA
g=26 τ0=976.0±85044 τ1=157.4±1066.9 a=126.0±6983.3 χ²=0.6 ; σ=1.6 t0=-25.2±22.5 m c=-4.5±2.3 nA
g=27 τ0=7467.0±42124581.8ms τ1=21.8±178.6ms a=23049.6±8322.1042.2nA χ²=1.9 ; σ=0.9 t0=106.7±0.3 ms c=1.6±0.1 nA
g=28 τ0=23.3±4.3ms τ1=32.4±1.9ms a=61.8±5.9nA χ²=0.9 ; σ=0.9 t0=111.2±0.3 ms c=-0.3±0.0 nA
g=29 τ0=17.7±3.4ms τ1=33.1±2.2ms a=38.0±3.4nA χ²=1.3 ; σ=0.8 t0=114.3±0.3 ms c=-0.5±0.0 nA
g=30 τ0=14.5±2.9ms τ1=64.8±5.2ms a=17.7±1.1nA χ²=4.4 ; σ=0.6 t0=115.0±0.8 ms c=1.4±0.1 nA
g=31 τ0=10.4±2.1ms τ1=30.5±2.2ms a=18.9±1.5nA χ²=0.5 ; σ=1.0 t0=118.7±0.4 ms c=0.1±0.0 nA
I [nA]
Time [ms]

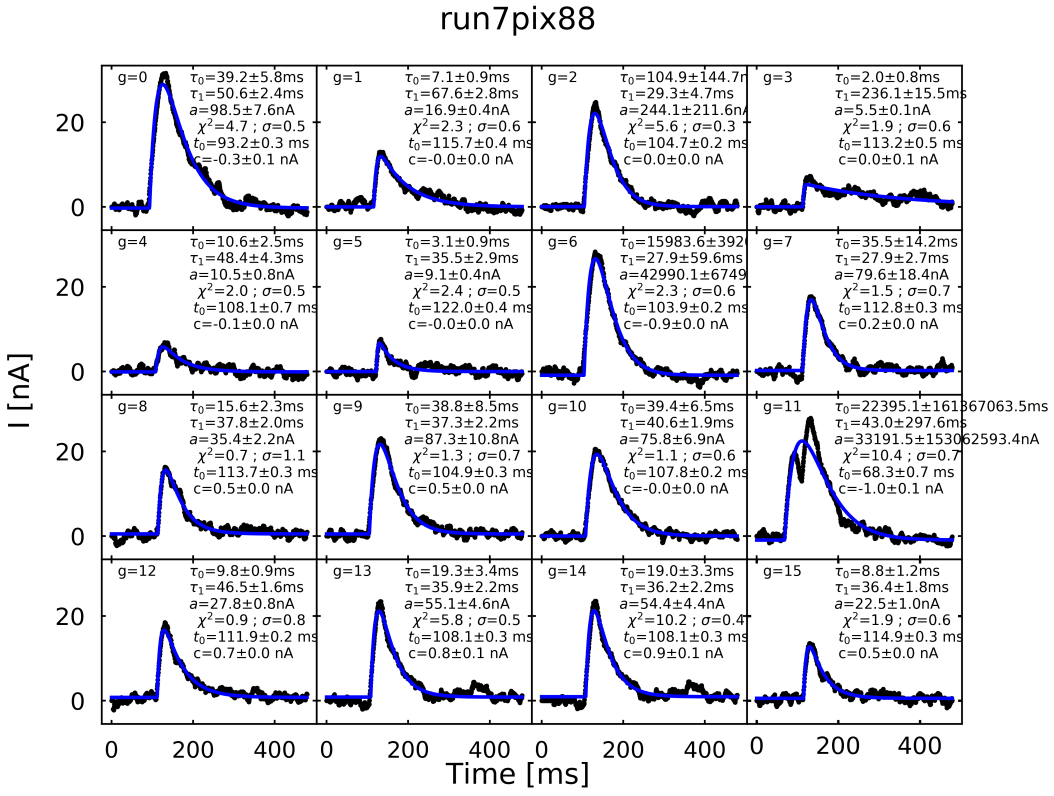
run7pix88
g=0 τ0=39.2±5.8ms τ1=50.6±2.4ms a=98.5±7.6nA χ²=4.7 ; σ=0.5 t0=93.2±0.3 ms c=-0.3±0.1 nA
g=1 τ0=7.1±0.9ms τ1=67.6±2.8ms a=16.9±0.4nA χ²=2.3 ; σ=0.6 t0=115.7±0.4 ms c=-0.0±0.0 nA
g=2 τ0=104.9±144.7r τ1=29.3±4.7ms a=244.1±211.6nA χ²=5.6 ; σ=0.3 t0=104.7±0.2 ms c=0.0±0.0 nA
g=3 τ0=2.0±0.8ms τ1=236.1±15.5ms a=5.5±0.1nA χ²=1.9 ; σ=0.6 t0=113.2±0.5 ms c=0.0±0.1 nA
g=4 τ0=10.6±2.5ms τ1=48.4±4.3ms a=10.5±0.8nA χ²=2.0 ; σ=0.5 t0=108.1±0.7 ms c=-0.1±0.0 nA
g=5 τ0=3.1±0.9ms τ1=35.5±2.9ms a=9.1±0.4nA χ²=2.4 ; σ=0.5 t0=122.0±0.4 ms c=-0.0±0.0 nA
g=6 τ0=15983.6±392 τ1=27.9±59.6ms a=42990.1±6749 χ²=2.3 ; σ=0.6 t0=103.9±0.2 ms c=-0.9±0.0 nA
g=7 τ0=35.5±14.2ms τ1=27.9±2.7ms a=79.6±18.4nA χ²=1.5 ; σ=0.7 t0=112.8±0.3 ms c=0.2±0.0 nA
g=8 τ0=15.6±2.3ms τ1=37.8±2.0ms a=35.4±2.2nA χ²=0.7 ; σ=1.1 t0=113.7±0.3 ms c=0.5±0.0 nA
g=9 τ0=38.8±8.5ms τ1=37.3±2.2ms a=87.3±10.8nA χ²=1.3 ; σ=0.7 t0=104.9±0.3 ms c=0.5±0.0 nA
g=10 τ0=39.4±6.5ms τ1=40.6±1.9ms a=75.8±6.9nA χ²=1.1 ; σ=0.6 t0=107.8±0.2 ms c=-0.0±0.0 nA
g=11 τ0=22395.1±161367063.5ms τ1=43.0±297.6ms a=33191.5±153062593.4nA χ²=10.4 ; σ=0.7 t0=68.3±0.7 ms c=-1.0±0.1 nA
g=12 τ0=9.8±0.9ms τ1=46.5±1.6ms a=27.8±0.8nA χ²=0.9 ; σ=0.8 t0=111.9±0.2 ms c=0.7±0.0 nA
g=13 τ0=19.3±3.4ms τ1=35.9±2.2ms a=55.1±4.6nA χ²=5.8 ; σ=0.5 t0=108.1±0.3 ms c=0.8±0.1 nA
g=14 τ0=19.0±3.3ms τ1=36.2±2.2ms a=54.4±4.4nA χ²=10.2 ; σ=0.4 t0=108.1±0.3 ms c=0.9±0.1 nA
g=15 τ0=8.8±1.2ms τ1=36.4±1.8ms a=22.5±1.0nA χ²=1.9 ; σ=0.6 t0=114.9±0.3 ms c=0.5±0.0 nA
I [nA]
Time [ms]

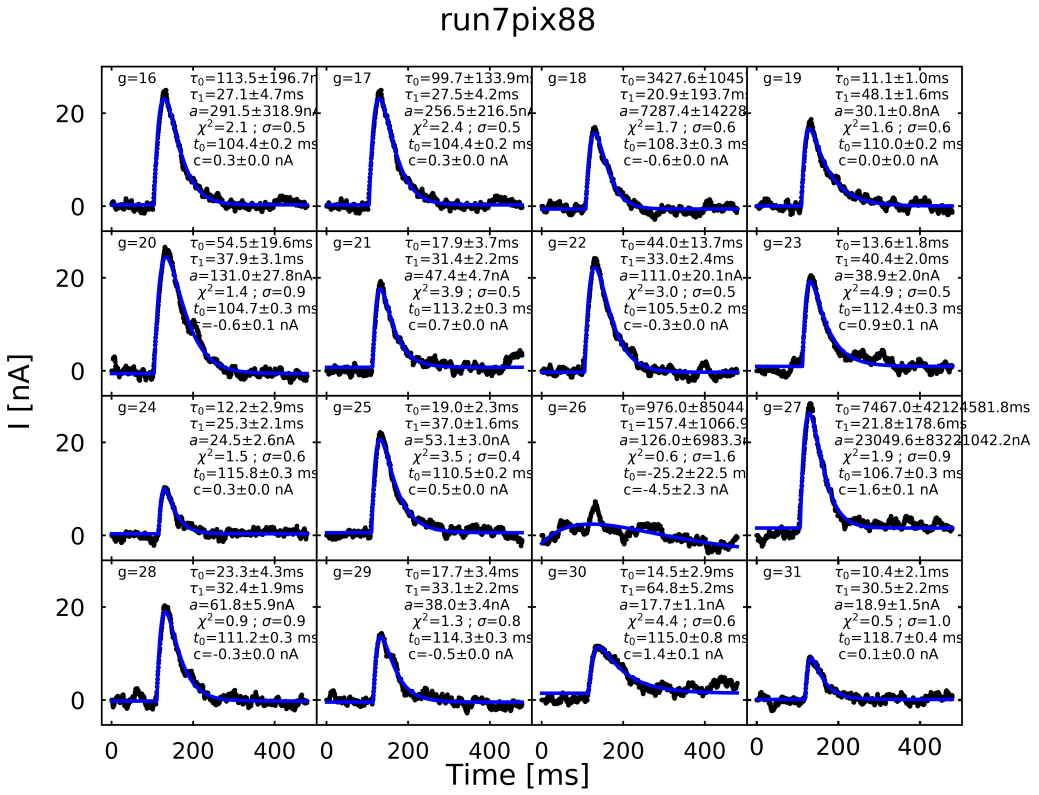
run7pix88
g=16 τ0=113.5±196.7r τ1=27.1±4.7ms a=291.5±318.9nA χ²=2.1 ; σ=0.5 t0=104.4±0.2 ms c=0.3±0.0 nA
g=17 τ0=99.7±133.9m τ1=27.5±4.2ms a=256.5±216.5nA χ²=2.4 ; σ=0.5 t0=104.4±0.2 ms c=0.3±0.0 nA
g=18 τ0=3427.6±1045 τ1=20.9±193.7m a=7287.4±14228 χ²=1.7 ; σ=0.6 t0=108.3±0.3 ms c=-0.6±0.0 nA
g=19 τ0=11.1±1.0ms τ1=48.1±1.6ms a=30.1±0.8nA χ²=1.6 ; σ=0.6 t0=110.0±0.2 ms c=0.0±0.0 nA
g=20 τ0=54.5±19.6ms τ1=37.9±3.1ms a=131.0±27.8nA χ²=1.4 ; σ=0.9 t0=104.7±0.3 ms c=-0.6±0.1 nA
g=21 τ0=17.9±3.7ms τ1=31.4±2.2ms a=47.4±4.7nA χ²=3.9 ; σ=0.5 t0=113.2±0.3 ms c=0.7±0.0 nA
g=22 τ0=44.0±13.7ms τ1=33.0±2.4ms a=111.0±20.1nA χ²=3.0 ; σ=0.5 t0=105.5±0.2 ms c=-0.3±0.0 nA
g=23 τ0=13.6±1.8ms τ1=40.4±2.0ms a=38.9±2.0nA χ²=4.9 ; σ=0.5 t0=112.4±0.3 ms c=0.9±0.1 nA
g=24 τ0=12.2±2.9ms τ1=25.3±2.1ms a=24.5±2.6nA χ²=1.5 ; σ=0.6 t0=115.8±0.3 ms c=0.3±0.0 nA
g=25 τ0=19.0±2.3ms τ1=37.0±1.6ms a=53.1±3.0nA χ²=3.5 ; σ=0.4 t0=110.5±0.2 ms c=0.5±0.0 nA
g=26 τ0=976.0±85044 τ1=157.4±1066.9 a=126.0±6983.3 χ²=0.6 ; σ=1.6 t0=-25.2±22.5 m c=-4.5±2.3 nA
g=27 τ0=7467.0±42124581.8ms τ1=21.8±178.6ms a=23049.6±8322.1042.2nA χ²=1.9 ; σ=0.9 t0=106.7±0.3 ms c=1.6±0.1 nA
g=28 τ0=23.3±4.3ms τ1=32.4±1.9ms a=61.8±5.9nA χ²=0.9 ; σ=0.9 t0=111.2±0.3 ms c=-0.3±0.0 nA
g=29 τ0=17.7±3.4ms τ1=33.1±2.2ms a=38.0±3.4nA χ²=1.3 ; σ=0.8 t0=114.3±0.3 ms c=-0.5±0.0 nA
g=30 τ0=14.5±2.9ms τ1=64.8±5.2ms a=17.7±1.1nA χ²=4.4 ; σ=0.6 t0=115.0±0.8 ms c=1.4±0.1 nA
g=31 τ0=10.4±2.1ms τ1=30.5±2.2ms a=18.9±1.5nA χ²=0.5 ; σ=1.0 t0=118.7±0.4 ms c=0.1±0.0 nA
I [nA]
Time [ms]

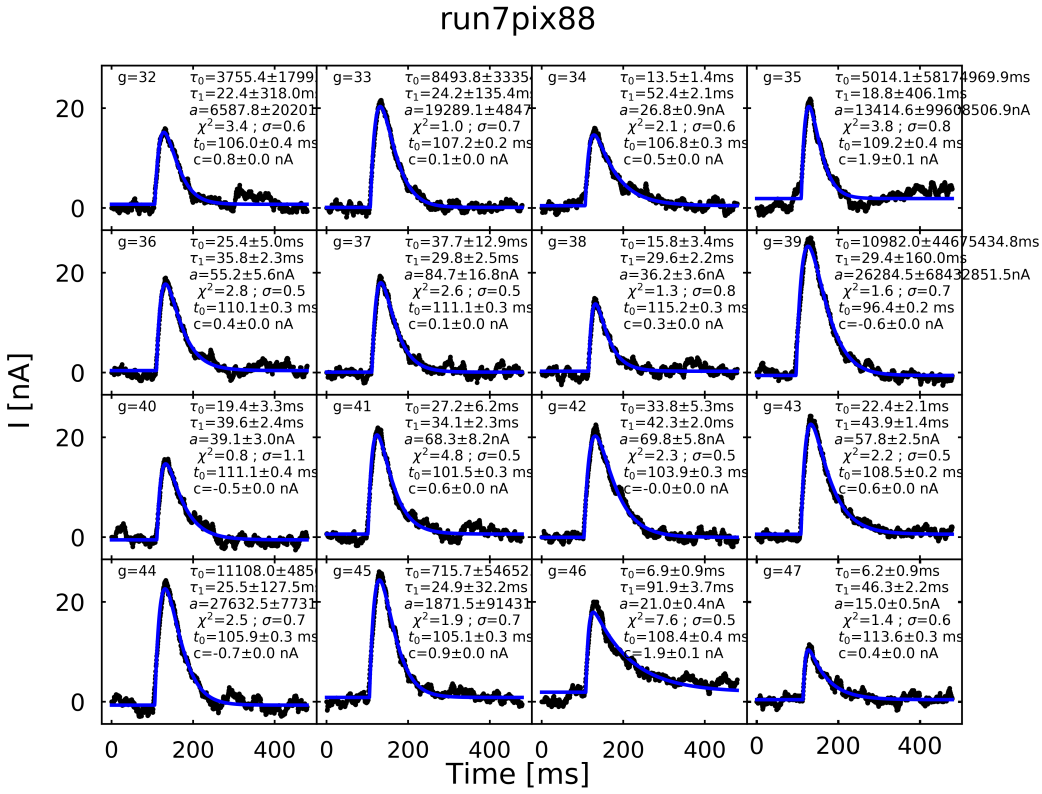
run7pix88
g=32 τ0=3755.4±1799 τ1=22.4±318.0m a=6587.8±20201 χ²=3.4 ; σ=0.6 t0=106.0±0.4 ms c=0.8±0.0 nA
g=33 τ0=8493.8±3335 τ1=24.2±135.4m a=19289.1±4847 χ²=1.0 ; σ=0.7 t0=107.2±0.2 ms c=0.1±0.0 nA
g=34 τ0=13.5±1.4ms τ1=52.4±2.1ms a=26.8±0.9nA χ²=2.1 ; σ=0.6 t0=106.8±0.3 ms c=0.5±0.0 nA
g=35 τ0=5014.1±58174969.9ms τ1=18.8±406.1ms a=13414.6±996.8506.9nA χ²=3.8 ; σ=0.8 t0=109.2±0.4 ms c=1.9±0.1 nA
g=36 τ0=25.4±5.0ms τ1=35.8±2.3ms a=55.2±5.6nA χ²=2.8 ; σ=0.5 t0=110.1±0.3 ms c=0.4±0.0 nA
g=37 τ0=37.7±12.9ms τ1=29.8±2.5ms a=84.7±16.8nA χ²=2.6 ; σ=0.5 t0=111.1±0.3 ms c=0.1±0.0 nA
g=38 τ0=15.8±3.4ms τ1=29.6±2.2ms a=36.2±3.6nA χ²=1.3 ; σ=0.8 t0=115.2±0.3 ms c=0.3±0.0 nA
g=39 τ0=10982.0±44675434.8ms τ1=29.4±160.0ms a=26284.5±68432851.5nA χ²=1.6 ; σ=0.7 t0=96.4±0.2 ms c=-0.6±0.0 nA
g=40 τ0=19.4±3.3ms τ1=39.6±2.4ms a=39.1±3.0nA χ²=0.8 ; σ=1.1 t0=111.1±0.4 ms c=-0.5±0.0 nA
g=41 τ0=27.2±6.2ms τ1=34.1±2.3ms a=68.3±8.2nA χ²=4.8 ; σ=0.5 t0=101.5±0.3 ms c=0.6±0.0 nA
g=42 τ0=33.8±5.3ms τ1=42.3±2.0ms a=69.8±5.8nA χ²=2.3 ; σ=0.5 t0=103.9±0.3 ms c=-0.0±0.0 nA
g=43 τ0=22.4±2.1ms τ1=43.9±1.4ms a=57.8±2.5nA χ²=2.2 ; σ=0.5 t0=108.5±0.2 ms c=0.6±0.0 nA
g=44 τ0=11108.0±485 τ1=25.5±127.5m a=27632.5±7731 χ²=2.5 ; σ=0.7 t0=105.9±0.3 ms c=-0.7±0.0 nA
g=45 τ0=715.7±54652 τ1=24.9±32.2ms a=1871.5±91431 χ²=1.9 ; σ=0.7 t0=105.1±0.3 ms c=0.9±0.0 nA
g=46 τ0=6.9±0.9ms τ1=91.9±3.7ms a=21.0±0.4nA χ²=7.6 ; σ=0.5 t0=108.4±0.4 ms c=1.9±0.1 nA
g=47 τ0=6.2±0.9ms τ1=46.3±2.2ms a=15.0±0.5nA χ²=1.4 ; σ=0.6 t0=113.6±0.3 ms c=0.4±0.0 nA
I [nA]
Time [ms]

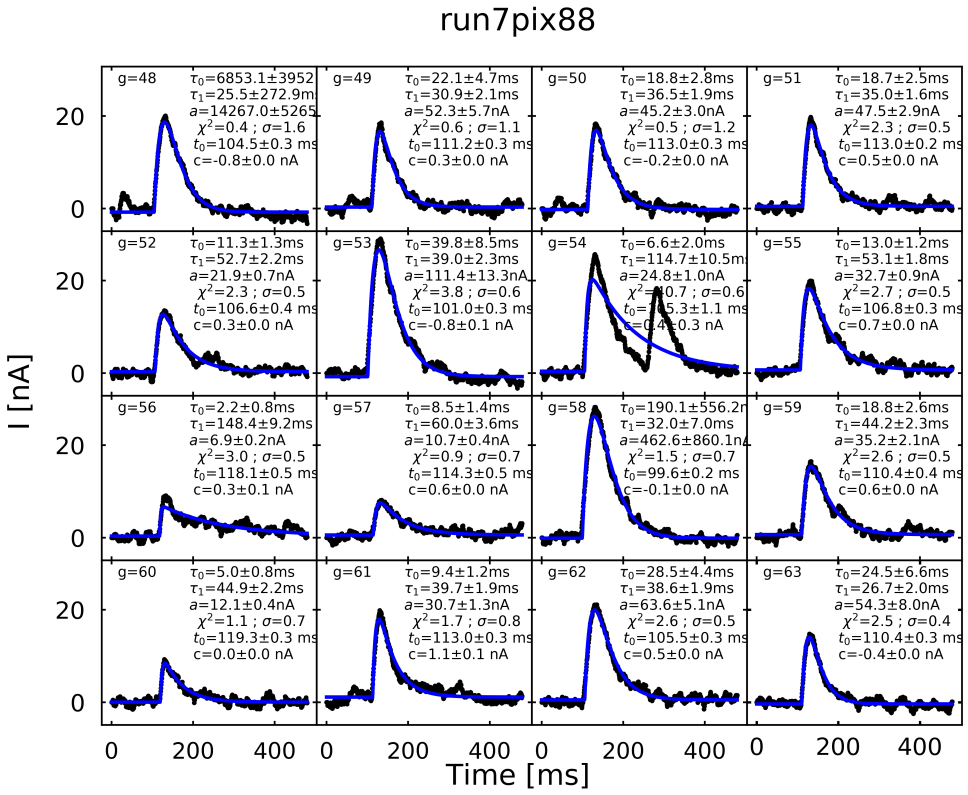
run7pix88
g=48 τ0=6853.1±3952 τ1=25.5±272.9m a=14267.0±5265 χ²=0.4 ; σ=1.6 t0=104.5±0.3 ms c=-0.8±0.0 nA
g=49 τ0=22.1±4.7ms τ1=30.9±2.1ms a=52.3±5.7nA χ²=0.6 ; σ=1.1 t0=111.2±0.3 ms c=0.3±0.0 nA
g=50 τ0=18.8±2.8ms τ1=36.5±1.9ms a=45.2±3.0nA χ²=0.5 ; σ=1.2 t0=113.0±0.3 ms c=-0.2±0.0 nA
g=51 τ0=18.7±2.5ms τ1=35.0±1.6ms a=47.5±2.9nA χ²=2.3 ; σ=0.5 t0=113.0±0.2 ms c=0.5±0.0 nA
g=52 τ0=11.3±1.3ms τ1=52.7±2.2ms a=21.9±0.7nA χ²=2.3 ; σ=0.5 t0=106.6±0.4 ms c=0.3±0.0 nA
g=53 τ0=39.8±8.5ms τ1=39.0±2.3ms a=111.4±13.3nA χ²=3.8 ; σ=0.6 t0=101.0±0.3 ms c=-0.8±0.1 nA
g=54 τ0=6.6±2.0ms τ1=114.7±10.5m a=24.8±1.0nA χ²=10.7 ; σ=0.6 t0=115.3±1.1 ms c=0.4±0.3 nA
g=55 τ0=13.0±1.2ms τ1=53.1±1.8ms a=32.7±0.9nA χ²=2.7 ; σ=0.5 t0=106.8±0.3 ms c=0.7±0.0 nA
g=56 τ0=2.2±0.8ms τ1=148.4±9.2ms a=6.9±0.2nA χ²=3.0 ; σ=0.5 t0=118.1±0.5 ms c=0.3±0.1 nA
g=57 τ0=8.5±1.4ms τ1=60.0±3.6ms a=10.7±0.4nA χ²=0.9 ; σ=0.7 t0=114.3±0.5 ms c=0.6±0.0 nA
g=58 τ0=190.1±556.2r τ1=32.0±7.0ms a=462.6±860.1nA χ²=1.5 ; σ=0.7 t0=99.6±0.2 ms c=-0.1±0.0 nA
g=59 τ0=18.8±2.6ms τ1=44.2±2.3ms a=35.2±2.1nA χ²=2.6 ; σ=0.5 t0=110.4±0.4 ms c=0.6±0.0 nA
g=60 τ0=5.0±0.8ms τ1=44.9±2.2ms a=12.1±0.4nA χ²=1.1 ; σ=0.7 t0=119.3±0.3 ms c=0.0±0.0 nA
g=61 τ0=9.4±1.2ms τ1=39.7±1.9ms a=30.7±1.3nA χ²=1.7 ; σ=0.8 t0=113.0±0.3 ms c=1.1±0.1 nA
g=62 τ0=28.5±4.4ms τ1=38.6±1.9ms a=63.6±5.1nA χ²=2.6 ; σ=0.5 t0=105.5±0.3 ms c=0.5±0.0 nA
g=63 τ0=24.5±6.6ms τ1=26.7±2.0ms a=54.3±8.0nA χ²=2.5 ; σ=0.4 t0=110.4±0.3 ms c=-0.4±0.0 nA
I [nA]
Time [ms]

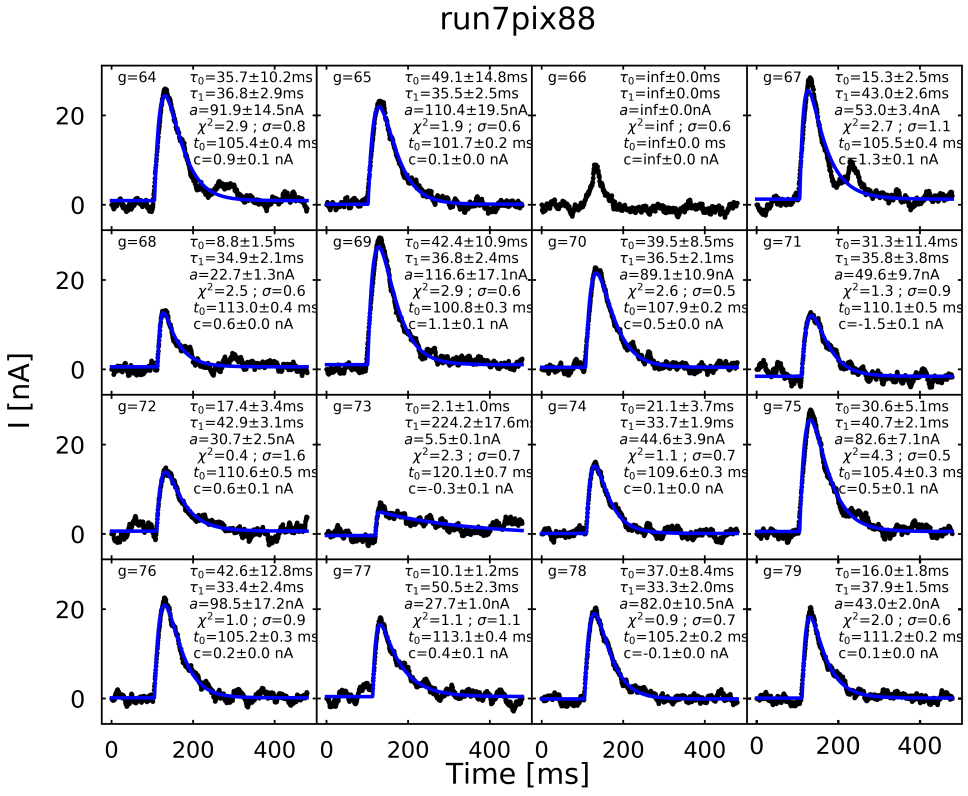
run7pix88
g=64 τ0=35.7±10.2ms τ1=36.8±2.9ms a=91.9±14.5nA χ²=2.9 ; σ=0.8 t0=105.4±0.4 ms c=0.9±0.1 nA
g=65 τ0=49.1±14.8ms τ1=35.5±2.5ms a=110.4±19.5nA χ²=1.9 ; σ=0.6 t0=101.7±0.2 ms c=0.1±0.0 nA
g=66 τ0=inf±0.0ms τ1=inf±0.0ms a=inf±0.0nA χ²=inf ; σ=0.6 t0=inf±0.0 ms c=inf±0.0 nA
g=67 τ0=15.3±2.5ms τ1=43.0±2.6ms a=53.0±3.4nA χ²=2.7 ; σ=1.1 t0=105.5±0.4 ms c=1.3±0.1 nA
g=68 τ0=8.8±1.5ms τ1=34.9±2.1ms a=22.7±1.3nA χ²=2.5 ; σ=0.6 t0=113.0±0.4 ms c=0.6±0.0 nA
g=69 τ0=42.4±10.9ms τ1=36.8±2.4ms a=116.6±17.1nA χ²=2.9 ; σ=0.6 t0=100.8±0.3 ms c=1.1±0.1 nA
g=70 τ0=39.5±8.5ms τ1=36.5±2.1ms a=89.1±10.9nA χ²=2.6 ; σ=0.5 t0=107.9±0.2 ms c=0.5±0.0 nA
g=71 τ0=31.3±11.4ms τ1=35.8±3.8ms a=49.6±9.7nA χ²=1.3 ; σ=0.9 t0=110.1±0.5 ms c=-1.5±0.1 nA
g=72 τ0=17.4±3.4ms τ1=42.9±3.1ms a=30.7±2.5nA χ²=0.4 ; σ=1.6 t0=110.6±0.5 ms c=0.6±0.1 nA
g=73 τ0=2.1±1.0ms τ1=224.2±17.6m a=5.5±0.1nA χ²=2.3 ; σ=0.7 t0=120.1±0.7 ms c=-0.3±0.1 nA
g=74 τ0=21.1±3.7ms τ1=33.7±1.9ms a=44.6±3.9nA χ²=1.1 ; σ=0.7 t0=109.6±0.3 ms c=0.1±0.0 nA
g=75 τ0=30.6±5.1ms τ1=40.7±2.1ms a=82.6±7.1nA χ²=4.3 ; σ=0.5 t0=105.4±0.3 ms c=0.5±0.1 nA
g=76 τ0=42.6±12.8ms τ1=33.4±2.4ms a=98.5±17.2nA χ²=1.0 ; σ=0.9 t0=105.2±0.3 ms c=0.2±0.0 nA
g=77 τ0=10.1±1.2ms τ1=50.5±2.3ms a=27.7±1.0nA χ²=1.1 ; σ=1.1 t0=113.1±0.4 ms c=0.4±0.1 nA
g=78 τ0=37.0±8.4ms τ1=33.3±2.0ms a=82.0±10.5nA χ²=0.9 ; σ=0.7 t0=105.2±0.2 ms c=-0.1±0.0 nA
g=79 τ0=16.0±1.8ms τ1=37.9±1.5ms a=43.0±2.0nA χ²=2.0 ; σ=0.6 t0=111.2±0.2 ms c=0.1±0.0 nA
I [nA]
Time [ms]

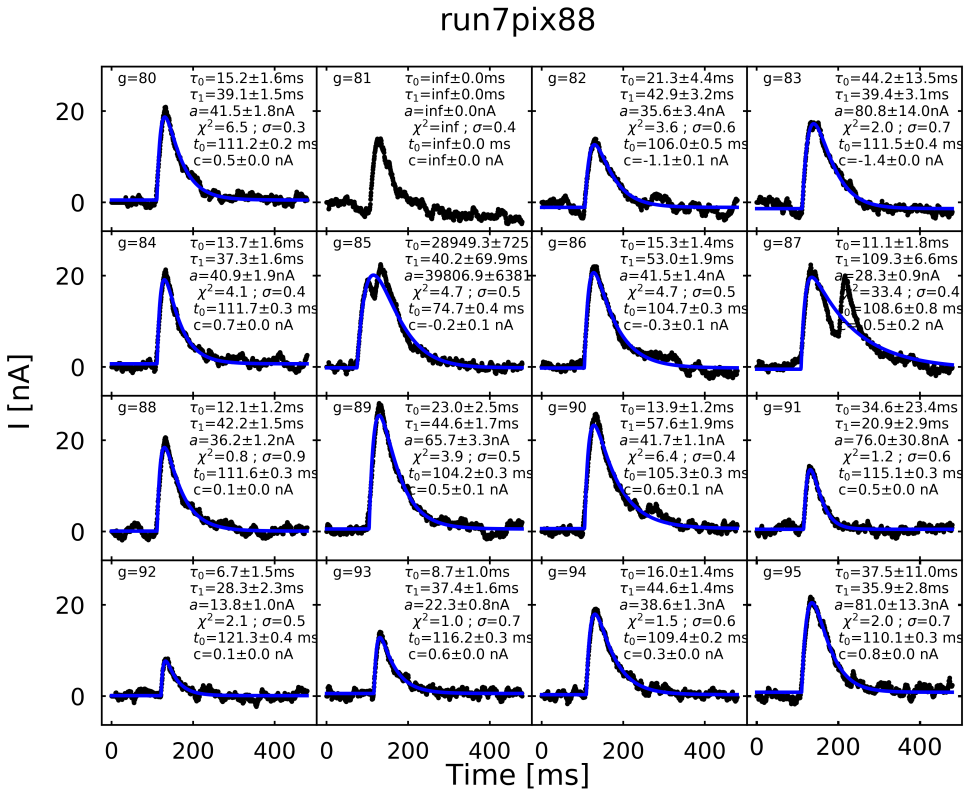
run7pix88
g=80 τ0=15.2±1.6ms τ1=39.1±1.5ms a=41.5±1.8nA χ²=6.5 ; σ=0.3 t0=111.2±0.2 ms c=0.5±0.0 nA
g=81 τ0=inf±0.0ms τ1=inf±0.0ms a=inf±0.0nA χ²=inf ; σ=0.4 t0=inf±0.0 ms c=inf±0.0 nA
g=82 τ0=21.3±4.4ms τ1=42.9±3.2ms a=35.6±3.4nA χ²=3.6 ; σ=0.6 t0=106.0±0.5 ms c=-1.1±0.1 nA
g=83 τ0=44.2±13.5ms τ1=39.4±3.1ms a=80.8±14.0nA χ²=2.0 ; σ=0.7 t0=111.5±0.4 ms c=-1.4±0.0 nA
g=84 τ0=13.7±1.6ms τ1=37.3±1.6ms a=40.9±1.9nA χ²=4.1 ; σ=0.4 t0=111.7±0.3 ms c=0.7±0.0 nA
g=85 τ0=28949.3±725 τ1=40.2±69.9ms a=39806.9±6381 χ²=4.7 ; σ=0.5 t0=74.7±0.4 ms c=-0.2±0.1 nA
g=86 τ0=15.3±1.4ms τ1=53.0±1.9ms a=41.5±1.4nA χ²=4.7 ; σ=0.5 t0=104.7±0.3 ms c=-0.3±0.1 nA
g=87 τ0=11.1±1.8ms τ1=109.3±6.6ms a=28.3±0.9nA χ²=33.4 ; σ=0.4 t0=108.6±0.8 ms c=0.5±0.2 nA
g=88 τ0=12.1±1.2ms τ1=42.2±1.5ms a=36.2±1.2nA χ²=0.8 ; σ=0.9 t0=111.6±0.3 ms c=0.1±0.0 nA
g=89 τ0=23.0±2.5ms τ1=44.6±1.7ms a=65.7±3.3nA χ²=3.9 ; σ=0.5 t0=104.2±0.3 ms c=0.5±0.1 nA
g=90 τ0=13.9±1.2ms τ1=57.6±1.9ms a=41.7±1.1nA χ²=6.4 ; σ=0.4 t0=105.3±0.3 ms c=0.6±0.1 nA
g=91 τ0=34.6±23.4ms τ1=20.9±2.9ms a=76.0±30.8nA χ²=1.2 ; σ=0.6 t0=115.1±0.3 ms c=0.5±0.0 nA
g=92 τ0=6.7±1.5ms τ1=28.3±2.3ms a=13.8±1.0nA χ²=2.1 ; σ=0.5 t0=121.3±0.4 ms c=0.1±0.0 nA
g=93 τ0=8.7±1.0ms τ1=37.4±1.6ms a=22.3±0.8nA χ²=1.0 ; σ=0.7 t0=116.2±0.3 ms c=0.6±0.0 nA
g=94 τ0=16.0±1.4ms τ1=44.6±1.4ms a=38.6±1.3nA χ²=1.5 ; σ=0.6 t0=109.4±0.2 ms c=0.3±0.0 nA
g=95 τ0=37.5±11.0ms τ1=35.9±2.8ms a=81.0±13.3nA χ²=2.0 ; σ=0.7 t0=110.1±0.3 ms c=0.8±0.0 nA
I [nA]
Time [ms]

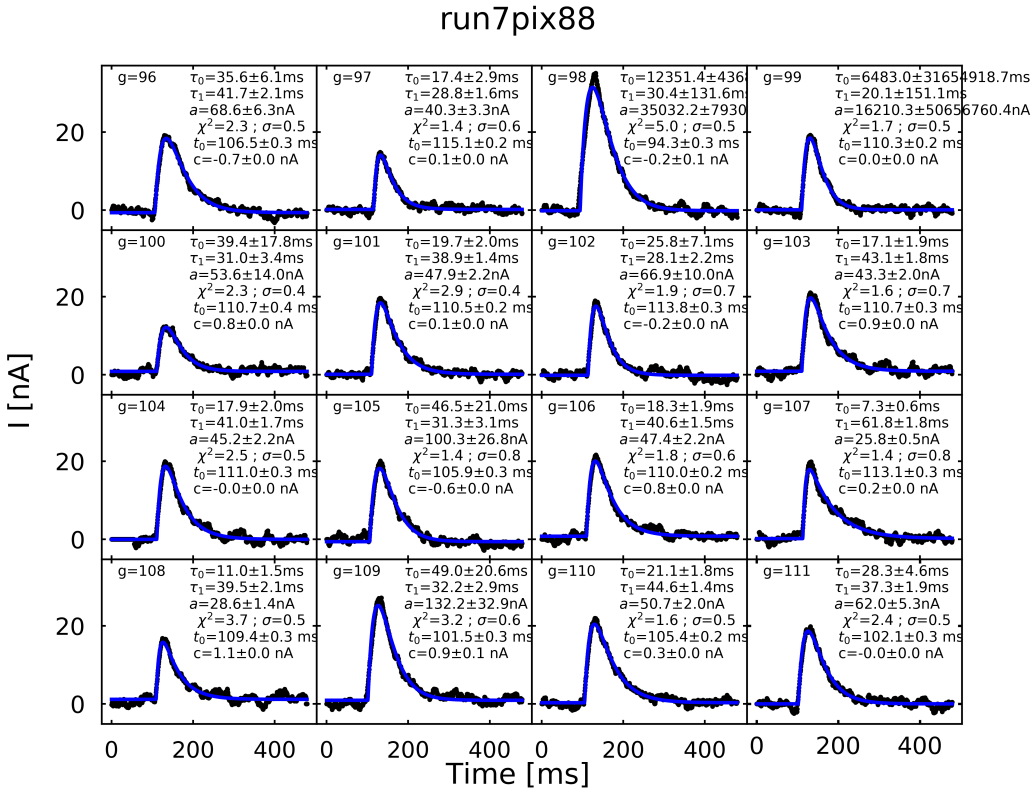
run7pix88
g=96 τ0=35.6±6.1ms τ1=41.7±2.1ms a=68.6±6.3nA χ²=2.3 ; σ=0.5 t0=106.5±0.3 ms c=-0.7±0.0 nA
g=97 τ0=17.4±2.9ms τ1=28.8±1.6ms a=40.3±3.3nA χ²=1.4 ; σ=0.6 t0=115.1±0.2 ms c=0.1±0.0 nA
g=98 τ0=12351.4±436 τ1=30.4±131.6m a=35032.2±7930 χ²=5.0 ; σ=0.5 t0=94.3±0.3 ms c=-0.2±0.1 nA
g=99 τ0=6483.0±31654918.7ms τ1=20.1±151.1ms a=16210.3±50656760.4nA χ²=1.7 ; σ=0.5 t0=110.3±0.2 ms c=0.0±0.0 nA
g=100 τ0=39.4±17.8ms τ1=31.0±3.4ms a=53.6±14.0nA χ²=2.3 ; σ=0.4 t0=110.7±0.4 ms c=0.8±0.0 nA
g=101 τ0=19.7±2.0ms τ1=38.9±1.4ms a=47.9±2.2nA χ²=2.9 ; σ=0.4 t0=110.5±0.2 ms c=0.1±0.0 nA
g=102 τ0=25.8±7.1ms τ1=28.1±2.2ms a=66.9±10.0nA χ²=1.9 ; σ=0.7 t0=113.8±0.3 ms c=-0.2±0.0 nA
g=103 τ0=17.1±1.9ms τ1=43.1±1.8ms a=43.3±2.0nA χ²=1.6 ; σ=0.7 t0=110.7±0.3 ms c=0.9±0.0 nA
g=104 τ0=17.9±2.0ms τ1=41.0±1.7ms a=45.2±2.2nA χ²=2.5 ; σ=0.5 t0=111.0±0.3 ms c=-0.0±0.0 nA
g=105 τ0=46.5±21.0ms τ1=31.3±3.1ms a=100.3±26.8nA χ²=1.4 ; σ=0.8 t0=105.9±0.3 ms c=-0.6±0.0 nA
g=106 τ0=18.3±1.9ms τ1=40.6±1.5ms a=47.4±2.2nA χ²=1.8 ; σ=0.6 t0=110.0±0.2 ms c=0.8±0.0 nA
g=107 τ0=7.3±0.6ms τ1=61.8±1.8ms a=25.8±0.5nA χ²=1.4 ; σ=0.8 t0=113.1±0.3 ms c=0.2±0.0 nA
g=108 τ0=11.0±1.5ms τ1=39.5±2.1ms a=28.6±1.4nA χ²=3.7 ; σ=0.5 t0=109.4±0.3 ms c=1.1±0.0 nA
g=109 τ0=49.0±20.6ms τ1=32.2±2.9ms a=132.2±32.9nA χ²=3.2 ; σ=0.6 t0=101.5±0.3 ms c=0.9±0.1 nA
g=110 τ0=21.1±1.8ms τ1=44.6±1.4ms a=50.7±2.0nA χ²=1.6 ; σ=0.5 t0=105.4±0.2 ms c=0.3±0.0 nA
g=111 τ0=28.3±4.6ms τ1=37.3±1.9ms a=62.0±5.3nA χ²=2.4 ; σ=0.5 t0=102.1±0.3 ms c=-0.0±0.0 nA
I [nA]
Time [ms]

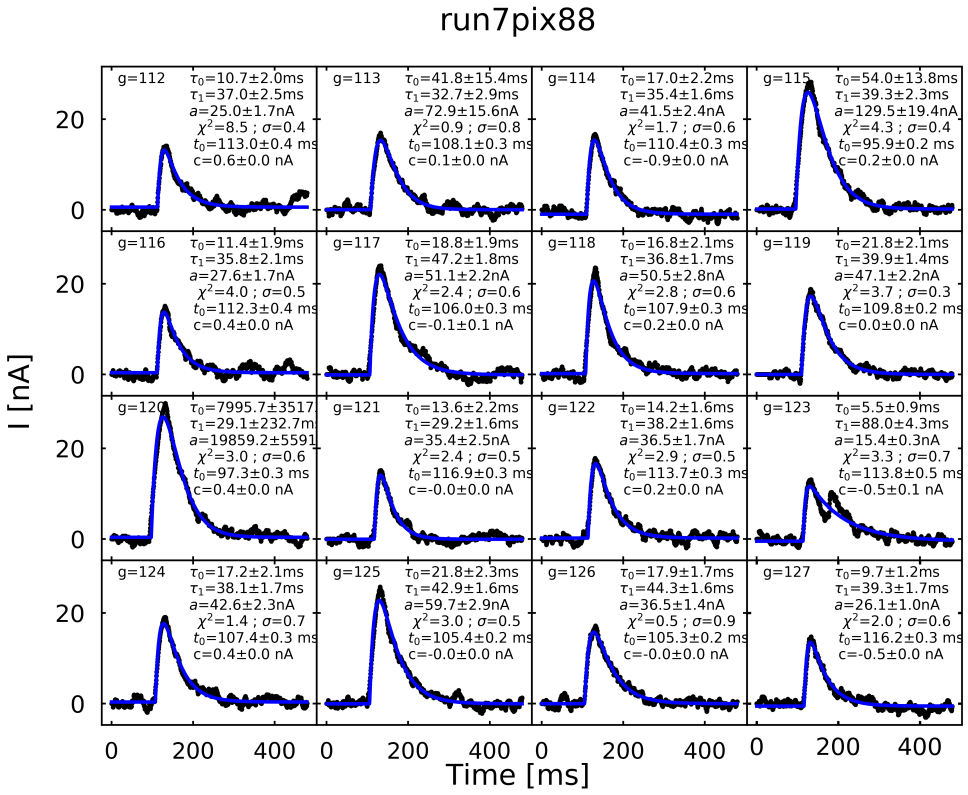
run7pix88
g=112 τ_0=10.7±2.0ms τ_1=37.0±2.5ms a=25.0±1.7nA χ^2=8.5 ; σ=0.4 t_0=113.0±0.4 ms c=0.6±0.0 nA
g=113 τ_0=41.8±15.4ms τ_1=32.7±2.9ms a=72.9±15.6nA χ^2=0.9 ; σ=0.8 t_0=108.1±0.3 ms c=0.1±0.0 nA
g=114 τ_0=17.0±2.2ms τ_1=35.4±1.6ms a=41.5±2.4nA χ^2=1.7 ; σ=0.6 t_0=110.4±0.3 ms c=-0.9±0.0 nA
g=115 τ_0=54.0±13.8ms τ_1=39.3±2.3ms a=129.5±19.4nA χ^2=4.3 ; σ=0.4 t_0=95.9±0.2 ms c=0.2±0.0 nA
g=116 τ_0=11.4±1.9ms τ_1=35.8±2.1ms a=27.6±1.7nA χ^2=4.0 ; σ=0.5 t_0=112.3±0.4 ms c=0.4±0.0 nA
g=117 τ_0=18.8±1.9ms τ_1=47.2±1.8ms a=51.1±2.2nA χ^2=2.4 ; σ=0.6 t_0=106.0±0.3 ms c=-0.1±0.1 nA
g=118 τ_0=16.8±2.1ms τ_1=36.8±1.7ms a=50.5±2.8nA χ^2=2.8 ; σ=0.6 t_0=107.9±0.3 ms c=0.2±0.0 nA
g=119 τ_0=21.8±2.1ms τ_1=39.9±1.4ms a=47.1±2.2nA χ^2=3.7 ; σ=0.3 t_0=109.8±0.2 ms c=0.0±0.0 nA
g=120 τ_0=7995.7±3517 τ_1=29.1±232.7m a=19859.2±5591 χ^2=3.0 ; σ=0.6 t_0=97.3±0.3 ms c=0.4±0.0 nA
g=121 τ_0=13.6±2.2ms τ_1=29.2±1.6ms a=35.4±2.5nA χ^2=2.4 ; σ=0.5 t_0=116.9±0.3 ms c=-0.0±0.0 nA
g=122 τ_0=14.2±1.6ms τ_1=38.2±1.6ms a=36.5±1.7nA χ^2=2.9 ; σ=0.5 t_0=113.7±0.3 ms c=0.2±0.0 nA
g=123 τ_0=5.5±0.9ms τ_1=88.0±4.3ms a=15.4±0.3nA χ^2=3.3 ; σ=0.7 t_0=113.8±0.5 ms c=-0.5±0.1 nA
g=124 τ_0=17.2±2.1ms τ_1=38.1±1.7ms a=42.6±2.3nA χ^2=1.4 ; σ=0.7 t_0=107.4±0.3 ms c=0.4±0.0 nA
g=125 τ_0=21.8±2.3ms τ_1=42.9±1.6ms a=59.7±2.9nA χ^2=3.0 ; σ=0.5 t_0=105.4±0.2 ms c=-0.0±0.0 nA
g=126 τ_0=17.9±1.7ms τ_1=44.3±1.6ms a=36.5±1.4nA χ^2=0.5 ; σ=0.9 t_0=105.3±0.2 ms c=-0.0±0.0 nA
g=127 τ_0=9.7±1.2ms τ_1=39.3±1.7ms a=26.1±1.0nA χ^2=2.0 ; σ=0.6 t_0=116.2±0.3 ms c=-0.5±0.0 nA
I [nA]
Time [ms]

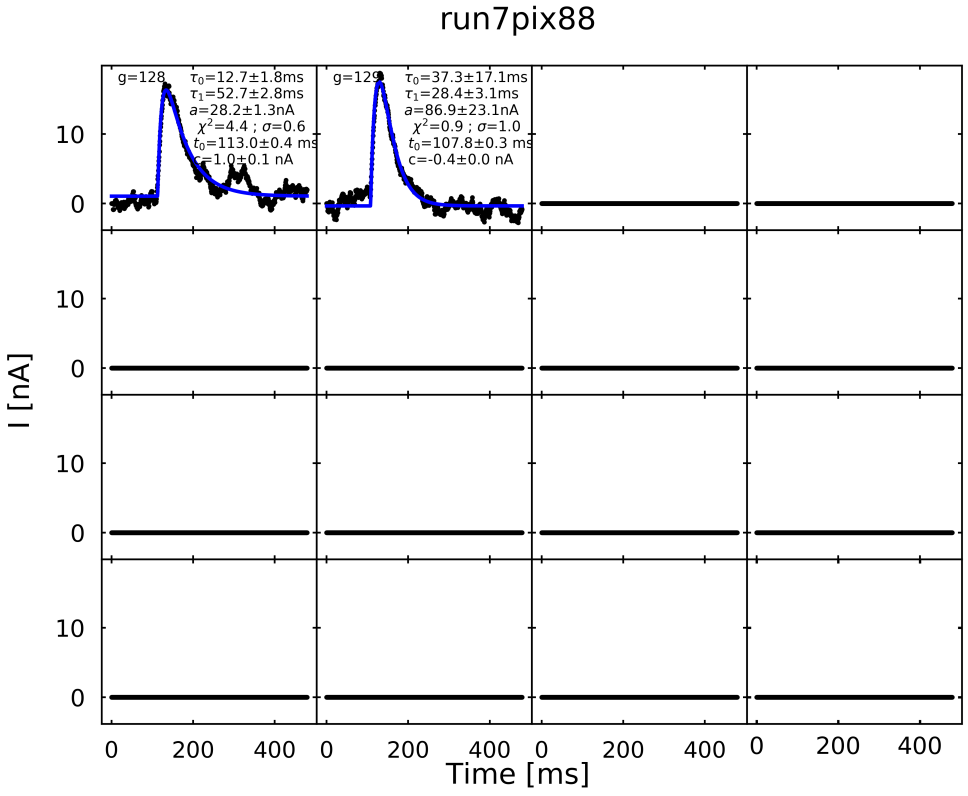
run7pix88
g=128 τ_0=12.7±1.8ms τ_1=52.7±2.8ms a=28.2±1.3nA χ^2=4.4 ; σ=0.6 t_0=113.0±0.4 ms c=1.0±0.1 nA
g=129 τ_0=37.3±17.1ms τ_1=28.4±3.1ms a=86.9±23.1nA χ^2=0.9 ; σ=1.0 t_0=107.8±0.3 ms c=-0.4±0.0 nA
I [nA]
Time [ms]

Bibliography

[1] *Mr.SQUID User's Guide.*

[2] *Low-noise electronic design.* John Wiley & Sons, Inc.

[3] *Triton 200/400.*

[4] The quantum theory of the electron. *Proceedings of the Royal Society of London A: Mathematical, Physical and Engineering Sciences*, 117(778):610–624, 1928. ISSN 0950-1207. doi: 10.1098/rspa.1928.0023. URL http://rspa.royalsocietypublishing.org/content/117/778/610.

[5] *Principles of physical cosmology.* Princeton University Press, 1993.

[6] *Introduction to superconductivity.* McGraw-Hill, Inc, 1996.

[7] *Modern cosmology.* Academic Press, 2003.

[8] *Primordial Cosmology.* Oxford University Press, 2009.

[9] *Observational cosmology.* Cambridde University Press, 2010.

[10] Mark Aartsen and et al. Neutrino emission from the direction of the blazar txs 0506+056 prior to the icecube-170922a alert. *Science*, 361(6398):147–151, 2018. ISSN 0036-8075. doi: 10.1126/science.aat2890. URL http://science.sciencemag.org/content/361/6398/147.

[11] B. P. et al. Abbott. Observation of gravitational waves from a binary black hole merger. *Phys. Rev. Lett.*, 116:061102, Feb 2016. doi: 10.1103/PhysRevLett.116.061102. URL https://link.aps.org/doi/10.1103/PhysRevLett.116.061102.

[12] R. A. Alpher, H. Bethe, and G. Gamow. The origin of chemical elements. *Phys. Rev.*, 73:803–804, Apr 1948. doi: 10.1103/PhysRev.73.803. URL https://link.aps.org/doi/10.1103/PhysRev.73.803.

[13] Lauren Anderson and et al. The clustering of galaxies in the sdss-iii baryon oscillation spectroscopic survey: baryon acoustic oscillations in the data releases 10 and 11 galaxy samples. *Monthly Notices of the Royal Astronomical Society*, 441(1):24–62, 2014. doi: 10.1093/mnras/stu523. URL http://dx.doi.org/10.1093/mnras/stu523.

[14] R. Banerji, G. Patanchon, M. Bucher, T. Matsumura, D.T. Hoang, H. Ishino, M. Hazumi, and J. Delabrouille. Bandpass mismatch error for satellite CMB experiments II: Correcting the spurious signal. *In preparation.*

[15] J. Bardeen, L. N. Cooper, and J. R. Schrieffer. Microscopic theory of superconductivity. *Phys. Rev.*, 106:162–164, Apr 1957. doi: 10.1103/PhysRev.106.162. URL https://link.aps.org/doi/10.1103/PhysRev.106.162.

[16] D. Baumann. TASI Lectures on Primordial Cosmology. *ArXiv e-prints*, July 2018.

[17] Daniel Baumann. Cosmology Part III Mathematical Tripos. URL: http://www.damtp.cam.ac.uk/user/db275/Cosmology/Lectures.pdf.

[18] Daniel Baumann. Inflation. In *Physics of the large and the small, TASI 09, proceedings of the Theoretical Advanced Study Institute in Elementary Particle Physics, Boulder, Colorado, USA, 1-26 June 2009*, pages 523–686, 2011. doi: 10.1142/9789814327183_0010. URL https://inspirehep.net/record/827549/files/arXiv:0907.5424.pdf.

[19] D. A. Bennett, R. D. Horansky, A. S. Hoover, N. J. Hoteling, M. W. Rabin, D. R. Schmidt, D. S. Swetz, L. R. Vale, and J. N. Ullom. An analytical model for pulse shape and electrothermal stability in two-body transition-edge sensor microcalorimeters. *Applied Physics Letters*, 97(10):102504, 2010. doi: 10.1063/1.3486477. URL https://doi.org/10.1063/1.3486477.

[20] BICEP2/Keck and Planck Collaborations. Joint Analysis of BICEP2/Keck Array and Planck Data. *Phys. Rev. Lett.*, 114(10):101301, March 2015. doi: 10.1103/PhysRevLett.114.101301.

[21] Bigot Sazy, M. A., Charlassier, R., Hamilton, J. Ch., Kaplan, J., and Zahariade, G. Self-calibration: an efficient method to control systematic effects in bolometric interferometry. *A&A*, 550:A59, 2013. doi: 10.1051/0004-6361/201220429. URL https://doi.org/10.1051/0004-6361/201220429.

[22] J. Bock, S. Church, M. Devlin, G. Hinshaw, A. Lange, A. Lee, L. Page, B. Partridge, J. Ruhl, M. Tegmark, P. Timbie, R. Weiss, B. Winstein, and M. Zaldarriaga. Task Force on Cosmic Microwave Background Research. *ArXiv Astrophysics e-prints*, April 2006. URL http://arxiv.org/abs/astro-ph/0604101.

[23] Jennifer Anne Burney. *Transition-Edge sensor imaging arrays for astrophysics applications*. PhD thesis, The department of physics, Stanford University, 2006.

[24] P. Cabella and M. Kamionkowski. Theory of Cosmic Microwave Background Polarization. *ArXiv Astrophysics e-prints*, March 2004.

[25] P. Cabella and M. Kamionkowski. Theory of Cosmic Microwave Background Polarization. *ArXiv Astrophysics e-prints*, March 2004. URL http://adsabs.harvard.edu/abs/2004astro.ph..3392C.

[26] M. Chiara Guzzetti, N. Bartolo, M. Liguori, and S. Matarrese. Gravitational waves from inflation. *ArXiv e-prints*, May 2016.

[27] J. Chluba. Science with CMB spectral distortions. *ArXiv e-prints*, May 2014.

[28] J. Chluba and R. A. Sunyaev. The evolution of cmb spectral distortions in the early universe. *Monthly Notices of the Royal Astronomical Society*, 419 (2):1294–1314, 2012. doi: 10.1111/j.1365-2966.2011.19786.x. URL http://dx.doi.org/10.1111/j.1365-2966.2011.19786.x.

[29] Jens Chluba. *Spectral Distortions of the Cosmic Microwave Background*. PhD thesis, der Fakultät für Physik der Ludwig, Maximilians-Universität München, 2005.

[30] QUBIC collaboration. Qubic: The qu bolometric interferometer for cosmology. *Astroparticle Physics*, 34(9):705 – 716, 2011. ISSN 0927-6505. doi: https://doi.org/10.1016/j.astropartphys.2011.01.012. URL http://www.sciencedirect.com/science/article/pii/S0927650511000223.

[31] QUBIC collaboration. QUBIC Technical Design Report. *ArXiv e-prints*, September 2016.

[32] CORE Collaboration. Exploring Cosmic Origins with CORE: The CORE mission. *JCAP, in preparation*.

[33] F. Couchot, J. Delabrouille, J. Kaplan, and B. Revenu. Optimised polarimeter configurations for measuring the Stokes parameters of the cosmic microwave background radiation. *aaps*, 135:579–584, March 1999. doi: 10.1051/aas:1999191.

[34] J. Delabrouille and et al. The pre-launch Planck Sky Model: a model of sky emission at submillimetre to centimetre wavelengths. *aap*, 553:A96, May 2013. doi: 10.1051/0004-6361/201220019.

[35] J. Delabrouille and et al. Exploring cosmic origins with core: Survey requirements and mission design. *Journal of Cosmology and Astroparticle Physics*, 2018(04):014, 2018. URL http://stacks.iop.org/1475-7516/2018/i=04/a=014.

[36] J. Delabrouille, J.F. Cardoso, and G. Patanchon. Multidetector multicomponent spectral matching and applications for cosmic microwave background data analysis. *Monthly Notices of the Royal Astronomical Society*, 346(4):1089–1102, 2003. doi: 10.1111/j.1365-2966.2003.07069.x. URL http://dx.doi.org/10.1111/j.1365-2966.2003.07069.x.

[37] Delabrouille, J., Cardoso, J.F., Le Jeune, M., Betoule, M., Fay, G., and Guilloux, F. A full sky, low foreground, high resolution cmb map from wmap. *A&A*, 493(3):835–857, 2009. doi: 10.1051/0004-6361:200810514. URL https://doi.org/10.1051/0004-6361:200810514.

[38] C. Dickinson. CMB foregrounds - A brief review. *ArXiv e-prints*, June 2016.

[39] B. T. Draine and A. Lazarian. Electric dipole radiation from spinning dust grains. *The Astrophysical Journal*, 508(1):157, 1998. URL http://stacks.iop.org/0004-637X/508/i=1/a=157.

[40] Apt. 1627 Mountain View CA 94040) Duhamel, Raymond H. (707 Continental Circle. Dual polarized sinuous antennas, April 1987. URL http://www.freepatentsonline.com/4658262.html.

[41] Albert Einstein. Cosmological Considerations in the General Theory of Relativity. *Sitzungsber. Preuss. Akad. Wiss. Berlin (Math. Phys.)*, 1917:142–152, 1917.

[42] H. K. Eriksen, J. B. Jewell, C. Dickinson, A. J. Banday, K. M. Górski, and C. R. Lawrence. Joint bayesian component separation and cmb power

spectrum estimation. *The Astrophysical Journal*, 676(1):10, 2008. URL http://stacks.iop.org/0004-637X/676/i=1/a=10.

[43] Johannes Hubmayr et al. Design of 280 ghz feedhorn-coupled tes arrays for the balloon-borne polarimeter spider, 2016. URL https://doi.org/10.1117/12.2231896.

[44] Leach, S. M. et al. Component separation methods for the planck mission. *A&A*, 491(2):597–615, 2008. doi: 10.1051/0004-6361:200810116. URL https://doi.org/10.1051/0004-6361:200810116.

[45] M. Hazumi et al. Litebird: a small satellite for the study of b-mode polarization and inflation from cosmic background radiation detection, 2012. URL https://doi.org/10.1117/12.926743.

[46] K. M. Górski, E. Hivon, A. J. Banday, B. D. Wandelt, F. K. Hansen, M. Reinecke, and M. Bartelmann. HEALPix: A Framework for High-Resolution Discretization and Fast Analysis of Data Distributed on the Sphere. *apj*, 622:759–771, April 2005. doi: 10.1086/427976.

[47] Alan H. Guth. Inflationary universe: A possible solution to the horizon and flatness problems. *Phys. Rev. D*, 23:347–356, Jan 1981. doi: 10.1103/PhysRevD.23.347. URL https://link.aps.org/doi/10.1103/PhysRevD.23.347.

[48] Antti Hamalainen. Cosmic perturbation theory and inflation. Master's thesis, University of Jyvaskyla, 2015.

[49] Duncan Hanson, Antony Lewis, and Anthony Challinor. Asymmetric beams and cmb statistical anisotropy. *Phys. Rev. D*, 81:103003, May 2010. doi: 10.1103/PhysRevD.81.103003. URL https://link.aps.org/doi/10.1103/PhysRevD.81.103003.

[50] Duc Thuong Hoang, Guillaume Patanchon, Martin Bucher, Tomotake Matsumura, Ranajoy Banerji, Hirokazu Ishino, Masashi Hazumi, and Jacques Delabrouille. Bandpass mismatch error for satellite cmb experiments i: estimating the spurious signal. *Journal of Cosmology and Astroparticle Physics*, 2017(12):015, 2017. URL http://stacks.iop.org/1475-7516/2017/i=12/a=015.

[51] W. Hu. Wandering in the Background: A CMB Explorer. *ArXiv Astrophysics e-prints*, August 1995.

[52] W. Hu and S. Dodelson. Cosmic Microwave Background Anisotropies. *araa*, 40:171–216, 2002. doi: 10.1146/annurev.astro.40.060401.093926.

[53] Wayne Hu. Weak lensing of the cmb: A harmonic approach. *Phys. Rev. D*, 62:043007, Jul 2000. doi: 10.1103/PhysRevD.62.043007. URL https://link.aps.org/doi/10.1103/PhysRevD.62.043007.

[54] Wayne Hu. Cmb temperature and polarization anisotropy fundamentals. *Annals of Physics*, 303(1):203 – 225, 2003. ISSN 0003-4916. doi: https://doi.org/10.1016/S0003-4916(02)00022-2. URL http://www.sciencedirect.com/science/article/pii/S0003491602000222.

[55] Wayne Hu and Takemi Okamoto. Mass reconstruction with cosmic microwave background polarization. *The Astrophysical Journal*, 574(2):566, 2002. URL http://stacks.iop.org/0004-637X/574/i=2/a=566.

[56] Wayne Hu and Naoshi Sugiyama. Toward understanding cmb anisotropies and their implications. *Phys. Rev. D*, 51:2599–2630, Mar 1995. doi: 10.1103/PhysRevD.51.2599. URL https://link.aps.org/doi/10.1103/PhysRevD.51.2599.

[57] Wayne Hu and Martin White. A cmb polarization primer. *New Astronomy*, 2(4):323 – 344, 1997. ISSN 1384-1076. doi: https://doi.org/10.1016/S1384-1076(97)00022-5. URL http://www.sciencedirect.com/science/article/pii/S1384107697000225.

[58] E. Hubble. A Relation between Distance and Radial Velocity among Extra-Galactic Nebulae. *Proceedings of the National Academy of Science*, 15:168–173, March 1929. doi: 10.1073/pnas.15.3.168.

[59] J. Hubmayr, J. Austermann, J. Beall, D. Becker, H. M. Cho, R. Datta, S. M. Duff, E. Grace, N. Halverson, S. W. Henderson, G. C. Hilton, S. P. Ho, K. D. Irwin, B. J. Koopman, D. Li, J. Mcmahon, C. Munson, M. D. Niemack, C. Pappas, B. L. Schmitt, S. M. Simon, S. T. Staggs, J. Van Lanen, and E. Wollack. Feedhorn-coupled transition-edge superconducting bolometer arrays for cosmic microwave background polarimetry. 1 2015. 26th International Symposium on Space Terahertz Technology, ISSTT 2015 ; Conference date: 16-03-2015 Through 18-03-2015.

[60] Kiyotomo Ichiki. Cmb foreground: A concise review. *Progress of Theoretical and Experimental Physics*, 2014(6):06B109, 2014. doi: 10.1093/ptep/ptu065. URL http://dx.doi.org/10.1093/ptep/ptu065.

[61] K.D. Irwin and G.C. Hilton. *Transition-Edge Sensors*, pages 63–150. Springer Berlin Heidelberg, Berlin, Heidelberg, 2005. ISBN 978-3-540-31478-3. doi: 10.1007/10933596_3. URL https://doi.org/10.1007/10933596_3.

[62] H. Ishino and et al. Litebird: lite satellite for the study of b-mode polarization and inflation from cosmic microwave background radiation detection. *Proc. SPIE*, 9904:99040X–99040X–8, 2016. doi: 10.1117/12.2231995. URL http://dx.doi.org/10.1117/12.2231995.

[63] N. Jarosik, C. Barnes, M. R. Greason, R. S. Hill, M. R. Nolta, N. Odegard, J. L. Weiland, R. Bean, C. L. Bennett, O. Doré, M. Halpern, G. Hinshaw, A. Kogut, E. Komatsu, M. Limon, S. S. Meyer, L. Page, D. N. Spergel, G. S. Tucker, E. Wollack, and E. L. Wright. Three-Year Wilkinson Microwave Anisotropy Probe (WMAP) Observations: Beam Profiles, Data Processing, Radiometer Characterization, and Systematic Error Limits. *apjs*, 170:263–287, June 2007. doi: 10.1086/513697.

[64] Marc Kamionkowski and Ely D. Kovetz. The quest for b modes from inflationary gravitational waves. *Annual Review of Astronomy and Astrophysics*, 54(1):227–269, 2016. doi: 10.1146/annurev-astro-081915-023433. URL https://doi.org/10.1146/annurev-astro-081915-023433.

[65] A. R. Kerr. Surface impedance of superconductors and normal conductors in em simulators. Technical report, National Radio Astronomy Observatory, 1999.

[66] W. H. Kinney. TASI Lectures on Inflation. *ArXiv e-prints*, February 2009.

[67] Alan Kogut, Jens Chluba, Dale J. Fixsen, Stephan Meyer, and David Spergel. The primordial inflation explorer (PIXIE). *Proc. SPIE*, 9904: 99040W–99040W–23, 2016. doi: 10.1117/12.2231090.

[68] Hannu Kurki-Suonio. Cosmological Perturbation Theory. URL: http://www.helsinki.fi/~hkurkisu/CosPer.pdf.

[69] A T Lee, J M Gildemeister, S F Lee, and P L Richards. Voltage-biased superconducting bolometers for IR and mm-wave astronomy. 1997. URL http://cds.cern.ch/record/868426.

[70] Shih-Fu Lee, Jan M. Gildemeister, Warren Holmes, Adrian T. Lee, and Paul L. Richards. Voltage-biased superconducting transition-edge bolometer with strong electrothermal feedback operated at 370 mk. *Appl. Opt.*, 37(16): 3391–3397, Jun 1998. doi: 10.1364/AO.37.003391. URL http://ao.osa.org/abstract.cfm?URI=ao-37-16-3391.

[71] Andrew R. Liddle. *An introduction to modern cosmology*. 1998.

[72] Andrew R. Liddle and D. H. Lyth. *Cosmological inflation and large scale structure*. 2000. ISBN 0521575982, 9780521575980, 9780521828499.

[73] LiteBIRD Collaboration. LiteBIRD Concept Design Report. *in preparation*.

[74] David H. Lyth. What would we learn by detecting a gravitational wave signal in the cosmic microwave background anisotropy? *Phys. Rev. Lett.*, 78:1861–1863, Mar 1997. doi: 10.1103/PhysRevLett.78.1861. URL https://link.aps.org/doi/10.1103/PhysRevLett.78.1861.

[75] Juan Maldacena. Non-gaussian features of primordial fluctuations in single field inflationary models. *Journal of High Energy Physics*, 2003(05):013, 2003. URL http://stacks.iop.org/1126-6708/2003/i=05/a=013.

[76] Joseph Martino. *Développement d'une chaine de détection bolométrique supraconductrice pour la mesure de la polarisation du Fond Diffus Cosmologique*. PhD thesis, Université de Paris 7 - Denis Diderot, 2013.

[77] John C. Mather. Bolometer noise: nonequilibrium theory. *Appl. Opt.*, 21(6): 1125–1129, Mar 1982. doi: 10.1364/AO.21.001125. URL http://ao.osa.org/abstract.cfm?URI=ao-21-6-1125.

[78] T. Matsumura and et al. Mission Design of LiteBIRD. *J. Low Temp. Phys.*, 176:733–740, September 2014. doi: 10.1007/s10909-013-0996-1.

[79] T. Matsumura et al. LiteBIRD: Mission Overview and Focal Plane Layout. *J. Low. Temp. Phys.*, 184(3-4):824–831, 2016. doi: 10.1007/s10909-016-1542-8.

[80] Tomotake Matsumura, Shaul Hanany, Peter Ade, Bradley R. Johnson, Terry J. Jones, Prashanth Jonnalagadda, and Giorgio Savini. Performance of

three- and five-stack achromatic half-wave plates at millimeter wavelengths. *Appl. Opt.*, 48(19):3614–3625, Jul 2009. doi: 10.1364/AO.48.003614. URL http://ao.osa.org/abstract.cfm?URI=ao-48-19-3614.

[81] J. McMahon, J. W. Appel, J. E. Austermann, J. A. Beall, D. Becker, B. A. Benson, L. E. Bleem, J. Britton, C. L. Chang, J. E. Carlstrom, H. M. Cho, A. T. Crites, T. Essinger Hileman, W. Everett, N. W. Halverson, J. W. Henning, G. C. Hilton, K. D. Irwin, J. Mehl, S. S. Meyer, S. Mossley, M. D. Niemack, L. P. Parker, S. M. Simon, S. T. Staggs, C. Visnjic, E. Wollack, K. U. Yen, K. W. Yoon, and Y. Zhao. Planar orthomode transducers for feedhorn-coupled tes polarimeters. *AIP Conference Proceedings*, 1185(1): 490–493, 2009. doi: 10.1063/1.3292386. URL https://aip.scitation.org/doi/abs/10.1063/1.3292386.

[82] J. McMahon, J. Beall, D. Becker, H.M. Cho, R. Datta, A. Fox, N. Halverson, J. Hubmayr, K. Irwin, J. Nibarger, M. Niemack, and H. Smith. Multi-chroic Feed-Horn Coupled TES Polarimeters. *Journal of Low Temperature Physics*, 167:879–884, June 2012. doi: 10.1007/s10909-012-0612-9.

[83] Melia, F. Angular correlation of the cosmic microwave background in the rh = ct universe. *A&A*, 561:A80, 2014. doi: 10.1051/0004-6361/201322285. URL https://doi.org/10.1051/0004-6361/201322285.

[84] A. et al. Mennella. QUBIC - The Q&U Bolometric Interferometer for Cosmology - A novel way to look at the polarized Cosmic Microwave Background. *ArXiv e-prints*, January 2018.

[85] B. Bélier A. Benoit L. Bergé A. Bounab E. Bréelle P. Camus S. Collin F. X. Désert L. Dumoulin C. Evesque H. Geoffray M. Giard C. Hoffmann Y. Jin G. Klisnick S. Marnieros A. Monfardini F. Pajot D. Prêle M. Redon D. Santos D. Stanescu G. Sou F. Voisin Michel Piat, Y. Atik. Bolometer arrays development in the dcmb french collaboration, 2008. URL https://doi.org/10.1117/12.789703.

[86] Y. Mnyukh and V. Vodyanoy. Superconducting State and Phase Transitions. *ArXiv e-prints*, July 2016.

[87] M. D. Niemack, J. Beall, D. Becker, H.M. Cho, A. Fox, G. Hilton, J. Hubmayr, K. Irwin, D. Li, J. McMahon, J. Nibarger, and J. Van Lanen. Optimizing feedhorn-coupled tes polarimeters for balloon and space-based cmb

observations. *Journal of Low Temperature Physics*, 167(5):917–922, Jun 2012. ISSN 1573-7357. doi: 10.1007/s10909-012-0554-2. URL https://doi.org/10.1007/s10909-012-0554-2.

[88] Daniel O'Dea, Anthony Challinor, and Bradley R. Johnson. Systematic errors in cosmic microwave background polarization measurements. *Monthly Notices of the Royal Astronomical Society*, 376(4):1767–1783, 2007. doi: 10.1111/j.1365-2966.2007.11558.x. URL http://dx.doi.org/10.1111/j.1365-2966.2007.11558.x.

[89] H. Kamerlingh Onnes. Leiden comm. 120b, 122b, 124c. 1911.

[90] Francesco Paci. *Gravitational Waves and Cosmic Microwave Anisotropies: from theory to data analysis for Planck*. PhD thesis, Universitá degli Studi di Bologna, 2009.

[91] J. A. Peacock. Large-scale surveys and cosmic structure. *ArXiv Astrophysics e-prints*, September 2003.

[92] A. A. Penzias and R. W. Wilson. A Measurement of Excess Antenna Temperature at 4080 Mc/s. *apj*, 142:419–421, July 1965. doi: 10.1086/148307.

[93] C. Perbost, S. Marnieros, B. Bélier, M. Piat, D. Prêle, F. Voisin, and T. Decourcelle. A 256-tes array for the detection of cmb b-mode polarisation. *Journal of Low Temperature Physics*, 184(3):793–798, Aug 2016. doi: 10.1007/s10909-016-1586-9. URL https://doi.org/10.1007/s10909-016-1586-9.

[94] Camille Perbost. *Matrices de bolomètres supraconducteurs pour la mesure de la polarisation du fond diffus cosmologique : application à léxpérience QUBIC*. PhD thesis, Université de Paris 7 - Denis Diderot, 2016.

[95] Saul Perlmutter. Supernovae, dark energy, and the accelerating universe. *Physics Today*, 56(4):53–60, 2003. doi: 10.1063/1.1580050. URL https://doi.org/10.1063/1.1580050.

[96] Planck Collaboration. Planck early results. xxv. thermal dust in nearby molecular clouds. *A&A*, 536:A25, 2011. doi: 10.1051/0004-6361/201116483. URL https://doi.org/10.1051/0004-6361/201116483.

[97] Planck Collaboration. Planck 2013 results. XIII. Galactic CO emission. *aap*, 571:A13, November 2014. doi: 10.1051/0004-6361/201321553.

[98] Planck Collaboration. Planck 2013 results. XI. All-sky model of thermal dust emission. *aap*, 571:A11, November 2014. doi: 10.1051/0004-6361/201323195.

[99] Planck Collaboration. Planck 2013 results. IX. HFI spectral response. *aap*, 571:A9, November 2014. doi: 10.1051/0004-6361/201321531.

[100] Planck Collaboration. Planck 2013 results. x. hfi energetic particle effects: characterization, removal, and simulation. *A&A*, 571:A10, 2014. doi: 10.1051/0004-6361/201321577. URL https://doi.org/10.1051/0004-6361/201321577.

[101] Planck Collaboration. Planck 2013 results. xi. all-sky model of thermal dust emission. *A&A*, 571:A11, 2014. doi: 10.1051/0004-6361/201323195. URL https://doi.org/10.1051/0004-6361/201323195.

[102] Planck Collaboration. Planck intermediate results. XXII. Frequency dependence of thermal emission from Galactic dust in intensity and polarization. *aap*, 576:A107, April 2015. doi: 10.1051/0004-6361/201424088.

[103] Planck Collaboration. Planck intermediate results. XLVI. Reduction of large-scale systematic effects in HFI polarization maps and estimation of the reionization optical depth. *aap*, 596:A107, December 2016. doi: 10.1051/0004-6361/201628890.

[104] Planck Collaboration. Planck 2015 results. X. Diffuse component separation: Foreground maps. *aap*, 594:A10, September 2016. doi: 10.1051/0004-6361/201525967.

[105] Planck Collaboration. Planck 2015 results - i. overview of products and scientific results. *A&A*, 594:A1, 2016. doi: 10.1051/0004-6361/201527101. URL https://doi.org/10.1051/0004-6361/201527101.

[106] Planck Collaboration. Planck 2015 results - x. diffuse component separation: Foreground maps. *A&A*, 594:A10, 2016. doi: 10.1051/0004-6361/201525967. URL https://doi.org/10.1051/0004-6361/201525967.

[107] Planck Collaboration. Planck 2015 results - iv. low frequency instrument beams and window functions. *A&A*, 594:A4, 2016. doi: 10.1051/0004-6361/201525809. URL https://doi.org/10.1051/0004-6361/201525809.

[108] Planck Collaboration. Planck 2015 results - iii. lfi systematic uncertainties. *A&A*, 594:A3, 2016. doi: 10.1051/0004-6361/201526998. URL https://doi.org/10.1051/0004-6361/201526998.

[109] Planck Collaboration. Planck 2015 results - xx. constraints on inflation. *A&A*, 594:A20, 2016. doi: 10.1051/0004-6361/201525898. URL https://doi.org/10.1051/0004-6361/201525898.

[110] Planck Collaboration. Planck 2015 results - xiii. cosmological parameters. *A&A*, 594:A13, 2016. doi: 10.1051/0004-6361/201525830. URL https://doi.org/10.1051/0004-6361/201525830.

[111] Planck Collaboration. Planck intermediate results - xlvi. reduction of large-scale systematic effects in hfi polarization maps and estimation of the reionization optical depth. *A&A*, 596:A107, 2016. doi: 10.1051/0004-6361/201628890. URL https://doi.org/10.1051/0004-6361/201628890.

[112] Planck Collaboration. Planck 2018 results. IV. Diffuse component separation. *ArXiv e-prints*, July 2018.

[113] Planck Collaboration. Planck 2018 results. I. Overview and the cosmological legacy of Planck. *ArXiv e-prints*, July 2018.

[114] Planck Collaboration. Planck 2018 results. XI. Polarized dust foregrounds. *ArXiv e-prints*, January 2018.

[115] Planck Collaboration. Planck 2018 results. XII. Galactic astrophysics using polarized dust emission. *ArXiv e-prints*, July 2018.

[116] Planck Collaboration. Planck 2018 results. VI. Cosmological parameters. *ArXiv e-prints*, July 2018.

[117] Planck Collaboration. Planck 2018 results. IV. Diffuse component separation. *ArXiv e-prints*, July 2018.

[118] Planck Collaboration. Planck 2018 results. X. Constraints on inflation. *ArXiv e-prints*, July 2018.

[119] Planck Collaboration, P. A. R. Ade, N. Aghanim, C. Armitage-Caplan, M. Arnaud, M. Ashdown, F. Atrio-Barandela, J. Aumont, C. Baccigalupi,

A. J. Banday, and et al. Planck 2015 results - xiii. cosmological parameters. *A&A*, 594:A13, 2016. doi: 10.1051/0004-6361/201525830. URL https://doi.org/10.1051/0004-6361/201525830.

[120] Planck Collaboration 2013GPlanck Collaboration VII. Planck 2013 results. vii. hfi time response and beams. *A&A*, 571:A7, 2014. doi: 10.1051/0004-6361/201321535. URL https://doi.org/10.1051/0004-6361/201321535.

[121] D. Prele. Front-end multiplexing—applied to squid multiplexing: Athena x-ifu and qubic experiments. *Journal of Instrumentation*, 10(08):C08015, 2015. URL http://stacks.iop.org/1748-0221/10/i=08/a=C08015.

[122] D. Prêle, M. Piat, L. Sipile, and F. Voisin. Operating point and flux jumps of a squid in flux-locked loop. *IEEE Transactions on Applied Superconductivity*, 26(2):1–5, March 2016. ISSN 1051-8223. doi: 10.1109/TASC.2015.2510606.

[123] D. Prêle, F. Voisin, M. Piat, T. Decourcelle, C. Perbost, C. Chapron, D. Rambaud, S. Maestre, W. Marty, and L. Montier. A 128 multiplexing factor time-domain squid multiplexer. *Journal of Low Temperature Physics*, 184(1):363–368, Jul 2016. ISSN 1573-7357. doi: 10.1007/s10909-015-1449-9. URL https://doi.org/10.1007/s10909-015-1449-9.

[124] D. Prêle, F. Voisin, C. Beillimaz, S. Chen, M. Piat, A. Goldwurm, and P. Laurent. Sige integrated circuit developments for squid/tes readout. *Journal of Low Temperature Physics*, Mar 2018. doi: 10.1007/s10909-018-1886-3. URL https://doi.org/10.1007/s10909-018-1886-3.

[125] Damien Prêle. Les détecteurs tes principes et technologie. URL: http://www-ecole-drtbt.neel.cnrs.fr/userfiles/file/drtbt2012/TES_DRTBT_Prele_v2.pdf.

[126] D. D. Reid, D. W. Kittell, E. E. Arsznov, and G. B. Thompson. The picture of our universe: A view from modern cosmology. *ArXiv Astrophysics e-prints*, September 2002.

[127] Mathieu Remazeilles, Jacques Delabrouille, and Jean-François Cardoso. Cmb and sz effect separation with constrained internal linear combinations. *Monthly Notices of the Royal Astronomical Society*, 410(4):2481–2487, 2011. doi: 10.1111/j.1365-2966.2010.17624.x. URL http://dx.doi.org/10.1111/j.1365-2966.2010.17624.x.

[128] Righi, M., Hernández-Monteagudo, C., and Sunyaev, R. A. Carbon monoxide line emission as a cmb foreground: tomography of the star-forming universe with different spectral resolutions. *A&A*, 489(2):489–504, 2008. doi: 10.1051/0004-6361:200810199. URL https://doi.org/10.1051/0004-6361:200810199.

[129] Barbara Ryden. *Introduction to Cosmology*. Department of Astronomy, The Ohio State University.

[130] R. K. Sachs and A. M. Wolfe. Perturbations of a Cosmological Model and Angular Variations of the Microwave Background. *apj*, 147:73, January 1967. doi: 10.1086/148982.

[131] M. Salatino, B. Bélier, C. Chapron, D. T. Hoang, S. Maestre, et al. Performance of NbSi transition-edge sensors readout with a 128 MUX factor for the QUBIC experiment. *Proc. SPIE Int. Soc. Opt. Eng.*, 10708:1070845, 2018. doi: 10.1117/12.2312080.

[132] Louis J. Salerno and Peter Kittel. Thermal contact conductance. Technical report, Ames Research Center, Moffett Field, California, 1997.

[133] Marcel M. Schmittfull, Anthony Challinor, Duncan Hanson, and Antony Lewis. Joint analysis of cmb temperature and lensing-reconstruction power spectra. *Phys. Rev. D*, 88:063012, Sep 2013. doi: 10.1103/PhysRevD.88.063012. URL https://link.aps.org/doi/10.1103/PhysRevD.88.063012.

[134] D. Scott and G. Smoot. Cosmic Background Radiation Mini-Review. *ArXiv Astrophysics e-prints*, June 2004.

[135] Uros Seljak. Measuring polarization in the cosmic microwave background. *The Astrophysical Journal*, 482(1):6, 1997. URL http://stacks.iop.org/0004-637X/482/i=1/a=6.

[136] Uros Seljak and Matias Zaldarriaga. Signature of gravity waves in the polarization of the microwave background. *Phys. Rev. Lett.*, 78:2054–2057, Mar 1997. doi: 10.1103/PhysRevLett.78.2054. URL https://link.aps.org/doi/10.1103/PhysRevLett.78.2054.

[137] Leonardo Senatore. *Lectures on Inflation*, chapter Chapter 8, pages 447–543. doi: 10.1142/9789813149441_0008. URL https://www.worldscientific.com/doi/abs/10.1142/9789813149441_0008.

[138] Kendrick M. Smith, Oliver Zahn, and Olivier Doré. Detection of gravitational lensing in the cosmic microwave background. *Phys. Rev. D*, 76:043510, Aug 2007. doi: 10.1103/PhysRevD.76.043510. URL https://link.aps.org/doi/10.1103/PhysRevD.76.043510.

[139] R. A. Sunyaev and I. B. Zeldovich. Microwave background radiation as a probe of the contemporary structure and history of the universe. *araa*, 18: 537–560, 1980. doi: 10.1146/annurev.aa.18.090180.002541.

[140] R. A. Sunyaev and Y. B. Zeldovich. Small-Scale Fluctuations of Relic Radiation. *apss*, 7:3–19, April 1970. doi: 10.1007/BF00653471.

[141] A. Suzuki, K. Arnold, J. Edwards, G. Engargiola, A. Ghribi, W. Holzapfel, A. Lee, X. Meng, M. Myers, R. O'Brient, E. Quealy, G. Rebeiz, and P. Richards. Multi-chroic dual-polarization bolometric focal plane for studies of the cosmic microwave background. *Journal of Low Temperature Physics*, 167(5):852–858, Jun 2012. ISSN 1573-7357. doi: 10.1007/s10909-012-0602-y. URL https://doi.org/10.1007/s10909-012-0602-y.

[142] A. Suzuki et al. The litebird satellite mission: Sub-kelvin instrument. *Journal of Low Temperature Physics*, May 2018. ISSN 1573-7357. doi: 10.1007/s10909-018-1947-7. URL https://doi.org/10.1007/s10909-018-1947-7.

[143] Hiroyuki Tashiro. Cmb spectral distortions and energy release in the early universe. *Progress of Theoretical and Experimental Physics*, 2014(6):06B107, 2014. doi: 10.1093/ptep/ptu066. URL http://dx.doi.org/10.1093/ptep/ptu066.

[144] Hiroyuki Tashiro, Nabila Aghanim, and Mathieu Langer. Secondary b-mode polarization from faraday rotation in clusters and galaxies. *Monthly Notices of the Royal Astronomical Society*, 384(2):733–746, 2008. doi: 10.1111/j.1365-2966.2007.12745.x. URL http://dx.doi.org/10.1111/j.1365-2966.2007.12745.x.

[145] Planck HFI Core Team. Planck early results. vi. the high frequency instrument data processing. *A&A*, 536:A6, 2011. doi: 10.1051/0004-6361/201116462. URL https://doi.org/10.1051/0004-6361/201116462.

[146] B. Thorne, J. Dunkley, D. Alonso, and S. Næss. The python sky model: software for simulating the galactic microwave sky. *Monthly Notices of the*

Royal Astronomical Society, 469(3):2821–2833, 2017. doi: 10.1093/mnras/stx949. URL http://dx.doi.org/10.1093/mnras/stx949.

[147] Hoang Duc Thuong. Cosmic ray interaction with detectors of the planck satellite for measurement of the cosmic microwave background radiation polarization. Master's thesis, University of science and technology of Hanoi, 2014.

[148] Rita Tojeiro. Understanding the cosmic microwave background temperature power spectrum. URL: http://www.roe.ac.uk/ifa/postgrad/pedagogy/2006_tojeiro.pdf.

[149] M Tristram and K Ganga. Data analysis methods for the cosmic microwave background. *Reports on Progress in Physics*, 70(6):899, 2007. URL http://stacks.iop.org/0034-4885/70/i=6/a=R02.

[150] C. G. R. Wallis, M. L. Brown, R. A. Battye, and J. Delabrouille. Optimal scan strategies for future CMB satellite experiments. *mnras*, 466:425–442, April 2017. doi: 10.1093/mnras/stw2577.

[151] Mike S. Wang. Mathematical tripos part iii essay: Primordial gravitational waves from cosmic inflation. *DAMTP, University of Cambridge*, 2017.

[152] B. Westbrook, A. Cukierman, A. Lee, A. Suzuki, C. Raum, and Holzapfel W. Development of the Next Generation of Multi-chroic Antenna-Coupled Transition Edge Sensor Detectors for CMB Polarimetry. *J. Low. Temp. Phys.*, 184:74–81, 2016. doi: 10.1007/s10909-016-1508-x.

[153] Matias Zaldarriaga and Uros Seljak. All-sky analysis of polarization in the microwave background. *Phys. Rev. D*, 55:1830–1840, Feb 1997. doi: 10.1103/PhysRevD.55.1830. URL https://link.aps.org/doi/10.1103/PhysRevD.55.1830.

[154] Matias Zaldarriaga, David N. Spergel, and Uros Seljak. Microwave background constraints on cosmological parameters. *The Astrophysical Journal*, 488(1):1, 1997. URL http://stacks.iop.org/0004-637X/488/i=1/a=1.

[155] Saleem Zaroubi. *The Epoch of Reionization*, pages 45–101. Springer Berlin Heidelberg, Berlin, Heidelberg, 2013. doi: 10.1007/978-3-642-32362-1_2. URL https://doi.org/10.1007/978-3-642-32362-1_2.

[156] Yue zhao. *Characterization of Transition Edge Sensors for the Millimeter Bolometer Array Camera on the Atacama Cosmology Telescope*. PhD thesis, Princeton University, 2010.

Publications and scientific activities

[1] Duc Thuong Hoang, Guillaume Patanchon, Martin Bucher, Tomotake Matsumura, Ranajoy Banerji, Hirokazu Ishino, Masashi Hazumi, Jacques Delabrouille, Bandpass mismatch error for satellite CMB experiments I: Estimating the spurious signal, Journal of Cosmology and Astroparticle Physics 2017-12-07 | journal-article DOI: 10.1088/1475-7516/2017/12/015

[2] P. Natoli et al., Exploring cosmic origins with CORE: mitigation of systematic effects, Journal of Cosmology and Astroparticle Physics 2018-4-05 | journal-article DOI: 10.1088/1475-7516/2018/04/022

[3] J. Delabrouille et al., Exploring Cosmic Origins with CORE: Survey requirements and mission design, Journal of Cosmology and Astroparticle Physics 2018-4-05 | journal-article DOI: 10.1088/1475-7516/2018/04/014

[4] LiteBIRD collaboration, Y. Sekimoto et al., Concept design of the LiteBIRD satellite for CMB B-mode polarization, SPIE Astronomical Telescopes + Instrumentation, 2018, Texas-USA, DOI: 10.1117/12.2313432

[5] XIIIth School of Cosmology, The CMB from A to Z, Cargès: Duc Thuong Hoang, Optimization of the next generation of CMB missions [talk]

[6] 53rd Rencontres de Moriond: Duc Thuong Hoang, Evaluating the level of the bandpass mismatch systematic effect for the future CMB satellites. [proceeding]

[7] 53rd Rencontres de Moriond: QUBIC collaboration, G. D'Alessandro et al., The QUBIC experiment [proceeding]

[8] QUBIC collaboration, M. Salatino, Benoit Bélier , Claude Chapron , Duc Thuong Hoang et al., Performance of NbSi Transition-Edge Sensors read out with a 128 MUX factor for the QUBIC experiment , SPIE Astronomical Telescopes + Instrumentation, 2018, Texas-USA, DOI: 10.1117/12.2312080

[9] QUBIC collaboration, D. Burke et al., Optical modelling and analysis of the Q and U bolometric interferometer for cosmology, International Society for Optics and Photonics, 2018, California-USA DOI: 10.1117/12.2287158

[10] QUBIC collaboration, C. O'Sullivan et al., QUBIC: the Q and U bolometric interferometer for cosmology, SPIE Astronomical Telescopes + Instrumentation, 2018, Texas-USA, DOI: 10.1117/12.2313332

[11] QUBIC collaboration, A. J. May et al., Thermal architecture for the QUBIC cryogenic receiver, SPIE Astronomical Telescopes + Instrumentation, 2018, Texas-USA, DOI: 10.1117/12.2312085

[12] QUBIC collaboration, C. O'Sullivan et al., Simulations and performance of the QUBIC optical beam combiner, SPIE Astronomical Telescopes + Instrumentation, 2018, Texas-USA, DOI: 10.1117/12.2313256

[13] QUBIC collaboration, P de Bernardis et al., QUBIC: Measuring CMB polarization from Argentina, Boletin de la Asociacion Argentina de Astronomia La Plata Argentina, Vol, 60

[14] QUBIC collaboration, Aniello Mennella et al., QUBIC: Exploring the primordial Universe with the Q&U Bolometric Interferometer

[15] Ranajoy Banerji, Jacques Delabrouille, Guillaume Patanchon, Duc Thuong Hoang, Martin Bucher, Tomotake Matsumura, Hirokazu Ishino, Masashi Hazumi, Bandpass mismatch error for satellite CMB experiments II: Correcting for the spurious signal. [in preparation]

[16] My initiative : 1st Meeting of Young Vietnamese Community of Astronomy (YVCA), 21-22 December 2017, APC laboratory, Université Paris Diderot, Paris-France, program: https://space.usth.edu.vn/en/news/news-events/yvca-program-127.html

Journal of Cosmology and Astroparticle Physics
An IOP and SISSA journal

Bandpass mismatch error for satellite CMB experiments I: estimating the spurious signal

Duc Thuong Hoang,[a,b] **Guillaume Patanchon,**[a] **Martin Bucher,**[a,c] **Tomotake Matsumura,**[d,e] **Ranajoy Banerji,**[a] **Hirokazu Ishino,**[f] **Masashi Hazumi**[g,e,d,h] **and Jacques Delabrouille**[a,i]

[a]Laboratoire Astroparticule et Cosmologie (APC), Université Paris Diderot, CNRS/IN2P3, CEA/Irfu, Observatoire de Paris, Sorbonne Paris Cité,
10, rue Alice Domon et Léonie Duquet, 75205 Paris Cedex 13, France
[b]Department of Space and Aeronautics, University of Science and Technology of Hanoi (USTH), Vietnam Academy of Science and Technology (VAST),
18 Hoang Quoc Viet, Cau Giay District, Hanoi, Vietnam
[c]Astrophysics and Cosmology Research Unit,
School of Mathematics, Statistics and Computer Science, University of KwaZulu-Natal,
Durban 4041, South Africa
[d]Kavli Institute for the Physics and Mathematics of the Universe (Kavli IPMU, WPI),
UTIAS, The University of Tokyo,
Kashiwa, Chiba 277-8583, Japan
[e]Institute of Space and Astronautical Science (ISAS),
Japan Aerospace Exploration Agency (JAXA),
Sagamihara, Kanagawa 252-0222, Japan
[f]Department of Physics, Okayama University,
3-1-1 Tsushimanaka, Kita-ku, Okayama 700-8530, Japan
[g]High Energy Accelerator Research Organization (KEK),
Tsukuba, Ibaraki 305-0801, Japan
[h]The Graduate University for Advanced Studies (SOKENDAI),
Miura District, Kanagawa 240-0115, Hayama, Japan
[i]Département d'Astrophysique, CEA Saclay DSM/Irfu,
91191 Gif-sur-Yvette, France
E-mail: hoang@apc.in2p3.fr, guillaume.patanchon@apc.univ-paris-diderot.fr, bucher@apc.univ-paris7.fr, tomotake.matsumura@ipmu.jp, banerji@apc.in2p3.fr, scishino@s.okayama-u.ac.jp, masashi.hazumi@kek.jp, delabrou@apc.in2p3.fr

Received July 4, 2017
Revised November 15, 2017
Accepted November 18, 2017
Published December 7, 2017

https://doi.org/10.1088/1475-7516/2017/12/015

JCAP12(2017)015

Abstract. Future Cosmic Microwave Background (CMB) satellite missions aim to use the B mode polarization to measure the tensor-to-scalar ratio r with a sensitivity $\sigma_r \lesssim 10^{-3}$. Achieving this goal will not only require sufficient detector array sensitivity but also unprecedented control of all systematic errors inherent in CMB polarization measurements. Since polarization measurements derive from differences between observations at different times and from different sensors, detector response mismatches introduce leakages from intensity to polarization and thus lead to a spurious B mode signal. Because the expected primordial B mode polarization signal is dwarfed by the known unpolarized intensity signal, such leakages could contribute substantially to the final error budget for measuring r. Using simulations we estimate the magnitude and angular spectrum of the spurious B mode signal resulting from bandpass mismatch between different detectors. It is assumed here that the detectors are calibrated, for example using the CMB dipole, so that their sensitivity to the primordial CMB signal has been perfectly matched. Consequently the mismatch in the frequency bandpass shape between detectors introduces differences in the relative calibration of galactic emission components. We simulate this effect using a range of scanning patterns being considered for future satellite missions. We find that the spurious contribution to r from the reionization bump on large angular scales ($\ell < 10$) is $\approx 10^{-3}$ assuming large detector arrays and 20 percent of the sky masked. We show how the amplitude of the leakage depends on the nonuniformity of the angular coverage in each pixel that results from the scan pattern.

Keywords: CMBR experiments, CMBR polarisation

ArXiv ePrint: 1706.09486

JCAP12(2017)015

Contents

JCAP12(2017)015

1 Introduction

Measurements of the cosmic microwave background (CMB) provide a rich data set for studying cosmology and astrophysics and for placing stringent constraints on cosmological models. In particular, the ESA Planck satellite mission has produced full sky maps in both temperature and polarization at unprecedented sensitivity in nine broad ($\Delta\nu/\nu \approx 0.3$) microwave frequency bands [1].

Conventional cosmological models predict that the CMB is linearly polarized, so that the fourth Stokes parameter V vanishes. CMB polarization patterns can be decomposed in two components known as the E and B modes, respectively of even and odd parity. In linear cosmological perturbation theory, *scalar* perturbations produce E mode polarization but are unable to produce any B mode polarization at linear order. The E mode polarization angular power spectrum can be predicted from a model fitted to the measured T anisotropies. The WMAP [2] and Planck [3] space missions, complemented on smaller angular scales by ACT [4] and SPT [5], have already measured the E mode polarization power spectrum up to high multipole number ℓ, even if the accuracy of the measurement can still be substantially improved. On the other hand, the odd parity (or pseudo-scalar) polarization pattern called the B mode arises either from primordial tensor perturbations, or equivalently primordial gravitational waves, presumably generated during inflation, or from scalar modes at higher nonlinear order, primarily through gravitational lensing. Gravitational lensing B modes dominate over primordial B modes on small angular scales. These gravitational lensing B modes have already been observed at $\ell \gtrsim 100$ by the POLARBEAR [6], SPT-Pol [7] and Bicep2/Keck [8] ground-based experiments. Primordial B modes have not been observed yet. Their predicted shape features a 'recombination bump' visible around $\ell \approx 80$, and a 'reionization bump' at $\ell \lesssim 10$. The overall amplitude of this primordial B mode spectrum depends linearly on the value of the tensor-to-scalar ratio r. The current upper limit is $r < 0.07$ at 95% c.l. [9, 10].

After Planck, a number of ground-based and balloon-borne experiments currently either taking data or in the planning stage aim to make the first detection of primordial B modes. In parallel, the space-borne mission concepts CORE [11], LiteBIRD [12, 13], and PIXIE [14] have

been designed to probe B modes at higher sensitivities and using frequency bands inaccessible from the ground. Constraining physically motivated inflation models requires sensitivities in the tensor-to-scalar ratio of $\sigma_r \lesssim 10^{-3}$, almost two orders of magnitude beyond the Planck sensitivity. Furthermore, systematic errors must be controlled so that their contribution to the final error budget is subdominant. The calibration requirements become correspondingly more stringent, and future experiments will have to devise novel calibration procedures to characterize the instrument at a level that makes it possible to correct the raw data at sufficient accuracy.

Typically experiments observe in a number of different frequency channels with many detectors for each frequency channel. Ideally, all detectors in a single channel should have the exact same bandpass function (i.e., the response $g(\nu)$ that defines the transmission of the system as a function of frequency) in order to construct single band maps, which are then analyzed to isolate the primordial cosmological signal. Many detectors are necessary in each channel to improve on the sensitivity of the current observations, which already use detectors that are very nearly at the quantum noise limit. If however the detectors that are meant to be identical have slightly different bandpasses, artifacts are introduced into the maps that are obtained by combining the signals from several detectors. After cross-calibration on the CMB, for instance using the bright CMB dipole, the amplitude of other astrophysical components is different in the different detectors, and residuals of the differences of integrated intensity leak into the reconstructed polarization maps. Such effects have been observed in Planck [15] and WMAP [16]. In this paper we call these artifacts 'bandpass mismatch errors'.

Obviously, such errors can be avoided if the observing strategy allows first to make polarization maps with each detector independently, hence without bandpass mismatch errors, and then to combine these individual detector maps into a global map. This however requires observing each sky pixel with enough independent orientations of the detector polarizer. This polarization modulation can be achieved either with the use of a rotating half-wave plate (HWP), or by rotating the whole instrument so that each pixel is observed with an optimized set of detector orientations. However, practical considerations may constrain the range of possible polarization orientations, leading to a loss of sensitivity after combining single detector polarization maps.

The objective of this paper is to evaluate the level of the bandpass mismatch effect for future space missions and to estimate its possible impact on the final determination of the tensor-to-scalar ratio r if no correction measures are taken. Our study first focuses on the case without a HWP, and we also verify that the effect is greatly reduced with an ideal rotating HWP without any chromaticity or other non-idealities. For a more detailed discussion of general issues pertaining to the use of a HWP for achieving polarization modulation and in particular a discussion of the issue of achromaticity, we refer the reader to the results of the ABS experiment [17] and the thesis [18] and references therein. We note that in the first case, making single detector maps that are subsequently combined to avoid bandpass mismatch errors, could be done at the price of increased final noise since the angular coverage in each pixel is sub-optimal. HWP non-idealities are not studied in this paper. Some of the issues considered in this paper are also discussed in ref. [19].

In section 2 we model the bandpass mismatch effect, and in section 3 we evaluate the impact on B mode measurements and relate the mismatch errors to the "crossing moment maps", that provide a measure of uniformity of polarizer angle coverage in each pixel. Correction methods are developed in a companion publication [20].

JCAP12(2017)015

2 Sky emission model and mismatch errors

The total intensity of the microwave sky can be expressed as a sum of components of different astrophysical origin. In intensity, the CMB anisotropies are dominant over most of the sky, but several diffuse components of galactic origin are also present as well as compact sources, which include extragalactic radio sources, IR sources (understood to be dusty galaxies), and Sunyaev-Zeldovich (SZ) distortions from the hot gas within galaxy clusters. We model the unpolarized sky emission at position $\hat{p}$ and frequency ν as

$$I_{\rm tot}(\hat{p},\nu) = I_0(\nu) + \left.\frac{\partial B(\nu;T)}{\partial T}\right|_{T_0} \Delta T_{\rm CMB}(\hat{p}) + \sum_{(c)} I_{(c)}(\hat{p},\nu) \tag{2.1}$$

where $B(\nu;T)$ is the spectrum of a blackbody at temperature T, T_0 is the average CMB temperature of about 2.7255 K, $\Delta T_{\rm CMB}(\hat{p})$ is the CMB temperature fluctuation around this mean value, $I_{(c)}(\hat{p},\nu)$ the emission spectrum of component (c) as a function of electromagnetic frequency ν, $I_0(\nu)$ is the monopole including all components. We have similar relationships for the Q and U Stokes parameters. All three Stokes parameters of the CMB at a given position on the celestial sphere have the factorized frequency dependence as given above. A similar factorizable form can be used for the SZ emission assuming that the hot gas is non-relativistic. The galactic components are more complicated at the accuracy required for future satellite missions, and an Ansatz where the frequency dependence of each component factorizes out breaks down. However for studying bandpass mismatch error to first order, a simple factorizable model suffices.

For this bandpass mismatch study, we consider only the CMB and the diffuse galactic components, which contribute the largest bandpass mismatch error. At frequencies $\approx 150\,$GHz where we focus our study, the galactic emission can be decomposed into thermal dust emission, which is the dominant component, and synchrotron, free-free, and spinning dust emissions. The carbon monoxide (CO) rotational emission at transition line frequencies $\nu = 115\,$GHz for $J = 1 \to 0$ and $\nu = 230\,$GHz for $J = 2 \to 1$ was a source of significant leakage in Planck experiment [21], but is not considered here because we anticipate that the filters used by future satellite experiments will avoid these lines.

For our study we assume that the galactic thermal dust emission is a greybody of temperature $T_d \approx 19.7\,$K [22] with an emissivity spectral index $\beta(\hat{p})$, which depends on sky position and whose average value is ≈ 1.62 as measured by Planck [22, 23]. The synchrotron and free-free emissions can be described by power law spectra with the negative spectral indices ≈ -3.1 and ≈ -2.3, respectively (see [24] and references therein). The fluctuation of the signal (relatively to the average CMB monopole) measured by the detector i is given by

$$\begin{aligned}\int d\nu\; g_i(\nu)\,\Big(I(\hat{p},\nu) - I_0(\nu)\Big) &= \int d\nu\; g_i(\nu) \left.\frac{\partial B(\nu;T)}{\partial T}\right|_{T_0} \Delta T_{\rm CMB}(\hat{p}) \\ &+ \int d\nu\; g_i(\nu)\; I_d(\hat{p},\nu_0)\; \left(\frac{\nu}{\nu_0}\right)^{\beta(\hat{p})} \frac{B(\nu;T_d)}{B(\nu_0;T_d)} + \ldots,\end{aligned} \tag{2.2}$$

where $I_0(\nu) = B(\nu;T_0)$ is the CMB monopole, $g_i(\nu)$ is the bandpass function of the detector i, $I_d(\hat{p},\nu_0)$ is the amplitude of the dust component at the reference frequency ν_0, and where the dots stand for other components (such as synchrotron and free-free) not explicitly written here. To first order we obtain for the total sky intensity $I_{\rm sky}(\nu_0)$ after converting the CMB

JCAP12(2017)015

temperature $\Delta T_{\rm CMB}$ to intensity $I_{\rm CMB}(\nu_0)$:

$$I_{\rm sky}(\nu_0) = I_{\rm CMB}(\nu_0) + \gamma_d\, I_{\rm dust}(\nu_0) + \gamma_s\, I_{\rm sync}(\nu_0) + \ldots, \tag{2.3}$$

where

$$\gamma_d = \left(\frac{\int d\nu\ g_i(\nu) \left(\frac{\nu}{\nu_0}\right)^{\beta} \frac{B(\nu;T_d)}{B(\nu_0;T_d)}}{\int d\nu g_i(\nu) \left(\frac{\partial B(\nu;T)}{\partial T}\right)\Big|_{T_0}} \right) \left(\frac{\partial B(\nu_0;T)}{\partial T}\right)\Big|_{T_0}. \tag{2.4}$$

The factor γ_s is similarly defined integrating over the synchrotron spectrum, etc.

Eq. (2.3) also holds for the polarization when I is replaced with Q and U. The unit normalization for the CMB component is justified because the data are calibrated using the CMB dipole (or higher order temperature anisotropies). The values of the γ parameters are close to unity when the bandwidth is narrow.

Differences in the bandpass function $g_i(\nu)$ from detector to detector result in corresponding variations in γ from detector to detector for each non-CMB component. Such variations have been observed in the Planck data (see figures 5 and 28 of [25] for the measured Planck filters and the mismatch parameters, respectively). Pre-flight Fourier Transform Spectrometer (FTS) ground measurements characterized variations of the filter edge positions at both the low and high frequencies at about the percent level. Ground measurements, however, were not accurate enough to detect variations near the center of the filters, and thus could not be used to determine the γ parameters with sufficient accuracy. The γ parameter variations had to be determined from the flight data to allow an accurate correction of the leakage (see the low-ℓ Planck paper [15] as well as [26]). It should be noted that the variations of the bandpass functions of the filters from detector to detector for a future satellite experiment will depend on the kind of detector technology used (see also [27] regarding the WMAP experiment).

As already stressed, for the above sky emission model where each component has a fixed (factorizable) frequency dependence, the bandpass mismatch maps depend only on the γ parameters and not on other details of the filters. The deviations from this simplified model due to the observed spatial variations of the spectral indices of component spectra and of thermal dust temperature produce a second order correction to the bandpass mismatch error, which is neglected for this study. Consequently, the intensity to polarization leakage due to bandpass mismatch can be obtained using only the γ's and no additional properties of the bandpass functions.

To relate these variations to filter properties, we assume a simple model in which each frequency band is a tophat bandpass function for which $g(\nu) = 1$ in the interval $[\nu_{\rm min}, \nu_{\rm max}]$ and $g(\nu) = 0$ elsewhere. We assume that the variations in $\nu_{\rm min}$ and $\nu_{\rm max}$ for each detector are generated independently according to a uniform distribution with a width of 1%.[1]

We also assume a bandwidth $(\nu_{\rm max} - \nu_{\rm min})/\nu_0$ of 0.25 on average, with $\nu_0 = 140.7\,$GHz. The resulting RMS of γ_d is 0.6% for this simple model. This is similar to the variations observed for Planck at 143 GHz. The fact that actual bandpass functions are more complex

[1] We thank Aritoki Suzuki for sharing with us that the measurement errors with FTS in the bandpass of the third-order Chebyshev filter placed between the broadband sinuous antennas and the bolometers of the focal plane panels of the Simons Array [28] give approximately this spread. Obviously, since these are values dominated by measurement error, the actual bandpass mismatch for these filters could be much smaller. These measurements merely serve to establish an upper bound on the mismatch. These values are also of the same order of magnitude as the values representing the bandpass mismatch of the metal mesh filters used as part of the Planck satellite HFI instrument. [See [29] for a discussion of the Planck bandpass mismatch.]

JCAP12(2017)015

functions of ν does not affect the applicability of the present work as long as the corresponding γ coefficients remain of the same order of magnitude. Results for other values may be obtained by trivial rescaling. We verified the expected linear scaling by increasing the width of the uniform distribution from 1% to 2% and observed that the leakage increases by a factor of 2, as expected.

This simple model for detector bandpasses is appropriate for the foreground components having a smooth frequency spectral dependence (e.g., synchrotron and dust emission), but for galactic line emission (such as galactic CO emission and other spectral lines) a more detailed model would be required. The γ's are computed as a random set from this distribution model, since those are the only quantities needed for the bandpass mismatch evaluation.

In this paper, we focus our analysis on a frequency channel centered at $\nu_0 = 140\,\mathrm{GHz}$, and so we restrict ourselves to the dominant galactic component, namely the thermal dust emission. More galactic components are included in the companion paper discussing the correction of the mismatch [20].

3 Calculating the bandpass mismatch

In this section we use a simplified model of the measurement, stripped of additional complications such as asymmetric beams, pixelization effects, etc. for estimating the dominant contribution to the bandpass mismatch error. A study of more than one source of systematic errors simultaneously would obviously be more complicated and also less intuitive to interpret. Here our purpose is to study bandpass mismatch error in isolation and in the simplest possible context.

We assume a scanning pattern that combines three rotations: a relatively fast spin of the payload around a spin axis that precesses around the anti-solar direction, which itself follows the yearly motion of the spacecraft around the Sun. Many of the proposed future CMB polarization space missions have adopted such a scan strategy [11, 13, 30]. The exact scanning pattern is characterized by the following parameters: α (precession angular radius), β (spin angular radius), τ_{prec} (precession period), and τ_{spin} (spin period). The motion of the satellites and the definitions of the scanning parameters are indicated in figure 1.

Our simulations use maps of the celestial sphere pixelized using HEALPix[2] [31] (with $n_{\mathrm{side}} = 256$). A sufficiently fast sampling rate is chosen so that several hits are recorded during each pixel crossing, so that altering this parameter does not significantly affect the results. White instrument noise of a stationary amplitude is assumed, and under this hypothesis we solve the map making equation:

$$\widehat{\mathbf{m}} = (\mathbf{A}^T\mathbf{N}^{-1}\mathbf{A})^{-1}(\mathbf{A}^T\mathbf{N}^{-1}\mathbf{d}). \tag{3.1}$$

Here the notation is such that $\widehat{\mathbf{m}}$ includes the estimated maps of Stokes parameters $\widehat{I}$, $\widehat{Q}$ and $\widehat{U}$; $\mathbf{A}$ is the pointing matrix relating data samples to the map; $\mathbf{N}$ is the noise covariance matrix in the time domain; and we denote the polarization angle of a detector ψ with respect to a reference axis. Individual measurements comprising the data vector $\mathbf{d}$ are given by

$$S_j = I(p) + Q(p)\cos 2\psi_j + U(p)\sin 2\psi_j + n_j \tag{3.2}$$

where n_j represents a stationary white noise source for observations indexed by j. Here the index j ($j = 1, \ldots, N_p$) labels the observations falling into the pixel labelled by p. The

[2] http://healpix.sourceforge.net.

JCAP12(2017)015

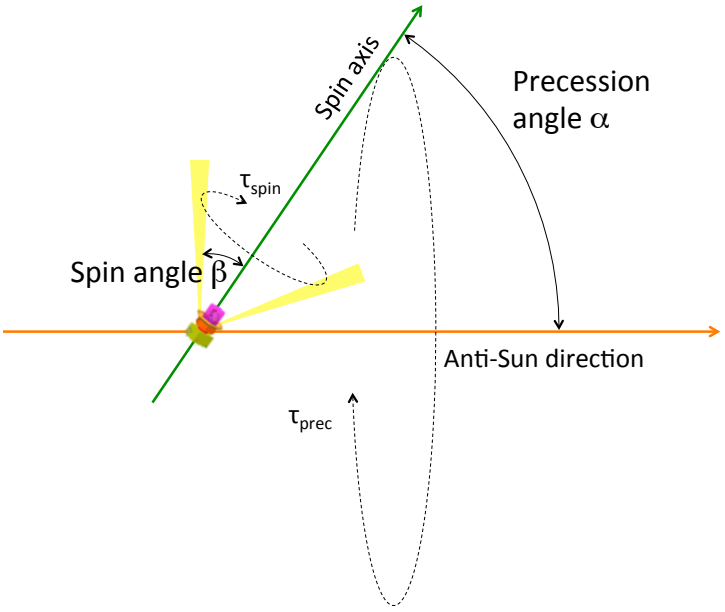

Figure 1. Representation of typical satellite scanning strategy.

normalization of the noise does not matter for our purpose. The model here assumes that all the beams are azimuthally symmetric and identical.

The hypothesis of white instrument noise provides considerable simplification because in this special case the map making equation [i.e., eq. (3.1)] can be cast into a block diagonal form, so that the equations for different pixels decouple from each other. Each block (labelled by the pixel index p) takes the form

$$\begin{pmatrix} \widehat{I}(p) \\ \widehat{Q}(p) \\ \widehat{U}(p) \end{pmatrix} = \frac{1}{N_p} \times \begin{pmatrix} 1 & \langle \cos 2\psi_j \rangle & \langle \sin 2\psi_j \rangle \\ \langle \cos 2\psi_j \rangle & \dfrac{1+\langle \cos 4\psi_j \rangle}{2} & \dfrac{\langle \sin 4\psi_j \rangle}{2} \\ \langle \sin 2\psi_j \rangle & \dfrac{\langle \sin 4\psi_j \rangle}{2} & \dfrac{1-\langle \cos 4\psi_j \rangle}{2} \end{pmatrix}^{-1} \times \begin{pmatrix} \sum_j S_j \\ \sum_j S_j \ \cos 2\psi_j \\ \sum_j S_j \ \sin 2\psi_j \end{pmatrix} \quad (3.3)$$

where the hats indicate the maximum likelihood estimator, and $\langle \cdot \rangle$ denotes the average of a quantity over all data samples j.

Computing the maps $\widehat{I}(p)$, $\widehat{Q}(p)$, and $\widehat{U}(p)$ as above gives the minimum variance estimator of the sky signal in the frequency band under consideration under the hypothesis that the noise of each detector is white (with no correlations in time giving rise to excess low-frequency noise, nor variation of the noise r.m.s. with time), that it is uncorrelated between detectors, and that its level is identical in all detectors [32]. It also assumes no source of systematic errors that may require a different detector weighting to estimate each of the Stokes parameters (and, in particular, no bandpass mismatch).

JCAP12(2017)015

Following eq. (3.2), for this map-making solution, bandpass mismatch causes the following map errors

$$\begin{pmatrix} \delta\widehat{I}_{BPM} \\ \delta\widehat{Q}_{BPM} \\ \delta\widehat{U}_{BPM} \end{pmatrix} = \begin{pmatrix} 1 & \langle\cos 2\psi_j\rangle & \langle\sin 2\psi_j\rangle \\ \langle\cos 2\psi_j\rangle & \frac{1+\langle\cos 4\psi_j\rangle}{2} & \frac{\langle\sin 4\psi_j\rangle}{2} \\ \langle\sin 2\psi_j\rangle & \frac{\langle\sin 4\psi_j\rangle}{2} & \frac{1-\langle\cos 4\psi_j\rangle}{2} \end{pmatrix}^{-1} \times \begin{pmatrix} \delta\langle S_j\rangle \\ \delta\langle S_j\cos 2\psi_j\rangle \\ \delta\langle S_j\sin 2\psi_j\rangle \end{pmatrix} \tag{3.4}$$

where $\delta\langle S_j\rangle$, $\delta\langle S_j\cos 2\psi_j\rangle$, and $\delta\langle S_j\sin 2\psi_j\rangle$ are functions of the underlying sky component maps. Here we assume that the normalization of the CMB component for each detector is perfect. This is obviously an idealization because in reality there are also systematic errors from uncorrected gain variation, but this is a separate issue that we do not analyze here. Moreover, since the relative gain of the detectors is calibrated using the CMB dipole, the approximation that the error is mostly in the relative contributions of the other components is a reasonable one.

Given a model of the microwave sky, the bandpass functions of the various detectors, and the scanning pattern on the sky, eq. (3.4) can be used to compute the bandpass mismatch errors in the reconstruction of a map of Stokes parameters. For future studies of the CMB polarization, and in particular for the search for primordial B modes, the error of greatest concern arises from the leakage of the I component of the foregrounds into the Q and U components of the maximum likelihood band sky maps. From eq. (3.4) we observe that the three terms $\delta\langle S_j\rangle$, $\delta\langle S_j\cos 2\psi_j\rangle$, and $\delta\langle S_j\sin 2\psi_j\rangle$ can potentially induce a bias on the polarization Stokes parameters. The first term $\delta\langle S_j\rangle$ has no impact if the maps of $\langle\cos 2\psi\rangle$ and $\langle\sin 2\psi\rangle$ vanish. This is the case in particular if the detectors are arranged in sets of perfectly orthogonal pairs observing the sky along the same scanning path. If in addition for each such pair there is a matching pair observing at an angle of 45° relative to the first one, we get an optimized configuration [32] for which the 3×3 matrix in eq. (3.3) takes the form

$$\begin{pmatrix} 1 & 0 & 0 \\ 0 & \frac{1}{2} & 0 \\ 0 & 0 & \frac{1}{2} \end{pmatrix}^{-1} . \tag{3.5}$$

This simple form is preserved when observations are made with a set of such 'optimized configurations' oriented at any angle with respect to each other. This type of detector arrangement was used for the Planck mission and is now standard for all proposed CMB polarization experiments. We then get

$$\begin{aligned} \delta\widehat{Q}_{BPM}(p) &= 2\delta\langle S_j\cos 2\psi_j\rangle , \\ \delta\widehat{U}_{BPM}(p) &= 2\delta\langle S_j\sin 2\psi_j\rangle , \end{aligned} \tag{3.6}$$

where under the sky model presented in section 2

$$\begin{aligned} \delta\langle S_j\cos 2\psi_j\rangle &= \sum_{(c)} I_{(c)}(p)\sum_i \gamma_{(c),i} f_i(p)\langle\cos 2\psi_{i,j}\rangle , \\ \delta\langle S_j\sin 2\psi_j\rangle &= \sum_{(c)} I_{(c)}(p)\sum_i \gamma_{(c),i} f_i(p)\langle\sin 2\psi_{i,j}\rangle . \end{aligned} \tag{3.7}$$

JCAP12(2017)015

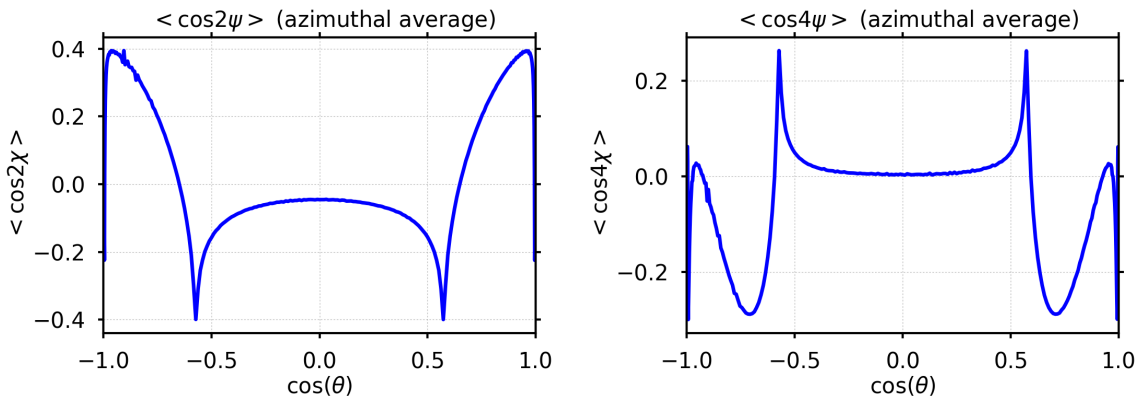

Figure 2. *Crossing moment map azimuthal averages.* We show the azimuthal average of $\langle \cos 2\psi \rangle$ and $\langle \cos 4\psi \rangle$ maps, constituting the totality of the component that is coherent on large angular scales. The corresponding $\langle \sin 2\psi \rangle$ and $\langle \sin 4\psi \rangle$ maps vanish for symmetry reasons.

Here the index (c) labels the non-CMB components of the sky model and i labels the detectors of the frequency channel under consideration (ideally supposed to have the same bandpass function). The coefficients $\gamma_{(c),i}$ vary from detector to detector as a function of the stochastic realizations for the bandpass variation $\delta\nu_{\rm min,i}$ and $\delta\nu_{\rm max,i}$. $f_i(p)$ denotes the fraction of the total hits in pixel p from the detector i, and $\langle \cos 2\psi_{i,j} \rangle$ and $\langle \sin 2\psi_{i,j} \rangle$ are the components of the second-order crossing moments in pixel p for the detector i.

Before describing the predictions of the level of residual due to bandpass mismatch, we briefly digress to examine the properties of the crossing moment maps $\langle \cos 2\psi \rangle$, $\langle \cos 4\psi \rangle$, $\langle \sin 2\psi \rangle$, and $\langle \sin 4\psi \rangle$ for an individual detector for our model scanning pattern characterized by the parameter values: $\alpha = 65°$, $\beta = 30°$, $\tau_{\rm spin} = 10.002$ min, and $\tau_{\rm prec} = 96.2079$ min. Those maps, which are studied into more detail in section 3.3, enter into the expression of the bandpass mismatch. In ecliptic coordinates, these quantities have a nearly symmetric pattern around the poles. Figure 2 shows the azimuthally averaged quantities (i.e., averaged over the ecliptic angle ϕ or ecliptic longitude) as a function of the sine of the latitude of the maps. We observe that for a large fraction of pixels, the spin-2 and spin-4 quantities (functions of period π and $\pi/2$, respectively) are less then 0.2.

3.1 Results

We now present numerical results for the bandpass mismatch maps and their power spectra based on simulations. We construct timestreams for each detector by reading a CMB map and a galactic map, both at $n_{\rm side} = 256$, which were preconvolved with a symmetric Gaussian beam of $\theta_{\rm FWHM} = 32'$. We use an instrument model with actual locations of detectors in the focal plane as described in [13] or [11] depending on the case being considered. We note however that the details of the arrangement of the detectors have little or no impact on the leakage power spectra. The galactic map is rescaled from detector to detector using random errors in the bandpass generated as described in detail in section 2. Then we construct combined I, Q, and U maps obtained by applying the map making equation as given in eq. (3.1). No noise is included in the simulation, because the map making method is linear and the noise does not affect the bias induced by the mismatch. For the same reason we do not introduce sky emission polarization in simulations. The bandpass mismatch properties

JCAP12(2017)015

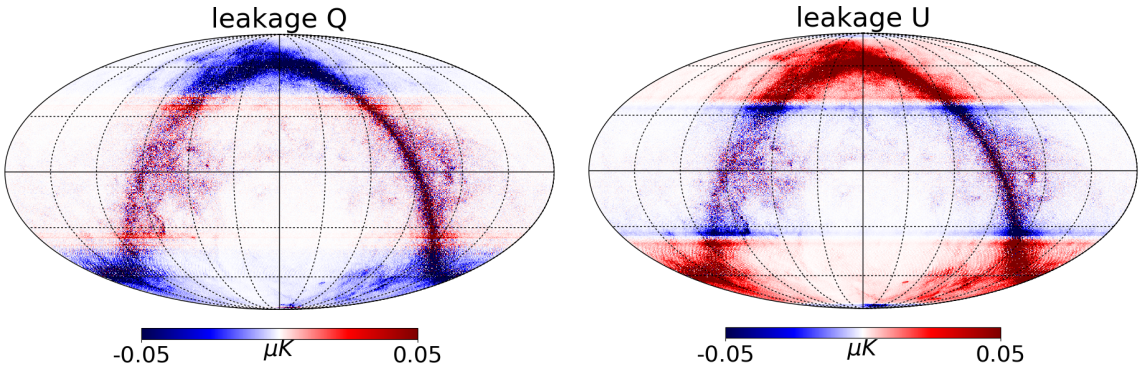

Figure 3. Q and U leakage maps, in ecliptic coordinates, with fiducial scanning parameters and $N_{\rm det} = 222$.

of each detector are generated randomly and in a statistically independent manner. Figure 3 shows the Q and U leakage maps $\delta Q_{\rm BPM}$ and $\delta U_{\rm BPM}$ for one particular realization. The output polarization maps result from optimal map making using our simulated noiseless and polarizationless timestreams for the 140 GHz channel and are shown in ecliptic coordinates. The simulation assumed 222 detectors, which is the number of detectors composing the LiteBIRD arrays described in [13], spread over a large focal plane approximatively 10 degrees wide observing with no HWP. The detector polarizer covers the full range of angles in the focal plane with 22.5 degree separation. We assume the fiducial scanning parameters $\alpha = 65°$, $\beta = 30°$, $\tau_{\rm spin} = 10\,{\rm min}$, and $\tau_{\rm prec} = 96.1803\,{\rm min}$ for the center of the focal plane (see section 3.3 for a discussion of the choice of $\tau_{\rm spin}$ and $\tau_{\rm prec}$ to minimize the inhomogeneity of the scanning pattern which is responsible for Moiré effects in the crossing moment maps). At 140 GHz the bandpass mismatch error in polarization is dominated by the I component of the thermal dust emission, although there are subdominant contributions from the diffuse galactic synchrotron emission and other non-primordial (non-CMB) components. The length of the survey in this simulation is exactly one sidereal year in order to ensure as uniform and complete sky coverage as possible and hence to facilitate the interpretation of those results. We observe that the leakage is concentrated near the galactic plane, as expected. The bands at equal latitude visible in the leakage maps correspond to regions where the second order crossing moments depart significantly from zero (figure 2), and as can be seen from eq. (3.7), there is a strong correlation between the relative leakage amplitude and these moments.

Figures 4, 5, and 6 show the bandpass mismatch leakage contributions to the EE and BB power spectra in different observing configurations. The power spectra are computed after the 20% of the sky where the thermal dust emission is strongest is masked. The data in this masked region is set to zero with no apodization (which is unnecessary since the small-scale power in the leakage maps dominates over the spurious power induced by the masking). For comparison we also show the CMB B mode spectrum for two different values of r. The dashed curves show how the signal is attenuated by beam smearing assuming the 140 GHz FWHM beamwidth of 32' fitted to a Gaussian profile for the present LiteBIRD configuration [33]. As will be demonstrated later, neglecting the discreteness of the scans, the overall amplitude of the leakage due to bandpass mismatch is nearly Gaussian and of zero mean, and the variations of γ_{dust} impact all multipoles of the leakage map power spectrum in a correlated way. For this reason, an accurate estimate of the average leakage power spectrum

JCAP12(2017)015

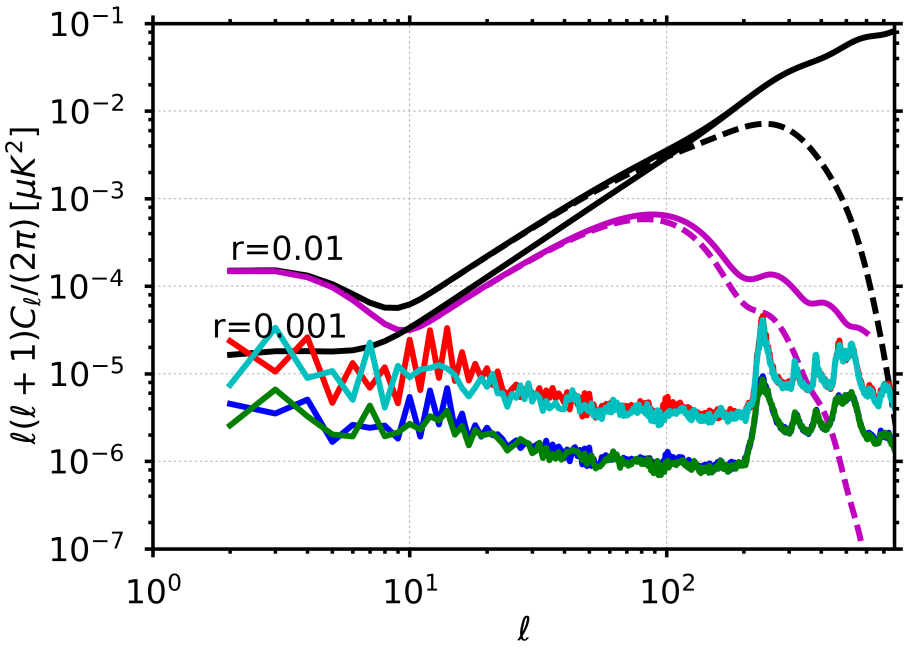

Figure 4. EE and BB leakage power spectra for $\alpha = 65°$, $\beta = 30°$, $\tau_{\rm spin} = 10\,{\rm min}$, $\tau_{\rm prec}$= 96.1803 min, and combining data for either 74 or 222 detectors. The red curve corresponds to BB with 74 detectors, the cyan to EE with 74 detectors, the blue to BB with 222 detectors and the green to EE with 222 detectors. The purple curve represents a model of primordial B mode power spectrum with fiducial cosmological parameters after Planck for $r = 0.01$, the black curves are including lensing for $r = 0.01$ and $r = 0.001$. The dashed curves show the effect of convolving with a 32 arcmin beam. This plot demonstrates the $1/N_{\rm det}$ dependance of the level of the power spectra.

requires averaging over many independent realizations even if many detectors are used for the simulations. At least on large angular scales, the fluctuations in the power spectrum due to different realizations is roughly an overall amplitude varying as the square of a Gaussian.

We find that with all other parameters equal, the bandpass mismatch error amplitude scales as $1/\sqrt{N_{\rm det}}$ where $N_{\rm det}$ is the number of detectors (and hence the power spectrum scales as $1/N_{\rm det}$). This scaling becomes more accurate when $N_{\rm det}$ becomes large, as shown by comparing the EE and BB leakage power spectra for $\tau_{\rm spin} = 10\,{\rm min}$, $\tau_{\rm prec}$= 96.1803 min and $N_{\rm det}$ of either 74 or 222. The pairs of spectra have the same shape but the ratio of power spectrum amplitudes is consistent with the predicted ratio $222/74 = 3$.

Figure 5 shows the BB power spectra for $\alpha = 65°$, $\beta = 30°$ for several spin and precession period combinations. We see that the characteristics of the leakage power spectrum (and in particular the location of the peaks at $\ell \leq 100$) depend on the exact values of $\tau_{\rm spin}$ and $\tau_{\rm prec}$. A proper value of the ratio $\tau_{\rm prec}/\tau_{\rm spin}$ moves the peaks in the bandpass leakage spectrum to higher ℓ, away from the location of the maximum of the primordial B mode recombination bump.

Figure 6 compares the BB power spectra for different opening angles α and β, and also different scan rates. With the constraint $\alpha + \beta = 95°$, scan strategies with larger precession angle produce less leakage because they allow for more homogeneous scan angle coverage per pixel, and hence lower $|\langle\cos 2\psi_j\rangle|$ and $|\langle\sin 2\psi_j\rangle|$ per individual detector.

JCAP12(2017)015

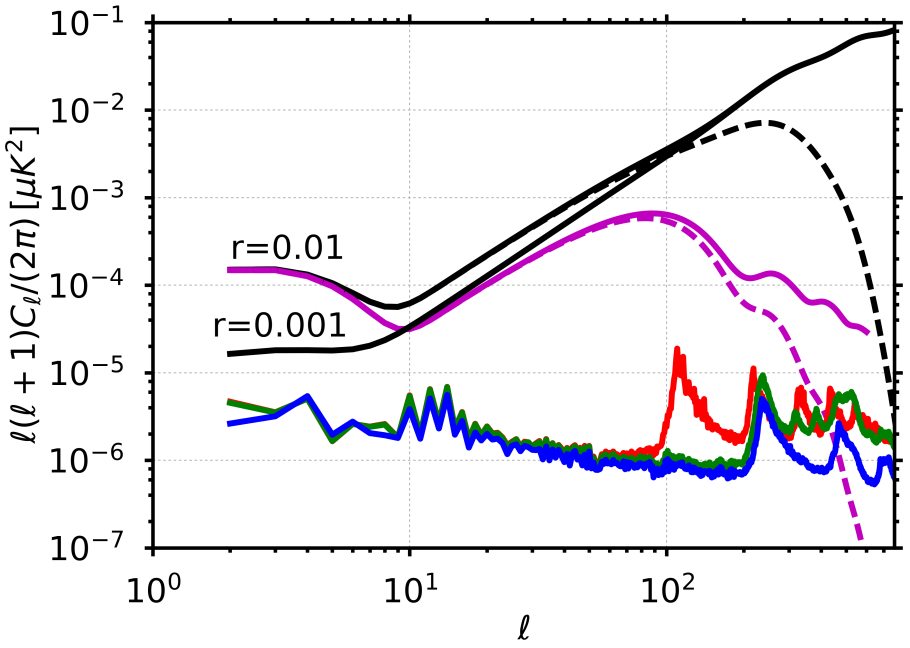

Figure 5. BB leakage power spectra for $\alpha = 65°$, $\beta = 30°$, $\tau_{\rm spin}$=10 min, $\tau_{\rm prec}$=93 min (red); $\tau_{\rm spin}$=10 min, $\tau_{\rm prec}$=96.1803 min (green); and $\tau_{\rm spin}$=10/3 min, $\tau_{\rm prec}$=96.1803 min (blue). Simulations include 222 detectors and 365 days observation. See the figure 4 caption for a description of the model curves.

We observe that the power spectra above (without a HWP) are approximately proportional to $\ell^{-\eta}$ where $\eta \approx 2.5$. This angular power spectrum is less steep than that of dust emission itself. The shape of the resulting leakage spectrum can be expressed as a kind of convolution between the harmonic coefficients of the crossing moment maps and of the dust component map (see ref. [34] for an analytical explanation of this power law). This spectral shape is problematic on very large scales, for example near the reionization bump, because the ratio of the bandpass mismatch to the white noise component of the detector noise (having an $\eta \approx 0$ spectrum) increases toward lower multipole number ℓ. We observe some dependance of the amplitude of the leakage spectra with respect to the scanning strategy parameters α and β. Scanning strategies with more uniform angular coverage (provided by larger precession angles for the studied cases) have a lower leakage amplitude.

When the experiment observes with a rotating HWP, the equivalent of an optimized polarimeter configuration is straightforwardly obtained when the HWP observes a given sky position $\hat{p}$ during an integer number of turns (and, thus, for an evenly spread set of angles between 0 and 2π). In practice, however, the pointing direction moves while the HWP rotates, and hence data samples are not usually so evenly distributed. However, when the HWP rotates at 1.467 Hz (88 rpm) while the instrument beam scans the sky with a spin period of $\tau_{\rm spin}$ = 10 minutes and with a 30° angle, the beam is displaced by 0.204° (about 12.3′) each time the HWP makes one turn. Neglecting this displacement, single detector timelines of I, Q, and U with no bandpass mismatch leakage can be straightforwardly obtained from the data set, and projected onto sky maps with optimal noise averaging, i.e., equivalent to the generalized least square solution of eq. (3.1). Of course, a real-life HWP is not

JCAP12(2017)015

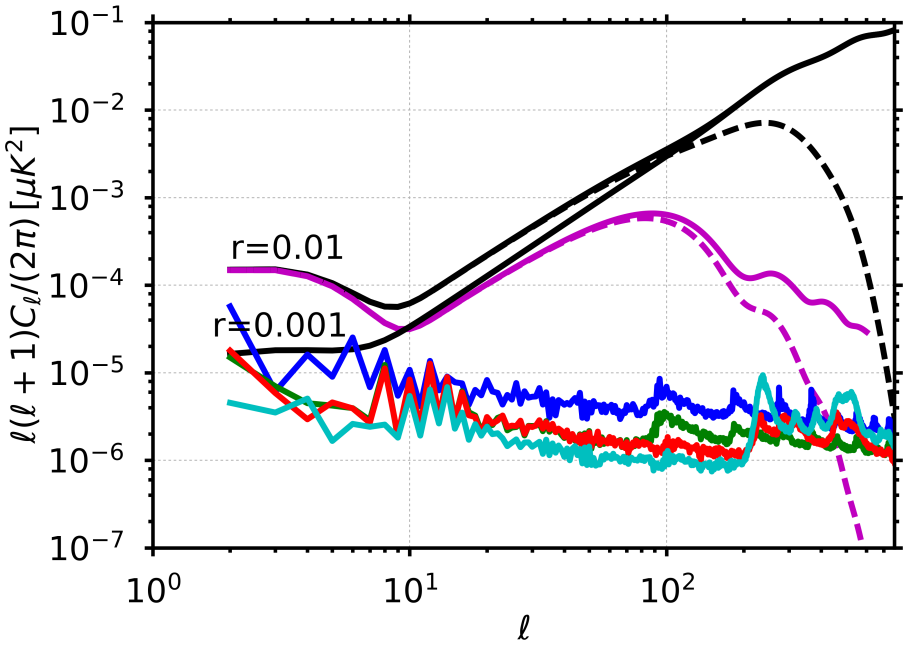

Figure 6. BB leakage power spectra for different scanning parameters. In cyan: $\alpha = 65°$, $\beta = 30°$, $\tau_{\rm spin}$=10 min, $\tau_{\rm prec}$=96.1803 min, red: $\alpha = 50°, \beta = 45°$, $\tau_{\rm spin}$=10 min, $\tau_{\rm prec}$=96.1803 min, green: $\alpha = 50°$, $\beta = 45°$, $\tau_{\rm spin}$=2 min, $\tau_{\rm prec}$=4 day, blue: $\alpha = 30°, \beta = 65°$, $\tau_{\rm spin}$=2 min, $\tau_{\rm prec}$=4 day. Spectra are computed for 222 detectors. Curves for the B mode model are described in the figure 4 caption. For the scanning strategies with a long precession period, we computed spectra for 100 detectors rescaling to 222 equivalent detectors using the $1/N_{\rm det}$ dependence.

perfectly achromatic and hence is likely to introduce bandpass mismatch effects of its own. We postpone to future work the study of this effect.

To illustrate the added value of a perfect HWP, we perform a simple set of simulations in which the input sky (smoothed by a $32'$ beam) is a Healpix map pixelized at $n_{\rm side} = 256$. The pixel size is well matched to the rotation speed of the HWP, which makes about one turn while it crosses a pixel. However, numerical effects will generate unevenness in the angular coverage of each pixel, and thus, when multi-detector maps are made using eq. (3.1), small bandpass leakage mismatch effects will subsist. Simulating the observation of this model sky with the use of a HWP spinning at 88 rpm and other parameters set to $\alpha = 65°$, $\beta = 30°$, $\tau_{\rm spin}$ =10 min, $\tau_{\rm prec}$ = 96.1803 min, we obtain the small residual leakage shown in figure 7, which confirms the effectiveness of the HWP in reducing bandpass leakage by homogenizing the angular coverage in each pixel. The shape of the spectrum of the residual is similar to that of white noise. Its origin is in the small unevenness of the angle distributions across the pixels and is an artefact of sky pixelization.

We verify that in case of a perfect HWP, the multi-detector solution for the polarization is close to the solution consisting in combining single detector (including the HWP) polarization maps, as the residual leakage and its impact of r that can be read off the plot, is negligible.

Table 1 shows the contribution to r that would result from uncorrected bandpass mismatch based on its power spectrum averaged over many realizations, calculated using the

JCAP12(2017)015

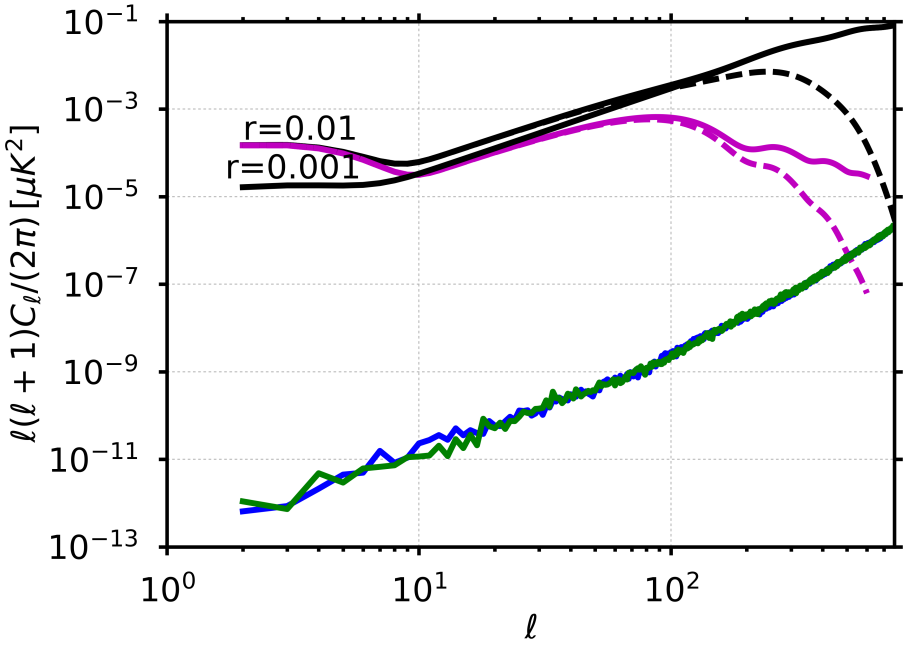

Figure 7. *EE and BB leakage power spectra with rotating HWP* for $\alpha = 65°$, $\beta = 30°$ and spin period of 10 min with a HWP rotating at 88 rpm for 50 detectors.

	$2 \leq \ell \leq 10$	$10 \leq \ell \leq 200$
$\alpha = 30°$; $\beta = 65°$; $\tau_{\rm prec} = 4$ days; $\omega_{\rm spin} = 0.5$ rpm	1.83×10^{-3}	9.32×10^{-5}
$\alpha = 50°$; $\beta = 45°$; $\tau_{\rm prec} = 4$ days; $\omega_{\rm spin} = 0.5$ rpm	6.49×10^{-4}	4.66×10^{-5}
$\alpha = 50°$; $\beta = 45°$; $\tau_{\rm prec} = 96$ min; $\omega_{\rm spin} = 0.1$ rpm	6.32×10^{-4}	3.08×10^{-5}
$\alpha = 65°$; $\beta = 30°$; $\tau_{\rm prec} = 93$ min; $\omega_{\rm spin} = 0.1$ rpm	3.29×10^{-4}	7.61×10^{-5}
$\alpha = 65°$; $\beta = 30°$; $\tau_{\rm prec} = 96$ min; $\omega_{\rm spin} = 0.1$ rpm	3.27×10^{-4}	2.11×10^{-5}
$\alpha = 65°$; $\beta = 30°$; $\tau_{\rm prec} = 96$ min; $\omega_{\rm spin} = 0.3$ rpm	3.03×10^{-4}	1.77×10^{-5}

Table 1. Contribution of bandpass mismatch error to the tensor-to-scalar ratio r computed according to eq. (3.8). The level of the bandpass leakage relative to primordial B mode signals is acceptable at the angular scale of the recombination bump, but problematic for the reionization bump at $\ell \lesssim 10$. Scanning strategies with larger α and smaller β perform better, as they provide more uniform angular coverage in each pixel.

projection

$$\hat{\delta r} = \frac{\sum_{\ell=\ell_{\rm min}}^{\ell_{\rm max}} (2\ell+1) C_\ell \hat{C}_\ell}{\sum_{\ell=\ell_{\rm min}}^{\ell_{\rm max}} (2\ell+1) C_\ell^2}. \tag{3.8}$$

Here C_ℓ is the power spectrum for the primordial B mode signal normalized to $r = 1$. The table shows δr calculated for two ranges of ℓ: one with $\ell \in [2, 10]$ to isolate the signal from the re-ionization bump, and another with $\ell \in [10, 100]$ to isolate the signal arising from the recombination bump. The results in the table assume $N_{\rm det} = 222$ detectors, but can be rescaled based on the $1/N_{\rm det}$ dependence to other numbers of detectors. These results are only an order of magnitude estimate because they are based on a single 140 GHz channel,

JCAP12(2017)015

and it has been assumed that very low and very high frequency channels have been used to removed the non-primordial components completely. We stress that the bandpass mismatch power spectrum is not a simple bias that can be predicted and subtracted away because its overall amplitude suffers large fluctuations, which are of the same order of magnitude as the average bias itself.

3.2 Analytic estimates

With the objective of finding fast and easy ways to predict the magnitude of potential leakage without running many Monte Carlo simulations, and in order to understand how the patterns shown in the leakage map in figure 3 are related to the scanning strategy, we now study theoretically in more detail how the leakage manifests itself in the polarization maps. To this end, we expand the solution of the map making equation [eq. (3.1)].

We derive a simple expression for the leakage originating from differencing the signal from a pair of orthogonally polarized detectors observing instantaneously at the same location in the sky, so that data of the two detectors of the pair i at time t in pixel p denoted as $S_{i;a}(t)$ and $S_{i;b}(t)$ are given by

$$\begin{aligned} S_{i;a}(t) &= I_{i;p} + Q_p \cos 2\psi(t) + U_p \sin 2\psi(t) + M_{i;p}, \\ S_{i;b}(t) &= I_{i;p} - Q_p \cos 2\psi(t) - U_p \sin 2\psi(t) - M_{i;p}. \end{aligned} \tag{3.9}$$

Here we assume no noise and perfect calibration on the CMB (e.g., using the CMB dipole), and ψ is the polarizer angle for detector a. $I_{i;p}$, Q_p, U_p are the Stokes parameters of the sky signal, $I_{i;p}$ being the mean intensity parameter for the detector pair i, and $M_{i;p}$ represents the bandpass mismatch component, which is given by

$$M_{i;p} = \frac{1}{2} \sum_{(c)} \left(\gamma^a_{(c)} - \gamma^b_{(c)} \right) \; I_{p,(c)}. \tag{3.10}$$

Here the index (c) labels the non-CMB sky components. The coefficient differences $\left(\gamma^a_{(c)} - \gamma^b_{(c)}\right)$ vary from detector pair to detector pair, as explained in section 2 (see in particular eq. (2.3)). To minimize clutter, we have suppressed the index i labelling the detector pairs. We neglect the subdominant effect of bandpass mismatch on the polarized sky components. As in the previous section, we neglect noise in our analysis. The estimated noiseless Stokes parameter maps $\widehat{Q_p}$ and $\widehat{U_p}$ can be expanded as $\widehat{Q_p} = Q_p + \delta Q_p$ and $\widehat{U_p} = U_p + \delta U_p$, where δQ and δU represent the leakages to polarization resulting from bandpass mismatch. Ideal solutions with no leakage are given in eq. (3.9).

The map making equation gives

$$\begin{pmatrix} \widehat{I}_p \\ \widehat{Q}_p \\ \widehat{U}_p \end{pmatrix} = \begin{pmatrix} 1 & 0 & 0 \\ 0 & \frac{1}{2}\left(1 + \langle \cos 4\psi \rangle\right) & \frac{1}{2}\langle \sin 4\psi \rangle \\ 0 & \frac{1}{2}\langle \sin 4\psi \rangle & \frac{1}{2}\left(1 - \langle \cos 4\psi \rangle\right) \end{pmatrix}^{-1} \begin{pmatrix} \langle S \rangle \\ \langle \frac{1}{2}(S_a - S_b) \cos 2\psi \rangle \\ \langle \frac{1}{2}(S_a - S_b) \sin 2\psi \rangle \end{pmatrix}, \tag{3.11}$$

and the zeros in the 3×3 matrix result because the exact orthogonality of the two detectors of each pair insures that $\langle \cos 2\psi \rangle$ and $\langle \sin 2\psi \rangle$ vanish exactly [compare with eq. (3.4)], so that the expression for $\widehat{I}_p$ decouples from the expressions for $\widehat{Q}_p$ and $\widehat{U}_p$. Consequently, the

JCAP12(2017)015

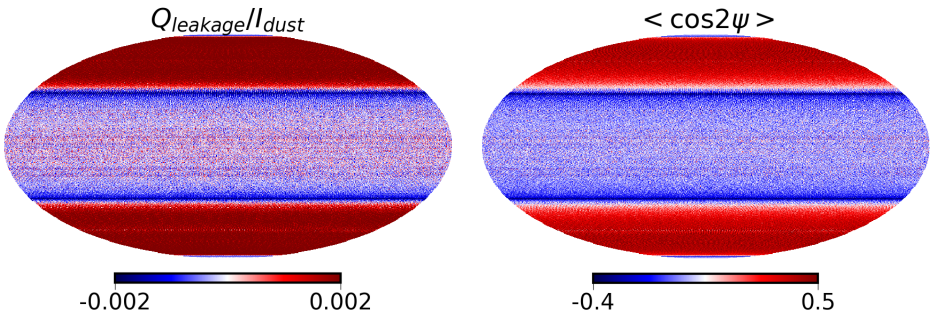

Figure 8. Left: leakage for the Q component relative to the dust temperature ($\delta Q/I_{\rm Gal}$) after polarization reconstruction using one bolometer pair only and a one year observation time. Right: averaged $\cos 2\psi$ in each pixel for one bolometer after one year observation time. This quantity is strongly correlated with the relative leakage Q component with respect to the dust intensity.

leakages are given by

$$\begin{aligned}\begin{pmatrix}\delta Q_p\\ \delta U_p\end{pmatrix} &= \begin{pmatrix}\frac{1}{2}(1+\langle\cos 4\psi\rangle) & \frac{1}{2}\langle\sin 4\psi\rangle\\ \frac{1}{2}\langle\sin 4\psi\rangle & \frac{1}{2}(1-\langle\cos 4\psi\rangle)\end{pmatrix}^{-1}\begin{pmatrix}\langle M_p\cos 2\psi\rangle\\ \langle M_p\sin 2\psi\rangle\end{pmatrix}\\ &= \frac{2}{(1-\langle\cos 4\psi\rangle^2-\langle\sin 4\psi\rangle^2)}\begin{pmatrix}1+\langle\cos 4\psi\rangle & -\langle\sin 4\psi\rangle\\ -\langle\sin 4\psi\rangle & 1-\langle\cos 4\psi\rangle\end{pmatrix}\begin{pmatrix}\langle M_p\cos 2\psi\rangle\\ \langle M_p\sin 2\psi\rangle\end{pmatrix}. \quad (3.12)\end{aligned}$$

Assuming that $\langle\cos 4\psi\rangle^2+\langle\sin 4\psi\rangle^2 \ll 1$ (which is not so bad an approximation except very near the poles), we obtain

$$\begin{pmatrix}\delta Q_p\\ \delta U_p\end{pmatrix} \approx 2\begin{pmatrix}\langle M_p\cos 2\psi\rangle\\ \langle M_p\sin 2\psi\rangle\end{pmatrix}. \quad (3.13)$$

For one Galactic component, by replacing M_p by its expression in eq. (3.10), the relative amplitude of the leakage can be written as

$$\begin{pmatrix}\frac{\delta Q_p}{I_{{\rm Gal};p}}\\ \frac{\delta U_p}{I_{{\rm Gal};p}}\end{pmatrix} = \left(\gamma^a_{\rm Gal}-\gamma^b_{\rm Gal}\right)\begin{pmatrix}\langle\cos 2\psi\rangle\\ \langle\sin 2\psi\rangle\end{pmatrix}. \quad (3.14)$$

The term on the right-hand side is one of the crossing moment terms for a single detector. We should then observe a large correlation between the two maps on the two sides of the equation. We have verified, with the help of simulations of data for one detector pair, this relationship for two different scanning strategies: $\alpha = 65°$ and $\beta = 30°$ and $\alpha = 50°$ and $\beta = 45°$. Figure 8 shows the relative leakage map $\delta Q_p/I_{{\rm Gal};p}$ and the quantity $\sum\cos 2\psi/n_p$. The U component (not shown here) exhibits similar properties.

Figure 9 shows the correlation of the two maps by plotting the values of one map versus the other for a subset of pixels. We observe a high correlation between the two maps. We verify that the slope is given by the coefficient $\Delta\gamma = \gamma_a - \gamma_b$ as derived in eq. (3.14). This figure shows the tight link between the crossing moments and the relative leakage due to bandpass mismatch. It also shows that the approximations made to derive eq. (3.14) are valid since we observe a relatively small scatter around the linear slope. The outliers in the figure are due to pixels near the ecliptic poles where the angle coverage is less uniform for the scanning parameters used as a baseline in this work.

JCAP12(2017)015

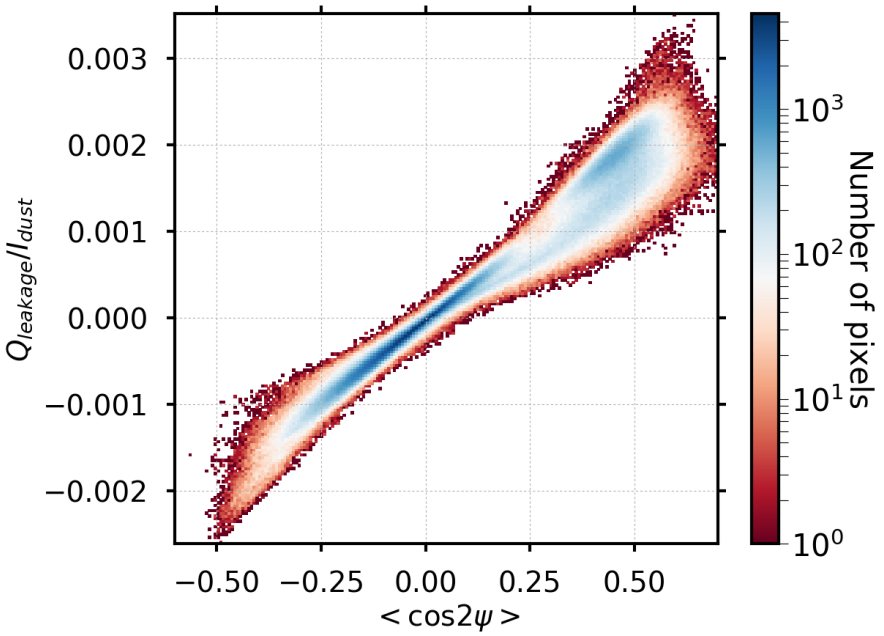

Figure 9. Values of the relative leakage $\delta Q_p / I_{\mathrm{Gal};p}$ for a pair of detectors with orthogonal polarizations of a function of the scanning strategy parameter $(1/n_p)\sum \cos 2\psi$ (see text) after map making with two detectors only. We observe a tight correlation between the relative leakage and the second order crossing moments.

We now consider the solution combining more detectors. The generalization of eq. (3.13) gives for the resulting leakage component

$$\begin{pmatrix} \delta Q_p \\ \delta U_p \end{pmatrix} = \begin{pmatrix} \frac{1}{2}\sum_i \sum_j (1+\cos 4\psi_i^j) & \frac{1}{2}\sum_i \sum_j \sin 4\psi_i^j \\ \frac{1}{2}\sum_i \sum_j \sin 4\psi_i^j & \frac{1}{2}\sum_i \sum_j (1-\cos 4\psi_i^j) \end{pmatrix}^{-1} \begin{pmatrix} \sum_i \sum_j \cos 2\psi_i^j \, M_{i,p} \\ \sum_i \sum_j \sin 2\psi_i^j \, M_{i,p} \end{pmatrix} \quad (3.15)$$

where we sum over all the detector pairs indexed by i and over all samples j falling in pixel p for each detector. In this case, for which we consider the realistic configuration of more than one pair of detectors per pixel, the covariance matrix above becomes nearly diagonal. As the number of detectors is increased, the matrix in eq. (3.15) becomes increasingly diagonal. The total leakage is then simply, replacing the leakage term M_p by its expression:

$$\frac{\delta Q_p}{I_{\mathrm{Gal};p}} \approx \frac{2}{N_{\mathrm{hit}}} \sum_i \Delta\gamma_i \sum_j \cos 2\psi_i^j, \quad (3.16)$$

using eq. (3.10), where we have defined N_{hit} as the total number of hits including all detectors (and not only count 1 per detector pair which explains the cancellation of the 1/2 factors since the sum runs over detector pairs), and $\Delta\gamma_i = \gamma_i^a - \gamma_i^b$. The leakage vanishes if each individual detector has uniform angle coverage. We observe that the relevant quantities to estimate the level of leakage for a given scanning strategy are the individual detector second order crossing moments. Following our hypothesis that the γ parameters are random and

JCAP12(2017)015

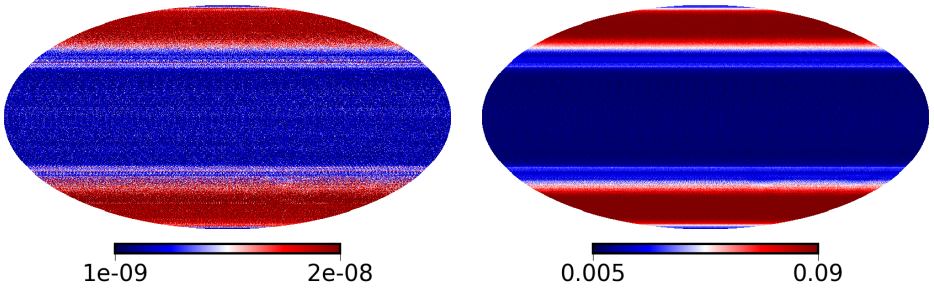

Figure 10. Left: estimated leakage variance of the Q component relative to the dust temperature ($\mathrm{Var}\,(\delta Q_p/I_{\mathrm{Gal};p})$) after polarization reconstruction using all bolometer pairs and one year of observations. We used 10 independent realizations of the bandpass to estimate the variance. Right: averaged $\left\langle \left((1/\bar{n}_p) \sum \cos 2\psi_i^j \right)^2 \right\rangle_{\mathrm{det}}$ in each pixel for all bolometers after one year observation time. As for the detector pair case, we observe a tight correlation of the two maps on large angular scales.

uncorrelated, we express the variance of the leakage map as:

$$\mathrm{Var}\left(\frac{\delta Q_p}{I_{\mathrm{Gal};p}}\right) \approx \sum_i \mathrm{Var}(\Delta\gamma_i) \left(\sum_j \cos 2\psi_i^j\right)^2 \left(\frac{2}{N_{\mathrm{hit}}}\right)^2, \tag{3.17}$$

which gives, since $\mathrm{Var}(\Delta\gamma) = 2\mathrm{Var}(\gamma)$:

$$\mathrm{Var}\left(\frac{\delta Q_p}{I_{\mathrm{Gal};p}}\right) \approx 4\frac{\mathrm{Var}(\gamma)}{N_{\mathrm{det}}} \left\langle \left(\frac{\sum \cos 2\psi_i^j}{\bar{n}_p}\right)^2 \right\rangle_{\mathrm{det}}, \tag{3.18}$$

where $\langle \cdot \rangle_{\mathrm{det}}$ denotes average over all detectors, and $\bar{n}_p = \frac{N_{\mathrm{hit}}}{N_{\mathrm{det}}}$ is the average number of hits per detector. The expression for the U component is similar with the cosine replaced by a sine. This expression for the variance of the leakage map is also valid if detectors are not arranged by pairs.

Figure 10 compares the maps of the variance on the left-hand side of the previous relationship which was estimated with ten independent realizations of the bandpass parameters, with the quantity $\left\langle \left((1/\bar{n}_p) \sum \cos 2\psi_i \right)^2 \right\rangle_{\mathrm{det}}$. Figure 11 shows the correlations between the two quantities on a scatter plot. We observe a significant correlation of the two quantities, especially on large scales. The dispersion is partly due to the limited number of realizations to estimate the variance. Nevertheless, this shows that the level of leakage can be evaluated by estimating the second order crossing moments only for different scanning strategies without the need of running large simulations. This result explains what was observed in figure 6, showing the level of the leakage with respect to the scanning parameters α and β. The strategies with more uniform angle distribution (the ones with larger precession angle) show lower residuals (see also [35] for the link with other systematic effects).

Results show that contamination from bandpass mismatch even if small could contribute to the B mode spectrum at a non-negligible level, close to the detection limit of primordial B modes with future satellite missions. Systematic variation of the bandpass functions across the focal plane, as opposed to the uncorrelated random variations assumed in this study, could produce larger errors. These considerations motivate developing correction methods, which we present in the companion paper [20].

JCAP12(2017)015

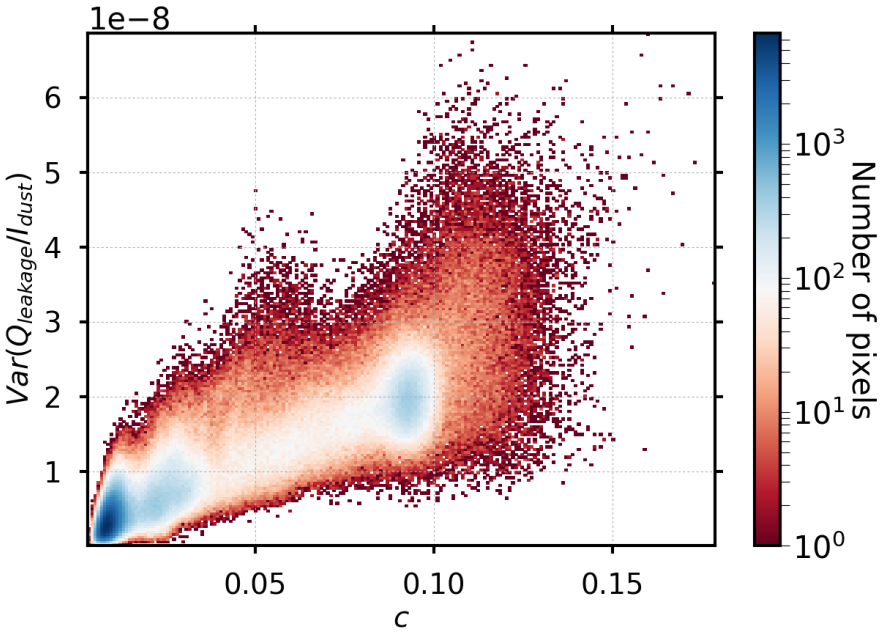

Figure 11. Estimated variance distribution of the relative leakage parameter: Var $(\delta Q_p/I_{\mathrm{Gal};p})$ as a function of $c = \left\langle \left((1/\bar{n}_p) \sum \cos 2\psi_{t;i} \right)^2 \right\rangle_{\mathrm{det}}$ (see text) after map making including all detectors. We have averaged over ten realizations to estimate the variance.

3.3 Importance of avoiding resonances

Here we briefly explain some considerations for choosing the scan frequency parameters ω_{spin} and ω_{prec}. We found that to obtain good crossing moment maps, careful attention must be paid to choosing the ratios of the hierarchy of scan frequencies $\omega_{\mathrm{ann}} \ll \omega_{\mathrm{prec}} \ll \omega_{\mathrm{spin}}$, and when there is a continuously rotating HWP also ω_{HWP}. For $\omega_{\mathrm{prec}}/\omega_{\mathrm{ann}}$, we choose to make this number an integer so that the scan pattern closes. In all the simulations reported here, we assumed a single survey of exactly one year in duration. Given the large number of precession cycles in a year, this requirement can be achieved by means of a very small adjustment in ω_{prec}. One might also want to do the same for the spin period, but this is less critical because of its shortness compared to a year.

More critical is the ratio $\theta = \omega_{\mathrm{spin}}/\omega_{\mathrm{prec}}$, which must be chosen so that θ cannot be well approximated by simple fractions of the form p/q where p and q are relatively prime and q is small in a sense that we shall make more precise shortly. Of concern are exact or near exact resonances where q is less than of order $\omega_{\mathrm{prec}}/\omega_{\mathrm{spin}}$.

Before entering into the theory of how the ratio θ should be chosen (and jumping ahead slightly), we show what goes wrong when θ is not well chosen. For example, our first try had $\tau_{\mathrm{spin}} = 10$ min and $\tau_{\mathrm{prec}} = 93$ min and gave hit count and crossing moment maps with clearly visible Moiré patterns at intermediate angular scales, as shown in figure 12, showing clear evidence of a near resonance. However, when ω_{prec} was sped up by the Golden ratio $\Phi = (1 + \sqrt{5})/2 = 1.61803398875$ (reputed to be the "most irrational" number),[3] these

[3]See for example Michael Berry, (1978, September), *Regular and irregular motion*, in S. Jorna (Ed.), AIP Conference proceedings (Vol. 46, No. 1, 16–120), AIP for a nice discussion of these questions in a different context, that of perturbations of integrable systems in classical mechanics, KAM theory, and the stability of the solar system.

JCAP12(2017)015

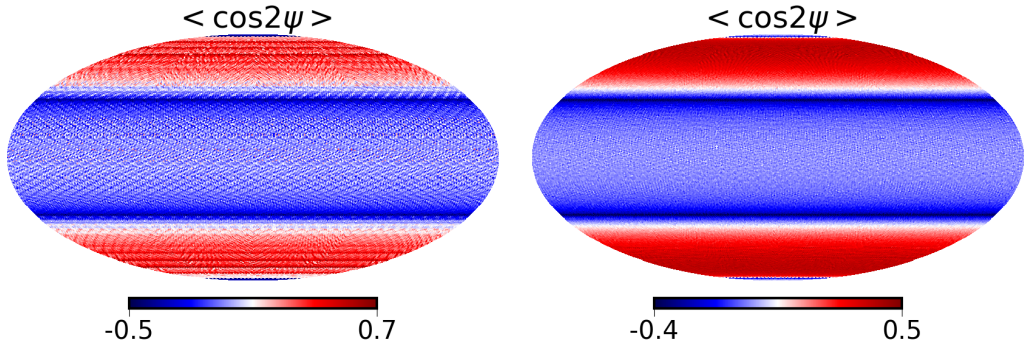

Figure 12. *Effect of a poorly chosen scanning frequency ratios.* The map on the left has $\theta = \omega_{\rm spin}/\omega_{\rm prec} = 9.3$, whose continued fraction representation is $[9, 3, 3]$, whereas the lower map has the more irrational ratio $\theta = 9.61803$, whose continued fraction representation is $[9, 1, 1, 1, ...]$. A series of Moiré patterns on intermediate angular scales is clearly visible in the map on the left, which lead to spikes in the crossing moment map power spectra, and also in the final bandpass mismatch power spectra. The artefacts can be avoided by choosing ratios of frequencies judiciously in order to avoid good rational approximations.

undesirable Moiré patterns disappear, as shown in the bottom right panel of the figure. The same effect could be achieved by altering the ratio θ by just 5%, so that the spin cycle has the same phase as with the Golden ratio sped up. We note that the effect of these Moiré patterns on the bandpass mismatch power spectra is to introduce peaks at multipole numbers at which the bandpass mismatch error is increased by up to about an order of magnitude beyond the baseline, where it would be if θ had been well chosen to avoid near resonances. We also note that when a continuously rotating HWP is introduced, there are two independent ratios to worry about, although the artefacts are less acute than in the case of no rotating HWP.

The theory of choosing ratios to avoid near resonances relates to problems well studied by pure mathematicians in the area of number theory, or more specifically the theory of Diophantine approximations, and we discussed these issues in more detail elsewhere [36]. The tool for characterizing the near resonance properties of real numbers is the continued fraction representation, where we expand

$$\theta = [a_0, a_1, a_2, \ldots] = a_o + \cfrac{1}{a_1 + \cfrac{1}{a_2 + \ldots}} \tag{3.19}$$

where a_0 is an integer and $a_1, a_2, \ldots$ are positive integers. For a rational number, the continued fraction representation terminates; for an irrational number it is of infinite length. The partial sums, known as 'convergents,' generate a sequence of 'best rational approximations' p/q to θ,[4] with q ascending. When a coefficient a_n is large compared to one, the preceding convergent is a particularly good approximation to θ considering the magnitude of q. The Golden ratio Φ has the continued fraction representation $[1, 1, 1, \ldots]$, and thus has among the worst approximation properties of any number.

For the parameters used in the simulations reported below, we adjusted the precession period so that there are an integer number 5467 cycles in a sidereal year, giving a precession

[4] An irreducible fraction p/q is a 'best approximation' to θ if $|\theta - p'/q'| > |\theta - p/q|$ whenever $q' < q$.

JCAP12(2017)015

period of 96.2080 minutes, and we replaced the ratio of $\theta = 9.3$, which in terms of continued fractions is represented by $[9, 3, 3]$, with the ratio 9.618033988749895,[5] whose continued fraction representation is $[9, 1, 1, 1, ...]$, giving a spin period of 10.002876 minutes. One may ask: approximately to what accuracy would one wish to maintain this ratio? Certainly more accuracy than the inverse of the number of precession cycles in a year would be superfluous. In fact, less accuracy would be adequate, the exact number depending on the precise scanning parameters, but we postpone further assessment of the required precision to future work. Moreover, it is more the absolute pointing that matters and not so much a question of maintaining precise ratios at any particular moment.

An important practical question is what accuracy is required in the ratios of the frequencies in order to avoid the Moiré patterns due to near resonances. It is not possible to provide a general answer to this question, but we performed some numerical experiments for the scanning frequencies considered in this paper and found that tuning the ratio of the frequencies to about 0.2% sufficed. It should be stressed that it is the relative phase rather than the instantaneous ratio of frequencies that matters for avoiding Moiré artifacts. In the above discussion we considered only a single ratio, but for more complicated situations with several frequencies, there is more than one ratio to keep away from near resonant values. A rotating half-wave plate, for example, introduces another frequency, and in principle the annual drift also allows other dimensionless ratios of frequencies to be formed. These complications will be investigated elsewhere.

3.4 Hitcount and crossing moment map properties

We now examine the properties of the hitcount map $H_a(p)$ for a particular detector labeled by the index a (where the index p denotes a particular discrete pixel) as well as maps of $\langle \cos 2\psi(p) \rangle_a$, $\langle \sin 2\psi(p) \rangle_a$, $\langle \cos 4\psi(p) \rangle_a$, and $\langle \sin 4\psi(p) \rangle_a$, which, as already stressed enter into the expressions for the bandpass mismatch.

Figures 13 and 14 show the maps $H_a(p)$, $\langle \cos 2\psi(p) \rangle_a$, $\langle \sin 2\psi(p) \rangle_a$, $\langle \cos 4\psi(p) \rangle_a$, and $\langle \sin 4\psi(p) \rangle_a$ for a typical detector with the fiducial scan parameters given above for a full-year scan (so that there are no boundaries).

These figures demonstrate that in all the maps (except for the $\langle \sin 2\psi(p) \rangle_a$, and $\langle \sin 4\psi(p) \rangle_a$ maps), when small-scale structure is ignored, there is an azimuthally symmetric non-uniformity. From the azimuthally averaged quantities shown in figure 2, we can see that superimposed on this azimuthally symmetric component is a component almost completely devoid of large-angle power resulting from the discreteness of the scans. Figure 15 shows the power spectra of the crossing moment maps. We note that given the finite size of the focal plane, the spin opening angle β varies from detector to detector. This variation in β induces an azimuthally symmetric component having large-scale power in the difference map of moments for different detectors at different locations in the focal plane. Also present will be a small-scale component, which would disappear in the limit $\omega_{\rm spin}$, $\omega_{\rm prec} \to +\infty$ along with the sampling rate while keeping the ratio $\omega_{\rm spin}/\omega_{\rm prec}$ fixed. This small scale power is somewhat akin to shot noise.

[5] In any specific application, the objective of avoiding near resonances obviously requires an accuracy involving only a finite number of terms of the continued fraction expansion. Moreover, it is less the instantaneous ratio of frequencies that matters but rather the relative phase. We have found using numerical simulations that avoiding Moiré patterns is achieved when the ratios are maintained with a relative accuracy of 1 part in 10^3, although the exact accuracy needed will depend on the particular application.

JCAP12(2017)015

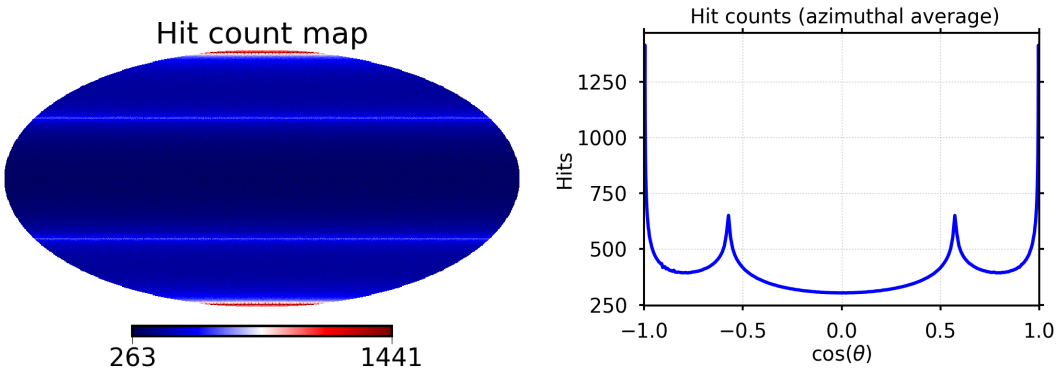

Figure 13. *Hitcount map and azimuthal average for fiducial scanning pattern.* The hitcount map is roughly uniform except for some localized spikes of high density around the ecliptic poles and at the caustics at ecliptic latitude $\pm(\alpha - \beta) = \pm(65° - 30°) = \pm 35°$. In the bottom plot the horizontal axis is $\cos\theta$ where θ is the angle from the north ecliptic pole.

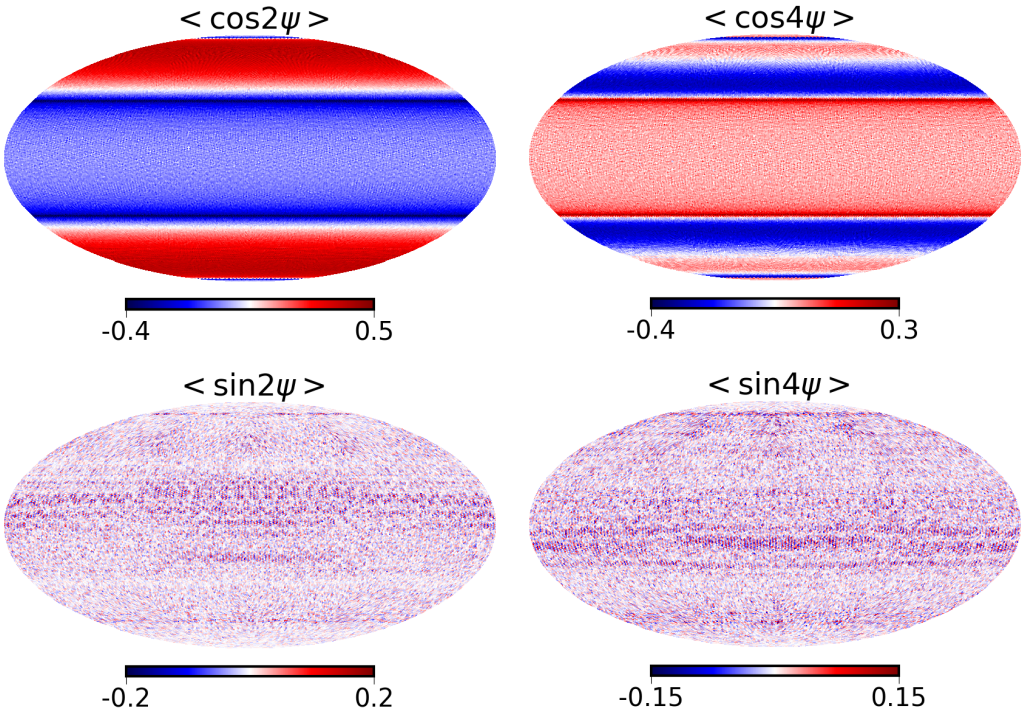

Figure 14. *Crossing moment maps for the fiducial scanning pattern.* The four relevant crossing moment maps $\langle \cos 2\psi \rangle$, $\langle \cos 4\psi \rangle$, $\langle \sin 2\psi \rangle$, $\langle \sin 4\psi \rangle$ (left to right, top to bottom) are shown for the fiducial scanning pattern (defined in the text) for a single detector whose polarization axis is oriented along the line running from the center of the beam to the spin axis. The corresponding maps for other polarizer orientations can be obtained trivially using the property that the first two maps transform as a spin-2 vector and the second two as a spin-4 vector under rotations of the polarization orientation. We observe that the cosine maps have structures coherent on large scales and azimuthally symmetric in ecliptic coordinates, whereas the sine maps include only small-scale noise (which is also present in the cosine maps) but have no structure coherent on large angular scales.

JCAP12(2017)015

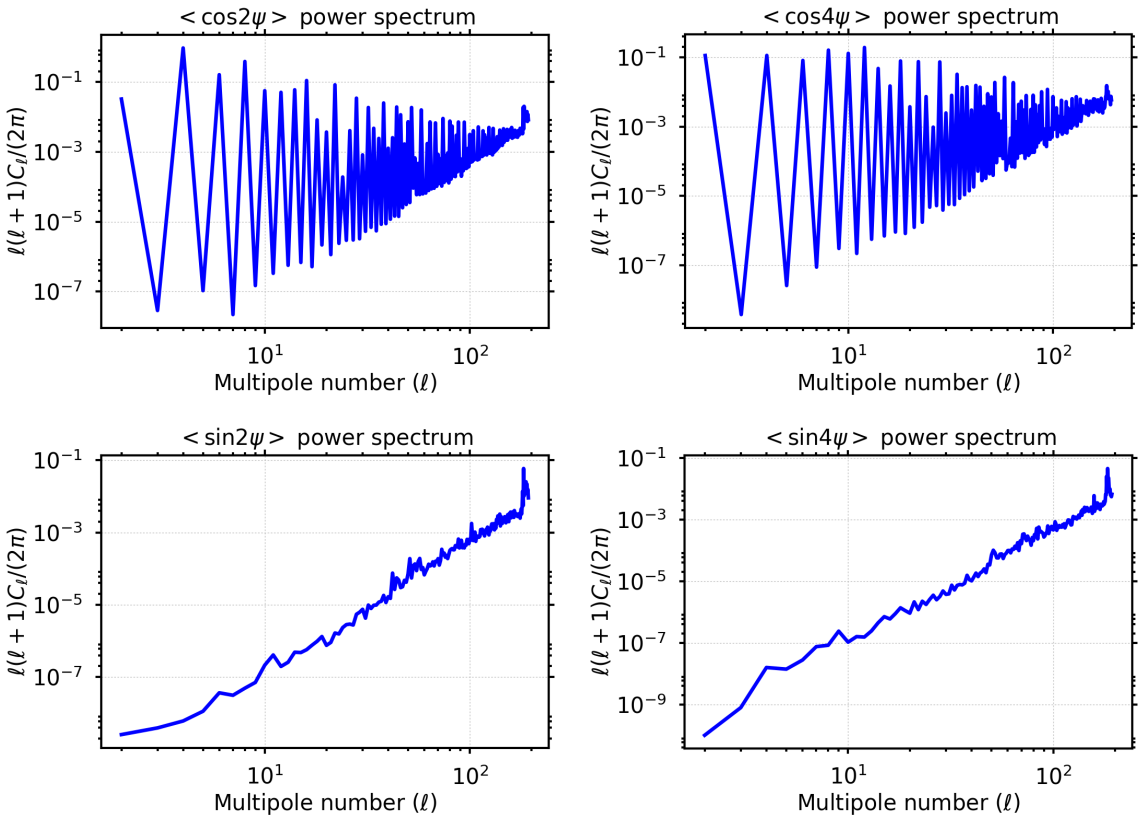

Figure 15. *Crossing moment map power spectra.* We show the power spectra of the maps of figure 14. The spectra of the two cosine maps, because of the azimuthally symmetric large power coherent on large scales shown in figure 2, have power spectra scaling similar to ℓ^{-2} for the even moments, whereas the two sine maps (bottom) row exhibit spectra resembling pure white noise.

We now consider the effect of a continuously rotating HWP on the second- and fourth-order crossing moment maps, as shown in figures 16 and 17. We see that the azimuthally symmetric structures coherent on large angular scales disappear as a consequence of the continuously rotating HWP. The main consequence is to beat down by many orders of magnitude the $(\ell^{-2.5})$-like power present on large angular scales in cosine maps, but there is also substantial reduction in the power at all multipole numbers compared to the no-HWP case.

We point out that much the same beneficial effect could also be obtained using a discretely stepped HWP (with a stepping pattern tailored to produce the necessary cancellations). Alternatively, less complete cancellations could also be obtained by stepping the orientation of the focal plane about its optical axis. These rotations are called "deck rotations" in the BICEP2 papers (see e.g., [8]), a terminology that we shall also adopt. Allowing for such deck rotations, however, would also require additional complexity in the satellite design beyond the simplest no HWP design. Moreover, for the deck rotations alone, the cancellations would be imperfect because the values of β for the individual detector scanning patterns change as the focal plane is rotated (except possibly for one detector situated at the optical axis, assumed to coincide with the deck rotation axis).

JCAP12(2017)015

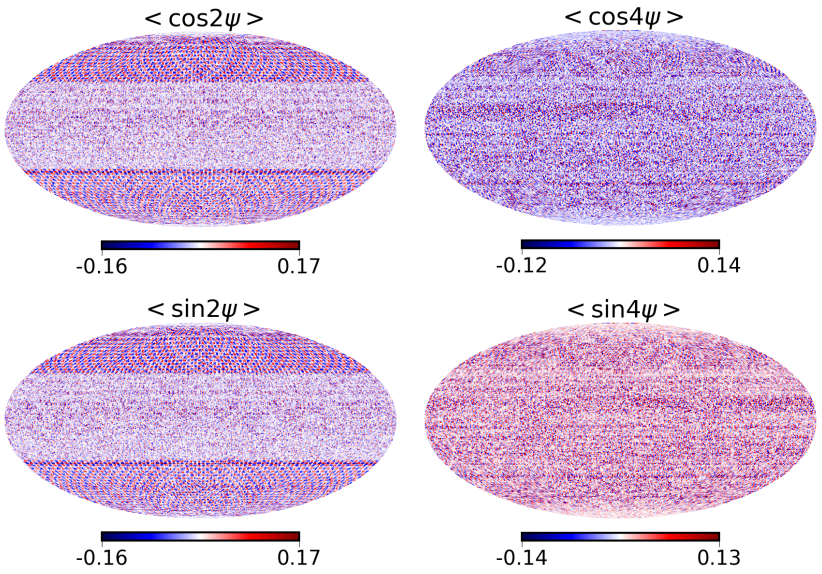

Figure 16. *Crossing moment maps (with rotating HWP).* We show the same maps as in figure 14 except that there is a rotating HWP, as explained in the main text. We observe that the coherent power in the cosine maps has been scrambled as a result of the presence of the HWP and the overall power in all the maps has greatly been reduced.

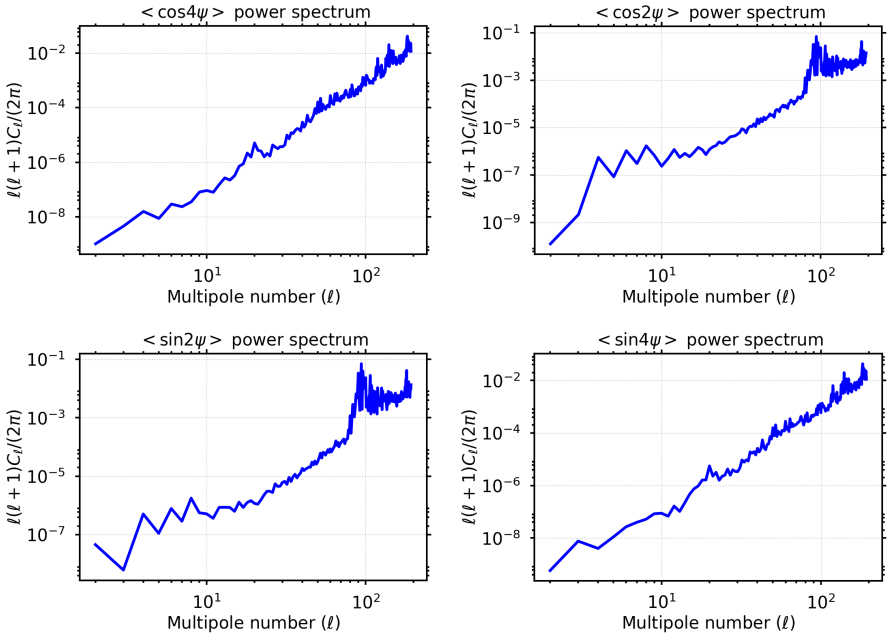

Figure 17. *Crossing moment map power spectra (with rotating HWP).* We show the power spectra for the maps in figure 16. The power spectra of the $\langle \cos 2\psi \rangle$ and $\langle \cos 4\psi \rangle$ have a white noise-like spectrum rather than an (ℓ^{-2})-like spectrum because the HWP has scrambled azimuthally symmetric component coherent on large-scale present in the case with no HWP.

JCAP12(2017)015

4 Conclusions

This paper presented estimates of the contribution of bandpass mismatch error to the final determination of the tensor-to-scalar ratio r, both for the window situated at the 're-ionization bump,' and for the window at the 'recombination bump', for a set of observation strategies considered for future CMB polarization experiments. In the case without a HWP, requiring in the optimal case the combination of multi-detector data, we show that the bandpass mismatch error in polarization has a red power spectrum resembling $\ell^{-2.5}$. The contribution to r is of the order of 10^{-3} at the reionization bump, assuming random variations of the detector filters for typical arrays at 140 GHz, such that the variation of the dust component amplitude is of the order of 0.6 %. However, with a continuously rotating HWP the spectrum is similar to that of white noise, with the power on the largest scales many orders of magnitude smaller than without a HWP. This is due to the fact that an ideal HWP allows nearly uniform angle coverage in each pixel, and hence the multi-detector solution is almost equivalent to the combination of single detector maps of Q and U. The HWP also cancels correlations in the non-uniformity in the angular coverage between different pixels, hence the efficient reduction in power of the bandpass mismatch on large angular scales. We further note that a stepped HWP would reduce bandpass mismatch in a similar way provided that its discrete rotations are properly synchronized with the scan pattern. We show that even with a simplistic multi-detector map-making approach, the HWP suppresses the bandpass leakage power by several orders of magnitude on large scales. We note however that this conclusion ignores the problem of HWP imperfections, in particular chromaticity effects, which would generate bandpass mismatch systematics of its own.

To obtain accurate estimates of the bandpass mismatch error, more precise information would be needed concerning (1) the scan pattern assumed, (2) the variations in the bandpass functions from detector to detector, and (3) the foreground removal process. For (1) we used one of the LiteBIRD candidate scan patterns. Likewise, for (2) we based our model for variations in the bandpass function from preliminary results that have actually been achieved in the laboratory between different detectors without a HWP, but there may be effects not properly taken into account that could lead to larger errors, or conversely further technological development could lead to reduced mismatch between bandpass functions. With respect to (3), we simply calculated the bandpass error in a 140 GHz map, assuming that but for this error, the dominant dust and synchrotron components could be removed by subtraction using a perfect foreground component templates. This is certainly a simplification which provides a simple estimate that can be described in a simple term. If the foregrounds turn out to be very complicated, the CMB clean map might be the result of a linear combination of maps whose coefficients (or varying sign) are much larger than one (assuming the maps are normalized to the CMB). A foreground cleaning of this sort (if necessary) may lead to larger bandpass errors than our estimate. Finally, we mention one caveat of our analysis: we did not include $1/f$ noise in our modeling, a feature that allowed us to carry out pixel-by-pixel map making and avoid including extra model parameters.

In this paper we have estimated bandpass mismatch error assuming that no measures have been taken to correct for or otherwise mitigate this systematic error. In the companion paper ref. [20] we explore paths to correct for and mitigate bandpass mismatch error with a dedicated data processing step.

JCAP12(2017)015

Acknowledgments

Duc Thuong Hoang thanks the Vietnam International Education Cooperation Department (VIED) of the Ministry of Education and Training for support through a Ph.D. fellowship grant. We thank Aritoki Suzuki for useful discussions and sharing with us data on filter bandpass measurements.

References

[1] Planck collaboration, P.A.R. Ade et al., *Planck Early Results. I. The Planck mission*, *Astron. Astrophys.* **536** (2011) A1 [arXiv:1101.2022] [INSPIRE].

[2] WMAP collaboration, C.L. Bennett et al., *Nine-year Wilkinson Microwave Anisotropy Probe (WMAP) Observations: Final Maps and Results*, *Astrophys. J. Suppl.* **208** (2013) 20 [arXiv:1212.5225] [INSPIRE].

[3] Planck collaboration, N. Aghanim et al., *Planck 2015 results. XI. CMB power spectra, likelihoods and robustness of parameters*, *Astron. Astrophys.* **594** (2016) A11 [arXiv:1507.02704] [INSPIRE].

[4] ACTPol collaboration, T. Louis et al., *The Atacama Cosmology Telescope: Two-Season ACTPol Spectra and Parameters*, *JCAP* **06** (2017) 031 [arXiv:1610.02360] [INSPIRE].

[5] SPT collaboration, A.T. Crites et al., *Measurements of E-Mode Polarization and Temperature-E-Mode Correlation in the Cosmic Microwave Background from 100 Square Degrees of SPTpol Data*, *Astrophys. J.* **805** (2015) 36 [arXiv:1411.1042] [INSPIRE].

[6] POLARBEAR collaboration, P.A.R. Ade et al., *A Measurement of the Cosmic Microwave Background B-Mode Polarization Power Spectrum at Sub-Degree Scales with POLARBEAR*, *Astrophys. J.* **794** (2014) 171 [arXiv:1403.2369] [INSPIRE].

[7] SPT collaboration, R. Keisler et al., *Measurements of Sub-degree B-mode Polarization in the Cosmic Microwave Background from 100 Square Degrees of SPTpol Data*, *Astrophys. J.* **807** (2015) 151 [arXiv:1503.02315] [INSPIRE].

[8] BICEP2, Keck Array collaboration, P.A.R. Ade et al., *BICEP2 /Keck Array V: Measurements of B-mode Polarization at Degree Angular Scales and 150 GHz by the Keck Array*, *Astrophys. J.* **811** (2015) 126 [arXiv:1502.00643] [INSPIRE].

[9] BICEP2, Planck collaboration, P.A.R. Ade et al., *Joint Analysis of BICEP2/Keck Array and Planck Data*, *Phys. Rev. Lett.* **114** (2015) 101301 [arXiv:1502.00612] [INSPIRE].

[10] BICEP2, Keck Array collaboration, P.A.R. Ade et al., *Improved Constraints on Cosmology and Foregrounds from BICEP2 and Keck Array Cosmic Microwave Background Data with Inclusion of 95GHz Band*, *Phys. Rev. Lett.* **116** (2016) 031302 [arXiv:1510.09217] [INSPIRE].

[11] CORE collaboration, J. Delabrouille et al., *Exploring Cosmic Origins with CORE: Survey requirements and mission design*, arXiv:1706.04516 [INSPIRE].

[12] M. Hazumi et al., *LiteBIRD: a small satellite for the study of B-mode polarization and inflation from cosmic background radiation detection*, *Proc. SPIE Int. Soc. Opt. Eng.* **8442** (2012) 844219 [INSPIRE].

[13] T. Matsumura et al., *LiteBIRD: Mission Overview and Focal Plane Layout*, *J. Low. Temp. Phys.* **184** (2016) 824 [INSPIRE].

[14] A. Kogut, J. Chluba, D. J. Fixsen, S. Meyer and D. Spergel, *The primordial inflation explorer (PIXIE)*, *Proc. SPIE* **9904** (2016) 99040W.

[15] Planck collaboration, N. Aghanim et al., *Planck intermediate results. XLVI. Reduction of large-scale systematic effects in HFI polarization maps and estimation of the reionization optical depth*, *Astron. Astrophys.* **596** (2016) A107 [arXiv:1605.02985] [INSPIRE].

JCAP12(2017)015

[16] WMAP Science Team collaboration, E. Komatsu et al., *Results from the Wilkinson Microwave Anisotropy Probe*, *PTEP* **2014** (2014) 06B102 [arXiv:1404.5415] [INSPIRE].

[17] the ABS collaboration, T. Essinger-Hileman et al., *Systematic effects from an ambient-temperature, continuously rotating half-wave plate*, *Rev. Sci. Instrum.* **87** (2016) 094503 [arXiv:1601.05901] [INSPIRE].

[18] T. Matsumura, *A cosmic microwave background radiation polarimeter using superconducting magnetic bearings*, Ph.D. Thesis, University of Minnesota, Minnesota U.S.A. (2006).

[19] CORE collaboration, P. Natoli et al., *Exploring cosmic origins with CORE: mitigation of systematic effects*, arXiv:1707.04224 [INSPIRE].

[20] R. Banerji et al., *Bandpass mismatch error for satellite CMB experiments II: Correcting the spurious signal*, in preparation.

[21] Planck collaboration, P.A.R. Ade et al., *Planck 2013 results. XIII. Galactic CO emission*, *Astron. Astrophys.* **571** (2014) A13 [arXiv:1303.5073] [INSPIRE].

[22] Planck collaboration, A. Abergel et al., *Planck 2013 results. XI. All-sky model of thermal dust emission*, *Astron. Astrophys.* **571** (2014) A11 [arXiv:1312.1300] [INSPIRE].

[23] Planck collaboration, P.A.R. Ade et al., *Planck intermediate results. XXII. Frequency dependence of thermalemissionfromGalacticdustinintensity and polarization*, *Astron. Astrophys.* **576** (2015) A107 [arXiv:1405.0874] [INSPIRE].

[24] Planck collaboration, R. Adam et al., *Planck 2015 results. X. Diffuse component separation: Foreground maps*, *Astron. Astrophys.* **594** (2016) A10 [arXiv:1502.01588] [INSPIRE].

[25] Planck collaboration, P.A.R. Ade et al., *Planck 2013 results. IX. HFI spectral response*, *Astron. Astrophys.* **571** (2014) A9 [arXiv:1303.5070] [INSPIRE].

[26] Planck collaboration, R. Adam et al., *Planck 2015 results. VIII. High Frequency Instrument data processing: Calibration and maps*, *Astron. Astrophys.* **594** (2016) A8 [arXiv:1502.01587] [INSPIRE].

[27] WMAP collaboration, N. Jarosik et al., *Three-year Wilkinson Microwave Anisotropy Pr (WMAP) observations: beam profiles, data processing, radiometer characterization and systematic error limits*, *Astrophys. J. Suppl.* **170** (2007) 263 [astro-ph/0603452] [INSPIRE].

[28] B. Westbrook et al., *Development of the Next Generation of Multi-chroic Antenna-Coupled Transition Edge Sensor Detectors for CMB Polarimetry*, *J. Low. Temp. Phys.* **184** (2016) 74.

[29] Planck collaboration, N. Aghanim et al., *Planck intermediate results. XLVI. Reduction of large-scale systematic effects in HFI polarization maps and estimation of the reionization optical depth*, *Astron. Astrophys.* **596** (2016) A107 [arXiv:1605.02985] [INSPIRE].

[30] EPIC collaboration, J. Bock et al., *Study of the Experimental Probe of Inflationary Cosmology (EPIC)-Intemediate Mission for NASA's Einstein Inflation Probe*, arXiv:0906.1188 [INSPIRE].

[31] K.M. Górski et al., *HEALPix: A Framework for high resolution discretization and fast analysis of data distributed on the sphere*, *Astrophys. J.* **622** (2005) 759 [astro-ph/0409513] [INSPIRE].

[32] F. Couchot, J. Delabrouille, J. Kaplan and B. Revenu, *Optimized polarimeter configurations for measuring the Stokes parameters of the cosmic microwave background radiation*, *Astron. Astrophys. Suppl. Ser.* **135** (1999) 579 [astro-ph/9807080] [INSPIRE].

[33] H. Ishino et al., *LiteBIRD: lite satellite for the study of B-mode polarization and inflation from cosmic microwave background radiation detection*, *Proc. SPIE* **9904** (2016) 99040X.

[34] M. Bucher et al., *Predicting bandpass mismatch power spectra*, in preparation.

[35] C.G.R. Wallis, M.L. Brown, R.A. Battye and J. Delabrouille, *Optimal scan strategies for future CMB satellite experiments*, *Mon. Not. Roy. Astron. Soc.* **466** (2017) 425 [arXiv:1604.02290] [INSPIRE].

[36] M. Bucher, *Maximum irrationality for optimal scanning of the CMB Sky*, in preparation.

JCAP12(2017)015

Evaluating the level of the bandpass mismatch systematic effect for the future CMB satellites

DUC THUONG HOANG [1,2]

[1] *Laboratoire Astroparticule et Cosmologie (APC), Université Paris Diderot, CNRS/IN2P3, CEA/Irfu, Observatoire de Paris, Sorbonne Paris Cité, 10, rue Alice Domon et Léonie Duquet, 75205 Paris Cedex 13, France.*

[2] *Department of Space and Aeronautics, University of Science and Technology of Hanoi (USTH), Vietnam Academy of Science and Technology (VAST), 18 Hoang Quoc Viet, Cau Giay, Hanoi, VietNam*

Bandpass mismatch error is one of the important systematic effects that can affect current and next generation measurement of the polarization of the Cosmic Microwave Background radiation (CMB). The slightly different frequency bandpasses among detectors introduce leakage from intensity into CMB polarization. The amplitude of the leakage depends on the scanning strategy and impacts the estimation of the tensor-to-scalar ratio r. With the help of full focal plane simulations we found that the spurious angular power spectrum could potentially bias r at the reionization bump (l≤10) at the level of 10^{-4}.

1 Introduction

The future Cosmic Microwave Background (CMB) satellite concepts LiteBird [1], CORE [2], PIXIE [3] have been proposed to probe B modes polarization to measure the tensor-to-scalar r ratio with a sensitivity $\sigma_r \leq 10^{-3}$, which is almost two orders of magnitude beyond the Planck sensitivity. Several important systematic effects could contribute to final observation as 1/f noise, asymmetric beams, bandpass mismatches, interaction of cosmic rays with the focal plane etc. The bandpass mismatch between the two orthogonal polarized detectors introduces the leakage into the polarization maps. The evaluation of the level of the bandpass mismatch systematic effect for future CMB satellites and the estimation of its possible impact on the final determination of the tensor-to-scalar ratio r are presented in this paper [4].

2 Simulation

The total sky intensity $I_{sky}(\nu_0)$ can be modeled as the sum of different components.

$$I_{\rm sky}(\nu_0) = I_{\rm CMB}(\nu_0) + \gamma_d\, I_{\rm dust}(\nu_0) + \gamma_s\, I_{\rm sync}(\nu_0) + \ldots, \tag{1}$$

where, for dust

$$\gamma_d = \left(\frac{\int d\nu\ g_i(\nu) \left(\frac{\nu}{\nu_0}\right)^{\beta} \frac{B(\nu;T_d)}{B(\nu_0;T_d)}}{\int d\nu g_i(\nu) \left(\frac{\partial B(\nu;T)}{\partial T}\right)\Big|_{T_0}} \right) \left(\frac{\partial B(\nu_0;T)}{\partial T}\right)\Big|_{T_0}. \tag{2}$$

The factor γ_s is similarly defined integrating over the synchrotron spectrum, etc. The $g_i(\nu)$ is the tophat bandpass filter function of the detector i. $T_0 = 2.725$ K is the CMB temperature. $B(\nu;T)$ is the Planck function. In this study, we only consider the CMB and the galactic thermal dust emission which is assumed as a grey body of temperature $T_d \approx 19.7K$ with the spectral index $\beta \approx 1.62$. We also assumed a bandwidth 0.25 on average with random variations of the order of those found in Planck, with $\nu_0 = 140.7$ GHz. The resulting RMS of dust factor γ_d is

~ 0.6 %. We simulate time streams by scanning input template maps without polarization, nor noise as well as same pixelisation between input and output maps using several detectors. We use detectors with nominal locations in the focal plane and polarizer orientations for LiteBIRD.

3 Result

We projected data using the simplest map-making *coaddition* method. Power spectra of residual EE and BB coming from the leakage maps are computed for 80 % sky fraction excluding the galactic plane.

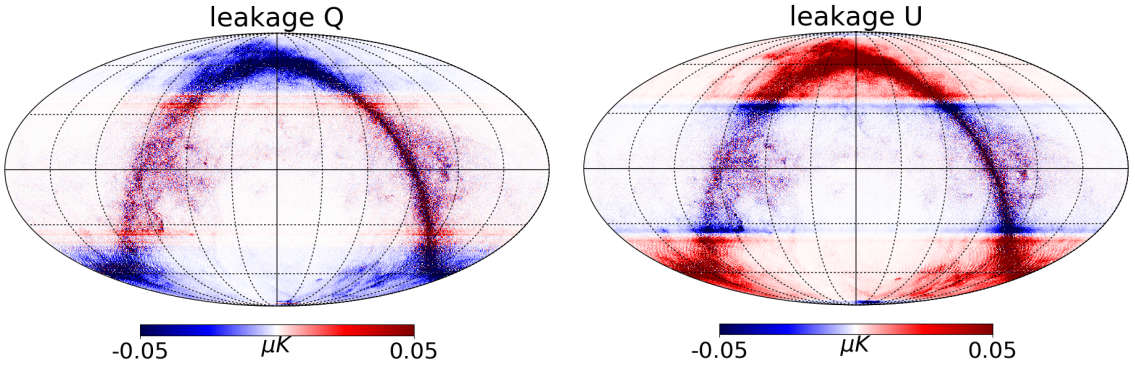

Figure 1 – Q and U leakage maps, in the ecliptic coordinates, width fiducial scanning parameters $\alpha = 65^\circ$ $\beta = 30^\circ$ $\tau_{spin} = 10\,mins$, $\tau_{prec} = 96.1803\,min$, number of detector are $N_{det} = 222$, one year observation.

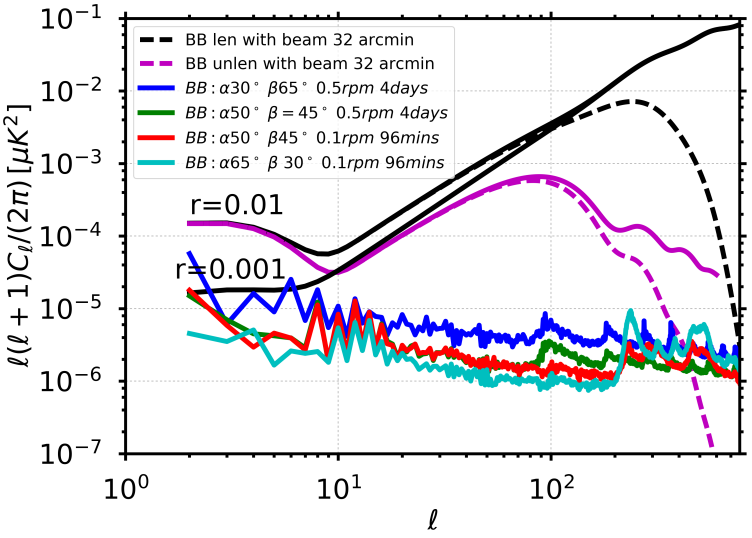

Figure 2 – BB leakage power spectra for different scanning parameters, the label indicates the configuration of scanning parameters, precession angle α, spin angle β, spin Ω_{spin}, precession time Ω_{prec}. The model curves of primordial B mode show the effect of convolving with a 32 arcmin beam. Spectra are computed for 222 detectors. For the scanning strategies with a long precession period, we computed spectra for 100 detectors rescaling to 222 equivalent detectors using the $1/N_{\rm det}$ dependance.

The residual power spectra of bandpass mismatch error give a bias of about 5×10^{-4} at the reionization bump and the amplitude scales as $\frac{1}{N_{det}}$. We have shown the tight correlation between leakage maps and the average angle $< \cos 2\psi >, < \sin 2\psi >$. The effect is negligible in case of an ideal HWP [4].

References

1. T. Matsumura *et al.*, J. Low. Temp. Phys. 184 (2016), DOI: 10.1007/s10909-016-1542-8.
2. CORE collaboration, J. Delabrouille *et al.*, arXiv: 1706.04516.
3. JA. Kogut *et al.*, Proc. SPIE 9904 (2016) 99040W, DOI: 10.1117/12.2231090.
4. Duc Thuong Hoang *et al.*, JCAP12(2017)015, DOI: 10.1088/1475-7516/2017/12/015.